Lecture Notes in Electrical Engineering 411

Mohammed Chadli
Sofiane Bououden
Ivan Zelinka
Editors

Recent Advances in Electrical Engineering and Control Applications

Springer

Lecture Notes in Electrical Engineering

Volume 411

About this Series

"Lecture Notes in Electrical Engineering (LNEE)" is a book series which reports the latest research and developments in Electrical Engineering, namely:

- Communication, Networks, and Information Theory
- Computer Engineering
- Signal, Image, Speech and Information Processing
- Circuits and Systems
- Bioengineering

LNEE publishes authored monographs and contributed volumes which present cutting edge research information as well as new perspectives on classical fields, while maintaining Springer's high standards of academic excellence. Also considered for publication are lecture materials, proceedings, and other related materials of exceptionally high quality and interest. The subject matter should be original and timely, reporting the latest research and developments in all areas of electrical engineering.

The audience for the books in LNEE consists of advanced level students, researchers, and industry professionals working at the forefront of their fields. Much like Springer's other Lecture Notes series, LNEE will be distributed through Springer's print and electronic publishing channels.

More information about this series at http://www.springer.com/series/7818

Mohammed Chadli · Sofiane Bououden
Ivan Zelinka
Editors

Recent Advances in Electrical Engineering and Control Applications

Springer

Editors
Mohammed Chadli
MIS (EA 4290)
Université de Picardie Jules Verne
Amiens
France

Ivan Zelinka
VŠB-Technical University of Ostrava
Ostrava-Poruba
Czech Republic

Sofiane Bououden
Laboratoire d'Automatique et de Robotiqu
Université Abbes Laghrour, Khenchela
Khenchela
Algeria

ISSN 1876-1100 ISSN 1876-1119 (electronic)
Lecture Notes in Electrical Engineering
ISBN 978-3-319-48928-5 ISBN 978-3-319-48929-2 (eBook)
DOI 10.1007/978-3-319-48929-2

Library of Congress Control Number: 2016957849

Printed on acid-free paper

This Springer imprint is published by Springer Nature
The registered company is Springer International Publishing AG
The registered company address is: Gewerbestrasse 11, 6330 Cham, Switzerland

Foreword

This proceedings book Recent Advances in Electrical Engineering and Control Applications contains accepted papers presenting the most interesting state of the art in this field of research.

Presented topics are focused on classical as well as modern methods for modeling, control, identification and simulation of complex systems with applications in science and engineering. Topics presented in this book include (but not limited to) control and systems engineering, renewable energy, faults diagnosis-faults tolerant control, large scale systems, fractional order systems, unconventional algorithms in control engineering, signal and communications, and much more.

The control and design of complex systems dynamics, and analysis and modeling of its behavior and structure is an important problem today in engineering, economics and science in general. Examples of such systems can be seen in the world around us and are a part of our everyday lives. Application of modern methods for control, electronics, signal processing and more can be found in our mobile phones, car engines, and home devices as washing machines as well as in advanced devices as space probes and communication with them.

The main aim of the conference is to create periodical possibility for students, academics, and researchers to exchange their ideas and share their novel methods with others. This conference will establish a forum for the presentation and discussion of recent trends in the area of applications of various modern as well as classical methods for researchers, students, and academics.

The accepted selection of papers was very rigorously reviewed in order to maintain the high quality of the conference that is supported by organizing universities and related research grants. Regular as well as student's papers have been submitted to the conference, and in accordance with review process, have been accepted after a positive review.

We would like to thank the members of the Program Committees and reviewers for their hard work. We believe that this conference represents a high-standard conference in the domain of above-mentioned topics.

We would like to thank all the contributing authors, as well as the members of the Program Committees and the Local Organizing Committee for their diligent and highly valuable work. Their work has definitely contributed to the success of the conference.

November 2016

Mohammed Chadli
Sofiane Bououden
Ivan Zelinka

Contents

Control and Systems Engineering (CSE)

Power Quality Improvement Based on Five-Level NPC Series APF Using Fuzzy Control Scheme

Salim Chennai(✉)

Birine Nuclear Research Center, BP. 180 Ain Oussera, 17200 Djelfa, Algeria
chenaisalimov@yahoo.fr

Abstract. This paper presents novel five-level NPC (Neutral Point Clamped) series APF (Active Power Filter) based on instantaneous reactive power control strategies for harmonic voltage compensation. The standard configuration based on voltage source inverter (VSI) with hysteresis controller presents several drawbacks such us uneven switching frequency and limited to lower power applications. Multilevel inverters are currently being investigated and used in various industrial applications. Five-level inverter is one of the most converters employed, their advantages include the capability to reduce the harmonic content and decrease the voltage or current ratings of the semiconductors. Fuzzy controllers are successfully employed in various industrial applications; they represent a good alternative to classic control systems. To benefit of all these advantages a novel control scheme for five-level series APF based on fuzzy techniques is proposed in this work. The proposed fuzzy voltage controller is designed to improve compensation capability of series active power filter by adjusting the voltage error using a fuzzy rule. The simulation is performed using MATLAB-Simulink and SimPowerSystem Toolbox. The obtained results demonstrate the effectiveness of the proposed Series APF control system.

Keywords: Fuzzy logic voltage controller · Series active power filter · Five-level (NPC) inverter · Harmonics voltage disturbances compensation · Instantaneous reactive power theory

1 Introduction

With the continuous proliferation of non linear loads, harmonic pollution is being considered as one of the major problems that degrade the power quality. Active power filters have been proposed as an interesting and high performance solution to improve the power quality [1]. Shunt active power filter is generally used to compensate current harmonics. Series active power filter is one of the control devices that feed modern industry with high quality power supply [2], it is used to compensate all types of voltage disturbances, such as voltage unbalances, sags, harmonics and voltage swells, these disturbances have harmful effects on the electric equipments [3]. The series active power filter is inserted in series between the load and the source voltage. Three single phase transformers are used to perform the series connection. The controller is the main

M. Chadli et al. (eds.), *Recent Advances in Electrical Engineering and Control Applications*, Lecture Notes in Electrical Engineering 411, DOI 10.1007/978-3-319-48929-2_1

part of any active power filter operation and has been a subject of many researches in recent years [4, 5], to improve the Series APF performances there's a great tendency to use intelligent control techniques, particularly fuzzy logic controllers. Fuzzy logic control theory is a mathematical discipline based on vagueness and uncertainty. The fuzzy control does not need an accurate mathematical model of a plant. It allows one to use non-precise or ill-defined concepts. Fuzzy logic control is also nonlinear and adaptive in nature that gives it robust performance under parameter variation and load disturbances [6–8].

The investigation in this paper concentrates on the fuzzy control approaches for five-level series APF to compensate particularly harmonics voltage disturbance using strategies control based on the instantaneous reactive power theory [9]. The performance of the proposed series active power filter is evaluated using Matlab-Simulink and SimPowerSystem Toolbox. The obtained results show the effectiveness of the proposed series APF filter systems.

The paper is structured as follows. The description of series APF based on five-level (NPC) inverter is presented in Sect. 2. The review of the instantaneous power theory is addressed in Sect. 3. The concept of the compensating voltage control using the fuzzy logic controller is described in Sect. 4. The simulation results and discussions of the harmonic elimination with the fuzzy logic controller are presented in Sect. 5. Finally, Sect. 6 is the conclusion of the paper.

2 Series APF Configuration System

The circuit configuration of the series active filter is shown in Fig. 1, the Series APF is inserted between the disturbed voltage source and a protected load. It is composed of three phase voltage source converter, LfCf filter to suppress switching ripples and series transformers which inject the compensating voltage to the line [10].

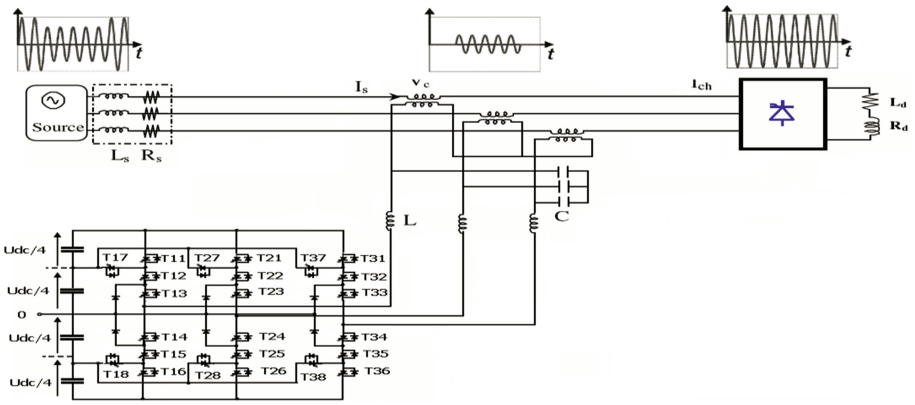

Fig. 1. Five-level (NPC) series active power filter

The five-level neutral point clamped inverter power circuit is given by Fig. 2, the DC bus capacitor is split into four parts to provide a three neutral-point. Each arm of the inverter is made up of eight IGBTs (Insulated Gate Bipolar Transistor) devices, and six clamping diodes connected to the neutral-point. The diodes are used to create the connection with the point of reference to obtain midpoint voltages. This structure allows the switches to endure larger dc voltage input on the premise that the switches will not raise the level of their withstand voltage. For this structure, five output voltage

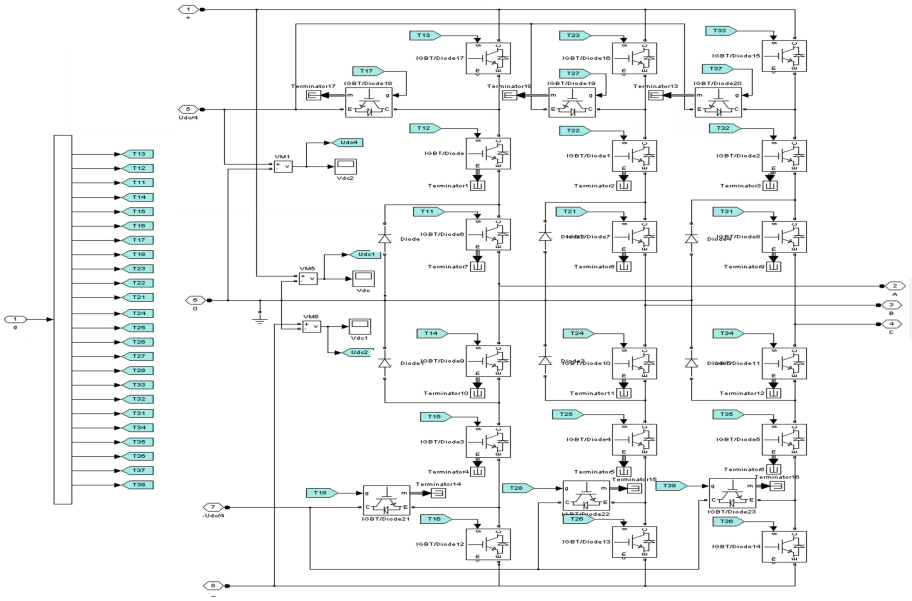

Fig. 2. Five-level (NPC) inverter

levels can be obtained, namely, Udc/2, Udc/4, 0, -Udc/4 and -Udc/2 corresponding to five switching states [10, 11].

The switch connection function F_{ks}, indicates the opened or closed state of the switch T_{ks}:

$$F_{ks} = \begin{cases} 1 & if \quad T_{ks} \quad closed \\ 0 & if \quad T_{ks} \quad open \end{cases} \tag{1}$$

For a leg K of the 3-phase, 5-level NPC VSI, several complementary control laws are possible. The optimal control law that allows the obtaining of a 5-level voltage (Udc1, Udc1 + Udc2, 0, -Udc3, -Udc3-Udc4) for each leg of this inverter is given below [12, 13]:

$$B_{k1} = \overline{B_{k5}}, \quad B_{k2} = \overline{B_{k4}}, \quad B_{k3} = \overline{B_{k6}} \tag{2}$$

$$B_{k7} = B_{k1}B_{k2}\overline{B_{k3}}, \quad B_{k8} = B_{k4}B_{k5}\overline{B_{k6}}$$

B_{ks} is the control signal of TD_{ks}.

In order to deduce the model of the inverter and using the proposed complementary law, we introduce the connection function F_{ks} of the switch TD_{ks} which describes the state of the switch (1 = turned ON and 0 = turned OFF). In this function, k is the number of the arm and s the number of the switch. The voltage of the three phases A, B, C relatively to the middle point M are given by VXM with X = point A, B or C.

$$V_{XM}(V) = \begin{bmatrix} F_{k1}F_{k2}F_{k3.}(U_{dc1} + U_{dc2}) \\ + F_{k1}F_{k2}\overline{F_{k3}}.(U_{dc1}) \end{bmatrix} - \begin{bmatrix} F_{k4}F_{k5}F_{k6.}(U_{dc3} + U_{dc4}) \\ + F_{k4}F_{k5}\overline{F_{k6}}.(U_{dc3}) \end{bmatrix} \tag{3}$$

Consider now, the connection function F_{ks} which describes the state of a half arm with k the number of the arm and m the number of the half arm (1 = upper half arm and 0 = lower half arm). The expression of the half arm connection function using the switch connection functions has the following form:

$$\begin{aligned} F^b_{k1} &= F_{k1}F_{k2}F_{k3} \\ F^b_{k0} &= F_{k4}F_{k5}F_{k6} \end{aligned} \tag{4}$$

$$\begin{aligned} F^b_{k1}\prime &= F_{k1}F_{k2}\overline{F_{k3}} \\ F^{b\prime}_{k0} &= F_{k4}F_{k5}\overline{F_{k6}} \end{aligned} \tag{5}$$

The voltage equation using the half arm connection functions will have the following form:

$$V_{XM}(V) = \begin{bmatrix} F^b_{k1}(U_{dc1} + U_{dc2}) + F_{k7.}(U_{dc1}) \\ -F^b_{k0}(U_{dc3} + U_{dc4}) + F_{k8.}(U_{dc3}) \end{bmatrix} \tag{6}$$

The output voltages of the inverter relative to point N of the load using the connection functions are given as follows [13]:

$$\begin{bmatrix} V_A \\ V_B \\ V_C \end{bmatrix} = \frac{1}{3}\begin{bmatrix} 2 & -1 & -1 \\ -1 & 2 & -1 \\ -1 & -1 & 2 \end{bmatrix}\begin{bmatrix} F_{17} + F^b_{11} \\ F_{27} + F^b_{21} \\ F_{37} + F^b_{31} \end{bmatrix} U_{dc1} + \begin{bmatrix} F^b_{11} \\ F^b_{21} \\ F^b_{31} \end{bmatrix} U_{dc2} - \frac{1}{3}\begin{bmatrix} 2 & -1 & -1 \\ -1 & 2 & -1 \\ -1 & -1 & 2 \end{bmatrix}\begin{bmatrix} F_{18} + F^b_{10} \\ F_{28} + F^b_{20} \\ F_{38} + F^b_{30} \end{bmatrix} U_{dc3} + \begin{bmatrix} F^b_{10} \\ F^b_{20} \\ F^b_{30} \end{bmatrix} U_{dc4} \tag{7}$$

3 Control Strategies

The proposed series active filter is adopted to compensate voltage harmonics. The control strategy used for extracting the reference voltages of series active power filter is based on the PQ theory described in [14, 15]. We assume that the three-phase voltage source in the grid is symmetric and distorted:

$$\begin{bmatrix} U_{sa} \\ U_{sb} \\ U_{sc} \end{bmatrix} = \begin{bmatrix} \sum_{n=1}^{\infty} \sqrt{2} U_n \sin(n\omega t + \theta_n) \\ \sum_{n=1}^{\infty} \sqrt{2} U_n \sin((n\omega t - \frac{2\pi}{3}) + \theta_n) \\ \sum_{n=1}^{\infty} \sqrt{2} U_n \sin((n\omega t + \frac{2\pi}{3}) + \theta_n) \end{bmatrix} \tag{8}$$

Un and θn are respectively the rms voltage and initial phase angle, n is the harmonic order. When n = 1, it means three-phase fundamental voltage source:

$$\begin{bmatrix} U_{sa} \\ U_{sb} \\ U_{sc} \end{bmatrix} = \begin{bmatrix} \sum_{n=1}^{\infty} \sqrt{2} U_1 \sin(n\omega t + \theta_1) \\ \sum_{n=1}^{\infty} \sqrt{2} U_1 \sin((\omega t - \frac{2\pi}{3}) + \theta_1) \\ \sum_{n=1}^{\infty} \sqrt{2} U_1 \sin((n\omega t + \frac{2\pi}{3}) + \theta_1) \end{bmatrix} \tag{9}$$

Equation (1) is transformed into (α–β) reference frame:

$$\begin{bmatrix} U_{s\alpha} \\ U_{s\beta} \end{bmatrix} = C_{32} \begin{bmatrix} U_{sa} \\ U_{sb} \\ U_{sc} \end{bmatrix} = \sqrt{3} \begin{bmatrix} \sum_{n=1}^{\infty} U_n \sin(n\omega t + \theta_n) \\ \sum_{n=1}^{\infty} \mp U_n \sin(n\omega t + \theta_n) \end{bmatrix} \tag{10}$$

Where:

$$C_{32} = \sqrt{2/3} \begin{bmatrix} 1 & -1/2 & -1/2 \\ 0 & \sqrt{3}/2 & -\sqrt{3}/2 \end{bmatrix} \tag{11}$$

Three-phase positive fundamental current template is constructed:

$$\begin{bmatrix} i_{sa} \\ i_{sb} \\ i_{sc} \end{bmatrix} = \sqrt{2/3} \begin{bmatrix} \sin(\omega t) \\ \sin(\omega t - \frac{2\pi}{3}) \\ \sin(\omega t + \frac{2\pi}{3}) \end{bmatrix} \tag{12}$$

Equation (5) is transformed to (α–β) reference frame:

$$\begin{bmatrix} i_{s\alpha} \\ i_{s\beta} \end{bmatrix} = C_{32} \begin{bmatrix} i_{sa} \\ i_{sb} \\ i_{sc} \end{bmatrix} = \begin{bmatrix} \sin(\omega t) \\ -\cos(\omega t) \end{bmatrix} \tag{13}$$

According to the instantaneous reactive power theory, then:

$$\begin{bmatrix} p \\ q \end{bmatrix} = \begin{bmatrix} u_{s\alpha} & u_{s\beta} \\ u_{s\beta} & -u_{s\alpha} \end{bmatrix} \begin{bmatrix} i_{s\alpha} \\ i_{s\beta} \end{bmatrix} \tag{14}$$

Where DC and AC components are included:

$$\begin{bmatrix} p \\ q \end{bmatrix} = \begin{bmatrix} \overline{p} + \overset{\approx}{p} \\ \overline{q} + \overset{\approx}{q} \end{bmatrix} \tag{15}$$

P and q are passed through low pass filter (LPF) and DC component are got:

$$\begin{bmatrix} \overline{p} \\ \overline{q} \end{bmatrix} = \sqrt{3} \begin{bmatrix} U_1 \cos(\theta_1) \\ U_1 \sin(\theta_1) \end{bmatrix} \tag{16}$$

According to (15), transformation is made:

$$\begin{bmatrix} p \\ q \end{bmatrix} = \begin{bmatrix} u_{s\alpha} & u_{s\beta} \\ u_{s\beta} & -u_{s\alpha} \end{bmatrix} \begin{bmatrix} i_{s\alpha} \\ i_{s\beta} \end{bmatrix} = \begin{bmatrix} i_{s\alpha} & i_{s\beta} \\ -i_{s\beta} & i_{s\alpha} \end{bmatrix} \begin{bmatrix} u_{s\alpha} \\ u_{s\beta} \end{bmatrix} \tag{17}$$

As for DC components of p and q:

$$\begin{bmatrix} \overline{p} \\ \overline{q} \end{bmatrix} = \begin{bmatrix} u_{s\alpha f} & u_{s\beta f} \\ u_{s\beta f} & -u_{s\alpha f} \end{bmatrix} \begin{bmatrix} i_{s\alpha} \\ i_{s\beta} \end{bmatrix} = \begin{bmatrix} i_{s\alpha} & i_{s\beta} \\ -i_{s\beta} & i_{s\alpha} \end{bmatrix} \begin{bmatrix} u_{s\alpha f} \\ u_{s\beta f} \end{bmatrix} \tag{18}$$

The fundamental voltages in (α–β) reference frame are:

$$\begin{bmatrix} u_{s\alpha f} \\ u_{s\beta f} \end{bmatrix} = \begin{bmatrix} i_{s\alpha} & i_{s\beta} \\ -i_{s\beta} & i_{s\alpha} \end{bmatrix}^{-1} \begin{bmatrix} \overline{p} \\ \overline{q} \end{bmatrix} = \begin{bmatrix} i_{s\alpha} & -i_{s\beta} \\ i_{s\beta} & i_{s\alpha} \end{bmatrix} \begin{bmatrix} \overline{p} \\ \overline{q} \end{bmatrix} \tag{19}$$

The three-phase fundamental voltage is:

$$\begin{bmatrix} U_{saf} \\ U_{sbf} \\ U_{scf} \end{bmatrix} = C_{23} \begin{bmatrix} u_{s\alpha f} \\ u_{s\beta f} \end{bmatrix} = \sqrt{2} U_1 \begin{bmatrix} \sin(\omega t + \theta_1) \\ \sin(\omega t + \theta_1 - \frac{2\pi}{3}) \\ \sin(\omega t + \theta_1 + \frac{2\pi}{3}) \end{bmatrix} \tag{20}$$

Where:

$$C_{23} = \sqrt{2/3} \begin{bmatrix} 1 & -1/2 & -1/2 \\ 0 & \sqrt{3}/2 & \sqrt{3}/2 \end{bmatrix}^T \tag{21}$$

The block diagram of the harmonic voltage identification based on PQ theory is presented in Fig. 3.

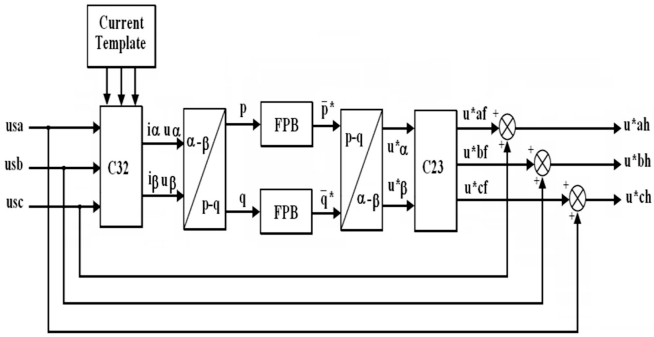

Fig. 3. Voltages reference identification based on PQ strategies

4 Fuzzy Logic Control

Fuzzy logic controllers (FLCs) have been interest a good alternative in more power electronics application. Their advantages are robustness, not need a mathematical model and accepting non-linearity. To benefit of these advantages new simple fuzzy logic voltage controller for five-level (NPC) inverter is designed. Fuzzy logic unlike Boolean or crisp logic, deal with problems that have vagueness, uncertainty or imprecision and uses membership functions with values varying between 0 and 1. The structure of fuzzy logic controller is shown in Fig. 4. There are four main parts for fuzzy logic approach [16]. The first part is 'fuzzification unit' to convert the input variable to the linguistic variable or fuzzy variable. The second part is 'knowledge base' to keep the necessary data for setting the control method by the expert engineer. The 'decision making logic' or the inference engine is the third part to imitate the human decision using rule bases and data bases from the second part. The final part is 'defuzzification unit' to convert the fuzzy variable to easy understanding variable [17, 18].

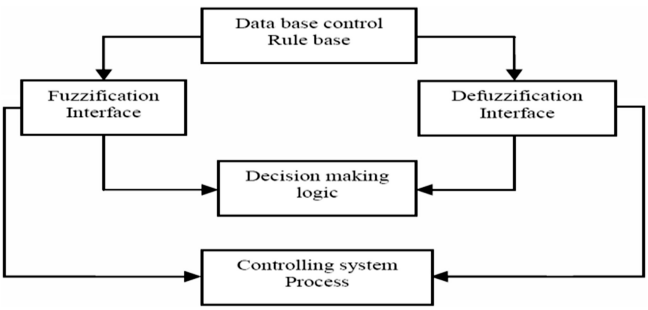

Fig. 4. Fuzzy inference system

The fuzzy voltage controller proposed in this paper is designed to improve compensation capability of series APF by adjusting the voltage error using fuzzy rules. The desired inverter switching signals of the five-level (NPC) series active power filter are determined according the error between the injected voltage and reference voltage. In this case, the fuzzy logic voltage controller has two inputs, error e and change of error de and one output s [19, 20]. To convert it into linguistic variable, we use seven fuzzy sets: NL (Negative Large), NM (Negative Medium), NS (Negative Small), ZE (Zero), PS (Positive Small), PM (Positive Medium) and PL (Positive Large). Figure 5 shows the membership functions used in fuzzification and defuzzification.

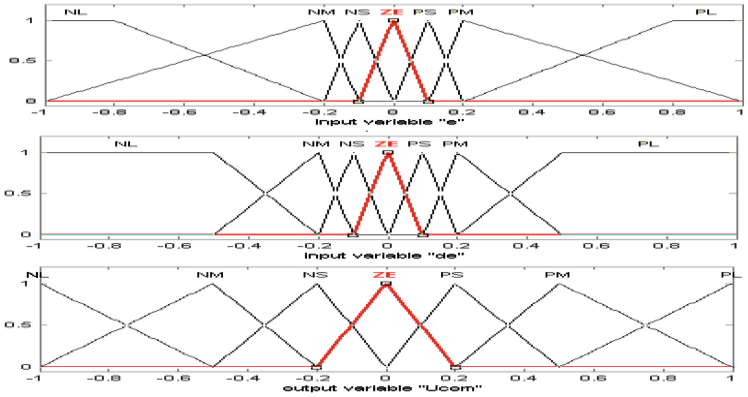

Fig. 5. Membership function (inputs and output variables)

The fuzzy controller for every phase is characterized for the following:

- Sept fuzzy sets for each input,
- Sept fuzzy sets for output,
- Triangular and trapezoidal membership function for the inputs and output,
- Implication using the “min” operator,
- Mamdani fuzzy inference mechanism based on fuzzy implication,
- Defuzzification using the “centroid” method.

Errors for each phase are discretized by the zero order hold blocks. The error rate is derivative of the error and it is obtained by the use of unit delay block. The saturation block imposes upper and lower bounds on a signal. When the input signal is within the range specified by the lower limit and upper limit parameters, the input signal passes through unchanged. When the input signal is outside these bounds, the signal is clipped to the upper or lower bound. The output of the saturation blocks are inputs to fuzzy logic controllers. The outputs of these fuzzy logic controllers are used in generation of pulses switching signals of the five-level (NPC) inverter. The switching signals are generated by means of comparing a four carrier signals with the output of the fuzzy logic controllers. The simulink model of the fuzzy logic switching signals generation is given by Fig. 6.

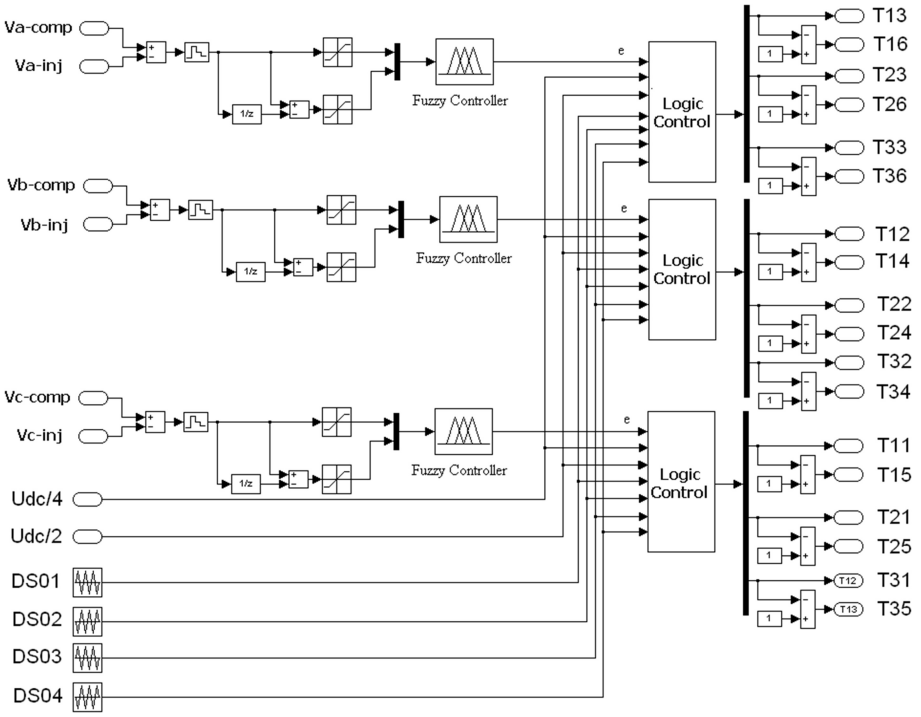

Fig. 6. Five-level (NPC) inverter switching signals generation

The difference between the injected voltages and the compensate voltages determines the reference signals, these error voltage signals pass through fuzzy controllers. The output of every fuzzy controller is compared with four triangular-carrying identical waves shifted from one to the other by a (+Upm, −Upm and −2Upm) and generating of switching pulses. The logic control of inverter is summarized in the two following stages:

Determination of the intermediate signals VK1 and VK0:

- If error Ec $\geq$ carrying 1 Then Vk11 = Udc/4,
- If error Ec $<$ carrying 1 Then VK11 = 0,
- If error Ec $\geq$ carrying 2 Then VK12 = Udc/4,
- If error Ec $<$ carrying 2 Then VK12 = 0.
- If error Ec $\geq$ carrying 3 Then VK10 = 0,
- If error Ec $<$ carrying 3 Then VK01 = −Udc/4,
- If error Ec $\geq$ carrying 4 Then VK02 = 0,
- If error Ec $<$ carrying 4 Then VK02 = −Udc/4,

With: VK1 = Vk11 + VK12 and VK0 = VK01 + VK02

Determination of control signals of the switches Tij (i = 1, 2, 3; j = 1, 2, 3):

- If (VK1 + VK0) = + Udc/2 Then Ti1 = 1, Ti2 = 1, Ti3 = 0,

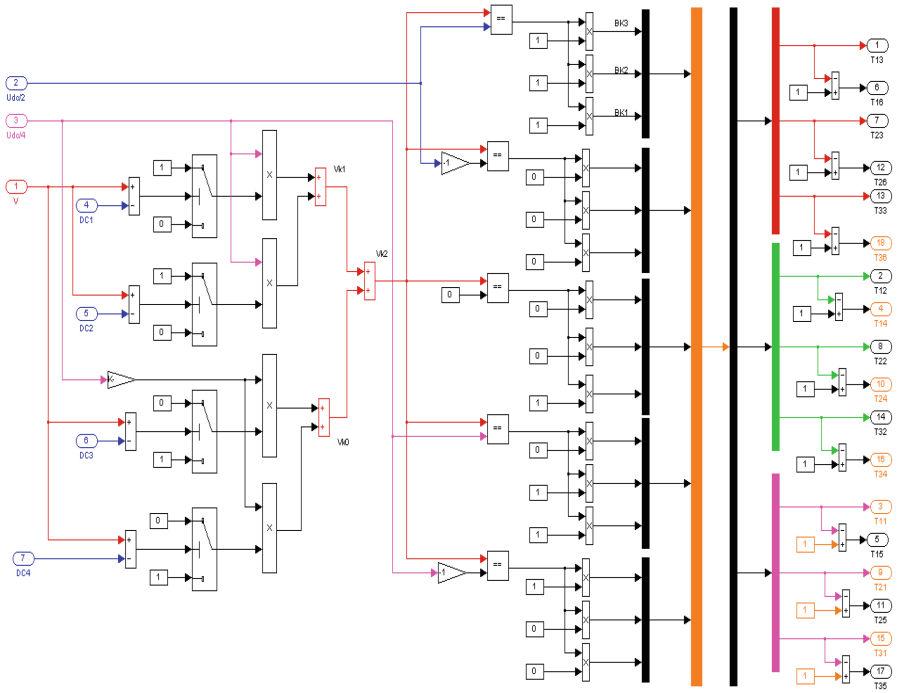

Fig. 7. Five-level (NPC) inverter logic control

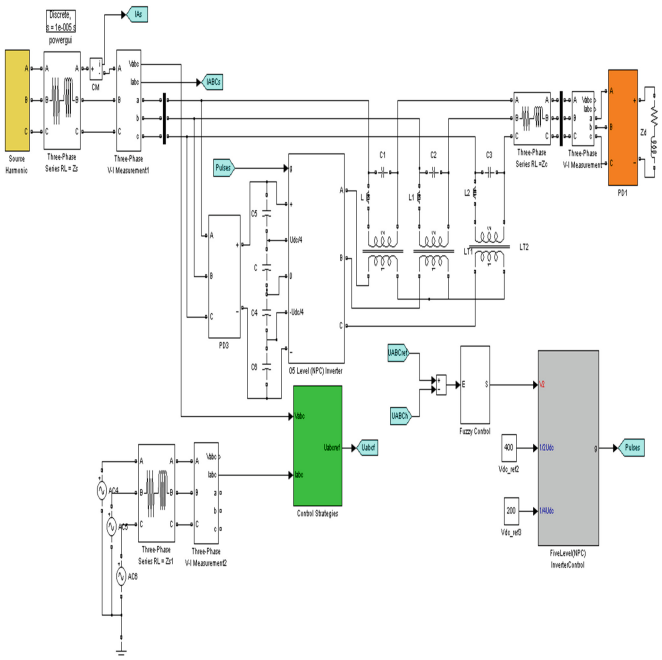

Fig. 8. Five-level series APF based on PQ control strategies

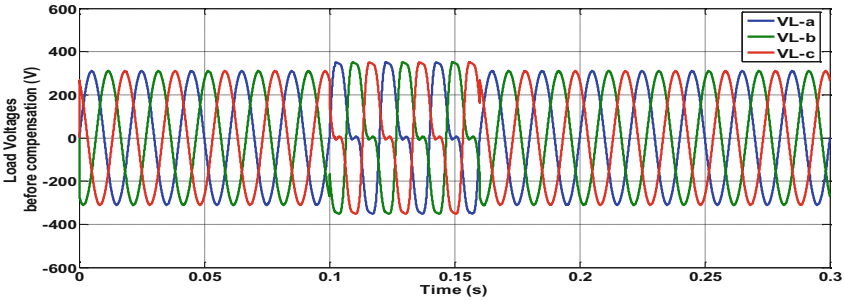

(a) Load voltage before compensation VL-abc(V)

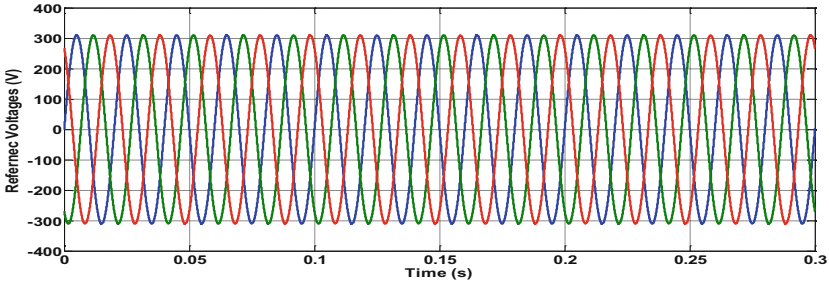

(b) Reference voltages Vref-abc(V)

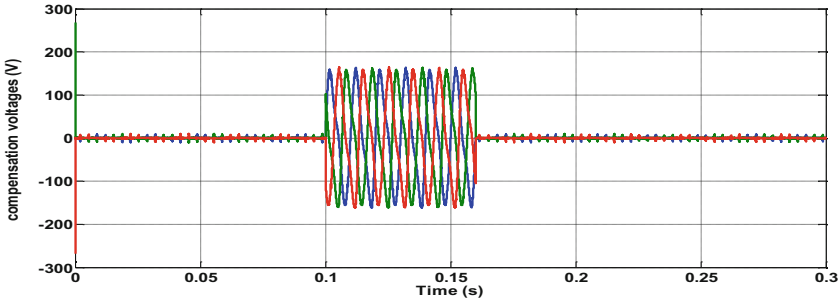

(c) Compensation voltages Vcomp-abc(V)

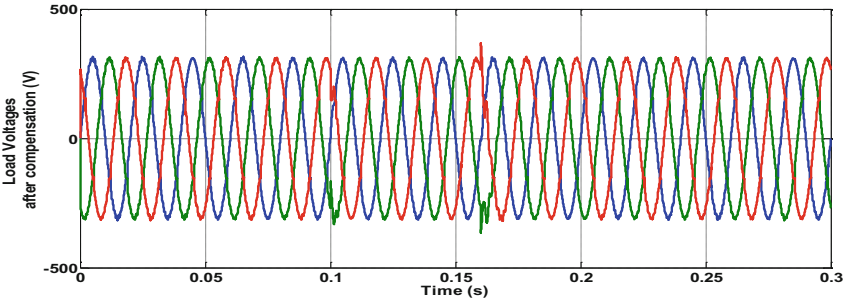

(d) Load voltage after compensation VL-abc(V)

Fig. 9. Load voltage before series compensation, reference voltage, injected voltage delivered by series APF and the load voltage after compensation

- If (VK1 + VK0) = + Udc/4 Then Ti1 = 1, Ti2 = 1, Ti3 = 0,
- If (VK1 + VK0) = 0 Then Ti1 = 1, Ti2 = 0, Ti3 = 0,
- If (VK1 + VK0) = −Udc/4 Then Ti1 = 0, Ti2 = 0, Ti3 = 1,
- If (VK1 + VK0) = −Udc/2 Then Ti1 = 0, Ti2 = 0, Ti3 = 0,

The logic control designed using simulink for the five-level (NPC) inverter is shown in Fig. 7.

5 Simulation Results and Discussion

The block diagram and Matlab-Simulink simulation model of the five-level (NPC) series active power filter based on PQ control strategies using fuzzy voltage controller is shown in Fig. 8.

The harmonic voltage disturbances is introduced voluntarily at t1 = 0.1 s to t2 = 0.16 s. Between t2 = 0.16 s and t3 = 0.2 s, the system is again at normal working condition. The series APF starts compensating voltage harmonics instantly. Figure (9) shows the load voltage before series compensation, reference voltage, injected voltage delivered by series APF and the load voltage after compensation. The harmonic spectrum of the load voltage before compensation is shown in Fig. 10 and the harmonic spectrum of the load voltage after compensation is shown in Fig. 11.

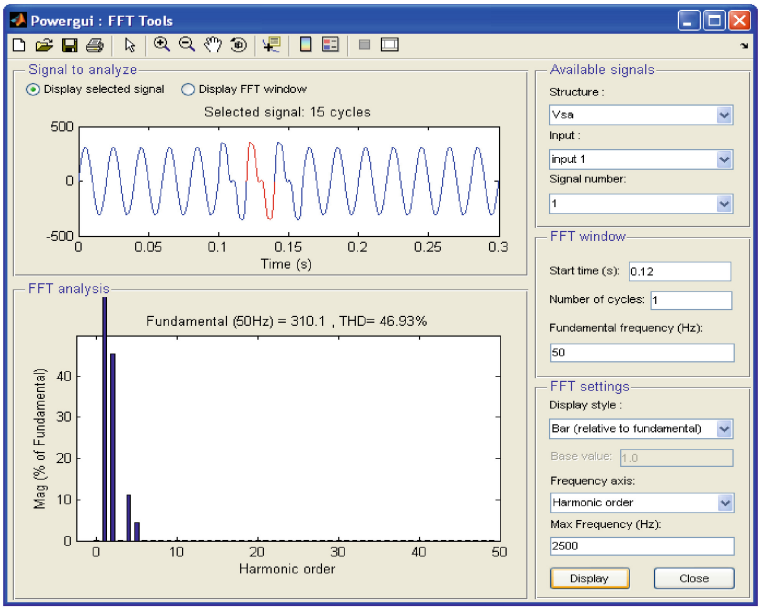

THDv (%) = 46.93%

Fig. 10. Load voltage harmonic spectrum without series AF

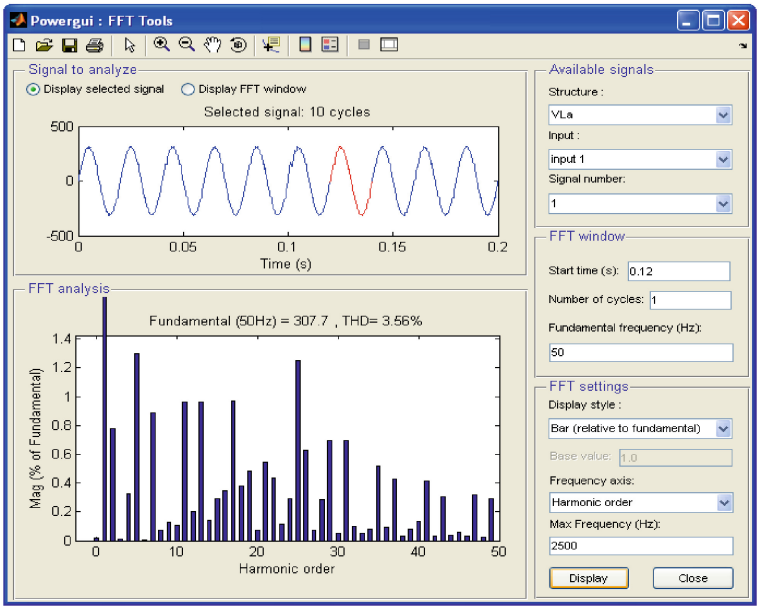

Fundamental (50Hz) = 307.7, THDv(%) = 3.56%

Fig. 11. Load voltage harmonic spectrum after compensation with series AF

6 Conclusion

The performance of the proposed Series APF system based on PQ control strategies is tested under distorted voltage supply. The simulation result shows that the load voltage before compensation is highly distorted; its THDv(%) is equal 46.93 %. After compensation the THDv(%) is reduced to 3.56 %. The simulation results obtained using MATLAB-Simulink and SimPowerSystem show the effectiveness of the proposed series APF based on fuzzy control techniques to ensure a pure sinusoidal voltage for loads at distorted supply network.

References

1. Hong, H.Z., Pingping, C., Zhengyu, L., Zhaoming, Q.: Novel control scheme based on per-phase reference current calculation for hybrid series active power filter with fundamental current bypass channel in unbalanced conditions. In: 35th Annual Power Electronics Specialists Conference, pp. 999–1002. IEEE (2004)
2. Bhim, S., Vishal, V.: A new control scheme for a series active filter for varying rectifier load. In: 2003 The Fifth International Conference on Power Electronics and Drive Systems, PEDS, vol. 1, pp. 554–559, 17–20 November 2003
3. Ambra, S., Jan, S., Tomas, L.: Power electronic solutions to power quality problems. Electr. Power Syst. Res. **66**, 71–83 (2003)

4. Guiying, L., Shiping, S., Peng, P.: Intelligent control and application of all-function active power filter. In: IEEE International Conference on Intelligent Computation Technology and Automation, pp. 1078–1081 (2008)
5. Kerrouche, S., Fateh, K.: Three-phase active power filter based on fuzzy logic controller. Int. J. Sci. Tech. Autom. Control Comput. Eng. **3**(1), 942–955 (2009)
6. Li, Y.F., Lau, C.C.: Development of fuzzy algorithms for servo systems. IEEE Control Syst. Mag. **9**, 65–72 (1989)
7. Correa, J.M., et al.: A fuzzy-controlled pulse density modulation strategy for a series resonant inverter with wide load range. In: Proceeding of the Conference on Power Electronics Specialists, PESC 2003, Acapulco, Mexico, pp. 15–19 (2003)
8. Sayeed, A., et al.: Fuzzy controller for inverter fed induction machines converter. IEEE Trans. Ind. Electron. **30**(1), 78–84 (1994)
9. Kim, Y.S., Ko, S.H.: Three-phase three-wire series active power filter, which compensates for harmonics and reactive power. IEE Proc. Electr. Power Appl. **151**(3), 276–282 (2004)
10. Mekri, F., Machmoum, M., Ait Ahmed N., Mazari, B.: A comparative studies of voltage controllers of series active power filter. Electr. Power Syst. Res., 1–12 (2009). Article in press, Elsevier
11. Thameur, A., Berkouk, E.-M., Benamrane, K., Benslimane, T.: Study and control of 5-level PWM rectifier-5-level NPC active power filter cascade using feedback control and redundant vectors. Turk. J. Electr. Eng. Comput. Sci. **20**(5), 655–677 (2012)
12. Chibani, R., Berkouk, E.-M., Boucherit, M.-S.: Five-Level NPC VSI: Different ways to balance input DC link voltages. ELEKTRIKA **11**(1), 19–33 (2009)
13. Morsli, A., Tlemçani, A., Cherchali, N.O., Boucherit, M.S.: Commande d'un filtre actif série de puissance à cinq niveaux pour améliorer la qualité de la tension électrique. In: 8ème Conférence sur le Génie Electrique 2013, CGE 2013, 16–17 Avril 2013, EMP, Bordj El Bahri, Alger, Algérie, (2013)
14. Hamadi, A., Rahmani, S., Al-Haddad, K.: A novel hybrid series active filter for power quality compensation. IEEE, pp. 1099–1104 (2007)
15. Reyes, H.H., Patricio, S., Hoyosung, K.: Instantaneous reactive power theory applied to active power filter compensation: different approaches, assessment, and experimental results. IEEE Trans. Ind. Electron. **55**, 184–196 (2008)
16. Narasa, T.R., Subramanyam, M.V.: Fuzzy logic controlled shunt active power filter for mitigation of harmonics with different membership. In: IEEE International Conference on Advances in Computing, Control, and Telecommunication, pp. 616–620 (2009)
17. Chennai, S., Benchouia, M.T., Goléa, A.: Harmonic currents compensation based on three-phase three-level shunt active filter using fuzzy logic current controller. J. Electr. Eng. Technol. JEET (KIEE) **6**(5), 595–604 (2011)
18. Chennai, S., Benchouia, M.-T.: Intelligent controllers for shunt active filter to compensate currents harmonics based on SRF and SRC control strategies. Int. J. Electr. Eng. Inf. IJEEI **3** (3), 372–393 (2011)
19. Chennai, S., Benchouia, M-T., Goléa, A.: Series active power filter for harmonic voltage compensation based on instantaneous reactive power theory strategy using fuzzy controller. In: International Conference on Electrical Engineering, ICEE 2012, 07–09 Mai 2012, Alger, Algeria (2012)
20. Chennai, S., Benchouia, M-T.: Shunt active power filter performances based on three-level (NPC) inverter to compensate current harmonics using intelligent controller. In: 8ème Conférence sur le Génie Electrique 2013, CGE 2013, 16–17 Avril 2013, EMP, Bordj El Bahri, Alger, Algérie (2013)

Adaptive Backstepping Control Using Combined Direct and Indirect σ–Modification Adaptation

Y. Soukkou[1(✉)] and S. Labiod[2]

[1] Research Center in Industrial Technologies CRTI (ex-CSC), P. O. Box. 64 Cheraga, 16014 Algiers, Algeria
soukkou_yassine@yahoo.fr

[2] LAJ, Department of Automatic Control, University of Jijel, BP. 98 Ouled Aissa, Jijel, Algeria
labiod_salim@yahoo.fr

Abstract. In this paper, by using the dynamic surface control technique, an adaptive backstepping controller using combined direct and indirect σ-modification adaptation is proposed for a class of parametric strict-feedback systems. In this approach, a σ-modification parameter adaptation law that combines direct and indirect update laws is proposed. At first, the x-swapping identifier with a gradient-type update law is presented for a class of parametric strict-feedback nonlinear systems. Next, the main steps of the controller design for a class of nonlinear systems in parametric strict-feedback form are described. The closed-loop error dynamics is shown to be globally stable by using the Lyapunov stability approach. Finally, simulation results for a single-link flexible-joint robot manipulator are given to illustrate the tracking performance of the proposed adaptive control scheme.

Keywords: Backstepping control · Direct and indirect adaptive control · Adaptive dynamic surface control · Lyapunov stability · Flexible joint manipulators

1 Introduction

Backstepping has been a powerful method for synthesizing adaptive controllers for the class of nonlinear systems with linearly parameterized uncertainties [1]. The uncertainties are assumed to be linear in the unknown constant parameters [2]. The adaptive backstepping control techniques have been found to be particularly useful for controlling parametric strict-feedback nonlinear systems [3], which achieve boundedness of the closed-loop states and convergence of the tracking error to zero. However, adaptive backstepping control can result in overparametrization and adaptation laws differentiations [3], a significant drawback that can be eliminated by introducing tuning functions [4]. For nonlinear systems with parametric lower-triangular form, several adaptive approaches were also presented in [5].

Though, backstepping technique has become one of the most popular design methods for a large class of single-input single-output (SISO) nonlinear systems [3, 5].

M. Chadli et al. (eds.), *Recent Advances in Electrical Engineering and Control Applications*, Lecture Notes in Electrical Engineering 411, DOI 10.1007/978-3-319-48929-2_2

A drawback in the traditional backstepping technique is the problem of "explosion of complexity" [2, 6, 7]. That is, the complexity of the controller grows drastically as the system order increases [1]. This problem is caused by the repeated differentiations of certain nonlinear functions such as virtual controls [2, 6, 7]. In [6], a procedure to deal with this problem for the non-adaptive case has been presented for a class of strict-feedback nonlinear systems, and it is called dynamic surface control (DSC). This problem is eliminated by introducing a first-order filtering of the synthetic virtual control input at each step of the traditional backstepping approach [1, 6–8]. In [2], authors are extending this technique to the adaptive control approach and it is called adaptive dynamic surface control.

The methodology proposed in this paper is an extension of the ideas presented in [9–11] for the adaptive backstepping design. This paper presents a new approach that combines direct and indirect σ-modification adaptation mechanism for adaptive backstepping control of parametric strict-feedback nonlinear systems. In fact, the tracking error based parameter adaptation law of the direct adaptive backstepping control with DSC [2, 11] will be combined with an identification error based parameter adaptation law of the indirect adaptive backstepping control [5, 11–14]. The combined adaptive law is introduced in order to achieve better parameter estimation and hence better tracking performance. The stability analysis of the closed-loop system is performed by using the Lyapunov stability theorem.

This paper is organized as follows. In Sect. 2, the identification based x-swapping is provided. The combined direct/indirect adaptive backstepping control with DSC is presented in Sect. 3. The stability analysis of the closed-loop system is given in Sect. 4. In Sect. 5, numerical example for a single-link flexible-joint robot manipulator is used to demonstrate the effectiveness of the proposed approach. Conclusion is contained in Sect. 6.

2 Identification Based x-Swapping

The goal of a swapping filter is to transform a dynamic parametric model into a static form, such that standard parameter estimation algorithms can be used. The term swapping describes the fact that the order of the transfer function describing the dynamics and the time varying parameter error $\tilde{\theta}$ is exchanged [14]. Two types of swapping schemes are presented in [5, 12–14], the z-swapping-based identifier derived from the tracking error model and the x-swapping-based identifier derived from the state dynamics [14]. Each of these two swapping-based identifiers allows application of gradient and least squares update laws. In this paper we use the gradient update law. To illustrate the x-swapping-based identifier procedure, we consider the following nonlinear system in parametric x-model [5, 12–14]

$$\dot{x}_i = f_i(x,u) + F_i^T(x,u)\theta_i \tag{1}$$

where

$$\begin{cases} f_i(x,u) &= x_{i+1}, i = 1, \cdots, n-1 \\ f_n(x,u) &= u \end{cases} \\ F_i^T(x,u) = \varphi_i^T(\bar{x}_i), \bar{x}_i = [\, x_1 \quad x_2 \quad \cdots \quad x_i \,]^T, i = 1, \cdots, n \tag{2}$$

$\theta_i \in \mathbb{R}^{p_i}$.

Then, we introduce the following two filters

$$\dot{\Omega}_{0i} = A_i(x,t)(\Omega_{0i} + x_i) - f_i(x,u), \Omega_{0i} \in \mathbb{R} \tag{3}$$

$$\dot{\Omega}_i^T = A_i(x,t)\Omega_i^T + F_i^T(x,u), \Omega_i \in \mathbb{R}^{p_i} \tag{4}$$

where, $i = 1, \cdots, n$, and $A_i(x,t) < 0$ is a negative definite matrix for each x continuous in t. We define the estimation error vector as

$$e_i = x_i + \Omega_{0i} - \Omega_i^T \hat{\theta}_i, e_i \in \mathbb{R} \tag{5}$$

with $\hat{\theta}_i$ the estimate of θ_i and let

$$\tilde{e}_i = x_i + \Omega_{0i} - \Omega_i^T \theta_i, \tilde{e}_i \in \mathbb{R} \tag{6}$$

Then, we obtain

$$e_i = \Omega_i^T \tilde{\theta}_i + \tilde{e}_i \tag{7}$$

The error signal $\tilde{e}_i$ satisfies

$$\dot{\tilde{e}}_i = \dot{x}_i + \dot{\Omega}_{0i} - \dot{\Omega}_i^T \theta_i = A_i(x,t)\tilde{e}_i \tag{8}$$

To guarantee boundedness of Ω_i when $F_i(x,u)$ grows unbounded, a particular choice of $A_i(x,t)$ is made [5, 14]

$$A_i(x,t) = A_{0i} - \lambda_i F_i^T(x,u) F_i(x,u) P_i \tag{9}$$

where $\lambda_i > 0$ and A_{0i} is an arbitrary constant matrix satisfying

$$P_i A_{0i} + A_{0i}^T P_i = -I, P_i = P_i^T > 0 \tag{10}$$

The update law for $\hat{\theta}_i$ employs the estimation error e_i and the filtered regressor Ω_i. The gradient update law is given by

$$\dot{\hat{\theta}}_i = \Gamma_i \frac{\Omega_i e_i}{1 + v_i \mathrm{tr}\{\Omega_i^T \Omega_i\}}, \Gamma_i = \Gamma_i^T > 0, v_i \geq 0 \tag{11}$$

where, $i = 1, \cdots, n$.

To establish the identifier properties, let $[0, t_f)$ be the maximal interval of existence of solutions of (1), the x-swapping filters (3) and (4), and the gradient update law (11). Then for $v_i \geq 0$ the following properties hold [5, 12–14]

(i) $\tilde{\theta}_i \in L_\infty[0, t_f)$
(ii) $e_i \in L_2[0, t_f) \cap L_\infty[0, t_f)$
(iii) $\dot{\hat{\theta}}_i \in L_2[0, t_f) \cap L_\infty[0, t_f)$

We consider the following Lyapunov function

$$V_i = \frac{1}{2}\tilde{\theta}_i^T \Gamma_i^{-1} \tilde{\theta}_i + \tilde{e}_i^T P_i \tilde{e}_i \tag{12}$$

Along of Eqs. (8) and (11), the derivative of the Lyapunov function (12) is

$$\begin{aligned}
\dot{V}_i &= \tilde{\theta}_i^T \Gamma_i^{-1} \dot{\tilde{\theta}}_i + \dot{\tilde{e}}_i^T P_i \tilde{e}_i + \tilde{e}_i^T P_i \dot{\tilde{e}}_i \\
&= \tilde{\theta}_i^T \Gamma_i^{-1} \dot{\tilde{\theta}}_i + \tilde{e}_i^T A_i^T(x,t) P_i \tilde{e}_i + \tilde{e}_i^T P_i A_i(x,t) \tilde{e}_i \\
&\leq -\tilde{\theta}_i^T \Gamma_i^{-1} \dot{\hat{\theta}}_i - \tilde{e}_i^T \tilde{e}_i = -\frac{\tilde{\theta}_i^T \Omega_i e_i}{1 + v_i \mathrm{tr}\{\Omega_i^T \Omega_i\}} - \tilde{e}_i^T \tilde{e}_i \\
&= -\frac{e_i^T e_i}{1 + v_i \mathrm{tr}\{\Omega_i^T \Omega_i\}} + \frac{e_i^T}{1 + v_i \mathrm{tr}\{\Omega_i^T \Omega_i\}} \tilde{e}_i - \tilde{e}_i^T \tilde{e}_i \\
&\leq -\frac{3}{4}\frac{e_i^T e_i}{1 + v_i \mathrm{tr}\{\Omega_i^T \Omega_i\}} - \frac{1}{4}\frac{e_i^T e_i}{\left(1 + v_i \mathrm{tr}\{\Omega_i^T \Omega_i\}\right)^2} + \frac{e_i^T}{1 + v_i \mathrm{tr}\{\Omega_i^T \Omega_i\}} \tilde{e}_i - \tilde{e}_i^T \tilde{e}_i \\
&= -\frac{3}{4}\frac{e_i^T e_i}{1 + v_i \mathrm{tr}\{\Omega_i^T \Omega_i\}} - \left(\frac{e_i}{2\left(1 + v_i \mathrm{tr}\{\Omega_i^T \Omega_i\}\right)} - \tilde{e}_i\right)^T \left(\frac{e_i}{2\left(1 + v_i \mathrm{tr}\{\Omega_i^T \Omega_i\}\right)} - \tilde{e}_i\right) \\
&\leq -\frac{3}{4}\frac{e_i^T e_i}{1 + v_i \mathrm{tr}\{\Omega_i^T \Omega_i\}}, i = 1, \cdots, n
\end{aligned} \tag{13}$$

Since $\dot{V}_i$ is negative semi-definite, one has $\tilde{\theta}_i \in L_\infty[0, t_f)$. From $e_i = \Omega_i^T \tilde{\theta}_i + \tilde{e}_i$ and the boundedness of Ω_i, one concludes that e_i and $\dot{\hat{\theta}}_i \in L_2[0, t_f) \cap L_\infty[0, t_f)$.

3 Direct/Indirect Adaptive Backstepping Control with DSC

In the direct/indirect adaptive backstepping control with DSC procedure, the control law and the parameter estimation are not separated. In this paper, the parameter update law for $\hat{\theta}_i$ combine gradient-type update laws based on the x-swapping identifier and tracking error based update laws. The control objective is to achieve the asymptotic tracking of a reference signal y_r by x_1. The reference signal y_r and its derivatives $\dot{y}_r, \ldots, y_r^{(n)}$ are assumed piecewise continuous and bounded. In the following, we

describe the main steps of the controller design for the nonlinear system in parametric strict-feedback form

$$\begin{aligned}\dot{x}_1 &= x_2 + \varphi_1^T(x_1)\theta_1 \\ \dot{x}_i &= x_{i+1} + \varphi_i^T(\bar{x}_i)\theta_i, i = 2, \cdots, n-1 \\ \dot{x}_n &= u + \varphi_n^T(x)\theta_n\end{aligned} \tag{14}$$

where, $x = [x_1 \quad x_2 \quad \cdots \quad x_n]^T \in \mathbb{R}^n$ and $u \in \mathbb{R}$ are the state variables vector and the input of the system, respectively. $\theta_i \in \mathbb{R}^{p_i}$ are unknown constant parameter vectors, $\bar{x}_i = [x_2 \quad x_3 \quad \cdots \quad x_i]^T$. The nonlinear functions $\varphi_i^T(\bar{x}_i) : \mathbb{R}^i \to \mathbb{R}^{p_i}$ are known.

Step $1(i = 1)$

The first surface is defined by $S_1 = x_1 - x_{1d}$, and its time derivative is given by

$$\dot{S}_1 = \dot{x}_1 - \dot{x}_{1d} = x_2 + \varphi_1^T(x_1)\theta_1 - \dot{x}_{1d} \tag{15}$$

we choose $\bar{x}_2$ to drive S_1 towards zero with

$$\bar{x}_2 = -\varphi_1^T(x_1)\hat{\theta}_1 + \dot{x}_{1d} - K_1 S_1 \tag{16}$$

we pass $\bar{x}_2$ through a first order filter, with time constant τ_2, to obtain x_{2d}

$$\tau_2 \dot{x}_{2d} + x_{2d} = \bar{x}_2, x_{2d}(0) = \bar{x}_2(0) \tag{17}$$

$$\dot{x}_{2d} = \frac{1}{\tau_2}\left(-x_{2d} - \varphi_1^T(x_1)\hat{\theta}_1 + \dot{x}_{1d} - K_1 S_1\right) \tag{18}$$

Step $i(i = 2, \cdots, n-1)$

The i^{th} surface is defined by $S_i = x_i - x_{id}$, and its time derivative is given by

$$\dot{S}_i = \dot{x}_i - \dot{x}_{id} = x_{i+1} + \varphi_i^T(\bar{x}_i)\theta_i - \dot{x}_{id} \tag{19}$$

we choose $\bar{x}_{i+1}$ to drive S_i towards zero with

$$\bar{x}_{i+1} = -\varphi_i^T(\bar{x}_i)\hat{\theta}_i + \dot{x}_{id} - K_i S_i \tag{20}$$

we pass $\bar{x}_{i+1}$ through a first order filter, with time constant τ_{i+1}, to obtain x_{i+1d}

$$\tau_{i+1}\dot{x}_{i+1d} + x_{i+1d} = \bar{x}_{i+1}, x_{i+1d}(0) = \bar{x}_{i+1}(0) \tag{21}$$

$$\dot{x}_{i+1d} = \frac{1}{\tau_{i+1}}\left(-x_{i+1d} - \varphi_i^T(\bar{x}_i)\hat{\theta}_i + \dot{x}_{id} - K_i S_i\right) \tag{22}$$

Step n

The n^{th} surface is defined by $S_n = x_n - x_{nd}$, and its time derivative is given by

$$\dot{S}_n = \dot{x}_n - \dot{x}_{nd} = u + \varphi_n^T(x)\theta_n - \dot{x}_{nd} \tag{23}$$

we choose the control input u to drive S_n towards zero with

$$u = -\varphi_n^T(x)\hat{\theta}_n + \dot{x}_{nd} - K_n S_n \tag{24}$$

The update laws (direct part) for the parameter estimates are given by [2, 11]

$$\begin{aligned} \dot{\hat{\theta}}_1 &= \bar{\Gamma}_1 S_1 \varphi_1(x_1) \\ \dot{\hat{\theta}}_i &= \bar{\Gamma}_i S_i \varphi_i(\bar{x}_i), i = 2, \cdots, n-1 \\ \dot{\hat{\theta}}_n &= \bar{\Gamma}_n S_n \varphi_n(x) \end{aligned} \tag{25}$$

where, $\bar{\Gamma}_i > 0 (i = 1, \cdots, n)$ are design parameters that can be adjusted for the rate of convergence of the parameter estimates.

Let us introduce the following two filters

$$\dot{\Omega}_{0i} = A_i(x,t)(\Omega_{0i} + x_i) - f_i(x,u), \Omega_{0i} \in \mathbb{R} \tag{26}$$

$$\dot{\Omega}_i^T = A_i(x,t)\Omega_i^T + F_i^T(x,u), \Omega_i \in \mathbb{R}^{p_i} \tag{27}$$

where, $i = 1, \cdots, n$, and

$$A_i(x,t) = A_{0i} - \lambda_i F_i^T(x,u) F_i(x,u) P_i \tag{28}$$

where $\lambda_i > 0$ and A_{0i} is an arbitrary constant matrix satisfying

$$P_i A_{0i} + A_{0i}^T P_i = -I, P_i = P_i^T > 0 \tag{29}$$

The gradient update law (indirect part) is given by [5, 11–14]

$$\dot{\hat{\theta}}_i = \Gamma_i \frac{\Omega_i e_i}{1 + v_i \mathrm{tr}\{\Omega_i^T \Omega_i\}}, \Gamma_i = \Gamma_i^T > 0, v_i \geq 0 \tag{30}$$

where, $i = 1, \cdots, n$ and $e_i = x_i + \Omega_{0i} - \Omega_i^T \hat{\theta}_i, e_i \in \mathbb{R}$.

Now we propose the following combined direct and indirect σ-modification adaptation law [11]

$$\dot{\hat{\theta}}_i = \bar{\Gamma}_i S_i \varphi_i(\bar{x}_i) - \bar{\Gamma}_i \sigma_i \left(\hat{\theta}_i - \bar{\theta}_i\right), \bar{\Gamma}_i > 0 \tag{31}$$

where, $i = 1, \cdots, n$, σ_i is a small positive constant, $\bar{\Gamma}_i$ is a positive definite constant matrix and $\bar{\theta}_i$ is computed with the gradient method as follows

$$\dot{\hat{\theta}}_i = \Gamma_i \frac{\Omega_i e_i}{1 + v_i \mathrm{tr}\{\Omega_i^T \Omega_i\}}, \Gamma_i = \Gamma_i^T > 0, v_i \geq 0 \tag{32}$$

where, Γ_i is a positive definite constant matrix and $e_i = x_i + \Omega_{0i} - \Omega_i^T \bar{\theta}_i, e_i \in \mathbb{R}$.

4 Stability Analysis

We define the boundary layer error as [2, 11, 15]

$$y_i = x_{id} - \bar{x}_i, i = 2, \cdots, n \tag{33}$$

and the parameter estimate errors as

$$\tilde{\theta}_i = \theta_i - \hat{\theta}_i, i = 1, 2, \cdots, n \tag{34}$$

Then the closed-loop dynamics can be expressed in terms of the surfaces S_i, the boundary layer errors y_i, and the parameter estimate errors $\tilde{\theta}_i$.

The dynamics of the surfaces are expressed, for $i = 1$, as

$$\begin{aligned} \dot{S}_1 &= \dot{x}_1 - \dot{x}_{1d} = x_2 + \varphi_1^T(x_1)\theta_1 - \dot{x}_{1d} \\ &= S_2 + x_{2d} + \varphi_1^T(x_1)\theta_1 - \dot{x}_{1d} \\ &= S_2 + y_2 + \bar{x}_2 + \varphi_1^T(x_1)\theta_1 - \dot{x}_{1d} \\ &= S_2 + y_2 - K_1 S_1 + \varphi_1^T(x_1)\tilde{\theta}_1 \end{aligned} \tag{35}$$

For $i = 2, \cdots, n-1$

$$\begin{aligned} \dot{S}_i &= \dot{x}_i - \dot{x}_{id} = x_{i+1} + \varphi_i^T(\bar{x}_i)\theta_i - \dot{x}_{id} \\ &= S_{i+1} + x_{i+1d} + \varphi_i^T(\bar{x}_i)\theta_i - \dot{x}_{id} \\ &= S_{i+1} + y_{i+1} + \bar{x}_{i+1} + \varphi_i^T(\bar{x}_i)\theta_i - \dot{x}_{id} \\ &= S_{i+1} + y_{i+1} - K_i S_i + \varphi_i^T(\bar{x}_i)\tilde{\theta}_i \end{aligned} \tag{36}$$

For $i = n$

$$\dot{S}_n = \dot{x}_n - \dot{x}_{nd} = u + \varphi_n^T(x)\theta_n - \dot{x}_{nd} = -K_n S_n + \varphi_n^T(x)\tilde{\theta}_n \tag{37}$$

The dynamics of the boundary layer errors y_i are expressed, for $i = 2$, as

$$\begin{aligned} \dot{y}_2 &= \dot{x}_{2d} - \dot{\bar{x}}_2 = \frac{1}{\tau_2}\left(-x_{2d} - \varphi_1^T(x_1)\hat{\theta}_1 + \dot{x}_{1d} - K_1 S_1\right) - \dot{\bar{x}}_2 \\ &= \frac{1}{\tau_2}(-x_{2d} + \bar{x}_2) - \dot{\bar{x}}_2 = \frac{1}{\tau_2}(-y_2 - \bar{x}_2 + \bar{x}_2) - \dot{\bar{x}}_2 = -\frac{1}{\tau_2} y_2 - \dot{\bar{x}}_2 \end{aligned} \tag{38}$$

For $i = 3, \cdots, n$

$$\begin{aligned}\dot{y}_i &= \dot{x}_{id} - \dot{\bar{x}}_i = \frac{1}{\tau_i}\left(-x_{id} - \varphi_{i-1}^T(\bar{x}_{i-1})\hat{\theta}_{i-1} + \dot{x}_{i-1d} - K_{i-1}S_{i-1}\right) - \dot{\bar{x}}_i \\ &= \frac{1}{\tau_i}(-x_{id} + \bar{x}_i) - \dot{\bar{x}}_i = \frac{1}{\tau_i}(-y_i - \bar{x}_i + \bar{x}_i) - \dot{\bar{x}}_i = -\frac{1}{\tau_i}y_i - \dot{\bar{x}}_i\end{aligned} \tag{39}$$

Let us consider the following Lyapunov function

$$V = \sum_{i=1}^{n} V_{is} + \sum_{i=2}^{n} V_{iy} + \sum_{i=1}^{n} V_i \tag{40}$$

where

$$V_{is} = \frac{1}{2}S_i^2, V_{iy} = \frac{1}{2}y_i^2, V_i = \frac{1}{2}\tilde{\theta}_i^T\bar{\Gamma}_i^{-1}\tilde{\theta}_i \tag{41}$$

Then, one has

$$\begin{aligned}\dot{V}_{is} &= S_i\dot{S}_i = S_iS_{i+1} + S_iy_{i+1} - K_iS_i^2 + S_i\varphi_i^T(\bar{x}_i)\tilde{\theta}_i \\ &\leq |S_i||S_{i+1}| + |S_i||y_{i+1}| - K_iS_i^2 + S_i\varphi_i^T(\bar{x}_i)\tilde{\theta}_i \\ &\leq (1 - K_i)S_i^2 + \frac{1}{2}S_{i+1}^2 + \frac{1}{2}y_{i+1}^2 + S_i\varphi_i^T(\bar{x}_i)\tilde{\theta}_i, i = 1, \cdots, n-1\end{aligned} \tag{42}$$

$$\dot{V}_{ns} = S_n\dot{S}_n = -K_nS_n^2 + S_n\varphi_n^T(x)\tilde{\theta}_n \leq -K_nS_n^2 + S_n\varphi_n^T(x)\tilde{\theta}_n \tag{43}$$

We assume that, $|y_i\dot{\bar{x}}_i| \leq M_{1i}y_i^2 + M_{2i}S_i^2 + \delta_i^2$, where, M_{1i} and M_{2i} are positive constants, and δ_i are bounded functions, then, we can write

$$\begin{aligned}\dot{V}_{iy} &= y_i\dot{y}_i = -\frac{1}{\tau_i}y_i^2 + y_i\dot{\bar{x}}_i \leq -\frac{1}{\tau_i}y_i^2 + |y_i\dot{\bar{x}}_i| \\ &\leq -\frac{1}{\tau_i}y_i^2 + M_{1i}y_i^2 + M_{2i}S_i^2 + \delta_i^2, i = 2, \cdots, n\end{aligned} \tag{44}$$

$$\begin{aligned}\dot{V}_i &= \tilde{\theta}_i^T\bar{\Gamma}_i^{-1}\dot{\tilde{\theta}}_i = -\tilde{\theta}_i^T\bar{\Gamma}_i^{-1}\dot{\hat{\theta}}_i \\ &= -\tilde{\theta}_i^T\bar{\Gamma}_i^{-1}\left(\bar{\Gamma}_iS_i\varphi_i(\bar{x}_i) - \bar{\Gamma}_i\sigma_i\left(\hat{\theta}_i - \bar{\theta}_i\right)\right) \\ &= -\tilde{\theta}_i^TS_i\varphi_i(\bar{x}_i) + \tilde{\theta}_i^T\sigma_i\left(\hat{\theta}_i - \bar{\theta}_i\right), i = 1, \cdots, n\end{aligned} \tag{45}$$

One has: $\theta_i - \bar{\theta}_i$ is bounded, thus: $e_{\theta_i} = \theta_i - \bar{\theta}_i$ is bounded, $\bar{\theta}_i = \theta_i - e_{\theta_i}$ and $\tilde{\theta}_i = \theta_i - \hat{\theta}_i$.

$$\begin{aligned}\dot{V}_i &= -\tilde{\theta}_i^T S_i \varphi_i(\bar{x}_i) + \tilde{\theta}_i^T \sigma_i \left(\hat{\theta}_i - \theta_i + e_{\theta_i}\right) \\ &= -\tilde{\theta}_i^T S_i \varphi_i(\bar{x}_i) - \sigma_i \tilde{\theta}_i^T \tilde{\theta}_i + \sigma_i \tilde{\theta}_i^T e_{\theta_i} \\ &\leq -\tilde{\theta}_i^T S_i \varphi_i(\bar{x}_i) - \sigma_i \tilde{\theta}_i^T \tilde{\theta}_i + \frac{\sigma_i}{2} \tilde{\theta}_i^T \tilde{\theta}_i + \frac{\sigma_i}{2} e_{\theta_i}^T e_{\theta_i} \\ &\leq -\tilde{\theta}_i^T S_i \varphi_i(\bar{x}_i) - \frac{\sigma_i}{2} \tilde{\theta}_i^T \tilde{\theta}_i + \frac{\sigma_i}{2} e_{\theta_i}^T e_{\theta_i}\end{aligned} \tag{46}$$

$$\begin{aligned}\dot{V} &= \sum_{i=1}^{n} \dot{V}_{is} + \sum_{i=2}^{n} \dot{V}_{iy} + \sum_{i=1}^{n} \dot{V}_i \\ &\leq \sum_{i=1}^{n-1} \left[(1 - K_i) S_i^2 + \frac{1}{2} S_{i+1}^2 + \frac{1}{2} y_{i+1}^2 + S_i \varphi_i^T(\bar{x}_i) \tilde{\theta}_i\right] - K_n S_n^2 + S_n \varphi_n^T(x) \tilde{\theta}_n \\ &+ \sum_{i=2}^{n} \left(-\frac{1}{\tau_i} y_i^2 + M_{1i} y_i^2 + M_{2i} S_i^2 + \delta_i^2\right) - \sum_{i=1}^{n} \tilde{\theta}_i^T S_i \varphi_i(\bar{x}_i) - \sum_{i=1}^{n} \frac{\sigma_i}{2} \tilde{\theta}_i^T \tilde{\theta}_i + \sum_{i=1}^{n} \frac{\sigma_i}{2} e_{\theta_i}^T e_{\theta_i} \\ &\leq -(K_1 - 1) S_1^2 - \sum_{i=2}^{n-1} \left(K_i - M_{2i} - \frac{3}{2}\right) S_i^2 - \left(K_n - M_{2n} - \frac{1}{2}\right) S_n^2 - \sum_{i=2}^{n} \left(\frac{1}{\tau_i} - \frac{1}{2} - M_{1i}\right) y_i^2 \\ &+ \sum_{i=2}^{n} \delta_i^2 - \sum_{i=1}^{n} \frac{\sigma_i}{2} \tilde{\theta}_i^T \tilde{\theta}_i + \sum_{i=1}^{n} \frac{\sigma_i}{2} e_{\theta_i}^T e_{\theta_i}\end{aligned} \tag{47}$$

If we assume that, $\delta_i \in L_\infty$, $e_{\theta_i} \in L_\infty$, $K_1 > 1$, $K_i > M_{2i} + \frac{3}{2}$, $K_n > M_{2n} + \frac{1}{2}$ and $\frac{1}{\tau_i} > \frac{1}{2} + M_{1i}$, we obtain the boundedness of all signals S_i, y_i and $\tilde{\theta}_i$. Moreover, the surface S_i can be made arbitrarily small by adjusting the design parameters K_i.

5 Numerical Example

Consider the single-link flexible-joint robot shown in Fig. 1. The dynamic model of this robot is given as follow [16, 17]

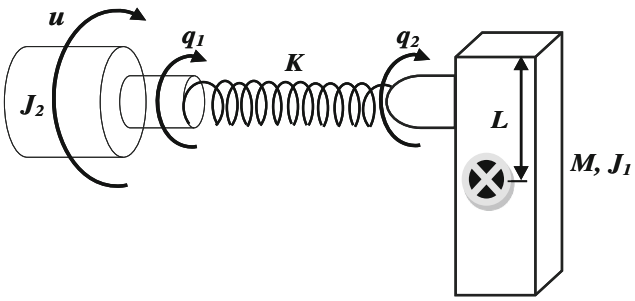

Fig. 1. Single link flexible joint robot.

$$\begin{aligned} J_1\ddot{q}_1 + MgL\sin(q_1) + K(q_1 - q_2) &= 0 \\ J_2\ddot{q}_2 - K(q_1 - q_2) &= u \end{aligned} \tag{48}$$

where u is the input torque. J_1 and J_2 are the inertias of the link and the motor respectively. M is the link mass. g is the gravity. L is the link length. K is the stiffness. q_1 and q_2 are the angular positions of the link and the motor shaft, respectively.

Let the state variables defined as follows: $x_1 = q_1$, $x_2 = \dot{q}_1$, $x_3 = q_2$ and $x_4 = \dot{q}_2$, and its dynamic model becomes

$$\begin{aligned} \dot{x}_1 &= x_2 \\ \dot{x}_2 &= f_1(x_1, x_3) + g_1 x_3 \\ \dot{x}_3 &= x_4 \\ \dot{x}_4 &= f_2(x_1, x_3) + g_2 u \end{aligned} \tag{49}$$

with

$$\begin{aligned} f_1(x_1, x_3) &= -\frac{MgL}{J_1}\sin(x_1) - \frac{K}{J_1}x_1, g_1 = \frac{K}{J_1} \\ f_2(x_1, x_3) &= \frac{K}{J_2}(x_1 - x_3), g_2 = \frac{1}{J_2} \end{aligned} \tag{50}$$

The single-link flexible-joint robot model used in this paper is given by (49) where the parameter values are given in Table 1 [17].

For the numerical simulation, the unknown parameter θ_1 of the system is selected as $\theta_1 = MgL$. Our objective is to force the output of the system to follow the reference trajectory given by: $y_d = 0.1\sin(t)$.

We choose $\bar{x}_2$, $\bar{x}_3$ and $\bar{x}_4$ to drive S_1, S_2 and S_3 towards zero with

$$\bar{x}_2 = \dot{x}_{1d} - K_1 S_1 = \tau_2 \dot{x}_{2d} + x_{2d}, x_{2d}(0) = \bar{x}_2(0) \tag{51}$$

$$\dot{x}_{2d} = \frac{1}{\tau_2}(-x_{2d} + \dot{x}_{1d} - K_1 S_1) \tag{52}$$

Table 1. Single-link flexible-joint robot model parameters.

Symbols	Values	Units
g	9, 81	$[m/s^2]$
M	1	$[kg]$
L	1	$[m]$
J_1	0.4	$[kg.m^2]$
J_2	0.02	$[kg.m^2]$
K	100	$[N.m/rad]$

$$\bar{x}_3 = \frac{1}{g_1}\left(\frac{\hat{\theta}_1}{J_1}\sin(x_1) + \frac{K}{J_1}x_1 + \dot{x}_{2d} - K_2 S_2\right) = \tau_3 \dot{x}_{3d} + x_{3d}, x_{3d}(0) = \bar{x}_3(0) \tag{53}$$

$$\dot{x}_{3d} = \frac{1}{\tau_3}\left(-x_{3d} + \frac{1}{g_1}\left(\frac{\hat{\theta}_1}{J_1}\sin(x_1) + \frac{K}{J_1}x_1 + \dot{x}_{2d} - K_2 S_2\right)\right) \tag{54}$$

$$\bar{x}_4 = \dot{x}_{3d} - K_3 S_3 = \tau_4 \dot{x}_{4d} + x_{4d}, x_{4d}(0) = \bar{x}_4(0) \tag{55}$$

$$\dot{x}_{4d} = \frac{1}{\tau_4}(-x_{4d} + \dot{x}_{3d} - K_3 S_3) \tag{56}$$

We choose the control u to drive S_4 towards zero with

$$u = \frac{1}{g_2}\left(-\frac{K}{J_2}(x_1 - x_3) + \dot{x}_{4d} - K_4 S_4\right) \tag{57}$$

For the swapping-based identifier we use the following filters

$$\dot{\Omega}_0 = \left(-\frac{1}{2} - \lambda\left(-\frac{\sin(x_1)}{J_1}\right)^2\right)(\Omega_0 + x_2) + \frac{K}{J_1}x_1 - g_1 x_3 \tag{58}$$

$$\dot{\Omega}^T = \left(-\frac{1}{2} - \lambda\left(-\frac{\sin(x_1)}{J_1}\right)^2\right)\Omega^T - \frac{\sin(x_1)}{J_1} \tag{59}$$

The combined direct and indirect σ-modification adaptation law is given by

$$\dot{\hat{\theta}}_1 = -\frac{\bar{\Gamma}}{J_1} S_2 \sin(x_1) - \bar{\Gamma}\sigma\left(\hat{\theta}_1 - \bar{\theta}\right), \bar{\Gamma} > 0 \tag{60}$$

where, $\bar{\theta}$ is computed with the gradient method as

$$\dot{\bar{\theta}} = \Gamma \frac{\Omega e}{1 + \nu \mathrm{tr}\{\Omega^T \Omega\}}, \Gamma = \Gamma^T > 0, \nu \geq 0. \tag{61}$$

where, $e = x_2 + \Omega_0 - \Omega^T \bar{\theta}$.

The selected initial conditions are: $x(0) = \begin{bmatrix} 0.1 & 0 & 0.1 + \frac{MgL}{K}\sin(0.1) & 0 \end{bmatrix}^T$, $\hat{\theta}_1(0) = \bar{\theta}(0) = 0$ and $\Omega_0(0) = \Omega^T(0) = 0$. The design parameters are selected as follows: $K_1 = 1$, $K_2 = 80$, $K_3 = 10$, $K_4 = 100$, $\bar{\Gamma} = 15$, $\sigma = 0.5$, $\Gamma = 20$, $\tau_2 = \tau_3 = \tau_4 = 0.009$ and $\lambda = \nu = 0.1$.

Numerical simulation results are shown in Figs. 2, 3, 4, 5, 6, 7, 8, 9, 10 and 11. Figures 2, 3, 4 and 5 show actual and desired trajectories of the angular position and velocity of the link and the motor shaft. Figures 6, 7, 8 and 9 show the trajectories of the surfaces. Figure 10 shows the trajectory of the control input signal u. Figure 11

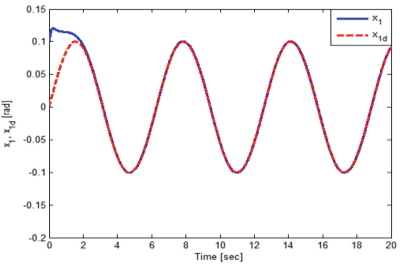

Fig. 2. Angular position of the link: actual x_1 (“−”) and desired $x_{1\mathrm{d}}$ (“− −”).

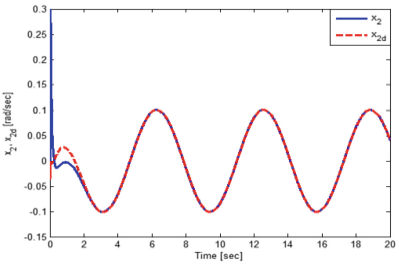

Fig. 3. Angular velocity of the link: actual x_2 (“−”) and desired $x_{2\mathrm{d}}$ (“− −”).

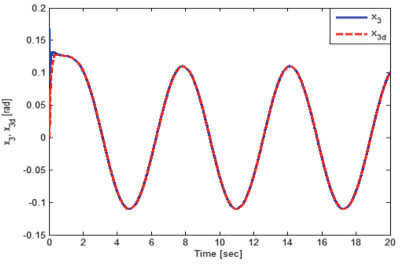

Fig. 4. Angular position of the motor shaft: actual x_3 (“−”) and desired $x_{3\mathrm{d}}$ (“− −”).

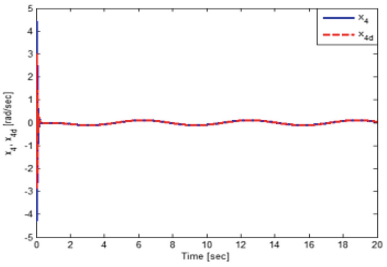

Fig. 5. Angular velocity of the motor shaft: actual x_4 (“−”) and desired $x_{4\mathrm{d}}$ (“− −”).

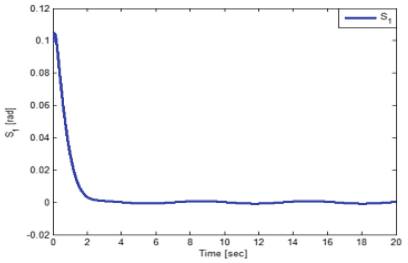

Fig. 6. Surface S_1.

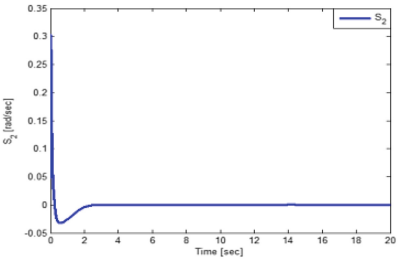

Fig. 7. Surface S_2.

shows the trajectory of the estimated parameter $\hat{\theta}_1$. From these results, we observe that the actual trajectories converge towards the desired trajectories, and that the errors converge to zero and the estimated parameter $\hat{\theta}_1$ converge towards θ_1. We can see that the results show that the proposed method has good tracking performance.

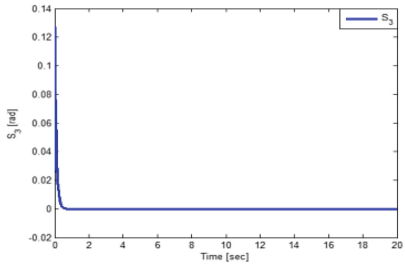

Fig. 8. Surface S_3.

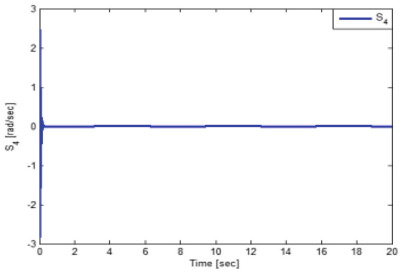

Fig. 9. Surface S_4.

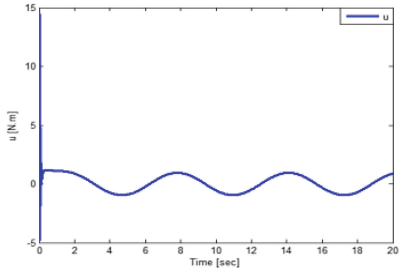

Fig. 10. Control input u.

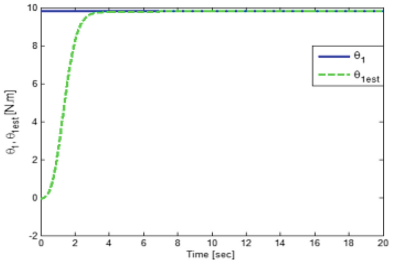

Fig. 11. Estimated parameter $\hat{\theta}_1$.

6 Conclusion

In this paper, adaptive backstepping control using combined direct and indirect σ-modification adaptation based gradient update law is designed using the DSC technique for a class of parametric strict-feedback nonlinear systems. The proposed approach eliminates the problem of explosion of complexity of the traditional backstepping approach. Stability analysis shows that the uniform ultimate boundedness of all signals in the closed-loop system can be guaranteed, and the tracking error can be made arbitrarily small by adjusting the control design parameters. Numerical simulation results demonstrate the effectiveness of the proposed approach.

References

1. Sun, G., Wang, D., Li, X., Peng, Z.: A DSC approach to adaptive neural network tracking control for pure-feedback nonlinear systems. Appl. Math. Comput. **219**(11), 6224–6235 (2013)
2. Yip, P.P., Hedrick, J.K.: Adaptive dynamic surface control: a simplified algorithm for adaptive backstepping control of nonlinear systems. Int. J. Control **71**(5), 959–979 (1998)
3. Kanellakopoulos, I., Kokotovic, P.V., Morse, A.S.: Systematic design of adaptive controllers for feedback linearizable systems. IEEE Trans. Autom. Control **36**(11), 1241–1253 (1991)

4. Krstic, M., Kanellakopoulos, I., Kokotovic, P.V.: Adaptive nonlinear control without overparametrization. Syst. Control Lett. North-Holland **19**(3), 177–185 (1992)
5. Krstic, M., Kanellakopoulos, I., Kokotovic, P.V.: Nonlinear and Adaptive Control Design. Wiley-Interscience Publication, New York (1995)
6. Swaroop, D., Gerdes, J.C., Yip, P.P., Hedrick, J.K.: Dynamic surface control of nonlinear systems. In: Proceedings of the American Control Conference, Albuquerque, New Mexico, pp. 3028–3034 (1997)
7. Swaroop, D., Hedrick, J.K., Yip, P.P., Gerdes, J.C.: Dynamic surface control for a class of nonlinear systems. IEEE Trans. Autom. Control **45**(10), 1893–1899 (2000)
8. Zhang, T.P., Ge, S.S.: Adaptive dynamic surface control of nonlinear systems with unknown dead zone in pure feedback form. Automatica **44**(7), 1895–1903 (2008)
9. Soukkou, Y., Labiod, S.: Adaptive backstepping control using combined direct and indirect adaptation based gradient update law for a single-link flexible-joint robot. In: 5th International Conference on Electrical Engineering and Automatic Control, Setif, Algeria, 24–26 November 2013
10. Soukkou, Y., Labiod, S.: Adaptive backstepping control using combined direct and indirect adaptation based least squares update law for a single-link flexible-joint robot. In: Proceedings of the 3rd International Conference on Industrial Engineering and Manufacturing, Batna, Algeria, pp. 272–279, 11–13 May 2014
11. Soukkou, Y.: Commande adaptative par backstepping d'une classe des systèmes non linéaires incertains. Magister Thesis, University of Jijel (2014)
12. Krstic, M., Kokotovic, P.V.: Adaptive nonlinear control with nonlinear swapping. In: Proceedings of the 32nd Conference on Decision and Control, San Antonio, Texas (1993)
13. Krstic, M., Kokotovic, P.V.: Adaptive nonlinear design with controller-identifier separation and swapping. IEEE Trans. Autom. Control **40**(3), 426–440 (1995)
14. Oort, E.R.V.: Adaptive backstepping control and safety analysis for modern fighter aircraft. Ph.D. Thesis, Delft University of Technology, Netherlands (2011)
15. Hou, M.Z., Duan, G.R.: Robust adaptive dynamic surface control of uncertain nonlinear systems. Int. J. Control Autom. Syst. **9**(1), 161–168 (2011)
16. Li, Y., Tong, S., Li, T.: Fuzzy adaptive dynamic surface control for a single link flexible joint robot. Nonlinear Dyn. **70**(3), 2035–2048 (2012)
17. Nicosia, S., Tomei, P.: A tracking controller flexible joint robots using only link position feedback. IEEE Trans. Autom. Control **40**(5), 885–890 (1995)

Linear Stochastic Model Validation for Civil Engineering Structures Under Earthquakes

Mohamed Azira(✉) and Lakhdar Guenfaf

LSEI Laboratory, Electrical Engineering Department, USTHB University, El Alia, BP 32, 16111 Bab Ezzouar, Algiers, Algeria
mohamed.azira@yahoo.fr, lakhdar.guenfaf@yahoo.fr

Abstract. The autoregressive moving average exogenous (ARMAX) model validation of civil engineering structure under earthquake is developed in this paper. The Kanai-Tajimi and Clough-Penzien seismic models are developed. An identification process is used to estimate the polynomial parameters for unknown simulated seismic signal in order to take into account the soil-structure interaction (SSI) within the structural model. The results show that the ARMAX model presents an interesting representation for the linear stochastic systems in control point of view. Simulation tests using a single-degree-of-freedom structure are performed to show the efficiency of introducing the SSI, by identification, in the response of the structure under the seismic ground motion.

Keywords: Dynamics of structures · ARMAX model · Seismic ground motion · Soil structure interaction · Identification

1 Introduction

The impact of control theory in the different domains of engineering and applied sciences has become increasingly important in the last few decades, and the specialists of civil engineering structures are very interested in structural control against earthquakes. One of the important missions of structural control is to ensure the safety of structures and cities in large earthquakes. In spite of the unpredicted nature and the uncertainty of the seismic phenomenon, the structural control should provide the structure the possibility to control itself during perturbation [10, 17]. Vigorous researches on structural control have given more interesting solutions; some of them have already been adopted in actual building structures. These researches have also stimulated global and interdisciplinary activities giving rise to a wide variety of interesting work in many fields [3, 10].

It has been shown in the literature that in the last two decades, control devices and algorithms have been interesting to enhance the structural control performances [17]. The performance of such systems under environmental loads has improved greatly as a result of theoretical and experimental research and related development efforts [11].

Several models of the structures have been developed in the literature. *Kareem et al.* use state-space representation of the linear stochastic model for real-time model predictive control [11]. Whereas *Sheng-Guo Wang*, *Shafieezadeh et al.*, *Purohit and*

M. Chadli et al. (eds.), *Recent Advances in Electrical Engineering and Control Applications*, Lecture Notes in Electrical Engineering 411, DOI 10.1007/978-3-319-48929-2_3

Chandiramani use the state-space model to develop different strategies of optimal control [13, 15, 16]. Indeed, *Guenfaf and Allaoua* have presented an active control strategy using a state-space model to develop the linear quadratic controller for structural vibration control [6]. Also, *J. Awrejcewicz and P. Olejnik* have presented an active control law of buildings for the general concept of stabilization against external excitations. The problem was analyzed in a two case studies for not excited and externally loaded two degrees-of-freedom dynamical system by using state-space model [2, 17]. They developed a LQR algorithm with an augmented model introducing seismic excitation as external loading. An augmented state space model is used for calculating this control law. But the excitation dynamical model is not introduced in the system model and the obtained law is deduced from deterministic criterion [12].

Nonlinear model has been presented by *Guenfaf el al.* for a Generalized Minimum Variance Gain Scheduling Controller using Nonlinear Structural Systems under Seismic Ground Motion [7]. *Ying* also presented a nonlinear model for Stochastic Optimal Control of Structural Systems [18].

In the last few years there has been increased interest in the study of soil-structure interaction (SSI) effects on the structures subjected to active control. The dynamic response of massive structures, such as high-rise buildings and dams, may be influenced by soil-structure interaction as well as the characteristics of exciting loads and structures. The effect of soil-structure interaction is noticeable especially for stiff and massive structures resting on relatively soft ground. It may alter the dynamic characteristics of the structural response significantly. As a result, these interaction effects have to be considered in the dynamic analysis of structures [5].

Although, different investigations have been conducted to soil-structure interaction analysis, depending on the modeling method for the soil region. For earthquake resistant design of critical structures, a dynamic analysis, either response spectrum or time history is frequently required. To provide input excitations to structural models for sites with no strong ground motion data, it is necessary to generate artificial excitations. In practice, it has long been established that different earthquake records show different characteristics; this is due to parameters such as geological conditions of the site, distance from the source, fault mechanism, etc. Thus, the simulated earthquake records must have realistic duration, frequency content, and intensity, representing the physical conditions of the site. Therefore, it is reasonable to identify certain parameters to measure the resulting differences in the strong ground motion data [14].

2 Dynamic Model of the Structure

In this section, a motion equation is developed for a single degree of freedom (SDOF) structure under a seismic motion as illustrated in Fig. 1. First the following assumptions are considered:

- The structure is supposed to be a lumped mass m in the beam.
- The two vertical axes are weightless and inextensible in the vertical direction with spring constant $k/2$ each.

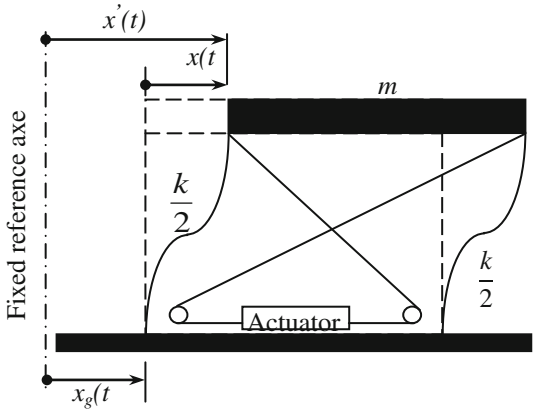

Fig. 1. Model of single degree of freedom structure

The essential physical properties of any linearly elastic structural system subjected to dynamic load include its mass, elastic properties and, energy-loss mechanism (damping), and the external source of excitation or loading. In the simplest model of

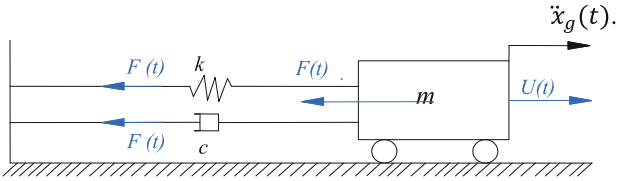

Fig. 2. Idealized SDOF structure model

SDOF system, each of these properties is assumed to be concentrated in a single physical element. The system as described is shown in Fig. 2 [4].

The entire mass m of this system is included in the rigid block. Rollers constrain this block so that it can move only in simple translation; thus the single displacement coordinate x completely defines its position. The elastic resistance of the displacement is provided by the weightless spring of stiffness k, while the energy-loss mechanism is represented by the damper c. The external-loading mechanism producing the dynamic response of this system is the time varying load $\ddot{x}_g(t)$.

The equation of motion for the system presented in Fig. 2 can be derived by directly expressing the equilibrium of all forces acting on the mass as follows:

$$m\ddot{x}'(t) + c\dot{x}(t) + kx(t) = u(t) \tag{1}$$

Where:

$$x(t)' = x(t) + x_g(t) \tag{2}$$

With $x_g(t)$ being the ground motion, and *u(t)* the external control force.
Using Eqs. (1) and (2), we have:

$$m\ddot{x}(t) + c\dot{x}(t) + kx(t) = u(t) - m\ddot{x}_g(t) \tag{3}$$

$\ddot{x}_g(t)$ is the ground acceleration.

Here, we developed the dynamic model of single-degree-of-freedom structure with its physical characteristics submitted to a seismic motion.

3 Seismic Dynamic Model

The aim of this work is to develop a model which takes into account the soil-structure

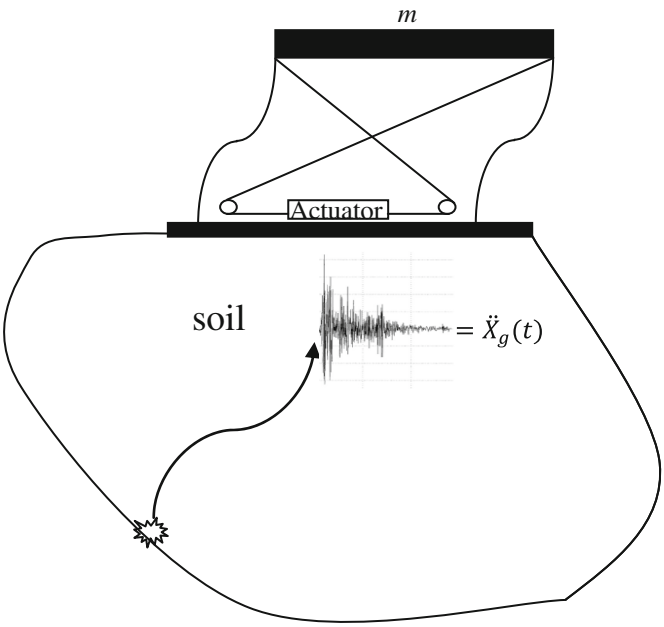

Fig. 3. Structural model under seismic motion

interaction in order to have a response which represents closely the displacement of the structure under the seismic motion (ε: the smaller the better) as shown in Fig. 3. For this, the ground motion model is given, so that the earthquake will be a white noise filtered by a function taken into account the specific soil parameters in where the structure is built as we can see it in Fig. 6.

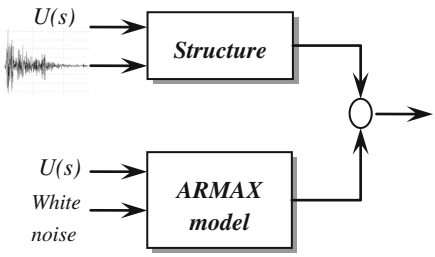

Fig. 4. Block diagram of comparing structural model with the ARMAX model

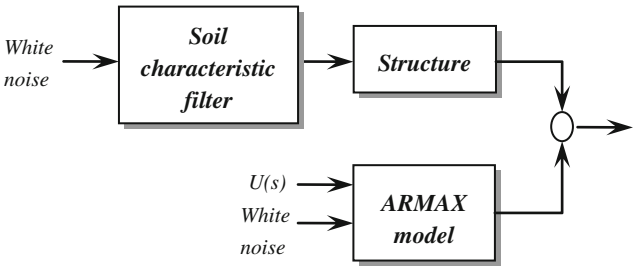

Fig. 5. Block diagram of comparing structural model with introducing soil characteristics (SSI) and the ARMAX model

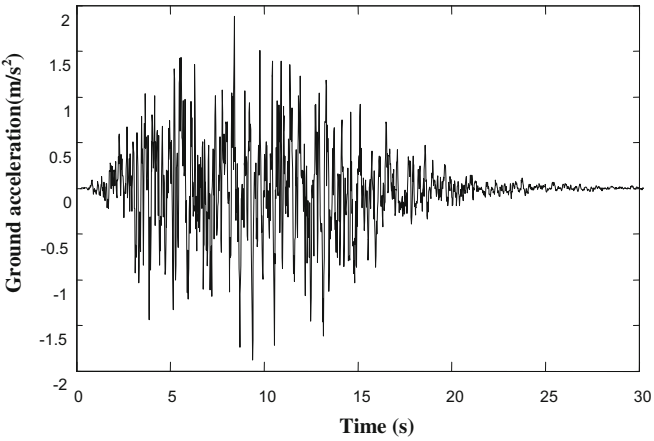

Fig. 6. Kanai-Tajimi seismic model simulated

To formulate an optimal problem, it is necessary to specify the process dynamics and its environment. It is assumed that the influence of the environment can be characterized by disturbances which are stochastic process [1]. As the system is linear,

we can represent all disturbances as single disturbance acting on the output as shown in Figs. 4 and 5.

Kanai-Tajimi and Clough-Penzien have presented a seismic model based on a filtered white noise depending on soil characteristics.

The earthquake ground acceleration is modeled as a uniformly modulated non-stationary random process [10].

$$\ddot{x}_g(t) = \psi(t)\ddot{x}_s(t) \tag{4}$$

Where $\psi(t)$ a deterministic non-negative envelope is function and $\ddot{x}_s(t)$ is a stationary random process with zero mean and a Kanai-Tajimi power spectral density.

$$\Phi_g(\omega) = \left[\frac{1+4\xi_g^2(\frac{\omega}{\omega_g})^2}{(1-\left(\frac{\omega}{\omega_g}\right)^2)^2+4\xi_g^2(\frac{\omega}{\omega_g})^2}\right] S_0^2 \tag{5}$$

Where ξ_g, ω_g filter parameters which depend on the site soil characteristics and S0 are is the constant spectral density of the white noise which reflects the seismic intensity [4]. Using such a second high-pass filter the Kanai-Tajimi spectrum is modified as follows to obtain the Clough-Penzien spectrum:

$$\Phi_c(\omega) = \left[\frac{1+4\xi_g^2(\frac{\omega}{\omega_g})^2}{(1-\left(\frac{\omega}{\omega_g}\right)^2)^2+4\xi_g^2(\frac{\omega}{\omega_g})^2}\right]\left[\frac{(\frac{\omega}{\omega_c})^4}{(1-\left(\frac{\omega}{\omega_c}\right)^2)^2+4\xi_c^2(\frac{\omega}{\omega_c})^2}\right] S_0^2 \tag{6}$$

A particular envelope function $\psi(t)$ given below will be used:

$$\psi(t) = \begin{cases} 0 & for\ t<0 \\ \left(\frac{t}{t_1}\right)^2 & for\ 0\le t\le t_1 \\ 1 & for\ t_1\le t\le t_2 \\ exp[-a(t-t_2)] & for\ t\ge t_2 \end{cases} \tag{7}$$

Where t_1, t_2 and a are parameters that should be selected appropriately to reflect the shape and the duration of the earthquake ground acceleration. Numerical values of parameters are t1 = 3 s, t2 = 13 s, a = 0.26, ξ_g = 0.65, ω_g = 19 rad/s, S0 = 0.8*10 −2 m/s [7, 9] (Fig. 7).

4 ARMAX Model of the Structure

Determination of the ARMAX model of the structure under seismic excitation can be done using equation of motion (3).

After dividing this equation by m and introducing the notations below Eq. (3) becomes

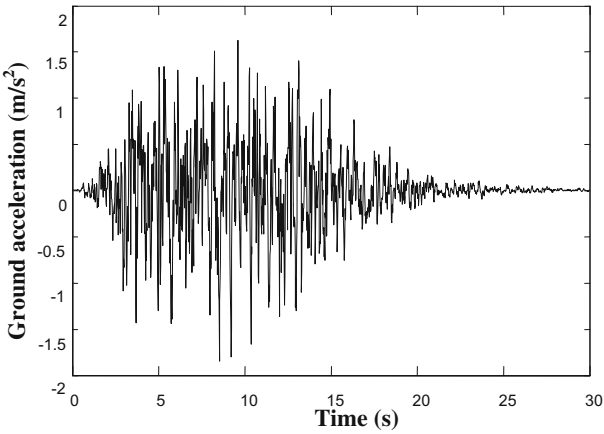

Fig. 7. Clough-Penzien seismic model simulated

$$\ddot{x}(t) + 2\xi\omega_0\dot{x}(t) + \omega_0^2 x(t) = \frac{1}{m}u(t) - \ddot{x}_g(t) \tag{8}$$

Applying Laplace transform to Eq. (8), we obtain

$$X(s) = \frac{\frac{1}{m}}{s^2 + 2\xi\omega_0 s + \omega_0^2}U(s) - \frac{1}{s^2 + 2\xi\omega_0 s + \omega_0^2}\ddot{X}_g(s) \tag{9}$$

Where $X(s)$, $\ddot{X}_g(s)$ and $U(s)$ are the Laplace transform of *x(t)*, $\ddot{x}_g(t)$ and *u(t)* respectively.

Depending on the model of seismic excitation, different ARMAX models can be obtained, and the following cases [8]:

The seismic excitation model is unknown or is not taken into consideration. Equation (9) has the form:

$$X(s) = \frac{H_{1N}(s)}{H_D(s)}U(s) + \frac{H_{2N}(s)}{H_D(s)}\ddot{X}_g(s) \tag{10}$$

The ARMAX model of the structure is obtained by discretization of Eq. (10) using computer programs (MATLAB R2010a).

$$x(t) = \frac{B(q^{-1})}{A(q^{-1})}u(t) + \frac{C(q^{-1})}{A(q^{-1})}\ddot{x}_g(t) \tag{11}$$

Kanai-Tajimi model: In this case we take into consideration the SSI. The ground acceleration is described by the Kanai-Tajimi model as shown in Fig. 8 and in the following equation:

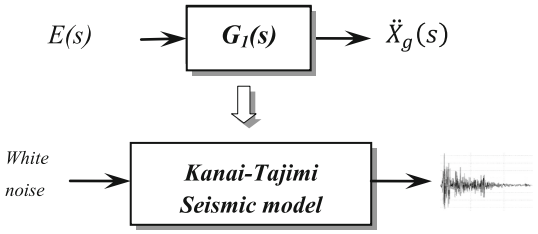

Fig. 8. Block diagram of the structural Kanai-Tajimi model.

$$\ddot{X}_g(s) = G_1(s)E(s) \tag{12}$$

Where

$$G_1(s) = \frac{G_{1N}(s)}{G_{1D}(s)} = \left(2\xi_g\omega_g s + \omega_g^2\right)/(s^2 + 2\xi_g\omega_g s + \omega_g^2)$$

And *E(s)* is the Laplace transform of white noise.

Clough-Penzien model: In this case the ground acceleration is described by Clough-Penzien model and introduced in the dynamic model of the structure as shown in Fig. 9. This excitation is described by the following equations.

$$\ddot{X}_g(s) = G_2(s)E(s) \tag{13}$$

Where $G_2(s) = \frac{G_{2N}(s)}{G_{2D}(s)} = \left(\frac{2\xi_g\omega_g s + \omega_g^2)}{s^2 + 2\xi_g\omega_g s + \omega_g^2}\right)\left(\frac{s^2}{s^2 + 2\xi_c\omega_c s + \omega_c^2}\right)$

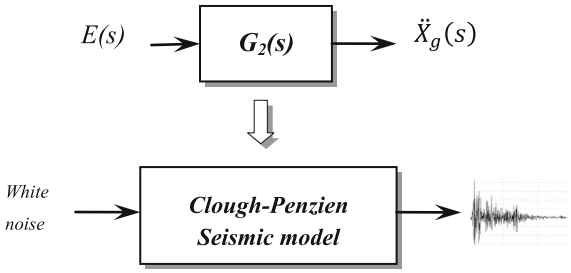

Fig. 9. Block diagram of the structural Clough-Penzien model.

It has been shown that the response without taking the SSI into account is not close to the structural one. Also, it has been presented a model taking wrong soil parameters into account, whereas, the best results has been given by the model response which included SSI with the right parameters [8].

5 ARMA Model Identification

According to the previous results, it is suitable to use an identification process to estimate the parameters of unknown earthquakes. We can find in the literature several identification algorithms such as 'recursive least square' (RLS) one, as represented in Fig. 10.

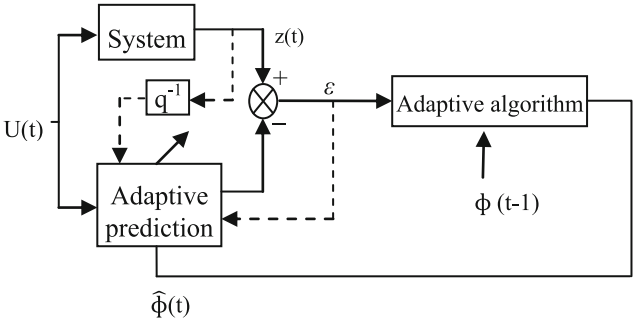

Fig. 10. Block diagram of the recursive identification method.

The recursive least square identification algorithm has been used to estimate the model parameters. It is based on the minimization of a quadratic criterion as follows:

$$J(t) = \sum_{i=0}^{t} [z(i) - \hat{z}(i)]^2 = \sum_{i=0}^{t} \varepsilon^2(t) \tag{14}$$

With
z(t) Actual output of the system, $\hat{z}$(t) Model output, ε Error.

$$\hat{z}(t) = \hat{\theta}^T(t)\phi(t-1) \tag{15}$$

With

$$\hat{\theta}^T(t) = [\widehat{a_1}, \ldots, \widehat{a_n}, \widehat{c_1}, \ldots, \widehat{c_l}] \tag{16}$$

$$\phi^T = [-z(t-1), .., -z(t-n), \varepsilon(t-1), .., \varepsilon(t-l)]$$

Where

$$J(t) = \sum_{i=0}^{t} \left[z(i) - \hat{\theta}^T(i)\phi(i-1)\right]^2 \tag{17}$$

The minimization of J gives the parametric adaptation of recursive least square algorithm:

$$\hat{\theta}(t+1) = \hat{\theta}(t) + F(t)\phi(t)\varepsilon(t+1) \tag{18}$$

$$F(t+1)^{-1} = F(t)^{-1} + \phi(t)\phi(t)^{T} \tag{19}$$

$$F(t+1) = F(t) - \frac{F(t)\phi(t)\phi(t)^{T}F(t)}{1+\phi(t)^{T}F(t)\phi(t)} \tag{20}$$

$$\varepsilon(t+1) = \frac{z(t+1) - \hat{\theta}^{T}(t)\phi(t)}{1+\phi(t)^{T}F(t)\phi(t)} \tag{21}$$

With F(t) is the adaptation of the gain matrix.

We consider in this paper a structure under an unknown earthquake. For this, a simulated seismic signal is carried out which is a linear combination between the Kanai-Tajimi and the Clough-Penzien models (described by Eqs. (12) and (13) respectively) as follows (Fig. 11):

$$\ddot{X}_n = 1/2(G_1(s) + G_2(s))E(s) \tag{22}$$

In order to show the effect of the SSI, we compare both the structural and the ARMA model responses following the cases:

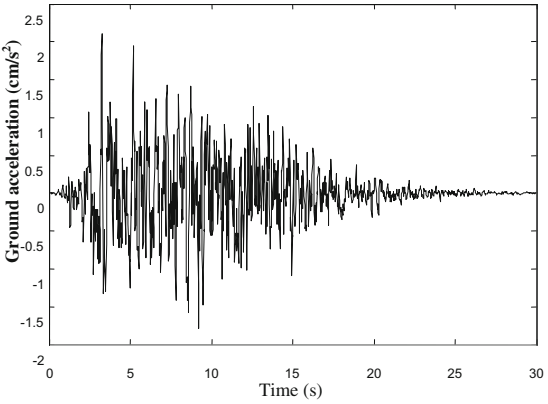

Fig. 11. Simulated earthquake ($\ddot{X}_n$)

Case 1: We compare the structural response model with the ARMA one described by Eq. (11), without introducing the soil characteristics (without considering SSI). Figure 12 shows the block diagram which calculates the error (ε) between the structural response and the ARMA model response with no control force (open loop).

Case 2: In this case, we have taken the estimated ARMA model with taking into account the soil-structure interaction. The soil characteristics had been identified by RLS algorithm and introduced in the structural model with no control force (U(s) = 0) as it is shown in Fig. 13.

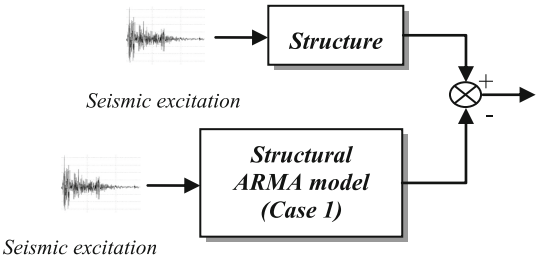

Fig. 12. Comparing model responses without considering soil-structure interaction (*Case 1*)

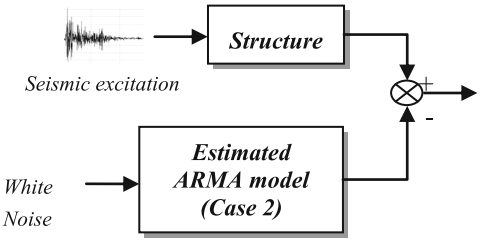

Fig. 13. Comparing model responses with considering soil-structure interaction (*Case 2*)

6 Simulation Results

A single-degree-of-freedom (SDOF) structure with the following structural properties is used [8, 9] m = 2921 kg, k = 1389kN/m, ξ = 0.0124. The sampling period Te = 0.02 s.

The Table 1 shows the error variance between structural response and the ARMAs models in different cases.

Table 1. Different error's variance

Cases	Case 1	Case 2
Errors variance ($\boldsymbol{\delta}^2$)	5.6524e-007	4.8807e-008

Parameters of ARMA model for the different cases are shown in the Table 2.

Simulations results have shown that the response without taking SSI into account is not close to the structural response as represented in Figs. 14 and 16. Whereas it is shown that the best results are obtained when we consider the soil characteristics (estimated model) as presented in Figs. 15 and 17.

Table 2. Parameters of ARMA models

	Case 1	Case 2
a_0	1	1
a_1	−1.803	−3.4003
a_2	0.9892	4.5455
a_3	–	−2.7995
a_4	–	0.6689
c_0	0	0
c_1	$-1.961*10^{-4}$	$0.2872*10^{-4}$
c_2	$-1.954*10^{-4}$	$0.8853*10^{-4}$
c_3	–	$-0.7033*10^{-4}$
c_4	–	$-0.2634*10^{-4}$

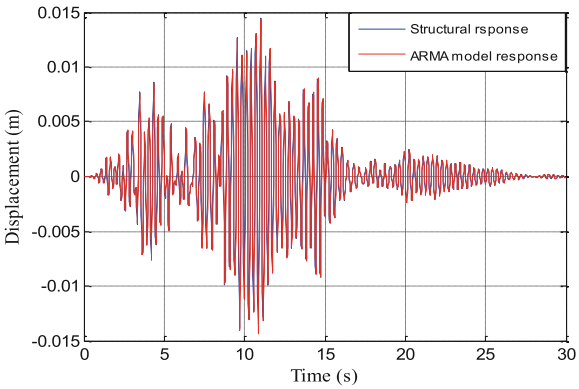

Fig. 14. Model responses under an unknown earthquake (Case 1).

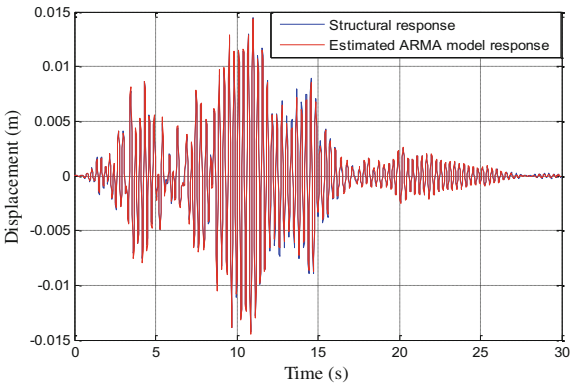

Fig. 15. Model responses under an unknown earthquake (Case 2).

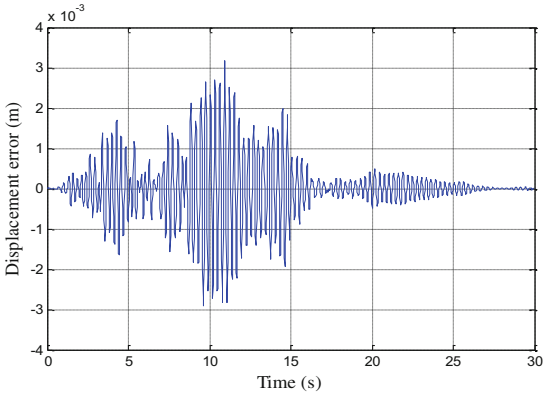

Fig. 16. Model error responses (Case 1).

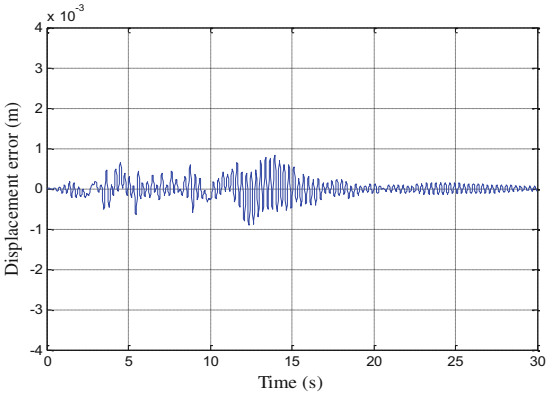

Fig. 17. Model error responses (Case 2).

7 Conclusions

The autoregressive moving average exogenous (ARMAX) of the structure has been developed in this paper. The Kanai-Tajimi and Clough-Penzien Seismic models have been presented and introduced in the dynamic of the structure. The earthquake signal identification study has been carried out and has given us the possibility to introduce the SSI within the structural ARMA model. We have chosen as example a structure built upon unknown soil. A simulated seismic signal has been formulated by a linear combination between Clough-Penzien and Kanai-Tajimi characteristics. The results leads us to conclude that the ARMA model with introducing SSI represents faithfully the complete structural model under a seismic ground motion.

References

1. Åström, K.J.: Computer-Controlled Systems. Prentice Hall Inc., Englewood Cliffs (1990)
2. Awrejcewicz, J., Olejnik, P.: Active control of two degrees-of-freedom building-ground system. Arch. Control Sci. **17**(4), 393–408 (2007)
3. Awrejcewicz, J., Tomczak, K., Lamarque, C.-H.: Controlling system with impacts. Int. J. Bifurcat. Chaos **9**(3), 547–553 (1999)
4. Clough, R.W., Penzien, J.: Dynamics of Structures. McGraw-Hill, New York (1993)
5. Luco, E.J.: A simple model for structural control including soil-structure interaction effects. Earthquake Eng. Struct. Dynam. **27**, 225–242 (1998)
6. Guenfaf, L., Allaoua, S.: Optimal choice of actuator for AMD linear quadratic controller. J. Electr. Control Eng. **3**(3), 31–38 (2013)
7. Guenfaf, L., Allaoua, S., Djebiri, M., Boucherit, M.S., Boujema, F.: Generalized minimum variance gain scheduling controller for nonlinear structural systems under seismic ground motion. J. Electr. Syst. **8**(4), 472–480 (2012)
8. Guenfaf, L., Azira, M.: ARMAX model calculation for structures under seismic ground motion including soil-structure interaction. J. Electr. Control Eng. **4**(1), 8–15 (2013)
9. Guenfaf, L., Djebiri, M., Boucherit, M.S., Boudjema, F.: Generalized minimum variance control for buildings under seismic motion. Earthquake Eng. Struct. Dynam. **30**, 945–960 (2001)
10. Kobori, T.: Future perspective of structural control in earthquake engineering. In: 12th World Conference on Earthquake Engineering, Auckland, New Zealand, 30 January – 4 February 2000, vol. 2841 (2000)
11. Mei, G., Kareem, A., Kantor, J.C.: Real-time model predictive control. Earthquake Eng. Struct. Dynam. **30**, 995–1019 (2001)
12. Olejnik, P., Awrejcewicz, J.: One-dimensional discrete LQR control of compression of the human chest impulsively loaded by fast moving point mass. Commun. Nonlinear Sci. Numer. Simul. **16**(5), 2225–2229 (2010)
13. Purohit, S., Chandiramani, N.K.: Optimal static output feedback control. Struct. Control Health Monit. **18**, 852–868 (2011)
14. Rofooei, F.R., Mobarake, A., Ahmadi, G.: Generation of artificial earthquake records with a nonstationary Kanai-Tajimi model. Eng. Struct. **23**, 827–837 (2001)
15. Shafieezadeh, A., Ryan, K., Chen, Y.Q.: Fractional order filter enhanced LQR for seismic protection of civil structures. J. Comput. Nonlinear Dyn. **3**(2), 021404 (2008). doi:10.1115/1.2833947. Pages 7
16. Wang, S.-G.: LQG-α control and its simulations for structural benchmark problems against winds and earthquakes. In: Proceedings of the 42nd IEEE Conference on Decision and Control, Maui, Hawaii USA, vol. 6, pp. 6572–6577, December 2003
17. Spencer Jr., B.F., Nagarajaiah, S.: State of the art of structural control. J. Struct. Eng. **129**(7), 845–856 (2003)
18. Ying, Z.G.: Stochastic optimal control of structural systems. Open Autom. Control Syst. J. **1**, 44–49 (2008)

Adaptive Fuzzy Control-Based Projective Synchronization Scheme of Uncertain Chaotic Systems with Input Nonlinearities

Sarah Hamel(✉) and Abdesselem Boulkroune

Department of Electronic, LAJ Laboratory, University of Jijel, BP. 98, Ouled-Aissa, 18000 Jijel, Algeria
m. sarahamel@gmail. com, boulkroune2002@yahoo. fr

Abstract. In this paper, a projective synchronization scheme for a class of master–slave chaotic systems subject to dynamic disturbances and input nonlinearities (dead-zone and sector nonlinearities) is investigated. To practically achieve this synchronization, an adaptive fuzzy variable-structure control system is designed. The fuzzy systems are used to appropriately approximate the uncertain nonlinear functions. A Lyapunov approach is employed to prove the boundedness of all signals of the closed-loop control system as well as the exponential convergence of the synchronization errors to an adjustable region. Simulations results are presented to illustrate the effectiveness of the proposed projective synchronization scheme.

Keywords: Projective synchronization · Adaptive control · Fuzzy control · Dead-zones · Uncertain chaotic system

1 Introduction

Chaos synchronization is an important topic in nonlinear science. It has received increasing attention thanks to their applications in information processing, secure communications, pattern recognition, power convertors, chemical reactions, laser systems, ecological and biological systems, and so on [1–5]. The initial configuration of chaos synchronization consists of master-slave systems. The master system drives the slave one via the transmitted signals. In the past two decades, various types of the chaos synchronization have been revealed, such as complete synchronization (CS) [6], phase synchronization (PHS) [7], projective synchronization (PS) [8, 9], and so on. In PS, the state vectors of two synchronized systems evolve in a proportional scale.

Based on the universal approximation theorem [10], many adaptive fuzzy control systems have been incorporated in the synchronization schemes [11–16] to solve the problem of uncertainties. The problem of the input nonlinearities has been also considered in [17–19] in the designing of the control-based synchronization systems for a class of uncertain chaotic systems. However, the class of chaotic systems considered in these works is relatively simple, affine and free of the dynamical disturbances.

Therefore, in this paper, we aim at addressing the projective synchronization problem of a class of multivariable nonaffine chaotic systems subject to both dynamic

M. Chadli et al. (eds.), *Recent Advances in Electrical Engineering and Control Applications*, Lecture Notes in Electrical Engineering 411, DOI 10.1007/978-3-319-48929-2_4

disturbances and input nonlinearities. This synchronization can be achieved via a suitable fuzzy adaptive variable-structure controller. The main difficulties of this work are how to deal with unknown nonlinear functions, nonaffine multivariable control, the uncertain input nonlinearities and the combined effect of the uncertain dynamic disturbances, fuzzy approximation errors together with the higher-order terms (HOT) issued from the use of the Taylor series expansion. In this study, these difficulties can be, respectively, solved by fuzzy system approximation, Taylor series expansion, variable structure control and robust dynamical control. A Lyapunov approach is adopted to carry out the parameter adaptation design, the convergence of the synchronization error and the stability analysis involved in this proposed synchronization scheme. The main contributions of this paper lie in the following:

(1) A new projective synchronization scheme based on fuzzy adaptive controller is proposed for uncertain perturbed chaotic systems with input nonlinearities (i.e. dead-zone and sector nonlinearities).
(2) The model of the considered chaotic systems is assumed to be completely unknown (except its relative degree), multivariable, nonaffine in control, subject to both input nonlinearities and dynamical disturbances. To our best knowledge, such a class of chaotic systems with all these features has not been already studied in the literature.

The rest of the paper is organized in the following manner. Section 2 presents the problem formulation and preliminaries, followed by the design of fuzzy adaptive controller to practically achieve a projective synchronization in Sect. 3. The simulation results are presented to demonstrate the effectiveness of proposed synchronization scheme in Sect. 4. Section 5 contains the conclusion.

2 Problem Statements and Preliminaries

Consider the following class of uncertain chaotic master systems:

$$\dot{Y} = H_1(Y) \tag{1}$$

where $Y = [y_1, \ldots, y_n]^T \in R^n$ is the overall state vector of the master system which is assumed to be measureable. $H_1(Y) = [h_{11}(Y), \ldots, h_{1n}(Y)]^T \in R^n$ is a vector of smooth unknown nonlinear functions.

The uncertain chaotic multivariable slave system affected by unknown dynamic disturbances can be given as:

$$\dot{X} = H_2(X, v) + \wedge(X) \tag{2}$$

Where $X = [x_1, \ldots .., x_n]^T \in R^n$ is the overall state vector of the slave system which is assumed to be measureable. $H_2(X, v) = [h_{21}(X, v), \ldots .., h_{2n}(X, v)]^T \in R^n$ denotes unknown nonaffine functions vector, with $v = \varphi(u) = \varphi_1(u_1), \ldots, \varphi_n(u_n)]^T$ is a

nonlinear input functions vector satisfying some properties which will be given later and $\wedge(X) = [\wedge_1(X), \ldots, \wedge_n(X)]^T$ is the unknown external disturbance vector.

Assumption 1: *The matrix $\partial H_2(X, v)/\partial v$ is non-singular and its sign is assumed to be known.*

Design Objective: *Determine an adaptive fuzzy variable- structure law u_i (for all i = 1, ...,n) which achieves a practical projective synchronization between the master system (1) and the slave one (2) and ensures the boundedness of all the signals in the derived closed-loop system remain.*

To quantify this objective, we define the *synchronization error* between systems (1) and (2) for this PS, as follows

$E = X - BY$, with $E = (e_1, \ldots, e_n)^T$, $B = Diag(b_1, \ldots, b_n)$
and $e_i = x_i - b_i y_i$ $(i = 1, 2, \ldots, n)$.

Definition 1: *For the master system (1) and the slave system (2), there is said to be projective synchronization if there exists a nonzero constant B such that $lim_{t\to\infty}\|X - BY\| = 0$, where $\|.\|$ represents the Euclidean norm.*

Definition 2: *The PS is said to be practically achieved, if there exists a strictly positive constant ε such that $lim_{t\to\infty}\|X - BY\| \le \varepsilon$, where ε depends on the design parameters.*

The dynamics of the synchronization error vector are

$$\dot{E} = H_2(X, v) + \wedge(X) - BH_1(Y) \tag{3}$$

Let us define a PI sliding surface as follows:

$$S = [S_1, S_2, \ldots, S_n]^T = \frac{d\left[\int_0^t E(\tau)d\tau\right]}{dt} + \lambda\left[\int_0^t E(\tau)d\tau\right] = E + \lambda\int_0^t E(\tau)d\tau \tag{4}$$

where λ is a positive design constant. The time derivative of S is given by

$$\dot{S} = H_2(X, v) + \wedge(X) - BH_1(Y) + \lambda E \tag{5}$$

By means of Taylor series expansion, the nonaffine system (5) can be transformed into an affine system in control, around an unknown ideal control $v = v^*(X)$ as follows:

$$H_2(X, v) = F(X) + G(X)v + HOT(X, v) \tag{6}$$

with

$$G(X) = [g_{ij}(X)] = \left[\frac{\partial H_2(X, v)}{\partial v}\right]_{v=v^*(X)}$$

and

$$F(X) = H_2(X, v^*(X)) - \left[\frac{\partial H_2(X,v)}{\partial v}\right]_{v=v^*(X)} v^*(X)$$

where $HOT(X, v)$ is the higher order terms (HOT) of the expansion, and $v = v^*(X)$ is an unknown smooth function minimizing the HOT.

Since the matrix $G(X)$ is not necessarily symmetric, the following important lemma will be used in the control design and the stability analysis [20–23]:

Lemma 1: *Any real matrix $G(X) \in R^{n\times n}$ with non-zero leading principal minors can be factorized as follows:*

$$G(X) = G_s(X)DT(X) \tag{7}$$

where $G_s(X) \in R^{n\times n}$ is a symmetric and positive-definite matrix, $D \in R^{n\times n}$ is a diagonal matrix with +1 or −1 on its diagonal, and $T(X) \in R^{n\times n}$ is a unity upper-triangular matrix. The diagonal elements of Dare nothing else than the ratios of the signs of the leading principal minors of $G(X)$.

Using the matrix factorization (7) and the expression (6), the dynamics of S can be expressed as follows:

$$\dot{S} = F(X) + G_s(X)DT(X)\varphi(u) + HOT(X, \varphi(u)) + \wedge(X) - H_3(Y, E) \tag{8}$$

where

$$H_3(Y, E) = BH_1(Y) - \lambda E \tag{9}$$

Assumption 2: *The matrix $G(X)$ is of class C^1 and satisfies the following property:*

$$\frac{1}{2}\left\|\frac{dG_s(X)}{dt}\right\| = \frac{1}{2}\left\|\frac{\partial G_s(X)}{\partial X}\dot{X}\right\| \le \bar{g}(X),$$

where $\bar{g}(X)$ is an unknown positive function.

A. Input Nonlinearity. The mathematical model of the input nonlinearity $\varphi(u) = [\varphi_1(u_1), \ldots, \varphi_n(u_n)]^T$ under consideration (i.e. sector nonlinearity and dead-zone) is given by [17]:

$$\varphi_i(u_i) = \begin{cases} \varphi_{i+}(u_i)(u_i - u_{i+}), & u_i > u_{i+} \\ 0, & -u_{i-} \le u_i \le u_{i+} \\ \varphi_{i-}(u_i)(u_i + u_{i-}), & u_i < -u_{i-} \end{cases} \tag{10}$$

where $\varphi_{i+}(u_i) > 0$ and $\varphi_{i-}(u_i) > 0$ are nonlinear functions of u_i, and $u_{i+} > 0$ and $u_{i-} > 0$.

We can show that $\varphi_i(u_i)$ satisfies the following properties:

$$\begin{aligned}(u_i - u_{i+})\varphi_i(u_i) &\geq m^*_{i+}(u_i - u_{i+})^2,\ u_i > u_{i+},\\ (u_i + u_{i-})\varphi_i(u_i) &\geq m^*_{i-}(u_i + u_{i-})^2,\ u_i < -u_{i-},\end{aligned} \tag{11}$$

where m^*_{i+} and m^*_{i-} are strictly positive constants witch called *"gain reduction tolerances"*.

Assumption 3: *Assume that:*

(a) *The functions* $\varphi_{i+}(u_i)$ *and* $\varphi_{i-}(u_i)$ *and the constants* m^*_{i+} *and* m^*_{i-} *are uncertain,*
(b) *The constants* u_{i+} *and* u_{i-} *are known and strictly positive.*

B. Description of the Fuzzy Logic System. The fuzzy system is based on particular knowledge of four main modules, namely: the rule base, fuzzifier, the inference engine and defuzzifier, as shown in Fig. 1.

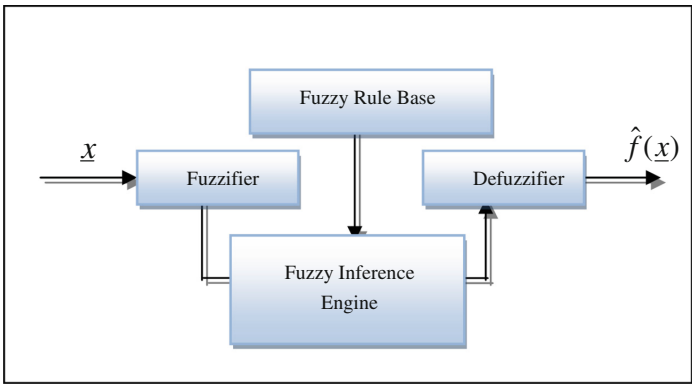

Fig. 1. Basic configuration of a fuzzy logic system.

The fuzzy inference engine uses the IF–THEN rules to achieve a mapping from an input vector $\underline{x}^T = [x_1, x_2, \ldots, x_n] \in R^n$ to an output scalar $\hat{f} \in R$. The ith fuzzy rule can be written as:

$$R^{(i)}: \textit{if } x_1 \textit{ is } A^i_1 \textit{ and}\ldots\textit{and } x_n \textit{ is } A^i_n \textit{ then } \hat{f} \textit{ is } f^i \tag{12}$$

where $A^i_1, A^i_2, \ldots\ldots$ and A^i_n are fuzzy sets and f^i is the fuzzy singleton for the output in the ith rule. The fuzzy-logic system can be expressed in the following form:

$$\hat{f}(\underline{x}) = \frac{\sum_{i=1}^{m}\left(f^i \prod_{j=1}^{n} \mu_{A^i_j}(x_j)\right)}{\sum_{i=1}^{m}\prod_{j=1}^{n}\mu_{A^i_j}(x_j)} = \theta^T \psi(\underline{x}) \tag{13}$$

where $\mu_{A_j^i}(x_j)$ is the membership function of A_j^i, m is the number of fuzzy rules, $\theta^T = [f^1, f^2, \ldots, f^m]$ is the adjustable parameter vector (composed of consequent parameters), and $\psi^T = [\psi^1 \psi^2 \ldots \psi^m]$ with

$$\psi^i(\underline{x}) = \frac{\prod_{j=1}^{n} \mu_{A_j^i}(x_j)}{\sum_{i=1}^{m} \left(\prod_{j=1}^{n} \mu_{A_j^i}(x_j) \right)} \tag{14}$$

being the fuzzy basis function (FBF). Throughout the paper, it is assumed that the FBFs are properly chosen so that there is always at least one active rule, i.e. $\sum_{i=1}^{m} (\prod_{j=1}^{n} \mu_{A_j^i}(x_j)) > 0$, [10].

3 Design of Fuzzy Adaptive Controller

Multiplying the Eq. (8) by $G_s^{-1}(X)$ and by posing $\bar{S} = D^{-1}S$ or $\bar{S}_i = d_{ii}S_i$ (as $D^{-1} = D^T = D$ and $d_{ii} = +1 \; or \; -1$), we get

$$G_1(X)\dot{\bar{S}} = D^{-1}F_1(X,Y) + \varphi(u) + D^{-1}P(X, \varphi(u)) \tag{15}$$

where $G_1(X) = D^{-1}G_s^{-1}(X)D$,
$F_1(X,Y) = G_s^{-1}(X)[F(X) - H_3(Y,E)] + [DT(X) - D]\varphi(u)$,
$P(X, \varphi(u)) = G_s^{-1}(X)HOT(X, \varphi(u)) + G_s^{-1}(X)\Lambda(X)$.
The dynamics (15) can be rewritten as follows

$$\frac{1}{2}\dot{G}_1(X)\bar{S} + G_1(X)\dot{\bar{S}} = \alpha(z) + \varphi(u) + \frac{1}{2}\dot{G}_1(X)\bar{S} - \bar{g}(X)\bar{S} + R(X, \varphi(u)) \tag{16}$$

with $R(X, \varphi(u)) = D^{-1}P(X, \varphi(u))$,

$$\alpha(z) = [\alpha_1(z_1), \ldots, \alpha_n(z_n)]^T = \bar{g}(X)\bar{S} + D^{-1}F_1(X,Y) \tag{17}$$

where $z = [z_1^T, \ldots, z_n^T]^T$. The vectors z_i will be determined later.

Assumption 4: *There exists an unknown continuous positive function* $\bar{\alpha}_i(z_i)$ *such that:* $|\alpha_i(z_i)| \leq \eta\bar{\alpha}_i(z_i), \forall z_i \in \Omega_{z_i}$ *with* $\eta = min\{m_{i+}^*, m_{i-}^*\}$ *for* $i = 1, \ldots, n$.

By examining the expressions of $F_1(X,Y,u)$ and $\alpha(z)$, and because the state vector of the master system *Y*is always bounded, the vectors z_i can be determined as follows:

$$\begin{aligned} z_1 &= [X^T, u_2, \ldots, u_n]^T \\ z_2 &= [X^T, u_3, \ldots, u_n]^T \\ &\vdots \\ z_{n-1} &= [X^T, u_n]^T \\ z_n &= X \end{aligned} \tag{18}$$

The corresponding operating compact sets are defined as follows:

$$\Omega_{z_i} = \left\{ [X^T, u_{i+1}, \ldots, u_n]^T | X \in \Omega_X \subset R^n, Y \in \Omega_Y \right\},$$
$$\Omega_{z_n} = \{ X | X \in \Omega_X \subset R^n \}.$$

It is clear that z_1 depends on control inputs $u_2, \ldots, u_n, z_2$ depends on $u_3, \ldots, u_n$, and so on. In fact, the structure of the nonlinearities $\alpha(z)$ is known under the name *"upper triangular control structure"*.

The unknown nonlinear function $\bar{\alpha}_i(z_i)$ can be approximated, on the compact set Ω_{z_i}, by the fuzzy systems (13) as follows:

$$\hat{\bar{\alpha}}_i(z_i, \theta_i) = \theta_i^T \psi_i(z_i), \quad with\, i = 1, \ldots, n \tag{19}$$

where $\psi_i(z_i)$ is the fuzzy basis function (FBF) vector, which is fixed a priori by the designer, and θ_i is the adjustable parameter vector of the fuzzy system. Then, we define:

$\theta_i^* = \arg min \left[sup | \bar{\alpha}_i(z_i) - \hat{\bar{\alpha}}_i(z_i, \theta_i) | \right]$ as the optimal value of θ_i which is mainly introduced for analysis purposes as its value is not needed when implementing the controller.

Define

$$\begin{aligned} \tilde{\theta}_i &= \theta_i - \theta_i^* \\ \varepsilon_i(z_i) &= \bar{\alpha}_i(z_i) - \hat{\bar{\alpha}}_i\left(z_i, \theta_i^*\right) = \bar{\alpha}_i(z_i) - \theta_i^{*T} \psi_i(z_i) \end{aligned} \tag{20}$$

as the parameter estimation error and the fuzzy approximation error, respectively. As in [10, 17–22], the fuzzy approximation error is assumed to be bounded for all $z_i \in \Omega_{z_i}$, i.e.:

$$|\varepsilon_i(z_i)| \leq \bar{\varepsilon}_i \ , \ \forall z_i \in \Omega_{z_i} \tag{21}$$

where $\bar{\varepsilon}_i$ is an unknown constant.

Now, let us denote

$$\begin{aligned} \hat{\bar{\alpha}}(z, \theta) &= \left[\hat{\bar{\alpha}}_1(z_1, \theta_1), \ldots, \hat{\bar{\alpha}}_n(z_n, \theta_n) \right]^T = \left[\theta_1^T \psi_1(z_1), \ldots, \theta_n^T \psi_n(z_n) \right]^T \\ \varepsilon(z) &= [\varepsilon_1(z_1), \ldots, \varepsilon_n(z_n)]^T, \\ \bar{\varepsilon}(z) &= [\bar{\varepsilon}_1, \ldots, \bar{\varepsilon}_n]^T. \end{aligned}$$

Then, we have

$$\begin{aligned} \hat{\bar{\alpha}}(z, \theta) - \bar{\alpha}(z) &= \hat{\bar{\alpha}}(z, \theta) - \hat{\bar{\alpha}}(z, \theta^*) + \hat{\bar{\alpha}}(z, \theta^*) - \bar{\alpha}(z) \\ &= \hat{\bar{\alpha}}(z, \theta) - \hat{\bar{\alpha}}(z, \theta^*) - \bar{\varepsilon}(z) = \tilde{\theta}^T \psi(z) - \bar{\varepsilon}(z) \end{aligned} \tag{22}$$

where $\tilde{\theta}^T \psi(z) = \left[\tilde{\theta}_1^T \psi_1(z_1), \ldots, \tilde{\theta}_n^T \psi_n(z_n) \right]$ and $\tilde{\theta}_i = \theta_i - \theta_i^*$, for $i = 1, \ldots, n$.

Assumption 5: *We assume that:*

$$|\varepsilon(z) + R(X, \varphi(u))| \leq \eta \bar{R}(X, u)\kappa^*$$

with $\bar{R}(X,u) = 1 + \|X\| + \|u\|$, *where* $\kappa^* = [\kappa_1^*, \ldots, \kappa_n^*]^T$ *is an unknown constant vector to be estimated.*

To practically achieve a projective synchronization between the master system (1) and the slave system (2), we can consider the following fuzzy adaptive variable-structure controller:

$$u_i = \begin{cases} -\rho_i(t)sign(\bar{S}_i) - u_{i-}, & \bar{S}_i > 0 \\ 0, & \bar{S}_i = 0 \\ -\rho_i(t)sign(\bar{S}_i) + u_{i+}, & \bar{S}_i < 0 \end{cases} \tag{23}$$

with

$$\rho_i(t) = |u_{ri}| + k_{0i} + k_{1i}|\bar{S}_i| + \theta_i^T \psi_i(z_i) \; \forall i = 1, \ldots, n \tag{24}$$

$$\dot{\theta}_i(t) = -\gamma_{\theta i}\sigma_{\theta i}\theta_i + \gamma_{\theta i}|\bar{S}_i|\psi_i(z_i), \; with \; \theta_{ij}(0) > 0 \tag{25}$$

where $\gamma_{\theta i}, \sigma_{\theta i}$, k_{0i} and k_{1i} for $i = 1, \ldots, n$ are free positive design constants and $u_r = [u_{r1}, \ldots, u_{rn}]$, $u_{ri}(0) > 0$ is an adaptive control term added in order to dynamically compensate for the uncertain nonlinearity.

$$\dot{u}_r = -\gamma_r u_r + \gamma_r \left[E_{ur}|\bar{S}| - \frac{sign(u_r)}{\sum_{i=1}^n |u_{ri}| + \delta^2} \bar{R}(X,u)\kappa^T |\bar{S}| \right] \tag{26}$$

$$\dot{\delta} = -\gamma_\delta \sigma_\delta \delta - \gamma_\delta \frac{\delta}{\sum_{i=1}^n |u_{ri}| + \delta^2} \bar{R}(X,u)\kappa^T |\bar{S}|, \; \delta(0) > 0 \tag{27}$$

$$\dot{\kappa} = -\gamma_\kappa \sigma_\kappa \kappa + \gamma_\kappa \bar{R}(X,u)|\bar{S}|, \kappa_i(0) \geq 0 \tag{28}$$

where $E_{ur} = diag[sign(u_{r1}), \ldots, sign(u_{rn})]$, γ_κ, σ_κ, γ_δ, σ_δ and γ_r are strictly positive design parameters.

By exploiting Eq. (22), Assumptions 2, 4 and 5, and control law (23)–(25), (16) can be rewritten as follows

$$\begin{aligned} \frac{d}{dt}\left[\frac{1}{2\eta}\bar{S}^T G_1(X)\bar{S}\right] &\leq \sum_{i=1}^n |\bar{S}_i|\bar{\alpha}_i(z_i) + \frac{1}{\eta}\bar{S}^T\varphi(u) \\ &\quad + \bar{R}(X,u)\kappa^{*T}|\bar{S}| - \bar{S}^T\varepsilon(z) \\ &\leq -\sum_{i=1}^n |\bar{S}_i|\left(|u_{ri}| + k_{1i}|\bar{S}_i| + \tilde{\theta}_i^T\psi_i(z_i)\right) \\ &\quad + \sum_{i=1}^n |\bar{S}_i|\left(|u_{ri}| + k_{1i}|\bar{S}_i| + \theta_i^T\psi_i(z_i)\right) \\ &\quad + \frac{1}{\eta}\bar{S}^T\varphi(u) + \bar{R}(X,u)\kappa^{*T}|\bar{S}| \end{aligned} \tag{29}$$

Theorem 1. *Consider the master-slave system (1) and (2) with Assumptions 1–5. Then, the control law given by (23)–(28) can guarantee the following properties:*

- *All the variables in the closed-loop control system are semi-globally uniformly ultimately bounded (SUUB).*
- *The synchronization errors S_i exponentially converge to an adjustable domain defined as:*

$$\Omega_{Si} = \left\{ S_i \| S_i | \leq \left(\frac{2\pi}{\sigma_{g1}\mu} \right)^{1/2} \right\} \tag{30}$$

where π, μ and σ_{g1} will be defined later.

Proof. Consider the following Lyapunov function candidate:

$$V = \frac{1}{2\eta}\bar{S}^T G_1(X)\bar{S} + \frac{1}{2}\sum\nolimits_{i=1}^{n} \frac{1}{\gamma_{\theta_i}}\tilde{\theta}_i^T\tilde{\theta}_i + \frac{1}{2\gamma_\kappa}\tilde{\kappa}^T\tilde{\kappa} + \frac{1}{2\gamma_\delta}\delta^2 + \frac{1}{2\gamma_r}u_r^T u_r \tag{31}$$

The time derivative of V is given by

$$\dot{V} = \frac{1}{\eta}\bar{S}^T G_1(X)\dot{\bar{S}} + \frac{1}{2\eta}\bar{S}^T \dot{G}_1(X)\bar{S} + \sum\nolimits_{i=1}^{n} \frac{1}{\gamma_{\theta_i}}\tilde{\theta}_i^T\dot{\theta}_i + \frac{1}{\gamma_\kappa}\tilde{\kappa}^T\dot{\kappa} + \frac{1}{\gamma_\delta}\delta\dot{\delta} + \frac{1}{\gamma_r}u_r^T\dot{u}_r \tag{32}$$

From (11) and Eq. (23), we can easily get the following expressions:

$$u_i < -u_{i-} for\, \bar{S}_i > 0 \Rightarrow$$

$$(u_i + u_{i-})\varphi_i(u_i) \geq m_{i-}^*(u_i + u_{i-})^2 \geq \eta(u_i + u_{i-})^2 \tag{33}$$

and

$u_i > u_{i+}$ *for* $\bar{S}_i < 0 \Rightarrow$

$$(u_i - u_{i+})\varphi_i(u_i) \geq m_{i-}^*(u_i - u_{i+})^2 \geq \eta(u_i - u_{i+})^2 \tag{34}$$

From the above analysis and (23), we can conclude that

$$\begin{aligned} \bar{S}_i > 0 \Rightarrow (u_i + u_{i-})\varphi_i(u_i) &= -\rho_i(t)sign(\bar{S}_i)\varphi_i(u_i) \\ &\geq m_{i-}^*\rho_i^2(t)[sign(\bar{S}_i)]^2 \geq \eta\rho_i^2(t) \end{aligned} \tag{35}$$

$$\begin{aligned} \bar{S}_i < 0 \Rightarrow (u_i - u_{i+})\varphi_i(u_i) &= -\rho_i(t)sign(\bar{S}_i)\varphi_i(u_i) \\ &\geq m_{i+}^*\rho_i^2(t)[sign(\bar{S}_i)]^2 \geq \eta\rho_i^2(t) \end{aligned} \tag{36}$$

Using the fact that $\bar{S}_i sign(\bar{S}_i) = |\bar{S}_i|$, for $\bar{S}_i > 0$ and $\bar{S}_i < 0$, we have

$$-\rho_i(t)\bar{S}_i^2 sign(\bar{S}_i)\varphi_i(u_i) \geq \eta\rho_i^2(t)\bar{S}_i^2 = \eta\rho_i^2(t)|\bar{S}_i|^2 \tag{37}$$

Finally, while $\rho_i(t) > 0$, for all $\bar{S}_i$ we have

$$\bar{S}_i\varphi_i(u_i) \leq -\eta\rho_i(t)|\bar{S}_i| \tag{38}$$

Using expressions (24)–(28), (29) and (38), (32) becomes

$$\begin{aligned}\dot{V} &\leq -\sum_{i=1}^{n}|\bar{S}_i|(|u_{ri}| + k_{0i} + k_{1i}|\bar{S}_i|) - \sum_{i=1}^{n}\sigma_{\theta i}\tilde{\theta}_i^T\theta_i + \bar{R}(X,u)|\bar{S}|^T\kappa^* + \frac{1}{\gamma_\kappa}\tilde{\kappa}^T\dot{\kappa} \\ &\quad + \frac{1}{\gamma_\delta}\delta\dot{\delta} + \frac{1}{\gamma_r}u_r^T\dot{u}_r \\ &\leq -\sum_{i=1}^{n}u_{ri}^2 - \sum_{i=1}^{n}k_{1i}\bar{S}_i^2 - \sum_{i=1}^{n}\sigma_{\theta i}\tilde{\theta}_i^T\theta_i - \sigma_\kappa\tilde{\kappa}^T\kappa - \sigma_\delta\delta^2\end{aligned} \tag{39}$$

Now, we can use the following inequalities

$$-\sigma_\kappa\tilde{\kappa}^T\kappa \leq -\frac{\sigma_\kappa}{2}\|\tilde{\kappa}\|^2 + \frac{\sigma_\kappa}{2}\|\kappa^*\|^2$$

$$-\sigma_{\theta_i}\tilde{\theta}_i^T\theta_i \leq -\frac{\sigma_{\theta_i}}{2}\left\|\tilde{\theta}_i\right\|^2 + \frac{\sigma_{\theta_i}}{2}\left\|\theta_i^*\right\|^2$$

Then, (39) becomes

$$\begin{aligned}\dot{V} &\leq -\sum_{i=1}^{n}u_{ri}^2 - \sum_{i=1}^{n}k_{1i}\bar{S}_i^2 - \sum_{i=1}^{n}\frac{\sigma_{\theta_i}}{2}\left\|\tilde{\theta}_i\right\|^2 + \sum_{i=1}^{n}\frac{\sigma_{\theta_i}}{2}\left\|\theta_i^*\right\|^2 \\ &\quad -\frac{\sigma_\kappa}{2}\|\tilde{\kappa}\|^2 + \frac{\sigma_\kappa}{2}\|\kappa^*\|^2 - \sigma_\delta\delta^2\end{aligned} \tag{40}$$

Thanks to the property of $G_s(x)$, there exists a positive scalar σ_{gs} such that $G_s(x) \geq \sigma_{gs}I_n$ yields

$$\bar{S}^T G_1(x)\bar{S} = S^T G_s^{-1} S \leq \frac{1}{\sigma_{gs}}\|\bar{S}\|^2 \tag{41}$$

And using (40) and (41), we obtain

$$\dot{V} \leq -\mu V + \pi \tag{42}$$

with $= \sum_{i=1}^{n}\frac{\sigma_{\theta_i}}{2}\left\|\theta_i^*\right\|^2 + \sum_{i=1}^{n}\frac{\sigma_{\kappa_i}}{2}\|\kappa^*\|^2$, and

$$\mu = min\left\{min\left\{2\eta\sigma_{gs}k_{1i}\right\}, min\{\gamma_{\theta i}\sigma_{\theta i}\}, 2\gamma_\delta\sigma_\delta, 2\gamma_r, \gamma_k\sigma_k\right\}$$

Multiplying (42) by $e^{\mu t}$, we get

$$\frac{d(Ve^{\mu t})}{dt} \leq \pi e^{\mu t} \tag{43}$$

And integrating (43) over [0,t], we have

$$0 \leq V(t) \leq \frac{\pi}{\mu} + \left(V(0) - \frac{\pi}{\mu}\right)e^{-\mu t} \tag{44}$$

Thus, all signals in the closed-loop control system are SUUB. And hence the input u_i is bounded.

From (43) and (31), and using the properties (the symmetry and its sign) of $G_1(x)$ i.e. *there exists an unknown positive constant* σ_{g1} *such that:* $G_1(x) \geq \sigma_{g1} I_n$. Then the following inequality results:

$$|\bar{S}_i| = |S_i| \leq \left(\frac{2}{\sigma_{g1}}\left(\frac{\pi}{\mu} + \left(V(0) - \frac{\pi}{\mu}\right)e^{-\mu t}\right)\right)^{1/2} \tag{45}$$

i.e. the solution of S_i exponentially converges to a bounded adjustable domain defined as follows:

$\Omega_{Si} = \left\{ S_i \middle| |S_i| \leq \left(\frac{2\pi}{\sigma_{g1}\mu}\right)^{1/2} \right\}$. This ends the proof.

4 Simulation Results

This section is carried out to show the effectiveness of the proposed synchronization scheme. For this end, we consider the following two identical chaotic satellites systems [2]:

The master system

$$\begin{cases} \dot{y}_1 = \frac{1}{3} y_2 y_3 - 0.4 y_1 + \frac{\sqrt{6}}{6} y_3 \\ \dot{y}_2 = -y_1 y_3 + 0.175 y_2 \\ \dot{y}_3 = y_1 y_2 - \sqrt{6} y_1 - 0.4 y_3 \end{cases} \tag{46}$$

The slave system controlled and being subject to input nonlinearities and dynamical external disturbances is described by:

$$\begin{cases} \dot{x}_1 = \frac{1}{3} x_2 x_3 - 0.4 x_1 + \frac{\sqrt{6}}{6} x_3 + \varphi_1(u_1) + \varphi_1(u_1)^3 + \wedge_1 (X) \\ \dot{x}_2 = -x_1 x_3 + 0.175 x_2 + \varphi_2(u_2) + \wedge_2 (X) \\ \dot{x}_3 = x_1 x_2 - \sqrt{6} x_1 - 0.4 x_3 + \varphi_3(u_3) + 2\varphi_3(u_3)^3 + \wedge_3 (X) \end{cases} \tag{47}$$

where the external disturbances are selected as follows:$\wedge_1(X) = 0.5x_1$, $\wedge_2(X) = 0.5x_2^2$ and $\wedge_3(X) = 0.5x_3^3$. The input nonlinearities $\varphi_i(u_i)$ for $i = 1, 2, 3$ are described by:

$$\varphi_i(u_i) = \begin{cases} (u_i - 3)(1 - 0.3\sin(u_i)), & u_i > 3 \\ 0, & -3 \le u_i \le 3 \\ (u_i + 3)(0.8 - 0.3\cos(u_i)), & u_i < -3 \end{cases} \tag{48}$$

The initial conditions of master-slave systems and the adaptation laws are respectively selected as: $Y(0) = [5, 3, -1]$, $X(0) = [3, 4.1, 2]$, $u_{r1}(0) = u_{r2}(0) = u_{r3}(0) = 0$, $\delta(0) = 2$, $\kappa_1(0) = \kappa_2(0) = \kappa_3(0) = 10$ and $\theta_{1_j}(0) = \theta_{2_j}(0) = \theta_{3_j}(0) = 0.001$, for $j = 1,\ldots,m$, where m is the number of the fuzzy rules.

The design parameters are chosen as: $\gamma_{\theta_1} = \gamma_{\theta_2} = \gamma_{\theta_3} = 300$, $\sigma_{\theta 1} = \sigma_{\theta 2} = \sigma_{\theta 3} = 10^{-3}$, $\gamma_{r_1} = \gamma_{r_2} = \gamma_{r_3} = 200, \gamma_{\kappa_1} = \gamma_{\kappa_2} = \gamma_{\kappa_3} = 200$, $\sigma_{\delta 1} = \sigma_{\delta 2} = \sigma_{\delta 3} = 10^{-7}$, $\gamma_{\delta_1} = \gamma_{\delta_2} = \gamma_{\delta_3} = 10^{-5}$, $\sigma_{\kappa 1} = \sigma_{\kappa 2} = \sigma_{\kappa 3} = 2 \times 10^{-3}$.

The proposed synchronization scheme is simulated in several cases according to the value of the scaling factor B, as shown in Figs. 2, 3 and 4. Firstly, when $B = 2$, a projective synchronization is achieved as shown in Fig. 2. Furthermore, we choose $B = 1$, Fig. 3 shows a complete synchronization where the trajectories of the master system converge to those of the slave one. And finally, with $B = -1$, an anti-phase synchronization is effectively obtained in Fig. 4.

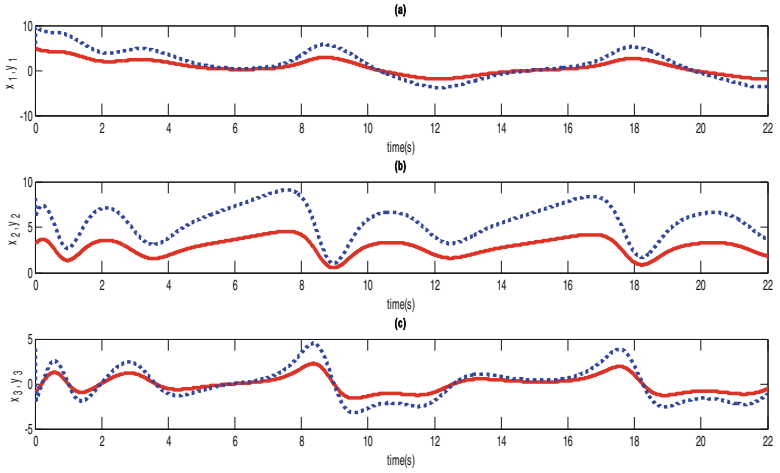

Fig. 2. Projective synchronization ($B = 2$): (a) x_1 (solid line) and y_1 (dotted line). (b) x_2 (solid line) and y_2 (dotted line). (c) x_3 (solid line) and y_3 (dotted line).

In summary, we can conclude that all simulation results demonstrate the effectiveness of the proposed projective synchronization scheme.

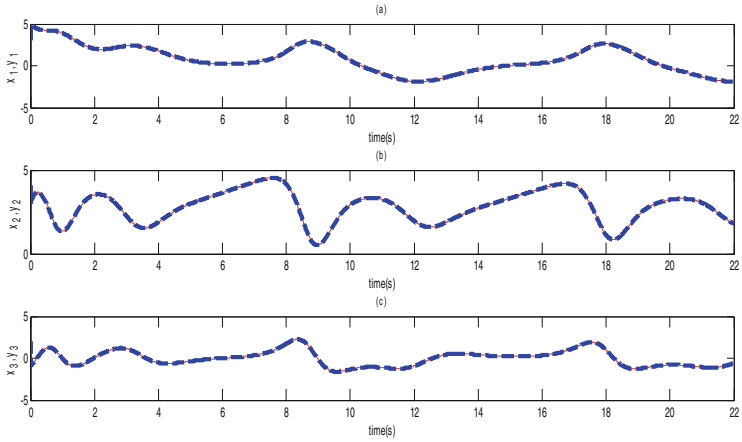

Fig. 3. Complete synchronization ($B = 1$): (a) x_1 (solid line) and y_1 (dotted line). (b) x_2 (solid line) and y_2 (dotted line). (c) x_3 (solid line) and y_3 (dotted line).

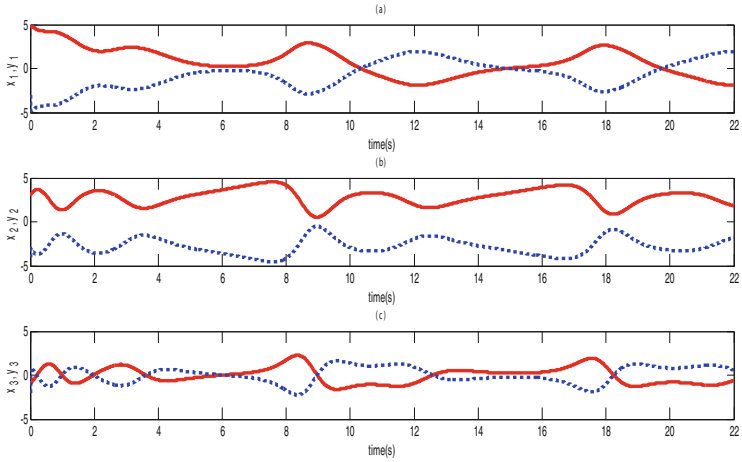

Fig. 4. Anti-phase synchronization ($B = -1$): (a) x_1 (solid line) and y_1 (dotted line). (b) x_2 (solid line) and y_2 (dotted line). (c) x_3 (solid line) and y_3 (dotted line).

5 Conclusion

In this paper, we have presented a projective synchronization scheme of two uncertain (chaotic or hyper-chaotic) systems subject to dynamic nonlinear disturbances and input nonlinearities (namely, dead-zone and sector nonlinearities). A fuzzy adaptive variable-structure controller has been designed to adequately achieve this projective synchronization. A Lyapunov based analysis has been carried out to conclude about the stability of the closed-loop system as well as the convergence of the synchronization error. Numerical simulations are presented to demonstrate the effectiveness of the proposed synchronization system.

References

1. Chen, G., Dong, X.: From Chaos to Order: Methodologies, Perspectives and Applications. World-Scientific, Singapore (1998)
2. Sadaoui, D., Boukabou, A., Merabtine, N., Benslama, M.: Predictive synchronization of chaotic satellites systems. Expert Syst. Appl. **38**, 9041–9045 (2011)
3. Boulkroune, A., Chekireb, H., Tadjine, M., Bouatmane, S.: An adaptive feedback controller with observer for linearizable chaotic systems. Control Intell. Syst. **35**(2), 1–8 (2007)
4. Yu, X., Song, Y.: Chaos synchronization via controlling partial state of chaotic systems. Int. J. Bifurcat. Chaos **11**, 1737–1741 (2001)
5. Pecora, L.M., Carroll, T.L.: Synchronization in chaotic systems. Phys. Rev. Lett. **64**, 821–824 (1990)
6. Bowonga, S., Kakmenib, M., Koinac, R.: Chaos synchronization and duration time of a class of uncertain systems. Math. Comput. Simulat. **71**, 212–228 (2006)
7. Pikovsky, A.S., Rosenblum, M.G., Osipov, G.V., Kurths, J.: Phase synchronization of chaotic oscillators by external driving. Physica D **104**, 219–238 (1997)
8. Jianping, Y., Changpin, L.: Generalized projective synchronization of a unified chaotic system. Chaos Solitons Fractals **26**, 1119–1124 (2005)
9. Li, G.: Projective synchronization of chaotic system using backstepping control. Chaos Solitons Fractals **29**, 490–598 (2006)
10. Wang, L.X.: Adaptive fuzzy systems and control: design and stability analysis. Prentice-Hall, Englewood Cliffs (1994)
11. Lin, T.-C., Lee, T.-Y., Balas, V.E.: Adaptive fuzzy sliding mode control for synchronization of uncertain fractional order chaotic systems. Chaos Solitons Fractals **44**(10), 791–801 (2011)
12. Poursamad, A., Davaie-Markazi, A.H.: Robust adaptive fuzzy control of unknown chaotic systems. Appl. Soft Comput. **9**, 970–976 (2009)
13. Roopaei, M., Jahromi, M.Z.: Synchronization of two different chaotic systems using novel adaptive fuzzy sliding mode control. Chaos **18**, 033133 (2008)
14. Hwang, E., Hyun, C., Kim, E., Park, M.: Fuzzy model based adaptive synchronization of uncertain chaotic systems: Robust tracking control approach. Phys. Lett. A **373**(22), 1935–1939 (2009)
15. Wang, J., Chen, L., Deng, B.: Synchronization of ghostburster neuron in external electrical stimulation via H∞ variable universe fuzzy adaptive control. Chaos Solitons Fractals **39**(5), 2076–2085 (2009)
16. Liu, Y., Zheng, Y.: Adaptive fuzzy approach to control unified chaotic systems. Nonlinear Dyn. **57**, 431–439 (2009)
17. Boulkroune, A., M'Saad, M.: A fuzzy adaptive variable-structure control scheme for uncertain chaotic MIMO systems with sector nonlinearities and dead-zones. Expert Syst. Appl. **38**(12), 14744–14750 (2011)
18. Boulkroune, A., M'Saad, M.: A practical projective synchronization approach for uncertain chaotic systems with dead-zone input. Commun. Nonlinear Sci. Numer. Simulat. **16**, 4487–4500 (2011)
19. Boulkroune, A., M'Saad, M.: Fuzzy adaptive observer-based projective synchronization for nonlinear systems with input nonlinearity. J. Vib. Control **18**, 437–450 (2012)
20. Boulkroune, A., M'Saad, M., Farza, M.: Adaptive fuzzy controller for multivariable nonlinear state time-varying delay systems subject to input nonlinearities. Fuzzy Sets Syst. **164**, 45–65 (2011)

21. Boulkroune, A., M'saad, M., Chekireb, H.: Design of a fuzzy adaptive controller for MIMO nonlinear time-delay systems with unknown actuator nonlinearities and unknown control direction. Inf. Sci. **180**, 5041–5059 (2010)
22. Boulkroune, A., M'Saad, M., Tadjine, M., Farza, M.: Fuzzy adaptive controller for MIMO nonlinear systems with known and unknown control direction. Fuzzy Sets Syst. **161**, 797–820 (2010)
23. Chen, J., Behal, A., Dawson, D.M.: Adaptive output feedback control for a class of MIMO nonlinear systems. In: American Control Conference, Minneapolis, MN, pp. 5300–5305, June 2006

A Novel State Representation of Electric Powered Wheelchair

Djamila Boubekeur[1(✉)], Zaki Sari[1], Abdelmadjid Boumédiène[2], and Souad Tahraoui[2]

[1] Manufacturing Engineering Laboratory of Tlemcen (MELT), Tlemcen, Algeria
djml.boubekeur@gmail.com, zaki_sari@yahoo.com
[2] Automatic Laboratory of Tlemcen (LAT), Tlemcen, Algeria
alOboumediene@yahoo.fr, Sd.tahraoui@gmail.com

Abstract. This paper describes a kinematic and dynamic modeling of an electric powered wheelchair (EPW) with a new state representation. In order to simplify the control design of the EPW, decoupling problem dynamics is considered. Afterwards a PID controller is implemented to achieve our purpose.

Keywords: Electric power wheelchair · EPW · Modeling · Decoupling · PID controller

1 Introduction

There are many people with either lower and upper extremity impairments or severe motor dysfunctions. For them, it is difficult or impossible to drive a conventional wheelchair. A robotic wheel-chair is developed to let these people, with physical disabilities, overcome the difficulties in driving a wheelchair. The robotic wheelchair system integrates a sensory subsystem, a navigation and control module and a user-machine interface to guide the wheelchair in automatic or semi-automatic mode. Bourhis et al. [1]; Mazo [2]; Parikh et al. [3]; Zengo et al. [4]; De la Cruz et al. [5].

The application of methods from robotics mobile on electric wheelchairs, allows users who do not have the possibility of using standard wheelchairs to benefit from a device with automatic features.

The electric powered wheelchair is an under actuated system, because of the uncontrollability of the two freedom wheels.

The literature offers several works in this field. Ruei et al. [6], presented a novel model which describe an information flow between the driving commands and wheel speed, he is composed of three function: the command interpretation, the speed estimation, and the speed servo blocks.

The work of Bourhis et al. [1] describes a prototype of a robotic wheelchair. This prototype has manual, semi-autonomous and autonomous mode. The choice of the mode usually depends on parameters such as: single-switch or proportional man–machine interface sensors, modeled or non-modeled environment, etc. [5].

M. Chadli et al. (eds.), *Recent Advances in Electrical Engineering and Control Applications*, Lecture Notes in Electrical Engineering 411, DOI 10.1007/978-3-319-48929-2_5

Fuji &Wada [7, 8] developed a dynamic modeling to agree both with the already known pilot model results and the empirical knowledge on the strategy of the EPW manipulation of the human pilot.

Shimada et al. [9], developed the experimental EPW which can measure dynamic posture changes of electric wheelchair and passenger, simultaneously. Their model is obtained in order to assume that the passenger and wheelchair are described by a spring mass system, and a point mass as passenger mores moves sliding on the smooth surface.

Sahnoun et al. [10], Worked on VAHM project (Véhicule Autonome pour Handicapé Moteur) in order to improve the conduct of electric wheelchairs equipping of environmental sensors and control methods from the mobile robotics. The dynamic model is obtained by the mathematical equation or by identification which they are oriented.

The main objective of this study is to establish a new state representation from the dynamic modeling given in [7], with a slope angle. To simplify the control design of the EPW, a decoupling model is considered.

Finally, a PID controller is inserted to the EPW for checking track trajectory and disturbances rejection.

2 Descripting and Modeling

In this section, we process with the method of modeling an electric powered wheelchair described in [7]. The chair has two stabilizing free wheels and two drive wheels which facilitate it's displacement by means of their differential movements.

Kinematic model is similar to the model of a mobile robot with independent drive wheels. From knowledge of position q of EPW at 't' time expressed in a fixed referential R0 and measuring the drive wheels, it's permit to estimate the posture at 't+1' [11] (Fig. 1).

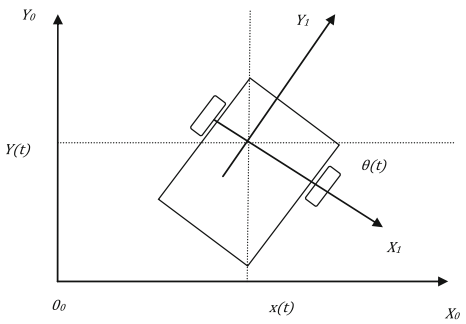

Fig. 1. q posture of EPW

3 Dynamic Modeling

The modeling of EPW can be done by two approaches: the Newtonian approach and Lagrangian approach.

We proceed using the Newtonian approach in this development, to analyze the motion of this robot, at fixed coordinate O-xy has been assigned as shown in Figs. 2 and 3.

Fig. 2. Electric powered wheelchair

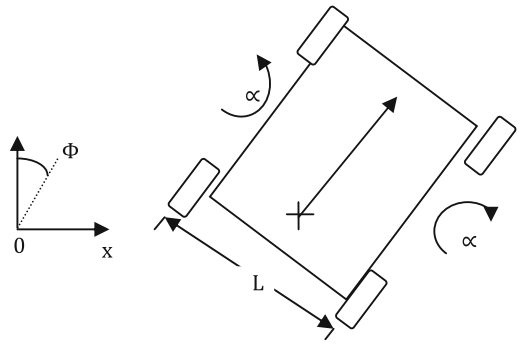

Fig. 3. Coordinate setup for analyzing the dynamics of the two motor EPW

Terms used in this part have the following meaning summarized in Table 1.

It's assumed that the EPW is going through the slope with ψ as shown in Fig. 4.

$$\begin{cases} J_a \ddot{\alpha}_{mr} + C_a \dot{\alpha}_{mr} + C_r = c_r \\ J_a \ddot{\alpha}_{ml} + C_a \dot{\alpha}_{ml} + C_l = c_l \end{cases} \quad (1)$$

The dynamics of the right and the left driving wheel is obtained from the 2nd law of Newton:

$$\sum \vec{F} = m\dot{v}$$

Table 1. Nomenclature

J_a	Moment of Inertia of the armature
C_a	Viscous friction of the motor bearing
c_r, c_l	Torque generated by the motors (right, left)
C_r, C_l	Load Torque required to driving
m_w	Masse of driving wheel
α_{mr}, α_{ml}	Rotational angle of the motor axes
ψ	Slope angle
J_w	Moment of Inertia of the driving wheel
C_w	Viscous friction coefficient
M	Masse of EPW including the operator
F_r, F_l	Reaction forces of the friction acting the driving wheels
J	Moment of Inertia of EPW around z axis
L	Distance between the two driving wheels
σ	Ratio of a gear box (< 1)
R	Radius of the driving wheel
α_r, α_l	Rotational angle of the EPW
v	Longitudinal velocity of EPW
ϕ	Yaw angle of EPW

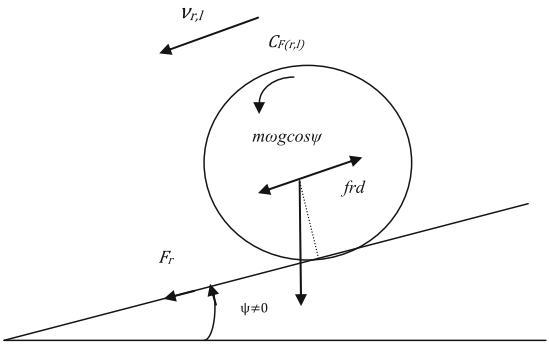

Fig. 4. Forces end torques acting on the driving wheel when the EPW is going down the slope

$$\begin{cases} m_w \dot{v}_r = m_w g sin\,\psi + F_r - f_{rd} \\ m_w \dot{v}_l = m_w g sin\,\psi + F_l - f_{ld} \end{cases} \tag{2}$$

For translational motion and for rotation:

$$\begin{aligned} J_w \ddot{\alpha}_r + C_w \dot{\alpha}_r &= C_{Fr} - RF_r \\ J_w \ddot{\alpha}_l + C_w \dot{\alpha}_l &= C_{Fl} - RF_l \end{aligned} \tag{3}$$

Given by the 2nd law of Newton:

$$J_w\ddot{\alpha} = \sum moments$$

Equation of motion of the EPW body with the operator can be written as:

$$M\dot{v} = Mgsin\,\psi + f_{rD} + f_{lD} \tag{4}$$

$$J\dot{w} = \frac{L}{2}(-f_{rD} + f_{lD}) \tag{5}$$

For longitudinal and yaw motion.

Under conditions of rolling without sliding, the longitudinal speed v and rotational w of the robot are related to the angular velocities of the driving wheels by the following relation:

Longitudinal:

$$v = \frac{\dot{v}_r + \dot{v}_l}{2} = \frac{R}{2}(\dot{\propto}_r + \dot{\propto}_l) \tag{6}$$

Rotational:

$$w = \dot{\alpha} = \frac{\dot{v}_r + \dot{v}_l}{L} = \frac{R}{2}(\dot{\propto}_r - \dot{\propto}_l) \tag{7}$$

With

$$\dot{v}_{r,l} = R\dot{\alpha}_{r,l}$$

After the combination of these equations, we obtain the dynamic of state vector $[\dot{\alpha}_r, \dot{\alpha}_l]^T$ as follow:

$$J_e\begin{bmatrix}\ddot{\alpha}_r \\ \ddot{\alpha}_l\end{bmatrix} + C_e\begin{bmatrix}\dot{\alpha}_r \\ \dot{\alpha}_l\end{bmatrix} = \begin{bmatrix}c_r \\ c_l\end{bmatrix} + T \tag{8}$$

Where *Je* and *Ce* are symmetric matrices of the form:

$$J_e = \begin{bmatrix}a & b \\ b & a\end{bmatrix}, C_e = \begin{bmatrix}c & 0 \\ 0 & c\end{bmatrix}$$

a, b, c are functions of the physical parameters of the form:

$$a = \frac{1}{\sigma}J_a + \sigma\left\{J_w + \left(\frac{M}{4} + m_w\right)R^2 + \left(\frac{R}{L}\right)^2 J\right\}$$

$$b = \sigma R^2\left(\frac{M}{4} - \frac{1}{L^2}J\right)$$

$$c = \frac{1}{\sigma} C_a + \sigma C_w$$

$$T = \sigma \left(\frac{M}{2} + m_w \right) g R sin\, \psi \begin{bmatrix} 1 \\ 1 \end{bmatrix}$$

$$y = \begin{bmatrix} v \\ w \end{bmatrix} = \begin{bmatrix} R/2 & R/2 \\ -R/L & R/L \end{bmatrix} \begin{bmatrix} \dot{\alpha}_r \\ \dot{\alpha}_l \end{bmatrix}$$

4 New State Representation

Our system has two degrees of freedom $[\alpha_r, \alpha_l]$, where their values stored are displacement $S_{r,l}$ as follow:

$$\dot{S}_{r,l} = R\dot{\alpha}_{r,l} \tag{9}$$

We replace (9) in (8), we obtain:

$$\frac{1}{R} \begin{bmatrix} a & b \\ b & a \end{bmatrix} \begin{bmatrix} \ddot{S}_r \\ \ddot{S}_l \end{bmatrix} + \frac{1}{R} \begin{bmatrix} c & 0 \\ 0 & c \end{bmatrix} \begin{bmatrix} \dot{S}_r \\ \dot{S}_l \end{bmatrix} = \begin{bmatrix} c_r \\ c_l \end{bmatrix} + T \begin{bmatrix} 1 \\ 1 \end{bmatrix}$$

The new state representation is:

$$\begin{cases} \dot{x} = Ax + \dot{B}u + B_v V \\ y = Cx + Du \end{cases} \tag{10}$$

We consider:

$$x = \begin{bmatrix} S_r & \dot{S}_r & S_l & \dot{S}_l \end{bmatrix}^T, \quad u = \begin{bmatrix} c_r & c_l \end{bmatrix}^T, \quad B_v = \begin{bmatrix} 0 & 1 & 0 & 1 \end{bmatrix}^T, \quad V = T$$

$$\begin{cases} \frac{a}{R}\ddot{S}_r + \frac{a}{R}\ddot{S}_l + \frac{c}{R}\dot{S}_r = c_r + T \\ \frac{b}{R}\ddot{S}_r + \frac{a}{R}\ddot{S}_l + \frac{c}{R}\dot{S}_l = c_l + T \end{cases} \tag{11}$$

Where:

$$\dot{x}_2 = \frac{aR}{a^2 - b^2} c_r - \frac{bR}{a^2 - b^2} c_l + \frac{bc}{a^2 - b^2} x_4 - \left[\frac{ac}{a^2 - b^2} \right] x_2 + \left[\frac{R}{a+b} \right] T$$

$$\dot{x}_4 = \frac{aR}{a^2 - b^2} c_r - \frac{bR}{a^2 - b^2} c_l - \frac{bc}{a^2 - b^2} x_4 + \frac{ac}{a^2 - b^2} x_2 + \frac{R}{a+b} T$$

The new state representation is defined by:

$$\begin{cases} [\dot{x}] = \begin{bmatrix} 0 & 1 & 0 & 0 \\ 0 & -\frac{ac}{a^2-b^2} & 0 & \frac{bc}{a^2-b^2} \\ 0 & 0 & 0 & 1 \\ 0 & \frac{bc}{a^2-b^2} & 0 & -\frac{ac}{a^2-b^2} \end{bmatrix} [x] + \begin{bmatrix} 0 & 0 \\ \frac{aR}{a^2-b^2} & -\frac{bR}{a^2-b^2} \\ 0 & 0 \\ -\frac{bR}{a^2-b^2} & \frac{aR}{a^2-b^2} \end{bmatrix} [u] \\ \qquad + T \begin{bmatrix} 0 \\ \frac{R}{a+b} \\ 0 \\ \frac{R}{a+b} \end{bmatrix} \\ \begin{bmatrix} S_r \\ S_l \end{bmatrix} = \begin{bmatrix} 1 & 0 & 0 & 0 \\ 0 & 0 & 0 & 0 \\ 0 & 0 & 1 & 0 \\ 0 & 0 & 0 & 0 \end{bmatrix} [x] \end{cases} \tag{12}$$

5 Decoupling System

To simplify the control design of the EPW, a decoupling method was employed to separate the control of the two wheels and transform the torque generate by the motors c_r, c_l to the new torque c_θ, c_δ [12].

$$\begin{bmatrix} c_l \\ c_r \end{bmatrix} = \begin{bmatrix} D_{11} & D_{12} \\ D_{21} & D_{22} \end{bmatrix} \begin{bmatrix} c_\theta \\ c_\delta \end{bmatrix} \tag{13}$$

This is shown schematically in Fig. (5).

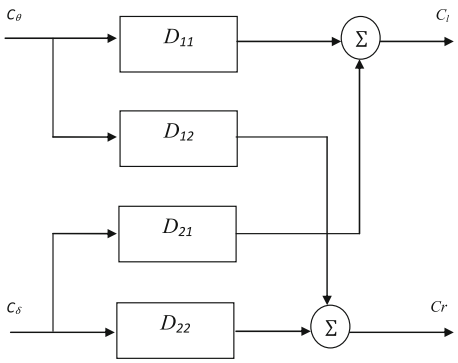

Fig. 5. Graphical representation of the decoupling method

Let rename the system constants as follows:

$$B_{21} = -\frac{ac}{a^2 - b^2}, B_{22} = \frac{bc}{a^2 - b^2}, B_{41} = \frac{bc}{a^2 - b^2}, B_{42} = -\frac{ac}{a^2 - b^2}$$

$$\begin{bmatrix} 0 & 0 \\ B_{21} & B_{22} \\ 0 & 0 \\ B_{41} & B_{42} \end{bmatrix} \begin{bmatrix} D_{11} & D_{12} \\ D_{21} & D_{22} \end{bmatrix} = \begin{bmatrix} 0 & 0 \\ B_{21} & 0 \\ 0 & 0 \\ 0 & B_{42} \end{bmatrix} \tag{14}$$

The matrix [D] is determinate from (14), and we obtained:

$$[D] = \begin{bmatrix} 0.9677 & 0.0163 \\ 0.0161 & 0.9837 \end{bmatrix}$$

6 EPW Control System

This section gives the design of the internal control of the EPW, which guarantees the regularity of the response characteristics against the parametric uncertainties.

To ensure the track reference and disturbance rejection, a classical controller PID (Proportional Integral Derivate) is employed seen these benefits in industrial implantation and reduces cost. Its transfer function is expressed as:

$$C(s) = k_p + k_i/s + k_d s$$

With k_p, k_i, k_d are parameters of the controller for the proportional, integral and derivate action respectively (Fig. 6).

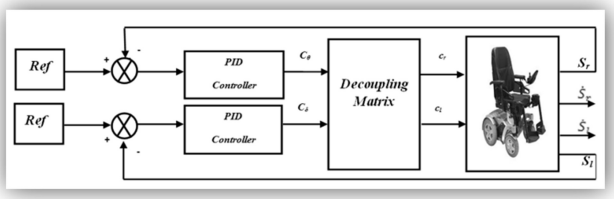

Fig. 6. Closed loop control system for the model based control of the EPW

7 Results and Discussion

To improve the performance of our system we take the parameters values of the controller as: $k_p = 50$, $k_i = 0.5$, $k_p = 0.9$.

The simulation results of the evolution of the position and the speed are presented in the following Figs. 7 and 8.

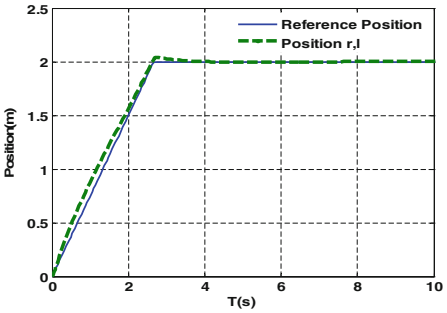

Fig. 7. The evolution of the right and left wheel position of EPW

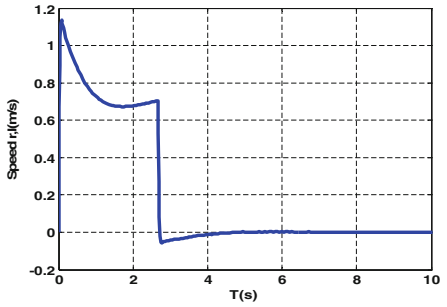

Fig. 8. The speed of right and left wheel of EPW

The simulation of the decoupled system (open loop) has allowed us to observe the divergence of the right and left wheels, where the implementation of the controller is indispensable.

The tracking test for straight trajectory (same reference) is verified for the two wheels. After integration of the PID controller, we obtained the performance:

$$\begin{cases} Overflow = 2\% \\ TimeRise_{5\%} = 2.49s \\ Error = 0.003 \end{cases}$$

We observed the convergence of the results and important improvement in performance of the system, such as stability of the system, preciseness, and time rise of the position response.

8 Conclusion

The system EPW-driver is an under actuated system, his dynamic model is obtained by the mathematical equation or by identification. It's a coupled system and multivariable, this is the reason for which we have used its state representation instead of the transfer function.

A novel state representation of the EPW model is developed in the first, to make the control system easier and to check its performance. We pass from the multi output case to the single output case, using a decoupling law quoted in [12].

Our simulations show the convergence of the driver wheels in closed loop after the implementation of the PID controller. The results showed us that the error is canceled, the response time has been reduced in contrast to overflow we can reduced it by varying the parameters of the corrector.

As prospects, we will apply another controller to the coupled multi output system and make a comparison between the results. Similarly, we will try to ensure the robustness.

References

1. Bourhis, G., Horn, O., Habert, O., Pruski, A.: An autonomous vehicle for people with motor disabilities. IEEE Robot. Autom. Mag. **8**(1), 20–28 (2001)
2. Mazo, M.: An integral system for assisted mobility. IEEE Robot. Autom. Mag. **8**(1), 46–56 (2001)
3. Parikh, S.P., Grassi, V., Kumar, V., Okamoto, J.: Integrating human inputs with autonomous behaviors on an intelligent wheelchair platform. IEEE Intell. Syst. **22**(2), 33–41 (2007)
4. Zeng, Q., Teo, C.L., Rebsamen, B., Burdet, E.: A collaborative wheelchair system. IEEE Trans. Neural Syst. Rehab. Eng. **16**(2), 161–170 (2008)
5. De La Cruz, C., Celeste, W.C., Bastos, T.F.: A robust navigation system for robotic wheelchairs. Control Eng. Pract. **19**, 575–590 (2010)
6. Chen, R.X., Chen, L.G., Chen, L.: System design consideration for digital wheelchair controller. IEEE Trans. Ind. Electr. **47**(4), 898–907 (2000)
7. Fuji, F., Wada, K.: For a better maneuverability of the electrically powered wheelchair a pilot model based approach. In: Micro mechatronics and Human Science, pp. 125–132 (2003)
8. Fujii, F., Wada, K.: Analysis on the manual control characteristics of the human pilot during the operation of the powered wheelchair. Adv. Robot. **19**(2), 121–139 (2005)
9. Shimada, S., Ishimura, K., Wada, M.: System design of electric wheelchair for realizing adaptive operation to human intention. In: International Conference on Robotic, Intelligent Systems and Signal Processing, Changsha, China (2003)
10. Sahnoun, M., Bouris, G.: Retour Haptique pour l'Aide au Pilotage des Fauteuils Roulants Electriques. In: National Conférence Handicap (2006)
11. Sahnoun, M., Bourhis, G.: Haptic feedback to assist powered wheelchair piloting. AMSE Periodicals **67**, 53–63 (2006)
12. Baker, N.P., Brown, C.P., Dowling, D.R.S., Modra, J.L., Tootell, D.J.: Son of EDGAR. Department Mechanical Engineering, Adelaide University, Australia, October 2006

Single and Multi Objective Predictive Control of Mobile Robots

H. Merabti[1(✉)], K. Belarbi[2], and I. Bouchachi[1]

[1] Research Center in Industrial Technologies Crti, Cheraga, P.O.Box 64, 16014 Algiers, Algeria
h.merabti@csc.dz, fingroo@yahoo.fr
[2] Ecole Nationale Polytechnique de Constantine Campus, Constantine 3, Nouvelle ville Ali Mendjeli, Constantine, Algeria
kbelarbi@yahoo.com

Abstract. In this work, we present a comparison between the use of a simple and multi objective MBPC in robots control for tracking trajectories and obstacle avoidance. Two cases were considered, in the first each robot has its own MPC controller where in the second a single two- objectives MPC controller is used for both robots. In the second case; two approaches were proposed to solve the multi objective optimization problem arising in the MOMPC: the multi objective Particle Swarm Optimization (MOPSO) and weighted sum method. The simulation results show that the robots movement is more stable by the MOPSO-NMPC than the PSO-NMPC. Computation times as expected are shorter PSO-NMPC; however MOPSO-NMPC although more time consuming is still feasible.

Keywords: Model predictive control · Metaheuristics · Multiobjective optimization

1 Introduction

Model based predictive control (MBPC) is based on the use of a model for predicting the future behavior of the system over a finite future horizon. The current control action is obtained by solving on-line, at each sampling instant, a finite horizon optimal control problem, using the current state of the plant as the initial state [1]. The optimization yields an optimal control sequence and the first control in this sequence is applied to the plant. The solution of the optimization problem depends on the nature of the model and constraints.

Multi objective model based predictive control (MOMBPC) has been proposed by a number of authors with improved performance. For example, in [2], the authors use multi objective optimization to tune nonlinear model predictive controllers based on a weighted sum objective function and in [3] authors shown that it is possible to compute a Pareto optimal solution as an explicit piecewise affine function after recasting the optimization problem associated with the multi objective MPC as a multi parametric multi objective linear or quadratic program.

M. Chadli et al. (eds.), *Recent Advances in Electrical Engineering and Control Applications*, Lecture Notes in Electrical Engineering 411, DOI 10.1007/978-3-319-48929-2_6

In this work, we present a comparison between the use of a simple and multi objective MBPC in robots control for tracking trajectories and obstacle avoidance. Each robot tracks a specified reference trajectory. In the first case, each robot has its own MPC controller and the Particle Swarm Optimization algorithm PSO is used for the solution of the optimization problem arising in the MPC. In the second case, a single two- objectives MPC controller is used for both robots. This last problem was solved using two approaches: the first is the use of multi-objectives PSO for the solution of the multi objective optimization problem arising in MOMPC, the second is to transform the multi objective optimization problem to simple optimization one using the weighted sum method.

The paper is organized as follows: Sect. 2 gives the formulation of simple and Multi objective nonlinear model predictive control, Sect. 3 provides the description of the MOPSO and the weighted sum method, Sect. 4 simulation results are given.

2 Model Predictive Control

Consider a nonlinear system described by the discrete state space model:

$$x(k+1) = f(x(k), u(k)) \tag{1}$$

where *x(k)* is the state, *u(k)* the control signal and *f* are a continuous mapping.

The control signal $u(k)$ is such that:

$$u(k) \in \mathbb{U} \subset \mathbb{R}^m \tag{2}$$

U is a compact convex set with $0 \in int(\mathbb{U})$ and $f(0,0) = 0$. Moreover the state may be constrained to stay into a convex and closed set:

$$x(k) \in \mathbb{X} \tag{3}$$

The problem solved by the non linear model predictive control is to regulate the state to the origin by solving the following optimization problem:

$$\min_{\mathcal{U}} J_N(x, k, \mathcal{U}) \tag{4}$$

With (1), (2) and (3) Where

$$J_N(x, k, \mathcal{U}) = F(x(k+N)) + \sum_{i=k}^{k+N-1} L(x(i), u(i)) \tag{5}$$

Where N is the optimization horizon. *F(x(k + N))* is a weight of the final state. Moreover, the final state may be constrained to be in a final region:

$$x(k+N) \in X_f \subset \mathbb{X} \tag{6}$$

The weight F and the final region are introduced to guarantee stability of the nonlinear MPC.

The solution gives the control sequence up to N

$$\mathcal{U} = [\, u(k) \quad u(k+1) \quad \cdots \quad u(k+N-1) \,] \in \mathbb{U}^N$$

and only u(k) is applied at sampling instant k. The procedure is repeated at each sampling instant.

The optimization problem (5), (6) is generally non convex. The straightforward algorithm for solving this problem is the sequential quadratic programming, SQP, an extension of the active set method used for solving quadratic program [4]. This method is difficult to code and time consuming. A number of algorithms have been proposed for solving this problem in a reasonable amount of time such that the multiple shooting method [5] and nonlinear sum of squares [6, 7]. In this work, Particle Swarm Optimization algorithm [8], PSO, is applied to the solution of this problem.

The problem of multi objective model predictive control is to minimize, at each sampling time, the l follows functions cost:

$$\begin{aligned} J_i(U,x) &= F_i(x(k+N)) \\ &\quad + \sum_{k=j}^{k+N-1} L_i(x(j),u(j)) \; with \; i = 1,\cdots,l \end{aligned} \tag{7}$$

$F_i(x(k+N))$ is a weight on the final state. Moreover, the final state may be constrained to be in a final region $(k+N) \in X_f \subset X$. The weight F_i and the final region are introduced to guarantee stability of the nonlinear MPC.

The solution gives the set of Pareto front and only one Pareto optimal solution is selected and applied at sampling instant k. The procedure is repeated at each sampling time. In this work we use Multi Objective Particle Swarm Optimization, MOPSO [9], to generate a set of approximately Pareto-optimal solutions in a single run and we use a weighted sum approach to convert the multi objective MPC to a single one.

3 Solution of the Multi Objective Predictive Control Problem

1. The MOPSO

Particle swarm optimization is an evolutionary computation technique developed by Kennedy and Eberhart in 1995 [8]. The particle swarm concept originated as a simulation of a simplified social system. The success of the particle swarm optimization algorithm motivated the researchers to apply it to multi-objective optimization problems. The MOPSO [9] is one of the algorithms proposed to solve the multi objective optimization problem using particle swarm optimization algorithm. The MOPSO maintains two archives, one for storing the global non-dominated solutions and the other for storing the individual best solutions attained by each particle. Basically, the updating of the particle is performed as follows:

$$V(t+1) = w * V(t) + R_1 * (p_{best}(t) - p(t)) + R_2 * (Rep(h) - p(t)) \tag{8}$$

$$p(t+1) = p(t) + V(t+1) \tag{9}$$

Where V is the particle velocity, $p(t)$ is the current position of the particle, w is a constant, R_1 and R_2 are random numbers in [0 1]. *REP* is a repository where are stored the positions of the non dominated particles and h is an index in the repository that is introduced to ensure some fitness sharing [10].

REP is updated by inserting the currently non dominated positions and dominated positions are eliminated. The size of the repository being limited when it becomes full and particles in less populated areas are given priority over those highly populated regions.

2. Weighted sum method for multi-objective optimization

This method is the simplest and widely used classical method. It allows the transformation of the objective functions vector into a single-objective function. The single criterion is obtained by the sum of the weighted criteria as follows:

$$\min \sum_{i=1}^{k} w_i J_i(x) \text{ With } w_i \geq 0 \tag{10}$$

w_i: is the affected weight to the objective i where:

$$\sum_{i=1}^{k} w_i = 1$$

Weights Value depends on the relative importance of each objective. In this work, objectives have the same weight.

4 Application

We consider four mobile robots, two real and two virtual, the real robots track the virtual ones. It is assumed that there is a pure rolling. The contact between the wheels and the ground is supposed to be frictionless. The kinematic model of the real robots is given by:

$$\dot{x}_i(t) = \frac{v_{ri}(t) + v_{li}(t)}{2} cos\, \theta_i(t) \tag{11}$$

$$\dot{y}_i(t) = \frac{v_{ri}(t) + v_{li}(t)}{2} sin\, \theta_i(t) \tag{12}$$

$$\dot{\theta}_i(t) = \frac{v_{ri}(t) - v_{li}(t)}{b} \tag{13}$$

$$\omega_i = (v_{ri} - v_{li}/b) \tag{14}$$

Where $i = 1, 2$, $v_{ri} \in R$ and $v_{li} \in R$ are the right and the left wheels linear velocities of the real robot i, $b \in R$ is the distance between the wheel centers. θ_i are the robots orientation and ω_i are the angular velocities. The objective is to find a control law defined by $v_{ri}(t)$, $v_{li}(t)$ ($i = 1, 2$) that allows the robots to:

- track a given reference trajectories defined by:$[x_{ri}(t)y_{ri}(t)], i = 1, 2$, respectively
- Avoid fixed obstacles on the trajectories
- Avoid collisions

This problem is set as a single objective MPCs and multi-objective MPC with constraints. The optimization problem arising in the MPCs is solved by the particle swarm optimization meta-heuristic, PSO. The optimization problem arising in MOMPC is solved using two different approaches. The first consists in converting the multi objective optimisation problem to single one where the resulting objective function is a weighted sum of the two objective functions. The second approach consists of using the multi objective particle swarm optimisation algorithm (MOPSO) to generate a set of optimal Pareto solutions.

The first reference trajectory is given by:

$\boldsymbol{x_{r1}(t) = cos(\omega_0 t)}$; $\boldsymbol{y_{r1}(t) = sin(2 * \omega_0 t)}$; $\omega_0 = 0.02$ *rad/s* is the signal pulsation, the second reference trajectory is given by: $\boldsymbol{x_{r2}(t) = cos(\omega_0 t + \varphi)}$; $\boldsymbol{y_{r2}(t) = sin(2 * \omega_0 t + \varphi)}$;

The control signals are constrained to:

$$\boldsymbol{-0.7 \leq v_{ri} \leq 0.7 - 0.7 \leq v_{li} \leq 0.7} \tag{15}$$

and the angular velocity is constrained to:

$$\boldsymbol{-5 \leq \omega_i \leq 5} \tag{16}$$

These algorithms are run until a satisfactory response is obtained. The collision point of the robots is m(0,0). The robots start from their initial positions (0.25, 0), (−0.75, 0) and track their own trajectories. It is observed that both have good tracking and avoid all fixed obstacles on their trajectories. However, the behavior of the robots in the collision point is different for each algorithm where:

- For the first and the second algorithms (PSO-NMPCs and MOPSO-NMPC), it is observed that the second robot continues its tracking while the first avoids it by decreasing its velocity to keep a safe distance. Then, they continue their tracking and avoid the obstacles encountered. One can also observe that their movement is more stable by the MOPSO-NMPC than the PSO-NMPC (Fig. 1).
- For the last algorithm, the WS-MOMPC, it is observed that each robot avoids the collision with the other. Then, they continue their tracking and avoid fixed obstacles encountered. We also observe a dynamic movement of the robots.

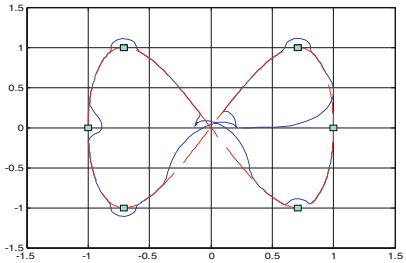

(a) Robot 1 trajectory

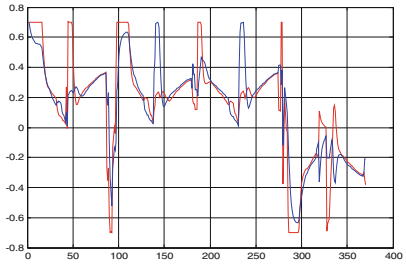

(b) Robot1 velocities

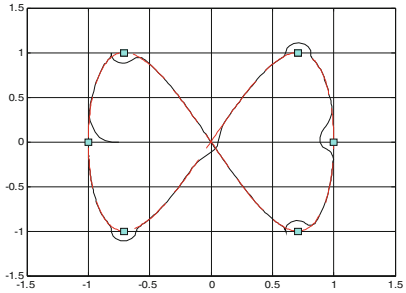

(c) Robot2 trajectory

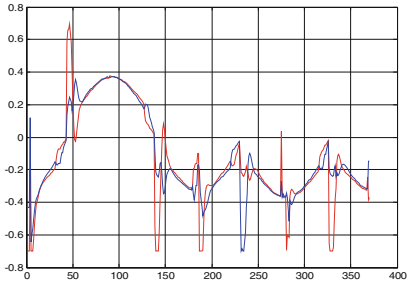

(d) Robot2 velocities

Fig. 1. Results with Two PSO-NMPC controllers. (a) Robot 1 trajectory (b) Robot1 velocities (c) Robot2 trajectory (d) Robot2 velocities

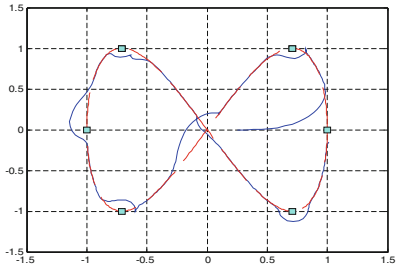

(a) Robot1 trajectory

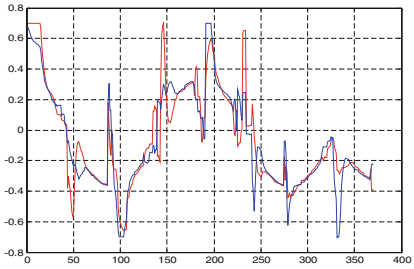

(b) Robot1 velocities

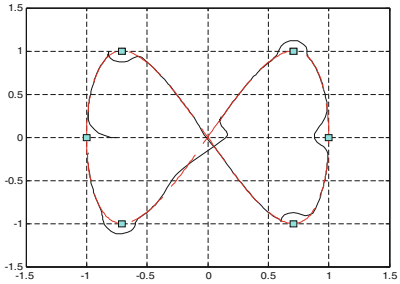

(c) The second robot trajectory

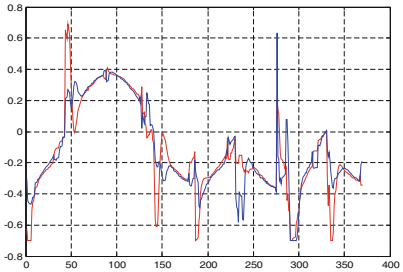

(d) The second robot velocities

Fig. 2. Results with the Pareto: MOPSO-NMPC (a) Robot1 trajectory (b) Robot1 velocities (c) The second robot trajectory (d) The second robot velocities

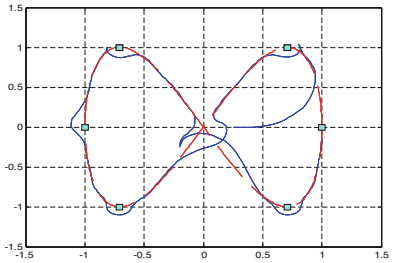

(a) Robot1 trajectory

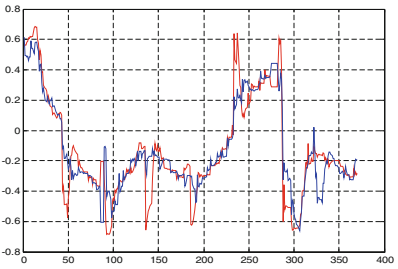

(b) Robot1 velocities

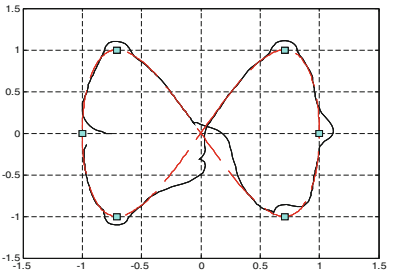

(c) Robot2 trajectory

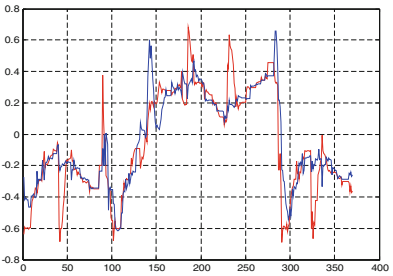

(d) Robot2 velocities

Fig. 3. Results with WS-MOMPC (a)Robot1 trajectory (b)Robot1 velocities. (c) Robot2 trajectory (d) Robot2 velocities

Table 1. COMPUTATION TIMES

	PSO-NMPC	MOPSO-NMPC	WS-MOMPC
Computation time	$\leq$ 4 ms	$\leq$ 11 ms	$\leq$ 12 ms

Computation times are given in Table 1, where it can be seen that PSO-NMPC outperforms the other algorithms. The constraints on the control signals are always satisfied as shown in Figs. 2 and 3.

5 Conclusion

In this work, we have developed a comparison between single objective and multi objective MBPC in robots control for tracking trajectories and obstacle avoidance. Each robot tracks a specified reference trajectory. In the first case, each robot has its own MPC controller and the Particle Swarm Optimization algorithm PSO is used for the solution of the optimization problem arising in the MPC. In the second case, a single two- objectives MPC controller is used for both robots. This last problem was solved using two approaches: the first is the use of multi-objectives PSO for the solution of the multi objective optimization problem arising in MOMPC, the second is to transform the multi objective optimization problem into a single objective optimization using the weighted sum method. The simulation results show that the robots movement is more stable by the MOPSO-NMPC than the PSO-NMPC. Computation times as expected are shorter PSO-NMPC, however MOPSO-NMPC although more time consuming, is still feasible.

References

1. Maciejowski, J.M.: Predictive Control with Constraints. Prentice Hall, Upper Saddle River (2001)
2. De Vito, D., Scattolini, R.: A receding horizon approach to the multiobjective. In: Proceedings of the 46th IEEE Conference on Decision and Control New Orleans, LA, USA, 12–14 December 2007
3. Bemporad, A., de la Peña, D.M.: Multiobjective model predictive control. Automatica **45**, 2823–2830 (2009)
4. Biegler, L.T., Rawlings, J.B.: Optimization approaches to nonlinear model predictive control. In: Arkun, Y., Ray, W.H. (eds.) CPC IV, The CACHE Corp., Austin, Texas (1991)
5. Diehl, M., Bock, H., Leineweber, D., Schlöder, J.: Efficient direct multiple shooting in nonlinear model predictive control. In: Keil, F., Mackens, W., Vos, H., Werther, J. (eds.) Scientific Computing in Chemical Engineering II, vol. 2. Springer, Berlin (1999)
6. Casavola, A., Famularo, D., Franzè, G.: Predictive control of constrained nonlinear systems via LPV linear embeddings. Int. J. Robust Nonlinear Control **13**(3–4), 281–294 (2003)
7. Franzè, G.: A nonlinear sum-of-squares model predictive control approach. IEEE Trans. Autom. Control **55**(6), 1466–1471 (2010)

8. Eberhart, R.C., Shi, Y.: Particle swarm optimization: developments, applications and resources. In: Proceedings of the Congress on Evolutionary Computation 2001, Seoul, Korea. Piscataway, NJ. IEEE Service Center (2001)(b)
9. Coello, C., Lechuga, M.: MOPSO: a proposal for multiple objective particle swarm optimization. In: Proceedings of the Congress on Evolutionary Computation, part of the 2002. IEEE World Congress on Computational Intelligence, Hawaii, pp. 1051–1056. IEEE (2002)
10. Li, X.: A non-dominated sorting particle swarm optimizer for multiobjective optimization. In: Cantú-Paz, E., et al. (eds.) GECCO 2003. LNCS, vol. 2723, pp. 37–48. Springer, Heidelberg (2003). doi:10.1007/3-540-45105-6_4

Comparison Between Predictive Sliding Mode Control and Sliding Mode Control with Predictive Sliding Function

Houda Ben Mansour(✉), Khadija Dehri, and Ahmed Said Nouri

Research Unit: Numerical Control of Industrial Processes,
National of Engineering School of Gabes, University of Gabes,
Street of medenine, 6029 Gabes, Tunisia
Houda.b.mansour@gmail.com, Khadija.dehri@gmail.com,
ahmedsaid.nouri@enig.rnu.tn

Abstract. This paper shows comparison between the Predictive Sliding Mode Controller (PSMC) and the Sliding Mode Controller with Predictive Sliding Function (SMC-PSF). The proposed controllers combine the design of Sliding Mode Control (SMC) with Model Predictive Control (MPC). This combination improves the performance of these two control laws. In fact, using a non-minimum phase system, the performances of the (PSMC) and the (SMC-PSF), in terms of strong robustness to external disturbance, parameters variation, chattering elimination and fast convergence were judged better, in comparison with SMC and MPC. Comparing the two controllers PSMC and SMC-PSF, the simulation results show that the SMC-PSF is more able to eliminate oscillations at the phase of convergence and at the presence of hard parameters variation.

Keywords: Sliding mode control · Model predictive control · Predictive sliding mode control · Predictive sliding function · Non minimum phase systems

1 Introduction

Many industrial systems are multivariable, nonlinear, also with external disturbances, parameter uncertainties, and time delays. These complexities of the system make difficult the design of an exact mathematical model and the development of a suitable control. Research in this area continues to grow. In fact, over the last 20 years much research has been developed, particularly, in Sliding Mode Control (SMC) and in Model based Predictive Control (MPC) [1, 2].

The SMC approach is derived from Variable Structure Control (VSC) which was studied originally by Utkin (1978) [3].

For a large class of systems, the SMC is particularly interesting due to its ability to deal with non linearities, uncertainties, modeling error and disturbances [4].

Sliding mode control design is composed of two steps. At the first step, a custom-made surface must to be designed. While on the sliding surface the plant's dynamics are restricted to the equations of the surface (and are robust to parameters

M. Chadli et al. (eds.), *Recent Advances in Electrical Engineering and Control Applications*,
Lecture Notes in Electrical Engineering 411, DOI 10.1007/978-3-319-48929-2_7

uncertainties and external disturbances). At the second step, a feedback control law is designed to provide convergence of a system trajectory to the sliding surface; and the sliding surface should be reached in a finite time. The system's motion on the sliding surface is called the sliding mode. However, undesired chattering produced by the high frequency switching of the control may be considered as a problem for implementing the sliding mode control methods for some real applications [5, 27].

Many approaches have been proposed to solve this problem such as high order sliding mode control [5–7].

On the other hand, Model based Predictive Control (MPC) has been successfully implemented in many industrial applications, showing good performance. The basic idea of MPC is to calculate a sequence of future control signals in such a way that it minimizes a multistage cost function defined over a prediction horizon. The index to be optimized is a difference between the predictive system output and predictive reference sequence over the prediction horizon plus a quadratic function measuring control effort [8, 9, 20, 21].

In order to implement the MPC, a plant's model is used to predict the future plant output. This prediction is based on past and current values of the input and the output of the plant. In spite of these advantages, MPC has some limitations. The computational cost can be very high, particularly if a high control horizon is chosen and when constraints are present. Nevertheless the control law is model dependent, so a perfect model is required to guarantee the success of MPC control strategies. Because of the finite horizon, the stability and the robustness of the process is difficult to analyze and guarantee, especially when constraints are present [22–24].

In this paper, for a class of discrete-time systems, in order to obtain desired closed-loop performances, such as wonderful chattering elimination, strong robustness and fast convergence, we combine the model predictive control with the sliding mode control.

Among the first contribution, in this kind of control strategy, we can cite Camacho [10], Gabin [11, 25], Xiao [12, 13], De la Parte [14], these works are based on the using of the MPC to choose the coefficient of the discontinuous part of the law control.

Zaholan [18] and Ben Mansour [15–17, 28], introduce the prediction of the sliding surface into the control objective function, by applying a predictive sliding surface and a reference trajectory, in the predictive control strategy.

The main idea of this work is to compare the Predictive Sliding Mode Control (PSMC) with the Sliding Mode Control with Predictive Sliding Function (SMC-PSF).

The paper is organized as follows: Sect. 2 is giving the system description. The synthesis of the predictive sliding mode controller is presented in Sect. 3.

Section 4 describes the synthesis of the sliding mode controller with predictive sliding function. In Sect. 5 a comparative study of the proposed controllers is presented by the simulation for a non minimum phase system with the presence of disturbances and parameter variations. Finally, Sect. 6 draws conclusions of the paper.

2 System Description

Let's consider the uncertain discrete time system defined by [19]:

$$\begin{cases} x(k+1) = (A + \Delta A)x(k) + (B + \Delta B)(u(k) + v(k)) \\ y(k) = Hx(k) + Du(k) \end{cases} \quad (1)$$

Where:

- $x(k) \in R^n$ is the state vector,
- $u(k) \in R$ is the scalar input control,
- The matrices A, B, H and D are the nominal model matrices with adequate dimensions,
- ΔA and ΔB are the parameter uncertainties,
- $v(k) \in R$ is the disturbance input.

The system (1) can be presented by the following form:

$$\begin{cases} x(k+1) = Ax(k) + Bu(k) + w(k) \\ y(k) = Hx(k) + Du(k) \end{cases} \quad (2)$$

with:

$$w(k) = \Delta Ax(k) + \Delta Bu(k) + (B + \Delta B)v(k) \quad (3)$$

3 Synthesis of Discrete Predictive Sliding Mode Controller

The principle of the Predictive Sliding Mode Controller (PSMC) is given by the bloc diagram shown in Fig. 1, where the primary loop is a Sliding Mode Control (SMC) and the secondary loop is a Model Predictive Control (MPC) [27].

The main purpose is to approximate the predictive sliding function (S_p) to the sliding reference function (S_r), penalizing at the same time the variation in the control signal.

We consider, now, the sliding mode control problem for system (1).

The objective is to design a predictive sliding mode controller taking the following reaching law [15]:

$$s(k+1) = \varphi s(k) - m\ sign(s(k)) \quad (4)$$

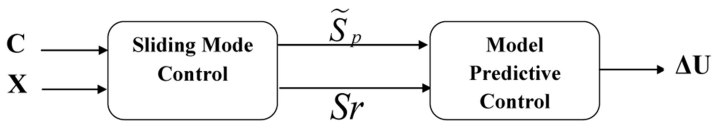

Fig. 1. PSMC Controller block diagram.

Where:

$$sign(s(k)) := \begin{cases} -1 & if\ s(k) < 0 \\ 1 & if\ s(k) > 0 \end{cases}$$

and m is the discontinuous term magnitude and $\varphi \in [0 \quad 1]$.

Knowing that the sliding function is defined as:

$$s(k+1) = Cx(k+1) = C[Ax(k) + Bu(k)] + Cw(k) \tag{5}$$

Without disturbances, the sliding function (5) value at time (k + p) is [16, 17]:

$$\begin{aligned} s(k+p) &= Cx(k+p) \\ &= CA^p x(k) + \sum_{j=1}^{p} CA^{j-1} Bu(k+p-j) \end{aligned} \tag{6}$$

where $k \in \mathbb{Z}$ and $p \in \mathbb{N}$

The sliding surface at the instance k + 1, k + 2 and k + 3 can be presented as:

$$\begin{cases} s(k+1) = Cx(k+1) \\ \quad = CAx(k) + CB(u(k) - u(k-1)) + CBu(k-1) \\ \quad = CAx(k) + CB\,\delta u(k) + CBu(k-1) \\ s(k+2) = Cx(k+2) \\ \quad = CAx(k+1) + CBu(k+1) \\ \quad = CA^2 x(k) + CB\,\delta u(k+1) + CAB\,\delta u(k) + CB\,\delta u(k) \\ \quad\quad + CB\,\delta u(k) + CAB\,\delta u(k-1) \\ \quad = CA^2 x(k) + CB\,\delta u(k+1) + C(A+I)B\,\delta u(k) \\ \quad\quad + C(A+I)Bu(k-1) \\ s(k+3) = Cx(k+3) \\ \quad = CA[A[Ax(k) + Bu(k)]] + CABu(k+1) + CBu(k+2) \\ \quad = CA^3 x(k) + CB\,\delta u(k+2) + C(A+I)B\,\delta u(k+1) \\ \quad\quad + C(A^2 + A + I)B\,\delta u(k+1) + C(A^2 + A + I)Bu(k-1) \end{cases}$$

where I is the identity matrix.

Then s(k + p) can be written as:

$$\begin{aligned} s(k+p) = {} & CA^p x(k) + CB\delta u(k+p-1) + C(A+I)\delta u(k+p-2) \\ & + \cdots + C\left[\sum_{j=0}^{p-1} A^j\right] B\delta u(k) + C\left[\sum_{j=0}^{p-1} A^j\right] Bu(k-1) \end{aligned} \tag{7}$$

where

$$\delta u(k) = u(k) - u(k-1) \tag{8}$$

Equation (7) can be developed in vector form as follows:

$$S_p(k+1) = \Gamma x(k) + \Omega^F \Delta U(k) + \Omega^P u(k-1) \tag{9}$$

where:

$$S_p(k+1) = [s(k+1), s(k+2), \ldots, s(k+N)]^T$$
$$\Delta U(k) = [\delta u(k), \delta u(k+1), \ldots, \delta u(k+M-1), 0, \ldots, 0]^T$$
$$\Gamma = \left[(CA)^T (CA^2)^T \ldots (CA^N)^T\right]^T$$

$$\Omega^p = \begin{bmatrix} CB \\ \vdots \\ C\left[\sum_{j=0}^{M-1} A^j\right]B \\ \vdots \\ C\left[\sum_{j=0}^{N-1} A^j\right]B \end{bmatrix}$$

$$\Omega^F = \begin{bmatrix} CB & 0 & \cdots & \cdots & 0 \\ C(A+I)B & CB & 0 & \cdots & 0 \\ \vdots & \vdots & \vdots & \vdots & \vdots \\ C\left[\sum_{j=0}^{M-1} A^j\right]B & \cdots & \cdots & C(A+I)B & CB \\ \vdots & \vdots & \vdots & \vdots & \vdots \\ C\left[\sum_{j=0}^{N-1} A^j\right]B & \cdots & \cdots & C\left[\sum_{j=0}^{N-M-1} A^j\right]B & C\left[\sum_{j=0}^{N-M} A^j\right]B \end{bmatrix}$$

with N is the horizon of prediction, M is control horizon.

To correct the future predictive sliding mode value s(k + p), in practice, we introduce the error between the practical sliding mode value s(k) and the predictive sliding mode value s(k/k−p). So, the output of sliding mode prediction sp(k + p) is given as follows:

$$\begin{aligned} \tilde{s}_p(k+p) &= s(k+p) + h_p e(k) \\ \tilde{s}_p(k+p) &= CA^p x(k) + CB\delta u(k+p-1) + C(A+1)\delta u(k+p-2) \\ &\quad + \cdots + C\left[\sum_{j=0}^{p-1} A^j\right] B\delta u(k) + C\left[\sum_{j=0}^{p-1} A^j\right] Bu(k-1) + h_p e(k) \end{aligned} \tag{10}$$

where

$$e(k) = s(k) - s(k/k-p)$$

$$s(k/k-p) = CA^p x(k-p) + \sum_{j=1}^{p} CA^{j-1} Bu(k-j)$$

and h_p is a correct coefficient.

In vector form, Eq. (10) is written as:

$$\widetilde{S}_p(k+1) = S_p(k+1) + H_p E(k) \tag{11}$$

where:

$$\begin{aligned}
&\widetilde{S}_p(k+1) = \left[\widetilde{s}_p(k+1), \widetilde{s}_p(k+2), \ldots \widetilde{s}_p(k+N)\right]^T \\
&H_p = diag[h_1, h_2, \ldots, h_N] \\
&E(k) = S(k) - S_{mp}(k) \\
&S(k) = [s(k), s(k), \ldots, s(k)]^T_{1\times N} \\
&S_{mp}(k) = [s(k/k-1), s(k/k-2), \ldots, s(k/k-N)]
\end{aligned}$$

The optimization cost function is defined as:

$$j_{PSMC} = \sum_{j=1}^{N} q_j \left[\widetilde{s}_p(k+j) - s_r(k+j)\right]^2 + \sum_{l=1}^{M} g_l[\delta u(k+l-1)] \tag{12}$$

where sr(k + j) are the sliding mode reference trajectory, qj and gl are weight coefficients.

We consider (qj = 1) and (gl = g), in order to simplify the synthesis of the controller. Then, the following corresponding optimization cost function is written by:

$$j_{PSMC} = \sum_{j=1}^{N} \left[\widetilde{s}_p(k+j) - s_r(k+j)\right]^2 + \sum_{l=1}^{M} g[\delta u(k+l-1)] \tag{13}$$

In vector form, Eq. (13) can be written as:

$$\begin{aligned}
J_{PSMC} &= \left\|\widetilde{S}_p(k+1) - S_r(k+1)\right\|^2 + \|\Delta U(k)\|^2_G \\
&= \left[\Gamma x(k) + \Omega^F \Delta U(k) + \Omega^P u(k-1) + H_p E(k)\right. \\
&\quad - S_r(k+1)\left.\right]^T \left[\Gamma x(k) + \Omega^F \Delta U(k) + \Omega^p u(k-1)\right. \\
&\quad \left. + H_p E(k) - S_r(k+1)\right] + \Delta U(k)^T G \Delta U(k)
\end{aligned} \tag{14}$$

where

$$G = [g, g, \ldots, g]$$
$$S_r(k+1) = [s_r(k+1), s_r(k+2), \ldots, s_r(k+N)]^T$$

and sr(k + p) is the reference sliding mode trajectory, verifying the reaching law (4) and written as:

$$\begin{cases} s_r(k+p) = \varphi s_r(k+p-1) - m\, sign(s(k)) \\ s_r(k) = s(k) \end{cases}$$

Let $\frac{\partial J_{PSMC}}{\partial \Delta U(k)} = 0$, the optimal control law can be calculated as:

$$\Delta U(k) = -((\Omega^F)^T \Omega^F + G)^{-1} (\Omega^F)^T \left[\Gamma x(k) + H_p E(k) - S_r(k+1)\right] \tag{15}$$

Due to the rolling optimization, only the present increment of control input signal is implemented, the next time increment of control signal $\delta u(k)$ will be calculated by:

$$\delta u(k) = [1, 0, \ldots, 0]^T \Delta U(k) \tag{16}$$

Then, we have:

$$u(k) = u(k-1) + \delta u(k) \tag{17}$$

4 Synthesis of Discrete Sliding Mode Controller with Predictive Sliding Function

A block diagram of the Sliding Mode Controller with Predictive Sliding Function (SMC-PSF) is shown in Fig. 2, where the primary loop is a model predictive controller and the secondary loop is a sliding mode controller. Model predictive control allows optimal sliding function based on a specific objective. Sliding mode control is a stabilizing control law that computes quickly [29].

In this section, we consider the sliding mode control problem for system (1), taking reaching law (4).

For the sliding mode controller, the control law is given by the following expression:

$$u(k) = u_{eq}(k) + u_{dis}(k) \tag{18}$$

with:

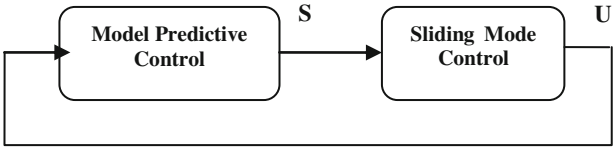

Fig. 2. SMC-PSF block diagram.

$$u_{eq}(k) = (CB)^{-1}[\varphi s(k) - CAx(k)] \tag{19}$$

$$u_{dis}(k) = -(CB)^{-1} m\ sign(s(k)) \tag{20}$$

Define the vector ΔUeq(k + 1) as:

$$\Delta U_{eq}(k+1) = \begin{bmatrix} u_{eq}(k+1) - u_{eq}(k) \\ u_{eq}(k+2) - u_{eq}(k+1) \\ \vdots \\ u_{eq}(k+M) - u_{eq}(k+M-1) \\ 0 \\ \vdots \\ 0 \end{bmatrix}_{(N\times 1)} \tag{21}$$

Considering the Eq. (19), the vector $\Delta U_{eq}(k+1)$ can be written as:

$$\Delta U_{eq}(k+1) = (CB)^{-1}\left[\varphi\begin{bmatrix} s(k+1) - s(k) \\ s(k+2) - s(k+1) \\ \vdots \\ s(k+M) - s(k+M-1) \\ \vdots \\ \vdots \\ s(k+N) - s(k+N-1) \end{bmatrix} - \begin{bmatrix} CA(x(k+1) - x(k)) \\ CA(x(k+2) - x(k+1)) \\ \vdots \\ CA(x(k+M) - x(k+M-1)) \\ \vdots \\ \vdots \\ CA(x(k+N) - x(k+N-1)) \end{bmatrix}\right] \tag{22}$$

Or we have:

$$
\begin{cases}
x(k+2)-x(k+1)=A(x(k+1)-x(k))+B(u_{eq}(k+1)-u_{eq}(k)) \\
x(k+3)-x(k+2)=A^2(x(k+1)-x(k))+AB(u_{eq}(k+1)-u_{eq}(k)) \\
\qquad\qquad +B(u_{eq}(k+2)-u_{eq}(k+1)) \\
\vdots \\
x(k+M)-x(k+M-1)=A^{M-1}(x(k+1)-x(k)) \\
\qquad\qquad +A^{M-2}B(u_{eq}(k+1)-u_{eq}(k)) \\
\qquad\qquad +A^{M-3}B(u_{eq}(k+2)-u_{eq}(k+1)) \\
\qquad\qquad +\cdots+B(u(k+M-1)-u(k+M-2)) \\
\vdots \\
x(k+N)-x(k+N-1)=A^{N-1}(x(k+1)-x(k)) \\
\qquad\qquad +A^{N-2}B(u_{eq}(k+1)-u_{eq}(k)) \\
\qquad\qquad +A^{N-3}B(u_{eq}(k+2)-u_{eq}(k+1)) \\
\qquad\qquad +\cdots+A^{N-M-1}B(u_{eq}(k+M)-u_{eq}(k+M-1))
\end{cases}
$$

Then the vector ΔUeq(k + 1) can be represented by:

$$
\Delta U_{eq}(k+1)=(CB)^{-1}\left[\varphi\begin{bmatrix} s(k+1)-s(k) \\ s(k+2)-s(k+1) \\ \vdots \\ s(k+M)-s(k+M-1) \\ \vdots \\ \vdots \\ s(k+N)-s(k+N-1) \end{bmatrix}-\Pi\,(x(k+1)-x(k))-\Psi\begin{bmatrix} u_{eq}(k+1)-u_{eq}(k) \\ u_{eq}(k+2)-u_{eq}(k+1) \\ \vdots \\ u_{eq}(k+M)-u_{eq}(k+M-1) \\ 0 \\ \vdots \\ 0 \end{bmatrix}\right] \tag{23}
$$

with:

$$
\Pi=\begin{bmatrix} CA \\ CA^2 \\ CA^3 \\ \vdots \\ CA^M \\ \vdots \\ CA^N \end{bmatrix}
$$

$$\Psi = \begin{bmatrix} 0 & 0 & \cdots & \cdots & 0 & \cdots & 0 \\ CAB & 0 & \cdots & \cdots & 0 & \cdots & 0 \\ \vdots & \vdots & \vdots & \vdots & \vdots & \vdots & \vdots \\ CA^{M-1}B & CA^{M-2}B & \cdots & 0 & 0 & \cdots & 0 \\ \vdots & \vdots & \vdots & \vdots & \vdots & \vdots & \vdots \\ CA^{N-1}B & CA^{N-2}B & \cdots & CA^{N-M-1}B & 0 & \cdots & 0 \end{bmatrix}$$

Equation (23) can be written as:

$$(I + (CB)^{-1}\Psi)\Delta U_{eq}(k+1) = (CB)^{-1}[\varphi \Delta S(k+1) - \Pi(x(k+1) - x(k))] \tag{24}$$

with:

$$\Delta S(k+1) = \begin{bmatrix} s(k+1) - s(k) \\ s(k+2) - s(k+1) \\ \vdots \\ s(k+M) - s(k+M-1) \\ \vdots \\ \vdots \\ s(k+N) - s(k+N-1) \end{bmatrix}$$

Equation (24) can be written as:

$$\Delta U_{eq}(k+1) = (I + (CB)^{-1}\Psi)^{-1}\Big[(CB)^{-1}[\varphi \Delta S(k+1) - \Pi(x(k+1) - x(k))]\Big] \tag{25}$$

So:

$$\Delta U_{eq}(k+1) = K\Delta S(k+1) + L(x(k+1) - x(k)) \tag{26}$$

with:

$$\begin{cases} K = (I + (CB)^{-1}\Psi)^{-1}(CB)^{-1}\varphi \\ L = -(I + (CB)^{-1}\Psi)^{-1}(CB)^{-1}\Pi \end{cases}$$

The following corresponding optimization cost function is defined:

$$j_{SMC-PSF}(k) = \sum_{j=1}^{N} q_j' \big[\delta s_p(k+j) - \delta s_r(k+j)\big]^2 + \sum_{l=1}^{M} g_l' \big[\delta u_{eq}(k+l-1)\big]^2 \tag{27}$$

Where δsr(k + j) is the increment of the sliding mode reference trajectory, δsp (k + j) is the increment of the sliding mode function, qj and gl are weight coefficients.

In order to simplify the synthesis of the controller, we consider (qj' = q') and (gl' = g'). So, the following corresponding optimization cost function is written by:

$$j_{SMC-PSF}(k) = \sum_{j=1}^{N} q' \left[\delta s_p(k+j) - \delta s_r(k+j)\right]^2 + \sum_{l=1}^{M} g' \left[\delta u_{eq}(k+l-1)\right]^2 \quad (28)$$

Rewrite Eq. (25) in vector form:

$$J_{SMC-PSF}(k) = \left\|\Delta S_p(k) - \Delta S_r(k)\right\|_{Q'}^2 + \left\|\Delta U_{eq}(k)\right\|_{G'}^2 \quad (29)$$

Since the control objective is to keep states on the sliding surface, the desired sliding mode reference value should be: Sr(k) = 0 ∀ k, so ΔSr(k) = 0 ∀ k [26]. Then, the optimization cost function can be written as:

$$J_{SMC-PSF}(k) = \left\|\Delta S_p(k)\right\|_{Q'}^2 + \left\|\Delta U_{eq}(k)\right\|_{G'}^2 \quad (30)$$

Using Eq. (25), $J_{SMC\text{-}PSF}(k)$ can be written as:

$$\begin{aligned} J_{SMC-PSF}(k) = {} & \Delta S_p(k)^T Q' \Delta S_p(k) + \left[K \Delta S_p(k)\right. \\ & \left. + L(x(k) - x(k-1))\right]^T G' \left[K \Delta S_p(k) + L(x(k) - x(k-1))\right] \end{aligned} \quad (31)$$

The optimal sequence of the sliding function is obtained by minimizing the cost function JSMC-PSF:

$$\frac{\partial J_{SMC-PSF}(k)}{\partial \Delta S_p(k)} = 0 \quad (32)$$

Then, the sliding function can be calculated as:

$$\Delta S_p(k) = -(G' K^T K + Q')^{-1} G' K^T L(x(k) - x(k-1)) \quad (33)$$

Or δs(k) is the first element of the vector ΔSp(k). Then the sliding function s(k) is given as:

$$s(k) = s(k-1) + \delta s(k) \quad (34)$$

So, the control law $u_{eq}(k)$ can be calculated as:

$$u_{eq}(k) = (CB)^{-1}[\varphi s(k) - CAx(k)] \quad (35)$$

Or we have:

$$u_{dis}(k) = -(CB)^{-1} m \, sign(s(k)) \quad (36)$$

So:

$$u(k) = u_{eq}(k) + u_{dis}(k) \tag{37}$$

5 Comparison Between PSMC and SMC-PSF

To evaluate the performances of the control laws (17) and (37), we consider the isothermal Van de Vussen systems [25].

It is a non linear, non minimum phase process. That's why, it has been used to show the controller performances.

After linearization and discretization, the state space representation of the isothermal Van de Vussen systems is given as follows:

$$\begin{cases} x(k+1) = Ax(k) + Bu(k) \\ y(k) = Hx(k) + Du(k) \end{cases}$$

where:

$$A = \begin{bmatrix} 1.2573 & -0.7902 \\ 0.5 & 0 \end{bmatrix};\ B = \begin{bmatrix} 0.5 \\ 0 \end{bmatrix}$$

$$H = \begin{bmatrix} -0.1878 \\ 0.698 \end{bmatrix};\ \mathrm{D} = [-0.0939]$$

The retained synthesis parameters are: $m = 1.5$, $N = 10$, $M = 5$, $C = [1\ \ -1]$, $G = 0.01\,\mathrm{I}_{\mathrm{N}\times\mathrm{N}}$, $Q = \mathrm{I}_{\mathrm{N}\times\mathrm{N}}$, $x(0) = [3\ \ 1]^{\mathrm{T}}$, $G' = 0.01\,\mathrm{I}_{\mathrm{N}\times\mathrm{N}}$, $Q' = \mathrm{I}_{\mathrm{N}\times\mathrm{N}}$.

The simulation results are obtained with the presence of disturbances, whose evolution is given in Fig. 3. The parameters variations are given by:

$$\Delta A = 0.1 \begin{bmatrix} 5\sin(-\frac{2K\pi}{10}) & 6\sin(-\frac{2K\pi}{10}) \\ 3\sin(-\frac{2K\pi}{10}) & 3\sin(-\frac{2K\pi}{10}) \end{bmatrix}$$

$$\Delta B = 0.1 \begin{bmatrix} 2\sin(-\frac{2K\pi}{10}) \\ 3\sin(-\frac{2K\pi}{10}) \end{bmatrix};\quad \mathrm{k} \geq 300$$

Comparing between the PSMC, the SMC-PSF, the SMC and the MPC, the states response, the sliding mode function and the control input are given respectively, in Figs. 4, 5, 6 and 7.

It can be seen that the performances of the PSMC and the SMC-PSF are better than the SMC or the MPC. Not only, in rejecting disturbances and hard parameters variation, but also in eliminating the chattering problem (k ≥ 300).

Comparing, only, between the PSMC and the SMC-PSF, Figs. 8, 9, 10 and 11 illustrate respectively the states response, the sliding mode function and the control input.

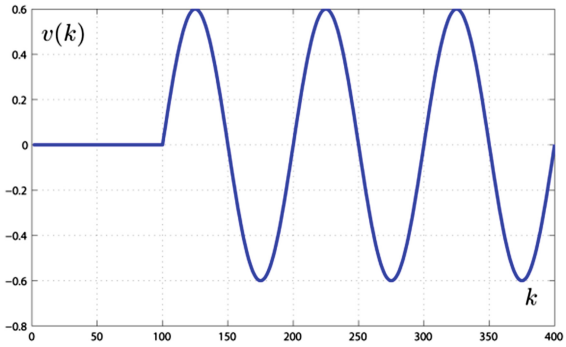

Fig. 3. Evolutions of disturbances.

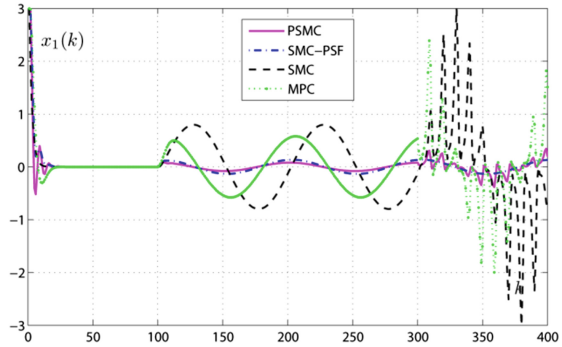

Fig. 4. Evolutions of the state $x_1(k)$.

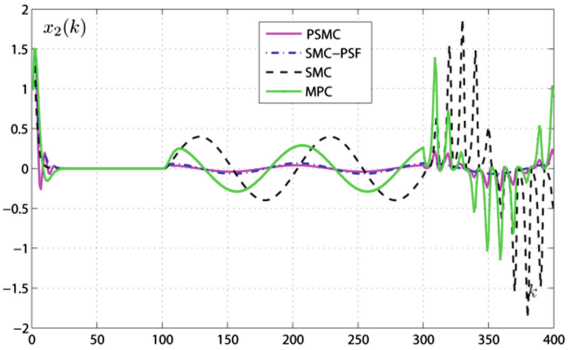

Fig. 5. Evolutions of the state $x_2(k)$.

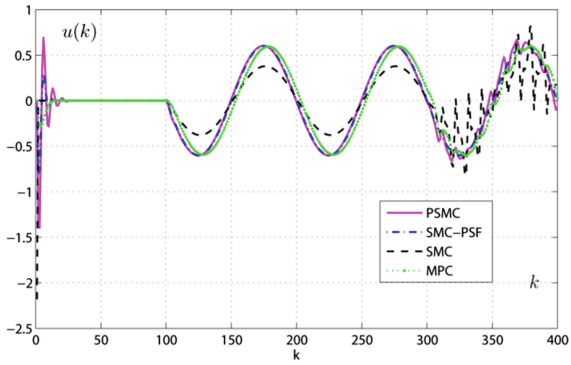

Fig. 6. Evolutions of the control input *u(k)*.

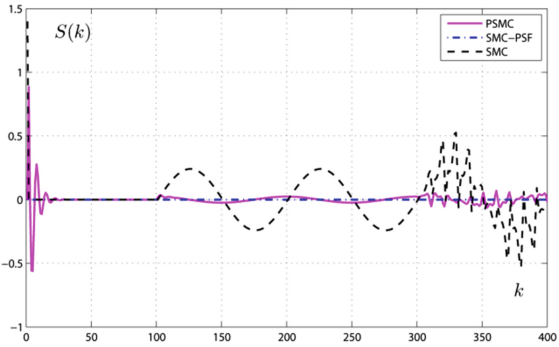

Fig. 7. Evolutions of the sliding function *s(k)*.

At the attainability phase (for $k \leq 10$), these figures prove that the SMC-PSF and PSMC converge at the same time, but without oscillations for the SMC-PSF and with three oscillations for the PSMC.

With disturbances and without parameter variation, (for $100 \leq k \leq 300$), the PSMC reduce better disturbances than the SMC-PSF.

But at the presence of disturbances and parameter variation (for $k \geq 300$), SMC is more able to eliminate chattering. In fact, it can eliminate oscillation better, than the PSMC.

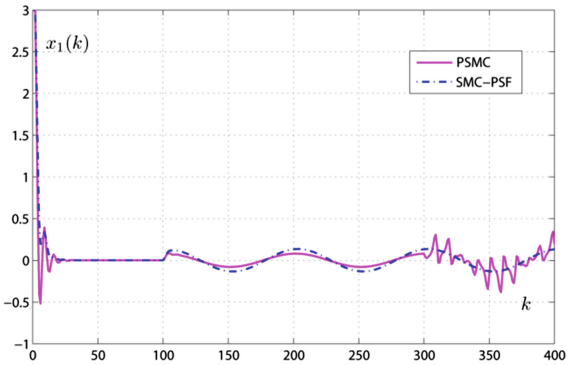

Fig. 8. Evolutions of the state $x_1(k)$.

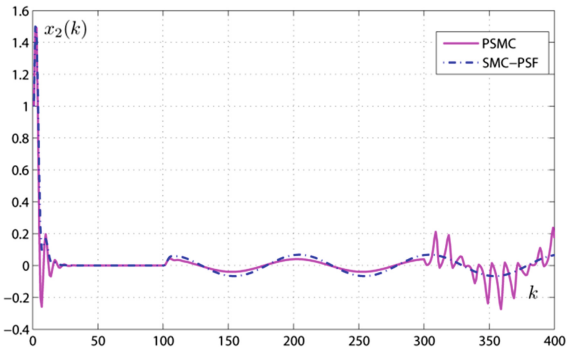

Fig. 9. Evolutions of the state $x_2(k)$.

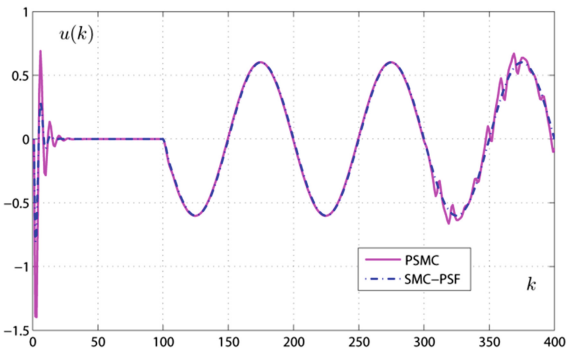

Fig. 10. Evolutions of the control input $u(k)$.

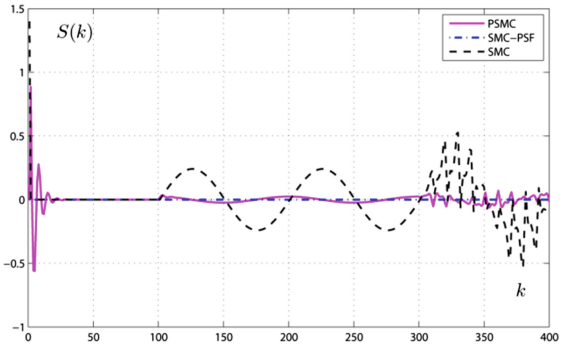

Fig. 11. Evolutions of the sliding function *s(k)*.

6 Conclusion

The two sliding mode prediction control design approaches proposed in this paper, combines the design technique of the SMC and MPC.

Firstly, a predictive sliding mode control strategy is proposed and a discrete-time reaching law is improved by applying a predictive sliding surface and a reference trajectory.

Secondly, a cascade control strategy is proposed to determine the optimal linear surface parameters of the Sliding Mode Control.

It is shown that mixing both control techniques gives news controllers with better robustness properties in rejecting disturbances, hard parameters variation and in eliminating the chattering problem.

Comparing the two controllers PSMC and SMC-PSF, it is true that the PSMC reduce better the disturbances, but, it can be seen that the SMC-PSF is more able to eliminate chattering, by eliminating oscillations at the phase of convergence and at the presence of hard parameters variation.

Acknowledgment. This work was supported by the Ministry of the Higher Education and Scientific Research Tunisia.

References

1. Lopez, P., Nouri, A.S.: Théorie élémentaire et pratique de la commande par les régimes glissants. Springer, Heidelberg (2006)
2. Yu, X., Kaynak, O.: Sliding mode control with soft computing: a survey. IEEE Trans. Industr. Electron. **56**(9), 3275–3285 (2009)
3. Utkin, V.I., Wang, Y., Wang, D.: Variable structure systems with sliding mode. IEEE Trans. Autom. Control **22**(2), 212–222 (1977)
4. Utkin, V.I., Chang, H.C.: Sliding mode control on electro-mechanical systems. Math. Prob. Eng. **8**, 451–473 (2002)

5. Mihoub, M., Nouri, A.S., Ben Abdennour, R.: Real time application of discrete second order sliding mode control to a chemical reactor. Control Eng. Pract. **17**, 1–7 (2009)
6. Bartolini, G., Ferrara, A., Usani, E.: Chattering avoidance by second-order sliding mode control. IEEE Trans. Autom. Control **43**(2), 241–246 (1998)
7. Cavallo, A., Natale, C.: High-order sliding control of mechanical systems: theory and experiments. Automatica **12**, 1139–1149 (2004)
8. Clarke, D., Mohtadi, W., Tuffs, P.: Generalized predictive control Part I. The basic algorithm. Automatica **23**(2), 137–148 (1992)
9. Clarke, D., Scattolini, R.: Constrained receding horizon predictive control. IEEE Trans. Autom. Control **23**(2), 347–354 (1991)
10. Camacho, O.: A predictive approach based sliding mode control. In: 15th Triennial World Congress, IFAC, Barcelone, Spain (2002)
11. Gabin, W.G., Zambrano, D., Camacho, E.F.: Sliding mode predictive control of a solar air conditioning plant. Control Eng. Pract. **17**, 652–663 (2009)
12. Xiao, L., Su, H., Zhang, X.: Variable structure control with sliding mode prediction for discrete time nonlinear systems. J. Control Theor. Appl. **2**, 140–146 (2006)
13. Xiao, L.F., Zhang, H.Y., Chu, J.: Discrete variable structure control algorithm for nonlinear systems via sliding mode prediction. In: Proceeding of American Control Conference, Minneapolis, Minnesota, USA, pp. 4712–4717. IEEE (2006)
14. De La Parte, M., Camacho, O., Camacho, E.: Developement of a GPC-based sliding mode controller. ISA Trans. **41**, 19–30 (2002)
15. Ben Mansour, H., Nouri, A.S.: Discrete predictive sliding mode control of uncertain systems. In: Proceedings of the 9th International Multi-Conference on System, Signals and Devices (2012)
16. Ben Mansour, H., Abdennabi, N., Nouri, A.S.: Predictive sliding mode control for perturbed discrete time delay systems: robustness analysis. In: Proceedings of the International Conference on Electrical Engineering and Software Applications, ICEESA 2013, Hammamet, Tunisia, 21–23 March 2013 (2013)
17. Abdennebi, N., Ben Mansour, H., Nouri, A.S.: A new sliding function for discrete predictive sliding mode control of time delay systems. In: 13th International conference on Sciences and Techniques of Automatic Control and Computer Engineering (2012)
18. Zaholan, H., Mao, W., Shuhuan, L.: Discrete sliding mode prediction control of uncertain switched systems. J. Syst. Eng. Electron. **20**, 1065–1071 (2009)
19. Gao, W., Wang, Y., Homaifa, A.: Discrete-time variable structure control systems. IEEE Trans. Industr. Electron. **42**(2), 117–122 (1995)
20. Camacho, E.F., Bordon, C.: Model Predictive Control. (2nd edn.). Springer, London (2004)
21. Culi, R.J., Bordon, C.: Iterative nonlinear model predictive control. Stability, robustness and applications. Control Eng. Pract. **16**, 1023–1034 (2008)
22. Maciejowski, J.M.: Predictive Control with Constraints. Prentice Hall, Harlow (2011)
23. Clarke, D.W., Mohtadi, M., Tuffs, P.S.: Generalized predictive control: Part II: extensions and interpretation. Automatica **23**(2), 149–160 (1987)
24. Bitmead, R.R., Gevers, M., Wertz, V.: Adaptative Optimal Control: The Thinking Man's GPC. Prentice Hall, Brunswick (1990)
25. Gabin, W.G., Camacho, E.F.: Sliding mode model based predictive control for non minimum phase systems. In: European Control Conference, Cambridge UK (2003)
26. Zhao, J., Meng, J., Zhang, L.: Passivity-based sliding mode predictive control of discrete-time singular systems with time varying delay. In: Proceeding of International Conference on Consumer, Electronics, Communication and Networks (CECNET) (2011)
27. Ben Mansour, H., Dehri, K., Nouri, A.S.: New predictive sliding mode control for non minimum phase systems. Int. J. Comput. Appl. IJCA **70**(11), 1–8 (2013)

28. Abdennabi, N., Ben Mansour, H., Nouri, A.S.: A new sliding function for discrete predictive sliding mode control of time delay systems. Int. J. Comput. Appl. **10**(4), 288–295 (2013)
29. Ben Mansour, H., Dehri, K., Nouri, A.S.: New discrete sliding mode controller with predictive sliding function. Int. Rev. Autom. Control **6**(4), 529–536 (2013)

Discrete Variable Structure Model Reference Adaptive Control for Non Strictly Positive Real Systems Using Only I/O Measurements

Aicha Znidi(✉), Khadija Dehri, and Ahmed Said Nouri

Research Unit: Numerical Control of Industrial Processes, National Engineering School of Gabes, University of Gabes, Street of Medenine, 6029 Gabes, Tunisia
aicha.zneidi@gmail.com, khadija.dehri@gmail.com, ahmedsaid.nouri@enig.rnu.tn

Abstract. Solving the problem of unpredictable transient responses and tracking reference trajectories has recently becomes one of the challenging aspects of Model Reference Adaptive Control (MRAC). In this paper, a Discrete Variable Structure Model Reference Adaptive Control using only input output measurements (D-VS-MRAC-IO) for linear non strictly positive real systems with relative degree two and relatively important parameter variations was proposed. The D-VSMRAC- IO was designed in order to improve the performances of the MRAC control. Simulation results show a good reference trajectory tracking in spite of the presence of parameter uncertainties.

Keywords: Model reference adaptive control · Variable structure control · Relay · Discrete Non-strictly positive real systems · Relative degree two · Parameter uncertainties

1 Introduction

In recent years, there has been a considerable interest in the control of dynamical systems with parameter uncertainties. Several techniques such as adaptive control techniques appeared in the literature. Model Reference Adaptive Control (MRAC) has especially received a fair amount of attention and attracted many researchers [2, 6–8, 10, 20, 22, 25]. The MRAC control is based on the modification of the controller parameters to achieve reference trajectory tracking in spite of the presence of unknown or uncertain parameters using a pre-designed stable reference model. However, this control was confronted with several problems resulting in transient closed-loop behavior, problem of stability, and large control signal, etc. In order to solve these problems and to achieve global stability, good robustness and well behaving tracking performances, numerous works are available for continuous time systems as well as sampled data systems [2, 9, 11–13, 18, 19]. One of these solutions is achieving robustness of the controller under the condition of Persistency of Excitation (PE) [17, 20, 21]. The second focus in modifying the parameter adaptation law: using the concept of dead zone introduced by Egardt [23]; the addition of a linear term $(-\sigma\theta)$ in the parameter update law adopted by Ioannou [24]. Other solutions are based on the combination of the model reference adaptive control

M. Chadli et al. (eds.), *Recent Advances in Electrical Engineering and Control Applications*, Lecture Notes in Electrical Engineering 411, DOI 10.1007/978-3-319-48929-2_8

and intelligent control as neural network and fuzzy logic control [1, 3, 31], as well as iterative learning control [14]. Variable Structure Control (VSC) is another well-known technique, for its robustness against external disturbances and parameter uncertainties [1, 4, 5, 7, 15, 16]. The VSC is based on the switching functions of the state variables, whose purpose is to force the trajectories of the system to reach the desired sliding manifold in finite time and to stay on it.

However, the original VSC requires the knowledge of all state coordinate values which cannot be measured in most cases. The use of state observers is a natural way to circumvent these requirements [29]. Another recent solution for this problem is based on measuring the system inputs and outputs [4, 7, 16]. Most of these solutions are still limited to systems with relative degree $n^* = 1$. An extension of this approach to continuous-time systems with relative degree $n^* = 2$ had been developed [7].

The combination of the variable structure control and the adaptation mechanisms was firstly proposed by G. Ambrosino in [30] and it was based on the same controller structure of the parameters adaptive scheme. But, it suffers from a mathematically ill-defined algorithm. It has been shown that a globally stable algorithm, designated VS-MRAC, can be constructed for systems with relative degree one. The controller was obtained by replacing the integral adaptation law by an appropriate VSC law. Significant advantages were shown: proper transient behavior and robustness with respect to unmodelled dynamics.

Unlike to the case $n^* = 1$, when the relative degree is greater than one, the controller design becomes more complicated. The difference between them is that in the first case the reference model can be chosen Strictly Positive Real (SPR). Besides, the control structure can easily be obtained. However, in the second case the reference model is not SPR so that the controller and the analysis technique in relative degree one cannot be applied directly. A solution for the general case was presented in [7], which requires n^* auxiliary errors.

In this paper, we are interested in improving the performances and the robustness of model reference adaptive control for discrete linear not strictly positive real systems with relative degree two. Firstly, we proposed a modified MRAC control, based on adding a second term. It was shown through suitable simulation that the second term insured stability. But, it was not a potential solution for the required performance improvements. Then, we developed a discrete relay-variable structure model reference adaptive control. This paper is organized as follow.

Section 2 will present the basic definitions and assumptions of the considered system. In Sect. 3, we will formulate the modified discrete model reference adaptive control for linear systems with relative degree two and parameter uncertainties. The development of a discrete variable structure model reference adaptive control using only input output measurements will be presented in Sect. 4. Section 5 will give the simulation results. Finally, we will give the conclusion.

2 Basic Definitions

Consider a linear single-input single-output discrete-time system with relative degree $n^* = 2$. The system can be described by the following transfer function:

$$\mathrm{W}\left(q^{-1}\right) = k_p q^{-d} \frac{B(q^{-1})}{\mathrm{A}(\mathrm{q}^{-1})} \tag{1}$$

where y(k) and u(k) are respectively the output and the input.

$\mathrm{A}(\mathrm{q}^{-1})$ and $\mathrm{B}(\mathrm{q}^{-1})$ are two polynomials defined as follows:

$$\mathrm{A}\left(\mathrm{q}^{-1}\right) = 1 + a_1\mathrm{q}^{-1} + a_2\mathrm{q}^{-2} + \ldots + a_n\mathrm{q}^{-\mathrm{n}}$$
$$\mathrm{B}\left(\mathrm{q}^{-1}\right) = 1 + b_1\mathrm{q}^{-1} + b_2\mathrm{q}^{-2} + \ldots + b_m\mathrm{q}^{-\mathrm{m}}$$

k_p is a positive constant gain.

- We note n^* the relative degree of the system, with $n^* = n$ - m.
- d: is the time delay system.

In this work, we were concerned with input-output not strictly positive real (NSPR) systems whose relative degree is 2. To define this type of system, we first defined positive real (PR) and strictly positive real (SPR) transfer function [26, 27].

Definition 1: A discrete-time rational transfer function $W(q^{-1})$ is said to be positive real (PR) if:

1. $W(q^{-1})$ is analytic in $|q| > 1$.
2. $Re[W(q^{-1})] \forall \mathrm{q}\ ;\ |q| > 1$.

Definition 2: A discrete-time rational transfer function $W(q^{-1})$ is said to be strictly positive real (SPR) if:

1. $\mathrm{B}(\mathrm{q}^{-1})$ and $\mathrm{A}(\mathrm{q}^{-1}) \in S$, with S is the set of Schur ploynomials, i.e. the set of all ploynomials in q^{-1} whose roots lie in $\left|q^{-1}\right| < 1$.
2. $Re[W(e^{-j\omega})] \geq 0,\ \forall \omega \in [0\ 2\pi]$.

If one of the above conditions is not satisfied the transfer function is called Non Strictly Real Positive (NSPR) function. In this paper, we are interested in NSPR systems with relative degree two.

3 The Modified Discrete Model Reference Adaptive Control

Model reference adaptive control (MRAC) is one of the main approaches to adaptive control. The basic structure of the MRAC scheme consists in an adaptive controller whose parameters were directly adjusted by an adaptation scheme so that the closed loop plant follows the conceptual model, which defines the desired performances.

The desired behavior of the system was described by a model reference, characterized by the following transfer function:

$$W_m(q^{-1}) = k_m q^{-d_1} \frac{B_m(q^{-1})}{A_m(q^{-1})} \tag{2}$$

where $y_m(k)$ and $y_c(k)$ are respectively the output and the input.

$$A_m(q^{-1}) = 1 + a_{m1}q^{-1} + a_{m2}q^{-2} + \ldots + a_{mn}q^{-n}$$
$$B_m(q^{-1}) = 1 + b_{m1}q^{-1} + b_{m2}q^{-2} + \ldots + b_{mz}q^{-z}$$

with $z \leq m$.

- k_m: is a positive constant gain.
- d_1: is the delay of the desired model.

The purpose is to elaborate a suitable control law u(k) such that the output error tends asymptotically to zero for arbitrary initial conditions and arbitrary piece-wise uniformly bounded reference signals $r(k)$.

$$e(k)y(k) - y_m(k) \tag{3}$$

In order to meet the control objective, we made the following standard assumptions [4]:

- ←the plant and the reference model were completely observable and controllable,
- ← the plant transfer function was minimum phase,
- ← the reference model had the same relative degree $n^* = n - m$ as the plant.

The MRAC law was structured as:

$$u(k) = \theta^T(k)\varphi(k) \tag{4}$$

where θ^T (k) is a vector of adjustable parameters and is considered as an estimate of a vector of unknown system parameters θ * (k) and φ^T(k) is the regression vector.

θ^T (k) and φ^T(k) are defined as:

$$\theta^T(k) = \left[k_0(k)C^T(k)D^T(k)d_0(k)\right] \tag{5}$$

$$\varphi^T(k) = \left[r(k)V_1^T(k)V_2^T(k)y(k)\right] \tag{6}$$

with V_1(k) and V_2(k) are generated by input/output filters according to following equation [4]:

$$\begin{cases} V1(k+1) = \Lambda V1(k) + gu(k) \\ V2(k+1) = \Lambda V2(k) + gy(k) \end{cases} \tag{7}$$

With $\Lambda \in R^{(n-1)\times(n-1)}$; $\det(qI - \Lambda) = q^{n-1} + \lambda_{n-2}q^{n-2} + \ldots + \lambda_1 q^{-1} + \lambda_0$ is a Hurwitz polynomial whose roots include the zeros of the reference model.

Since the relative degree $n^* = 2$, the reference model cannot be chosen SPR, a polynomial $L(q^{-1})$ was introduced by Monopoli [31], so that $W_m(q^{-1})L(q^{-1})$ is SPR.

In this case, an augmented error was generated by adding $y_a(k)$ to the true output error:

$$e_a(k) = e(k) - y_a(k) \tag{8}$$

where

$$y_a(k) = W_m(q^{-1})L(q^{-1}))\left[L^{-1}\theta^T - \theta^T L^{-1}\right]\varphi(k) + \alpha\xi^T(k)\Gamma\xi(k)e_a(k) \tag{9}$$

With $\xi(k) = L^{-1}(q^{-1})\varphi(k)$

$\Gamma(k)$: is the gain matrix, which is important for a successful adaptation.

The design task is to find adaptive laws to update the parameter $\hat{\theta}(k)$.

We chose the gradient adaptive laws given by:

$$\hat{\theta}(k) = \hat{\theta}(k-1) - \Gamma\xi(k)e_a(k) \tag{10}$$

The retained structure of the model reference adaptive control law is represented in Fig. 1.

In the MRAC scheme, the adaptation algorithm is based on parameter estimation and contains pure integral action which leads to unacceptable and unpredictably transient behavior and lack of robustness even under ideal conditions.

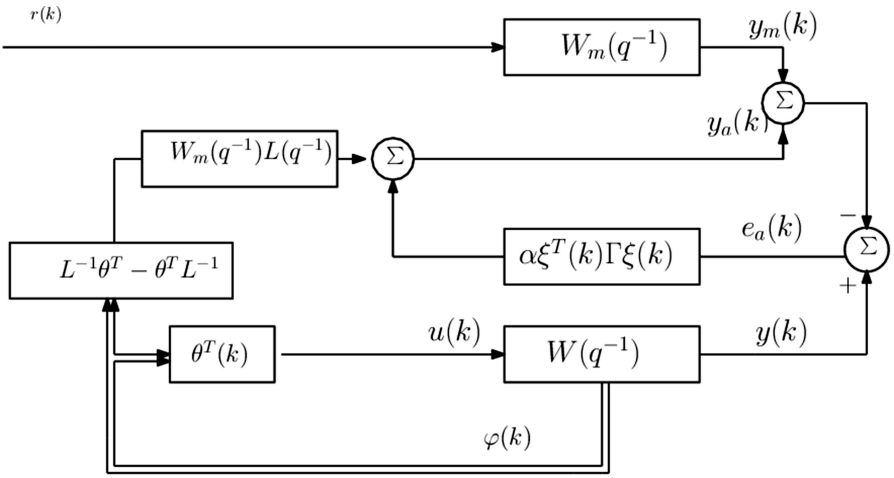

Fig. 1. The structure of model reference adaptive control $n^* = 2W_m(q^{-1})$, *is NSPR).*

In order to insure the stability and solve the problem of bad transient behavior, we proposed the development of a new control which is a combination of the MRAC and the variable structure control based on the Relay method.

The resulting control scheme was called Discrete Variable Structure Model Reference Adaptive Control using only Input-Output measurements (D-VS-MRAC-IO).

4 The Discrete Variable Structure Model Reference Adaptive Control Using Only Input-Output Measurements

Variable structure model reference adaptive control (VSMRAC) is a combination of the MRAC control with the Variable Structure Control (VSC). The original VS- MRAC requires the knowledge of all state vectors [28], which is difficult in certain cases. To overcome this problem, numerous trials attempt to extend the VS-MRAC technique to systems with only input and output measurements. However, most of these extensions can only be applied to systems with relative degree $n^* = 1$. This shortcoming was solved in [7], where an extension of the VS-MRAC-IO was developed in general case $n^* \geq 2$. But the resulting controller was much more complex for practical applications. Also, some new VS-MRAC-IO versions were proposed including a very simplified one the relay-VS-MRAC. The first attempt to develop Relay-VS-MRAC was made in continuous time, which was proposed by Liu HSU [4]. This algorithm consists in using positive $k_i (i = 0, \ldots, n^* - 1)$ and choosing $\theta_j^{nom}(k) = 0$ except, possibly, those corresponding to the output of system and the desired ouput. It only requires n* constant amplitude relays and a few linear filters [4]. Our aim is to extend this algorithm in the discrete framework and to show its effectiveness in reducing the effect of parameter uncertainties and unmodelled dynamics. The algorithm of this method is given below:

The control law can be defined by:

$$u(k) = -u_2(k) + r(k) \tag{11}$$

The two auxiliary control are expressed as follows:

$$u_1(k) = \mathrm{k_1 sign(s_1(k))} \tag{12}$$

$$u_2(k) = \mathrm{k_2 sign(s_2(k))} \tag{13}$$

With $sign(x(k)) = \begin{cases} 1 \, if \, x(k) > 0 \\ -1 \, if \, x(k) < 0 \end{cases}$; $x(k)$ can be $\mathrm{s_1(k)}$ or $\mathrm{s_2(k)}$.

As in the case of continuous time, the two sliding surfaces $\mathrm{s_1}$ (k) and $\mathrm{s_2}$ (k) are defined by:

$$\mathrm{s_1(k) = y(k) - y_m(k) - y_a(k)} \tag{14}$$

$$\mathrm{s_2(k) = (u(k))^*_{eq} - L^{-1}(q^{-1}) u_2(k)} \tag{15}$$

The term $(\mathrm{u(k)})^{*}_{\mathrm{eq}}$ is the equivalent control, which is approximately implemented in practice via averaging filter $F(q^{-1})$ defined by:

$$F(q^{-1}) = \frac{\mathrm{k_f q^{-2}}}{1 + 2\xi\omega \mathrm{q}^{-1} + \omega_0 \mathrm{q}^{-2}}$$

with high enough cut-off frequency ω_0. The operator $(\mathrm{u(k)})^{*}_{\mathrm{eq}}$ can be replaced by $F(q^{-1})$ in the VS-MRAC algorithm so the expression of $\mathrm{s_2(k)}$ became:

$$\mathrm{s_2(k)} = F(q^{-1})u_1(k) - L^{-1}(q^{-1})u_2(k) \tag{16}$$

The auxiliary signal is given by:

$$y_{a1}(k) = W_m(q^{-1})L(q^{-1})\left[u_1(k) - L^{-1}(q^{-1})u_2(k)\right] \tag{17}$$

The Hurwitz polynomial $L(q^{-1})$ is of the form:

$$\mathrm{L}(q^{-1}) = \mathrm{L_1(q^{-1})L_2(q^{-1})}\ldots\mathrm{L_j(q^{-1})} \text{ with } j = n^{*} - 1$$

Where $\mathrm{L_i(q^{-1})} = (q^{-1} - \delta_i)$ with $\delta_i > 0 \quad (\mathrm{i} = 1\ldots\mathrm{j})$.
The principle of this algorithm is given by the block diagram (Fig. 2):

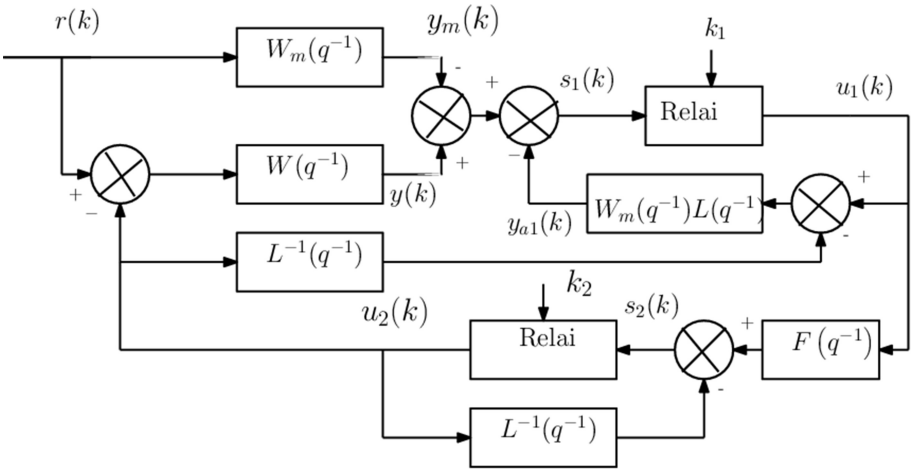

Fig. 2. Block diagram of the discrete VS-MRAC-IO control.

5 Simulation Example

In order to evaluate the robustness of the discrete model reference adaptive control and the discrete variable structure model reference adaptive control using only input-output measurements and to make a comparison between them, some simulations were made

to illustrate the difference of the tracking performance in the presence of parameter uncertainties.

Considere the single-input single-output system described by the following equation:

$$W(q^{-1}) = \frac{b_1 q^{-2}}{1 + a_1(k)q^{-1} + a_2(k)q^{-2}} \tag{18}$$

with $b_1 = 2.5.10^{-5}$

The parameters $a_1(k)$ and $a_2(k)$ are a time varying parameters.

These parameters are defined as:

$$a_1(k) = -1.9944 - 0.3 \times \cos(\mathrm{k})$$

$$a_2(k) = -0.9944 - 0.3 \times \cos(\mathrm{k})$$

The reference model was chosen as:

$$W_m(q^{-1}) = \frac{2.5.10^{-5} q^{-2}}{1 - 1.99\mathrm{q}^{-1} + 0.990025 q^{-2}} \tag{19}$$

As shown in Fig. 3 the reference model is not strictly positive real.

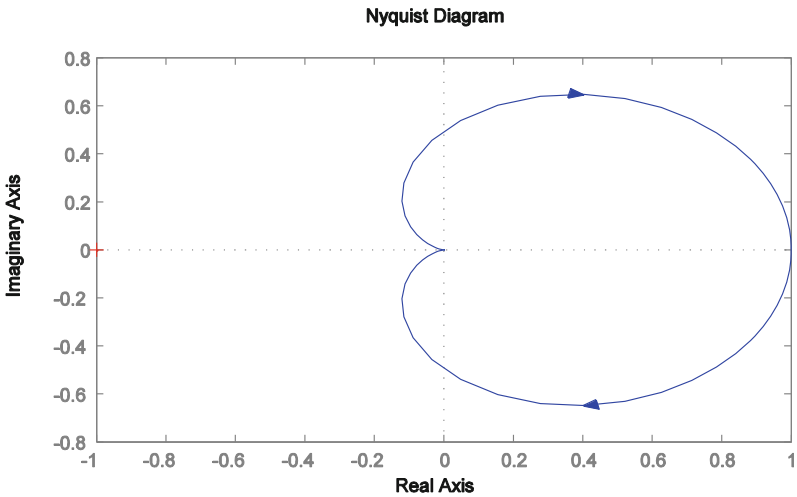

Fig. 3. The Nyquist diagram for the reference transfer function $W_m(q^{-1})$.

The reference input $r(k)$ is given by:

$$r(k) = \begin{cases} \sin(0.001k) & if\ k \leq \frac{2N}{3} \\ 1 & if\ k > 1 + \frac{2N}{3} \end{cases} \tag{20}$$

N is equal to 12000.

5.1 Mrac

Firstly, we applied the control law (4) to the considered system (1). In our case, the adaptation gain was given as follows:

$$\Gamma(k) = \Gamma(k-1) - \frac{\Gamma(k)\varphi(k)\varphi^T(k)\Gamma(k)}{1 + \varphi^T(k)\Gamma(k)\varphi(k)}$$

Since $W_m(q^{-1})$ was NSPR, we proposed a first order filter given by the following equation:

$$L^{-1}(q^{-1}) = \frac{0.001q^{-1}}{1 - 0.995q^{-1}}$$

So that $W_m(q^{-1})L(q^{-1})$ was SPR, as shown in Fig. 4.

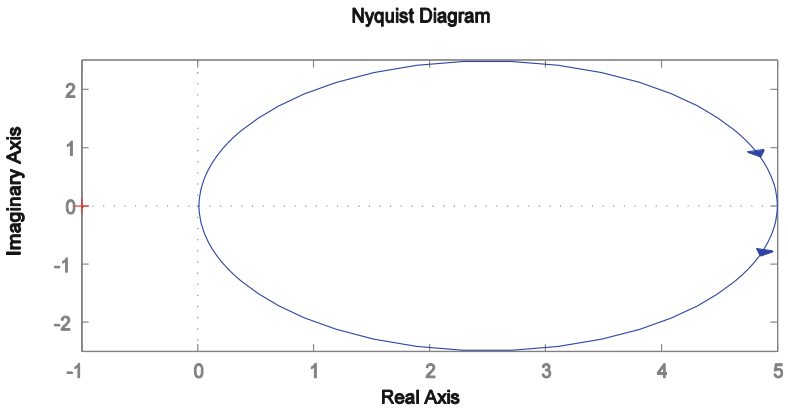

Fig. 4. The Nyquist diagram for the transfer function $W_m(q^{-1})L(q^{-1})$

To assess the effectiveness of MRAC against parameter uncertainties two cases were considered: without and with the second term.

Case 1: without $\alpha\xi^T(\boldsymbol{k})\boldsymbol{\Gamma}\boldsymbol{\xi}(\boldsymbol{k})\boldsymbol{e_a}(\boldsymbol{k})$ The Fig. 5 shows the evolutions of the desired reference trajectories $y_m(k)$ and the output of the system y(k).

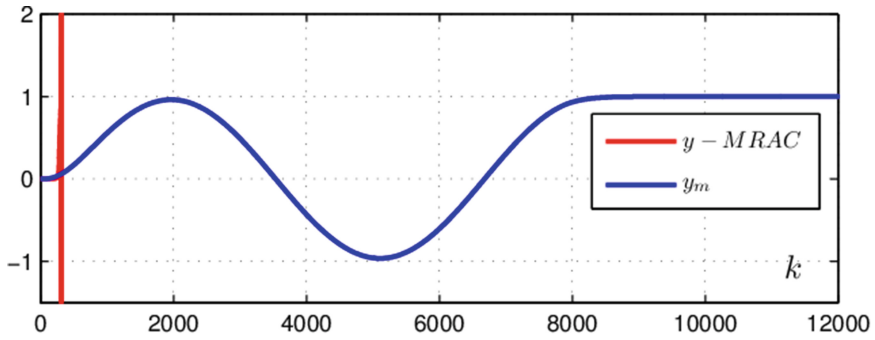

Fig. 5. Evolution of the system output and the model reference output (MRAC control without $\alpha\xi^T(k)\Gamma\xi(k)e_a(k)$)

This figure demonstrates that the system output is far from being representative of the desired behavior, the output could not follow the desired output.

Case 2: with $\alpha\xi^T(\boldsymbol{k})\boldsymbol{\Gamma\xi}(\boldsymbol{k})\boldsymbol{e_a}(\boldsymbol{k})$ In order to insure stability with respect to unmodeled dynamics, we proposed adding the second term, introduced by Narendra and Annaswamy [17] to the error equation.

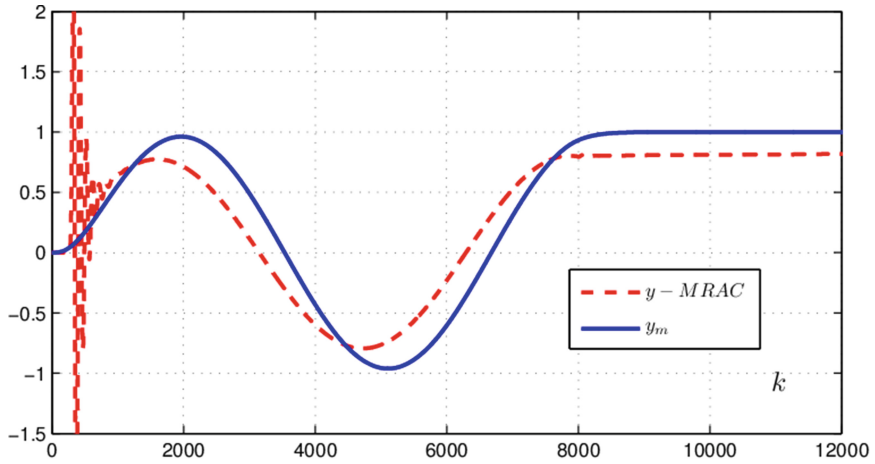

Fig. 6. Evolution of the system output and the model reference output (MRAC control with $\alpha\xi^T(k)\Gamma\xi(k)e_a(k)$)

Simulation results are shown in Figs. 6, 7 and 8. Figure 6 illustrates the evolution of the output y(k) and the desired reference trajectory $y_m(k)$, Fig. 7 presents the evolution of the controller u(k) and Fig. 8 shows the evolution of the control parameters.

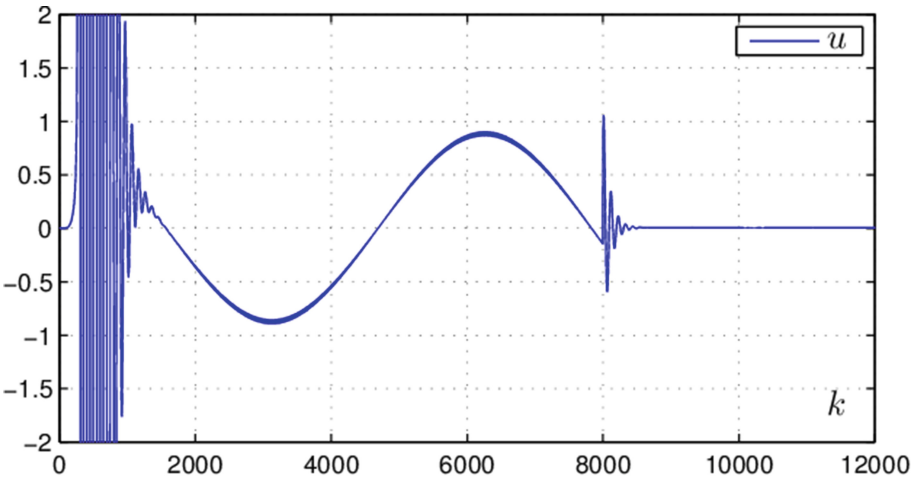

Fig. 7. Evolution of the control signal (MRAC control $\alpha\xi^T(k)\Gamma\xi(k)e_a(k)$).

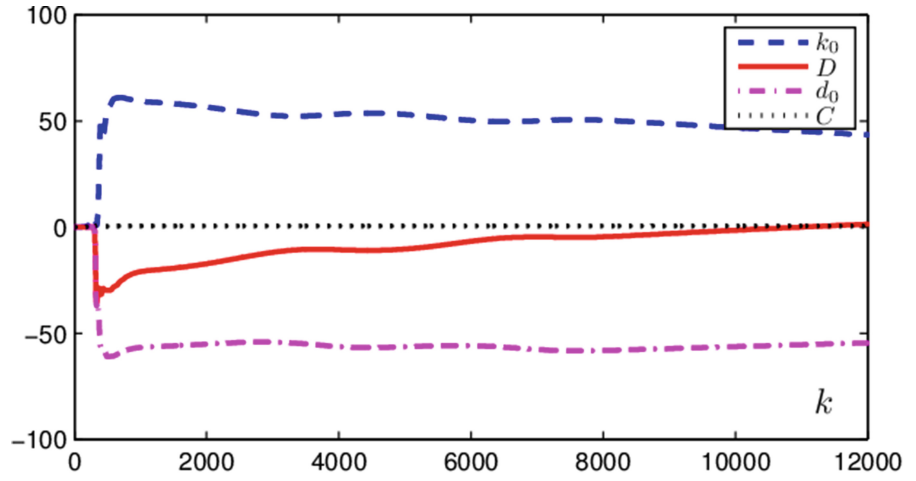

Fig. 8. Evolution of the control parameters (MRAC control with $\alpha\xi^T(k)\Gamma\xi(k)e_a(k)$).

According to the above simulation, the second term $\alpha\xi^T(k)\Gamma\xi(k)e_a(k)$ was essential to establish the stability of the system. But, some undesirable transient behaviors between $y(k)$ and $y_m(k)$ are observed in Fig. 6.

In fact, the gradient adaptation law was unable to follow the desired performances, even when we added the second term. To overcome this problem, we used the proposed discrete relay variable structure model reference adaptive input-output measurements control.

5.2 D-Vs-Mrac-Io

To demonstrate its importance interest and contribution to the performances of the synthesized discrete variable structure model reference adaptive control using only input output measurements, we took the same non stationary system described by the Eq. (18) again.

The low-pass filter is defined as:

$$F\left(q^{-1}\right) = \frac{0.01\mathrm{q}^{-2}}{1 - 1.8586\mathrm{q}^{-1} + 0.8686\mathrm{q}^{-2}}$$

The coefficients of the control law were chosen as $k_1 = 1$ and $k_2 = 1$.

The simulation results are shown in Figs. 9, 10, 11 and 12. Figure 9 shows the evolutions of the desired reference trajectory $y_m(k)$ and the output of the system $y(k)$

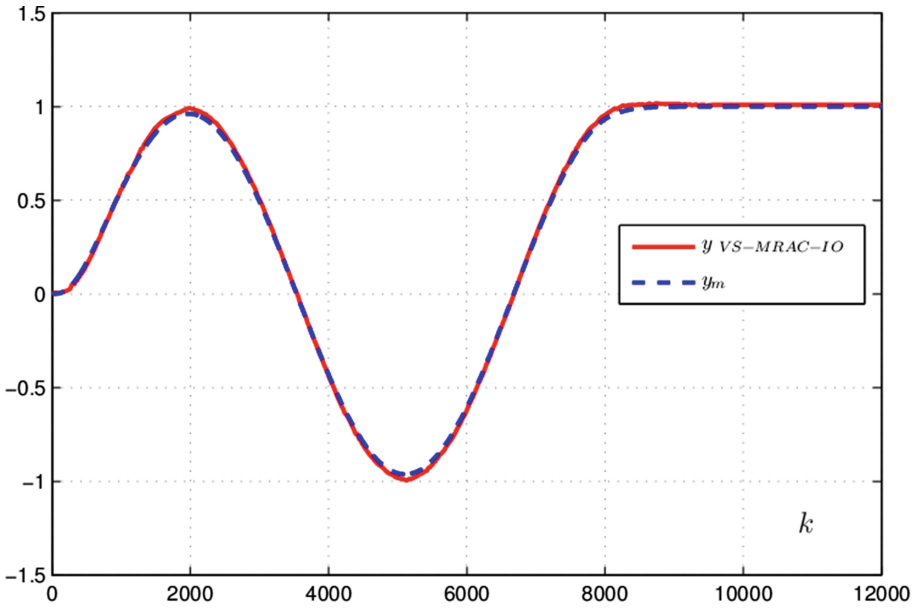

Fig. 9. Evolution of the system output and the model reference output (D-VS-MRAC-IO control).

Figure 10 presents the evolution of the controller $u(k)$. The evolution of the sliding surfaces $s_1(k)$ and $s_2(k)$ is presented in Figs. 11 and 12.

The D-VS-MRAC-IO was a reliable solution to solve the problem of the modified discrete MRAC: the system follows the desired behavior with more precision the desired behavior.

In fact, the output $y(k)$ tracks the reference $y_m(k)$ very accurately, the auxiliary sliding surfaces converge exponentially to zero.

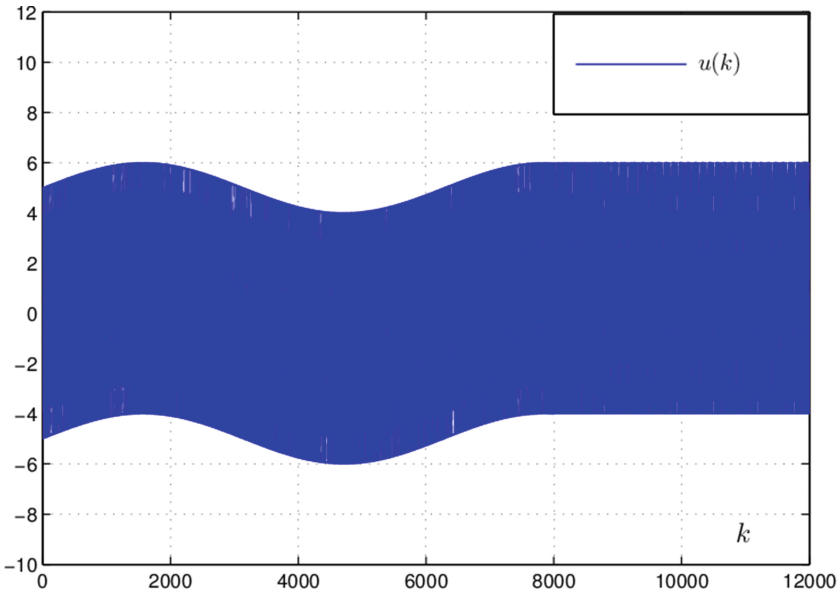

Fig. 10. Evolution of the control signal (D-VS-MRAC-IO).

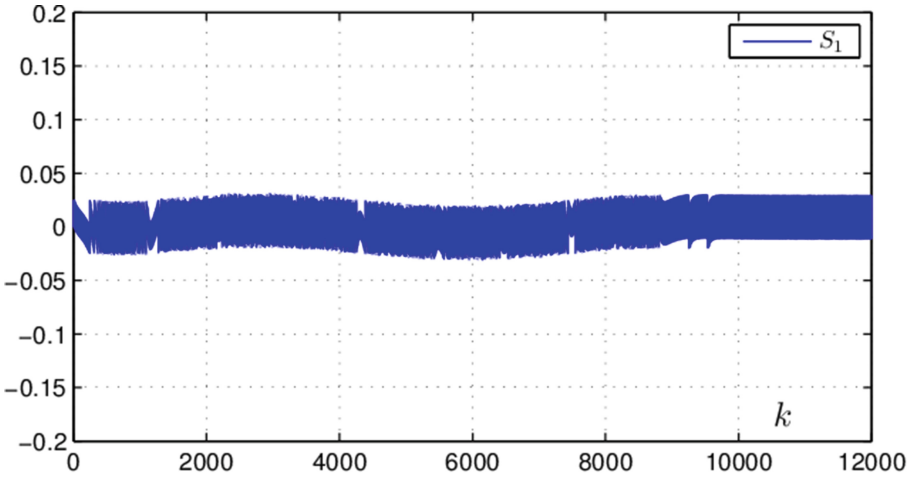

Fig. 11. Evolution of the sliding surfaces $s_1(k)$(discrete VS-MRAC-IO control).

5.3 Comparison Between Discrete MRAC and D-VS-MRACIO

Figure 13 shows the limits of the gradient adaptation law in the presence of unmodeled dynamics: unpredictable and unacceptable transient behavior and lack of robustness. However significant advantages are underlined compared to the model reference adaptive control.

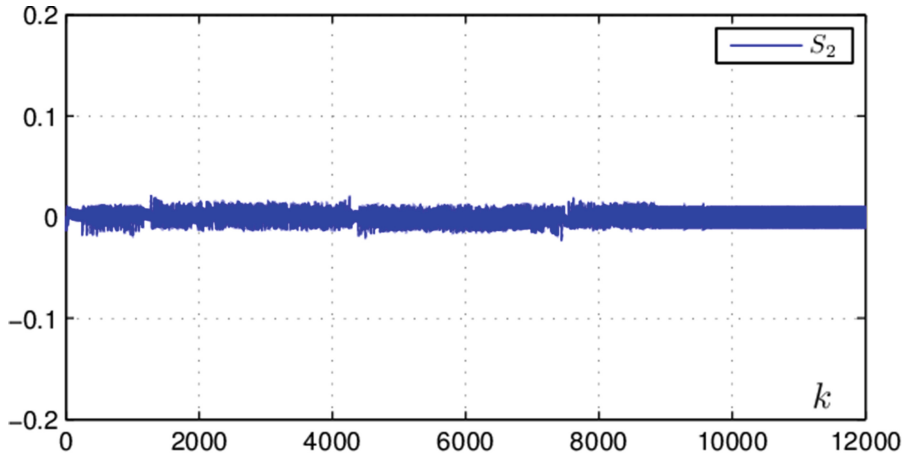

Fig. 12. Evolution of the sliding surfaces $s_2(k)$ (discrete VS-MRAC-IO control).

- remarkable transient behavior,
- good asymptotic stability,
- insensitivity to the parameters-variations,
- robustness to unmodeled dynamics.

Finally, the results show the effectiveness of the proposed DVS- MRAC-IO scheme and prove its performance superiority to the MRAC technique (Fig. 13).

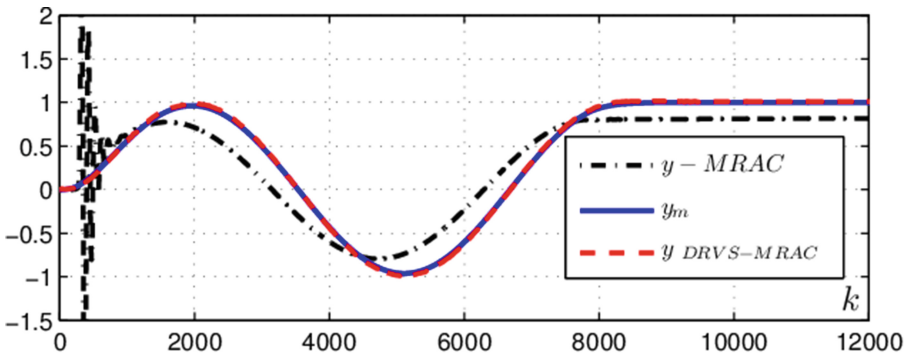

Fig. 13. Evolution of the system output and the model reference output.

6 Conclusion

The objective of this paper was to improve the performances of the standard MRAC for discrete time varying NSPR systems with relative degree $n^* = 2$ by exploring the intervention of Narendra and Annaswamy [17] as well as the VS-MRAC-IO.

The first solution was based on adding a second term $\alpha\xi^T(k)\Gamma\xi(k)e_a(k)$ to the error equation, which was unable to provide the required performance enhancements with respect to those achieved by the standard MRAC.

The second solution was the very simplified variable structure model reference adaptive control (discrete VS-MRAC IO), which was found to be efficient to insure stability, good robustness and well-behaving tracking performances.

Simulation results were included to highlight the theoretical results and the outstanding performances of discrete variable structure control using only input output measurements.

Acknowledgment. This work was supported by the Ministry of the Higher Education and Scientific Research Tunisia.

References

1. Mohore, S., Shukla, S.: Fuzzy based model adaptive reference controller for non linear systems. Int. J. Dig. Appl. Contemp. Res. **1**(6) (2013)
2. Ezzeldin, M., Van Den. Bosch, P.P.J., Waarsing, R.: Improved convergence of MRAC design for printing system. In: American Control Conference, pp. 3232–3237 (2009)
3. Murugananadham, A., Prakash, R.: A novel model reference intelligent adaptive control using neural network and fuzzy logic controller. J. Theor. Appl. Inf. Technol. **62**(1), 288–302 (2014)
4. Hsu, L., Araujo, A.D., Costa, R.: Analysis and design of I/O based variable structure adaptive control. IEEE Trans. Autom. Control **39**(1), 4–21 (1994)
5. Lopez, P., Nouri, A.S.: Théorie élémentaire et pratique de la commande par régimes glissants. Mathématiques et applications, vol. 55. Springer, Heidelberg (2006). SAMAI
6. Elkhalil, M., Ltaif, M., Nouri, A.S., Ben Abedennour, R., M'ssad, M.: Performance sampled data model reference controlenhancements using multimodel and variable structure control. In: International Conference on Automation, Robotics and Control Systems (ARCS 2008) 2008
7. Hsu, L.: Variable structure model-reference adaptive control (VS-MRAC) using only input and output measurements: the general case. IEEE Trans. Autom. Control **35**, 1238–1243 (1990)
8. Wen-Han, D., Xiu-Xia, S., Yan, L.: Variable structure model reference adaptive control with unknown high frequency gain sign. Acta Automatica Sincia **33**(4), 404–408 (2007)
9. da Cunha, J.P.V.S., Hsu, L., Costa, R.R., Lizarralde, F.: Output-feedback model-reference sliding mode control of uncertain multivariable systems. IEEE Trans. Automatica Control **48** (12), 2245–2250 (2003)
10. Trajkov, T.N., Koppe, H., Galbbert, U.: Direct model refernce adaptive control (MRAC) design and simulation for the vibration suppression of piezoelectr smart sructure. Commun. Nonlinear Sci. Numer. Simul. **13**, 1896–1909 (2008)
11. Rong, Z., De-wen, Z., Gun-chen, G.: A model adaptive variable structure controller for system with time delay. In: Chinese control and Decision conference (2009)
12. Hsu, L., da cunha, J.P.V.S., Costa, R.R., Lizarralde, F.: Unit vector control of multivariable systems. In: IFAC World Congress Barcelona (2002)
13. Tayebi, A.: Model reference adaptive iterative learning control for linear systems. Int. J. Adap. Control Sig. Process. **20**, 475–489 (2006)

14. Pourboghrat, F., Vlastos, G.: Model reference adaptive sliding control for linear systems. Comput. Electr. Eng. **28**, 361–374 (2002)
15. Fu, L.C.: A new robust MRAC using variable structure design for relative degree tow plants. Comput. Electr. Eng. Autom. **28**(5), 911–925 (1992)
16. Elkhalil, M., Ltaif, M., Ben Abdennour, R., M'Saad, M.: Sampled data model refernce control: performance enhancements using multimodel and variable structure control. In: International Conference on Automation, Robotics and Control Sytems, ARCS 2008 (2008)
17. Narendra, K., Annaswamy, M.: A new adaptive law for robust adaptation without persistent excitation. IEEE Trans. Aut. Control **32**, 134–145 (1987)
18. Oliveira, J.B., Araujo, A.D., Dias, S.M.: A simplified indirect adaptive sliding mode scheme. Eng. Prac. **18**, 577–584 (2010)
19. Coman, S., Boldisor, C.: Model reference adaptive control for a DC electrical drive. Bull. Transilvanic Univ. Brasov Ser. I: Eng. Sci. **6**(2), 33–38 (2013)
20. Xue-Jun, X., Jun-Ling, L.: A systematic analysis approach to discret time indirect model reference adaptive control. Acta Automatica Sincia **33**(11), 1170–1175 (2007)
21. Bodson, Stability, Convergence and robustness of adaptive systems, Ph. D. dissertation, University of California, Berkeley (1986)
22. Fei, J., Zhang, S., Zhou, J.: Adaptive sliding mode control of single phase shunt active power filter. Math. Prob. Eng. 1–22 (2012)
23. Egardt, B.: Stability analysis of adaptive control systems with disturbances. In: Proceedings of JACC, San Francisco (1980)
24. Ioannou, P.A.: Robust adaptive controller with zero residual tracking errors. IEEE Trans. Autom. Control **31**, 773–776 (1986)
25. Jain, P., Nigam, M.J.: Design of a model reference adaptive controller using modified MIT rule for a second order system. In: Advance in Electric and Electronic Engineering, vol. 3, No. 4, pp. 477–484 (2013). ISSN 2231–1297
26. Bianchini, G.: Synthesis of robust strictly positive real discrete-time systems with l2 parametric perturbations. IEEE Trans. Circ. Syst. I Fundam. Theor. Appl. **49**, 1221–1225 (2002)
27. Tao, G., Ioannou, P.A.: Necessary and sufficient conditions for strictly positive real matrices. IEE Proc. G-Circ. Dev. Syst. **137**(5), 360–366 (1990)
28. Slotine, J.J., Li, W.: Applied nonlinear control. Prentice-Hall, Englewood Cliff (1991)
29. Bondarev, A.G., Bondareva, S.A., Kostyleva, N.E., Utkin, V.I.: Sliding modes in systems with asymptotic state observers. Autom. Remote Control **46**(6), 679–684 (1985)
30. Hsu, L., Costa, R.R.: Variable structure model reference adaptive control using only input and output measurement: part I. Int. J. Control **6**(2), 399–416 (1989)
31. Douratsos, I., Gomm, J.B.: Neural network based model reference adaptive control for processes with time delay. Int. J. Inf. Syst. Sci. **3**(1), 161–179 (2007)

Stable Adaptive Fuzzy Sliding-Mode Controller for a Class of Underactuated Dynamic Systems

Soumia Moussaoui(✉) and Abdesselem Boulkroune

LAJ Laboratory, Department of Automatic Control, University of Jijel, Ouled-Aissa, BP. 98, 18000 Jijel, Algeria
soumia_moussaoui@hotmail.fr, boulkroune2002@yahoo.fr

Abstract. In this paper, a novel stable adaptive fuzzy sliding–mode controller (AFSMC) is investigated for a class of uncertain underactuated nonlinear dynamic systems. The underactuated system is decoupled into two subsystems. In the controller design, a sliding surface for each subsystem is defined and a suitable adaptive fuzzy system is used to reasonably approximate the uncertain functions. The stability of the closed-loop system is proven by Lyapunov approach. The effectiveness of the proposed AFSMC is illustrated throughout simulation results.

Keywords: Adaptive control · Sliding-mode control · Fuzzy control · Underactuated systems

1 Introduction

Recently, there has been an increasing interest in underactuated systems [1–9]. These systems have fewer actuators than degree of freedom to be controlled. Examples of this kind of systems can be found in several applications such as free-flying space robots, underwater robots, and manipulators with structural flexibility, overhead crane. It is obvious that underactuated systems have many advantages which include: the decreasing of the actuators number can decrease the volume and the weight of system.

Many control techniques to treat the underactuated systems have been proposed in the literature [1–11]. In [1], an adaptive control for an underactuated spherical robot based on hierarchical sliding mode approach has been proposed. An optimal control of underactuated nonholonomic mechanical systems was studied by Hussein and Bloch in [2]. Hao et al. have proposed a robust controller using incremental sliding mode control system method for a class of underactuated mechanical systems with mismatched uncertainties [3]. A sliding mode controller of double-pendulum crane systems has been developed in [4]. Authors of [5] have investigated an adaptive multiple-surface sliding controller based on function approximation techniques (FAT) for underactuated mechanical systems with disturbances and mismatched uncertainties. In [6], a motion planning-based adaptive control method of underactuated crane systems has been proposed. An adaptive fuzzy sliding mode control for a class underactuated system has been developed in [7]. Here, the underactuated system is decoupled into two

M. Chadli et al. (eds.), *Recent Advances in Electrical Engineering and Control Applications*, Lecture Notes in Electrical Engineering 411, DOI 10.1007/978-3-319-48929-2_9

subsystems, and a sliding surface is respectively define for each subsystem. Shine et al. [8] have designed a controller to achieve a globally asymptotical stability for a class of uncertain underactuated mechanical systems. A direct adaptive fuzzy sliding mode decoupling control for a class of underactuated mechanical systems has been developed in [9]. A stable sliding mode controller has been designed in [10] for a class of second-order underactuated systems. In [11], a disturbance adaptive control for an under-actuated spherical robot based on hierarchical sliding-mode technology has been investigated.

In this paper, motivated by works in [1–11], we will propose a novel adaptive fuzzy sliding mode controller (AFSMC) for a class of underactuated systems. The difficulties met in the control design are how to deal with unknown nonlinear functions, and to establish a control law which ensures the stability of the underactuated systems. These difficulties can be solved by using a fuzzy system approximation, a sliding mode control and a robust dynamic compensation.

Compared to the above works [1–11], the main contributions of this paper lie in the following:

(1) A novel and simple AFSMC for a class of uncertain underactuated systems is proposed.
(2) The model of these underactuated systems is assumed to be unknown, except the relative degree.
(3) Unlike many previous works (e.g. [1, 7, 10, 11]), the stability analysis of the closed-loop system is rigorously derived with mild assumptions.

2 System Description and Problem Formulation

Consider a class of underactuated nonlinear systems which can be expressed in the following form:

$$\begin{aligned} \dot{x}_1 &= x_2 \\ \dot{x}_2 &= f_1(X) + b_1(X)u \\ \dot{x}_3 &= x_4 \\ \dot{x}_4 &= f_2(X) + b_2(X)u \end{aligned} \tag{1}$$

where $X = [x_1, x_2, x_3, x_4] \in \Re^4$ is the state vector, $u \in \Re$ is the control input, $f_i(X)$ and $b_i(X)$, $i = 1, 2$, are unknown continuous nonlinear functions.

Assumption 1 [12, 13]: The functions $b_1(X)$ and $b_2(X)$ are non-singular and depend only on the variables x_1 and x_3.

Assumption 2: The desired trajectory vector $x_d(t) = [x_{d1} \quad x_{d2} \quad x_{d3} \quad x_{d4}] = [x_{d1} \quad \dot{x}_{d1} \quad x_{d3} \quad \dot{x}_{d3}] \in \Re^4$ is supposed to be continuous, bounded and available for measurement.

Assumption 3: The sign of the functions $b_1(X)$ and $b_2(X)$ is assumed to be known. Without loss of generality, we assume that the functions $b_1(X)$ and $b_2(X)$ are strictly positive.

The objective of this paper is to design an AFSMC for a class of underactuated systems described by (1) that guarantees the stability of the closed-loop system and the tracking error convergence to zero.

3 Control System Design and Stability Analysis

To quantify this control objective, we define the tracking error vector as follows:

$$e = \begin{bmatrix} e_1 \\ e_2 \\ e_3 \\ e_4 \end{bmatrix} = \begin{bmatrix} x_{d1} - x_1 \\ x_{d2} - x_2 \\ x_{d3} - x_3 \\ x_{d4} - x_4 \end{bmatrix} \tag{2}$$

The sliding surfaces are selected as follows:

$$\begin{cases} s_1 = \dot{e}_1 + c_1 e_1 \\ s_2 = \dot{e}_2 + c_2 e_2 \end{cases} \tag{3}$$

where c_1 and c_2 are positive design constants.

Differentiating (3) with respect to time yields:

$$\begin{cases} \dot{s}_1 = c_1 \dot{e}_1 + \dot{x}_{2d} - f_1(X) - b_1(X)u \\ \dot{s}_2 = c_2 \dot{e}_2 + \dot{x}_{4d} - f_2(X) - b_2(X)u \end{cases} \tag{4}$$

To facilitate the control system design, we rewrite the dynamics (4) as follows:

$$\begin{cases} \frac{1}{2}\frac{db_1^{-1}(X)}{dt} s_1 + \frac{\dot{s}_1}{b_1(X)} = \frac{1}{2}\frac{db_1^{-1}(X)}{dt} s_1 + \frac{c_1\dot{e}_1 + \dot{x}_{2d} - f_1(X)}{b_1(X)} - u \\ \frac{1}{2}\frac{db_2^{-1}(X)}{dt} s_2 + \frac{\dot{s}_2}{b_2(X)} = \frac{1}{2}\frac{db_1^{-1}(X)}{dt} s_2 + \frac{c_2\dot{e}_2 + \dot{x}_{4d} - f_2(X)}{b_2(X)} - u \end{cases} \tag{5}$$

Now, let's denote

$$\alpha_1(X) = \frac{1}{2}\frac{db_1^{-1}(X)}{dt} s_1 + \frac{c_1\dot{e}_1 + \dot{x}_{2d} - f_1(X)}{b_1(X)},$$
$$\alpha_2(X) = \frac{1}{2}\frac{db_2^{-1}(X)}{dt} s_2 + \frac{c_2\dot{e}_2 + \dot{x}_{4d} - f_2(X)}{b_2(X)}.$$

Multiplying by s_1 and s_2, the expression (5) becomes

$$\begin{cases} \frac{1}{2}\frac{db_1^{-1}(X)}{dt}s_1^2 + \frac{s_1\dot{s}_1}{b_1(X)} = (\alpha_1(X) - u)s_1 \\ \frac{1}{2}\frac{db_2^{-1}(X)}{dt}s_2^2 + \frac{s_2\dot{s}_2}{b_2(X)} = (\alpha_2(X) - u)s_2 \end{cases} \tag{6}$$

Since the nonlinear functions $\alpha_1(X)$ and $\alpha_2(X)$ are unknown, the design of a stable controller for dynamics (1) is very difficult. To solve this problem, we will use an adaptive fuzzy system to approximate these unknown nonlinear functions.

A. **Description of fuzzy logic system**

The basic configuration of a fuzzy logic system consists of following collection fuzzy IF-THEN rules:

$$R^{(l)} : \text{IF } x_1 \text{ is } F_1^l \text{ and} \ldots x_4 \text{ is } F_4^l \text{ THEN } y \text{ is } G^l \tag{7}$$

where $X = [x_1, x_2, x_3, x_4] \in \Re^4$ and $y \in \Re$ are the input and output of the fuzzy systems respectively, F_i^l and G^l are fuzzy sets, and $l = 1, 2, \ldots, N$, N is the total numbers of fuzzy rules for each the fuzzy model. By using the singleton fuzzifier, product inference, and center-average defuzzifier, the output of the fuzzy system can be expressed as follows:

$$y = \theta^T \psi(X) \tag{8}$$

where $\theta^T = \begin{bmatrix} \theta^1 & \theta^2 & \ldots & \theta^N \end{bmatrix} \in \Re^N$ with each variable θ^l as the point at which the fuzzy membership function of G^l achieves the maximum value, and the fuzzy basis function $\psi^T = \begin{bmatrix} \psi^1(X) & \psi^2(X) & \ldots & \psi^N(X) \end{bmatrix} \in \Re^N$, with $\psi^l(X)$ expressed as follows:

$$\psi^l(X) = \prod_{i=1}^{4} \mu_{F_i^l}(x_i) \Big/ \sum_{l=1}^{N} \left(\prod_{i=1}^{4} \mu_{F_i^l}(x_i) \right) \tag{9}$$

where $\mu_{F_i^l}(x_i)$ is the membership function of fuzzy set.

It is worth nothing that the fuzzy system (8) is commonly used in control applications. Following the universal approximation theorem, the fuzzy system (8) is able to approximate any nonlinear smooth function y on compact operating space to an arbitrary degree of accuracy. Of particular importance, it is assumed that the structure of the fuzzy system, namely the pertinent inputs, the number of membership functions for each input and the number of rules, and the membership function parameters are properly specified beforehand. The consequent parameters are then determined by appropriate parameter adaptation algorithms [14–17].

B. **Design of adaptive fuzzy sliding-mode controller**

To facilitate the control system design, the following assumption is presented and will used the subsequent developments.

Assumption 4: *There exists an unknown continuous positive function* $\bar{\alpha}_2(X)$, *such as that:*

$$|\alpha_2(X) - \alpha_1(X)| \leq \bar{\alpha}_2(X), \quad \forall X \in \Omega_X \subset \Re^4. \tag{10}$$

The unknown nonlinear function $\alpha_1(X)$ and $\bar{\alpha}_2(X)$ can be approximated by the linearly parameterized fuzzy systems (8), as follows:

$$\hat{\alpha}_1(X) = \theta_1^T \psi_1(X) \tag{11a}$$

$$\hat{\bar{\alpha}}_2(X) = \theta_2^T \psi_2(X) \tag{11b}$$

where $\psi_1(X)$ and $\psi_2(X)$ are fuzzy basis functions, and θ_1 and θ_2 are the adjustable parameters vector of the fuzzy systems.

Let's define the following optimal parameter vectors:

$$\begin{aligned} \theta_1^* &= \arg_{\theta_1} \min \left[\sup_{X \in \Omega_X} |\alpha_1(X) - \hat{\alpha}_1(X, \theta_1)| \right] \\ \theta_2^* &= \arg_{\theta_2} \min \left[\sup_{X \in \Omega_X} \left|\bar{\alpha}_2(X) - \hat{\bar{\alpha}}_2(X, \theta_2)\right| \right] \end{aligned} \tag{12}$$

Note that the optimal values of θ_1 and θ_2 are artificial constant quantities introduced only for analysis purposes, and their values are not needed when implementing the controller. Define $\tilde{\theta}_1 = \theta_1 - \theta_1^*$ and $\tilde{\theta}_2 = \theta_2 - \theta_2^*$ as the parameter estimation error, and $\varepsilon_1(X) = \alpha_1(X) - \hat{\alpha}_1(X, \theta_1^*)$ and $\varepsilon_2(X) = \bar{\alpha}_2(X) - \hat{\bar{\alpha}}_2(X, \theta_2^*)$ are the fuzzy approximation errors, where

$$\hat{\alpha}_1(X, \theta_1^*) = \theta_1^{*T} \psi_1(X) \tag{13a}$$

$$\hat{\bar{\alpha}}_2(X, \theta_2^*) = \theta_2^{*T} \psi_2(X) \tag{13b}$$

As in the literature [12–17], we assume that the used fuzzy systems do not violate the universal approximator property on the compact set Ω_X, which is assumed large enough so that the input vector of the fuzzy system remains in Ω_X under closed-loop control system. So it is logical that the fuzzy approximation error is bounded for all $x \in \Omega_X$, i.e. $|\varepsilon_i(X)| \leq \bar{\varepsilon}_i \ \forall X \in \Omega_X$, where $\bar{\varepsilon}_i$ is an unknown constant.

From the above analysis, one has

$$\begin{aligned} \hat{\alpha}_1(X, \theta_1) - \alpha_1(X) &= \hat{\alpha}_1(X, \theta_1) - \hat{\alpha}_1(X, \theta_1^*) + \hat{\alpha}_1(X, \theta_1^*) - \alpha_1(X) \\ &= \hat{\alpha}_1(X, \theta_1) - \hat{\alpha}_1(X, \theta_1^*) - \varepsilon_1(X) \\ &= \tilde{\theta}_1^T \psi_1(X) - \varepsilon_1(X) \end{aligned} \tag{14a}$$

$$\begin{aligned}\hat{\bar{\alpha}}_2(X,\theta_2)-\bar{\alpha}_2(X) &= \hat{\bar{\alpha}}_2(X,\theta_2)-\hat{\bar{\alpha}}_2(X,\theta_2^*)+\hat{\bar{\alpha}}_2(X,\theta_2^*)-\bar{\alpha}_2(X)\\ &= \hat{\bar{\alpha}}_2(X,\theta_2)-\hat{\bar{\alpha}}_2(X,\theta_2^*)-\varepsilon_2(X)\\ &= \tilde{\theta}_2^T\psi_2(X)-\varepsilon_2(X)\end{aligned} \tag{14b}$$

To meet the control objective, a suitable adaptive fuzzy sliding mode controller is proposed as follows:

$$u = k_1(s_1+s_2)+k_2 sign(s_1+s_2)+\theta_1^T\psi_1(X)+v_r \tag{15}$$

The associated adaptive laws are given by

$$\dot{v}_r = -\gamma_v v_r+\gamma_v\left[(s_1+s_2)-v_r\left(\frac{\theta_2^T\psi_2(X)|s_2|+k_3|s_2|+k_4 s_2^2}{v_r^2+\delta^2}\right)\right] \tag{16}$$

$$\dot{\delta} = -\gamma_\delta\delta\left(\frac{\theta_2^T\psi_2|s_2|+k_3|s_2|+k_4 s_2^2}{v_r^2+\delta^2}\right) \tag{17}$$

$$\dot{\theta}_1 = \gamma_{\theta_1}(s_1+s_2)\psi_1(X) \tag{18}$$

$$\dot{\theta}_2 = \gamma_{\theta_2}|s_2|\psi_2(X) \tag{19}$$

where $k_1, k_2, k_3, k_4, \gamma_v, \gamma_\delta, \gamma_{\theta_1}$ and γ_{θ_2} are positive design constants.

Theorem 1: Consider the system (1) and suppose that Assumptions 1–4 are satisfied. Then, the proposed control law (15)–(19) ensures that:

- all signals in the closed-loop system are bounded, and
- the tracking errors asymptotically converge to zero.

Proof of Theorem 1: Let us consider the following Lyapunov function candidate:

$$V = \frac{1}{2b_1(X)}s_1^2+\frac{1}{2b_2(X)}s_2^2+\frac{1}{2\gamma_v}v_r^2+\frac{1}{2\gamma_\delta}\delta^2+\frac{1}{2\gamma_{\theta_1}}\tilde{\theta}_1^T\tilde{\theta}_1+\frac{1}{2\gamma_{\theta_2}}\tilde{\theta}_2^T\tilde{\theta}_2 \tag{20}$$

Differentiating (20) with respect to time yields

$$\begin{aligned}\dot{V} = &\frac{d}{dt}\left(b_1^{-1}(X)\right)\frac{s_1^2}{2}+\frac{1}{b_1(X)}s_1\dot{s}_1+\frac{d}{dt}\left(b_2^{-1}(X)\right)\frac{s_2^2}{2}+\frac{1}{b_2(X)}s_2\dot{s}_2+\frac{1}{\gamma_v}v_r\dot{v}_r+\frac{1}{\gamma_\delta}\delta\dot{\delta}\\ &+\frac{1}{\gamma_{\theta_1}}\tilde{\theta}_1^T\dot{\theta}_1+\frac{1}{\gamma_{\theta_2}}\tilde{\theta}_2^T\dot{\theta}_2\end{aligned} \tag{21}$$

Using (6), (21) becomes

$$\begin{aligned}\dot{V} &= (\alpha_1(X)-u)s_1+(\alpha_2(X)-u)s_2+\frac{1}{\gamma_v}v_r\dot{v}_r+\frac{1}{\gamma_\delta}\delta\dot{\delta}+\frac{1}{\gamma_{\theta_1}}\tilde{\theta}_1^T\dot{\theta}_1+\frac{1}{\gamma_{\theta_2}}\tilde{\theta}_2^T\dot{\theta}_2\\ &= (s_1+s_2)\alpha_1(X)+(\alpha_2-\alpha_1)s_2-(s_1+s_2)u+\frac{1}{\gamma_v}v_r\dot{v}_r\\ &+\frac{1}{\gamma_\delta}\delta\dot{\delta}+\frac{1}{\gamma_{\theta_1}}\tilde{\theta}_1^T\dot{\theta}_1+\frac{1}{\gamma_{\theta_2}}\tilde{\theta}_2^T\dot{\theta}_2\end{aligned} \tag{22}$$

Substituting (14a) and (15) into (22), we get

$$\begin{aligned}\dot{V}\leq &-(s_1+s_2)\tilde{\theta}_1^T\psi_1(X)+(s_1+s_2)\varepsilon_1(X)+\bar{\alpha}_2|s_2|-k_1(s_1+s_2)^2\\ &-k_2|s_1+s_2|-(s_1+s_2)v_r+\frac{1}{\gamma_v}v_r\dot{v}_r+\frac{1}{\gamma_\delta}\delta\dot{\delta}+\frac{1}{\gamma_{\theta_1}}\tilde{\theta}_1^T\dot{\theta}_1+\frac{1}{\gamma_{\theta_2}}\tilde{\theta}_2^T\dot{\theta}_2\end{aligned} \tag{23}$$

The design constants k_2 and k_3 should be selected such as $k_2 \geq \bar{\varepsilon}_1$ and $k_3 \geq \bar{\varepsilon}_2$, respectively.

Using the adaptive laws (16)–(19) and the expression (14b), (23) can be simplified as:

$$\dot{V}\leq -k_1(s_1+s_2)^2-v_r^2-k_4s_2^2 \tag{24}$$

Therefore all signals s_1, s_2, s_1+s_2, v_r, δ, θ_1, θ_2, X and u are bounded. Then, from (4), we can conclude about the boundedness of $\dot{s}_1$, $\dot{s}_2$ and $\dot{s}_1+\dot{s}_2$. Also, we can demonstrate from (24) that s_2 and $s_1+s_2 \in L_2$. By using the Barbalat's lemma, we can obtain the asymptotic convergence to zero of the signals s_2 and s_1+s_2. Hence, the signal s_1 can converge asymptotically to zero. The tracking error convergence of e_1 and e_2 follow that of the surfaces s_1 and s_2.

4 Simulation Study

In this section, the spherical robot in Fig. 1 is used to verify the performance of the proposed controller.

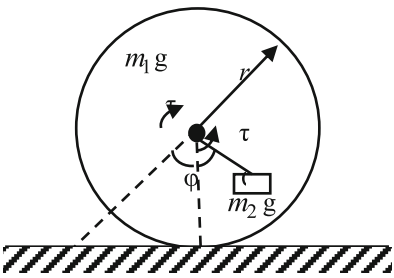

Fig. 1. The spherical robot system.

From Fig. 1, we can note that τ is the driving torque, φ is the angle that shell rolls away from the start point and ϕ is the inner suspension swing angle with respect to its equilibrium position in vertical direction [11].

The equation of dynamic behavior of this spherical robot can be governed by:

$$M(q)\ddot{q} + C(q,\dot{q})\dot{q} + G(q) = \tau \tag{25}$$

where $q = [\,q_1 \quad q_2\,]^T = [\,\varphi \quad \phi\,]^T$ represent the output vector and τ is input vector of robot system. $M(q)$ is a symmetric positive definite inertia matrix, $C(q,\dot{q})$ is damping matrix and $G(q)$ is gravity matrix. These system matrices can be given as follows:

$$M(q) = \begin{bmatrix} a & b\cos q_2 \\ b\cos q_2 & c \end{bmatrix},\ C(q) = \begin{bmatrix} 0 & b\dot{q}_2 \cos q_2 \\ 0 & 0 \end{bmatrix},\ M(q) = \begin{bmatrix} 0 \\ d\sin q_2 \end{bmatrix}.$$

where $a = \frac{1}{3}(5m_1 + 3m_2)r^2$, $b = m_2 r l^2$, $c = m_2 l^2 d = m_2 g l$.

Because the inertia matrix M is invertible., then the system (25) can be rewritten as

$$\ddot{q} = M^{-1}(\tau - C\dot{q} - G) = F(q) + B(q)\tau \tag{26}$$

with

$$F(q) = [f_1(q) \quad f_2(q)\,]^T,\ B(q) = [\,b_1(q) \quad b_2(q)\,]^T.$$

Let us denote $X = [\,x_1 \quad x_2 \quad x_3 \quad x_4\,]^T = [\,q_1 \quad \dot{q}_1 \quad q_2 \quad \dot{q}_2\,]^T$.

So

$$\begin{cases} \dot{x}_1 = x_2 \\ \dot{x}_2 = f_1(X) + b_1(X)u \\ \dot{x}_3 = x_4 \\ \dot{x}_4 = f_2(X) + b_2(X)u \end{cases} \tag{27}$$

where $f_1(X) = \frac{bd\,\sin x_3 \cos x_3 + bcx_4^2 \sin x_3}{ac - b^2\cos^2 x_3}$, $f_2(X) = \frac{-ad\,\sin x_3 - b^2 x_4^2 \sin x_3 \cos x_3}{ac - b^2\cos^2 x_3}$

$$b_1(X) = \frac{c - b\,\cos x_3}{ac - b^2\cos^2 x_3},\ b_2(X) = \frac{a - b\,\cos x_3}{ac - b^2\cos^2 x_3}.$$

In which $m_1 = 3$, $m_2 = 5$, $r = 0.175$, $l = 0.094$, $g = 9.81$. The desired output vector $x_d = [\,20 \quad 0 \quad 0 \quad 0\,]^T$, the initial conditions $X(0) = [\,0.5 \quad 0 \quad 0 \quad 0\,]^T$.

The fuzzy systems $\theta_1^T\psi_1(X)$ and $\theta_2^T\psi_2(X)$ have the state vector X as input. For each input variable of these fuzzy systems, we defined three (triangular and trapezoidal) membership functions uniformly distributed on the interval $[-10, 10]$. Therefore, the number of fuzzy rules used in each fuzzy system is 81.

The design parameters are chosen as follows: $\gamma_{\theta_1} = 600, \gamma_{\theta_2} = 600, \gamma_v = 0.5$, $\gamma_\delta = 0.005$, $k_1 = k_2 = 1, k_3 = 2$. The initial conditions of the adaptive parameters are chosen as $\delta(0) = 1, \theta_1(0) = \theta_2(0) = 0$, $v_r(0) = 0.1$.

Figure 2 shows the simulation results obtained with the proposed adaptive fuzzy sliding mode control law. It demonstrates that AFSMC can control all states of spherical robot to their desired states.

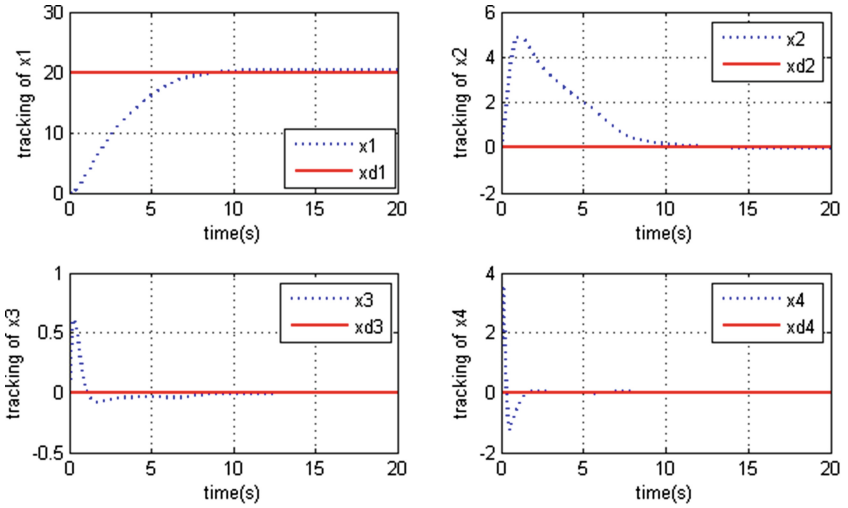

Fig. 2. Output states of spherical robot.

Figure 3 illustrates the convergence towards zero of the sliding mode surfaces and the tracking errors as well as the boundedness of the control signals.

Figure 4 illustrates the boundedness of the norm of fuzzy parameters.

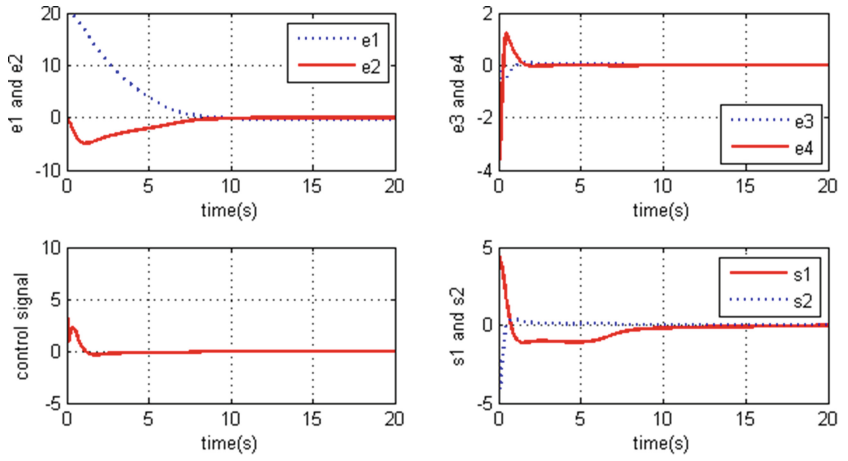

Fig. 3. Curves of all sliding surfaces and trajectories errors and curves of control input.

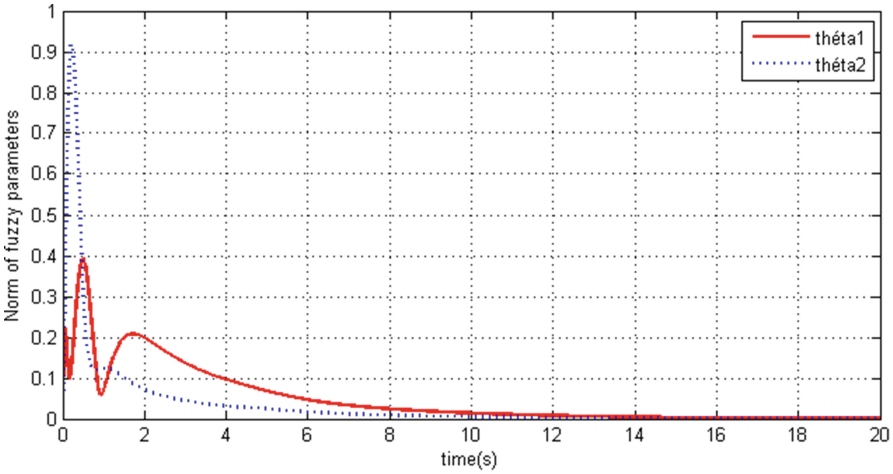

Fig. 4. Norm of fuzzy parameters.

5 Conclusion

In this paper, an adaptive fuzzy sliding mode controller is developed for a class of underactuated systems. The adaptive fuzzy systems are used to approximate the unknown non-linear functions. The adaptive learning algorithms are constructed based on Lyapunov stability analysis. The numerical simulations have been carried out to evaluate the performance of the proposed controller.

References

1. Yue, M., Liu, B.: Adaptive control of an under-actuated spherical robot with a dynamic stable equilibrium point using hierarchical sliding mode approach. J. Adapt. Control Sig. Proc. **44**(10), 1–13 (2013)
2. Hussein, I.I., Bloch, M.: Optimal control of under-actuated non-holonomic mechanical systems. IEEE Trans. Autom. Control **53**(3), 668–682 (2008)
3. Hao, Y., Yi, J., Zhao, D., Qian, D.: Robust control using incremental sliding mode for under-actuated systems with mismatched uncertainties. In: IEEE American Control Conference, pp. 532–537 (2008)
4. Tuan, L., Lee, S.: Sliding mode controls of double-pendulum crane systems. J. Mech. Sci. Technol. **23**(10), 1863–1873 (2013)
5. Huang, A.-C., Chen, Y.-F.: Adaptive control for a class of under-actuated system with mismatched uncertainties. In: IEEE Chinese Control Conference, Bejing, China, pp. 2053–2059 (2010)
6. Fang, Y., Ma, B., Wang, P., Zhang, X.: A motion planning-based adaptive control method for an under-actuated crane system. IEEE Trans. Autom. Control **20**(1), 241–682 (2012)
7. Kung, C.C., Chen, T.H., Huang, L.C.: Adaptive fuzzy sliding mode control for a class under-actuated systems. In: IEEE-Fuzz Conference, vol. 14, no. 1, pp. 1791–1795 (2009)

8. Shine, K., Yang, Y., Cheng, C.: Robust adaptive controller design for second-order under-actuated mechanical systems. In: International Conference in Electric, Communication and Automatic Control, pp. 711–719 (2012)
9. Nafa, F., Labiod, S., Chekired, H.: Direct adaptive fuzzy sliding mode decoupling control for a class of under-actuateed mechanical systems. Turk J. Electr. Eng. Comput. Sci. **21**, 1615–1630 (2012)
10. Wang, W., Zhao, J., Liu, D.: Design of a stable sliding-mode controller for class of second-order under-actuated systems. IEEE Proc. Control Theor. Appl. **151**(6), 683–690 (2004)
11. Ming, Y., Baoyin, L.: Disturbance adaptive control for an under-actuated spherical robot based on hierarchical sliding-mode technology. In: Chinese Control Conference, Hefei, China, pp. 4787–4791 (2012)
12. Park, J.H., Kim, S.H.: Direct adaptive output feedback fuzzy controller for a nonaffine of nonlinear systems. IEEE Proc. Control Theor. Appl. **151**, 65–72 (2004)
13. Ge, S.S., Zhang, J.: Neural-network control of nonaffine nonlinear system with zero dynamics by state and output feedback. IEEE Trans. Neural Netw. **14**, 900–918 (2003)
14. Wang, L.X.: Adaptive Fuzzy Systems and Control: Design and Stability Analysis. Prentice-Hall, Englewood Cliffs (1994)
15. Boulkroune, A., M'Saad, M., Farza, M.: Adaptive fuzzy controller for multivariable nonlinear state time-varying delay systems subject to input nonlinearities. Fuzzy Sets Syst. **164**, 45–65 (2011)
16. Boulkroune, A., M'saad, M., Tadjine, M., Farza, M.: Fuzzy adaptive controller for MIMO nonlinear systems with known and unknown control direction. Fuzzy Sets Syst. **161**, 797–820 (2010)
17. Boulkrune, A., Tadjine, M., M'saad, M.: General adaptive observer based fuzzy control of uncertain nonaffine systems. Arch. Control Sci. **16**, 363–390 (2006)

Indirect Robust Adaptive Fuzzy Control of Uncertain Two Link Robot Manipulator

Bounemeur Abdelhamid[1(✉)], Chemachema Mouhamed[1], and Essounbouli Najib[2]

[1] Laboratory of Automatic, Robotic and Control Systems, Faculty of Engineering, Department of Electronics, University of frères Mentouri, Constantine, Algeria
hamidsie4@gmail.com, m_chemachema@yahoo.com
[2] Laboratory of Research in Science and Information Technical and Communication, Department of Mechanical Engineering, University of Troyes, Troyes cedex, France
najib.essounbouli@univ-reims.fr

Abstract. This paper presents an adaptive fuzzy logic modeling and control of two link robot manipulator with uncertainties. To estimate the uncertain parts of the process, fuzzy logic systems are used. The uncertain nonlinearities of the system are captured by fuzzy systems that have been proven to be universal approximators. The proposed control scheme completely overcomes the singularity problem that occurs in the indirect adaptive feedback linearizing control. Projection in the estimate parameters is not required and the stability analysis of the closed-loop system is performed using Lyapunov approach. Simulation results are provided to verify the effectiveness of the proposed design.

Keywords: Adaptive fuzzy control · Feedback linearization · Nonlinear systems · Lyapunov stability

1 Introduction

In practical control engineering, fuzzy system based adaptive control methodologies have received much attention for controlling uncertain and nonlinear dynamical systems. Based on the universal approximation theorem [1], during the last two decades, several adaptive fuzzy control schemes for a class of multi-input multi-output (MIMO) nonlinear uncertain systems are investigated [2–4]. Conceptually, there are two distinct approaches that have been formulated in the design of a fuzzy adaptive control system: direct and indirect schemes. The direct approach consists to approximate the ideal control law by a fuzzy system [5, 6]. However, in the indirect approach the nonlinear dynamics of the system are approximated by fuzzy systems to develop a control law based on these systems [3, 7]. In the indirect adaptive schemes, the possible controller singularity problems are usually met.

In the aforementioned papers, the adjustable parameters of the fuzzy systems are updated by adaptive laws based on a Lyapunov approach, i.e., the parameter adaptive laws are designed in such a way to ensure the convergence of a Lyapunov function.

M. Chadli et al. (eds.), *Recent Advances in Electrical Engineering and Control Applications*, Lecture Notes in Electrical Engineering 411, DOI 10.1007/978-3-319-48929-2_10

However, for an effective adaptation, it is more judicious to directly base the parameter adaptation process on the identification error between the unknown function and its adaptive fuzzy approximation [6].

Inspired by [6, 8], this paper presents indirect adaptive fuzzy control schemes for a class of continuous-time uncertain MIMO nonlinear dynamical systems. The proposed scheme is based on the results in [6] such that the fuzzy systems are used to approximate the system's unknown nonlinearities. To achieve the tracking of a desired output, new learning algorithms are proposed in the presented controller which permits superior control performance compared to the same class of controllers [8, 9]. In the proposed controller, a robustifying control term is added to the basic fuzzy controller to deal with approximation errors. The regularized inverse matrix is employed to solve problem of singularity and the stability of the closed-loop system is studied using Lyapunov method.

The outline of the paper is as follows. Section 2 presents the problem formulation. Section 3 presents a brief description of the used fuzzy system. In Sect. 4, a new control law and adaptive algorithms are proposed and stability analysis is given. Simulation examples are illustrated in Sect. 5. The conclusion is finally given in Sect. 6.

2 Problem Formulation

Let we consider a class of uncertain MIMO nonlinear systems modeled by

$$\begin{aligned} y_1^{r1} &= f_1(x) + \textstyle\sum_{j=1}^{p} g_{1j}(x)u_j \\ &\vdots \\ y_p^{rp} &= f_p(x) + \sum_{j=1}^{p} g_{pj}(x)u_j \end{aligned} \tag{1}$$

where

$x = \left[y_1, \dot{y}_1, \ldots, y_1^{(r_1-1)}, \ldots y_p, \dot{y}_p, \ldots, y_p^{(r_p-1)}\right]^T$ is the overall state vector which is assumed available for measurement, $u = [u_1, \ldots, u_p]^T$ is the control input vector, $y = [y_1, \ldots, y_p]^T$ is the output vector, and $f_i(x)$ et $g_{ij}(x), i,j = 1, \ldots, p$ are unknown smooth nonlinear functions.

Let us denote

$$y^{(r)} = \left[y_1^{(r_1)} \ldots y_p^{(r_p)}\right]$$

$$F(x) = \left[f_1(x) \ldots f_p(x)\right]^T$$

$$G(x) = \begin{bmatrix} g_{11}(x) & \ldots & g_{1p}(x) \\ \vdots & \ddots & \vdots \\ g_{p1}(x) & \ldots & g_{pp}(x) \end{bmatrix}$$

Then, dynamic system (1) can be written in the following compact form

$$y^{(r)} = F(x) + G(x)u \tag{2}$$

The control objective is to design adaptive control $u_i(t)$ for system (1) such that the output $y_i(t)$ follows a specified desired trajectory $y_{di}(t)$ under boundedness of all signals.

Assumption 1: The matrix $G(x)$ is symmetric positive definite and bounded as $G(x) \geq \sigma_0 I_P$, where σ_0 is a positive constants.

Assumption 2: The desired trajectory $y_{di}(t), i = 1, \ldots, P$, is a known bounded function of time with bounded known derivatives $\dot{y_{di}}(t), \ldots, y_{di}^{(r_i)}$ i.e. $y_{di}(t)\mathcal{C}^{r_i}$.

Remark 1: Notice that Assumption 1 is a sufficient condition ensuring that the matrix $G(x)$ is always regular and, therefore, system (1) is feedback linearizable by a static state feedback. Although this assumption restricts the considered class of MIMO nonlinear systems, many physical systems, such as robotic system [10], fulfill such a property.

Define the tracking errors as

$$\begin{aligned} e_1(t) &= y_{d1}(t) - y_1(t) \\ &\vdots \\ e_p(t) &= y_{dp}(t) - y_p(t) \end{aligned} \tag{3}$$

while the feedback control is given by:

$$u = G(x)^{-1}[-F(x) + V] \tag{4}$$

where

$$V = \begin{bmatrix} v_1 \\ \vdots \\ v_p \end{bmatrix} = \begin{bmatrix} y_{d1}^{(r_1)} + k_{1r1}e_1^{(r_1-1)} + \ldots + k_{11}e_1 \\ \vdots \\ y_{dp}^{(r_p)} + k_{prp}e_p^{(r_p-1)} + \ldots + k_{p1}e_p \end{bmatrix} \tag{5}$$

we can write

$$\begin{cases} e_1^{(r_1)} + k_{1r1}e_1^{(r_1-1)} + \ldots + k_{11}e_1 = 0 \\ \vdots \\ e_p^{(r_p)} + k_{prp}e_p^{(r_p-1)} + \ldots + k_{p1}e_p = 0 \end{cases}. \tag{6}$$

where the coefficients k_{ij} are chosen such that all the polynomials in Eq. 6 are of the type Hurwitz. So we can conclude that $\lim_{t\to\infty} e_i(t) = 0$ which is the main objective of the command. However in this case, the nonlinear functions $f_i(x)$ and $g_i(x) i = 1, \ldots, p$ are

assumed unknown, then obtaining the feedback control law (4) is difficult. For this reason the dynamics of these functions is approximated by using fuzzy systems.

3 Description of Fuzzy Systems

In this work we will consider a fuzzy zero order (TS0).

Each rule has a numerical conclusion, the total output of the fuzzy system is obtained by calculating a weighted average, and in this manner the time consumed by the procedure of defuzzification is avoided. Then the output of fuzzy system is given by following relationship [13–15]:

$$y(x) = \frac{\sum_{k=1}^{N} \mu_k(x) f_k(x)}{\sum_{k=1}^{N} \mu_k(x)} \tag{7}$$

with $\mu_k(x) = \prod_{i=1}^{n} \mu_{\underset{\sim}{F}_i^k}$, $\underset{\sim}{F}_i^k \in \{F_i^1, \ldots, F_i^{m_i}\}$ which represents the degree of confidence or activation rule R_k and $f_k(x)$ is a polynomial of zero order.

$$f_k(x) = a^k \tag{8}$$

We can simplify the output of fuzzy system as follows:

$$y(x) = \frac{\sum_{k=1}^{N} \mu_k(x) a^k}{\sum_{k=1}^{N} \mu_k(x)} \tag{9}$$

By introducing the concept of fuzzy basis functions [16], the output of fuzzy system TS0 can be written as:

$$y(x) = w^T(x)\theta \tag{10}$$

with

- $\theta = [a^1 \ldots a^N]$: Vector of parameters of the conclusion of rules fuzzy part.
- $w(x) = [w_1(x) \ldots w_N(x)]^T$:Basic function of the vector each component is given by:

$$w_N(x) = \frac{\mu_k(x)}{\sum_{j=1}^{N} \mu_j(x)}, k = 1, \ldots, N \tag{11}$$

4 Indirect Adaptive Fuzzy Control

In this section we propose to indirectly approximate the unknown ideal (4) by identifying the unknown functions $f_i(x)$ and $g_{ij}(x)$ using fuzzy systems.

$$\hat{f}_i(x,\theta) = w_{f_i}^T(x)\theta_{f_i},\ i = 1,\ldots,p \tag{12}$$

$$\hat{g}_{ij}(x,\theta) = w_{g_{ij}}^T(x)\theta_{g_{ij}}, i,j = 1,\ldots,p \tag{13}$$

With $w_{f_i}^T$ and $w_{g_{ij}}^T$ are vectors of fuzzy basic functions supposed properly fixed in prior by the user,θ_{f_i} and $\theta_{g_{ij}}$ are vectors of the fitted parameters. The functions $f_{ij}(x)$ and $g_{ij}(x)$ can be expressed in terms of fuzzy approximations in the following manner:

$$\begin{cases} f_i(x) = \hat{f}_l\left(x,\theta_{fi}^*\right) + \varepsilon_{f_i}(x) \\ g_{ij}(x) = \hat{g}_{ij}\left(x,\theta_{g_{ij}}^*\right) + \varepsilon_{g_{ij}}(x) \end{cases} \tag{14}$$

With $\varepsilon_{f_i}(x)$ and $\varepsilon_{g_{ij}}(x)$ represent the fuzzy approximation errors, $\theta_{f_i}^*$ and $\theta_{g_{ij}}^*$ are respectively of the optimum parameters of θ_{f_i} and $\theta_{g_{ij}}$, the values of parameters θ_{f_i} and $\theta_{g_{ij}}$ respectively minimizing the approximation errors $\varepsilon_{f_i}(x)$ and $\varepsilon_{g_{ij}}(x)$. These optimal parameters satisfy:

$$\theta_{fi}^* = arg\min_{\theta_{f_i}}\left\{\sup_x\left|f_i(x) - \hat{f}_i(x,\theta_{f_i})\right|\right\} \tag{15}$$

$$\theta_{gij}^* = arg\min_{\theta_{f_i}}\left\{\sup_x\left|g_{ij}(x) - \hat{g}_{ij}(x,\theta_{gij})\right|\right\} \tag{16}$$

Note that the optimal parameters $\theta_{f_i}^*$ and $\theta_{g_{ij}}^*$ are unknown constants artificial introduced only to the theoretical study of the stability of the control algorithm. In fact, the knowledge of their values is not necessary for implementation of adaptive control law. From the above analysis, we can write:

$$f_i(x) - \hat{f}_i(x,\theta_{f_i}) = w_{f_i}^T(x)\tilde{\theta}_{f_i} + \varepsilon_{f_i}(x) \tag{17}$$

$$g_{ij}(x) - \hat{g}_{ij}(x,\theta_{gij}) = w_{g_{ij}}^T(x)\tilde{\theta}_{g_{ij}} + \varepsilon_{g_{ij}}(x) \tag{18}$$

where

$\tilde{\theta}_{f_i} = \theta_{f_i}^* - \theta_{f_i}$ and $\tilde{\theta}_{g_{ij}} = \theta_{g_{ij}}^* - \theta_{g_{ij}}$, are the parameter estimation errors.

Assumption 3: The fuzzy approximation errors $\varepsilon_{f_i}(x)$ and $\varepsilon_{g_{ij}}(x)$ are bounded for all $x\epsilon\Omega_x$ as $\left|\varepsilon_{f_i}(x)\right| \le \bar{\varepsilon}_{f_i}$ and $\left|\varepsilon_{g_{ij}}(x)\right| \le \bar{\varepsilon}_{g_{ij}}$, where $\bar{\varepsilon}_{f_i}$ and $\bar{\varepsilon}_{g_{ij}}$ are unknown positive constants.

This assumption is reasonable, since we assume that fuzzy systems used for approximating unknown functions have the universal approximator property.

Denote

$$\hat{F}(x,\theta_f) = \left[\hat{f}_1(x,\theta_{f1})\ldots\hat{f}_p(x,\theta_{fp})\right]^T$$

$$\hat{G}(x,\theta_g) = \begin{bmatrix} \hat{g}_{11}(x) & \ldots & \hat{g}_{1p}(x) \\ \vdots & \ddots & \vdots \\ \hat{g}_{p1}(x) & \ldots & \hat{g}_{pp}(x) \end{bmatrix}$$

$$\theta_f = \left[\theta_{f1},\ldots,\theta_{fp}\right]^T;\ \theta_f^* = \left[\theta_{f1}^*,\ldots,\theta_{fp}^*\right]^T$$

$$\theta_g = \begin{bmatrix} \theta_{g11} & \ldots & \theta_{g1p} \\ \vdots & \ddots & \vdots \\ \theta_{gp1} & \ldots & \theta_{gpp} \end{bmatrix}$$

$$\theta_g^* = \begin{bmatrix} \theta_{g11}^* & \ldots & \theta_{g1p}^* \\ \vdots & \ddots & \vdots \\ \theta_{gp1}^* & \ldots & \theta_{gpp}^* \end{bmatrix}$$

$$W_f(x) = diag[w_{f1}(x),\ldots,w_{fp}(x)]$$

$$W_g(x) = diag[w_{g1}(x),\ldots,w_{gp}(x)]$$

$$\varepsilon_f(x) = \left[\varepsilon_{f1}(x)\ldots\varepsilon_{fp}(x)\right]^T$$

$$\varepsilon_g(x) = \begin{bmatrix} \varepsilon_{g11}(x) & \ldots & \varepsilon_{g1p}(x) \\ \vdots & \ddots & \vdots \\ \varepsilon_{gp1}(x) & \ldots & \varepsilon_{gpp}(x) \end{bmatrix}$$

$$\overline{\varepsilon_f} = \left[\bar{\varepsilon}_{f1}\ldots\bar{\varepsilon}_{fp}\right]^T$$

$$\bar{\varepsilon}_g = \begin{bmatrix} \bar{\varepsilon}_{g11} & \ldots & \bar{\varepsilon}_{g1p} \\ \vdots & \ddots & \vdots \\ \bar{\varepsilon}_{gp1} & \ldots & \bar{\varepsilon}_{gpp} \end{bmatrix}$$

$$F(x) - \hat{F}(x,\theta_f) = \hat{F}(x,\theta_f^*) - \hat{F}(x,\theta_f) + \varepsilon_f(x) \tag{19}$$

$$G(x) - \hat{G}(x,\theta_g) = \hat{G}\left(x,\theta_g^*\right) - \hat{G}(x,\theta_g) + \varepsilon_g(x) \tag{20}$$

Now we can write an expression for the adaptive law

$$u_c = \hat{G}^T(x,\theta_g)\left(\varepsilon_0 I_P + \hat{G}(x,\theta_g)\hat{G}^T(x,\theta_g)\right)^{-1}\left[-\hat{F}(x,\theta_f)+V\right] \tag{21}$$

where ε_0 is a small positive constant.

In the control law (21), we replaced $\hat{G}(x,\theta_g)^{-1}$ by the regularized inverse

$$\hat{G}^T(x,\theta_g)\left(\varepsilon_0 I_P + \hat{G}(x,\theta_g)\hat{G}^T(x,\theta_g)\right)^{-1} \tag{22}$$

The regularized inverse given by (22) is always defined even when $\hat{G}(x,\theta_g)$ is not invertible, hence the control law (21) is well defined.

Note that even if the control law (22) is well defined, it cannot alone ensure the stability of the closed loop system. This is due, on the one hand, the error introduced by the approximation of actual functions $F(x)$ and $G(x)$ by fuzzy systems and from one side to the error introduced by the use of the regularized inverse matrix in place of the inverse matrix. For these reasons and in order to have a control law does not depend on any initialization phase we propose, a control law which is composed of two terms, a term adaptive control u_c introduced to overcome the problems of non-linearity of the system, and a second term u_r proposed, to circumvent the problem of approximation errors and, compensate for the error due to the use of the inverse regularized instead of the inverse matrix, then the resulting control law is represented as follows:

$$u = u_c + u_r \tag{23}$$

The adaptive control term u_c is given by

$$u_c = \hat{G}^T(x,\theta_g)\left(\varepsilon_0 I_P + \hat{G}(x,\theta_g)\hat{G}^T(x,\theta_g)\right)^{-1}\left[-\hat{F}(x,\theta_f)+V\right] \tag{24}$$

The robust control term u_r is given by

$$u_r = \frac{B^T P E |E^T P B|\left(\hat{\varepsilon}_f + \hat{\varepsilon}_g |u_c| + |u_O|\right)}{\sigma_0 \|E^T P B\|^2 + \delta} \tag{25}$$

where

$$u_r = \begin{bmatrix} u_{r1} \\ \vdots \\ u_{rp} \end{bmatrix}$$

$$u_0 = \varepsilon_0\left[\varepsilon_0 I_p + \hat{G}(x,\theta_g)\hat{G}^T(x,\theta_g)\right]^{-1}\left(-\hat{F}(x,\theta_f)+V\right) \tag{26}$$

$\hat{\varepsilon}_f$ and $\hat{\varepsilon}_g$ are respectively the estimated of $\bar{\varepsilon}_f$ and $\bar{\varepsilon}_g$, δ is a time-varying parameter defined below. To achieve the control objectives, we define the parameter adaption laws as follows:

$$\dot{\theta}_f = -\gamma_f B^T P E w_f(x) \tag{27}$$

$$\dot{\theta}_{gij} = -\gamma_g B^T P E u_j w_{gi}(x)\, i,j = 1,\ldots,p \tag{28}$$

$$\dot{\hat{\varepsilon}}_f = n_f \left| B^T P E \right| \tag{29}$$

$$\dot{\hat{\varepsilon}}_g = n_g \left| u_c^T \right| \left| B^T P E \right| \tag{30}$$

$$\dot{\delta} = -\eta \frac{|E^T P B| \left(\hat{\varepsilon}_f + \hat{\varepsilon}_g |u_c| + |u_O| \right)}{\sigma_0 \|E^T P B\|^2 + \delta} \tag{31}$$

$\gamma_f > 0, \gamma_g > 0, n_f > 0, n_g > 0, n_0 > 0$ and $\delta(0) > 0$.

Theorem 1. Consider the nonlinear system (1), and suppose that the assumptions (1–3) are satisfied. Then the control law defined by Eqs. (24) and (25) with adaptation law (27)–(31) applied to the system (1) ensures boundedness of all signals of the closed loop and the convergence to zero of tracking errors,, $e_i^{(j)} \to 0$ when $t \to \infty$ for $i = 1,\ldots,P$ and, $j = 0,1,\ldots,r_i - 1$.

Proof

$$E^{(n)} = Y_d^{(n)} - Y^{(n)} \tag{32}$$

$$E^{(n)} = Y_d^{(n)} - F(x) - G(x)u \tag{33}$$

We can write as follows:

$$E^{(n)} = Y_d^{(n)} - F(x) - G(x)u_c - G(x)u_r \tag{34}$$

substitute (24) and (26), Eq. (34) becomes

$$E^{(n)} = -K^T E - \left(F(x) - \hat{F}(x,\theta_f) \right) - \left(G(x) - G(x,\theta_g) \right) u_c - G(x)u_r + u_0 \tag{35}$$

substitute (19) and (20), Eq. (35) becomes

$$E^{(n)} = -K^T E - \left(\hat{F}(x,\theta_f^*) - \hat{F}(x,\theta_f) + \varepsilon_f(x) \right) - \left(\hat{G}(x,\theta_g^*) - \hat{G}(x,\theta_g) + \varepsilon_g(x) \right) u_c - G(x)u_r + u_0 \tag{36}$$

$$E^{(n)} = -K^T E - \left(W_f^T \tilde{\theta}_f + \varepsilon_f(x) \right) - \left(\sum_{i=1}^{p} \sum_{j=1}^{p} \tilde{\theta}_{gij} u_{cj} \right) - \varepsilon_g(x) u_c - G(x)u_r + u_0 \tag{37}$$

While the dynamics of the error can be written as follows:

$$\dot{E} = AE + B\left[-\left(W_f^T\tilde{\theta}_f + \varepsilon_f(x)\right) - \left(\sum_{i=1}^{p}\sum_{j=1}^{p}\tilde{\theta}_{gij}u_{cj}\right) - \varepsilon_g(x)u_c - G(x)u_r + u_0\right] \tag{38}$$

where

$$A = \begin{bmatrix} 0 & I_{n\times n} & \dots & 0 \\ \vdots & \ddots & & \vdots \\ 0 & 0 & 0 & I_{n\times n} \\ -K_1 & -K_2 & \dots & -K_n \end{bmatrix} B = \begin{bmatrix} 0 \\ \vdots \\ 0 \\ I_{n\times n} \end{bmatrix}$$

Until $(|sI - A|) = s^{(n)} + K_1 s^{(n-1)} + \ldots + K_n$ is stable (A stable), we know that there exists a symmetric positive definite matrix $P(n, n)$ that satisfies the Lyapunov equation:

$$A^T P + PA = -Q \tag{39}$$

where Q is a symmetric positive definite matrix of arbitrary dimensions $(n\,x\,n)$.

To minimize the tracking error and the approximation error, we consider the following Lyapunov function:

$$V = \frac{1}{2}E^T PE + \frac{1}{2\gamma_f}\tilde{\theta}_f^T\tilde{\theta}_f + \frac{1}{2\gamma_g}tr(\tilde{\theta}_g^T\tilde{\theta}_g) + \frac{1}{2\eta_f}\tilde{\varepsilon}_f^T\tilde{\varepsilon}_f + \frac{1}{2\eta_g}tr\left(\tilde{\varepsilon}_g^T\tilde{\varepsilon}_g\right) + \frac{1}{2\eta}\delta^2 \tag{40}$$

with δ is a time-varying parameter, $\tilde{\varepsilon}_f = \bar{\varepsilon}_f - \hat{\varepsilon}_f$, $\tilde{\varepsilon}_g = \bar{\varepsilon}_g - \hat{\varepsilon}_g$

Using (38) and (39), the time derivative of V can be write in the following form

$$\begin{aligned}\dot{V} = &-\frac{1}{2}E^T QE + E^T PB\left[-\left(W_f^T\tilde{\theta}_f + \varepsilon_f(x)\right) - \left(\sum_{i=1}^{p}\sum_{j=1}^{p}W_{gi}^T\tilde{\theta}_{gij}u_{cj}\right) - \varepsilon_g(x)u_c - G(x)u_r + u_0\right] \\ &-\frac{1}{\gamma_f}\tilde{\theta}_f^T\dot{\theta}_f - \sum_{i=1}^{p}\sum_{j=1}^{p}\frac{1}{\gamma_{gij}}\tilde{\theta}_{gij}^T\dot{\theta}_{gij} - \frac{1}{\eta_f}\tilde{\varepsilon}_f^T\dot{\tilde{\varepsilon}}_f - \frac{1}{\eta_g}tr\left(\tilde{\varepsilon}_g^T\dot{\tilde{\varepsilon}}_g\right) + \frac{1}{\eta}\delta\dot{\delta}\end{aligned} \tag{41}$$

Equation (41) can be simplified

$$\dot{V} = -\frac{1}{2}E^T QE + \dot{V}_1 + \dot{V}_2 \tag{42}$$

Remark 2: Writing the derivative of the Lyapunov function described in Eq. (42) facilitates the task of demonstrating negativity of the derivative $\dot{V}$.

$$\dot{V}_1 = -\frac{1}{\gamma_f}\tilde{\theta}_f^T\left[\gamma_f B^T PEW_f + \dot{\theta}_f\right] - \frac{1}{\gamma_g}\sum_{i=1}^{p}\sum_{j=1}^{p}\tilde{\theta}_{gij}^T\left[\gamma_g B^T PEu_j w_{gi} + \dot{\theta}_{gij}\right] \tag{43}$$

If adaptation laws (27) and (28), Eq. (43) becomes

$$\dot{V}_1 = 0 \tag{44}$$

$$\dot{V}_2 = -E^T PBG(x)u_r - E^T PB\varepsilon_f(x) - E^T PB\varepsilon_g(x)u_c + E^T PBu_0 - \frac{1}{\eta_f}\tilde{\varepsilon}_f^T\dot{\hat{\varepsilon}}_f - \frac{1}{\eta_g}tr\left(\tilde{\varepsilon}_g^T\dot{\hat{\varepsilon}}_g\right) + \frac{1}{\eta}\delta\dot{\delta} \tag{45}$$

Then $\dot{V}_2$ can be bounded as follows

$$\dot{V}_2 \leq -E^T PB\sigma_0 u_r + \left|E^T PB\right|\overline{\varepsilon_f} - \left|E^T PB\right|\overline{\varepsilon_g}|u_c| + \left|E^T PB\right||u_0| - \frac{1}{\eta_f}\tilde{\varepsilon}_f^T\dot{\hat{\varepsilon}}_f - \frac{1}{\eta_g}tr\left(\tilde{\varepsilon}_g^T\dot{\hat{\varepsilon}}_g\right) + \frac{1}{\eta}\delta\dot{\delta} \tag{46}$$

If we use the adaption laws (29) and (30), Eq. (46) becomes

$$\dot{V}_2 \leq -E^T PB\sigma_0 u_r + \left|E^T PB\right||u_0| + \frac{1}{\eta}\delta\dot{\delta} + \hat{\varepsilon}_f\left|E^T PB\right| + \hat{\varepsilon}_g\left|E^T PB\right||u_c| \tag{47}$$

Using (25) et (31), then (47) becomes

$$\dot{V}_2 = 0 \tag{48}$$

From results (44) and (48), (42) can be bounded as follows

$$\dot{V} \leq -\frac{1}{2}E^T QE \leq 0 \tag{49}$$

$$\dot{V} \leq -\frac{1}{2}\lambda_{Qmin}\|E\|^2 \tag{50}$$

where λ_{Qmin}The minimum Eigen value of the matrix Q, then by integrating both sides of Eq. (50) from [0,t]

$$\int_0^t \|E(\tau)\|^2 d\tau \leq \frac{2}{\lambda_{Qmin}}[V(0) - V(t)] \tag{51}$$

which gives us

$$\int_0^t \|E(\tau)\|^2 d\tau \leq \frac{2}{\lambda_{Qmin}}[\|V(0)\| + \|V(t)\|] \tag{52}$$

As shown by [17], this implies that $E(t) \in L_2$, according to the theory of Lyapunov, $E(t)$ is bounded. On the other hand, from (38) $\dot{E}(t) \in L_\infty$ (bounded) because all

members of the right are bounded. According to Barbalat's lemma, we conclude that $\lim_{t\to\infty}\|E(t)\| = 0$.

5 Simulation Results

In this section, we test the proposed indirect adaptive fuzzy control scheme on the tracking control of two-link rigid robot manipulator with the following dynamics [10, 18]:

$$\begin{pmatrix} \ddot{q}_1 \\ \ddot{q}_2 \end{pmatrix} = \begin{pmatrix} M_{11} & M_{12} \\ M_{21} & M_{22} \end{pmatrix}^{-1} \left\{ \begin{pmatrix} u_1 \\ u_2 \end{pmatrix} - \begin{pmatrix} -h\dot{q}_2 & -h\dot{q}_2(\dot{q}_1 + \dot{q}_2) \\ h\dot{q}_1 & 0 \end{pmatrix} \begin{pmatrix} \dot{q}_1 \\ \dot{q}_2 \end{pmatrix} \right\} \quad (53)$$

where

$$M_{11} = a_1 + 2a_3\cos(q_2) + 2a_4\sin(q_2)$$

$$M_{22} = a_2$$

$$M_{21} = M_{12} = a_2 + a_3\cos(q_2) + a_4\sin(q_2)$$

$$h = a_3\sin(q_2) - a_4\cos(q_2)$$

$$a_1 = I_1 + m_1 l_{c1}^2 + I_e + m_e l_{ce}^2 + m_e l_1^2$$

with

$$a_2 = I_e + m_e l_{ce}^2$$

$$a_3 = m_e l_1 l_{ce}\cos(\delta_e)$$

$$a_4 = m_e l_1 l_{ce}\sin(\delta_e)$$

In the simulation, the following parameter values are used

$$m_1 = 1,\ m_e = 2,\ l_1 = 1,\ l_{c1} = 0.5,\ l_{ce} = 0.6,\ I = 0.12,\ I_e = 0.5,\ \delta_e = 30^{\circ}.$$

$$y = [q_1 q_2] u = [u_1 u_2]$$

$$x = [q_1 \dot{q}_1 q_2 \dot{q}_2]$$

$$F(x) = \begin{pmatrix} f_1(x) \\ f_2(x) \end{pmatrix} = -M^{-1} \begin{pmatrix} -h\dot{q}_2 & -h\dot{q}_2(\dot{q}_1 + \dot{q}_2) \\ h\dot{q}_1 & 0 \end{pmatrix} \begin{pmatrix} \dot{q}_1 \\ \dot{q}_2 \end{pmatrix}$$

$$G(x) = \begin{pmatrix} g_{11}(x) & g_{12}(x) \\ g_{21}(x) & g_{22}(x) \end{pmatrix} = M^{-1} = \begin{pmatrix} M_{11} & M_{12} \\ M_{21} & M_{22} \end{pmatrix}^{-1}$$

Then, the robot system given by (54) can be expressed as $\ddot{y} = F(x) + G(x)u$

The control objective is to force the system output q_1 and q_2 to track the desired trajectories $y_{d1} = \sin(t)$ and $y_{d2} = \sin(t)$, respectively.

To synthesize the indirect adaptive fuzzy controller, six fuzzy systems in the form of (11) are used. Each fuzzy system has $x_1(t)$, $x_2(t)$, $x_3(t)$, and $x_4(t)$ as input, and for each input variable $x_i(t)$, five Gaussian functions are defined as

$$\mu_{F_i^1}(x_i) = \exp\left\{-\frac{1}{2}\left(\frac{x_i + 1.25}{0.7}\right)^2\right\}$$

$$\mu_{F_i^2}(x_i) = \exp\left\{-\frac{1}{2}\left(\frac{x_i + 0.75}{0.7}\right)^2\right\}$$

$$\mu_{F_i^3}(x_i) = \exp\left\{-\frac{1}{2}\left(\frac{x_i}{0.7}\right)^2\right\}$$

$$\mu_{F_i^4}(x_i) = \exp\left\{-\frac{1}{2}\left(\frac{x_i - 0.75}{0.7}\right)^2\right\}$$

$$\mu_{F_i^5}(x_i) = \exp\left\{-\frac{1}{2}\left(\frac{x_i - 1.25}{0.7}\right)^2\right\}, \quad i = 1, 2, 3, 4$$

The robot initial conditions are $x(0) = [0.5; 0; 0.5; 0]$, and the initial values of the parameter estimates $\theta_f(0)$ set equal to zero, and $\theta_g(0)$ between $[-2, 2]$.

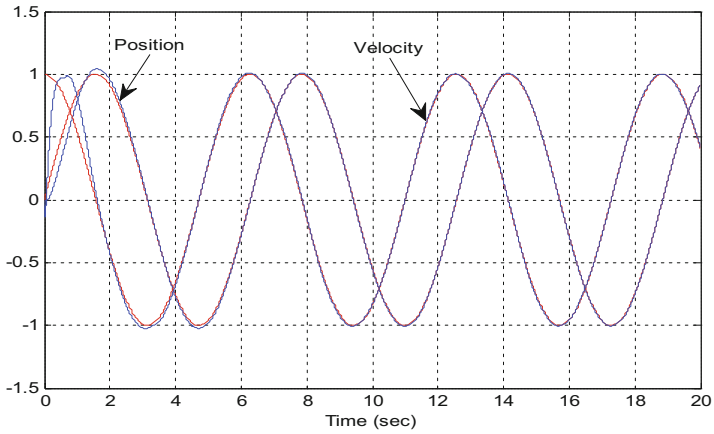

Fig. 1. Tracking curves of link 1: actual (blue lines); desired (red lines).

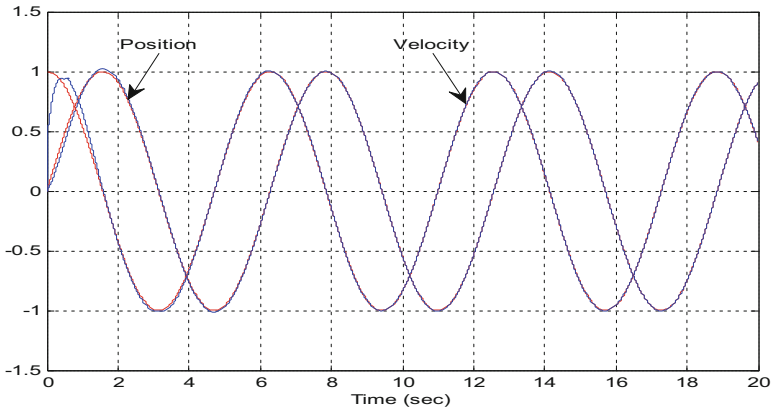

Fig. 2. Tracking curves of link 2: actual (blue lines); desired (red lines).

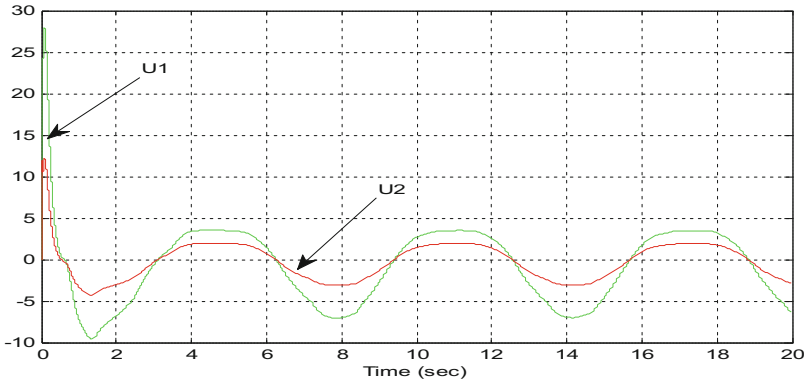

Fig. 3. Control input signals: u_1 (green line); u_2 (red line).

$$p = [8.1202.750; 08.1202.75; 2.7502.620; 02.7502.62]$$

$$Q = diag(5.5, 5.5, 5, 5),\ k = [10; 01; 20; 02],\ \varepsilon_f(0) = 0,\ \varepsilon_g(0) = 0\eta = 0.001,\ \delta(0) = 1,\ \sigma_0 = 0.1,\ \varepsilon_0 = 0.1,\ \gamma_f = \gamma_g = 10,\ \eta_f = \eta_g = 20.$$

The simulation results for the first link are shown in Fig. 1, those for the second link are shown in Fig. 2, and the control input signals are shown in Fig. 3. We can note that the actual trajectories converge to the desired trajectories and the control signals are almost smooth. These simulation results demonstrate the tracking capability of the proposed indirect adaptive controller and its effectiveness for control tracking of uncertain MIMO nonlinear systems.

6 Conclusion

In this paper, stable indirect adaptive fuzzy control for class of unknown (MIMO) nonlinear systems is developed. The scheme consists of an adaptive fuzzy controller with a robuste control term used to compensate for approximation errors. The adaptive schema is a free from singularity, and new adaptive parameters update law are used, besides, the proposed adaptive schemes allow initialization to zero of all adjustable parameters of the fuzzy systems. This approach do not require the knowledge of the mathematical model of the plant, guarantee the uniform boundedness of all the signals in the closed-loop system, and ensure the convergence of the tracking errors to a neighborhood of the origin. Simulation results performed on a two- link robot manipulator illustrate the method. Future works will focus on extension of the approach to more general MIMO nonlinear systems and its improvement by introducing a state observer to provide an estimate of the state vector.

References

1. Lilly, J.H.: Fuzzy Control and Identification, 1st edn. Wiley, New York (2011)
2. Shi, W., Zhang, M., Guo, W., Guo, L.: Stable adaptive fuzzy control for MIMO nonlinear systems. Comput. Math Appl. **62**, 2843–2853 (2011)
3. Qi, R.: T-S model based indirect adaptive fuzzy control for a class of MIMO uncertain nonlinear systems. In: IEEE Proceedings of the 6th World Congress on Intelligent Control and Automation, pp. 3943–3947, June 2006
4. Gao, Y.: Online adaptive fuzzy neural identification and control of a class of MIMO nonlinear sysytems. IEEE Trans. Fuzzy Syst. **11**, 3900–3904 (2003)
5. Tlemcani, A., Chekireb, H., Boucherit, M.S., Labiod, S.: Decentralized direct adaptive fuzzy control of nonlinear interconnected MIMO system class. Arch. Control Sci. **17**(4), 357–374 (2007)
6. Labiod, S., Guerra, T.M.: Direct adaptive fuzzy control for a class of MIMO nonlinear systems. Int. J. Syst. Sci. **38**(8), 665–675 (2007)
7. Wang, L.-X.: A Course in Fuzzy Systems and Control, 2nd edn. Prentice-Hall Inc., Englewood Cliffs (1997)
8. Labiod, S., Guerra, T.M.: Direct and indirect adaptive fuzzy control for a class of MIMO nonlinear systems. Adv. Robot Manipulators **31**, 280–298 (2010)
9. Babaie, A., Nikranjbar, A.: Adaptive fuzzy control of uncertain (P-R) robot manipulator using Lyapunov method compared to RLSE. MAjlesi J. Mechatron. Syst. **1**(2), 37–45 (2012)
10. Slotine, J.J., Li, W.: Applied Nonlinear Control. Prentice-Hall Inc., Englewood Cliffs (1991)
11. Wang, L.X., Mendel, J.M.: fuzzy basis functions, universal approximation and orthogonal least squares learning. IEEE Trans. Neural Netw. **3**(5), 807–814 (1992)
12. Takagi, T., Sugeno, M.: Fuzzy identification of systems and its application to modeling and control. IEEE Trans. Syst. Manand Cybern. **15**, 116–132 (1985)
13. Kosko, B.: Fuzzy systems as universal approximator. In: Proceedings of the IEEE Conference on Fuzzy Systems, pp. 1153–1162, San Diego, USA (1992)
14. Jang, J.R.: ANFIS: adaptive-network-based fuzzy inference system. IEEE Trans Syst Man, Cybern. **23**(3), 665–685 (1993)

15. Jang, J.S.R., Sun, C.T.: Neuro-fuzzy modeling and control. Proc. IEEE **83**(3), 378–406 (1995)
16. Wang, L.X.: Adaptive Fuzzy Systems and Control. Prentice-Hall, Englewood Cliffs (1994)
17. Wang, L.X.: Stable adaptive fuzzy control of nonlinear systems. IEEE Trans. Fuzzy Syst. **1** (2), 146–155 (1993)
18. Tong, S., Tang, J., Wang, T.: Fuzzy adaptive control of multivariable nonlinear systems. Fuzzy Sets Syst. **111**, 153–167 (2000)

Constrained Fuzzy Predictive Control Design Based on the PDC Approach

Abdelmalek Zahaf[1(✉)], Sofiane Bououden[2], and Mohamed Chadli[3]

[1] Department of Electronics, Faculty of Technology Sciences, University of Freres Mentouri, Constantine, Algeria
zaha_malek@yahoo.fr
[2] Faculty of Sciences and Technology, University Abess Lghrour, Khenchela, Algeria
ss_bououden@yahoo.fr
[3] University of Picardie Jules Verne, MIS (EA 4029), Amiens, France
mchadli@u-picardie.fr

Abstract. In this paper, we are considering a model based T-S fuzzy predictive control using LMI optimization. The purpose of T-S fuzzy predictive control law is to drive the state of the system to the original state. Adopting the PDC controller and using non quadratic case of the Lyapunov function to study the stability of the controlled systems were ensuring with the stabilizing controller. The stability is guaranteed based on the conditions expressed of terms of LMIs. In addition, input and output constraints of the fuzzy system are satisfied with the PDC controller. Where, the optimal solution has been obtained at each sampling time. The simulations results are show the effectiveness of this approach.

Keywords: Parallel distributed compensation PDC · Model predictive control (MPC) · Takagi-Sugeno (T-S) fuzzy systems · Linear matrix inequality (LMI)

1 Introduction

Constrained fuzzy model predictive control become among efficient techniques in control for its tolerance, and admiration of imposed constraints. MPC is based to use a model for the prediction of future behavior of the system [1]. A constrained optimal control problem is solved at each sampling instant in online MPC approaches; several schemes are offered to put ideas for adopting in online optimization for the control of medium and high speed systems [2–4]. Relaxed conditions in form of LMIs are introduced in [5]. This form is usually used for studying robustness and stability of fuzzy systems which are analyzing using Lyapunov function for the both cases: quadratic [6], and non-quadratic case for discrete time fuzzy systems [7].

The Lyapunov function is used to study the stability problems [8, 9] of optimization was employed and becomes the most using techniques to analysis stability, where fuzzy techniques are adopted for the optimization in MPC for nonlinear systems [10–14].

In addition, the fuzzy control law parallel distributed compensation (PDC) has been implemented during the last three decades [6, 15, 16]. This approach is based on

M. Chadli et al. (eds.), *Recent Advances in Electrical Engineering and Control Applications*, Lecture Notes in Electrical Engineering 411, DOI 10.1007/978-3-319-48929-2_11

quadratic Lyapunov function and becomes the most favorite control law has been applying for fuzzy systems.

In this work, we consider to study an optimal linear control law non quadratic based on the conception of model predictive control for discrete T-S model [14]. The main idea is to calculate the gains of the control law by solving the optimization of the LMIs constrained problem at each sampling time by correct some errors in [14], even in presence of extern uncertainties. The stability and also the robustness are ensured. The results show the effectiveness of the studying control law by stabilizing the constrained systems.

This paper is organized as follows: Sect. 2 introduces the notation and some preliminary results of the basic elements, MPC, T-S fuzzy system. Section 3 presents the proposed strategy to obtain control law for regulation of the closed-loop system. In Sect. 4, simulation results are presented.

2 Backgrounds

2.1 Model Predictive Control

Let us consider the following problem, which minimizes the following objective function in an infinite horizon [5]:

$$\min_{u(k+i/k)=F(x)x(k+i/k)} \max_{i>0} J_\infty(k) \tag{1}$$

$$\begin{aligned} y_{h,min} \le y_h(k+i/k) \le y_{h,max}, \quad i \ge 0, \quad h = 1,2,\ldots,q \\ u_{h,min} \le u_h(k+i/k) \le u_{h,max}, \quad i \ge 0, \quad h = 1,2,\ldots,p \end{aligned}$$

$$J_\infty(k) = \sum_{i=0}^{\infty} [X(k+i) + U(k+i)] \tag{2}$$

$$With \quad \begin{cases} X(k+i) = x^T(k+i/k) Q_0 x(k+i/k) \\ U(k+i) = u^T(k+i/k) R_0 u(k+i/k) \end{cases} \tag{3}$$

$Q_0 > 0$ *and* $R_0 > 0$, are two known weighting matrices.

2.2 Fuzzy Discrete Time T-S Model

Let us consider the following fuzzy discrete Time T-S system which represents a discrete time nonlinear system as follows:

$$\begin{aligned} &Rule\, \boldsymbol{i}: \textbf{\textit{if}} \;\; z_1(k) \; is \; M_{i1} \ldots \text{and} \; z_p(k) \; is \; M_{ip} \\ &\textbf{\textit{then}} \begin{cases} x(k+1) = A_i x(k) + B_i u(k) \\ y(k) = C_i x(k) \end{cases} \quad i = 1 \ldots r \end{aligned} \tag{4}$$

With fuzzy discrete Time T-S model

$$\begin{cases} x(k+1) = \sum_{i=1}^{r} h_i(z(k))(A_i x(k) + B_i u(k)) \\ y(k) = \sum_{i=1}^{r} h_i(z(k)) C_i x(k) \end{cases} \quad i = 1 \ldots r \tag{5}$$

And A_i, B_i *and* C_i are states matrices of system.

2.3 PDC Fuzzy Control Law

We use the PDC control law presented in [6]. Which describe and can writing as follows:

$$u(k) = -\left(\sum_{j=1}^{r} h_j(z(k)) F_j\right) x(k) = -\sum_{j=1}^{r} h_j(z(k)) Y_j G^{-1} x(k) \tag{6}$$

By substituting (6) in (5), the closed loop system is obtained as follows:

$$\begin{cases} x(k+1) = (A_z - B_z F_z) x(k) \\ y(k) = C_z x(k) \end{cases} \tag{7}$$

With:

$$A_z = \sum_{i=1}^{r} h_i(z(k)) A_i, B_z = \sum_{i=1}^{r} h_i(z(k)) B_i, C_z = \sum_{i=1}^{r} h_i(z(k)) C_i,$$
$$F_z = \sum_{j=1}^{r} h_j(z(k)) = \sum_{j=1}^{r} h_j(z(k)) Y_j G$$

3 Robust T-S Predictive Control Model Using PDC Controller

Theorem 1 [14].

Let us consider the constrained closed-loop system in (7) at time instant k, The equilibrium of the closed-loop discrete fuzzy model, given by (5), is globally asymptotically stable if there exists a matrix $P_i > 0$ define positive, Υ_{ij}, Y_j, G and $X_{ii} > 0$ and $X_{ij} = X_{ij}^T$, while:

$$\min_{\hat{P}_i, Y_j, G} \gamma \tag{8}$$

$$\begin{bmatrix} \gamma & x^T(k/k) \\ x(k/k) & \hat{P}_i \end{bmatrix} > 0 \tag{9}$$

$$\Upsilon_{ij} = \begin{bmatrix} G^T + G - \hat{P}_i & (A_i G - B_i Y_j)^T & Y_j^T R_0 & G^T Q_0 \\ (A_i G - B_i Y_j) & \hat{P}_i & 0 & 0 \\ R_0 Y_j & 0 & R_0 & 0 \\ Q_0 G & 0 & 0 & Q_0 \end{bmatrix} \tag{10}$$

$$\begin{bmatrix} W & C_i(A_i G - B_i Y_j) \\ (A_i G - B_i Y_j)^T C_i^T & G^T + G - \hat{P}_i \end{bmatrix} > 0 \tag{11}$$

$$\begin{bmatrix} U & Y_j \\ Y_j^T & G^T + G - \hat{P}_i \end{bmatrix} > 0 \tag{12}$$

$$\Upsilon_{ij} > X_{ii} \quad i \in \{1, \ldots, r\} \tag{13}$$

$$\Upsilon_{ij} + \Upsilon_{ij} > X_{ij} + X_{ij}^T \quad i,j \in \{1, \ldots, r\}, \quad i < j \tag{14}$$

$$With: \quad X_l = \begin{bmatrix} 2X_{11} & (*) & (*) & (*) \\ X_{12} & 2X_{22} & \cdots & (*) \\ \vdots & \vdots & \ddots & \vdots \\ X_{1r} & X_{2r} & \cdots & 2X_{rr} \end{bmatrix} > 0 \tag{15}$$

Proof: Recall the closed-loop system in (7) and consider the following Non-quadratic Lyapunov function candidate:

$$V(x(k/k)) = x^T(k/k) \left(\sum_{i=1}^{r} h_i P_i \right)^{-1} x(k/k) \tag{16}$$

To ensure the stability of (4), it's necessary to satisfy the next inequalities:

$$V(x(k+i+1/k)) - V(x(k+i/k)) \leq -[X(k+i) + U(k+i)] \tag{17}$$

$$-V(x(k/k)) \leq -J_\infty(k) \tag{18}$$

We can write it:

$$\max_{A_i, B_i, i > 0} J_\infty(k) \leq V(x(k/k)) \leq \gamma \tag{19}$$

While the problem of minimization become

$$\min_{\hat{P}_i, Y_j, G} \gamma \tag{20}$$

With:

$$x^T(k/k)\hat{P}_i^{-1}x(k/k) \leq \gamma \Leftrightarrow \gamma - x^T(k/k)\hat{P}_i^{-1}x(k/k) \geq 0 \tag{21}$$

Using schur's complement to (21) we obtain:

$$\begin{bmatrix} \gamma & x^T(k/k) \\ x(k/k) & \hat{P}_i \end{bmatrix} > 0 \tag{22}$$

In the next, the PDC control law will be used to introduce more conditions that are ensuring the stability of system (5).

We have (17) it can be writing as:

$$\begin{aligned} &V(x(k+i+1/k)) - V(x(k+i/k)) \\ &\quad \leq -\left[(x^T(k+i/k)Q_0x(k+i/k)) + (u^T(k+i/k)R_0u(k+i/k))\right] \end{aligned}$$

That can be writing as:

$$\begin{aligned} &[x^T(k+i+1/k)\hat{P}_i^{-1}x(k+i+1/k)] - [x^T(k+i/k)\hat{P}_i^{-1}x(k+i/k)] \\ &\quad < -\left[(x^T(k+i/k)Q_0x(k+i/k)) + (u^T(k+i/k)R_0u(k+i/k))\right] \end{aligned}$$

We replace $u(k+i/k)$ by (6):

$$\begin{aligned} &x^T(k+i/k)[x^T(k+1/k)\hat{P}_i^{-1}x(k+1/k) - \hat{P}_i^{-1}]x(k+i/k) \\ &\quad < -x^T(k+i/k)[Q_0 + G^{-T}Y_j^TR_0Y_jG^{-1}]x(k+i/k) \end{aligned}$$

With substitution of $x(k+1/k)$ by (7) we obtain:

$$\begin{aligned} &x^T(k+i/k)[(A_i - B_iY_jG^{-1})^T\hat{P}_i^{-1}(A_i - B_iY_jG^{-1}) - \hat{P}_i^{-1}]x(k+i/k) \\ &\quad < -x^T(k+i/k)[Q_0 + G^{-T}Y_j^TR_0Y_jG^{-1}]x(k+i/k) \end{aligned}$$

This inequality is equivalent to next inequality:

$$(A_i - B_iY_jG^{-1})^T\hat{P}_i^{-1}(A_i - B_iY_jG^{-1}) - \hat{P}_i^{-1} < -Q_0 - G^{-T}Y_j^TR_0Y_jG^{-1} \Leftrightarrow$$

We multiple in the left by G^T and by G in the right we get:

$$(A_iG - B_iY_j)^T\hat{P}_i^{-1}(A_iG - B_iY_j) - G^T\hat{P}_i^{-1}G < -G^TQ_0G - Y_j^TR_0Y_j \Leftrightarrow$$

Then we obtain:

$$G^T\hat{P}_i^{-1}G - (A_iG - B_iY_j)^T\hat{P}_i^{-1}(A_iG - B_iY_j) - G^TQ_0G - Y_j^TR_0Y_j > 0 \tag{23}$$

The term $G^T\hat{P}_i^{-1}G$, can be writing as follows:

$$\left(G^T-\hat{P}_i\right)\hat{P}_i^{-1}\left(G-\hat{P}_i\right)\geq 0\Rightarrow$$

$$G^T\hat{P}_i^{-1}G-G^T\hat{P}_i^{-1}\hat{P}_i-\hat{P}_i\hat{P}_i^{-1}G+\hat{P}_i\hat{P}_i^{-1}\hat{P}_i\geq 0\Leftrightarrow$$

$$G^T\hat{P}_i^{-1}G-G^T-G+\hat{P}_i\geq 0\Leftrightarrow$$

$$G^T+G-\hat{P}_i\leq G^T\hat{P}_i^{-1}G\Leftrightarrow$$

$$G^T+G-\hat{P}_i\leq G^T\hat{P}_i^{-1}G \tag{24}$$

We hold (24) in (23):

$$G^T+G-\hat{P}_i-(A_iG-B_iY_j)^T\hat{P}_i^{-1}(A_iG-B_iY_j)-G^TQ_0G-Y_j^TR_0Y_j>0$$

With a small addition of Q_0 *and* R_0 matrices to the precedent inequality, we find:

$$\begin{aligned}&(G^T+G-\hat{P}_i)-(A_iG-B_iY_j)^T\hat{P}_i^{-1}(A_iG-B_iY_j)-Y_j^TR_0R_0^{-1}R_0Y_j\\&\quad-G^TQ_0Q_0^{-1}Q_0G>0\end{aligned} \tag{25}$$

Using generalized schur's complement and propriety in [12] to (25), we obtain:

$$\begin{bmatrix}G^T+G-\hat{P}_i & (A_iG-B_iY_j)^T & Y_j^TR_0 & G^TQ_0\\(A_iG-B_iY_j) & \hat{P}_i & 0 & 0\\R_0Y_j & 0 & R_0 & 0\\Q_0G & 0 & 0 & Q_0\end{bmatrix}>0 \tag{26}$$

The inequality (26) represents the LMI form of model fuzzy predictive control. Now, we also must put the constraints in the form of LMIs.

– Output Constraints

$$y_{h,min}\leq y_h(k+i/k)\leq y_{h,max},\quad i\geq 0,\quad h=1,2,\ldots,q$$

$$|y_h(k+i/k)|\leq y_{h,max},\quad i\geq 0,\quad h=1,2,\ldots,q$$

$$y_{max}=W$$

$$\|y(k+i/k)\|_{max}\triangleq\max_i y_i(k+i/k)$$

With (7), we can write:

$$\max_{i>0}\|y(k)\|_{max}\geq\max_{i>0}\left\|C_i(A_i-B_iY_jG^{-1})\hat{P}_i^{-1}x(k)\right\|_{max}$$

Using the LMI constraints in [5]. We obtain:

$$\begin{bmatrix} W & C_i(A_i - B_i Y_j G^{-1}) \\ (A_i - B_i Y_j G^{-1})^T C_i^T & \hat{P}_i \end{bmatrix} > 0$$

By using Congruence property with full rank matrix $\begin{bmatrix} I & 0 \\ 0 & G^T \end{bmatrix}$ gives:

$$\begin{bmatrix} W & C_i(A_i G - B_i Y_j) \\ (A_i G - B_i Y_j)^T C_i^T & G^T + G - \hat{P}_i \end{bmatrix} > 0 \tag{27}$$

– Input Constraints

$$u_{h,min} \leq u_h(k+i/k) \leq u_{h,max}, \quad i \geq 0, \quad h = 1, 2, \ldots, p$$

$$|u_h(k+i/k)| \leq u_{h,max}, \quad i \geq 0, \quad h = 1, 2, \ldots, p$$

$$u_{max} = U$$

$$\|u(k+i/k)\|_{max} \triangleq \max_i u_i(k+i/k)$$

With (6), we can write:

$$\max_{i>0} \|u(k)\|_{max} \geq \max_{i>0} \left\| Y_j G^{-1} \hat{P}_i^{-1} x(k) \right\|_{max}$$

Use again the LMI constraints in [5]. We obtain:

$$\begin{bmatrix} U & (Y_j G^{-1}) \\ (Y_j G^{-1})^T & \hat{P}_i \end{bmatrix} > 0$$

By using Congruence property with full rank matrix $\begin{bmatrix} I & 0 \\ 0 & G^T \end{bmatrix}$ gives:

$$\begin{bmatrix} U & Y_j \\ Y_j^T & G^T + G - \hat{P}_i \end{bmatrix} > 0 \tag{28}$$

4 Simulation Results

In this section we present the design of conditions that ensure stability for nonlinear systems by the presented strategy, Constrained MPC for Fuzzy discrete time by PDC controller. Two examples are presented with and without uncertainties. The online set solutions were carried out using the YALMIP toolbox [17].

4.1 Example 1

The following system is taken from [18]:

$$\begin{cases} \textit{Rule}1 : \textit{if } \boldsymbol{x}_1(\boldsymbol{k}) \textit{ is } \boldsymbol{M}_1, \textit{ then } \begin{cases} \dot{\boldsymbol{x}}(\boldsymbol{t}) = \boldsymbol{A}_1 x(\boldsymbol{t}) + \boldsymbol{B}_1 u(\boldsymbol{t}) \\ y(\boldsymbol{t}) = \boldsymbol{C}_1 x(\boldsymbol{t}) \end{cases} \\ \textit{Rule}2 : \textit{if } \boldsymbol{x}_1(\boldsymbol{k}) \textit{ is } \boldsymbol{M}_2, \textit{ then } \begin{cases} \dot{\boldsymbol{x}}(\boldsymbol{t}) = \boldsymbol{A}_2 x(\boldsymbol{t}) + \boldsymbol{B}_2 u(\boldsymbol{t}) \\ y(\boldsymbol{t}) = \boldsymbol{C}_2 x(\boldsymbol{t}) \end{cases} \end{cases} \tag{29}$$

Using sector nonlinearity with the sampling time 1 s the T-S fuzzy discrete time system represents with:

$$\mathrm{A}_1 = \begin{bmatrix} 0.9504 & 0.9834 \\ -0.09834 & 0.9504 \end{bmatrix}, \quad \mathrm{A}_2 = \begin{bmatrix} 0.9635 & 0.6218 \\ -0.06218 & 0.3417 \end{bmatrix}$$

$$\mathrm{B}_1 = \begin{bmatrix} 0.4958 \\ 0.9834 \end{bmatrix}, \mathrm{B}_2 = \begin{bmatrix} 0.365 \\ 0.6218 \end{bmatrix}; \mathrm{C}_1 = [1 \quad 0], \mathrm{C}_2 = [1 \quad 0]$$

Weighting matrices and membership functions for rule 1 and rule 2 are:

$$\mathrm{Q}_0 = \begin{bmatrix} 1 & 0 \\ 0 & 1 \end{bmatrix}, \quad \mathrm{R}_0 = 0.5, \quad \mathrm{M}_1(x_1(k)) = -x_2^2 + 1, \quad \mathrm{M}_2(x_2(k)) = x_2^2$$

Under the constraints: $-2 < y(k) < 2, \quad -0.5 < u(k) < 0.5$.

With the initials conditions are: $x_1(0) = 0, \quad x_2(0) = 0$.

The results in Figs. 1 and 2 shows that the conception of control law with corrections gives a better responses when we compare the results with that given in [15]. It is clearly that the stability is guarantee with respect of imposed constraints.

Also results in Fig. 3 show the robustness behavior of the study approach in presence of extern uncertainties.

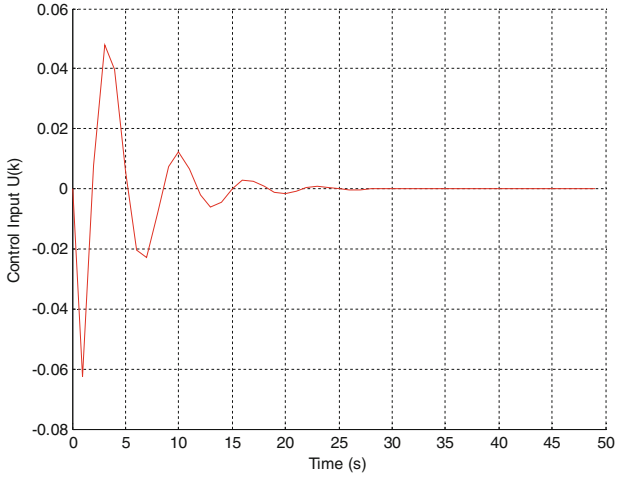

Fig. 1. Response of control input u(k)

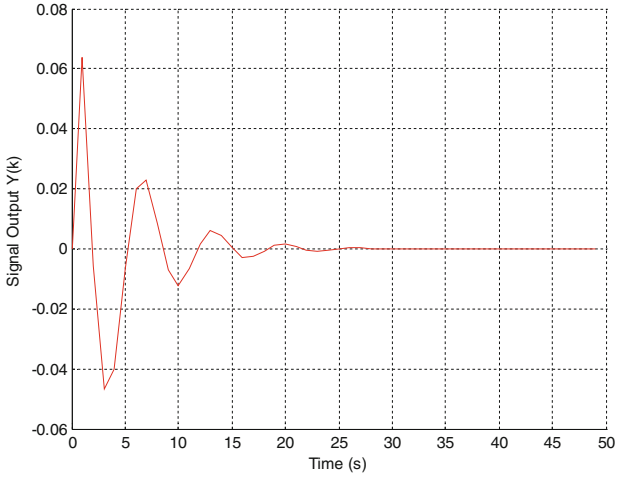

Fig. 2. Response of output signal y(k)

4.2 Example 2

The following system is taken from [14], with the states matrices:

$$A_1 = \begin{bmatrix} -0.5 & 2 \\ -0.1 & 1.1 \end{bmatrix}, \quad A_2 = \begin{bmatrix} -0.19 & 0.5 \\ -0.1 & -1.2 \end{bmatrix}$$

$$B_1 = \begin{bmatrix} 4.1 \\ 4.8 \end{bmatrix}, \quad B_2 = \begin{bmatrix} 3 \\ 0.1 \end{bmatrix}; \quad C_1 = [1 \quad 0.3], \quad C_2 = [0.8 \quad 0.2]$$

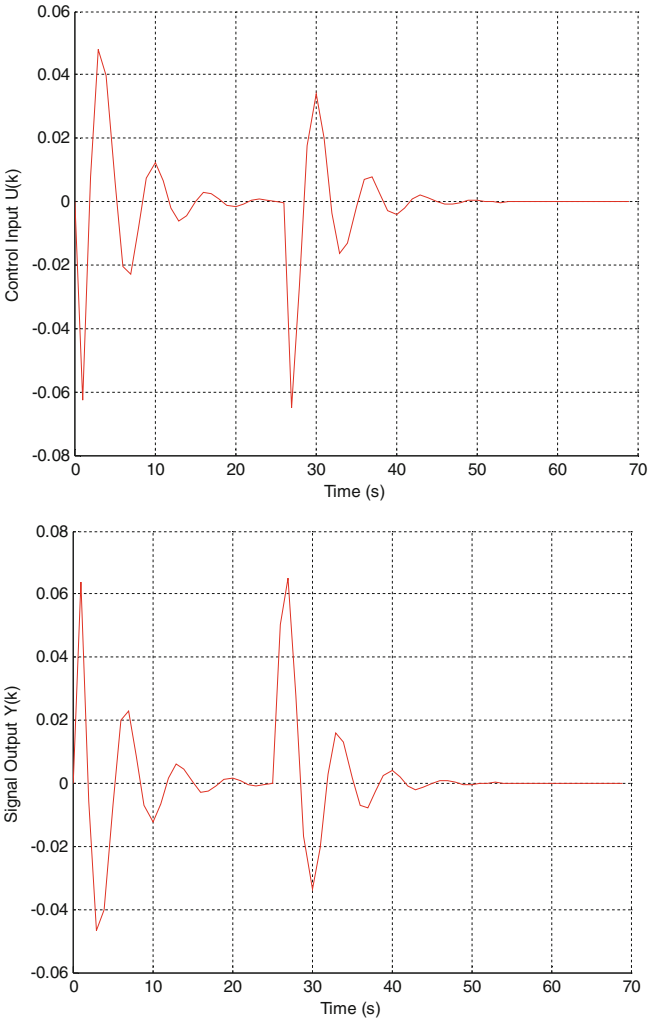

Fig. 3. Response of control input u(k) and output signal y(k)

Weighting matrices:

$$Q_0 = \begin{bmatrix} 0.8 & 0.1 \\ 0.1 & 0.95 \end{bmatrix}, \quad R_0 = 0.9.$$

And membership functions for rule 1 and rule 2 are:

$$M_1(x_1(k)) = \frac{1}{1 + \exp(-2x_1(k))}, \quad M_2(x_2(k)) = 1 - M_1(x_1(k))$$

Under the constraints: $-2.5 < y(k) < 2.5, \quad -1 < u(k) < 1.$
With the initials conditions are:

$$x_1(0) = -0.3, \quad x_2(0) = -1, \quad u(0) = -0.5, \quad y(0) = -0.5.$$

The results in Figs. 4 and 5 of the simulation show that the conception of corrected control law performance gives better results when we compare with [14]. The comparison is presented in Table 1.

Even in presence of extern uncertainties, results in Figs. 6 and 7 are showing that the robustness of this approach is ensured.

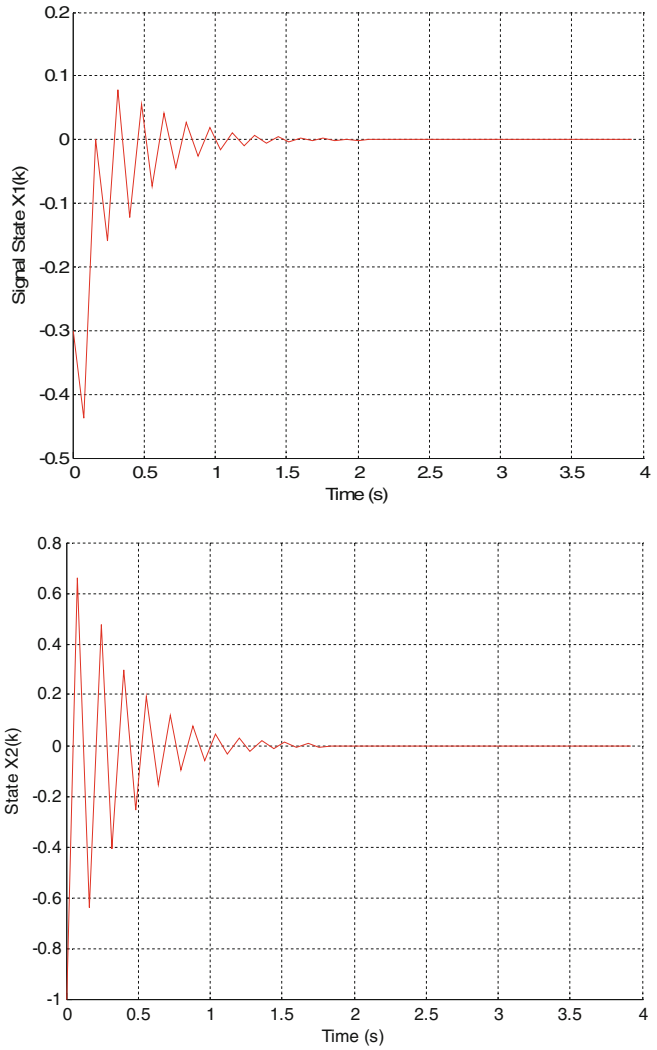

Fig. 4. Response of state X1(k) and X2(k)

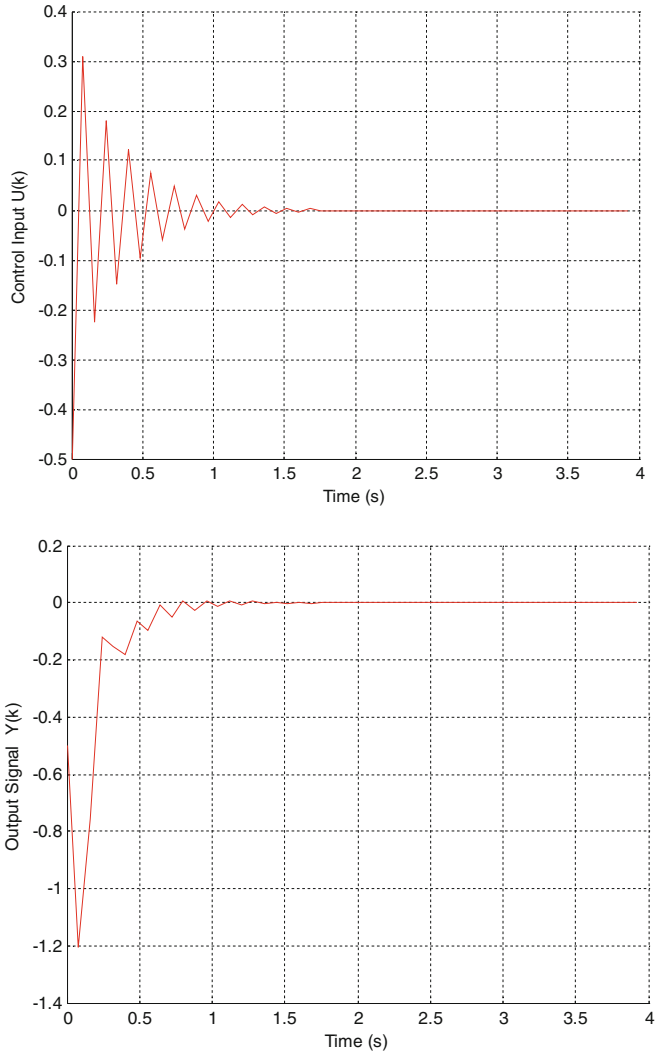

Fig. 5. Response of control input u(k) and output signal y(k)

Table 1. Comparison results with [14].

Comparison results	This paper	[14]
Chattering interval of x_1	−0.4–0.1	−3.3–3.2
Chattering interval of x_2	−0.7–0.7	−0.9–1.1
Chattering interval of u	−0.2–0.3	−0.9–0.7
Chattering interval of y	−1.2–0.1	−2.4–2.3
Convergence time at All	1.3–2.0	3.1–3.5

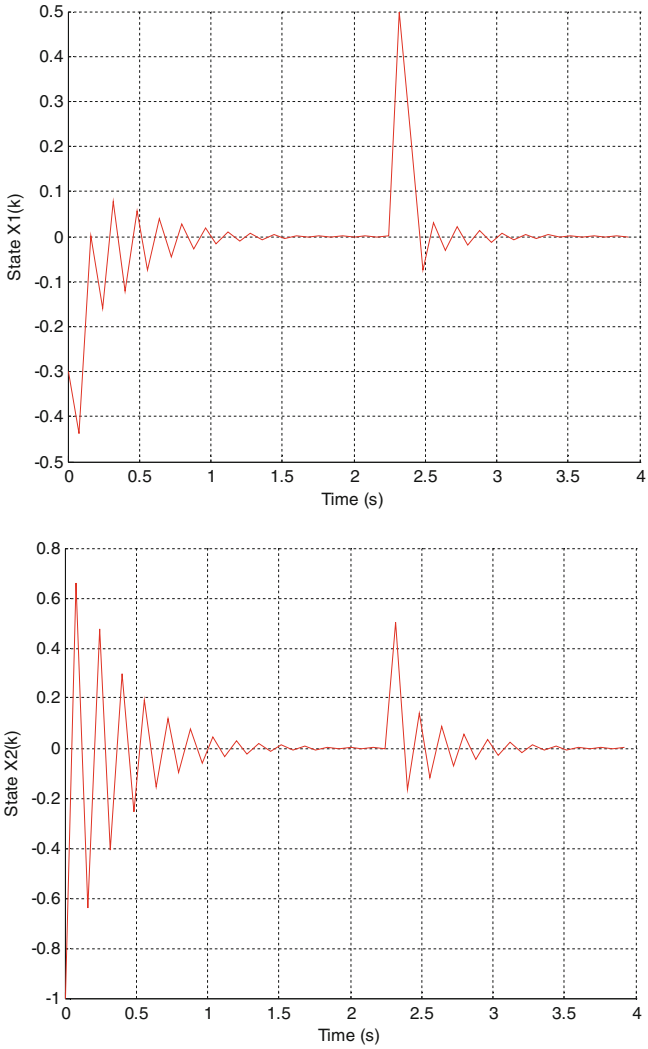

Fig. 6. Response of state X1(k) and X2(k)

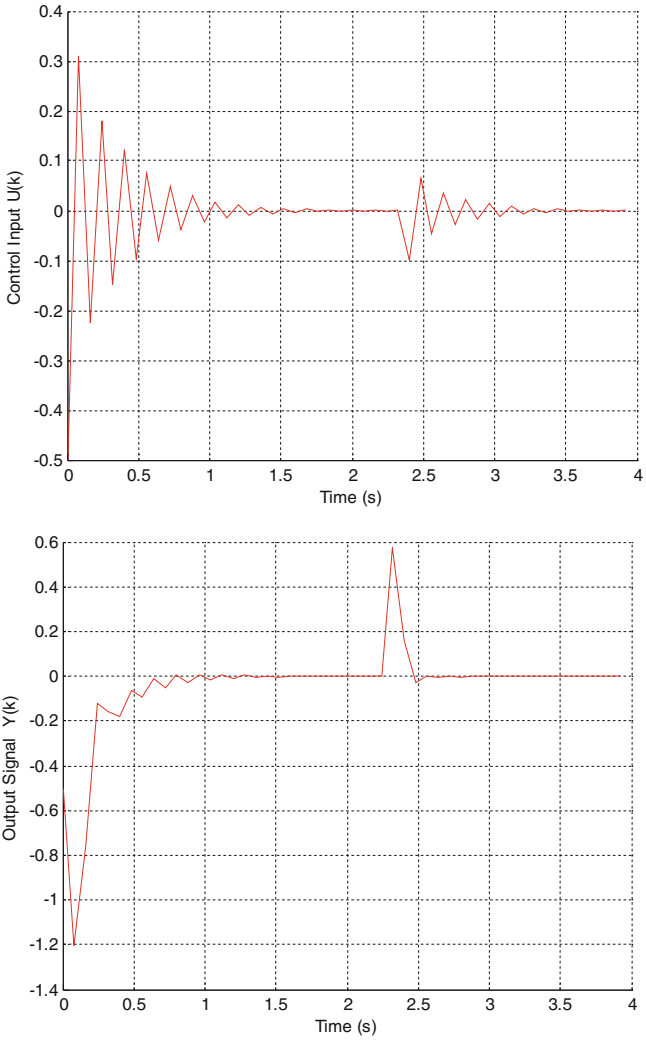

Fig. 7. Response of control input u(k) and output signal y(k)

5 Conclusion

In this paper, corrections of controller performance based T-S fuzzy predictive control under constraints was introduced. The PDC is designed with an infinite horizon predictive control; therefore the optimization problem with input constraint is transformed into constraint LMI problem. Thus LMI optimization is well suited for online implementation, which is essential for predictive control. The using of fuzzy controller PDC in this work shows good results for a class of nonlinear systems. Finally, the stability of the closed-loop system is guaranteed by the Lyapunov approach.

References

1. Camacho, E.F., Bordons, C.: Model Predictive Control. Springer, London (2004)
2. Zeilinger, M.N., Raimondo, D.M., Domahidi, A., Morari, M., Jones, C.N.: On real-time robust model predictive control. Automatica **50**, 683–694 (2014)
3. Ferreau, H.J., Bock, H.G., Diehl, M.: An online active set strategy to overcome the limitations of explicit MPC. Int. J. Robust Nonlinear Control **18**, 816–830 (2008)
4. Wang, Y., Boyd, S.: Fast model predictive control using online optimization. IEEE Trans. Control Syst. Technol. **18**(2), 267–278 (2010)
5. Kothare, M.V., Balakrishnan, V., Morari, M.: Robust constrained model predictive control using linear matrix inequalities. Automatica **32**(10), 1361–1379 (1996)
6. Tanaka, K., Sugeno, M.: Stability analysis and design of fuzzy control system. Fuzzy Sets Syst. **45**(2), 135–156 (1992)
7. Morère, Y.: Control laws for fuzzy models of Takagi–Sugeno, Thesis. University of Valenciennes & Hainaut Cambresis, January 2001
8. Tanaka, K., Ohtake, H., Wang, H.O.: A descriptor system approach to fuzzy control system via fuzzy Lyapunov functions. IEEE Trans. Control Syst. Technol. **15**(3), 333–341 (2007)
9. Kang, Q., Wang, W.: Guaranteed cost control for T-S fuzzy systems with time-varying delays. J. Control Theory Appl. **8**(4), 413–417 (2010)
10. Ding, B., Ping, X.: Output feedback predictive control with one free control move for nonlinear systems represented by a Takagi-Sugeno model. IEEE Trans. Fuzzy Syst. **22**(2), 249–263 (2014)
11. Bououden, S., Chadli, M., Filali, S., El Hajjaji, A.: Fuzzy model based multivariable predictive control of a variable speed wind turbine: LMI approach. Renew. Energy **37**(1), 434–439 (2012)
12. Bououden, S., Benelmir, O., Ziani, S., Filali, S.: A new adaptive fuzzy model and output terminal constraints in predictive control. Int. J. Inf. Syst. Sci. (IJISS) **3**(1), 25–35 (2007)
13. Zhang, T., Feng, G., Lu, J.: Fuzzy constrained min-max model predictive control based on piecewise Lyapunov functions. IEEE Trans. Fuzzy Syst. **15**(4), 686–698 (2007)
14. Xia, Y., Yang, H., Shi, P., Fu, M.: Constrained infinite-horizon model predictive control for fuzzy-discrete time systems. IEEE Trans. Fuzzy Syst. **19**(3), 429–436 (2010)
15. Tanaka, K., Wang, H.O.: Fuzzy Control Systems Design and Analysis: A Linear Matrix Inequalities Approach. Wiley, New York (2001)
16. Guechi, H., Lauber, J., Dambrine, M., Klancar, G., Blažic, S.: PDC control design for non-holonomic wheeled mobile robots with delayed outputs. J. Intell. Robot. Syst. **60**(4), 395–414 (2010)
17. Löfberg, J.: YALMIP: a toolbox for modeling and optimization in MATLAB. In: Proceedings of the CACSD Conference, Taipei, Taiwan. (2004)
18. Khairy, M., Elshafei, A.L., Emara, H.M.: LMI based design of constrained fuzzy predictive control. Fuzzy Sets Syst. **161**, 893–918 (2010)

Renewable Energy (RE)

Control of Grid-Connected Photovoltaic System with Batteries Storage

Seif Eddine Boukebbous[1,2(✉)], Djallel Kerdoun[1], and Messaoud Khelif[3]

[1] Laboratory of Electrical Engineering of Constantine (LGEC), Department of electrotechnics, University Constantine 1, Constantine, Algeria
boukebbous_seifeddine@hotmail.fr
[2] Unité de Recherche Appliquée en Energies Renouvelables, URAER, Centre de Développement des Energies Renouvelables, CDER, 47133 Ghardaïa, Algeria
[3] Centre de Développement des Energies Renouvelables, CDER, 16340 Algiers, Algeria
mkhelif@cder.dz

Abstract. This paper presents a control of grid-connected photovoltaic system with electrochemical batteries storage; the objective of this study is to supply active photovoltaic power to electrical grid in different atmospheric conditions (temperature, illumination), this presented work focused on decupled active and reactive power strategy, which makes it possible to control the level of the active and reactive power injected (or recovered) with the electrical grid, In other hand, the batteries complement the active power imposed in all situations. Simulation results in rigorous case illustrate the performances obtained.

Keywords: PV · Photovoltaic panels · MPPT · Battery · Active and reactive power control · Grid-connected

1 Introduction

With the decrease of conventional energy sources and the growing problem of environmental pollution, the research and utilization of the renewable energy, such as solar energy, wind energy as so on, has been concerned with more and more attention [1]. PV power is becoming more prevalent as its cost is becoming more competitive with traditional power sources. However, the utilization of dedicated energy storage systems needs to be taken into account because of the intermittent nature of the PV generation. Energy storage systems can open the possibility to employ renewable energy sources able to operate in stand-alone mode, grid-connected mode, and mode transitions from stand-alone to grid, or vice versa in micro-grid systems [2]. In this work we proposed a photovoltaic station with two electronics converter and batteries storage system connected to the grid, this structure is controlled for prescribed active and reactive power to the grid. The system performance has been evaluated in rigorous situation to prove the feasibility and the simplicity of this control.

M. Chadli et al. (eds.), *Recent Advances in Electrical Engineering and Control Applications*, Lecture Notes in Electrical Engineering 411, DOI 10.1007/978-3-319-48929-2_12

2 Photovoltaic Model

Starting from the widely known photovoltaic cell electrical equivalent circuit [3] (Fig. 1), an equivalent model for a more powerful PV generator made of an ($N_s \times N_p$) array of PV cells, is established [4, 5]:

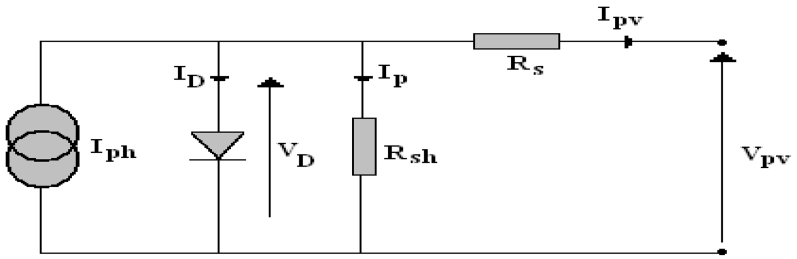

Fig. 1. Simple model of the photovoltaic cells.

$$I_{pv} = I_{ph} - I_D - I_p \tag{1}$$

I_D expression being deduced from the semiconductor diode theory, the above relation may be detailed as:

$$I_{pv} = I_{ph} - I_o(\exp(\frac{V_{pv} + R_s I_{pv}}{nKT/q}) - 1) - \frac{V_{pv} + R_s I_{pv}}{R_{sh}} \tag{2}$$

Where, I_{ph} is the light generated current (A), I_o the PV cell saturation current (A), q the electron charge (q = 1, 6 10^{-19} C), K the Boltzmann constant (K = 1, 38 10^{-23} J/K), n the cell ideality factor, T the cell temperature. R_{sh} and R_s are pure parasitic resistances characterizing respectively parallel current leakage and series connecting circuit.

In general, for a PVG involving an array of N_S cells connected in series and N_P in parallel, its output voltage current relation may be deduced from the basic cell Eq. (2) as follows [4, 5]:

$$I_{pv} = N_p I_{ph} - N_p I_o(\exp(\frac{q(V_{pv} + \frac{N_s}{N_p} R_s I_{pv})}{nKTN_s}) - 1) - \frac{V_{pv} + \frac{N_s}{N_p} R_s I_{pv}}{\frac{N_s}{N_p} R_{sh}} \tag{3}$$

From (2), an already temperature dependence of the cell external characteristic is established. Furthermore, all the cell parameters (I_o, n, R_s and R_{sh}), are equally temperature related. However, semiconductor diode theory, suggests that the most significant temperature effect comes from the reverse saturation current I_o. Variation of its value I_o (T) with working temperature T, is usually evaluated relatively to its evaluated value I_o (T_r) at a reference temperature T_r [3].

$$\frac{I_o(T)}{I_o(T_r)} = (\frac{T}{T_r})^3 \exp[\frac{qE_g}{nK}(\frac{1}{T_r} - \frac{1}{T})] \tag{4}$$

Where: E_g is the cell material band gap, supposed here no temperature dependant, and K is the Boltzmann constant.

The value of saturation current Io (T_r), may be evaluated through the open circuit voltage V_{oc} (T_r) and the short circuit current I_{SC} (T_r) deduced from (2).

$$I_o(T_r) = \frac{I_{sc}(T_r)}{(e^{\frac{qV_{oc}(T_r)}{nkT}} - 1)} \tag{5}$$

The equation of the illumination current brought back to the reference conditions (G_r = 1000 W/m^2, T_r = 25 C°) is given as follows:

$$I_{ph} = [I_{cc}\frac{G}{G_r} + I_t(T - T_r)] \tag{6}$$

I_t: Temperature coefficient of short-circuit current.
G_r: The reference illumination.
G: The actually illumination.

The model of the PVG precedent is implemented in environment MATLAB/ SIMULINK as indicates the (Fig. 2).

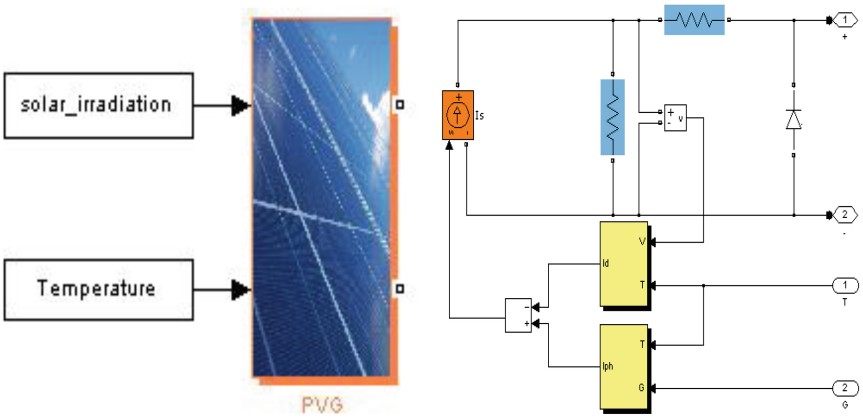

Fig. 2. Structure of the PVG Simulink model.

The main external reference characteristics of the PVG are established using the identified perturbation inputs (solar illumination, temperature) as parameters (Figs. 3, 4 and 5).

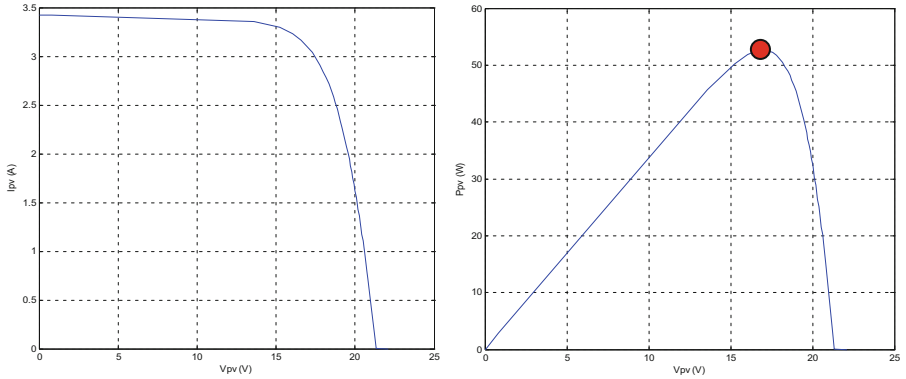

Fig. 3. PVG (current – voltage) and (power – voltage) characteristics for standards conditions.

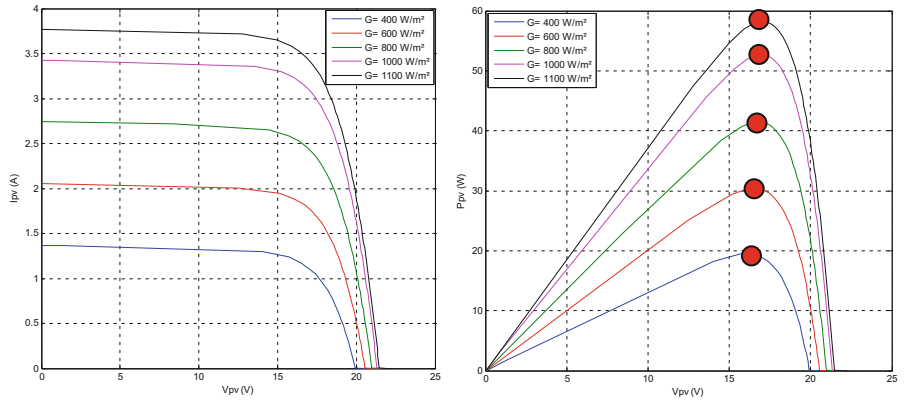

Fig. 4. PVG (current –voltage) and (power –voltage) characteristics for different solar illuminations.

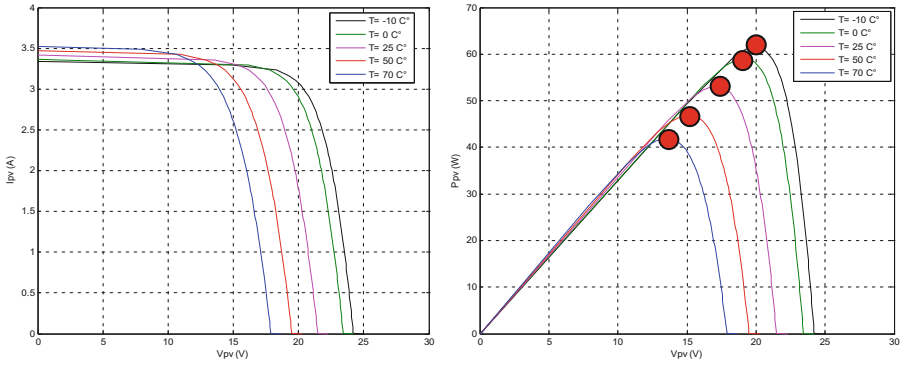

Fig. 5. PVG (current – voltage) and (power – voltage) characteristics for different temperatures.

3 Storage System

One of the principal disadvantages of solar energy is its intermittent character. For a permanent use, it is thus necessary to store part of produced energy. There are several methods of storage: in water form, hydrogen, supercondensator, or electrochemical battery [6]. The battery block of MATLAB-SIMULINK "Sim Power Systems" (Fig. 6) implements a generic dynamic model parameterized to represent most popular types of rechargeable batteries (Lead-Acid, Lithium-Ion, Nickel-Cadmium, Nickel-Metal-Hydride) [7].

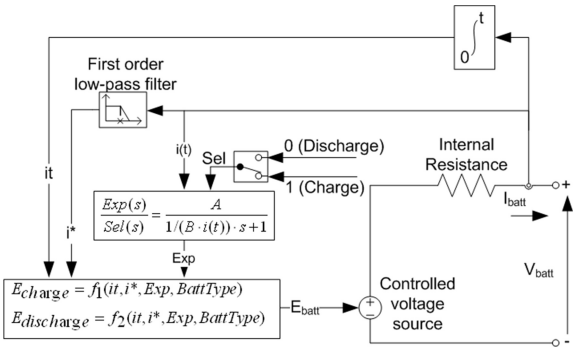

Fig. 6. Battery model [7].

The charge and discharge equations of the lead acid battery are given [7]:
Charge:

$$E_{batt} = E_o - R.i - K\frac{Q}{i_t - 0.1Q}i^* - K\frac{Q}{Q - i_t}i_t + Exp(t) \tag{7}$$

Discharge:

$$E_{batt} = E_o - R.i - K\frac{Q}{Q - i_t}(i_t + i^*) + Exp(t) \tag{8}$$

$$\dot{Exp}(t) = B.|i(t)|.(-Exp(t) + A.sel(t)) \tag{9}$$

Where:

Sel(t) = charge or discharge mode.
Exp(t) = exponentiel zone voltage (V).
E_{batt} = nonlinear voltage (V).
V_{batt} = battery voltage (V).
E_0 = battery constant voltage (V).
K = polarization constant (V/Ah) or polarization resistance.
Q = battery capacity (Ah).

i_t = actual battery charge (Ah).
A = exponentiel zone amplitude (V).
B = exponential zone time constant inverse $(Ah)^{-1}$.
R = internal resistance (Ω).
i = battery current (A).
i^* = filtered current (A).

4 Topology of the System

The photovoltaic system consists of (Fig. 7):

1. Photovoltaic panels.
2. Storage system: (batteries).
3. DC/DC converter.
4. DC/AC converter.
5. Filter.
6. Transformer for increasing the alternative voltage.

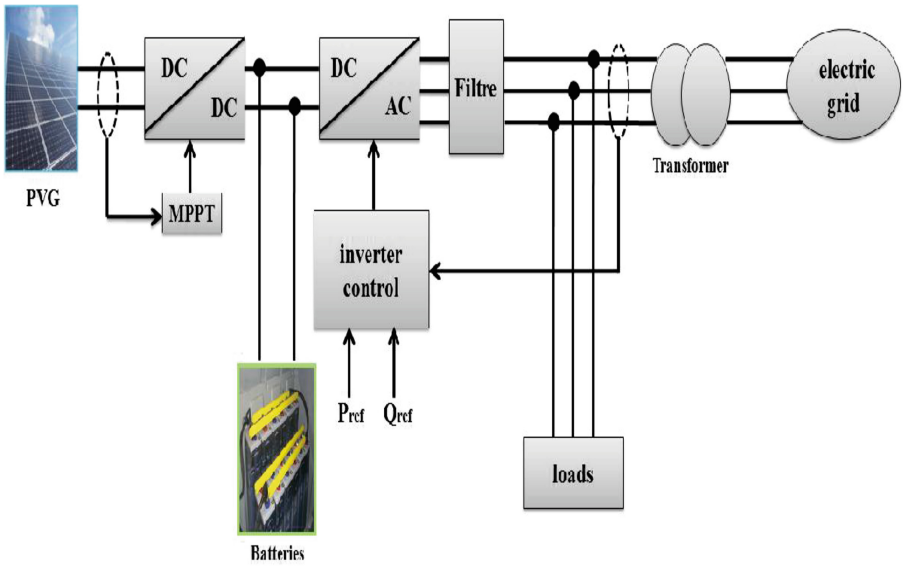

Fig. 7. Global architecture of Grid-connected photovoltaic system

5 Control Strategy

The control system is composed of two parts, the control of the boost chopper and the three phase inverter.

5.1 Boost Converter Control

Due to its nonlinear external current–voltage characteristic, the PVG maximum power output varies with its operating point. The latter being equally load related, this occurs even for a given solar irradiation and temperature. In this case only a unique load value may ensure the optimum operating point in terms of maximum power extraction from the PVG, which output voltage and current are then at their respective optimal values (V_{opt}, I_{opt}). Generally, all the inputs defining the optimum operating point of the PVG (Solar irradiation, temperature and load, shading being a particular situation), are imposed. However, it is known in power DC electrical circuits, that a switching DC-DC electronic power converter may be an efficient impedance adaptor tool (Fig. 8). Hence, it may be used to adjust the equivalent load impedance to the needed value for PVG optimal operating point, whatever are the solar irradiance, temperature and eventually shading rate [3].

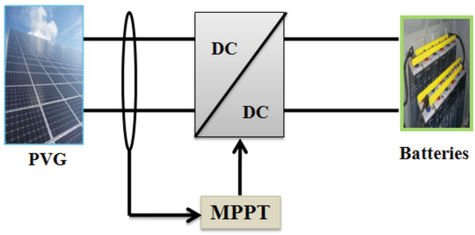

Fig. 8. Control of the boost chopper.

The MPPT algorithm used is a classical one and will not be detailed in this paper.

5.2 Inverter Control

The objective of this control is to impose the active and reactive power injected to grid. The diagram of the algorithm used in this work is shown in (Fig. 9).

1. *PLL Control*

Various disturbances can occur on the electrical supply network, the objective of synchronization system is to reconstitute information on the direct component of the fundamental voltage. The principle of the three-phase PLL (Fig. 10) consists in applying an inverse Park transformation to the grid voltages. The component V_q generated by this transformation is controlled to zero by action on the estimation angle of Park (θ_{est}). In mode established θ_{est} is equal to the angle of the network θ.

By using the park transformation and trigonometric methods, the V_d and V_q voltage can be written such:

$$\begin{cases} V_{dr} = \sqrt{\frac{3}{2}} V_m \cos(\theta - \theta_{est}) \\ V_{qr} = -\sqrt{\frac{3}{2}} V_m \sin(\theta - \theta_{est}) \end{cases}, \quad (\theta - \theta_{est}) = \delta \tag{10}$$

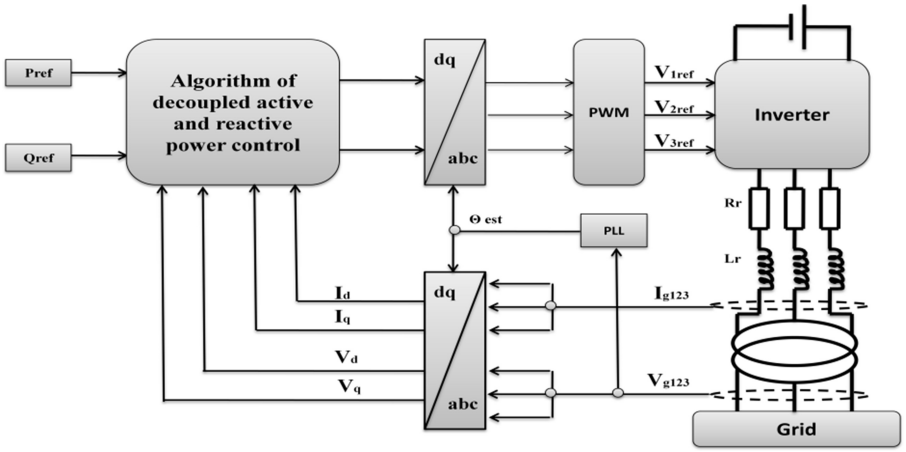

Fig. 9. Block diagram of the used power control algorithm.

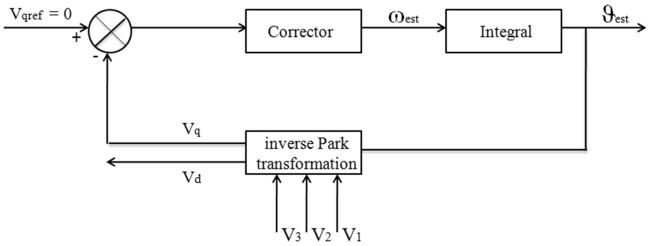

Fig. 10. Principe of three phases PLL.

The objective of the control is to cancel δ to obtain the frequency and the voltage angle at the connection point.

To be able to use the traditional techniques of corrector adjustment, it is necessary to linearize the PLL. Thus, if the system error is regarded as very small, the relation between this error and the error of estimation phase will be:

$$V_{qr} = -\sqrt{\frac{3}{2}} V_m \sin\delta \cong -\sqrt{\frac{3}{2}} V_m \delta \tag{11}$$

The diagram of three-phase PLL regulation is represented in (Fig. 11) [8]:

2. *Power Control*

The active and reactive power (P, Q) can be both expressed by using Park components of supply voltage (V_d, V_q) and line current (I_d, I_q) as follows [9–11]:

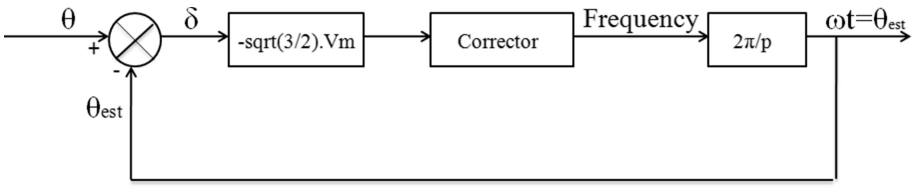

Fig. 11. PLL control system.

$$\begin{cases} P = V_d I_d + V_q I_q \\ Q = V_d I_q - V_q I_d \end{cases} \tag{12}$$

Reference currents (I_{dref}, I_{qref}) which allows setting the desired reference active and reactive powers (P_{ref}, Q_{ref}), as follows [9, 12–14]:

$$\begin{cases} I_{dref} = \dfrac{P_{ref} V_d - Q_{ref} V_q}{V_d^2 + V_q^2} \\ I_{qref} = \dfrac{P_{ref} V_q - Q_{ref} V_d}{V_d^2 + V_q^2} \end{cases} \tag{13}$$

The unity power factor is obtained simply by setting the reactive power reference null. We can also generate or absorb ($Q_{ref} < 0$ or $Q_{ref} > 0$).

3. *Current Control*

The vector current control in Park reference frame is carried out by using the synchronized reference with the grid voltage. The electric equations of the filter (R_r, L_r) connected to the grid are given bellow:

$$\begin{cases} V_d = R_r I_d + L_r \dfrac{dI_d}{dt} - \omega_s L_r I_d + V_d \\ V_q = R_r I_q + L_r \dfrac{dI_q}{dt} - \omega_s L_r I_q + V_q \end{cases} \tag{14}$$

The full diagram of a decoupled active and reactive power algorithm [10, 11] is shown in (Fig. 12).

6 Simulation Results

In this section, the photovoltaic grid-connected system is simulated using SIMULINK-MATLAB. Several numeric simulations of the proposed system are accomplished for different situations (Power injected and illuminations values). The most important parameters of the converter are shown in Table 1.

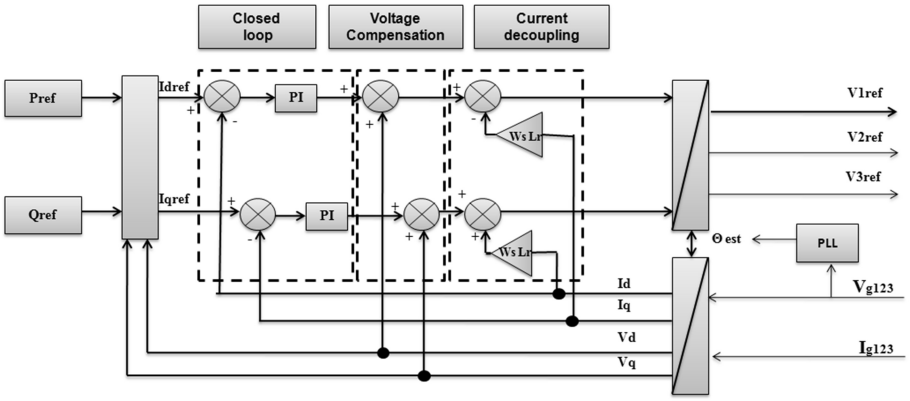

Fig. 12. Diagram of the decoupled active and reactive power control.

Table 1. Parameter values

Quantity	Values
Batteries voltage (V)	12*32
Transformer (Y/Y) (V)	220/380
Electric grid voltage (V)	220/380
Commutation frequency (Hz)	10000

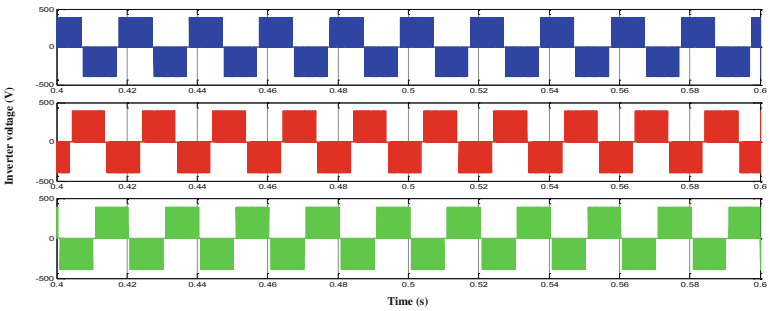

Fig. 13. Inverter voltages.

In the first scenario, we apply tow level of reference active power (6 kW at 0.2 s, and 2 kW at 0.6 s) with $Q_{ref} = 0$. The main simulation results are given in (Figs. 13, 14, 15, 16, and 17).

In the 2nd scenario, we inject the photovoltaic power (PV system to electrical grid) and we recovers the active power (electrical grid to PV system), we obtained many results shown in (Figs. 18, 19 and 20).

The control device makes it possible to impose the values desired of the active and reactive powers (image of current), with a very acceptable dynamics.

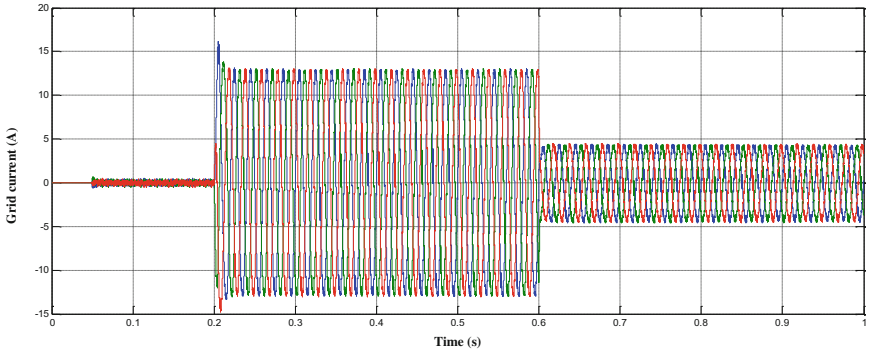

Fig. 14. Currents injected to the grid.

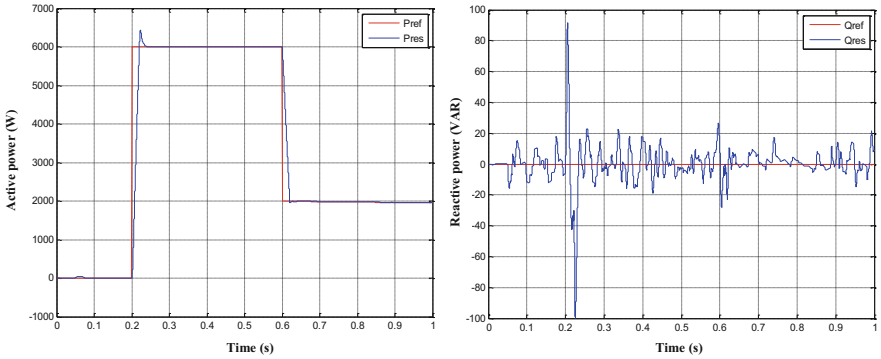

Fig. 15. Active and reactive power injected.

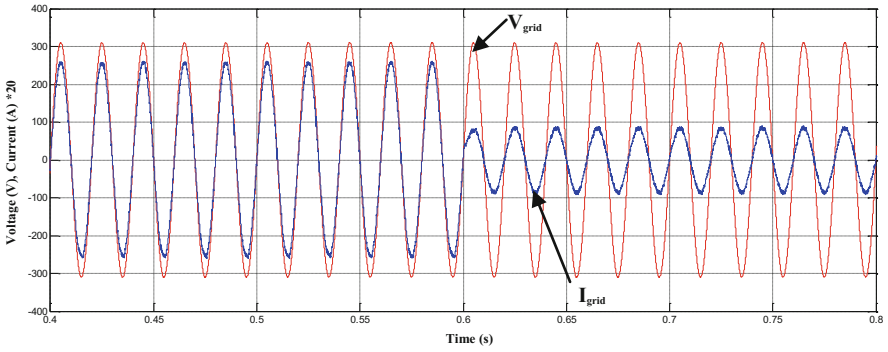

Fig. 16. Grid voltages and currents injected to the grid.

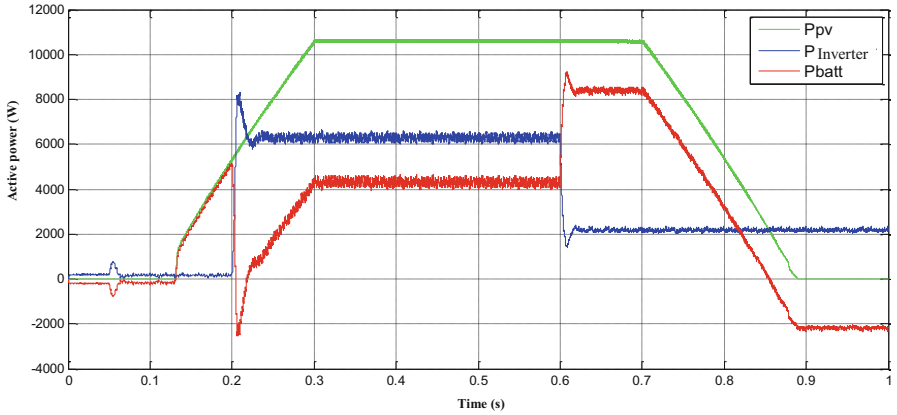

Fig. 17. Variation of the active power in the photovoltaic station.

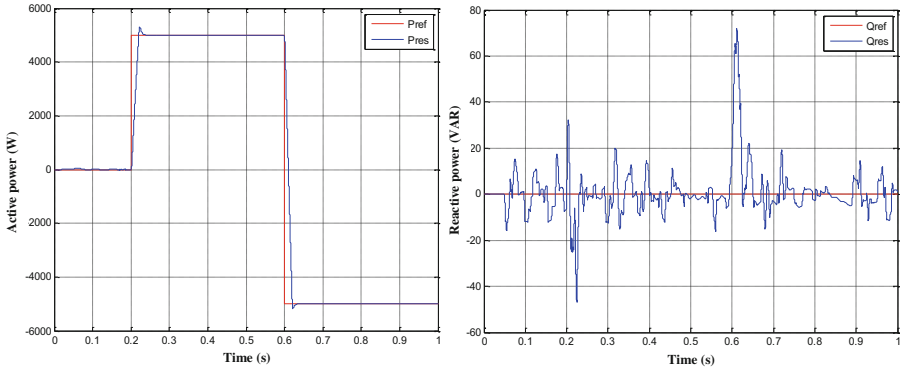

Fig. 18. Active and reactive power injected to the grid.

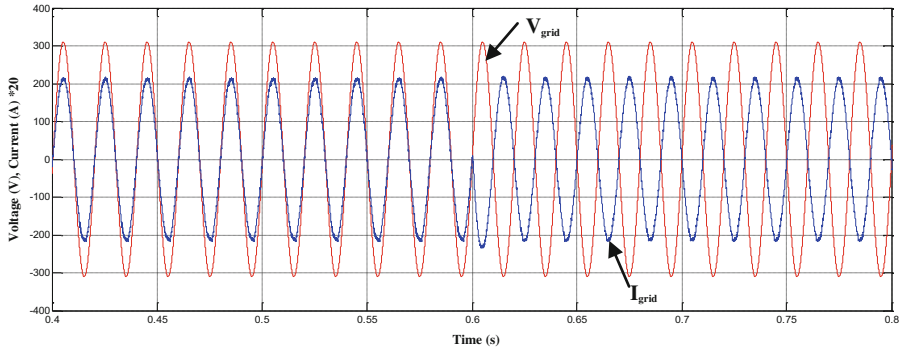

Fig. 19. Grid voltages and currents injected to the grid.

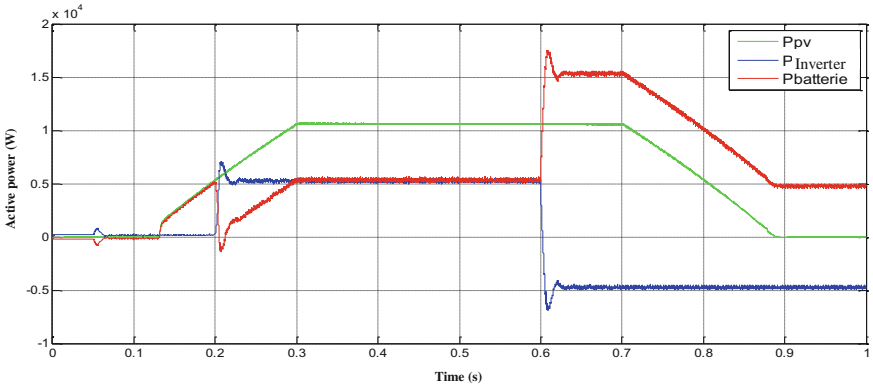

Fig. 20. Variation of the active power in the photovoltaic station.

The connection of the PV station is achieved at t = 0.05 s, for that the power injected is null, at t = 0.2 s we applied an active power reference of 6 kW, so it is directly transmitted to the electrical grid. If we change the active power reference the 6 kW to 2 kW at t = 0.6 s, the power injected follows this variation, so the currents injected decreased.

When the produced photovoltaic energy is higher than the reference imposed, more energy is stored in the batteries, in the contrary case, the batteries intervenes; therefore, we have a transfer of battery energy to the grid.

We can transmit the active power in two directions, the solar station to electrical grid or the grid to photovoltaic system. In the last case, the active power is stored in the electrochemical batteries, and the grid current is inversed.

While the reactive power is null (Figs. 16 and 19), the interval between the voltage and the current is zero, so, we have unit power factor.

7 Conclusion

In this paper, a simple control of grid-connected photovoltaic station with lead-acid batteries storage has been presented in order to inject the active photovoltaic power to the electrical grid. The storage systems make it possible to supplement the electrical power injected to the grid in the moments when the photovoltaic power is not sufficient, therefore the service continuity is ensured in all time. The simulation results obtained of this approach show and confirm the reliability and the simplicity of this strategy control.

References

1. Cai, W., Ren, H., Jiao, Y., Cai, M., Cheng, X.: Analysis and simulation for grid-connected photovoltaic system based on Matlab. IEEE, 978-1-4244-8165-1/11/$26.00 ©2011
2. Park, S.M., Park, S.Y.: Power weakening control of the photovoltaic-battery system for seamless energy transfer in microgrids. IEEE, 978-1-4673-4355-8/13/$31.00 ©2013

3. Khelif, M., M'raoui, A., Malek, A.: Simulation, optimization and performance analysis of an analog, easy to implement, perturb and observe MPPT technique to be used in a 1.5 kWp photovoltaic system. In: IRSEC 2013, Ouarzazate, 07–09 March 2013
4. Huan, L.T., Siang, C.T., Su, Y.J.: Development of generalized photovoltaic model using MATLAB/SIMULINK. In: Proceedings of the World Congress on Engineering and Computer Science 2008, WCECS 2008, 22–24 October 2008, San Francisco, USA (2008)
5. Francisco, M., Longatt, G.: Model of Photovoltaic Module in Matlab™. 2do congreso iberoamericano de estudiantes de ingeniería eléctrica, electrónica y computación (ii cibelec 2005)
6. Singo, A.T.: Système d'alimentation photovoltaïque avec stockage hybride pour l'habitat énergétiquement autonome. Doctorate thesis, Henri Poincare University, Nancy-I, February 2010
7. Fakham, H., Lu, D., Francois, B.: Power control design of a battery charger in a hybrid active PV generator for load following applications. IEEE Trans. Ind. Electron. **58**(1), 85–94 (2011). TIE-09-1370
8. Mogoş, E.F.: production décentralisée dans les réseaux de distribution. Étude pluridisciplinaire de la modélisation pour le contrôle des sources. doctorate thesis, école nationale supérieure d'arts et métiers (2005)
9. Himour, K., Ghedamsi, K., Berkouk, E.M.: A five-level diode clamped inverter for grid connection PV generation system. In: IRSEC 2013, Ouarzazate, 07–09 March 2013
10. Ghenam, T.: Supervision d'une ferme éolienne pour son intégration dans la gestion d'un réseau électrique, Apports des convertisseurs multi niveaux au réglage des éoliennes à base de machine asynchrone à double alimentation. doctorate thesis, Military polytechnic school and Central school of lille (2011)
11. Rami, G.: contrôle de tension auto adaptatif pour des productions décentralisées d'énergies connectées au réseau électrique de distribution. doctorate thesis, national polytechnic institute of grenoble (2006)
12. Tan, K.T., So, P.L., Chu, Y.C., Kwan, K.H.: Modeling, control and simulation of a photovoltaic power system for grid-connected and stand-alone applications. IEEE, 978-1-4244-7398-4/10/$26.00 ©2010
13. Kumar, R., Mohanty, A., Mohanty, S.R., Kishor, N.: Power quality improvement in 3-Φ grid connected photovoltaic system with battery storage. In: 2012 IEEE International Conference on Power Electronics, Drives and Energy Systems, 16–19 December, Bengaluru, India (2012)
14. Liu, L., Li, H., Xue, Y.: A coordinated active and reactive power control strategy for grid-connected cascaded photovoltaic PV system in high voltage high power applications. IEEE, 978-1-4673-4355-8/13/$31.00 ©2013

The Development of Empirical Photovoltaic/Thermal Collector

H. Ben cheikh el hocine[1(✉)], K. Touafek[1], and F. Kerrour[2]

[1] Centre de Développement des Energies Renouvelables, CDER, Unité de Recherche Appliquée en Energie Renouvelables, URAER, 47133 Ghardaïa, Algeria
bencheikh_80@yahoo.fr

[2] Laboratoire de Modélisation des Dispositifs à Énergies Renouvelables et Nanométriques, Département d'électronique, Université Constantine 1, Constantine, Algeria

Abstract. In the PV system, the electrical efficiency decreases rapidly as the PV module temperature increases. Therefore, in order to achieve higher electrical efficiency, the PV module should be cooled by removing the heat in some way. In order to eliminate an external electrical source and to cool the PV module, the PV module should be combined with the solar air/water heater collector. This type of system is called solar photovoltaic thermal (PV/T) collector. The PV/T collector produces thermal and electrical energy simultaneously. In this study, an attempt has been made to **develop** the hybrid PVT collector based on a new integrated absorber configuration **that is formed by two types of absorber**, the first **is parallel vertical tubes** and the second **is an** enclosure.

Keywords: Component · Solar energy · Hybrid collector · PV module photovoltaic · Photovoltaic-thermal (PV/T)

1 Introduction

Renewable energy technologies currently supply 13.3% of the world's primary energy needs and their future potential depends on exploiting the resources that are available locally and on overcoming the environmental challenges as well as winning public acceptance. Various forms of renewable energy depend primarily on incoming solar radiation, which totals about 3.8 million EJ per year.

The solar hybrid collectors are the fundamental elements in the transformation of solar energy into thermal and electrical energy; this allows an increase in the overall total conversion efficiency of solar energy received.

Research on solar began in the 1970s and has been intensified in the 1980s. In 2005, Zondag [1] provides a state of the art on the solar PVT hybrid based on the report of the European project PV-Catapult [2]. Among the first studies reviewed by Zondag [1], some of them focus on the evolution of the geometry and other components of modeling methods. Thus, Wolf [3] in 1976 performs the analysis of a solar thermal collector coupled to a heat storage system with PV modules based on silicon.

M. Chadli et al. (eds.), *Recent Advances in Electrical Engineering and Control Applications*, Lecture Notes in Electrical Engineering 411, DOI 10.1007/978-3-319-48929-2_13

Subsequently, the study by Kern and Russel in 1978 gives the basics of using solar water or air as a coolant. In 1982, Hendrie [4] developed a theoretical model of PVT hybrid collector based on correlations related to solar standards. In 1981, Raghuraman [5] presents numerical methods for predicting the performance of flat solar PVT water or air. Later, in 1985, Cox and Raghuraman [6] developed simulation software to study the performance of air hybrid PVT and focus on the influence of the optical properties of the glazing on the thermal performance and electrical components of solar. In 1986, Lalovic et al. [7] propose a new type of transparent amorphous a-Si cells as a cost effective solution for the construction of PV modules. Various experimental and theoretical studies have been carried out then, for the development of PVT hybrid collectors [8]. In 1997, Fujisawa and Tani [9] have designed and built solar hybrid PVT water on a university campus in Tokyo, Japan. In 2003, solar PVT hybrid water is investigated under dynamic conditions by Chow [10] which achieves an appropriate model for transient thermal simulations. It relies on the work of Bergen and Lovvik [11] that present in 1995. Chow et al. [12] presented the modeling and a comparison of the performance of solar PVT hybrid water, a solar PV and solar water. Two prototype solar hybrid collectors have been built, the first having been modeled in 2006 [13]. Other PVT systems have been investigated and discussed by many researchers for the last decade in the literature [14–21].

The design idea of the hybrid collector with galvanized steel sheet and tube as absorber came after it was noticed in previous studies and designs [21, 22] for its low cost.

In this paper, the thermal performance evaluation of a solar PV/T collector will be studied. A detailed model will be developed to calculate the thermal parameters of a hybrid PV/T collector.

2 Concept of Hybrid PVT Collector

2.1 Block Diagram of a PV/T System for the Production of Energy

The PV/T, merging PVs into the solar thermal module, represents a new direction for renewable heating and power generation. Figure 1 indicates the inter-relationship among different solar conversion technologies.

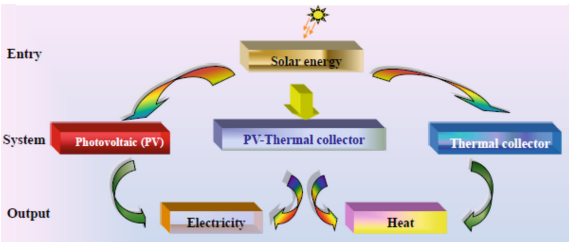

Fig. 1. Block diagram of a PV/T system for the production of energy

2.2 Constitution of the Hybrid Collector

Collector consists of an assembly of elements which are: The transparent cover, a monocristallin's photovoltaic module (with its three layers: tempered glass, layer of the cells with the ethylene vinyl acetate (EVA), and lay down Tedlar) type (UDTS50) of 1.29 m length and 0.33 m width, the form of absorber for the first collector is parallel vertical tubes wherein the heat transfer fluid, and the second is an enclosure. An insulation of the hybrid collector is necessary, it allows better thermal performances, and this insulation is ensured by glass wool (Fig. 2 and Table 1).

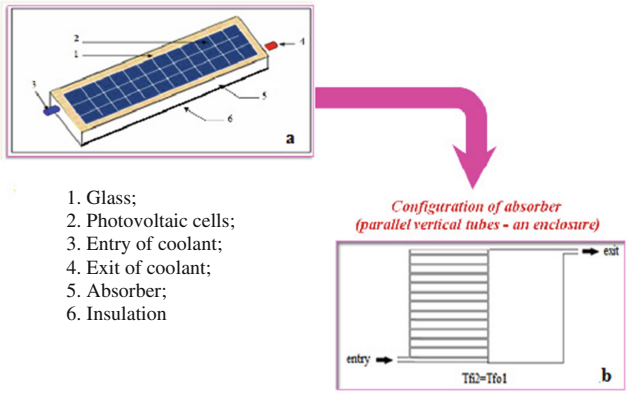

Fig. 2. a - New hybrid collector prototype, b - New configuration of absorber

Table 1. Parameter photovoltaic module

Parameter	Value
Courant de court circuit: Isc	2.99 A
Tension de circuit ouvert: Voc	20.8 V
Courant maximum: Imax	2.62 A
Tension maximum: Umax	14.9 V
Puissance maximum: Pmax	39.1 W

3 Thermal Analysis

3.1 Schematic of Heat Transfer

The heat exchange between the different layers of the collector in the prototype can be presented by the following figure (Fig. 3):

$U_{L,1}$ and $U_{L,2}$ are the overall thermal loss efficient of first and second PVT collector its value may be computed by using the concept of thermal network

The value of a heat loss at the upper surface (1D model) $U_{L,1}$ was calculated by, Formula of Klein (Duffie and Beckman, 1991, p. 260): [23].

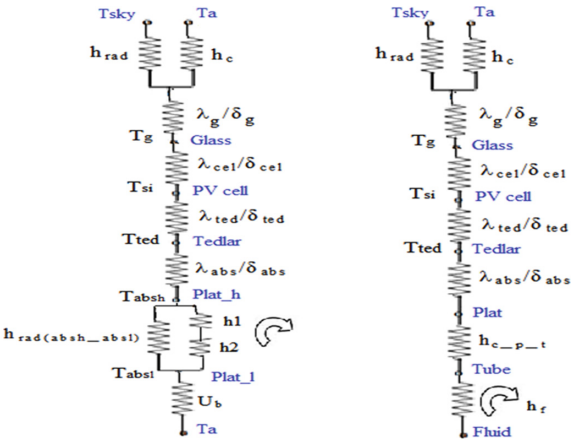

Fig. 3. Schematic of Heat Transfer in the PV/T

In the case of PVT in an enclosure the value of a heat loss $U_{L,2}$ is calculated by losses in different nodes;

It includes all of conduction, convection and radiation losses from the PV/T collector to the atmosphere.

$$U_1 = \left(\frac{1}{h_{rad} + h_c} + \frac{L_g}{\lambda_g}\right)^{-1} \tag{1}$$

$$h_c = 2.8 + 3V_w \tag{2}$$

$$h_{rad} = \varepsilon_v \sigma \left(T_c^2 + T_{sky}^2\right)\left(T_c + T_{sky}\right) \tag{3}$$

Where V_w is wind speed on the top surface of PV/T collector. The effective temperature of the sky (T_{sky}) is calculated from the following empirical relation [24]:

$$T_{sky} = 0.0552(T_a)^{1.5} \tag{4}$$

In the estimation of overall loss coefficient from cell to absorber (U_2), has been calculated from Eq. (5)

$$U_2 = \left(\frac{\delta_c}{\lambda_c} + \frac{\delta_{ted}}{\lambda_{ted}} + \frac{\delta_p}{\lambda_p}\right)^{-1} \tag{5}$$

A radiative loss exists from the top to the bottom part of absorber surface $h_{rad\,(absh\_absb)}$ [23].

$$h_{rad(abs_h - abs_b)} = \frac{4\sigma \overline{T}^3}{(1/\varepsilon_p)(1/\varepsilon_p) - 1} \tag{6}$$

The convective heat transfer coefficient inside the duct (hf) is calculated according to flow regime and its Nusselt number.

In the estimation of overall back loss coefficient (Ub), the convective heat transfer coefficient on the back surface of PV/T collector (hconv,b) has been calculated from Eq. (7)

$$U_b = \left(\frac{\delta_p}{\lambda_p} + \frac{\delta_i}{\lambda_i} + \frac{\delta_{tol}}{\lambda_{tol}} + \frac{1}{h_{conv,b}}\right)^{-1} \tag{7}$$

Solving equations expressing the conservation of energy for an element of volume between the glass, cell, the absorber and the fluid expressed in terms of different coefficient calculated above leads us to determine the U_{L2} and F_{R2} for the second collector coefficient of overall loss.

From energy balance consideration the useful energy gain is equal to:

$$Q_u = \dot{m}\, C_f \left(T_{fo} - T_{fi}\right) \tag{8}$$

Hottel *et al.* [25] proposed the expression of the useful energy calculated as function of the inlet fluid temperature

$$Q_{u,1} = A_1 F_{R_1} \left[S_1 - U_{L,1}\left(T_{fi} - T_a\right)\right] \tag{9}$$

The quantity F_R is equivalent to the effectiveness of conventional heat exchanger, which is defined as the ratio of the actual heat transfer to the maximum possible heat transfer.

The amount of solar energy available in the system will be reduced by heat extraction of electric energy from solar cells:

$$S_1 = (\tau\alpha)_{ef} G = \left((\tau_v \alpha_c) - \tau_v \eta_{pv} \frac{A_c}{A_1}\right) G \tag{10}$$

In our prototype the performance of the second module will not be the same as the first, the outlet temperature of the water at the outlet of the collector in parallel vertical tubes PVT given by T_{fo1} becomes the inlet temperature to the collector whose PVT absorber is an enclosure given by T_{fi2}, $T_{fi2} = T_{fo1}$. The energy useful in the second collector is given by

$$Q_{u,2} = A_2 F_{R_2}\left(S_2 - U_{L,2}\left(T_{fo,1} - T_a\right)\right) \tag{11}$$

With

$$S_2 = h_{p1}(\tau\alpha)_{ef} G = h_{p1}\left((\tau_v \alpha_c) - \tau_v \eta_{pv} \frac{A_c}{A_2}\right) G \tag{12}$$

And

$$h_{p1} = \frac{U_1}{(U_2 + U_2)}$$

Where hp1 is a penalty factor due to the presence of solar cell material, glass and EVA.

$\dot{m}$ and C_f are respectively, the mass flow rate and specific heat capacity of the coolant, T_{fi} and T_{fo} the coolant temperatures at the inlet and outlet, $A_1$and A_2 are the collector area of first and second collector;

In 1D model a Hottel-Whillier model (Duffie and Beckman, 1991, pp. 253–281) [24]. The thermal yield is given by

$$\eta_T = \frac{Q_{u,1+2}}{AG} = \frac{Q_{u,1} + Q_{u,2}}{AG} \tag{13}$$

$$\eta_T = a_1 - a_2 \frac{T_{fi} - T_a}{G} \tag{14}$$

For our configuration was found:

$$a_1 = \frac{A_1 F_{R_1} S_1 + A_2 F_{R_2} S_2}{AG} - \frac{A_1 A_2 F_{R_1} F_{R_2} U_{L,2} S_1}{AG\,\dot{m}\,C_f}$$

$$a_2 = \frac{A_1 F_{R_1} U_{L,1} + A_2 F_{R_2} U_{L,2}}{A} - \frac{A_1 A_2 F_{R_1} F_{R_2} U_{L,1} U_{L,2}}{A\,\dot{m}\,C_f}$$

4 Results and Discussions

Calculations are done for typical day of May 16/05/2014 in the site of Ghardaïa; for a given design and climatic parameters. The hourly variations of global radiation and ambient temperature.

The variation of solar intensity and ambient temperature for a typical day in the month of May 2014 for Ghardaïa condition is shown in Fig. 4.

Figure 5 shows thermal efficiency variation at various PVT-panels, these results are referred to thermal efficiency of water η_{th} in the mode of water heat exchanger; the ration $\Delta T/G$ ($KW^{-1}m^2$) is the reduced temperature, with $\Delta T = T_i - T_a$(K). The PV/T collector in parallel vertical tubes is obviously performing more at zero reduced temperature and represents a higher value.

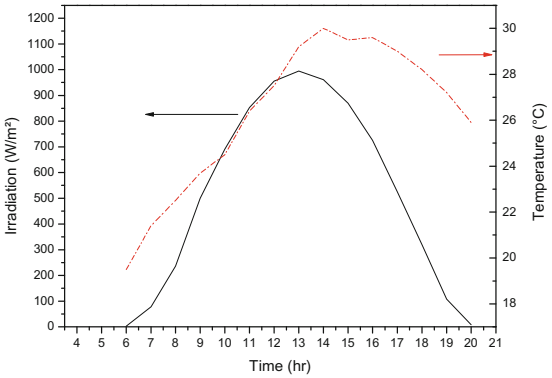

Fig. 4. Hourly variation of solar intensity and ambient temperature for the day of 16/05/2014.

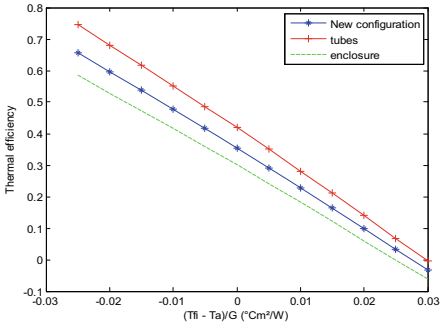

Fig. 5. Thermal efficiency according to the reduced temperature

5 Experimental Study

The heat exchanger used in the new PVT collector consists of galvanized steel tubes welded to galvanized steel plate [26], and a part of absorber in enclosure is constituted by a galvanized steel sheet of 3 mm length 640 mm, width 270 mm and depth of 35 mm, this interchange on the back of the photovoltaic module.

The dimensions of the tubes are: Outside diameter: 14 mm;
Inner diameter: 12 mm; Spacing between the tubes: 30 mm;

Figure 6 is a photo taken in the laboratory of the Unit for Applied Research in Renewable Energy in Ghardaïa; it shows the new hybrid PVT collector placed on the control structure.

Data acquisition of type 34970 (Data Acquisition/Switch Unit) is used to determine the values of temperature.

Figure 7 shows the variation of the temperature at the front and rear side of the hybrid collector, two thermocouples K-type are placed in two different points T_{av1} and T_{av2} of the front face, it is found that the variation between these two points is

Fig. 6. Photo of the new PVT collector

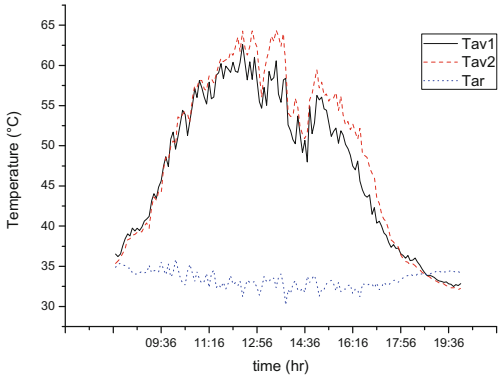

Fig. 7. Temperature of the glass in two different points

negligible and it explains the uniform distribution of the temperature front. The rear face temperature is nearly identical to the ambient temperature and it is up to the good insulation of the PVT collector.

The current-voltage (I-V) experimental characteristics of PV module and new PVT collector are displayed in Fig. 8.

The new PVT collector provides important electrical characteristics (short circuit current of 2.7 A and open circuit voltage of 18.5 V). The effect of heating water in the absorber has reduced the temperature of the solar cell and thus increases the electrical efficiency of the hybrid collector.

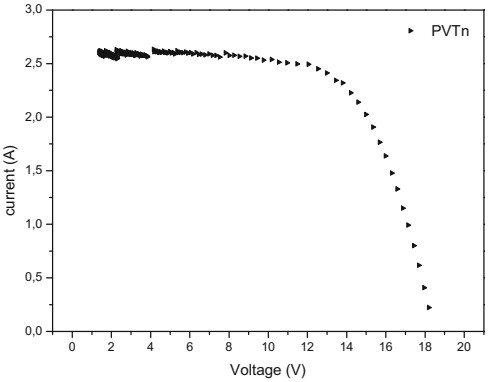

Fig. 8. Current–voltage characteristic curve

6 Conclusion

The work presented in this paper concerns the theoretical and experimental study of a hybrid photovoltaic thermal solar collector or PVT. New configuration of the absorber is used. This configuration is an assembly between two interchanges; the first is PVT in parallel vertical tubes and second in an enclosure.

The thermal model is steady-state, based on solving the heat balance for all the layers in the PVT collector.

This work allowed us to study the new hybrid PVT collector, determining its thermal and electrical performance.

References

1. Zondag, H.A.: Flat-plate, PV-thermal collectors and systems: a review. Renew. Sustain. Energy Rev. **12**, 891–959 (2005)
2. Zondag, H.A., Bakker, M., Helden, W.G.J. (eds.): PV/T Roadmap-a European guide for the development and market introduction of PV-thermal technology, Rapport EU-Project PV-Catapult, p. 87 (2005)
3. Wolf, M.: Performance analyses of combined heating and photovoltaic power systems for residences. Energy Convers. **16**(1–2), 79–90 (1976)
4. Hendrie, S.D.: Photovoltaic/thermal collector development program. Rapport final. Massachusetts Institute of Technology, Etats-Unis (1982)
5. Raghuraman, P.: Analytical predictions of liquid and air photovoltaic/thermal, flat-platz collector performance. J. Sol. Energy Eng. **103**(2), 291–298 (1981)
6. Cox, C.H., Raghuraman, P.: Design considerations for flat-plate-photovoltaic/thermal collectors. Sol. Energy **35**(3), 227–241 (1985)
7. Lalovic, B., Kiss, Z., Weakliem, H.A.: Hybrid amorphous silicon photovoltaic and thermal solar collector. Sol. Cells **19**(2), 131–138 (1986)

8. Tripanagnostopoulos, Y., Tzavellas, D.: Hybrid PV/T systems with dual heat extraction operation. In: Proceedings of the 17th European PV Solar Energy Conference, Munich, Allemagne, pp. 2515–2518 (2001)
9. Fujisawa, T., Tani, T.: Annual exergy evaluation on photovoltaic-thermal hybrid collector. Sol. Energy Mater. Sol. Cells **47**(1–4), 135–148 (1997)
10. Chow, T.T.: Performance analysis of photovoltaic-thermal collector by explicit dynamic model. Sol. Energy **75**, 143–152 (2003)
11. Bergene, T., Lovvik, O.M.: Model calculations on a flat-plate solar heat collector with integrated solar cells. Sol. Energy **55**(6), 453–462 (1995)
12. Chow, T.T., He, W., Ji, J.: Performance evaluation of photovoltaic-thermosyphon system for subtropical climate application. Sol. Energy **81**, 123–130 (2007)
13. Chow, T.T., He, W., Ji, J.: Hybrid photovoltaic-thermosyphon water heating system for residential application. Sol. Energy **80**(3), 298–306 (2006)
14. Kumar, S., Tiwari, A.: Design, fabrication and performance of a hybrid photovoltaic/thermal (PV/T) active solar still. Energy Convers. Manage. **51**, 1219–1229 (2010)
15. Li, M., Li, G., Ji, X., Yin, F., Xu, L.: The performance analysis of the trough concentrating solar photovoltaic/thermal system. Energy Convers. Manage. **52**, 2378–2383 (2011)
16. Gang, P., Huide, F., Jie, J., Tin-tai, C., Tao, Z.: Annual analysis of heat pipe PV/T systems for domestic hot water and electricity production. Energy Convers. Manage. **56**, 8–21 (2012)
17. Calise, F., Dentice d'Accadia, M., Vanoli, L.: Design and dynamic simulation of a novel solar trigeneration system based on hybrid photovoltaic/thermal collectors (PVT). Energy Convers. Manage. **60**, 214–225 (2012)
18. Rajoria, C.S., Sanjay, S., Tiwari, G.N.: Exergetic and enviroeconomic analysis of novel hybrid PVT array. Sol. Energy **88**, 110–119 (2013)
19. Ammar, M.B., Chaabene, M., Chtourou, Z.: Artificial neural network based control for PV/T panel to track optimum thermal and electrical power. Energy Convers. Manage. **65**, 372–380 (2013)
20. Othman, M.Y., Ibrahim, A., Jin, G.L., Ruslan, M.H., Sopian, K.: Photovoltaic-thermal (PV/T) technology – the future energy technology. Renew. Energy **49**, 171–174 (2013)
21. Touafek, K., Haddadi, M., Malek, A.: Modeling and experimental validation of a new hybrid photovoltaic thermal collector. IEEE Trans. Energy Convers. **26**(1), 176–183 (2011)
22. Touafek, K., Haddadi, M., Malek, A.: Conception and study of a low cost hybrid solar collector. In: 2nd International Conference on Nuclear and Renewable Energy Resources, Ankara Turkey, 4–7 July 2010
23. Duffie, J.A., Beckman, W.A.: Solar Engineering of Thermal Processes, 2nd edn. Wiley, New York (1991)
24. Bernards, J.: énergie solaire Calculs et optimisation, Août 2004 France
25. Hottel, H.C., Willier, A.: Evaluation of flat-plate solar collector performance. In: Transactions of the Conference on the Use of Solar Energy, vol. 2. University of Arizona Press, Tucson, Arizona (1958)
26. Touafek, K., Khelifa, A., Adouane, M.: Theoretical and experimental study of sheet and tubes hybrid PVT Collector. Energy Convers. Manage. **80**, 71–77 (2014)

A Mathematical Model to Determine the Shading Effects in the I-V Characteristic of a Photovoltaic Module

A. Fezzani[1(✉)], I. Hadj Mahammed[1], and S. Bazi[2]

[1] Centre de Développement des Energies Renouvelables CDER, Unité de Recherche Appliquée en Energie Renouvelables URAER, 47133 Ghardaïa, Algeria
amorfezzani@yahoo.fr
[2] Laboratory, LSP-IE, University of Batna, Rue Cahid Med El-Hadi Boukhl, 05000 Batna, Algeria
bazismail@yahoo.fr

Abstract. The performance of a photovoltaic (PV) array is affected by temperature, solar insolation, shading. Often, the PV arrays get shadowed, completely or partially, by the passing clouds neighboring buildings, towers or by trees, etc. The situation is of a particular interest in a case of the large PV power plants. In the case of the shading the characteristics of the PV module are more complex with the several peak values. Under such conditions, it is very difficult to determine the maximum power point (MPP). This paper presents a MATLAB-based modeling and simulation scheme suitable for studying the I–V and P–V characteristics of a PV under a no uniform insolation due to partial shading. The Photovoltaic model has been developed and used as Simulink subsystems. The proposed model facilitates simulating the dynamic performances of PV-based power systems and also has been validated by means of simulation study.

Keywords: MATLAB® · Photovoltaic cells · Partial shading · Reverse characteristics

1 Introduction

The photovoltaic system (PV) has attracted much attention due to the oil and environment pollution in recent years [1–3]. Its merits are: inexhaustible; pollution-free; abundant; silent and with no rotating parts and size-independent electricity conversion efficiently.

The main drawback is that: Form an operational point of the view, a photovoltaic array experiences large variation of its output power under intermittent weather conditions. These phenomena may cause operational problems at a central control center in a power utility, such as excessive frequency deviations, spinning reserve increase, etc.; its initial installation cost is considerably high.

M. Chadli et al. (eds.), *Recent Advances in Electrical Engineering and Control Applications*, Lecture Notes in Electrical Engineering 411, DOI 10.1007/978-3-319-48929-2_14

Integrating the PV power plant with other power sources such as diesel backup [2], fuel cell backup [3], battery backup [1, 3] super conductive magnetic energy storage backup are ways to overcome variations of its output power problem.

However, a major challenge in using a PV source is to tackle its nonlinear output characteristics, which vary with temperature and solar insolation.

The characteristics get more complicated if the entire array does not receive uniform insolation, as in partially cloudy (shaded) conditions, resulting in multiple peaks. The presence of multiple peaks reduces the effectiveness of the existing maximum power point tracking (MPPT) schemes [5–7] due to their inability to discriminate between the local and global peaks.

Nevertheless, it is very important to understand and predict the PV characteristics in order to use a PV installation effectively, under all conditions. Over the years, several researchers have studied the characteristics of PV modules and the factors that affect those [8–10].

This paper begins with the modeling and simulation of PV modules. The non-uniform insolation or partial shading occurs very frequently in solar PV system. To study the shading effects modeling of solar PV module in reverse biased conditions is required. Many models have been reported in literature. A more precise model, based on the one diode model was given by Bishop [11]. This model offers optimal conditions for description of the solar cell characteristics.

The main feature of the proposed model is to include the effect of complete or partial shading in the model. To study mismatch losses, mathematical modeling is done for the PV system and the simulation has been performed using MATLAB® environment. Further, the effects of partial shading with bypass diodes are investigated.

2 Model and Simulation Procedure

2.1 Model of Practical PV in First Quadrant

Forward Characteristics

Photovoltaic (PV) arrays are built up with combined series/parallel combinations of PV solar cells [4], which are usually represented by a simplified equivalent circuit model such as the one given in Fig. 1 and/or by (1).

During darkness, the solar cell is not an active device; it works as a diode, i.e. a p-n junction. It produces neither a current nor a voltage. However, if it is connected to an external supply it generates a current I_d, called diode (D) current or dark current. The diode determines the I-V characteristics of the cell.

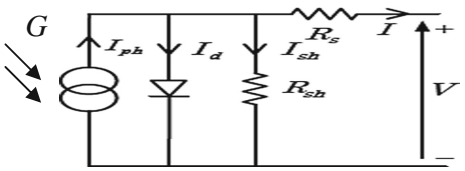

Fig. 1. Simplified equivalent circuit PV model.

$$I = I_{ph} - I_0\left[exp\left(\frac{V + IR_s}{V_t}\right) - 1\right] - \frac{V + IR_s}{R_{sh}} \quad (1)$$

Where $V_t = aKT_c/q$ is the thermal voltage, q is the electron charge (1.602×10^{-19} C), K is the Boltzmann constant (1.38×10^{-23} J/K), I is the cell output current (A), I_{ph} is the photocurrent, function of the irradiation level and junction temperature, I_0 is the reverse saturation current of diode, R_s and R_{sh} the series and shunt resistance respectively, T_c is the reference cell operating temperature (25 °C), V is the cell output voltage, V.

As example of simulation, the solar cell parameters used in this simulation, from model shown at the equivalent circuit of Fig. 1 or (1), are the following: Diode: a = 1.2, $I_0 = 10^{-8}$ A; $R_s = 0.005$ Ω, $R_{sh} = 9$ Ω.

The PV characteristic in under different irradiance level and PV characteristic under different temperature are plotted in Fig. 2. As illustrated in the figures, the open-circuit voltage (V_{oc}) is dominated by temperature, and solar irradiance has preeminent influence on short-circuit (I_{sc}). We can conclude that high temperature and low solar irradiance will reduce the power conversion capability. Figure 3 shows the influence of irradiance on the characteristic power - voltage (P-V) of a photovoltaic module.

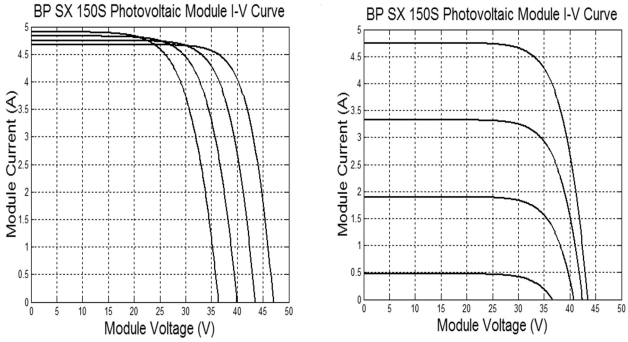

Fig. 2. PV characteristic under different temperature and irradiance.

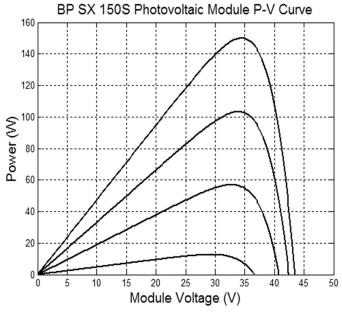

Fig. 3. PV characteristic under different irradiance (temperature = 25 °C).

2.2 Modeling of Reverse Characteristics of PV Cell

Reserve characteristics

Typically 72 cells are connected in series to get the requisite voltage of PV module. All the cells are forced to carry the same current called module current in series module. If one or more cells are not receiving the equal illumination or shaded these cells become reverse biased which leads to power dissipation and thus to heating effects. This situation is illustrated in Fig. 4 which shows the I-V characteristics of a cell in the whole range.

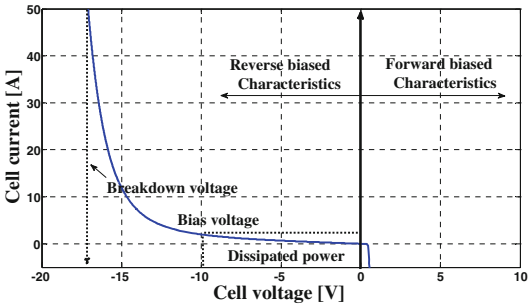

Fig. 4. I-V characteristic of the PV cell in the forward and reverse biased conditions.

The forward characteristic extends to the open circuit voltage of approximately 0.6 V; the reverse biased characteristic is much more extensive and limited by the breakdown voltage. If the cell is shaded, its short circuit current is less than the module current so that it is operated at the reverse characteristic, causing power to be dissipated. Hence it is required to model the reverse characteristics of the PV cell for the complete representation of it. The breakdown occurs in PV cell is not taken into account in the one diode model shown in Fig. 1. Therefore another model based on the model of Bishop [11] is described in this paper. This model includes an extension term which describes the diode breakdown at high negative voltages. The equivalent of this model is given in Fig. 5.

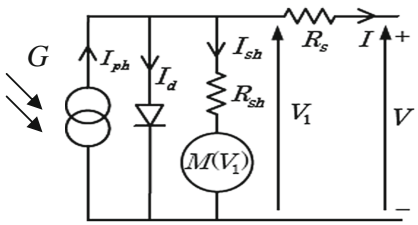

Fig. 5. Simplified equivalent circuit PV model.

Different I-V curves are obtained by substituting different numerical values for the parameters.

The I-V curve of this model is given by

$$I = I_{ph} - I_0\left[exp\left(\frac{V + IR_s}{V_t}\right) - 1\right] - I_{sh} \tag{2}$$

The leakage current term I_{sh}, which is a function of voltage and controls the cell reverse characteristic, consists of an ohmic term (current through the shunt resistance) and a non-linear multiplication factor [12–14] describing avalanche breakdown [15]:

$$I_{sh} = \frac{V_1}{R_{sh}}\left[1 + k\left(1 - \frac{V_1}{V_b}\right)^{-n}\right] \tag{3}$$

Where V_1 is the voltage across the junction (V), V_b is the junction break down voltage, k is the fraction of ohmic current involved in avalanche breakdown and n is the avalanche break down exponent.

Equation (2) is modified as:

$$I = I_{ph} - I_0\left[exp\left(\frac{V + IR_s}{V_t}\right) - 1\right] - \frac{V + IR_s}{R_{sh}}\left[1 + k\left(1 - \frac{V_1}{V_b}\right)^{-n}\right] \tag{4}$$

Manufacturers usually integrate bypass diodes for every 12 or 18 cells to a PV module as seen in Fig. 6. Although bypass diode numbers in a PV module is of great importance under partial shading conditions [17, 18].

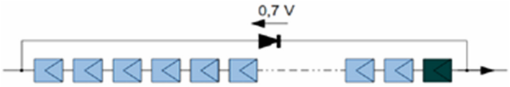

Fig. 6. Bypass diode covering 18 solar cells, one of these cells is working in shading conditions while the rest are free of shadow.

Typically, module consists of many solar cells, and for each 18 cells are equipped with one bypass diode, so bypass diode is connected with a string (one string corresponds to eighteen cells in series), Fig. 7.

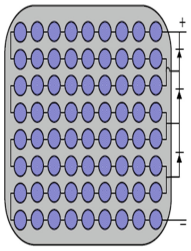

Fig. 7. Connection schematic of bypass diodes in the PV module.

The mathematical model has been implemented in the Matlab-Simulink environment. The solar cell parameters used in this simulation, from model shown at the equivalent circuit of Fig. 5 or (4), are the following:

Diode: a = 1.2, $I_0 = 10^{-8}$ A; $R_s = 0.005\ \Omega$, $R_{sh} = 9\ \Omega$; $V_t = 0.0258$ V; Bishop's term: $V_b = -20$ V, k = 0.1 and n = 3.

The current source I_{ph} is controlled by the irradiance level and temperature, the solar cell active area and its short circuit current density. The simulation I-V characteristics under reverse biased conditions for dark condition is shown in Fig. 8.

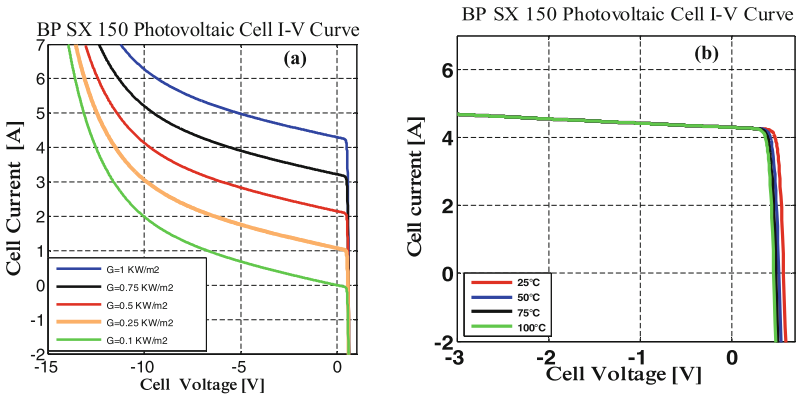

Fig. 8. I-V characteristic under different irradiance (a) and temperature (b).

The two-quadrant I-V characteristic of a cell can be plotted by setting the parameters k, n, and V_b to the desired values. More details can be found in [11, 19].

3 Study of Partial Shadowing Effects in the Solar PV

The performance of a Solar Photovoltaic (SPV) is affected by temperature, irradiance conditions, mismatch effects, shading and array configuration.

The presented model and simulation procedure can be applied to the study of SPV working in partial shadowing conditions. The application of this Matlab-based simulation procedure can help to a better understanding and prediction of the I–V and P–V characteristics of PV arrays. It can be used to study the effect of temperature and irradiance variation conditions, hot spot apparition and effects in output power reduction. It can be also useful in the study of bypass diodes configuration in the SPV and its effects in output power variation and apparition of peaks and new maximum power points in the power–voltage characteristic [17, 20–22].

4 Simulation Results

The diagram of the closed loop system for MATLAB® and Simulink is shown in Fig. 9, which includes the electrical circuit of the photovoltaic module BP SX 150S, whose characteristics are given as: maximum power $P_{Mpp} = 150$ w, rated voltage

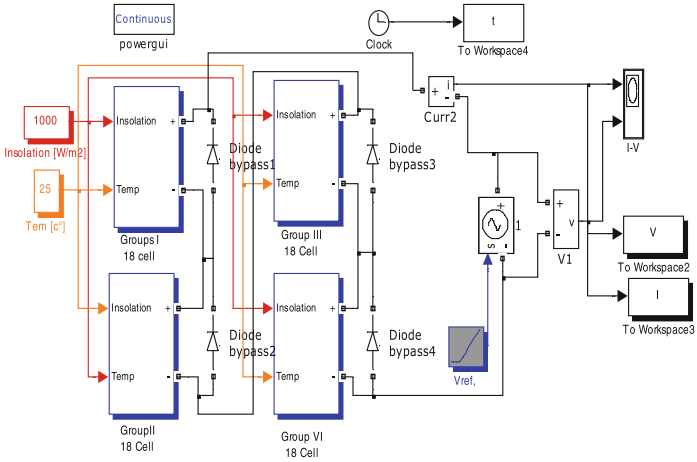

Fig. 9. Simulink simulation to illustrate the I-V and P-V module output characteristics.

V_{MPP} = 35 V, open circuit voltage V_{oc} = 43.5 V, rated current I_{MPP} = 4 A and short circuit current I_{sc} = 4.3 A. The photovoltaic module is modeled using the electrical characteristics to provide the current and voltage of the photovoltaic module output.

4.1 Influence of the Amount of Shading with Bypass Diode

A string with 18 cells has been considered, supposing that one of the cells is 25%, 50%, 75% or 100% shaded (Fig. 10a), 1st cell 50% and 2nd cell 75% shaded (Fig. 10b), one range horizontal shaded (Fig. 10c), four ranges horizontal shaded (Fig. 10d) and one cell for 3 groups shaded (Fig. 10e). A system formed by 4 strings serially connected has been simulated. Results are presented in Figs. 11.

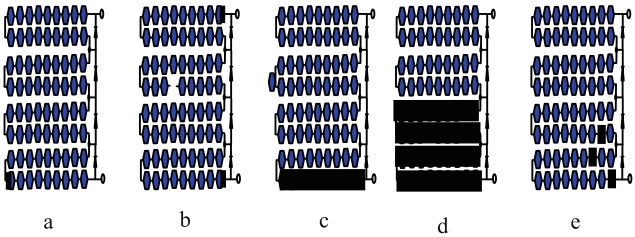

Fig. 10. Shading on the photovoltaic module.

Figure 11 show that also in the case when the solar cells are shaded in series with a bridging diode the shading influences on the I-V and the P-V characteristics of the module. When one solar cell (1.4% shading of the module) is shaded the maximum power decreases for approximately 25%.

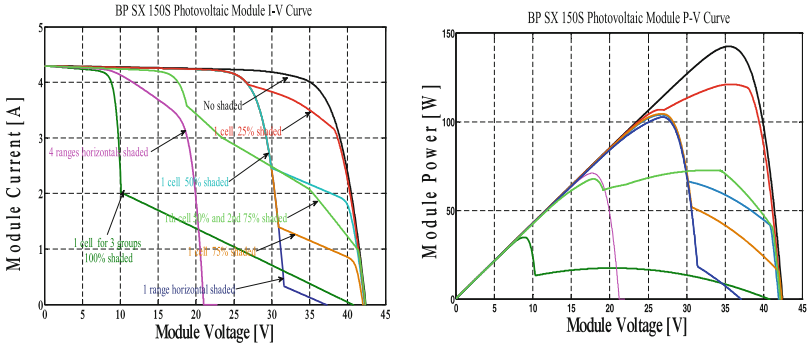

Fig. 11. Influence of shading one or more cell different percentages in an 18 cell strings in a module with four strings.

It is observed from the under results; the use of bypass diodes can save the poorly illuminated panels from damage and also make this energy available to the load. But the P-V characteristics under non uniform insolation with bypass diodes contain multiple peaks [16]. The magnitude of the global maxima is dependent on the array configuration and shading patterns.

Figure 12 reveals that, under partially shaded conditions, the bypass diodes introduce multiple steps in the I-V characteristics and multiple peaks in the P-V characteristics.

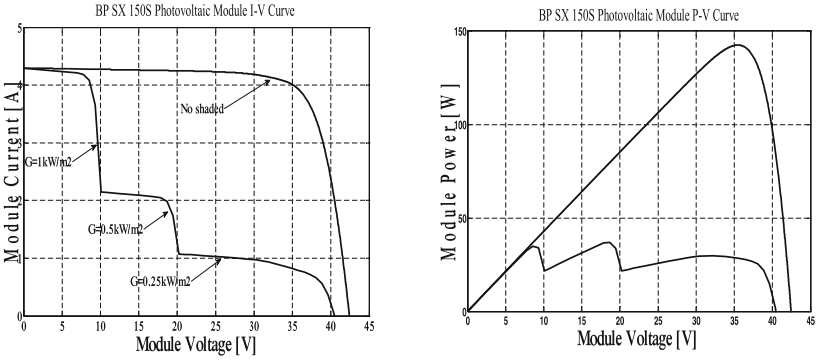

Fig. 12. I-V and P-V curves for varying insolation.

5 Conclusion

In this work we propose an approach to the study of solar cells working partially shadowed, based on the model proposed by Bishop. A simulation methodology for solar cells and PV modules working partially shadowed using the developed models in MATLAB® environment is proposed.

The focus is on the influence of the shading on the I-V and the P-V characteristics of the module. The results show that the influence of the shading cannot be neglected and it is necessary to consider it in the installation of the photovoltaic systems.

References

1. Bose, M.K.: Microcomputer control of a residential photovoltaic power conditioning system. IEEE Trans. Ind. Appl. **21**(5), 1182–1191 (1988)
2. Calloway, T.M.: Autonomous photovoltaic diesel power system design. In: Proceedings of IEEE PV Specialists Conference, Las Vegas, Nevada, pp. 280–284, October 1985
3. Ohnishi, M., Takeoka, A.: Advanced photovoltaic technologies and residential applications. Renew. Energy **6**(3), 275–282 (1995)
4. Fossas, E., Biel, D.: A sliding mode approach to robust generation on dc-to-dc nonlinear converters. In: IEEE International Workshop on Variable Structure Systems, pp. 67–71, December 1996
5. Koutroulis, E., Kalaitzakis, K., Voulgaris, N.C.: Development of a microcontroller-based photovoltaic maximum power point tracking control system. IEEE Trans. Power Electron. **16**(1), 46–54 (2001)
6. Hussein, K.H., Muta, I.: Maximum photovoltaic power tracking: an algorithm for rapidly changing atmospheric conditions. In: Proceedings of Institution of Electrical Engineers Generation, Transmission and Distribution, vol. 142, no. 1, pp. 59–64, January 1995
7. Jain, S., Agarwal, V.: A new algorithm for rapid tracking of approximate maximum power point in photovoltaics systems. IEEE Power Electron. Lett. **2**(1), 16–19 (2004)
8. Walker, G.: Evaluating MPPT converter topologies using a MATLAB PV model. J. Electr. Electron. Eng. Aust. **21**(1), 49–56 (2001)
9. Shimizu, T., Hirakata, M., Kamezawa, T., Watanabe, H.: Generation control circuit for photovoltaic modules. IEEE Trans. Power Electron. **16**(3), 293–300 (2001)
10. Patel, H., Agarwal, V.: Matlab- based modeling to study the effects of partial shading on PV array characteristic. IEEE Trans. Energy Convers. **23**(1), 302–310 (2008)
11. Bishop, J.W.: Computer simulation of the effects of electrical mismatches in photovoltaic cell interconnection circuits. Sol. Cells **25**(1), 73–89 (1988)
12. Alonso-Garciaa, M.C., Ruizb, J.M.: Analysis and modelling the reverse characteristic of photovoltaic cells. Sol. Energy Mater. Sol. Cells **90**, 1105–1120 (2006)
13. Quaschning, V., Hanitsch, R.: Numerical simulation of photovoltaic generators with shaded cells. In: 3Gh Universities Power Engineering Conference, Greenwich, pp. 583–586 (1995)
14. Hartman, R.A., Prince, J.L., Lathrop, J.W.: Second quadrant effects in silicon solar cells. In: Proceedings of 14th IEEE Photovoltaic Specialists' Conference, San Diego, CA, p. 119. IEEE, New York (1980)
15. Pace, S., Bishop, J., Magni, M.: Hot-spots in solar cells – test procedures and study of related phenomena. In: Proceedings of 6th Commission of the European Communities Conference on Photovoltaic Solar Energy, London, p. 304. Reidel, Dordrecht (1986)
16. Alonso, M.C., Arribas, L.M., Chenlo, F., Cruz, I.: Shading effects on a roof integrated grid-connected PV plants. In: Proceedings of the 14th European Photovoltaic Solar Energy Conference, pp. 1891–1894 (1997)
17. Silvestre, S., Boronat, A., Chouder, A.: Study of bypass diodes configuration on PV modules. Appl. Energy **36**, 1632–1640 (2009)

18. Bun, L.: Détection et Localisation de Défauts pour un Système PV. thèse doctorat Génie Electrique, université de Grenoble (2011)
19. Alonso-Garcia, M., Ruiz, J.: Analysis and modelling the reverse characteristic of photovoltaic cells. Sol. Energy Mater. Sol. Cells **90**(7–8), 1105–1120 (2006)
20. Hirata, Y., Noro, S., Aoki, T., Miyazawa, S.: Diagnosis photovoltaic failure by simple function method to acquire I–V curve of photovoltaic modules string. In: The Proceeding of 2012 IEEE PVSC (38th IEEE Photovoltaic Specialists Conference), Austin, TX, 3–8 June 2012, pp. 001340–001343 (2012)
21. Gana, O., Vasar, C., Babescu, M., Vartosu, A.: PV control system based on short-circuit current. In: The Proceeding of 2013 IEEE SACI (8th International Symposium on Applied Computational Intelligence and Informatics), Timisoara, Romania, 23–25 May 2013, pp. 387–390 (2013)
22. Olivares, B.E., Munoz, M.A., Orchard, M.E., Silva, J.F.: Particle-filtering-based prognosis framework for energy storage devices with a statistical characterization of state-of-health regeneration phenomena. IEEE Trans. Instrum. Measur. **62**(2), 364–376 (2013)

Hybrid Systems Using Thermal/Biomass Sources

Souad Belhour[1(✉)] and Abdelouahab Zaatri[2]

[1] Faculté des Sciences Exactes, Department of Physical Department, University of Constantine 1, Constantine, Algeria
souad_belhourl@yahoo.fr
[2] Faculty of Engineering, Department of Mechanical Department, University of Constantine 1, Constantine, Algeria

Abstract. The hybrid systems of renewable energy can contribute in a significant way to the durable development in several isolated areas. This paper discusses an optimization solution of an hybrid system of renewable energy. We consider the example of the combination of two common renewable energy resources namely thermal and biomass. We present the estimation of the energetic potential for each considered renewable energy resource that can be extracted from a given site; and then we propose their repartition in order to optimize the exploitation of these available resources while meeting the global specific energy demand. The general problem can be formulated as a problem of optimal allocation of limited resources constrained to meet specific demands. We consider two types of situations. The first type considers situations where the installed energetic capacity of each resource is continuous. The second type considers situations where the installed energetic capacity is only available as specific discontinuous units. The approach adopted to solve the first type uses the simplex linear programming method while for the second type; we use the integer linear programming method. We also present some examples to illustrate the proposed technique.

Keywords: Optimal energy distribution · Renewable energy · Integration of renewable energy · Thermal · Biodigester · Linear programming

1 Introduction

Hybrid renewable energetic systems are systems that integrate more than one renewable energy sources. As they are time, environment and site dependent, one expects that their judicious and complementary combination may overcome some limitations which are inherent to every individual system used alone. Hybrid systems may also reduce the need for energy storage which is very costly and space consuming. The application of renewable energy system has become an important alternative as power provider in rural electrification program when the price of oil is reaching its highest level. The topic of optimizing the integration of renewable energy sources in a complementary way is a very interesting but a challenging one both scientifically and technologically. The general issue of combining renewable energy sources we are considering can be stated

M. Chadli et al. (eds.), *Recent Advances in Electrical Engineering and Control Applications*, Lecture Notes in Electrical Engineering 411, DOI 10.1007/978-3-319-48929-2_15

as follows. In a specific site, given the capacities of some renewable energy sources and an energetic demand, how to determine the optimal repartition of these energies that meets the demand. We will consider the combination of two renewable resources such as thermal energy and biomass energy. We will firstly address the problem in case where the energy to be allocated can be continuous. Secondly, we will address the problem in case where the energy to be allocated is available as specific discrete units. For instance, manufacturers may provide photothermal panels as units with a specific capacity characterized by its provided energetic capacity. Manufacturer also may provide bioreactors as units with specific size and then with a specific energetic capacity according to the biodigester characteristics. Therefore, determining the optimal energy to be installed leads to determining the number of units from each source which are required to meet the specified energetic demand. There have been few proposed approaches to solving this problem with and without taking into account energy storage systems such as batteries, diesel engines, hydrogen, etc. Among these approaches, we can notice linear programming, dynamic programming, genetic algorithms techniques, etc. [1–4]. Some software for analysis and optimization of hybrid energetic systems has been developed and are actually largely used such as HOMER, SOMES, RAPSIM, SOSIM, etc. [5–7] revise some relevant papers concerning the simulation and optimization techniques, as well as the tools existing that are needed to simulate and design stand-alone hybrid systems for the generation of electricity and/or heat. We will address the first issue which concerns the case where the energy is continuous. As proposed in Ref. [1], we modeled the problem of resource allocation in terms of linear program and solve it with simplex algorithm. The second issue concerning the case of discrete units of energy requires integer numbers of renewable energetic units. We solve it with integer linear programming method has been formulated in many ways. But the most used approach seeks to minimize the Loss of Power Supply Probability (LPSP) [8]. Consider the case where they have photovoltaic panels and wind turbines as specific units. Thus, the problem consists of determining the numbers of PV panels, wind turbines, and batteries. Their formulation leads to a non linear integer programming problem. They solve the problem by using the LPSP in the framework of ant systems by minimizing the initial capital investment [9]. Present an optimal sizing method for stand-alone hybrid solar–wind system with LPSP technology based on genetic algorithms. It consists of determining, among other elements [10]. Uses a hybrid system and the formulation determine the number of micro-hydro, PV, wind turbines, and batteries by minimizing the life cycle cost [11]. The LPSP model is used and the lowest Levelised Cost of Energy is considered as the economical optimal configuration. Following the formulation using linear programming to model and solve the problem of sources repartition without taking into account the storage issue, we address the problem of optimal distribution of renewable energetic hybrid systems where the energies provided by each source are constituted of specific units. We formulate the problem as an integer linear programming one by minimizing the initial capital investment under constraints such as ensuring the annual required demand. The formulation requires the estimation of the annual energy that should be provided by each renewable energy unit as well as its cost. To illustrate our analysis, we provide examples combining Thermal and biodigester units.

2 An Experimental Hybrid System

The purpose of this study is to combine renewable energy sources to meet the energy demand of a given location (home, farm, urban…). Figure 1 shows an experimental prototype house that uses hybrid energy sources solar, and biomass. Energy sources appearing in pictures of Fig. 1 are experimental renewable energy systems that have been developed at our laboratory LATA, University of Constantine. The picture (a) shows a photo-thermal system, the image (b) shows an experimental bioreactor for the production of methane using wastewater and organic waste. The management system is used to adapt the energy available to meet the demand. As renewable energies are fluctuating, it is customary to add storage batteries as a reserve.

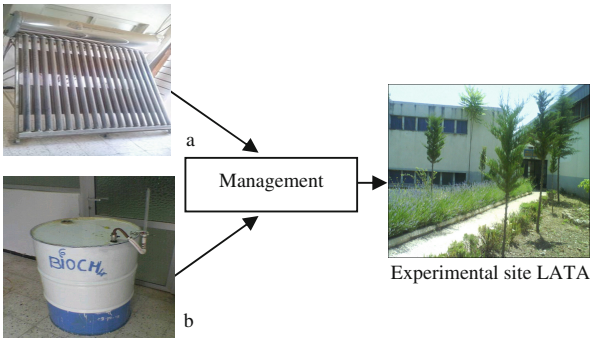

Fig. 1. Experimental Hybrid renewable energy systems (HRES).

3 Energy Resources Estimation

3.1 Estimation of Annual Thermal Energy

The power generated by a thermal solar simple flat collector can be estimated by the following expression [12, 13]:

$$P_{th} = S_{th} \cdot [F_R \cdot \tau \cdot \alpha \cdot G - F_R \cdot U_L \cdot (T_{fe} - T_a)] \quad (1)$$

Where:

S_{th} : Absorber area (m^2).
F_R : Heat removal factor.
$\tau \cdot \alpha$: Transmittance–absorptance product.
G : Total (direct plus diffuse) solar energy incident on the collector aperture $(\mathrm{W}/\mathrm{m}^2)$.
U_L : Solar collector heat transfer loss coefficient $(\mathrm{W}/\mathrm{m}^2\ \mathrm{C}^\circ)$.
T_{fe} : Temperatures of the fluid entering the collector (C°).
T_a : Ambient temperature (C°).

We can estimate the annual power produced by the thermal collector according to (1) and we can also use an empirical rule in a sunny zone like our site [12]. In our case; we consider a collector with an absorber surface of 2 m^2 which produces about 200 Watts. As we estimate the number of sunny hours per year to (2190), the temperature of the fluid entering the collector of 45 C° and the ambient temperature of 25 C°; therefore the annual energy transmitted to the water is about 438 kWh/year.

3.2 Estimation of Annual Biogas Energy

To estimate the power generated by a methane digester, we consider a completely mixed continuous anaerobic digester in steady state operation. We use the Chen-Hashimoto model which is given in [14]. The expression of methane production with respect to the different parameters that intervene in this model can be written as:

$$P_{bio} = [B \cdot (M0/TRH)] \cdot V \tag{2}$$

$$P_{bio} = \mathrm{Q_m} = \mathrm{B0} \cdot [1 - (\mathrm{K}/\mu\mathrm{m} - \mathrm{HRT} + \mathrm{K} - 1)](\mathrm{MO}/\mathrm{HRT})) \cdot \mathrm{V} \tag{3}$$

Where:

HRT: Hydraulic retention time.
MO: Matter oxidizable.
V: Biodigester volume (m^3).
B: Biological efficiency.
Q_m : Production of methane (m^3/d).
B0 Production potential of methane.
K: Constant of inhibition ($K = 0.6 + 0.021 \cdot 10^{0.05} \cdot Mo$).
μm : Kinetic coefficient ($\mu m = 0.013 * T - 0.129$).

This expression is used to estimate the annual energy produced by a given reactor under given conditions of exploitation. On the other hand, it can be used to designing a reactor given an expected estimate of the energy.

As example, let's consider a continuous bioreactor of Volume $V = 4\ m^3$, volumetric flow rate $Q = 0.3\ m^3/d$, the hydraulic retention time can be deduced as $HRT = V/Q = 13.33$ days. In our regional context, we use the organic fraction of solid waste mixed with the activated sludge in mesophilic condition, with matter oxidizable $MO = 5g/l$. At a temperature of 25 °C, the kinetic coefficient can be estimated as $\mu m = 0.013 * T - 0.129$ and $B0 = 0.1\ m^3/kgMO$; therefore the estimate energy produced by day is about $Q_m = 0.07\ m^3$. If we consider a functioning of the reactor during 335 days per year, we can estimate the annual production of energy as $E_{bio} = Q_m.335 = 23.5\ m^3/year$. This energy production can be converted into various other forms of energy such as heat, electricity and both. One m^3 provides, when converted into electricity, about 10 kWh. If we convert the annual methane production into electricity, we can expect energy of about 235 kWh/year [15].

4 Modeling the Hybrid System

4.1 Continuous Energy Case

Given the characteristics and the energy demand for a specific site, the problem under consideration is to determine the capacity of renewable resources to be installed in order to meet the demand. Such an approach was made by [1] to solve a problem of rural electrification based on the integration and distribution of renewable resources in India. We consider the renewable energy resources E_i with the available capacity limit L_i. We need to provide also the unit costs of each resource C_i as well as the global demand D to be met. The general form may be that of a linear programming problem of minimizing a cost function Z_T under given constraints. The problem can be expressed as follows:

$$\left\{\begin{array}{l} \min \mathrm{Z}_T = \sum C_i \cdot E_i \\ \sum E_i = D \\ E_i \leq L_i \\ E_i \geq 0 \end{array}\right\} \quad (\mathrm{i} = \mathrm{th},\ \mathrm{bio}\ldots) \tag{4}$$

4.2 Discrete Energy Case

The problem consists of determining the number of thermal units as well as the number of biodigester units. Therefore, it can be converted into an optimization program known as integer linear programming problem that requires pure integer solutions for the decision variables N_1 and N_2. A basic general formulation consists of minimizing a cost function Z_T while satisfying the demand D. The unit costs of each renewable unit are C_i and its annual energy production is E_i. The problem can be expressed as follows:

$$\left\{\begin{array}{ll} \min \mathrm{Z_T} = \sum\limits_{\mathrm{i}} \mathrm{C_i N_i} & \\ \sum\limits_{\mathrm{i}} \mathrm{E_i} \cdot \mathrm{N_i} = \mathrm{D} & \mathrm{i} = 1, 2, 3, \ldots \\ \mathrm{N_i} \geq 0 & \\ N_i \ \textit{Integers} & \end{array}\right. \tag{5}$$

Compared to linear programming problems, integer linear programming problems are more difficult to solve and have specific techniques for their resolution. In the last twenty years, the most effective technique has been based on dividing the problem into a number of smaller problems in a method called branch and bound. For simpler case with two decision variables, graphical representation can help to analyze and solve the problem if a solution exists.

5 Application

5.1 Continuous Energy Case

Let's consider too combination examples of renewable energies sources: the thermal energy E_{th} with the limit L_{th}, the biogas energy E_{bio} with the limit L_{bio}. Let's also provide the unit costs C_i of each energy as well as the global demand D.

The resolution of these problems can be done by techniques derived from the simplex or interior point methods. Many computer programs are available as (LINDO [16] LINSOLVE [17], Z-PL [18]…). In our case, we used the LINDO program to determine the optimal allocation of resources.

5.2 Discrete Energy Case

Let's consider the following example of a small Thermal/Biomass hybrid system. The estimated energy produced by a thermal (one unit) is $E_{th} = 160$ KWh/year and the estimated energy produced by a biodigester (one unit) is $E_{bio} = 83$ KWh/year. If we assume a cost of 0.8\$ per Watt of peak power, then the unit cost of a thermal is around $C_{th} = 70\$$. On the other hand, the reduced cost of the type of biodigester which has been built up at our laboratory can be estimated at about $C_2 = 100\$$. This leads to 2\$ /Watt. For simplicity, we may only consider in this analysis the investment for capital cost of the hybrid system which may involve the number of thermal units (N_1) and the number of biodigester units (N_2).

6 Results

We present in the following Table 1, the formulation; and the applicative examples for both cases; Continuous and discrete. These problems have been solved by Linear Programming technique. The optimal repartition of renewable energies and their percentage to participate to satisfy the global demand are given below.

Comments

- For the continuous energy case: we obtain the following distribution; biomass has the lowest cost, so it is completely consumed. Its capacity is completely used and it participates at 43.3%. Other resources were used according their lowest cost and capacity ($E_{th} = 56.7\%$). We notice that the management system works as follows: it initially selects the energy which has the lowest cost until it its completely consumed, then selects the next low cost and son on.
- For the Discrete Energy Case: There is a particular issue related to the demand. If we consider the demand as an equality constraint; therefore the solution is not guarantee. But; if we reformulate it as an inequality constraint; the possibility to find out a solution is much more obvious. For the studied case see Table l; if we consider the demand as an equality case, there no solution. In case where the demands is considered as an inequality; the solution gives an objective function

Table 1. Optimal Energy repartition

Continuous Energy Case	**general form**	$\begin{cases} \min Z_T = C_1 E_{th} + C_2 E_{bio} \\ E_{th} + E_{bio} = D \\ E_{th} \le L_{th} \\ E_{bio} \le L_{bio} \\ E_{th} \ge 0, \quad E_{bio} \ge 0 \end{cases}$
	Application	$\begin{cases} \min Z_T = 160\, E_{th} + 90 E_{bio} \\ E_{th} + E_{bio} = 3000\,(kWh/\,year) \\ E_{th} \le 2000\,(kWh/\,year) \\ E_{bio} \le 1300\,(kWh/\,year) \\ E_{th} \ge 0, \quad E_{bio} \ge 0 \end{cases}$
	Results Energy repartition (kWh/year)	Eth=1700 Ebip=1300 Min ZT=3.89e+005

			equality constraint	**inequality constraint**
Discrete Energy Case	**general form**		$\begin{cases} \min Z_T = C_1.N_1 + C_2.N_2 \\ Subject\ to \\ E_{th}.N_1 + E_{bio}.N_2 = D \\ N_1, N_2 \ge 0 \\ N_1, N_2\ Integers \end{cases}$	$\begin{cases} \min Z_T = C_1.N_1 + C_2.N_2 \\ Subject\ to \\ E_{th}.N_1 + E_{bio}.N_2 \ge D \\ N_1, N_2 \ge 0 \\ N_1, N_2\ Integers \end{cases}$
	Application	**first case**	$\begin{cases} \min Z_T = 70.N_1 + 100.N_2 \\ Subject\ to \\ 160.N_1 + 83.N_2 = 2000 \\ N_1, N_2 \ge 0 \\ N_1, N_2\ Integers \end{cases}$	$\begin{cases} \min Z_T = 70.N_1 + 100.N_2 \\ Subject\ to \\ 160N_1 + 83.N_2 \ge 2000 \\ N_1, N_2 \ge 0 \\ N_1, N_2\ Integers \end{cases}$
		Second case	$\begin{cases} \min Z_T = 70.N_1 + 100.N_2 \\ Subject\ to \\ 160.N_1 + 84.N_2 = 2000 \\ N_1, N_2 \ge 0 \\ N_1, N_2\ Integers \end{cases}$	
	Results Energy repartition (kWh/year)	**first case**	no solution	N_1=13 N_2=0 Min ZT=910
		second case	N_1=2 N_2=20 Min ZT=2140	

value $= 910\$$ with $N_1 = 13$ photothermal panels and $N_2 = 0$ Biodigesters (Table 2) whatever the variations of the cost of a photothermal panels. According to this result, the system will be only composed of photothermal panels because

Table 2. Sensitivity of the solution w.r.t E_{bio}

E_{bio} (cost of a Biodigester)	Z($):objective function		N_1 (photothermal Panels)		N_2 (Biodigester)	
	equality constraint	*Inequality* constraint	equality constraint	*Inequality* constraint	Equality constraint	*Inequality* constraint
80	940	910	12	13	1	0
81	No solution	910	//	13	//	0
82	No solution	910	//	13	//	0
83	No solution	910	//	13	//	0
84	2140	910	2	13	20	0
85	1880	910	4	13	16	0
86	No solution	910	//	13	//	0

a photothermal panels is cheaper than a Biodigesters. But; we may notice that this case is not realistic if we consider the variability of the produced energy with seasons. If we do not limit the maximum capacity of the RE; we cannot obtain a hybrid system (Table 2).

To illustrate the search of solutions in integer linear programming, we present and discuss the graphical solution of the following program with the equality constraint and $E_{bio} = 84$.

Let's analyze the sensitivity of the solution (if it exists) of the integer program with the equality constraint with respect to a small change in the unit cost characterizing the annual energy production of a biodigesters unit. Table 2 shows the sensitivity of the solution with respect to E_{bio}.

7 Graphic

The graphical analysis is presented in Fig. 2 where the x-axis represents N_1 and the y-axis represents N_2. The red line represents the equality constraint ($160 \cdot N_1 + 84 \cdot N_2 = 2000$). The blue lines represent the objective function ($Z = 70 \cdot N_1 + 100 \cdot N_2$) Which is parameterized by the value Z. So, by increasing the value of Z while moving the blue line in the direction of the arrows, we seek to interest the red line in a point where both N_1 and N_2 should be integers. If there are many points that meet this condition of integrality, we should select the point which corresponds to the minimal value of Z. In the example under consideration, the optimal value corresponds to the point M where $Z = 2140\,\$$ with

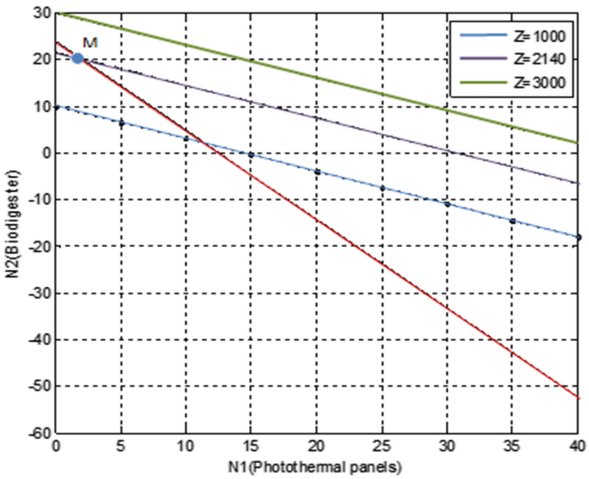

Fig. 2. Graphical analysis of a solution in Integer Linear programming. (Color figure online)

$N_1 = 2$ and $N_2 = 20$. If we consider the integer linear program given in (10), there will be no intersection between the equality constraint and the objective function that corresponds to a point with integer coordinates.

8 Conclusion

We have presented a formulation for optimally combining renewable energy sources in order to build up economical hybrid energetic systems in case where these energies are available in a continuous form. The proposed model directly relates the group of input parameters to the estimated power and annual energy production for each renewable energy source. These parameters depend on environmental conditions (solar irradiation, temperature), on geographical characteristics of the site (latitude, longitude, altitude), and on the design characteristics of each energetic system (panel orientation, volume of the biodigester, etc.). In case of continuous energy, given an estimation of the annual energy production and a cost of each unit of the renewable energy source as well as an annual demand, the simplex algorithm outputs (if possible) the optimal repartition of each renewable energy resource. Knowing the energy and the characteristics of the site, this enables to sizing the renewable energy system to be used. According to various simulations; we finally notice that the management system works as follows: it initially selects the energy which has the lowest cost until its capacity is completely consumed, and then selects the next low cost resource and son on. In case of discrete units, given an estimation of the annual energy production and the cost of each unit of the renewable energy source as well as an annual demand, the program outputs (if possible) the number of units from each source to meet the demand while satisfying all the constraints. Both approaches are generic since they are adaptive to various sites, demands, and different energy sources. Illustrative examples have been given

combining thermal and biomass sources. However, solving integer programs is much difficult than solving linear programs.

References

1. Akella, A.K., Sharma, M.P., Saini, R.P.: Optimum utilization of renewable energy sources in a remote area. Renew. Sustain. Energy Rev. **11**, 894–908 (2007)
2. Manolakos, D., Papadakis, G., Papantonis, D., Kyritsis, S.: A simulation-optimization program for designing hybrid energy systems for supplying electricity and fresh water through desalination to remote areas. J. Energy **26**, 679–704 (2001). Elsevier
3. Deshmukha, M.K., Deshmukhb, S.S.: Modeling of hybrid renewable energy systems. Renew. Sustain. Energy Rev. **12**, 235–249 (2008). Elsevier
4. Ramakumar, R., Shetty, P.S., Ashenai, K.: A linear programming approach to the design of integrated renewable energy systems for developing countries. IEEE Trans. Energy Convers. **EC-1**(4) (1986)
5. Bekele, G., Palm, B.: Feasibility study for a standalone solar–wind-based hybrid energy system for application in ethiopia. Appl. Energy **87**, 487–495 (2010). Elsevier
6. Farret, F.A., Simoes, M.G.: Integration of Alternative Sources of Energy. Wiley Inc., Hoboken (2006)
7. Bernal-Agustın, J.L., Dufo-Lopez, R.: Simulation and optimization of stand-alone hybrid renewable energy systems. Renew. Sustain. Energy Rev. **13**(8), 2111–2118 (2009). Elsevier
8. Xu, D., Kang, L.-y., Cao, B.-g.: Graph-based ant system for optimal sizing of standalone Hybrid Wind/PV power systems. In: Huang, D.-S., Li, K., Irwin, G.W. (eds.) ICIC 2006. LNCS (LNAI), vol. 4114, pp. 1136–1146. Springer, Heidelberg (2006)
9. Yang, H., Zhou, W., Lu, L., Fang, Z.: Optimal sizing method for stand-alone hybrid solar–wind system with LPSP technology by using genetic algorithm. Solar Energy **82**, 354–367 (2008). Elsevier
10. Ashok, S.: Optimized model for community-based hybrid energy system. Renew. Energy **32**, 1155–1164 (2007). Elsevier
11. Yang, H., et al.: A novel optimization sizing model for hybrid solar-wind power generation system. Solar Energy **81**, 76–84 (2007). Elsevier
12. Kalogirou, S.A.: Solar thermal collectors and applications. Progr. Energy Combust. Sci. **30**, 253–255 (2004)
13. www.tecsol.fr/letters/articles/documents/ecssolaire3.pdf
14. Hu, W.C., Thayanithy, K., Forster, C.F.: A kinetic study of the anaerobic digestion of ice-cream wastewater. Process. Biochem. **37**, 965–971 (2002)
15. Coudure, R., Castaing, J.: Bilan de Fonctionnement d'une Unité de Méthanisation de Lisier de Porc. JournéesRech. Porcine en France **29**, 335–342 (1997)
16. http://www.lindo.com/
17. http://archives.math.utk.edu/software/msdos/discrete.math/tslin/.html
18. Zaatri, A.: Les Techniques de la Recherche Opérationnelle: Algorithme du Simplexe. les mathématiques à l'université, Constantine, Mars (2002)

A Neural and Fuzzy Logic Based Control Scheme for a Shunt Active Power Filter

Hichem Laib[1(✉)], Abd Elaziz Chaghi[1], and Patrice Wira[1]

[1] LSPIE Laboratory, Electrical Engineering Department Batna University, Batna, Algeria
hichem_elt@yahoo.fr, az_chaghi@univ-batna.dz, patrice.wira@uha.fr
[2] MIPS Laboratory, University of Haute Alsace, Mulhouse, France

Abstract. In this paper, a three-phase shunt active filter is used to compensate for current harmonics and reactive power in three-phase distribution network system. In order to improve its performances, artificial neural networks and fuzzy logic approaches are used to control this device. The first controller, based on ADALINE networks, is used with the direct method in order to identify precisely the necessary currents to reduce the harmonics and to compensate reactive power. The neural network inputs are based on a decomposition of the measured currents. This decomposition is also based on the Fourier series analysis of the current signals and Least Mean Square (LMS) training algorithm to carry out the weights. In this case, three ADALINE are used to extract the fundamental component of the distorted line current directly from the three phase space. The second controller is the fuzzy logic controller, used to regulate the DC link capacitor voltage. This approach has the advantage to eliminate the PLL and Concordia, Park or Clark transformations method. Speed and accuracy of this approach results in improving the performance of the APF.

Keywords: Adaline · Fuzzy logic control · Active power filter · Power quality

1 Introduction

Nowadays there has been a rapid increase in the number of power electronic loads resulting in alarming levels of harmonic distortion in the distribution systems. These harmonics circulate in the electrical network, disturb the correct operation of the components and even it may damage them [1, 2]. Shunt Active Power Filters (APFs) are recognized solutions to compensate for harmonic distortions, to correct the power factor and to recover the balance in power distribution systems by injecting compensating currents [3, 4]. One important factor which influences the performance of the APFs is the speed and accuracy of the detection tool for the power line harmonic currents. APFs can be used with different control strategies. One of the most widely used is based on the conventional instantaneous power theory (*pq*-method) initiated by Akagi [3]. This approach works in the $\alpha\beta$-reference frames, calculates the real and imaginary instantaneous powers and separates their alternative parts from their continuous parts. The alternative parts of the powers are then used to deduce the

M. Chadli et al. (eds.), *Recent Advances in Electrical Engineering and Control Applications*, Lecture Notes in Electrical Engineering 411, DOI 10.1007/978-3-319-48929-2_16

compensation currents. This principle has been efficiently achieved through neural approaches in [5–7]. The main drawbacks of the *pq*-method for identifying harmonic terms are essentially the following [8]:

- It is not effective under distorted and unbalanced main voltage conditions.
- The time delays introduced by pass filters, which are used to separate the average and oscillating parts of powers, degrades the dynamic performance of the active filter.
- This method requires more computational calculation.

Recently, Artificial Neural Networks (ANNs) have been successfully applied to power systems [4]. With their learning capabilities, ANNs are able to take into account time-varying parameters [9, 10]. Inserted in an APF scheme, they can appreciably improve its performance compared to the one obtained with traditional methods. Several methods have been proposed in [5] where ADALINE neural networks have been used to on-line learn the expressions of the signals, i.e., either instantaneous powers or currents. The ADALINE is a simple and fast adaptive scheme which is suitable for on-line applications [11].

In this paper, a neural network and a fuzzy logic approach are proposed to enhance the performances of an APF. The adaptive neural network is used in an open-loop and extracts with high precision the fundamental components of the distorted line currents directly from the *abc* axis. The output of the ADALINE is compared with distorted supply current to obtain the reference current. The Fuzzy Logic Controller (FLC) is used in a closed-loop to maintain the DC-bus voltage constant at the reference value [1, 2]. The output of the closed-loop and the open-loop is summed to construct the modulating signals as shown by Fig. 1. These modulating signals are

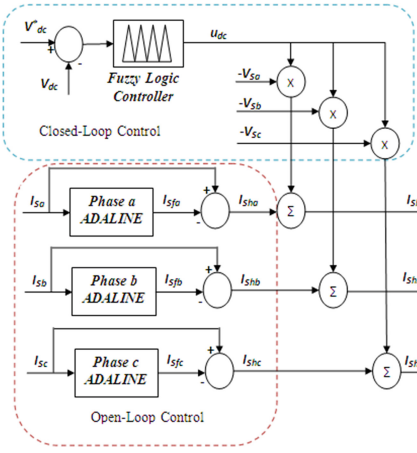

Fig. 1. The proposed strategy to control the power converter

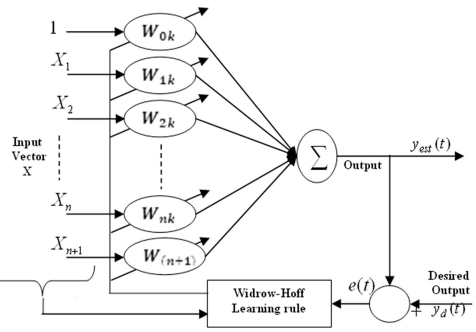

Fig. 2. The ADALINE network

used to generate the Pulse-Width Modulation (PWM) pulses to be fed into the APF in order to generate the compensating currents. This allows maintaining the electrical power to be in a good shape when transported to end-users.

2 Proposed Control Strategy

The main function of the controller is to create the PWM switching signals for the connected Voltage Source Inverter (VSI). Figure 1 shows the schematic diagram of the proposed control strategy for a shunt APF. The proposed control system consists of two control loops, an open and a closed loop. In the open loop, the signal containing the harmonics, I_{Sh}, is obtained from the output of the ADALINE and then its value is summed by $-V_S \times u_{dc}$. The output of the FLC, u_{dc}, is used to maintain the DC-side voltage at its reference value. The opposite of this signal is used as a current reference signal. The sum of the open loop control signal (the ADALINE current reference signal) and the closed-loop control signal (the FLC for regulating DC-side voltage) is used as a modulating signal for each of the three phases. The PWM control strategy then uses them to create the PWM switching pattern for driving the switches of the power converter.

In the next section, we describe the ADALINE approach and more specifically the direct method and the design of the FLC applied to the APF system.

3 Adaptive Linear Neural Networks Principle

The ADALINE is an algorithm having n input in the form of a vector and a scalar output signal. Its main applications are for adaptive filtering and signal prediction. The output of the ADALINE is a linear combination of its inputs. The ADALINE architecture is depicted by Fig. 2. The input to the ADALINE is the vector: $X = [X_0 \quad X_1 \quad X_2 \quad \ldots \quad X_n]$, where X_0 is a bias term, it set to 1. The ADALINE has the following weight vector: $W = [W_0 \quad W_1 \quad W_2 \quad \ldots \quad W_n]$ Then, its output can be simply written by: $Y = W^T X = W_0 + W_1 X_1 + W_2 X_2 + \ldots + W_n X_n$.

The weight adjustment, or adaptation, is performed during the training process of the ADALINE using a nonlinear adaptation algorithm. In order to update the weight vector and minimize the mean square error between the desired signal output $y_d(t)$ and the estimate output $y_{est}(t)$, the Widrow-Hoff learning delta rule is used [11–13]:

$$W(k+1) = W(k) + \alpha \left[\frac{e(k) \times X(k)}{X^T(k) \times X(k)} \right]$$

This expression uses the following parameters:

k	Is the time index of iteration,
$W(k)$	Is the weight vector at time k,

$X(k)$	Is the input vector at time k,
$e(k) = y_d(k) - y_{est}(k)$	Is the error at time k,
α	Represents the learning rate of the weight update law

We use this principle and apply it to according to the direct method [10].

4 ADALINE as Harmonic Estimator

The ADALINE network is used in order to identify the current harmonics in a distorted waveform [15, 16]. In our application, this is achieved according to the direct method which means that the ADALINE works directly the space of the measured current of the electrical supply network. So, three ADALINE networks must be used for the three phases of an electrical supply network. Each one can be decomposed into Fourier series in the following way [14–16]:

$$I_S(t) = I_{Sf}(t) + I_{Sh}(t) = I_{11}\cos(wt - \alpha) + I_{12}\sin(wt - \alpha) + \sum_{n=2}^{N} I_{n1}\cos\, n(wt - \alpha) + I_{n2}\sin n(wt - \alpha) \tag{1}$$

In this expression, I_S represents the current source, I_{Sf} is the fundamental component of current source and I_{Sh} is the harmonics current. Currents I_{Sf} and I_{Sh} can be expressed by:

$$I_{Sf}(t) = I_{11}\cos(wt - \alpha) + I_{12}\sin(wt - \alpha) \tag{2}$$

$$I_{Sh} = \sum_{n=2..n} I_{n1}\cos\, n(wt - \alpha) + I_{n1}\sin\, n(wt - \alpha) \tag{3}$$

In the previous expressions, W is the fundamental frequency, α is the phase shift between the current and the load voltage, I_{11} and I_{12} are the cosine and sine frequency components of the fundamental current, I_{n1} and I_{n2} are the cosine and sine frequency components of the harmonics current. The identification of the harmonics components is achieved with an ADALINE for each phase [14, 15]. This is shown by Fig. 3. The expression of the current expressed in (1) can be written as a linear combination which can be learned by an ADALINE network:

$$I_S(t) = W^T \cdot x(t) \tag{4}$$

Where $x(t)$ is the network input vector and W^T is the ADALINE weight vector. The input vector is chosen as follow:

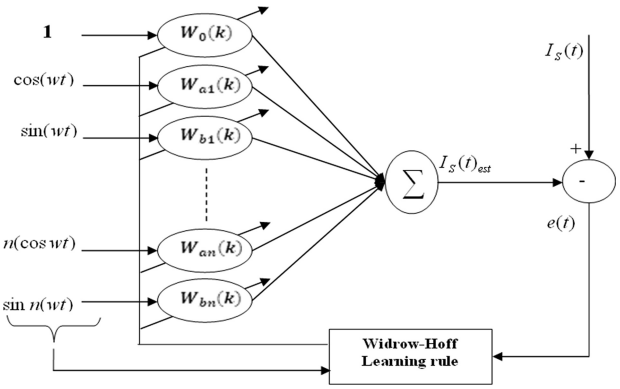

Fig. 3. Design of the ADALINE network for harmonic distortion identification (direct method).

$$x(t) = [\cos(wt - \alpha) \quad \sin(wt - \alpha) \quad \ldots\ldots \quad \cos n(wt - \alpha) \quad \sin n(wt - \alpha)] \tag{5}$$

Then, after learning and convergence, the weights of the ADALINE correspond to

$$W^T = [I_{11} \quad I_{12} \quad \ldots\ldots \quad I_{n1} \quad I_{n2}] \tag{6}$$

The amplitude of continuous component of the fundamental current will be determined by the weight $W_0(k)$ of a first neural network ADALINE multiplying by $\cos(wt)$ and $\sin(wt)$ as follows [13]:

$$I_{Sf} = I_{11}\cos(wt) + I_{12}\sin(wt) \tag{7}$$

Once the fundamental current is determined, the harmonic current can be obtained by subtracting the fundamental component of current estimated by the ADALINE from the measured current. This can be expressed by:

$$I_{Sh}(t) = I_S(t) - I_{Sf}(t) \tag{8}$$

This harmonic current $I_{Sh}(t)$ for one phase will then be injected phase-opposite in the electrical network via a controlled device, i.e., the VSI.

5 Design of the DC-bus Fuzzy Logic Controller

The voltage of the DC-bus should be maintained at a desired value, to compensate the losses in the active filter. The voltage control of the DC bus is achieved by adjusting a small amount of the real power flowing into the DC capacitor. Several methods can be used like PI, PID, or RST controllers. In our application, we utilize a FLC algorithm to control the APF in a closed loop. The DC-bus capacitor voltage is sensed and then compared with a desired reference value [1, 2, 17, 18, 19, 20]. The

error signal $e(t)$ and a variation of it given by $\Delta e(t) = e(t) - e(t-1)$ are used as the inputs of the FLC as shown in Fig. 4 [1, 2, 16]. The output of the fuzzy controller estimates the magnitude of the peak reference current I_{Max}. This current takes into account the active power demand of the non-linear load for harmonics and reactive power compensation. This peak reference current is then multiplied with the system voltage (V_{S-abc}) to output a synchronized reference current as shown by Fig. 1. In order to convert the real values into linguistic variables, we use seven fuzzy sets. These are: NL (negative big), NM (negative medium), NS (negative small), Z (zero), PS (positive small), PM (positive medium), and PB (positive big) [1, 2, 22, 23, 24, 25]. The seven fuzzy sets are for each input $(e, \Delta e)$ and for the output I_{Max} with triangular and trapezoidal membership functions with are characterized by:

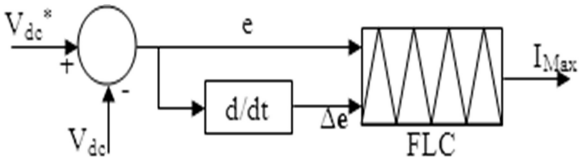

Fig. 4. The Fuzzy Logic Controller (FLC) strategy

- fuzzification step using a continuous universe of discourse;
- an implication using Mamdani's 'min' operator;
- a defuzzification step using the 'centroid' method.

The membership functions used for the input and output variables used here are shown by Fig. 5. As both inputs have seven subsets, a fuzzy rule base formulated for the present application is provide by Table 1.

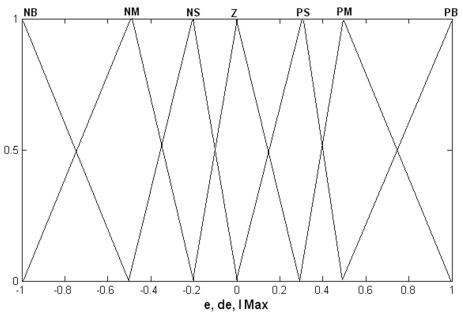

Fig. 5. Membership functions for the inputs and output variables

6 Simulations and Analysis of the Results

In order to evaluate our compensation approach based on ADALINE and a FLC, a digital simulation is carried out. This study examines an electrical distribution networks having a three-phase voltage source, a nonlinear load that generates a high level of harmonics and a shunt APF to compensate for them. Figure 6 shows the electrical scheme of the system and the values of the main parameters are given in Table 2.

Table 1. The fuzzy sets for the design of the FLC

de	e						
	NL	NM	NS	ZE	PS	PM	PL
NL	NL	NL	NL	NL	NM	NS	ZE
NM	NL	NL	NL	NM	NS	ZE	PS
NS	NL	NL	NM	NS	ZE	PS	PM
ZE	NL	NM	NS	ZE	PS	PM	PL
PS	NM	NS	ZE	PS	PM	PL	PL
PM	NS	ZE	PS	PM	PL	PL	PL
PL	NL	NM	NS	ZE	PS	PM	PL

Obviously, the proposed control scheme must be evaluated under changing and varying conditions. Thus, the nonlinear load is changed at $t = 0.125$ s and the converter is set up with a firing angle of 20°.

In the following, an ADALINE is used to estimate the fundamental current of each of the three phases. The compensating currents are injected in the electrical network. They are obtained from reference currents which are calculated by subtracting the fundamental current estimated by an ADALINE from the measured current issued from the electrical network. In addition, the FLC is used to maintain the value of the DC voltage at a fixed value.

The performances of the proposed technique are given by Figs. 7 and 8. The steady state and transient behaviors of the controlled system can be seen. Figure 7 shows the load current without compensation (the current of only one phase is represented for more clearness) with its harmonic spectrum, and the source currents and with its harmonic spectrum after compensation. Figure 8 shows for one phase, the compensating current issued by the APF, the resulting source current and source voltage, and the DC capacitor voltage. The overall performance of the compensating strategy can be seen with the active and reactive powers on the source side. They are represented by Fig. 9 and can be compared to the one on the nonlinear load side without compensation.

It can be seen from the previous figures that the proposed compensation technique of the APF is able to reduce the harmonics generated by the nonlinear load. Indeed, the resulting currents are sinusoidal and in phase with the source voltages, even under nonlinear load changes. The Total Harmonic Distortion (THD) rate and the

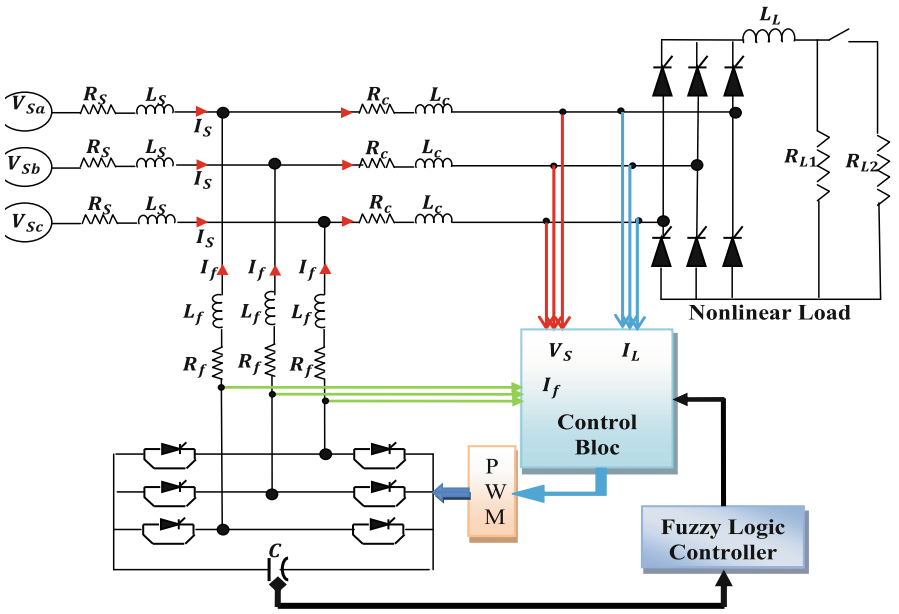

Fig. 6. Overall scheme of the compensation strategy based on a shunt APF inserted in the electrical distribution network

Table 2. Values of the electrical parameters

Phase to neutral source voltage	$240\sqrt{2}$ V, 50 Hz
Source impedance	$R_S = 3.5$ mΩ; $L_S = 0.05$ μH
Filter impedance	$R_C = 0.82$ mΩ; $L_C = 0.1$ mH
Load impedance	$R_{L1} = 1.5$ Ω; $R_{L2} = 3$Ω; $L_L = 6$ mH
DC side capacitance	$C = 8$ mF
DC-bus voltage reference	$V_{dc}^{*} = 850$ V

Power Factor (PF) have been recorded. Finally, the THD has been reduced from 28.47% without compensation to 0.82% with the compensation strategy. After the nonlinear load, the THD still remains under 1%. By using the FLC in a closed-loop control, the DC-bus voltage is maintained at the desired value when the nonlinear load changes. The transient response is also excellent. This can be observed from Fig. 9 where the active and reactive powers' fast evolutions are depicted. The reactive power is almost canceled. The real power from the AC source side is practically free of the alternating part due to the nonlinear property of the load.

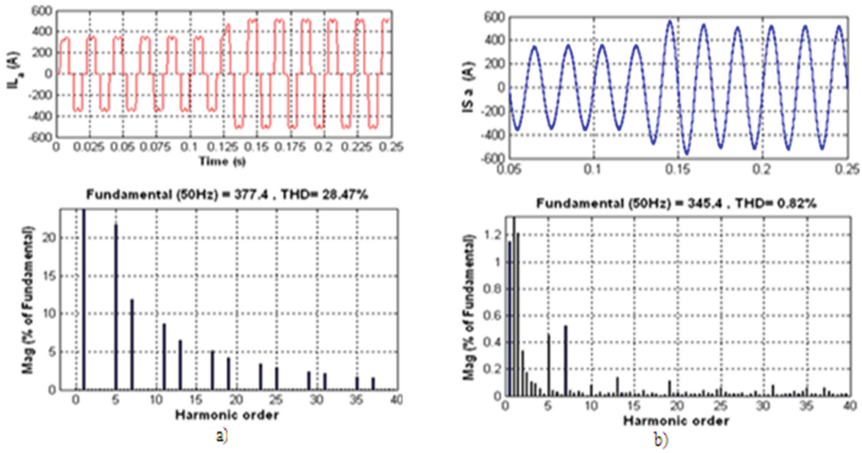

Fig. 7. Load and source currents and their harmonics spectrum. (a) Before compensation (THD = 28.47%), (b) After compensation (THD = 0.82%).

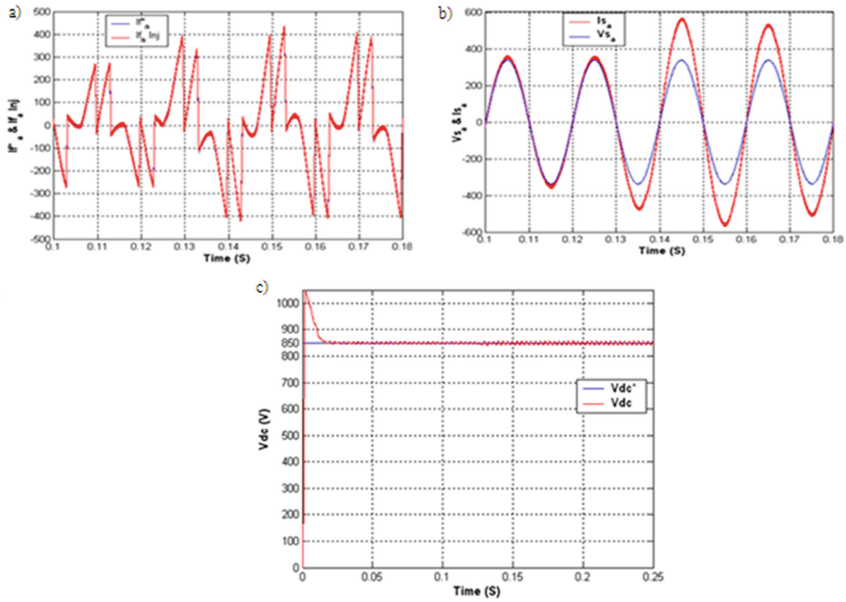

Fig. 8. Simulation results, (a) reference and compensation currents from the APF, (b) voltage and current source waveforms before compensation, (c) the DC capacitor voltage.

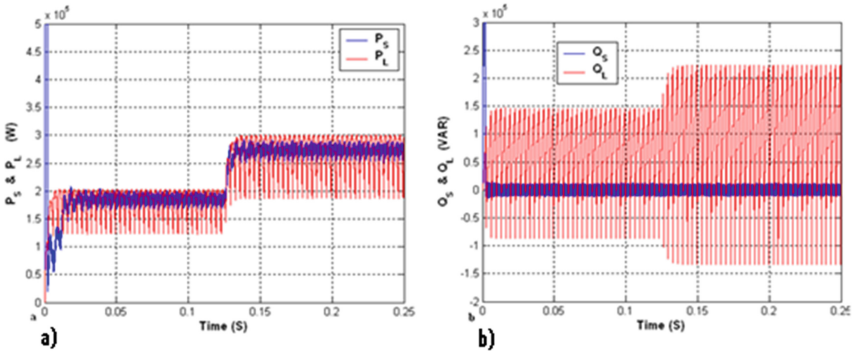

Fig. 9. (a) The instantaneous active power and, (b) the reactive powers at the load side and obtained after compensation on the source side

7 Conclusion

A shunt active power filter has been used to compensate for harmonics and reactive power produced by the presence of a nonlinear load inserted in a power distribution grid. The identification of the harmonic currents is achieved by a neural approach that relies on ADALINE networks. The identification is made directly in the measured current frame. This is called the direct method. In addition, a fuzzy controller is used to keep the DC voltage at the desired constant value. This closed loop will also be able to minimize the DC voltage fluctuations and the settling time. The effectiveness of the approach has been illustrated by the simulation results with the Matlab/Simulink toolbox Power System.

The results show that the proposed control approach can compensate for highly distorted line currents by generating and injecting appropriate compensation currents. In the various test cases simulated with different nonlinear loads, the THD of the supply current is always reduced to a value which is less than 5%. The performances obtained by the proposed method are better than those obtained by more traditional techniques.

In future work we plan to expand the use of artificial neural networks. We will intend to use other active compensation schemes and generalize their control strategies.

References

1. Laib, H., Kouara, H., Chaghi, A.E.: A new approach of modular active power filtering. Int. J. Adv. Sci. Technol. **50**, 11 (2013)
2. Laib, H., Kouara, H., Chaghi, A.E.: An advanced control approach for modular active power filtering. ACTA Technica Corviniensis- Bulletin of Engineering, Tome VI (year 2013)-Fascicule 2, April–June 2013. ISSN 2067-3809
3. Akagi, H., Watanabe, E.H., Aredes, M.: Instantaneous Power Theory and Applications to Power Conditioning. Wiley-IEEE Press, Hoboken (2007)

4. Nguyen, N.K., Wira, P., Flieller, D., Ould Abdeslam, D., Mercklé, J.: A comparative experimental study of neural and conventional controllers for an active power filter. In: 36th Annual Conference of the IEEE Industrial Electronics Society (IECON10) (2010)
5. Ould Abdeslam, D., Wira, P., Mercklé, J., Flieller, D., Chapuis, Y.-A.: A unified artificial neural network architecture for active power filters. IEEE Trans. Ind. Electron. **54**(1), 61–76 (2007)
6. Flieller, D., Ould Abdeslam, D., Wira, P., Mercklé, J.: Distortions identification and compensation based on artificial neural networks using symmetrical components of the voltages and the currents. Electron. Power Syst. Res. **79**(7), 1145–1154 (2009)
7. Nguyen, N.K., Flieller, D., Wira, P., Ould Abdeslam, D., Mercklé, J.: Neural networks for phase and symmetrical components estimations in power systems. In: 35th Annual Conference of the IEEE Industrial Electronics Society (IECON09) (2009)
8. Lamchich, M.T.: ANN current controller based on PI-Fuzzy adaptive system for shunt power active filter. Adv. Power Electron. **2012**, Article ID 237259, 6p (2012)
9. Vazquez, J., Salmeron, P.: Active power filter control using neural network technologies. IEE Proc. Electron. Power Appl. **150**(2), 139–145 (2003)
10. Ould Abdeslam, D., Mercklé, J., Ngwanyi. R., Chapuis, Y.A.: Artificial neural networks for harmonic estimation in low-voltage power systems. In: Fourth International ICSC Symposium on Engineering of Intelligent Systems (EIS 2004), Island of Madeira, Portugal (2004)
11. Widrow, B., Lehr, M.A.: 30 years of adaptive neural networks: perceptron, madaline and back propagation. Proc. IEEE **78**(9), 1415–1442 (1990)
12. Chandra Sekaran, E., Anbalagan, P.: Comparison of neural network and fast fourier transform based selective harmonic extraction and total harmonic reduction for power electronic converter. Asian Power Electron. J. **2**(1), 1–9 (2008)
13. Ould Abdeslam, D., Mercklé, J., Wira, P., Flieller, D.: Harmonic identification based on ANN: a comparative study. In: 9th International Conference on Engineering Applications of Neural Networks-(EANN 2005), Lille, France, 24–26 August 2005
14. Ould Abdeslam, D.: Techniques neuromimétiques pour la commande dans les systèmes électriques: application au filtrage actif parallèle dans les réseaux électriques basse tension. Thèse de doctorat. Université de Haute-Alsace, Mulhouse (2005)
15. EL Shatshat, R.A.: A novel modular approach to active power-line harmonic filtering in distribution systems. Thèse de doctorat. Université de Waterloo, Ontario (2001)
16. Narasa Reddy, T.M., Subramanyam, V.: Fuzzy logic controlled shunt active power filter for mitigation of harmonics with different membership functions. In: International Conference on Advances in Computing, Control, and Telecommunication Technologies (2009)

Faults Diagnosis-Faults Tolerant Control (FTC)

Robust Fault Detection Filter Design for Discrete-Time Fuzzy Models

Sabrina Aouaouda[1] and Mohammed Chadli[2(✉)]

[1] Souk-Ahras University, LEER, BP 1553 Souk-Ahras, Algeria
Sbrina.aouaouda@univ-soukahras.dz
[2] Laboratoire de MIS, Mohammed-Chadli, Université de Picardie Jules verne, 33, rue Saint-Leu, 80039 Amiens, France
mohammed.chadli@u-picardie.fr

Abstract. This New fault detection observer design conditions for discrete-time fuzzy systems with unmeasurable premise variables are proposed. In this study, the considered Takagi-Sugeno (T-S) fuzzy system is subject to sensor faults and unknown bounded disturbances. The T-S observer is used to estimate jointly states and faults by means of a mixed H_-/H_∞ performance index. Using the technique of descriptor system representation new conditions are proposed in terms of a Linear Matrix Inequality (LMI) by considering the sensor fault as an auxiliary state variable. Simulation results are presented to demonstrate the effectiveness of the approach.

Keywords: Discrete-time T-S fuzzy models · Descriptor approach · Sensor fault detection observer · Unmeasurable premise variables LMI

1 Introduction

Recently, fault detection observer has been strongly investigated and a lot of works, involving various specifications, are now available. Among this literature, many results have been reported for linear systems [1, 2], nonlinear models [3, 4] and descriptor systems [5]. Briefly, two main criteria dealing with the above observer design must be considered. The first one is that when the fault detection observers have to be robust, i.e. insensitive to disturbances. The second guarantees the sensitivity to faults. Moreover, a suitable performance index is to be optimized. For this purpose several performance indexes are reported in the literature such as [5, 6], H_- [4], and mixed H_-/H_∞ [2, 4, 7]. For every case, the result obtained are dependent on the Lyapunov function used to prove the stability (see for example, [8, 9] and references therein) by means of linear matrix inequalities (LMIs) [10]. Regrettably, in the literature the design of fault detection and diagnosis for nonlinear systems remain more complicated.

Furthermore, extensive studies are made on Takagi-Sugeno (T-S) models, which have proved their effectiveness in the analysis, control and observation of nonlinear systems [11]. It provides a representation of some nonlinear systems by means of a collection of linear models which are interconnected by nonlinear function as a convex combination. The presented work illustrates the design of a fault detection observer for discrete T-S model. The contribution of this work concerns the consideration of the

M. Chadli et al. (eds.), *Recent Advances in Electrical Engineering and Control Applications*, Lecture Notes in Electrical Engineering 411, DOI 10.1007/978-3-319-48929-2_17

case when the premise variables of the T-S model are not measurable (as the state of the system), this situation is commonly encountered when using the sector nonlinearity approach [15, 16]. This formalism is very important in both the exact representation of the nonlinear behavior by T-S model and in diagnosis method based on observer banks to detect and isolate actuator and sensor faults. In fact, the T-S models with unmeasurable premise variables may represent a larger class of nonlinear systems compared to the T-S model with measurable premise ones [7, 12].

In this note, robust observer design with maximum fault sensitivity and unmeasurable premise variables for discrete-time fuzzy models is discussed. Indeed, based on nonquadratic Lyapunov function, less conservative conditions for discrete fuzzy T-S system affected by sensor faults and unknown bounded disturbances are derived. The observer gains and the residual weighting matrix are obtained through the minimization of a H_∞ norm and the maximization of a H_- norm. The main objective is to find a fault detection observer which has the best robustness to disturbances and residual sensitivity to faults.

This paper is organized as follows. In the next section, the class of studied systems and the discrete T-S fuzzy descriptor observer are presented. In Sect. 3, the problem of residual generation and disturbance attenuation is proposed. Section 4 is devoted to the robustness conditions on fault detection observer and the fault sensitivity conditions are presented in Sect. 5. The multi-objective H_-/H_∞ fault detection observer is then detailed in Sect. 6. In the last section, a numerical example and a truck-trailer model are considered to illustrate the efficiency of the proposed approach.

The following notation is considered. $\mathcal{H}(P)$ denotes the Hermitian of the matrix P, i.e. $\mathcal{H}(P) = P + P^T$. The symbol * indicates the transposed element in the symmetric positions of a matrix; $\mathcal{R} = \{1, 2, .., r\}$.

2 Preliminaries on T-S Fuzzy Systems

Let us consider a discrete-time T-S fuzzy system represented by:

$$\begin{cases} x_{k+1} = \sum_{i=1}^{r} \mu_i(\xi_k)(A_i x_k + B_i u_k) \\ y_k = C x_k \end{cases} \tag{1}$$

where $x_k \in \mathbb{R}^n$, $y_k \in \mathbb{R}^p$, and $u_k \in \mathbb{R}^m$ represent respectively the state, the measured output and the bounded input vectors. $\{A_i, B_i\}$ are the submodels matrices with appropriate dimension and r is the number of submodels, and $\mu_i(\xi_k)$ are the weighting functions depending on the variables ξ_k. These functions verify the convex sum property

$$0 \le \mu_i(\xi_k) \le 1, \sum_{i=1}^{r} \mu_i(\xi_k) = 1 \quad \forall i \in \{1, 2, \cdots, r\} \tag{2a}$$

ξ_k is the decision variable assumed not fully measurable. Consider $\Im_{ij}$ a matrix and $\mu_i(.)$ some function sharing the convex sum property (2a). The single or double sums can be rewritten as:

$$\psi_\mu = \sum_{i=1}^{r} \mu_i(\xi_k)\psi_i \tag{2b}$$

and

$$\psi_{\mu\hat{\mu}} = \sum_{i=1}^{r}\sum_{j=1}^{r} \mu_i(\xi_k)\mu_j\left(\hat{\xi}_k\right)\psi_{ij} \tag{2c}$$

In this work, we consider the discrete-time T-S fuzzy model affected by sensor faults and unknown bounded disturbances.

$$\begin{cases} x_{k+1} = A_\mu x_k + B_\mu u_k + B_d d_k \\ y_{fk} = Cx_k + D_f f_k \end{cases} \tag{3}$$

where $f_k \in \mathbb{R}^s$ is the sensor fault vector, $d_k \in \mathbb{R}^d$ is the unknown bounded disturbance vector. Matrices B_d and D_f are of appropriate dimension and D_f is assumed to be full column rank. To ensure the estimation of both the state and sensor fault vectors, an augmented system is firstly constructed using the descriptor technique. The faulty system given by (3) can be rewritten as follows:

$$\begin{cases} \bar{E}\bar{x}_{k+1} = \bar{A}_\mu \bar{x}_k + \bar{B}_\mu u_k + \bar{B}_d d_k + \bar{D}_h h_k \\ y_k = \bar{C}\bar{x}_k = C^* \bar{x}_k + h_k \end{cases} \tag{4}$$

where

$$h_k = D_f f_k, \bar{x}_k^T = \left[x_k^T h_k^T\right] \tag{5a}$$

$$\bar{E} = \begin{bmatrix} I & 0 \\ 0 & 0 \end{bmatrix}, \quad \bar{A}_i \triangleq \begin{bmatrix} A_i & 0 \\ 0 & -I \end{bmatrix}, \quad \bar{B}_i \triangleq \begin{bmatrix} B_i \\ 0 \end{bmatrix}, \quad \bar{B}_d = \begin{bmatrix} B_d \\ 0 \end{bmatrix} \tag{5b}$$

$$\bar{D}_h = \begin{bmatrix} 0 \\ I \end{bmatrix}, \quad C^* = [C \quad 0], \text{ and } \bar{C} = [C \quad I] \tag{5d}$$

We consider an observer under the usual form:

$$\begin{cases} Ez_{k+1} = F_{\hat{\mu}} z_k + \bar{B}_{\hat{\mu}} u_k & (6a) \\ \hat{\bar{x}}_k = z_k + Ky_k & (6b) \\ \hat{y}_k = C^* \hat{\bar{x}}_k = C\hat{x}_k & (6c) \end{cases}$$

where $z_k \in \mathbb{R}^{n+p}$ is the auxiliary state vector of the observer and $\hat{\bar{x}}_k \in \mathbb{R}^{n+p}$ is the estimate state. $F_{\hat{\mu}}$, E and K are the observer gains to be determined.

3 Problem Statement

Let us define the state error and the residual signal:

$$r_k = \mathbb{S}_\mu(y_k - \hat{y}_k) \tag{7a}$$

$$e_k = \bar{x}_k - \hat{\bar{x}}_k \tag{7b}$$

where $\mathbb{S}$ is a weighting matrix.

Definition. Given the fuzzy system (3), two scalars $\gamma > 0$ and $\beta > 0$. The observer (6) is called an H_-/H_∞ fault detection observer if (6) is asymptotically stable, and the following inequalities are satisfied:

$$\sum_{i=0}^{\infty} r^T(i)r(i) \le \gamma^2 \sum_{i=0}^{\infty} d^T(i)d(i) \tag{8a}$$

$$\sum_{i=0}^{\infty} r^T(i)r(i) \ge \beta^2 \sum_{i=0}^{\infty} f^T(i)f(i) \tag{8b}$$

The goal is to find an admissible observer (6) to minimize γ and maximize β, i.e. an observer which has the best robustness to disturbances (d_k) and a maximal sensitivity to faults (f_k). In the following we give conditions to design the fuzzy observer and we also give a bound on the estimation error. After some manipulation with

$$F_{\hat{\mu}} = \begin{bmatrix} A_{\hat{\mu}} & 0 \\ -C & -I \end{bmatrix}, \quad K = \begin{bmatrix} 0 \\ I \end{bmatrix}, \quad E = \begin{bmatrix} I + \Theta C & \Theta \\ \mathcal{F}C & \mathcal{F} \end{bmatrix} \tag{9}$$

The augmented state estimation error dynamic is expressed as

$$e_{k+1} = S_{\hat{\mu}} e_k + \tilde{A}_{\mu\hat{\mu}} x_k + \tilde{B}_{\mu\hat{\mu}} u_k + G d_k \tag{10}$$

where

$$S_{\hat{\mu}} \triangleq \begin{bmatrix} A_{\hat{\mu}} + \Theta\mathcal{F}^{-1}C & \Theta\mathcal{F}^{-1} \\ -CA_{\hat{\mu}} - \left(\mathcal{F}^{-1} + C\Theta\mathcal{F}^{-1}\right)C & -\mathcal{F}^{-1} - C\Theta\mathcal{F}^{-1} \end{bmatrix} \tag{11}$$

$$\tilde{A}_{\mu\hat{\mu}} \triangleq \begin{bmatrix} A_\mu - A_{\hat{\mu}} \\ -C\left(A_\mu - A_{\hat{\mu}}\right) \end{bmatrix}, \quad \tilde{B}_{\mu\hat{\mu}} \triangleq \begin{bmatrix} B_\mu - B_{\hat{\mu}} \\ -C\left(B_\mu - B_{\hat{\mu}}\right) \end{bmatrix}, \quad G = \begin{bmatrix} B_d \\ -CB_d \end{bmatrix} \tag{12}$$

Consequently, the augmented state estimation error obeys to the following nonlinear system:

$$r_k = \mathbb{S}_\mu(C^* e_k + h_k) \tag{13}$$

$$\tilde{x}_{k+1} = M_{\mu\hat{\mu}}\tilde{x}_k + U_{\mu\hat{\mu}}u_k + Hd_k \tag{14a}$$

where

$$e_k = \begin{bmatrix} I_{n+nh} & 0 \end{bmatrix}\begin{bmatrix} e_k \\ x_k \end{bmatrix}, \quad M_{\mu\hat{\mu}} \triangleq \begin{bmatrix} S_{\hat{\mu}} & \tilde{A}_{\mu\hat{\mu}} \\ 0 & A_\mu \end{bmatrix}, \quad U_{\mu\hat{\mu}} = \begin{bmatrix} \tilde{B}_{\mu\hat{\mu}} \\ B_\mu \end{bmatrix}, \quad H = \begin{bmatrix} G \\ B_d \end{bmatrix} \tag{14b}$$

$$\text{and} \quad \tilde{x}_k^T = \begin{bmatrix} e_k^T & x_k^T \end{bmatrix} \tag{14c}$$

when $d_k = 0$, we have:

$$r_k^f = \mathbb{S}_\mu\left(C^* e_k^f + D_f f_k\right) \tag{15a}$$

$$\tilde{x}_{k+1}^f = M_{\mu\hat{\mu}}\tilde{x}_k^f + U_{\mu\hat{\mu}}u_k \tag{15b}$$

and when $f_k = 0$, we have :

$$r_k^d = \mathbb{S}_\mu C^* e_k^d \tag{16a}$$

$$\tilde{x}_{k+1}^d = M_{\mu\hat{\mu}}\tilde{x}_k^d + U_{\mu\hat{\mu}}u_k + Hd_k \tag{16b}$$

In the following two sections, expressions (15) and (16) will be independently used to study the problems of robustness and sensitivity. To avoid clutter, assume $\mu_\mu(\xi_k) = \mu_\mu$ and $\mu_\mu(\xi_{k+1}) = \mu_\mu^+$.

4 Robustness Conditions

This section recalls some results obtained for discrete TS fuzzy system by considering only robustness against disturbance problem. Conditions are derived by means of the H_∞ performance index.

Theorem 1. Consider the system (3) with the observer (6), system (16) is asymptotically stable satisfying (8) if there exist symmetric matrices X_i, and any matrices $L, \mathbb{S}_i$, R_{ijl}, $\mathcal{F}$, Θ and scalars $\rho = \sqrt{\gamma}$, $\delta = \sqrt{\lambda}$, such that the following conditions are satisfied for $i, j, l \in \mathcal{R}$

$$\min_{X_i, L, \mathbb{S}_i, R_{ijl}} \delta, \rho$$

$$\text{s.t. } \Pi_l - \Im_l - \Im_l^T < 0, X_i > 0, (i, l \in \mathcal{R}) \tag{17}$$

where

$$\Pi_l = \begin{bmatrix} \mathcal{Q}_{11l} & * & \cdots & * \\ \mathcal{Q}_{21l} & \mathcal{Q}_{22l} & \cdots & * \\ \vdots & \vdots & \ddots & \vdots \\ \mathcal{Q}_{r1l} & \mathcal{Q}_{r2l} & \cdots & \mathcal{Q}_{rrl} \end{bmatrix}, \quad \Im_l = \begin{bmatrix} O_{11l} & * & \cdots & * \\ O_{21l} & O_{22l} & \cdots & * \\ \vdots & \vdots & \ddots & \vdots \\ O_{r1l} & O_{r2l} & \cdots & O_{rrl} \end{bmatrix} \tag{18}$$

with

$$\mathcal{Q}_{ijl} = \begin{bmatrix} \frac{1}{2}\left(\Gamma_i + \Gamma_j\right) & * & * & * & * & * \\ 0 & -\delta I & * & * & * & * \\ 0 & 0 & -\rho I & * & * & * \\ \Phi_{ij} & \frac{1}{2}\left(U_{ij} + U_{ji}\right) & H & -X_l & * & * \\ N_1 L & 0 & 0 & 0 & -I & * \\ N_{2i} L & 0 & 0 & 0 & 0 & -I \end{bmatrix} \tag{19a}$$

$$O_l = \mathrm{diag}\left[R_{11l} \quad \cdots \quad R_{rrl} \right] \tag{19b}$$

$$\Gamma_i = X_i - L^T - L, \; \Phi_{ij} = \frac{1}{2}\left(M_{ij} + M_{ji}\right)L \tag{20a}$$

$$N_1 = \begin{bmatrix} I & (0) \\ (0) & (0) \end{bmatrix}, \quad N_{2i} = \begin{bmatrix} \mathbb{S}_i C^* & (0) \\ (0) & (0) \end{bmatrix} \tag{20b}$$

where M_{ij} and U_{ij} are defined in (14c). Then the system is stable with ρ-disturbance attenuation and the $\mathcal{L}_2$-gain from $u(t)$ to $e_d(t)$ is bounded by δ.

Proof. Let $V\left(\tilde{x}_k^d\right)$ denote the following candidate Lyapunov function:

$$V\left(\tilde{x}_k^d\right) = \tilde{x}_k^{dT} \mathcal{P}_\mu \tilde{x}_k^d \tag{20c}$$

where $\mathcal{P}_\mu$ is a symmetric positive definite matrix. By respecting the criterion (8), the $\mathcal{L}_2$ gain from u_k to e_k^d is bounded by λ if:

$$\Delta V\left(\tilde{x}_k^d\right) + e_k^{dT} e_k^d + r_k^{dT} r_k^d - \lambda^2 u_k^T u_k - \gamma^2 d_k^T d_k < 0 \tag{20d}$$

where

$$\Delta V\left(\tilde{x}_k^d\right) = \tilde{x}_{k+1}^{dT} \mathcal{P}_{\mu^+} \tilde{x}_{k+1}^d - \tilde{x}_k^{dT} \mathcal{P}_\mu \tilde{x}_k^d \tag{20e}$$

is the increment of the fuzzy Lyapunov function candidate $V\left(\tilde{x}_k^d\right)$, shown in (20c). According to (16), it follows that

$$\dot{V} = \mathcal{X}^T \left(\Lambda_{\mu\mu}^T \bar{\mathcal{P}}_{\mu^+} \Lambda_{\mu\mu} - \tilde{\mathcal{P}}_\mu\right)\mathcal{X} \tag{20f}$$

where $\mathcal{X}^T = \left[\tilde{x}_k^d u_k d_k\right]$ and

$$\Lambda_{\mu\mu} = \begin{bmatrix} M_{\mu\mu} & U_{\mu\mu} & H \\ N_1 & 0 & 0 \\ N_{2i} & 0 & 0 \end{bmatrix}, \quad \bar{\mathcal{P}}_{\mu^+} = \begin{bmatrix} \mathcal{P}_{\mu^+} & 0 & 0 \\ 0 & I & 0 \\ 0 & 0 & I \end{bmatrix}, \quad \widetilde{\mathcal{P}}_{\mu} = \begin{bmatrix} \mathcal{P}_{\mu} & 0 & 0 \\ 0 & \lambda^2 I & 0 \\ 0 & 0 & \gamma^2 I \end{bmatrix}$$

N_1, N_{2i} are given by (20b). By applying Lemma A.1, Eq. (20f) is equivalent to

$$V \leq \mathcal{A} = \mathcal{X}^T \left\{ \sum_{i=1}^{r} \mu_i^2 \, \overline{\Lambda}_{ii\mu^+} + 2 \sum_{i<j}^{r} \mu_i \mu_j \frac{\left(\overline{\Lambda}_{ij\mu^+} + \overline{\Lambda}_{ji\mu^+}\right)}{2} \right\} \mathcal{X}$$

where

$$\bar{\Lambda}_{ijl} = \begin{bmatrix} M_{ij}^T \mathcal{P}_l M_{ij} + N_1^T N_1 + N_{2i}^T N_{2i} - \mathcal{P}_i & * & * \\ U_{ij}^T \mathcal{P}_l M_{ij} & U_{ij}^T \mathcal{P}_l U_{ij} - \lambda^2 I & * \\ H^T \mathcal{P}_l M_{ij} & H^T \mathcal{P}_l U_{ij} & H^T \mathcal{P}_l H - \gamma^2 I \end{bmatrix}$$

For the stability of (16b) with H_∞ guaranteed cost given by γ and bounded the *L2* gain from u_k to e_k^d by λ, it is sufficient that $\bar{\Lambda}_{ii\,\mu^+} < 0$ and $\bar{\Lambda}_{ij\mu^+} < 0 (i < j, i, j \in \mathcal{R})$. This follows that $\mathcal{A} < 0$, which implies that (20c) holds.

At this point, Lemma B is used and more slack matrix variables are added to promote the less conservative LMIs proposed in Theorem 1.

Remark 1. The conditions (17) are not in LMI form due to the products $M_{ij}L$ in Φ_{ij} and $N_{2i}L$. An LMI solution is then proposed by the following corollary.

Corollary 1. Consider the system (3) with the observer (6), system (16) is asymptotically stable satisfying (8), for a given scalar $\varepsilon_1 \geq 0$, if there exist symmetric matrices X_i, matrices $L, \mathbb{S}_i, R_{ijl}$, T_1, T_2 and scalars ρ, δ, such that LMI conditions (17) are satisfied for $i, j, l = 1, \cdots, r$. with

$$\mathcal{Q}_{ijl} = \begin{bmatrix} \frac{1}{2}\left(\Gamma_i + \Gamma_j\right) & * & * & * & * & * & * \\ 0 & -\delta I & * & * & * & * & * \\ 0 & 0 & -\rho I & * & * & * & * \\ \Phi_{ij} & \frac{1}{2}\left(U_{ij} + U_{ji}\right) & H & -X_l & * & * & * \\ N_1 L & 0 & 0 & 0 & -I & * & * \\ 0 & 0 & 0 & 0 & L & -\varepsilon_1 I & * \\ N_{2i} & 0 & 0 & 0 & 0 & 0 & -\varepsilon_1^{-1} I \end{bmatrix} \tag{21a}$$

where Γ_i, Φ_{ij} are expressed by (20a), matrices M_{ij} and U_{ij} are defined in (14c) and N_1, N_{2i} are given by (20b). With

$$L = \begin{bmatrix} L_{11} & (0) \\ L_{12} & L_{22} \end{bmatrix} \tag{21b}$$

and

$$\mathrm{L}_{11} = \begin{bmatrix} \mathcal{L}_1^{11} & 0 \\ 0 & 0 \end{bmatrix} \tag{21c}$$

$$\begin{cases} \mathrm{T}_1 = \Theta \mathcal{F}^{-1} \mathrm{C} \mathcal{L}_1^{11} \\ \mathrm{T}_2 = \left(\mathcal{F}^{-1} + \mathrm{C} \Theta \mathcal{F}^{-1}\right) \mathrm{C} \mathcal{L}_1^{11} \end{cases} \tag{21d}$$

Remark 2. Since $\mathrm{D_f}$ is assumed to be of full column rank, then the sensor faults estimation can be obtained by

$$\hat{\mathrm{f}}(\mathrm{t}) = \left(\mathrm{D_f^T D_f}\right)^{-1} \mathrm{D_f^T} \hat{\mathrm{h}}(\mathrm{t}) \tag{22}$$

which guarantee the good estimation of faults.

5 Fault Sensitivity Conditions

For now, the sensitivity problem of the residual $\mathrm{r}(\mathrm{t})$ to the fault $\mathrm{f}(\mathrm{t})$ is treated in this section. In fact the main idea is to make the residual as sensitive as possible to faults. For this purpose, the $\mathrm{H_-}$ index is used hereafter.

Theorem 2. Consider the system (3) with observer (6), system (15) is asymptotically stable satisfying (9), if there exist some symmetric positive definite $\mathrm{X_i}$ and any matrices L, $\mathbb{S}_\mathrm{i}$, $\mathrm{W_{ijl}}$ T_1, T_2 and scalars $\eta = \sqrt{\beta}$, $\delta = \sqrt{\lambda}$ such that the following optimization conditions are satisfied for $\mathrm{i}, \mathrm{j}, \mathrm{l} \in \mathcal{R}$

$$\min_{\mathrm{X_i}, L, \mathbb{S}_\mathrm{i}, \mathrm{W_{ijl}}} \delta$$

$$\text{s.t. } \tilde{\Pi}_\mathrm{l} - \tilde{\Im}_\mathrm{l} - \tilde{\Im}_\mathrm{l}^\mathrm{T} < 0, \mathrm{X_i} > 0, (i, l \in \mathcal{R}) \tag{23}$$

where

$$\tilde{\Pi}_\mathrm{l} = \begin{bmatrix} \tilde{\mathcal{Q}}_{11\mathrm{l}} & * & \cdots & * \\ \tilde{\mathcal{Q}}_{21\mathrm{l}} & \tilde{\mathcal{Q}}_{22\mathrm{l}} & \cdots & * \\ \vdots & \vdots & \ddots & \vdots \\ \tilde{\mathcal{Q}}_{\mathrm{r}1\mathrm{l}} & \tilde{\mathcal{Q}}_{\mathrm{r}2\mathrm{l}} & \cdots & \tilde{\mathcal{Q}}_{\mathrm{rrl}} \end{bmatrix}, \quad \tilde{\Im}_\mathrm{l} = \begin{bmatrix} \tilde{\mathrm{O}}_{11\mathrm{l}} & * & \cdots & * \\ \tilde{\mathrm{O}}_{21\mathrm{l}} & \tilde{\mathrm{O}}_{22\mathrm{l}} & \cdots & * \\ \vdots & \vdots & \ddots & \vdots \\ \tilde{\mathrm{O}}_{\mathrm{r}1\mathrm{l}} & \tilde{\mathrm{O}}_{\mathrm{r}2\mathrm{l}} & \cdots & \tilde{\mathrm{O}}_{\mathrm{rrl}} \end{bmatrix},$$

and

$$\tilde{\mathcal{Q}}_{ijl} = \begin{bmatrix} \frac{1}{2}\left(\Gamma_i + \Gamma_j\right) & * & * & * & * & * & * \\ 0 & -\delta I & * & * & * & * & * \\ 0 & 0 & \eta I & * & * & * & * \\ -\Phi_{ij} & \frac{1}{2}\left(U_{ij} + U_{ji}\right) & 0 & -X_l & * & * & * \\ N_{2i}L & 0 & N_{3i} & 0 & -I & * & * \\ N_{2i}L & 0 & 0 & 0 & 0 & -I & * \\ N_1 L & 0 & 0 & 0 & 0 & 0 & -I \end{bmatrix}$$

$$\tilde{O}_l = \mathrm{diag}\left[W_{11l} \quad \cdots \quad W_{rrl} \right]$$

where Γ_i, Φ_{ij} are expressed by (20a), matrices M_{ij} and U_{ij} are defined in (14c), and N_1, N_{2i}, L are given by (20b), (21b) respectively.

Proof. Let $V\left(\tilde{x}_k^f\right)$ denote the following candidate Lyapunov function:

$$V\left(\tilde{x}_k^f\right) = \tilde{x}_k^{fT} \mathcal{P}_\mu \tilde{x}_k^f \tag{25}$$

where $\mathcal{P}_\mu$ is a symmetric positive definite matrix. Note that we seek to minimize the $\mathcal{L}_2$-gain of the transfer from u_k to the estimation error vector e_k^f, this is formulated by:

$$\sum_{k=0}^{\infty} e_f^T(k) e_f(k) \le \lambda^2 \sum_{k=0}^{\infty} u^T(k) u(k) \tag{26}$$

Then we get by considering (15):

$$\begin{aligned} J_- &= \sum_{k=0}^{\infty} r^T(k) r(k) - \beta^2 \sum_{k=0}^{\infty} f^T(k) f(k) \\ &= \sum_{k=0}^{\infty} \left[r_k^{fT} r_k^f - \beta^2 f_k^T f_k - \Delta V\left(\tilde{x}_k^f\right) \right] + V\left(\tilde{x}_k^f\right) \\ &= \sum_{k=0}^{\infty} \Big[\left[C^* e_k^f + D_f f_k \right]^T V^T V \left[C^* e_k^f + D_f f_k \right] \\ &\quad -\beta^2 f_k^T f_k - \tilde{x}_{k+1}^{fT} \mathcal{P}_{\mu^+} \tilde{x}_{k+1}^f - \tilde{x}_k^{fT} \mathcal{P}_\mu \tilde{x}_k^f \Big] + V\left(\tilde{x}_k^f\right) \\ &= \sum_{k=0}^{\infty} \left(\mathcal{X}^T \left(\Lambda_{\mu\hat{\mu}}^T \bar{\mathcal{P}}_{\mu^+} \Lambda_{\mu\hat{\mu}} - \tilde{\mathcal{P}}_\mu \right) \mathcal{X} + V\left(\tilde{x}_k^f\right) \right) \end{aligned} \tag{27}$$

where

$$\Lambda_{\mu\hat{\mu}} = \begin{bmatrix} M_{\mu\hat{\mu}} & U_{\mu\hat{\mu}} & 0 \\ N_1 & 0 & 0 \\ N_{2i} & 0 & N_{3i} \end{bmatrix}, \quad \bar{\mathcal{P}}_{\mu^+} = \begin{bmatrix} \mathcal{P}_{\mu^+} & 0 & 0 \\ 0 & I & 0 \\ 0 & 0 & I \end{bmatrix}, \quad \tilde{\mathcal{P}}_{\mu} = \begin{bmatrix} \mathcal{P}_{\mu} & 0 & 0 \\ 0 & \lambda^2 I & 0 \\ 0 & 0 & \beta^2 I \end{bmatrix},$$
$$N_{3i} = \begin{bmatrix} \mathbb{S}_i D_f & 0 \\ 0 & 0 \end{bmatrix}, \quad \mathcal{X} = \begin{bmatrix} \tilde{x}_k^f \\ u \\ f \end{bmatrix}$$

Using Lemma A.1 one can obtain:

$$J_- = \sum_{k=0}^{\infty} \left(\mathcal{X}^T \left\{ \Lambda_{\mu\mu}^T \bar{\mathcal{P}}_{\mu^+} \Lambda_{\mu\mu} - \tilde{\mathcal{P}}_{\mu} + \left[\left(\Lambda_{\mu\hat{\mu}} + \Lambda_{\mu\hat{\mu}} \right)^T \bar{\mathcal{P}}_{\mu^+} \left(\Lambda_{\mu\hat{\mu}} + \Lambda_{\mu\hat{\mu}} \right) - \tilde{\mathcal{P}}_{\mu} \right] \right\} \mathcal{X} + V\left(\tilde{x}_k^f \right) \right) \tag{28}$$

Now define

$$\bar{\Lambda}_{\mu\hat{\mu}\mu^+} = \begin{bmatrix} K_{\mu\hat{\mu}} & * & * \\ -U_{\mu\hat{\mu}}^T \mathcal{P}_{\mu}^+ M_{\mu\hat{\mu}} & -U_{\mu\hat{\mu}}^T \mathcal{P}_{\mu}^+ U_{\mu\hat{\mu}} + \lambda^2 I & * \\ N_{3i}^T N_{2i} & 0 & N_{3i}^T N_{3i} - \beta^2 I \end{bmatrix} \tag{29}$$

with

$$K_{\mu\hat{\mu}} = -M_{\mu\hat{\mu}}^T \mathcal{P}_{\mu}^+ M_{\mu\hat{\mu}} + N_1^T N_1 + N_{2i}^T N_{2i} + \mathcal{P}_{\mu}$$

and rewrite (28) as

$$J_- = \mathcal{X}^T \left\{ \bar{\Lambda}_{\mu\mu\mu^+} + 2 \left[\frac{\left(\bar{\Lambda}_{\mu\hat{\mu}\mu^+} + \overline{\Lambda}_{\hat{\mu}\mu\mu^+} \right)}{2} \right] \right\} \mathcal{X} \tag{30}$$

Hence if $\Lambda_{\mu\hat{\mu}\mu^+} \geq 0$, it follows that : $J_- \geq 0$, that is :

$$\bar{\Lambda}_{\mu\mu\mu^+} + 2 \left[\frac{\left(\bar{\Lambda}_{\mu\hat{\mu}\mu^+} + \bar{\Lambda}_{\hat{\mu}\mu\mu^+} \right)}{2} \right] \leq 0 \tag{31}$$

Following the same steps as in the proof of Theorem 1 and using linearization given by Corollary 1, the conditions (23) are fulfilled.

Remark 3. The objective is to find Θ, $\mathcal{F}$ and $\mathbb{S}_i$ which satisfy performance (9). However, as stated above, the H_- performance given by Theorem 2 leads to a non-linear problem in $\mathbb{S}_i$. To solve this problem, Lemma A.3 is used and the matrix $\tilde{\mathcal{Q}}_{ijl}$ in Theorem 2 is substituted by (32).

6 Mixed H_-/H_∞ Fault Detection Observer Design

In this section, a less conservative condition is proposed, towards a generalization of the previous results. The aim is to design a robust fault detection observer which generates residual signals that have the best robustness to disturbances, and the best sensitivity to fault. For that reason, the mix H_- and H_∞ performances is used to derive the following theorem:

Theorem 3. Consider the system (3) with observer (6), system (7) is asymptotically stable satisfying (8) and (9), for a given positive scalars $\varepsilon_1, \varepsilon_2, \varepsilon_3$, if there exist some symmetric positive definite matrices X_i , matrices L, T_1, T_2 and $\mathbb{S}_i$, R_{ijl}, W_{ijl} and scalars $\eta = \sqrt{\beta}$, $\rho = \sqrt{\gamma}$, $\delta = \sqrt{\lambda}$ such that LMI conditions (17) and (23) hold, with $\mathcal{Q}_{ijl}$ and $\tilde{\mathcal{Q}}_{ijl}$ defined by (21a) and (32) respectively. We deduce from (21d) the gains of the observer (6) satisfying the multi-objective H_-/H_∞ performance as following:

1. $\mathcal{F} = \left((T_2 - CT_1)\left(C\mathcal{L}_1^{11}\right)^{-1}\right)^{-1}$
2. $\Theta = T_1\left(R^{-1}\mathcal{C}\mathcal{L}_1^{11}\right)^{-1}$
3. and then F_j, K and E are computed from (13)

$$\tilde{\mathcal{Q}}_{ijl} = \begin{bmatrix} \frac{1}{2}(\Gamma_i + \Gamma_j) & * & * & * & * & * & * & * & * & * \\ 0 & -\delta I & * & * & * & * & * & * & * & * \\ 0 & 0 & \eta I & * & * & * & * & * & * & * \\ -\Phi_{ij} & \frac{1}{2}(U_{ij} + U_{ji}) & 0 & -X_l & * & * & * & * & * & * \\ 0 & 0 & N_{3i} & 0 & -I & * & * & * & * & * \\ N_1 L & 0 & 0 & 0 & 0 & -I & * & * & * & * \\ 0 & 0 & 0 & 0 & L & 0 & -\varepsilon_2 I & * & * & * \\ N_{2i} & 0 & 0 & 0 & 0 & 0 & 0 & -\varepsilon_2^{-1} I & * & * \\ 0 & 0 & 0 & 0 & 0 & L & 0 & 0 & -\varepsilon_3 I & * \\ N_{2i} & 0 & 0 & 0 & 0 & 0 & 0 & 0 & 0 & -\varepsilon_3^{-1} I \end{bmatrix} \tag{32}$$

7 Simulation Example

Let us consider the following discrete-time Takagi-Sugeno model:

$$\begin{cases} x_{k+1} = \sum_{i=1}^{r} \mu_i(\xi_k)(A_i x_k + B_i u_k + B_d d_k) \\ y_k = C x_k + D_f f_k \end{cases} \tag{33}$$

with

$$A_1 = \begin{bmatrix} 1 & -1.3 \\ -0.2 & 0.5 \end{bmatrix}, \quad A_2 = \begin{bmatrix} 1 & 1.3 \\ -0.2 & 0.5 \end{bmatrix}, \quad B_1 = \begin{bmatrix} 5.3 \\ 4.6 \end{bmatrix}, \quad B_2 = \begin{bmatrix} 4.7 \\ 4.6 \end{bmatrix}$$

$$C = \begin{bmatrix} 0.1 & 1 \\ 0 & 1 \end{bmatrix}, \quad D_f = \begin{bmatrix} 8 & 0 \\ 0 & 8 \end{bmatrix}, \quad B_d = \begin{bmatrix} 0.2 \\ 0.1 \end{bmatrix}$$

For simulation purpose, the weighting functions depend only on the first state variable x_k^1 . They are defined by the following membership functions:

$$\mu_1(x_k^1) = (1 - \sin(x_k^1))/2, \quad \mu_2(x_k^1) = 1 - \mu_1(x_k^1)$$

Let us consider the following fault signal $f(t) = (f_1(t) f_2(t))^T$ affecting the system behavior and described as follows:

$$f_1(k) = 0.1 * \sin(10(t - 0.4))e^{1.6t-10} \text{ occurs at } \begin{matrix} 6s \le t \le 9s \\ (60 \le k \le 90) \end{matrix}$$

$$f_2(k) = \begin{cases} 0.02(t-1) & \begin{matrix} 12s \le t < 14s \\ (20 \le k \le 40) \end{matrix} \\ 0.01(t-14) & \begin{matrix} 14s \le t \le 16s \\ (40 < k \le 60) \end{matrix} \\ 0 & \text{otherwise} \end{cases}$$

An unknown disturbance d_k with band-limited white noise as given by Fig. 1 is considered. Thus the simulation results are illustrated by the following figures.

To show the sensitivity of the residual signal $r(t)$ to the faults f_1, f_2, we perform two simulations: In the first one, robustness against disturbance is considered by applying the Theorem 1 H_∞ conditions. The second case concerns the multi-objective H_-/H_∞ observer design where the Theorem 3 is applied. As a result, considering $\varepsilon_1 = \varepsilon_2 = 10$, $\varepsilon_3 = 2$, the level of disturbance attenuation γ is reduced to 0.96, the attenuation rate λ to 0.60, and the H_- index bound $\beta = 20.61$. Then one obtains the matrices $\mathbb{S}_i$, $\mathcal{F}$, Θ and L

$$\mathbb{S}_1 = \begin{bmatrix} 2.8147 & -2.4063 \\ -2.9983 & 3.5411 \end{bmatrix}, \quad \mathbb{S}_2 = \begin{bmatrix} 2.7547 & -2.3689 \\ -2.9568 & 3.4705 \end{bmatrix}$$

$$\mathcal{F} = \begin{bmatrix} -0.0081 & 0.0073 \\ -0.0080 & 0.0073 \end{bmatrix}, \quad \Theta = \begin{bmatrix} -10 & 10 \\ 230 & -208 \end{bmatrix}$$

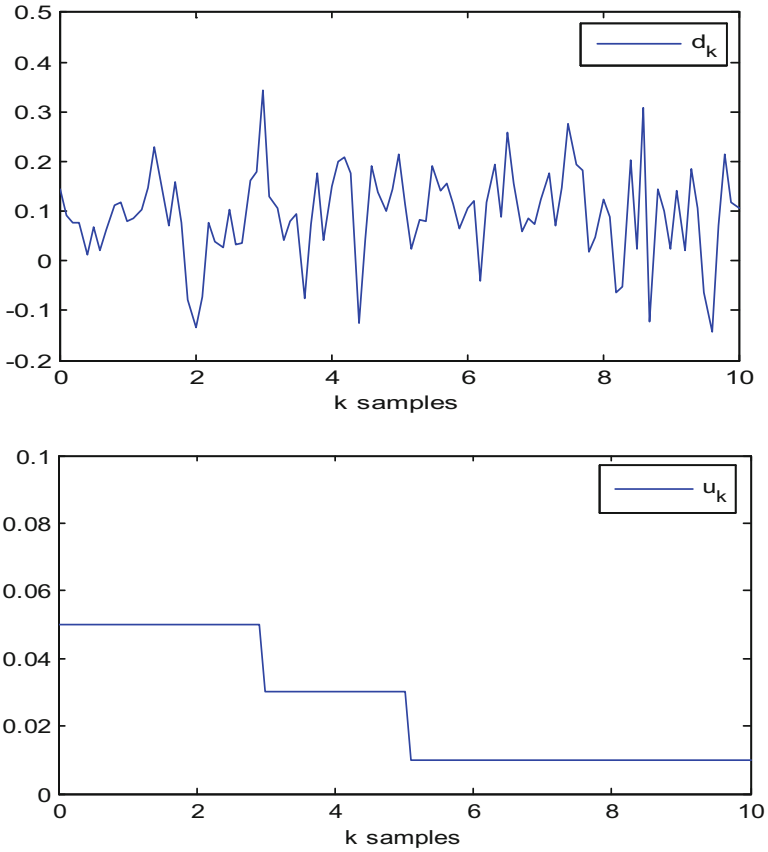

Fig. 1. Disturbance d(t) (top), inputs (bottom)

$$L = \begin{bmatrix} 0.0005 & -0.0001 & 0 & 0 & -0.5090 & -0.0060 \\ -0.0002 & -0.0008 & 0 & 0 & 0 & 0.0005 \\ 0 & 0 & 0 & 0 & 0.1229 & 0.0017 \\ 0 & 0 & 0 & 0 & -0.0001 & -0.0001 \\ -0.5090 & 0 & 0.1229 & -0.0001 & 70.6706 & 2.4924 \\ -0.0060 & 0.0005 & 0.0017 & -0.0001 & 1.7918 & 20.6290 \end{bmatrix}$$

The corresponding observer gain matrices and residual weighing matrix are:

$$F_1 = \begin{bmatrix} 1 & -1.3 & 0 & 0 \\ -0.2 & 0.5 & 0 & 0 \\ -0.1 & -1 & -1 & 0 \\ 0 & -1 & 0 & -1 \end{bmatrix}, \quad F_2 = \begin{bmatrix} 1 & 1.3 & 0 & 0 \\ -0.2 & 0.5 & 0 & 0 \\ -0.1 & -1 & -1 & 0 \\ 0 & -1 & 0 & -1 \end{bmatrix},$$

$$K = \begin{bmatrix} 0 & 0 & 1 & 0 \\ 0 & 0 & 0 & 1 \end{bmatrix}^T$$

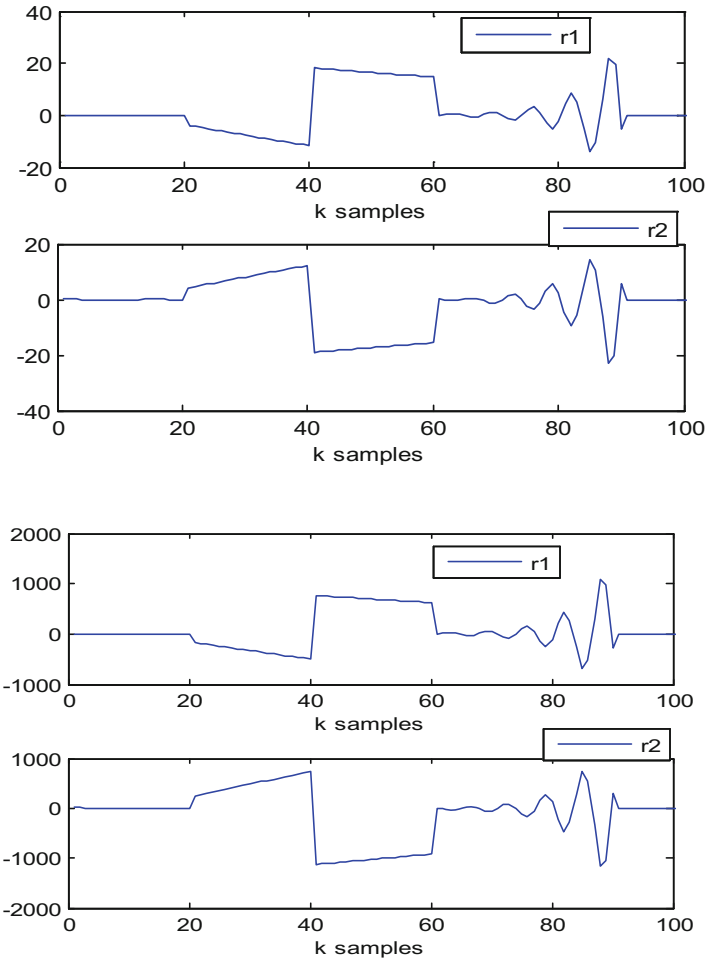

Fig. 2. Generated residuals r1, r2 Theorem 1 (top), Theorem 3 (bottom)

$$\mathrm{E} = \begin{bmatrix} -0.0000 & -0.0000 & -10.0000 & 10.0000 \\ 23.0000 & 23.0000 & 230.0000 & -208.0000 \\ -0.0008 & -0.0008 & -0.0081 & 0.0073 \\ -0.0008 & -0.0008 & -0.0080 & 0.0073 \end{bmatrix}$$

The Fig. 2 illustrates the residual trajectories of r_1 and r_2 generated from Theorems 1 and 3. Figure 3 shows estimation simulation result of both state and fault sensor affecting the system. From these latter, one can see that the synthesized observer shows their effectiveness, since the fault and the system states are well estimated. Figure 4 show simulation results of the output responses.

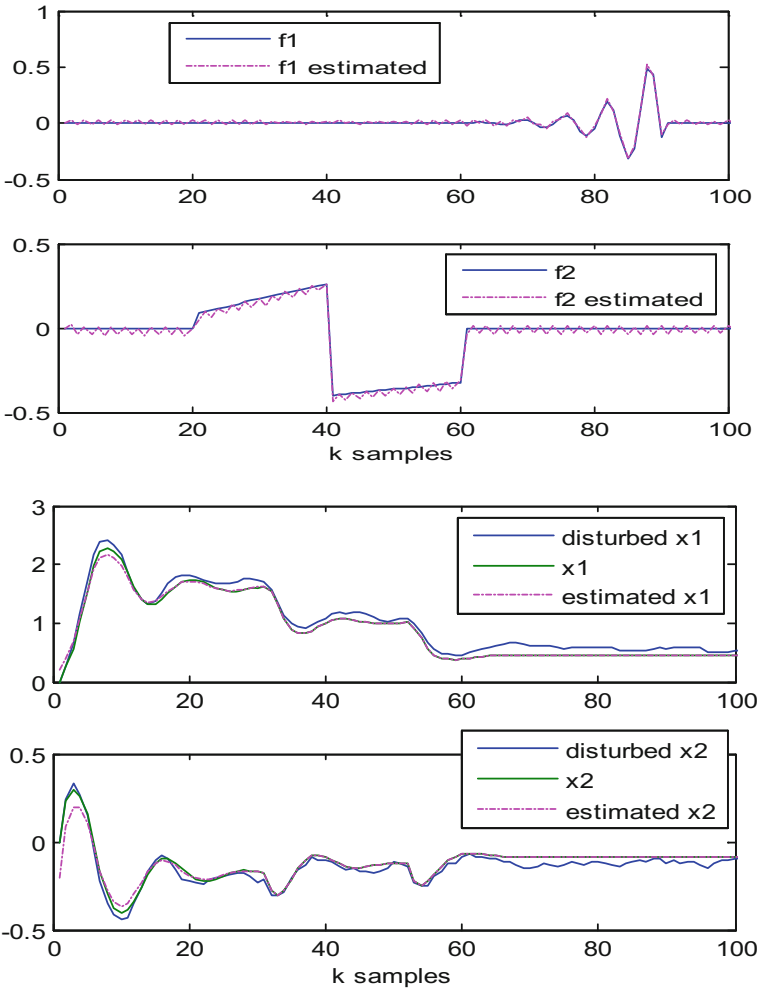

Fig. 3. Faults (f_1, f_2) and their estimates (top), states (x_1, x_2) and their estimates (bottom)

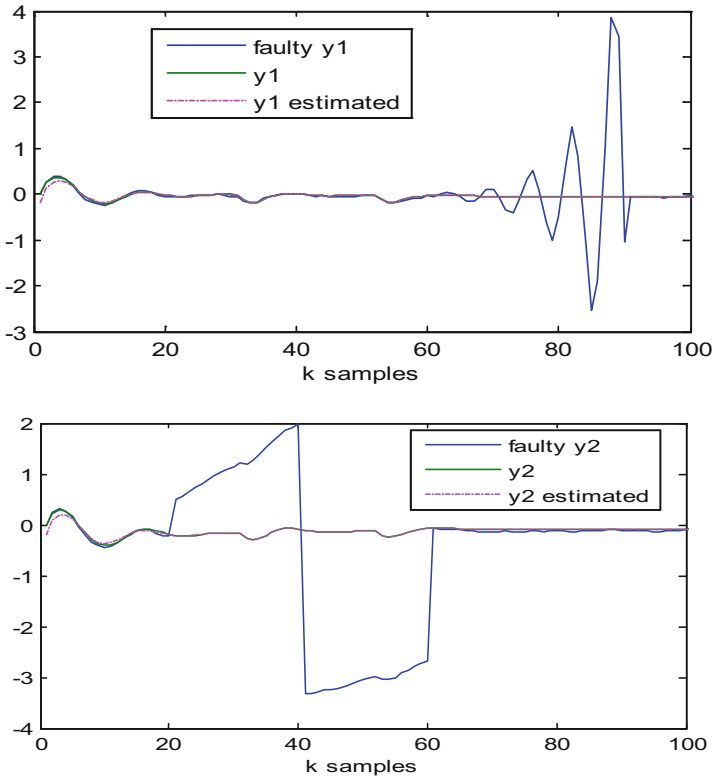

Fig. 4. Outputs (y_1, y_2) and their estimates

8 Conclusion

In this work, a multiobjective H_-/H_∞ fault detection observer has been designed for discrete-time T-S fuzzy model with unmeasurable premise variables subject to sensor faults and unknown bounded disturbances. By considering faults as an auxiliary state variable, different strategies were combined with fuzzy Lyapunov function and descriptor theory to promote the obtained LMI conditions. Simulation results are presented to show the effectiveness of the proposed approach.

Appendix A

The following Lemmas are required in the development of the Theorem 1 proof.

Lemma A.1. If $\Phi > 0$, then

$$\Xi_i^T \Phi \Xi_j + \Xi_j^T \Phi \Xi_i \leq \Xi_i^T \Phi \Xi_i + \Xi_j^T \Phi \Xi_j \tag{A.1}$$

Lemma A.2. if $Z > 0$, then

$$SZ^{-1}S^T \geq S^T + S - Z \tag{A.2}$$

Lemma A.3 [13]. Consider two real matrices X and Y with appropriate dimensions, for any positive scalar Ω the following inequality is verified:

$$X^T Y + Y^T X \leq X^T \Omega X + Y^T \Omega^{-1} Y \quad \Omega > 0 \tag{A.3}$$

Lemma B [14]. Consider the system (B.1). If there exist symmetric matrices X_i and any matrices L, such that the following stability conditions are satisfied for $i, j, l = 1, \cdots, r$

$$\Pi_l < 0, X_i > 0, \quad (i, l \in \mathcal{R}) \tag{B.1}$$

where

$$\Pi_l = \begin{bmatrix} \mathcal{Q}_{111} & * & \cdots & * \\ \mathcal{Q}_{211} & \mathcal{Q}_{22l} & \cdots & * \\ \vdots & \vdots & \ddots & \vdots \\ \mathcal{Q}_{r11} & \mathcal{Q}_{r2l} & \cdots & \mathcal{Q}_{rrl} \end{bmatrix} \tag{B.2}$$

$$\mathcal{Q}_{ijl} = \begin{bmatrix} \frac{1}{2}(\Gamma_i + \Gamma_j) & * \\ \frac{1}{2}(A_i + A_j)L & -X_l \end{bmatrix} \tag{B.3}$$

$$\Gamma_i = X_i - L^T - L \tag{B.4}$$

Then the closed loop fuzzy model is globally asymptotically stable.

References

1. Liang, W.J., Yang, G.-H., Liu, J.: An LMI approach to H_ index and mixed H_/H∞ fault detection observer design. Automatica **43**, 1656–1665 (2007)
2. Zhong, M., Ding, S.X., Lam, J., Wang, H.: An LMI approach to design robust fault filter for uncertain LTI systems. Automatica **39**, 543–550 (2003)
3. Gao, Z., Shi, X., Ding, S.-X.: Fuzzy state-disturbance observer design for T-S fuzzy systems with application to sensor fault estimation. IEEE Trans. SMC Part B **38**(3), 875–880 (2008)
4. Jaimoukha, I.M., Li, Z.: A matrix factorization solution to the H_/H∞ fault detection problem. Automatica **42**, 1907–1912 (2006)
5. Gao, Z., Ding, S.: Actuator fault robust estimation and fault tolerant control for a class of nonlinear descriptor systems. Automatica **43**, 912–920 (2007)
6. Aouaouda, S., Chadli, M., Cocquempot, V., Khadir, M.T.: Multi-objective H_/H∞ fault detection observer design for Takagi-Sugeno fuzzy systems with unmeasurable premise variables: descriptor approach. Int. J. Adapt. Control Signal Process. **27**(12), 1031–1047 (2013)
7. Yuesheng, L., Xinping, G.: Robust fault tolerant H2/H∞ controller design based on state feedback. In: Proceedings of IEEE International Conference on Automation and Logistics, Hong Kong and Macau, pp. 643–647 (2010)
8. Ding, B.C.: Quadratic boundedness via dynamic output feedback for constrained nonlinear systems in Takagi–Sugeno's form. Automatica **45**(5), 2093–2098 (2009)
9. Fang, C.H., Liu, Y.S., Kau, S.W., Hong, L., Lee, C.H.: A new LMI-based approach to relaxed quadratic stabilization of T-S fuzzy control systems. IEEE Trans. Fuzzy Syst. **14**(3), 386–397 (2006)
10. Boyd, S., El Ghaoui, L., Feron, E., Balakrishnan, V.: Linear matrix inequalities. In: System and Control Theory. SIAM Studies in Applied Mathematics, SIAM, Philadelphia, PA, USA, vol. 15 (1994)
11. Tanaka, K., Wang, H.O.: Fuzzy Control Systems Design and Analysis: A Linear Matrix Inequality Approach. Wiley, New York (2001)
12. Yoneyama, J.: H∞ filtering for fuzzy systems with immeasurable premise variables: an uncertain system approach. Fuzzy Sets Syst. **160**(12), 1738–1748 (2009)
13. Chadli, M., Hajjaji, A.E.: Comment on observer-based robust fuzzy control of nonlinear systems with parametric uncertainties. Fuzzy Sets Syst. **157**, 1276–1281 (2006)
14. Mozelli, L.A., Palhares, R.M.: Less conservative H∞ fuzzy control for discrete-time Takagi-Sugeno systems. Math. Prob. Eng. (2011). doi:10.1155/2011/361640
15. Aouaouda, S., Chadli, M., Karimi, H.R., Shi, P.: Robust fault tolerant tracking controller design for a VTOL aircraft. J. Franklin Inst. **9**, 2627–2645 (2013)
16. Chadli, M., Karimi, H.R., Shi, P.: On stability and stabilization of singular uncertain Takagi-Sugeno fuzzy systems. J. Franklin Inst. **351**(3), 1453–1463 (2014)

Feature Selection for Enhancement of Bearing Fault Detection and Diagnosis Based on Self-Organizing Map

Smail Haroun[1(✉)], Amirouche Nait Seghir[1], and Said Touati[2]

[1] Laboratoire des Systèmes Electriques et Industriels (LSEI), Faculté d'Électronique et Informatique, USTHB, BP 32 El Alia Bab Ezzouar, Algiers, Algeria
haroun.smail@yahoo.com, naitseghir_a@yahoo.fr
[2] Département de Génie Électrique (DGE), Centre de Recherche Nucleaire de Birine (CRNB), BP 180, Ain Oussera, Algeria
saidtouati@yahoo.fr

Abstract. Mechanical faults account for a large majority of the faults in the electrical rotating machinery, it can result in partial or total breakdown of a motor. Therefore, their diagnosis is an intensively investigated field of research. This paper investigates the application of the Self-Organizing Maps (SOM) for the detection of rolling element bearing damages in three phase induction motor. It discusses the integration of features selection methods in the fault classification system based on SOM. The bearings vibration signal is obtained from experiment in different conditions: normal bearing, bearing with inner race fault, bearing with outer race fault and bearings with balls fault. Then multiple features extraction techniques from time, frequency and time-frequency domains are used. ReliefF and min redundancy max Relevance (mRMR) features selection techniques are used to select the optimal features and reduce the dimension of calculated data. Finally, the SOM is used for classification of the different conditions. The obtained results show that the association of feature selection techniques to SOM classifier conduct to the improvement the classification performances of the fault detection process.

Keywords: Fault detection and diagnosis · Bearing faults · Feature selection · Self-Organizing map

1 Introduction

Electrical rotating machinery is very common in industrial applications, and represent the mainstay of various critical industries, from the turbine-compressor used in the petrochemical plants to the reactor coolant pump in nuclear power plants, that require accurate performance and continuous operation. Incipient Failures of these machines, if it left undetected, can lead to financial losses resulting from lapses in production, and even human lives fatalities.

The bearing failures is one of the principal causes of breakdown in rotating machines, it is responsible for about 41% of all machine failures [1]. Therefore,

M. Chadli et al. (eds.), *Recent Advances in Electrical Engineering and Control Applications*, Lecture Notes in Electrical Engineering 411, DOI 10.1007/978-3-319-48929-2_18

predicting incipient defects in bearings is quite necessary to avoid catastrophic malfunction and increase system availability. Thus, several techniques for bearing fault detection and diagnosis (FDD) have been reported in literature. Among these techniques, vibration analysis in the most used and well-known approach.

Vibration analysis Include many signal processing techniques [2], such as Auto Regressive (AR) Model parameters estimation [3], time domain analysis by monitoring the variation of some statistical parameters [4]. Frequency domain analysis is widely explored in vibration analysis using Fast Fourier Transform (FFT) for detecting the fault-related frequency components in the vibration spectrum [5]. However, these techniques are unsuitable for the analysis of non-stationary signals that are usually related to machinery defects. Therefore, time–frequency domain techniques were proposed. It's include Short Time Fourier Transform (STFT) [6], The S-transform [7], Empirical Mode Decomposition (EMD) [8], Wavelets, and Wavelet Packet Transform (WPT) [9–11].

The majority of these signal-processing techniques require a prior expert knowledge of the bearing defect frequency to accurate bearing failure detection and severity evaluation [3]. So, a decision-making process to classify the obtained features into different health condition categories is needed. Several automatic decision-making techniques have been reported in the literature, it includes Support vector machines (SVMs) [12], fuzzy technique [13], neuro-fuzzy inference system (ANFIS) [14], and many artificial neural networks as Multi-Layer Perceptron (MLP) [15], radial basis function (RBF) [16], Self-Organizing Map [17–19], and so on.

However, there are many effects that may obscure the detection of the bearing fault and cause false alarms. A diagnosis process based on multiple signatures, by combining different feature extraction methods should be more reliable in fault detection and reducing the effect of some misinterpreted signatures, but it can weighing down the classification process since much time is needed to calculate the results. So a subsequent necessary step to filter the most discriminative information is feature selection, which in general increases accuracy and reduces computational time of the fault classifier.

This paper aims at developing a bearing fault detection and severity evaluation methodology for based on multiple signature analysis extracted from time domain, frequency domain, and time-frequency domain of the vibration signal. For the classification process, the Self-Organizing Map (SOM) neural network was chosen as it has been applied successfully in many fault diagnosis applications. ReliefF and min Redundancy and max Relevancy (mRMR) methods as feature selection tools enhance the capability and the effectiveness of the SOM classifier.

The remainder of this paper is organized as follows: In Sect. 2 we present the theoretical back ground of the used feature selection methods and the SOM. The global bearing fault detection system is presented in Sect. 3. Section 4 presents the experimental implementation and results.

Conclusions and future works are shown in Sect. 5.

2 Theoretical Background

2.1 Feature Selection

The feature selection object is to select features that allow an accurate description of the bearing condition, and subsequently, reliable defect classification, and diagnosis [20]. At present, several feature selection algorithms have been proposed in recent literatures such as genetic algorithm [21], principle component analysis [22], sequential backward selection algorithm (SBS), minimum redundancy maximum relevancy (mRMR) algorithm [23], and Relief [24].

2.2 ReliefF Feature Selection

ReliefF is a simple yet efficient procedure to estimate the quality of attributes in problems with strong dependencies between attributes [25]. In practice, ReliefF is usually applied in data pre-processing as a feature subset selection method.

The key idea of the ReliefF is to estimate the quality of attributes according to how well their values distinguish between instances that are near to each other. Given a randomly selected instance *Insm* from class *L*, ReliefF searches for *K* of its nearest neighbors from the same class called nearest hits *H*, and also *K* nearest neighbors from each of the different classes, called nearest misses *M*. It then updates the quality estimation *Wi* for attribute *i* based on their values for *Insm*, *H,* and *M*. If instance *Insm* and those in *H* have different values on attribute *i*, then the quality estimation *Wi* is decreased. On the other hand, if instance *Insm* and those in *M* have different values on the attribute *i*, then *Wi* is increased. The whole process is repeated *n* times which is set by users. The algorithm is shown in Fig. 1 and updating W_i can use Eq. 1.

```
Input : Gene variables and labels
Output : W for the gene rank
Set all weights W:=0;
Foreach Iteration n do
|   Randomly select an instance Ins_m;
|   Find K nearest hits H;
|   Foreach class c ≠ Label_m do
|   |   From class c find K nearest misses M_c;
|   End
|   Foreach g_i do
|   |   Update W_i ;
|   End
End
```

Fig. 1. The reliefF algorithm.

$$W_i = W_i - \frac{\sum_{k=1}^{K} D_H}{n.K} + \sum_{c=1}^{C-1} P_c . \frac{\sum_{k=1}^{K} D_{H_c}}{n.K} \quad (1)$$

where nc is the number of instances in class c, D_H (or D_{Mc}) is the sum of distance between the selected instance and each H (or M_C), P_C is the prior probability of class c.

Detailed discussions on ReliefF can be found in [25].

2.3 Minimum Redundancy and Maximum Relevancy (MRMR)

The mRMR method is a filter based feature selection algorithm which measures the relevance and redundancy of the feature candidates based on mutual information, and selects the most relevant features that has maximal relevance and minimal redundancy [23]. Given g_i which represents the feature i, and the class label c, their mutual information is defined in terms of their frequencies of appearances $p\ (g_i)$, $p\ (c)$, and $p\ (g_i,\ c)$ as follows.

$$I(g_i, c) = \iint p(g_i, c) \ln \frac{p(g_i, c)}{p(g_i)p(c)} dg_i dc \quad (2)$$

The Maximum-Relevance method selects the top m features in the descent order of $I\ (g_i,\ c)$, i.e. the best m individual features correlated to the class labels.

$$\max_S \frac{1}{|S|} \sum_{g_i \in S} I(g_i, c) \quad (3)$$

Features selected based on Max-Relevance only can have a lot of redundancy because the dependency among these features is very large. Therefore, Min-Redundancy criteria is introduced:

$$\min_S \frac{1}{|S|^2} \sum_{g_i, g_j \in S} I(g_i, g_j) \quad (4)$$

The minimum redundancy – maximum relevance feature selection framework is obtained by optimizing the conditions in Eqs. (3) and (4) simultaneously.

2.4 Self-Organizing Map (SOM)

The Self-Organizing Map (also known as Kohonen map) is an unsupervised artificial neural network which is a powerful method for clustering and visualization of high dimensional data [26]. The SOM algorithm implements a nonlinear topology preserving mapping from a high-dimensional input data space onto a low dimension discrete space, called the topological map.

A SOM model is composed by two layers of neurons. The first is called input layer (composed by N neurons, one for each input variable), the second is the output layer (formed by M neurons) is in charge of information processing and the construction of map features. Usually, neurons in the output layer are organized in two-dimensional map [27], as shown in Fig. 2. Note that each neuron of the network is completely connected to all the nodes of the input layer. The number of neurons determines the accuracy and generalization capability of the SOM and it is determined by the heuristic equation:

$$M = 5\sqrt{N} \tag{5}$$

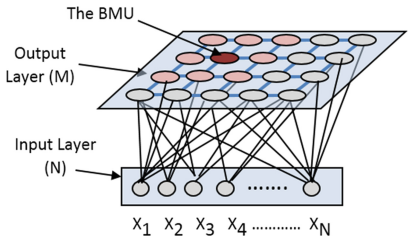

Fig. 2. SOM architecture.

Where M is the number of neurons and N is the number of samples of the training data. According to Eq. (6), the ratio between side-lengths of the map (n_1 and n_2) is the square root of the ratio between the two biggest eigenvalues of the training data (e_1 and e_2) [26].

$$n_1/n_2 = \sqrt{e_1/e_2} \tag{6}$$

During training phase, the weight vectors are adapted in such a way that close observations in the input space would activate two close neurons of the SOM [29]. The SOM is trained iteratively. At each training step, a sample input data vectors X is randomly presented from the training data sets, and the distance between the data and all the weight vectors of the SOM is calculated. The neuron whose weight vector is closest to the input vector is called the best-matching unit, often denoted *bmu*:

$$\|X - W_{bmu}\| = \min i\{\ \|X - W_i\|\}, \quad i \in \{1, \ldots, m\} \tag{7}$$

where W_{bmu} is the best-matching unit weight vector.

After finding the *bmu*, the weight vectors of the SOM are updated. The weight vectors of the *bmu* and its topological neighbors are moved closer to the input data vector. The weight-updating rule of the unit i is:

$$W_i(\tau + 1) = W_i(\tau) + \varepsilon(\tau) h_{bmu}(i, \tau)[X(\tau) - W_i(\tau)] \tag{8}$$

Where τ is time, $\varepsilon(\tau)$ is a learning rate and $h_{bmu}(i, \tau)$ is defined as the neighborhood kernel function around the *bmu*. Usually, $\varepsilon(\tau)$ is a decreasing function of time

and should be between 0 and 1. In this paper the Gaussian neighborhood function is chosen.

After the training phase of the SOM, the map quality should be evaluated by calculating the two parameters: quantization (*QE*) and topographic (*TE*) error. Lower *QE* and *TE* values specify superior mapping quality.

The quantization error *QE* indicates the quality of learning of a SOM and shows how well neurons of the trained network adapt to the input vectors [29] given by:

$$QE = \frac{\sum_{i=1}^{m} d(x_i, m_c)}{m} \tag{9}$$

where m_c is the reference vector associated to the *bmu* of x_i:

$$c = \arg_j \min\{ d(x_i, m_j) \} \tag{10}$$

$D\ (x_i, m_c)$ is the Euclidean distance, m is the number of input patterns.

Topographic error (*TE*) represents the proportion of all data vectors for which the first and second bmus are not closest to measure the topology preservation [29].

The *TE* represents the accuracy of the mapping in the preserving topology. It can be computed in the map as follows:

$$TE = \frac{1}{N} \sum_{k=1}^{N} u(x_k) \tag{11}$$

Where N is the number of input samples, and $u(x_k)$ is 1 if the first and second bmus of x_k are not next to each other, otherwise $u(x_k)$ is 0.

3 Proposed Fault Diagnosis System

The adopted fault diagnosis procedure is based on vibration signal analysis, which are acquired by accelerometers from test motors.

Then Feature extraction by combining most relevant techniques used in literature from time domain, frequency domain and time-frequency domain. In order to reduce the data set and improve the fault diagnosis, two feature selection methods are used: ReliefF and min Redundancy and Max Relevance technique. At the end, the Self Organising Map neural network is used as a classifier. The developed algorithm is depicted by the block diagram in Fig. 3.

3.1 Feature Extraction

A. Statistical Features. Time domain features often involve statistical features that are sensitive to impulse faults [4], in present work, ten (10) statistical parameters are extracted from the measured vibration signal. The mathematical expression of these parameters can be found in Table 1.

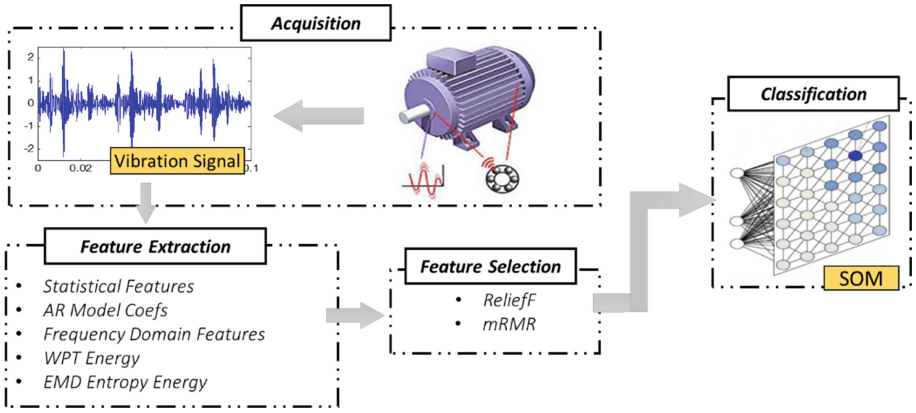

Fig. 3. Framework of the proposed intelligent fault diagnosis system.

B. Frequency Domain Features. Frequency domain analysis is another description of a signal that can reveal some information which cannot be found in the time domain [2]. In addition to the bearing fault-related characteristic frequencies components, e.g., the ball-pass frequency of outer ring (BPFO), ball-pass frequency of inner ring (BPFI), and ball-spin frequency (BSF) [30] presented in Table 2, 13 statistical features

Table 1. Time and frequency domain features.

Features from Time domain	Features from Frequency domain
$X_m = \frac{1}{n}\sum_{i=1}^{n} x_i$ $X_{PPV} = (\max(x_i) - \min(x_i))/2$ $X_{RMS} = \sqrt{\frac{1}{N}\sum_{i=1}^{n}(x_i^2)}$ $\sigma = \sqrt{\frac{1}{N}\sum_{i=1}^{N}(x_i - \overline{x})^2}$ $X_{KURT} = \frac{1}{N}\sum_{i=1}^{n}\left(\frac{x_i - \overline{x}}{\sigma}\right)^4$ $X_{SKEW} = \frac{1}{N}\sum_{i=1}^{n}\left(\frac{x_i - \overline{x}}{\sigma}\right)^3$ $X_{CLI} = \max\lvert x_i\rvert / \left(\frac{1}{N}\sum_{i=1}^{n}\sqrt{\lvert x_i\rvert}\right)^2$ $X_{IF} = \max(\lvert x_i\rvert) / \frac{1}{N}\sum_{i=1}^{n}\lvert x_i\rvert$ $X_{CF} = \max\lvert x_i\rvert / \sqrt{\frac{1}{N}\sum_{i=1}^{n}(x_i^2)}$ $X_{SF} = \sqrt{\frac{1}{N}\sum_{i=1}^{n}(x_i^2)} / \frac{1}{N}\sum_{i=1}^{n}\sqrt{\lvert x_i\rvert}$ where x_i is a vibration signal samples for $i = 1,2,\ldots,N$, N is the number of data samples	$F_1 = \sum_{k=1}^{K} s(k)/K$ $F_2 = \sum_{k=1}^{K}(s(k) - F_1)^2/(K-1)$ $F_3 = \sum_{k=1}^{K}(s(k) - F_1)^3 / \left(K(\sqrt{F_2})^3\right)$ $F_4 = \sum_{k=1}^{K}(s(k) - F_1)^4 / KF_2^2$ $F_5 = \sum_{k=1}^{K} f_k s(k) / \sum_{k=1}^{K} s(k)$ $F_6 = \sqrt{\sum_{k=1}^{K}(f_k - F_5)^2 s(k)/K}$ $F_7 = \sqrt{\sum_{k=1}^{K} f_k^2 s(k) / \sum_{k=1}^{K} s(k)}$ $F_8 = \sqrt{\sum_{k=1}^{K} f_k^4 s(k) / \sum_{k=1}^{K} f_k^2 s(k)}$ $F_9 = \frac{\sum_{k=1}^{K} f_k^2 s(k)}{\sqrt{\sum_{k=1}^{K} s(k) \sum_{k=1}^{K} f_k^4 s(k)}}$ $F_{10} = F_6/F_5$ $F_{11} = \sum_{k=1}^{K}(f_k - F_5)^3 s(k)/KF_6^3$ $F_{12} = \sum_{k=1}^{K}(f_k - F_5)^4 s(k)/KF_6^4$ $F_{13} = \frac{\sum_{k=1}^{K}(f_k - F_5)^{1/2} s(k)}{K\sqrt{F_6}}$ where $s(k)$ is a spectrum for $k = 1,2,\ldots,K$, K is the number of spectrum lines; f_k is the frequency value of the k^{th} spectrum line

(F1–F13), are extracted from the frequency spectrums of the vibration signal envelope [31]. These features are defined as presented in Table 1.

Table 2. Bearing fault-related frequencies components

Frequency component	Ball-pass frequency of outer ring (BPFO)	Ball-pass frequency of inner ring (BPFI)	Ball-spin frequency (BSF)
Expression	$\frac{N}{2}\left[f_i\left(1-\frac{d\cos(\theta)}{D}\right)\right]$	$\frac{N}{2}\left[f_i\left(1+\frac{d\cos(\theta)}{D}\right)\right]$	$\frac{D}{2d}f_i\left[1-\left(\frac{d\cos(\theta)}{D}\right)^2\right]$

where f_i is the shaft speed in; d is the diameter of the rolling element; D is the pitch diameter; θ is the contact angle.

C. AR Model Coefficients. Autoregressive (AR) model is a time sequence analysis method whose parameters comprise important information of the system condition. Therefore, the coefficients of the AR model can be effectively used to analyze the condition variation of dynamic systems [3]. The AR model of the vibration signal x_i (t) is given as:

$$x_i(t) + \sum_{k=1}^{m} \varphi_k x_i(t-k) = e(t) \tag{12}$$

where m is the order of the AR model and φ_k (k = 1, 2…m) are the coefficients of the AR model of x_i (t), $e(t)$ is the remnant of the model and is a white noises sequence whose mean value is zero and variance is σ^2.

In this study, the first 30 coefficients φ_k (k = 1, 2…,30) are chosen as vector to identify the bearing condition.

D. Wavelet Packet Decomposition Analysis. A wavelet packet transform is a simple generalization of a wavelet transform, it plays an important role in many aspects such as signal de-noising, filter, compression, the analysis and fault diagnosis about the non-stationary vibration signal of the mechanical and the technique of multi-carrier modulation. By applying 3-layer wavelet packet decomposition to the original vibration signal using "sym 6" as mother wavelet, we get at the third layer eight WPD coefficients noted R_{3j} (j = 0,1,…,7). Then the energy of each one of these coefficients is calculated according to the Eq. (13).

$$E_{3J} = \sqrt{\sum_{i=1}^{n} |R_{3J}(i)|^2} \tag{13}$$

E. EMD Entropy Energy. The EMD method proposed by Huang [32] is a technique which is able to decompose a non-stationary signal into some intrinsic mode functions (IMFs). An IMF is a function that satisfies the two following definitions: (1) in the whole data set, the number of extrema and the number of zero-crossings must either equal or differ at most by one, and (2) at any point, the mean value of the envelope

defined by local maxima and the envelope defined by the local minima is zero. The detail description of the EMD method can be found in [32].

The IMFs c_1,c_2,…,c_M include different frequency bands ranging from high to low. The frequency components contained in each frequency band are different and they change with the variation of the original signal [24].

In this paper, the first six IMFs containing almost all valid information are selected. Then the energy entropy (I_{EE}) is calculated from the IMFs according to the equation:

$$I_{EE} = -\sum_{i=1}^{M} P_E(i) \log P_E(i) \tag{14}$$

Where P_E is the normalized energy distribution. PE can be defined as:

$$P_E(\mathrm{i}) = E_i / \sum_{i=1}^{M} E_i \tag{15}$$

Now, a feature set containing 71 features is achieved, which simultaneously covers the most significant features from time domain, frequency domain and the time-frequency domain.

4 Experimental Implementation

4.1 Experimental Data

The proposed fault detection method is applied to bearing fault vibration data obtained from the Bearing Data Centre of Case Western Reserve University [33]. In this experiment, vibration signals are collected at a rate of 12 kHz from accelerometer mounted on the motor housing at the drive end of the three phase induction motor which is connected to a dynamometer as load as shown in Fig. 4.

In this work, we study four different operating conditions: normal condition (NO), outer race fault (ORF), inner race fault (IRF), and ball fault (BF), with fault diameters of 0.007 inches, 0.014 inches and 0.021 inches. All the experiments were repeated for four different load conditions: 0, 1, 2 and 3 Hp.

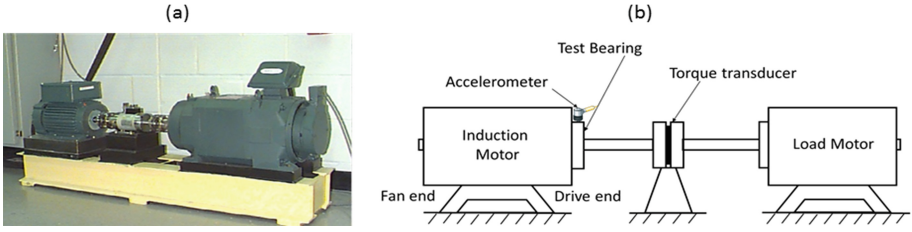

Fig. 4. The bearing test stand (a), and its Schematic diagram (b).

The collected experimental data are decomposed into 1120 samples (112 representatives from each case) of 4096 data points in length., Then the features were calculated from each signal to construct a data-base (size is 1120 × 71). Two thirds of this database serve to train the SOM, and the rest were kept for the testing. The self-organizing map network was implemented by using the SOM toolbox [28].

A classification process is constructed for testing the performance of proposed diagnosis system, it consists on a ten-class classifier corresponding to the four operating conditions with different extent of faults. A label is associated to each case as presented in Table 3.

Table 3. Description of classification task

Bearing condition	Defect size (inch)	Assigned labels
Normal		NO
Ball Fault	0.007	BF1
	0.014	BF2
	0.021	BF3
Inner Race Fault	0.007	IR1
	0.014	IR2
	0.021	IR3
Outer Race Fault	0.007	OR1
	0.014	OR2
	0.021	OR3

4.2 Results and Discussion

After feature calculation and data set construction, we present data set to dimensionality reduction based on ReliefF and mRMR Feature selection approaches.

Figure 5 present the classification accuracy of the SOM versus the number of selected features by the two methods feature selection algorithms for the classification task. According to these figures we can note that using 33 features selected by ReleliefF we get 100% in term of classification accuracy which means there is no false alarms or misclassified cases, versus 99.75% using 44 features selected by mRMR. While we get 99% using all the features together.

More performances parameters of the two selection methods and the classification using all the data set, which are: training time, quantization error, topographic error, and training and test accuracy are presented in Table 3.

For better visualization, analysis and get an overview of the classification performance status using all extracted features and those selected by the two methods reliefF and mRMR, the presented information on the Table 4 are illustrated as a performance radar chart in Fig. 6. Each axis on the chart corresponds to a column on the table, except the two last columns (training and test accuracy) which are replaced by training and test error. For that, the chart who a reduced area is the better case since it has the reduced training time, lower *QE* and *TE* and minimum of training and testing errors.

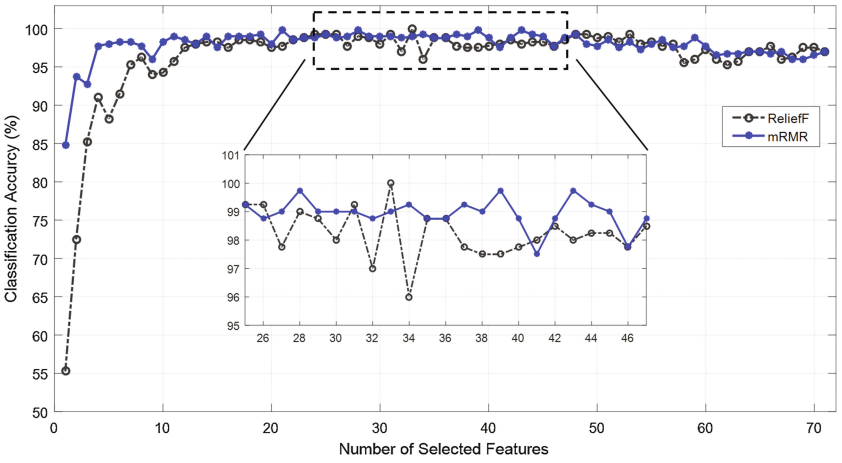

Fig. 5. Classification performance versus number of selected features.

Table 4. Classification results of the two classification tasks.

	Number of features	Training time (s)	*QE*	*TE*	Training (%)	Test (%)
All	70	1,435	2,887	0,018	97,91	97
Relief	33	0,234	1,292	0,009	99,58	100
mRMR	39	0,25	1,625	0,034	100	99,75

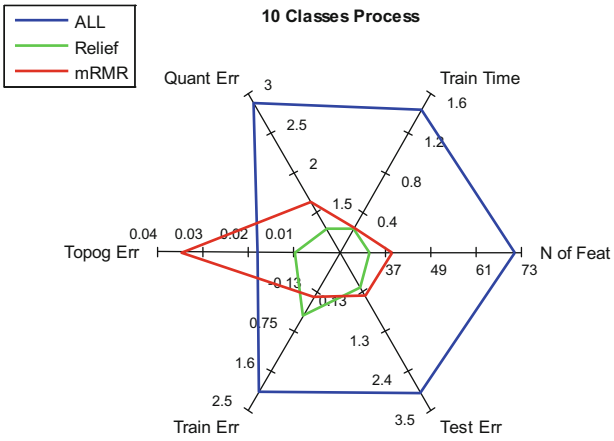

Fig. 6. Performance radar chart.

From this figure we can note that the training of the SOM using the selected features by the ReliefF and the mRMR features selection techniques is much better than the training using the whole training data set in term of the classification performances and the training Time.

By comparing the results of the two features selection methods, we see that the ReliefF feature selection technique is more reliable where we get best or at least the same classification performances, with a reduced number of selected features comparing to the mRMR feature selection.

5 Conclusion

This study presents a methodology for detection of bearing faults in electric motors based on self-organizing map (SOM) and feature selection techniques. This methodology incorporates multiple signature analysis techniques from time, frequency, and time-frequency domains.

From the experimental results, we can say that the fault diagnosis and classification accuracy of the SOM using the feature selection methods was clearly higher than those using the whole data set. In addition, the quality of the learned map and the training time greatly improved as well.

We can then conclude that the proposed approach is a very attractive tool for bearing fault detection and diagnosis in electric motors, because it is not only possible to detect the bearing faults, but it is also able to locate the fault and estimate the extent of the faults by separating the different faulty conditions.

In a future work, further investigation will be conducted t applicate this strategy to pother mechanical faults and to the implementation on real time application.

References

1. IAS Motor Reliability Working Group: Report of large motor reliability survey of industrial and commercial installations: Part I and Part II. IEEE Trans. Ind. Appl. 21(4), 853–872 (1985)
2. Bhende, A.R., Awari, G.K., Untawale, S.P.: Assessment of bearing fault detection using vibration signal analysis. VSRD-TNTJ **2**(5), 249–261 (2011)
3. Ayaz, E.: Autoregressive modeling based bearing fault detection in induction motors. In: IX Symposium Industrial Electronics INDEL, Banja Luka (2012)
4. Lei, Y., He, Z., Zi, Y.: New approach to intelligent fault diagnosis of rotating machinery. Expert Syst. Appl. **35**, 1593–1600 (2008)
5. Mechefske, C.K., Mathew, J.: Fault detection and diagnosis in low speed rolling element bearings Part I: the use of parametric spectra. Mech. Syst. Signal Process. **6**, 297–307 (1992)
6. Kaewkongka, T., Au, Y., Rakowski, R., Jones, B.: A comparative study of short time Fourier transform and continuous wavelet transform for bearing condition monitoring. Int. J. COMADEM **6**, 41–48 (2003)
7. Hou, Z., Yang, J., Zhang, X.: Bearing defect diagnosis based on S-transform and singular value ratio spectrum. J. Comput. Inf. Syst. **6**(10), 3285–3292 (2010)

8. Lei, Y., Lin, J., He, Z., Zuo, M.J.: A review on empirical mode decomposition in fault diagnosis of rotating machinery. Mech. Syst. Signal Process. **35**, 108–126 (2013)
9. Yadav, M., Wadhwani, S.: Automatic fault classification of rolling element bearing using wavelet packet decomposition and artificial neural network. Int. J. Eng. Technol. **3**(4), 270–276 (2011)
10. Wei, Z., Gao, J., Zhong, X., Jiang, Z., Ma, B.: Incipient fault diagnosis of rolling element bearing based on wavelet packet transform and energy operator. WSEAS Trans. Syst. **10**(3), 81–90 (2011)
11. Yan, R., Gao, R.X., Chen, X.: Wavelets for fault diagnosis of rotary machines: A review with applications. Sig. Process. **96**, 1–15 (2014)
12. Sugumaran, V., Ramachandran, K.I.: Effect of number of features on classification of roller bearing faults using SVM and PSVM. Expert Syst. Appl. **38**, 4088–4096 (2011)
13. Chen, Y.: A fuzzy decision system for fault classification using high levels of uncertainty. Trans. ASME J. Dyn. Syst. Meas. Control **117**, 108–115 (1995)
14. Samhouri, M., Al-Ghandoor, A., Alhaj Ali, S., Hinti, I., Massad, W.: An intelligent machine condition monitoring system using time-based analysis: neuro-fuzzy versus neural network. Jordan J. Mech. Ind. Eng. **3**(4), 294–305 (2009)
15. Zarei, J.: Induction motors bearing fault detection using pattern recognition techniques. Expert Syst. Appl. **39**, 68–73 (2012)
16. Onel, I.Y., Dalci, K.B., Senol, I.: Detection of bearing defects in three-phase induction motors using park's transform and radial basis function neural networks. Sadhana **31**(3), 235–244 (2006)
17. Moshou, D., Kateris, D., Sawalhi, N., Loutridis, S., Gravalos, I.: Fault severity estimation in rotating mechanical systems using feature based fusion and self-organizing maps. In: Diamantaras, K., Duch, W., Iliadis, L.S. (eds.) ICANN 2010. LNCS, vol. 6353, pp. 410–413. Springer, Heidelberg (2010). doi:10.1007/978-3-642-15822-3_49
18. Hu, J., Zhang, L., Liang, W.: Degradation assessment of bearing fault using SOM network. In: Seventh International Conference on Natural Computation ICNC 2011, pp. 561–565. IEEE (2011)
19. Beia, J., Lu, C., Tao, X., Wang, Z.: Performance assessment for rolling bearing based on EMD and SOM. In: FITMSE 2012. Lecture Notes in Information Technology, vol. 14, pp. 95–99 (2012)
20. Haroun, S., Seghir, A.N., Touati, S.: Stator faults detection and diagnosis in reactor coolant pump using kohonen self-organizing map. In: Amine, A., Otmane, A.M., Bellatreche, L. (eds.) Modeling Approaches and Algorithms for Advanced Computer Applications. Studies in Computational Intelligence, vol. 488, pp. 17–26. Springer, Heidelberg (2013)
21. Nguyen, N.T., Lee, H.H., Kwon, J.M.: Optimal feature selection using genetic algorithm for mechanical fault detection of induction motor. J. Mech. Sci. Technol. **22**(3), 490–496 (2008)
22. Malhi, A., Gao, R.X.: PCA-based feature selection scheme for machine defect classification. IEEE Trans. Instrum. Meas. **53**(6), 1517–1525 (2004)
23. Peng, H., Long, F., Ding, C.: Feature selection based on mutual information criteria of max-dependency, max-relevance, and min-redundancy. IEEE Trans. Pattern Anal. Mach. Intell. **27**(8), 1226–1238 (2005)
24. Li, B., Zhang, P., Ren, G., Xing, Z.: A two stage feature selection method for gear fault diagnosis using ReliefF and GA-Wrapper. In: International Conference on Measuring Technology and Mechatronics Automation, pp. 578–581 (2009)
25. Robink-Sikonja, M., Kononenko, I.: Theoretical and empirical analysis of relifF and RreliefF. Mach. Learn. J. **53**, 23–69 (2003)
26. Kohonen, T.: Self-Organizing Maps. Springer, Heidelberg (2001)

27. Bossio, J.M., De Angelo, C.H.: Self-organizing map approach for classification of mechanical and rotor faults on induction motors. Neural Comput. Appl. **23**, 41–51 (2013)
28. Vesanto, J., Himberg, J., Alhoniemi, E., Parhankangas, J.: Self-organizing map in matlab: the SOM toolbox. In: Proceedings of the Matlab, DSP Conference, pp. 35–40 (1999). http://www.cis.hut.fi/projects/somtoolbox
29. Kivilnoto, K.: Topology preservation in self-organizing maps. In: Proceedings of IEEE International Conference on Neural Networks ICNN 1996, pp. 294–299 (1996)
30. Harris, T.: Rolling Bearing Analysis, 3rd edn. Wiley, New York (1991)
31. Lei, Y., He, Z., Zi, Y.: New approach to intelligent fault diagnosis of rotating machinery. Expert Syst. Appl. **35**, 1593–1600 (2008)
32. Huang, N.E.: New method for nonlinear and nonstationary time series analysis: Empirical mode decomposition and hilbert spectral analysis. In: AeroSense 2000 International Society for Optics and Photonics, pp. 197–209 (2000)
33. Case Western Reserve University. Bearing data centre. http://www.eecs.cwru.edu/laborator/bearing

Small Signal Fractional Order Modeling of PN Junction Diode

F. Boulgamh[1(✉)], M. Remram[2], and A. Djouambi[1]

[1] Département des Sciences et Sciences Appliquées,
Université Larbi Ben M'Hidi, 04000 Oum-El-Bouaghi, Algeria
fel_boulgamh@yahoo.fr, djouambi_abdelbaki@yahoo.fr
[2] Département d'Electronique, Université Constantine 1,
Route Ain El-bey, 25011 Constantine, Algeria
moh_remram@yahoo.fr

Abstract. This paper deals with the dynamical fractional order model of PN junction diode based small signal equivalent circuits. With the advent of fractional calculus, it is seen that these concepts would have several advantages and applications in such fields. We present various small signal *PN* junction equivalent circuit models including their frequency responses. The equivalent models presented utilize the concepts of fractional calculus. Experimental data are used to validate the proposed approach.

Keywords: Fractional order models · PN junction · Diffusive systems · Small signal equivalent circuit models

1 Introduction

The diode is one of the most important elements used in modern electronic systems. It is used as a device in many applications such as rectifiers, variable capacitors, detectors, etc. [1]. However, diodes are difficult to model quantitatively.

One of the reason for this difficulty is that diode conduction is related to that the width of the intrinsic bulk region is a function of applied voltage. The conduction includes nonlinear carrier diffusion and a nonlinear junction capacitor. Also, the PN diode Model has a nonlinear I-V characteristics and tunable C-V characteristics [2].

In practice, diodes are used for digital and analog applications. In analog applications, the device is biased at some DC value. There are many cases where diodes are operated with small AC signals around a DC offset voltage. In such a case, conventional linear small-signal diode models are usually used. In forward bias, a diode is modeled with two components: a diode resistance r_d, and charge storage capacitance C_{SC}. In reverse bias, a diode is represented with only the depletion capacitance C_d. However, due to the non linear nature of these devices, conventional models may be note appropriate to represent its frequency behavior at high frequency.

Many researchers started building more or less complicated models in order to explain the small signal PN junction Diode behavior. Some authors focused on small signal PN junction Diode modeling using half-order systems [3]. Also, the dynamic

M. Chadli et al. (eds.), *Recent Advances in Electrical Engineering and Control Applications*,
Lecture Notes in Electrical Engineering 411, DOI 10.1007/978-3-319-48929-2_19

behavior of Diode has been modeled using the technique based on impedance frequency response [4, 5].

Fractional (or non integer order) systems are considered as a generalization of integer order systems [6, 7]. The advantages of fractional form become apparent in modeling mechanical and electrical properties of real devices as well as in the theory of dynamical systems. Sometimes, mathematical modeling of processes and physical phenomena leads to differential equations of fractional orders and so fractional order calculus is necessary to explain their behavior.

In this paper, small signal fractional order models of PN junction diodes is presented. Using the frequency measurements made, we will generalize, to fractional order, the small signal elements models, and use them to construct fractional order equivalent circuit of PN junction diode around the operating point.

2 Diode AC Small Signal Impedance-Experimental Setup

Ac small signal diode response is usually used to understand its frequency behavior [8–10]. Figure 1 presents the experimental setup used to frequency response measurements made. The diode is biased with a *dc* voltage V_{dc} superposed with an *ac* signal v_{in}. The Output signals v_s and i_s will be then measured a cross the diode and resistor R respectively. We can then consider frequency response of the transfer function representing the admittance G_s given by:

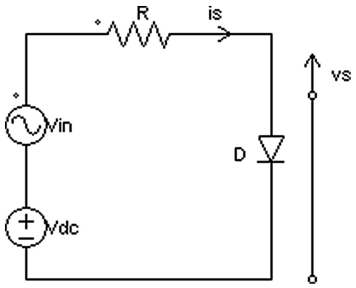

Fig. 1. Electrical circuit of ac-small signal experiment

$$\frac{I_s(f)}{V_s(f)} = \frac{1}{Z_s} = G_s \tag{1}$$

2.1 Diode Elements

In forward biased case using DC voltage V_{dc} superposed to an ac small signal V_{in}, the diode equivalent circuit can be considered as a resistance R_s, a junction capacitance C_j and a diffusion capacitance C_{diff} connected as shown in Fig. 3. Reference [3] is used to determine these elements. The small signal capacitance is, generally, given by the following equation:

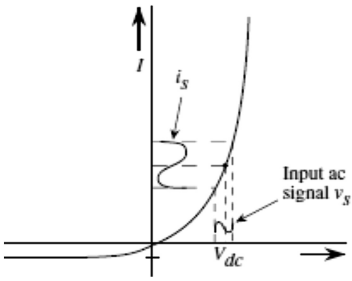

Fig. 2. Current changes in a diode under ac-small signal conditions.

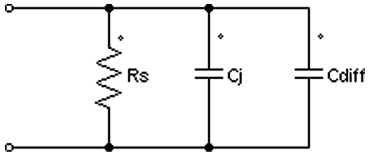

Fig. 3. The equivalent circuit of a forward biased diode.

$$C = \left|\frac{dQ}{dV}\right| = \frac{C_{j0}}{\left(1 - \frac{V}{V_{bi}}\right)^{1/2}} \tag{2}$$

where C_{jO} is the capacitance at zero applied bias, V the applied voltage and V_{bi} the built-in voltage.

In real diodes, the doping in the n-side and p-side gradually changes from n- region to p-one. In this case, the junction capacitance is given by:

$$C_j = \frac{C_{j0}}{\left(1 - \frac{V}{V_{bi}}\right)^{m_g}} \tag{3}$$

with m_g the grading parameter ($m_g = 1/2$ for abrupt junctions and $m_g = 1/3$ for graded ones).

We note that in reverse biased conditions, the junction capacitance is dominant. However, in direct polarization it can be neglected. The diffusion capacitance is due to the injected charge density. For injected hole charge, the diffusion capacitance can be given by:

$$C_{diff} = \frac{dQ_p}{dV} = \frac{q}{k_B T} I \tau_p \tag{4}$$

With q the electron charge, k_B the Boltzmann constant, T the temperature in Kelvin, τ_p the hole lifetime, and I is the dc current.

Finally, using the ac small signal response, the *ac* diode resistance R_s is given by:

$$R_s = \frac{dV}{dI} = \frac{k_B T/q}{I(V)} \tag{5}$$

We note that this resistance only holds at low frequencies.

2.2 Integer Order Models

(a) *Analytical model*

By considering a PN diode under forward-biased voltage V_{dc} as shown in Fig. 1, if an *ac* signal is superposed to the *dc* voltage, the current changes as shown in Fig. 2.

The small signal equivalent circuit of the diode is then given in Fig. 3.

Under forward bias conditions, the junction capacitance is neglected and using the equivalent circuit, the relationship between the current i_s and the applied voltage v_s is given by:

$$i_s = G_s v_s + C_{diff} \frac{dv_s}{dt} \tag{6}$$

In frequency domain, we will have:

$$i_s = \left(G_s + j\omega C_{diff}\right) v_s / G_s = 1/r_s \tag{7}$$

and the diode impedance is given by:

$$Z_s = \frac{v_s}{i_s} = \frac{1}{G_s + j\omega C_{diff}} = \frac{r_s}{\left(1 + j\omega r_s C_{diff}\right)} \tag{8}$$

To find G_s and C_{diff}, we have to use the time dependant continuity equation [3]. The solution of this equation enables us to calculate the current i_s which is found to be:

$$i_s = \frac{qI}{k_B T} \sqrt{1 + j\omega\tau_p} \cdot v_s \tag{9}$$

Then, the ac small signal impedance is:

$$Z_s = \frac{i_s}{v_s} = K_s \frac{1}{\left(1 + j\omega\tau_p\right)^{1/2}} \tag{10}$$

with $K_s = (k_B T/qI)$.

(b) *Classical model*

We will start now with the classical model of a PN diode represented in Fig. 4 [11]. The first component of the model is the series resistance R_s. This one incorporates the contact resistance and the resistance of the quasi-neutral region. A second resistance R_p is the probe resistance.

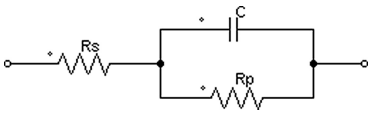

Fig. 4. Equivalent circuit of a pn diode under ac-small signal conditions

In parallel with R_p, the model take into account the diode capacitance C which arises from the junction capacitance C_j related to the depletion region and the diffusion capacitance C_{diff} due to injected carriers outside the depletion region. We note that under forward bias conditions, the diffusion capacitance dominates.

In the complex domain, an expression analogous to Ohm law is:

$$v = Z_c \cdot i \tag{11}$$

where Z_c is the circuit impedance given by:

$$Z_c = \frac{R_p}{1 + CR_p \cdot j\omega} + R_s \tag{12}$$

This expression can be written as:

$$Z_c = K_c \frac{1 + \tau_1(j\omega)}{1 + \tau_2(j\omega)} \tag{13}$$

with $K_1 = (R_p + R_s)$, $\tau_1 = \frac{CR_pR_s}{R_p + R_s}$ and $\tau_2 = CR_p$.

Here, we note that the impedance is expressed as a complex function with two time constants τ_1 and τ_2. Then, $Z_c(\omega)$ have a real and imaginary part which can be well represented by Bode plot.

3 Fractional Order Models

Fractional systems are considered as a generalization of integer order systems [6]. In this section, a generalized form of the above mentioned conventional models will be considered.

The generalization of the analytical model given by (10) in implicit fractional order form can be given by:

$$Z_s = \frac{K_{sf}}{1 + (j\omega\tau_p)^m} \tag{14}$$

where m is real number.

In the other hand, the corresponding implicit fractional order form of the classical model given by (13), is expressed by:

$$Z_{cf} = K_{cf} \frac{1 + (j\omega\tau_1)^{m_1}}{1 + (j\omega\tau_2)^{m_2}} \tag{15}$$

where m_1 and m_2 are real numbers.

4 Experimental Results

4.1 Analytical and Classical Models

To validate models described above, we use the ac small signal circuit of Fig. 1. To discuss results and for Bode diagram [8].

Data from which we have to identify the diode model is the frequency response of an *ac* small signal experiment. We applied a biased *dc* voltage $V_p = 15\text{V}$ to a BY402 diode and we superpose an *ac* signal $v_{in}(t) = V_0 sin\omega t$ with $V_0 = 4.4V$ and $\omega = 2\pi f$. We measure responses i_s and v_s in the frequency range $\left[10^4, 1.1 \cdot 10^5\right]$ Hz, and thus the impedance transfer function $Z_s(f) = \frac{v_s}{i_s}$ will be fitted according to the measured data. Figure 5 shows the Bode magnitude diagrams of such system using analytical and classical models.

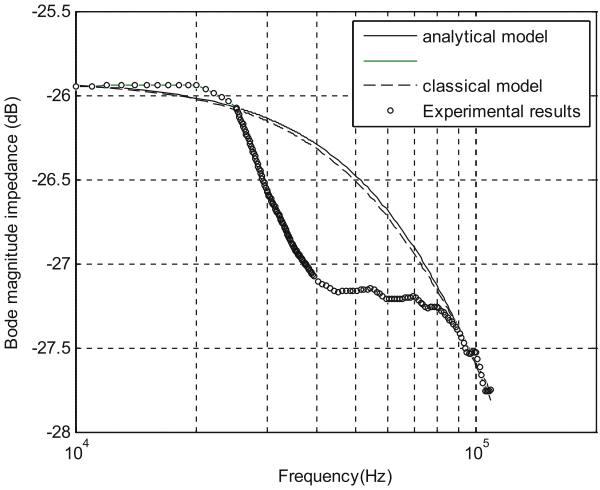

Fig. 5. Experimental diode impedance fitted by analytical and classical models.

From these results, we conclude that the analytical and classical models give the same results. At low and high frequencies, experimental curve is well fitted with $K_s = 50,6 \cdot 10^{-3}$, $\tau = 1,085 \cdot 10^{-5}\text{s}(\omega_c = 1/\tau = 9.22 \cdot 10^4\ \text{rad/s})$

Remember that at high frequencies, the asymptotic Bode diagram for analytical model is approximate to be:

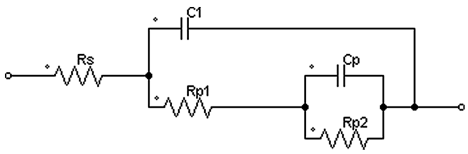

Fig. 6. Proposed equivalent circuit for a pn diode under small signal conditions

$$|Z_s|_{dB} \approx -10Log(\omega\tau) \tag{16}$$

which present a slope of $-10\,\mathrm{dB/dec}$.

In the other hand, *classical model* of the diode is an integer system with one pole and one zero. Asymptotic Bode diagram of such system can be approximated, at high frequencies, by:

$$|Z|_{dB} \approx 20Log\left(\frac{\tau_1}{\tau_2}\right) \tag{17}$$

The best fitting of the curve is obtained for $K = 50,6 \cdot 10^{-3}$, $\tau_2 = 1,009 \cdot 10^{-5}$ s, $\tau_1 = 6.0 \cdot 10^{-6}$. Remember that $\omega_{c1} = 1/\tau_1 = 1.7 \cdot 10^5$ rad/s is out of the range of frequencies used for experimental data $\left(\left[10^4, 1,09 \cdot 10^5\right]\right)$. In this frequency range, the system is described by the expression:

$$Z_c = K_c \frac{1}{1 + j\omega\tau_2} \tag{18}$$

which is a first order system having one pole and then a slope of $-20\,\mathrm{dB/dec}$.

4.2 Fractional Model with One Zero and One Pole

Reporting to experimental data, we found that the magnitude Bode diagram of diode impedance is well fitted by classical model only at low and high frequencies.

In order to well approximate experimental curve at intermediate frequencies, we use the fractional order generalized model. That is because the electrical impedance of a diode is related to conduction phenomena, based on carrier diffusion in the *PN* junction, which, generally, present a fractional behavior.

Then, the implicit fractional order form of classical model is given by (15).

The best fitting of experimental data using this model is obtained for: $K_{cf} = 51.5 \cdot 10^{-3}$, $m_1 = 0.6677$, $m_2 = 0.79$, $\tau_1 = 4.5 \cdot 10^{-7}$ s, $\tau_2 = 52.6 \cdot 10^{-7}$ s. The results are reported in Fig. 7. It can clearly be seen that this fractional model takes into account intermediate frequencies, but it can't describe precisely the behavior of the system in such frequencies.

That's for which we propose another fractional model with one zero and two poles.

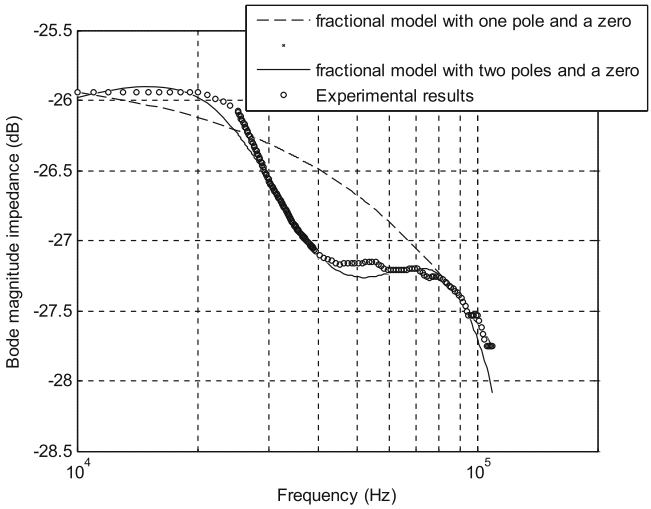

Fig. 7. Experimental diode impedance fitted by classical and proposed fractional models.

4.3 Fractional Model with One Zero and Two Poles

In this model, we use the Warburg impedance [12, 13]. Thus, the diode electrical impedance is presented by the electrical circuit of Fig. 6.

This circuit yield to a second order system with two poles and a zero. In his implicit fractional form, it is defined by the following expression:

$$Z_f = K_f \frac{\left(1 + \left(j\omega\tau_{1f}\right)^{m_{1f}}\right)}{\left(\left(1 + \left(j\omega\tau_{2f}\right)^{m_{2f}}\right)\left(1 + \left(j\omega\tau_{3f}\right)^{m_{3f}}\right)\right)} \tag{19}$$

The best fitting of experimental data is obtained for:

$K_f = 48.5 \cdot 10^{-3}$, $m_{1f} = 1.3300$, $m_{2f} = 1.3450$, $m_{3f} = 1.361$, $\tau_{1f} = 2.7165 \cdot 10^{-5}$ s, $\tau_{2f} = 3.2999 \cdot 10^{-5}$ s, $\tau_{3f} = 8.9 \cdot 10^{-5}$ s.

5 Conclusion

In this paper, we used the ac-small-signal impedance to model the PN junction diode using experimental data. In this experiment, the diode is considered as an integer or fractional order dynamical system. Then, to identify zero and poles of such system, we use the frequency response of the device using magnitude Bode plot.

The identification method was based on finding the proposed model parameters (poles, zero and fractional orders) using experimental data.

Several models were proposed and their equivalent electrical circuits were presented. First, we start with an analytical model obtained from physical study of conduction phenomena in diodes. This yields to a 0.5 order system with one pole.

Secondly, a classical model based on the diode equivalent circuit was used. It is presented as an integer order system with one pole and a zero.

These models gave the same results and fit well the experimental data only at low and high frequencies.

The third model used is the classical model generalized in the fractional form. This model takes into account the intermediate frequencies but it doesn't give well fitted results.

The fractional model which present the best fitting is that described by a zero and two poles with fractional orders upper than the unity.

References

1. Pulfrey, D.L.: Understanding Modern Transistors and Diodes, pp. 138–324. Cambridge University Press, Cambridge (2010)
2. Zhang, H., Pappas, J.A.: A moving boundary diffusion model for PIN diodes. IEEE Trans. Magn. **37**(1), 406–410 (2001)
3. Mushra, U.K., Singh, J.: Semiconductor Device Physics and Design, pp. 304–318. Springer, Netherlands (2008)
4. Oustaloup, A., Lanusse, P., Levron, F.: Frequency-domain synthesis of a filter using viète root functions. IEEE Trans. Autom. Control **47**(5), 837–841 (2002)
5. Valerio, D., Ortigueira, M.D., da Costa, J.S.: Identifying a transfer function from frequency response. Trans. ASME J. Comput. Nonlinear Dyn. **3**, 021207 (2008)
6. Oldham, K.B., Spanier, J.: The Fractional Calculus: Theory and Applications of Differentiation and Integration to Arbitrary Order. Springer (2006)
7. Sabatier, J., Agrawal, O.P., Tenreiro Machado, J.A.: Advances in Fractional Calculus: Theoretical Developments and Applications in Physics and Engineering. Springer, Netherlands (2006)
8. Ghanbari, M., Haeri, M.: Order and pole locator estimation in fractional order systems using bode diagram. Signal Process. **91**(2), 191–202 (2011)
9. Valério, D., Costa, J.: Identification of fractional models from frequency data. In: Advances in Fractional Calculus, Part 4, pp. 229–242 (2007)
10. Valerio, D., Ortigueira, M.D., da Costa, J.S.: Identifying a transfer function from a frequency response. J. Comput. Nonlinear Dyn. **3**(2), 021207 (2008)
11. Schroder, D.K.: Semiconductor Material and Device Characterization. 2nd edn., pp. 133–200. Wiley, New York (1998)
12. Barsoukov, E., Macdonald, J.R.: Impedance Spectroscopy-Theory, Experiment, and Applications, 2nd edn., pp. 205–537. Wiley, Hoboken (2005)
13. Sekushin, N.A.: Equivalent circuit of Warburg Impedance. Russ. J. Electrochem. **45**(7), 828–832 (2009)

Fractional Order Systems (Sofa)

Rational Function Approximation of a Fundamental Fractional Order Transfer Function

Djamel Boucherma[1(✉)], Abdelfatah Charef[2], and Hassene Nezzari[1]

[1] Research Center in Industrial Technologies (CRTI), P.O. Box 64, 16014 Cheraga, Algiers, Algeria
djamelboucherma25@yahoo.com, nezzarih@yahoo.fr
[2] Département d'Electronique, Université des frères Mentouri, Constantine, Algeria
afcharef@yahoo.com

Abstract. This paper introduces a rational function approximation of the fractional order transfer function $H(s) = \frac{(\tau_0 s)^{\alpha}}{[1+(\tau_0 s)^{2\alpha}]}$, *for* $0 < \alpha \leq 0.5$. This fractional order transfer function is one of the fundamental functions of the linear fractional system of commensurate order corresponding to pure complex conjugate poles or eigenvalues, in s^{α}. Hence, the proposed approximation will be used in the solution of the linear fractional systems of commensurate order. Illustrative examples are given to show the exactitude and the efficiency of the approximation method.

Keywords: Fractional power zero · Linear fractional system · Irrational transfer function · Rational transfer function

1 Introduction

The theory of fractional order systems has gained some importance during the last decades (Miller et al. 1993), (Podlubny 1999), (Kilbas et al. 2006), (Monje et al. 2010), (Caponetto et al. 2010). Therefore, active research work to find accurate and efficient methods to solve linear fractional order differential equations is still underway to establish a clear linear fractional order system theory accessible to the general engineering community. More recently, a great deal of effort has been expended in the development of analytical techniques to solve them. The goal of these methods is to derive an explicit analytical expression for the general solution of the linear fractional differential equations (Charef 2006a), (Bonilla et al. 2007), (Oturanç et al. 2008), (Hu et al. 2008), (Arikoglu et al. 2009), (Odibat 2010), (Charef et al. 2011).

A linear single input single output (SISO) fractional system of commensurate order is described by the following linear fractional order differential equation:

$$\sum_{i=0}^{N} a_i D^{i\alpha} y(t) = \sum_{j=0}^{M} b_j D^{j\alpha} u(t) \tag{1}$$

M. Chadli et al. (eds.), *Recent Advances in Electrical Engineering and Control Applications*, Lecture Notes in Electrical Engineering 411, DOI 10.1007/978-3-319-48929-2_20

where u(t) is the input, y(t) is the output, α is a real number such that $0 < \alpha < 1$, a_i ($1 \leq i \leq N$) and b_i ($0 \leq j \leq M$) are constant real numbers with $M \leq N$. With zero initial conditions, the fractional order system transfer function is given as:

$$G(s) = \frac{Y(s)}{U(s)} = \frac{\sum_{j=0}^{M} b_j (s^\alpha)^j}{\sum_{i=0}^{N} a_i (s^\alpha)^i} \tag{2}$$

This fractional transfer function can be decomposed into several elementary fundamental functions corresponding to different types of poles, in s^α, as:

$$G(s) = \sum_{k=1}^{K} H_k(s) \tag{3}$$

where the functions $H_k(s)$ are given, according to the poles of the fractional system, as:

- For a simple real pole:

$$H_k(s) = \frac{1}{(s^\alpha + p)} \tag{4}$$

- For a pair of complex poles with negative real part:

$$H_k(s) = \frac{\omega_n^2}{[s^{2\alpha} + 2\zeta\omega_n s^\alpha + \omega_n^2]} \tag{5}$$

$$H_k(s) = \frac{s^\alpha + \omega_n \zeta}{[s^{2\alpha} + 2\zeta\omega_n s^\alpha + \omega_n^2]} \tag{6}$$

- For a pair of complex poles with null real part:

$$H_k(s) = \frac{\omega_n^2}{[s^{2\alpha} + \omega_n^2]} \tag{7}$$

$$H_k(s) = \frac{\omega_n s^\alpha}{[s^{2\alpha} + \omega_n^2]} \tag{8}$$

In previous works (Charef 2006a) and (Charef et al. 2011), (Nezzari et al. 2011), (Boucherma et al. 2011), the elementary fundamental functions defined in (4), (5), (6) and (7) have been approximated by rational ones in order to represent them by linear

time-invariant system models so as to derive their closed form impulse and step responses as well as their performance characteristics. Using these approximations, simple analog circuits have been also derived to represent the above irrational functions of the fractional order system. This paper gives a rational function approximation of the fundamental function represented by the irrational transfer function of (8) which corresponds to pure complex conjugate poles or eigenvalues, in s^{α}. In (Boucherma et al. 2011), the approximation of (8) has been done for $0.5 < \alpha < 1$. In this work the approximation of (8) will be done for $0 < \alpha \leq 0.5$. First, the basic ideas and the derived formulations of the approximation technique are presented. Then, the impulse and step responses of this type of fractional system are derived. Finally, illustrative examples are presented to show the exactitude and the usefulness of the approximation method.

2 Rational Function Approximation

For $(\tau_0)^{\alpha} = \frac{1}{\omega_n}$, (8) can be rewritten as:

$$H(s) = \frac{X(s)}{E(s)} = \frac{(\tau_0 s)^{\alpha}}{[1 + (\tau_0 s)^{2\alpha}]}, \quad 0 < \alpha \leq 0.5 \tag{9}$$

The above irrational function is the transfer function of the linear fractional order system represented by the following fundamental linear fractional order differential equation:

$$(\tau_0)^{2\alpha} \frac{d^{2\alpha} x(t)}{dt^{2\alpha}} + x(t) = (\tau_0)^{\alpha} \frac{d^{\alpha} e(t)}{dt^{\alpha}} \tag{10}$$

In this context, the transfer function of (9) has two pure complex conjugate poles, in s^{α}. To represent the linear fractional order system of (10) by a linear time-invariant system model so as to derive their closed form impulse and step responses, its irrational transfer function of (9) will be approximated by a rational function. To do so, we will consider two cases based on the fractional derivative α.

2.1 Case 1: 0 < α < 0.5

For this case, the function of (9) can be decomposed in two functions as follows:

$$H(s) = H_1(s) \times H_2(s) = (\tau_0 s)^{\alpha} \times \frac{1}{1 + (\tau_0 s)^{2\alpha}} \tag{11}$$

where $H_1(s) = (\tau_0 s)^{\alpha}$ and $H_2(s) = \frac{1}{1 + (\tau_0 s)^{2\alpha}}$.

In a given frequency band of interest $[\omega_L, \omega_H]$, around the frequency $\omega_0 = (1/\tau_0)$, the fractional order differentiator $H_1(s) = (\tau_0 s)^{\alpha}$ can be approximated by a rational function as follows (b, 2006):

$$H_1(s) = (\tau_0 s)^{\alpha} \cong \tau_0^{\alpha} \left[K_D \frac{\prod_{i=0}^{N_1} \left(1 + \frac{s}{z_i}\right)}{\prod_{i=0}^{N_1} \left(1 + \frac{s}{p_i}\right)} \right] \tag{12}$$

where the poles pi and the zeros z_i ($0 \leq i \leq N1$), the constant K_D and the number N1 of the approximation are given by:

$$\begin{gathered} p_i = p_0\ (ab)^i,\ z_i = z_0\ (ab)^i, K_D = (\omega_c)^{\alpha}, \\ N_1 = \left\{ Integer \left[\frac{\log(\omega_{\max}/z_0)}{\log(ab)} \right] + 1 \right\} \end{gathered} \tag{13}$$

For some given real values y (dB), δ and β, the approximation parameters a, b, p_0, z_0, ω_c and ω_{max} can be calculated as:

$$\begin{gathered} a = 10^{\left[\frac{y}{10(1-\alpha)}\right]}, b = 10^{\left[\frac{y}{10\alpha}\right]}, \omega_c = \delta\omega_L, \\ \omega_{\max} = \beta\omega_H,\ z_0 = \omega_c\sqrt{b}\ and\ p_0 = az_0 \end{gathered} \tag{14}$$

By the decomposition of the rational function of (12), we will get:

$$H_1(s) = (\tau_0 s)^{\alpha} \cong \tau_0^{\alpha} \left(K_D + \sum_{i=0}^{N_1} \frac{k_i s}{\left(1 + \frac{s}{p_i}\right)} \right) \tag{15}$$

$$k_i = -\frac{K_D}{p_0 (ab)^i} \frac{\prod_{j=0}^{N_1} \left(1 - a(ab)^{(i-j)}\right)}{\prod_{j=0, i \neq j}^{N_1} \left(1 - (ab)^{(i-j)}\right)}, i = 0, 1, \ldots, N1 \tag{16}$$

Because $0 < \alpha < 0.5$ the number 2α is then $0 < 2\alpha < 1$; hence, in a given frequency band $[0, \omega_H]$, the fractional system $H_2(s) = \frac{1}{1 + (\tau_0 s)^{2\alpha}}$ can be approximated by a rational function as follows (Charef 2006a):

$$H_2(s) = \frac{1}{1 + (\tau_0 s)^{2\alpha}} \cong \sum_{j=1}^{2N_2 - 1} \frac{kk_j}{\left(1 + \frac{s}{pp_j}\right)} \tag{17}$$

where the poles pp_j and the residues kk_j (for $1 \leq j \leq 2N_2 - 1$), and the number N_2 of the approximation are given, for some given real values λ and β, by:

$$
\begin{aligned}
pp_j &= \frac{(\lambda)^{(j-N)}}{\tau_0} \\
kk_j &= \frac{1}{2\pi}\left[\frac{\sin[(1-\alpha)\pi]}{\cosh[\alpha\,\log(\frac{1}{\tau_0 pp_j})] - \cos[(1-\alpha)\pi]}\right] \\
N_2 &= Integer\left[\frac{\log[\tau_0\beta\omega_H]}{\log(\lambda)}\right] + 1
\end{aligned}
\tag{18}
$$

Therefore, the function of (11) is approximated by a rational function as follows:

$$
H(s) \cong \tau_0^{\alpha}\left(K_D + \sum_{i=0}^{N_1}\frac{k_i s}{\left(1+\frac{s}{p_i}\right)}\right)\left(\sum_{j=1}^{2N_2-1}\frac{kk_j}{\left(1+\frac{s}{pp_j}\right)}\right) \tag{19}
$$

$$
\begin{aligned}
H(s) \cong &\left(\sum_{j=1}^{2N_2-1}\frac{\left(\tau_0^{\alpha}K_D\right)\left(pp_j kk_j\right)}{\left(s+pp_j\right)}\right) \\
&+\left(\sum_{i=0}^{N_1}\sum_{j=1}^{2N_2-1}\frac{\left(\tau_0^{\alpha}\right)\left(p_i k_i\right)\left(pp_j kk_j\right)s}{\left(s+p_i\right)\left(s+pp_j\right)}\right)
\end{aligned}
\tag{20}
$$

By the decomposition of the rational function of (20), we will get:

$$
\begin{aligned}
H(s) \cong &\left(\sum_{j=1}^{2N_2-1}\frac{\left(\tau_0^{\alpha}K_D\right)\left(pp_j kk_j\right)}{\left(s+pp_j\right)}\right) \\
&+\left(\sum_{i=0}^{N_1}\sum_{j=1}^{2N_2-1}\frac{A_{ij}}{\left(s+p_i\right)}+\frac{B_{ij}}{\left(s+pp_j\right)}\right)
\end{aligned}
\tag{21}
$$

where the residues A_{ij} and B_{ij} (for $0 \le i \le N_1$ and $1 \le j \le 2N_2-1$) are given by:

$$
A_{ij} = \frac{\left(\tau_0^{\alpha}\right)\left(p_i^2 k_i\right)\left(pp_j kk_j\right)}{p_i - pp_j}, \quad B_{ij} = \frac{\left(\tau_0^{\alpha}\right)\left(p_i k_i\right)\left(pp_j^2 kk_j\right)}{pp_j - p_i} \tag{22}
$$

Hence, we can write that:

$$
\begin{aligned}
H(s) \cong &\left(\sum_{j=1}^{2N_2-1}\frac{\left(\tau_0^{\alpha}K_D\right)\left(pp_j kk_j\right)}{\left(s+pp_j\right)}\right) \\
&+\left(\sum_{j=1}^{2N_2-1}\frac{\sum_{i=0}^{N_1}B_{ij}}{\left(s+pp_j\right)}\right)+\left(\sum_{i=0}^{N_1}\frac{\sum_{j=1}^{2N_2-1}A_{ij}}{\left(s+p_i\right)}\right)
\end{aligned}
\tag{23}
$$

$$H(s) \cong \left(\sum_{i=0}^{N_1} \frac{\overline{A}_i}{(s+p_i)}\right) + \left(\sum_{j=1}^{2N_2-1} \frac{\overline{B}_j}{(s+pp_j)}\right) \tag{24}$$

where the residues $\overline{A}_i$ ($0 \leq i \leq N_1$), and $\overline{B}_j$ ($1 \leq j \leq 2N_2-1$), are given by:

$$\overline{A}_i = \sum_{j=1}^{2N_2-1} A_{ij}, \quad \overline{B}_j = \left[\left(\tau_0^{\alpha} K_D\right)\left(pp_j kk_j\right)\right] + \sum_{i=0}^{N_1} B_{ij} \tag{25}$$

2.2 Case 2: α = 0.5

For this case, the function of (9) can be rewritten as:

$$H(s) = \frac{(\tau_0 s)^{0.5}}{1+(\tau_0 s)} \tag{26}$$

From Eq. (15), the above function is approximated by a rational function as follows:

$$H(s) \cong \tau_0^{0.5}\left(K_D + \sum_{i=0}^{N_1} \frac{k_i s}{\left(1+\frac{s}{p_i}\right)}\right)\left(\frac{1}{1+(\tau_0 s)}\right) \tag{27}$$

$$H(s) \cong \left(\frac{\tau_0^{(-0.5)} K_D}{(s+1/\tau_0)}\right) + \left(\sum_{i=0}^{N_1} \frac{\left(\tau_0^{(-0.5)}\right)(p_i k_i)s}{(s+p_i)(s+1/\tau_0)}\right) \tag{28}$$

By the decomposition of the rational function of (28), we will get:

$$H(s) \cong \left(\frac{\tau_0^{(-0.5)} K_D}{(s+1/\tau_0)}\right) + \left(\sum_{i=0}^{N_1} \left(\frac{C_i}{(s+p_i)} + \frac{D_i}{(s+1/\tau_0)}\right)\right) \tag{29}$$

where the residues C_i and D_i (for $0 \leq i \leq N_1$) are given by:

$$C_i = \frac{\left(\tau_0^{(-0.5)}\right)\left(p_i^2 k_i\right)}{p_i - 1/\tau_0}, \quad D_i = \frac{\left(\tau_0^{(-1.5)}\right)(p_i k_i)}{1/\tau_0 - p_i} \tag{30}$$

Hence, we can write that:

$$H(s) \cong \left(\sum_{i=0}^{N_1} \frac{\overline{C}_i}{(s+p_i)}\right) + \left(\frac{\overline{D}}{(s+1/\tau_0)}\right) \tag{31}$$

with the residues $\overline{C}_i = C_i$ (for $0 \leq i \leq N_1$) and $\overline{D} = \left[\tau_0^{(-0.5)} K_D\right] + \left[\sum_{i=0}^{N_1} D_i\right]$.

3 Time Responses

3.1 Case 1: 0 < α < 0.5

From Eq. (24), we have that:

$$H(s) = \frac{X(s)}{E(s)} = \left(\sum_{i=0}^{N_1} \frac{\overline{A}_i}{(s+p_i)}\right) + \left(\sum_{j=1}^{2N_2-1} \frac{\overline{B}_j}{(s+pp_j)}\right) \tag{32}$$

then,

$$X(s) = \left[\left(\sum_{i=0}^{N_1} \frac{\overline{A}_i}{(s+p_i)}\right) + \left(\sum_{j=1}^{2N_2-1} \frac{\overline{B}_j}{(s+pp_j)}\right)\right] E(s) \tag{33}$$

For e(t) = δ(t) the unit impulse E(s) = 1, we will have:

$$X(s) = \left[\left(\sum_{i=0}^{N_1} \frac{\overline{A}_i}{(s+p_i)}\right) + \left(\sum_{j=1}^{2N_2-1} \frac{\overline{B}_j}{(s+pp_j)}\right)\right] \tag{34}$$

Hence, the impulse response of (10) is:

$$\begin{aligned} x(t) = L^{-1}\{X(s)\} = &\left(\sum_{i=0}^{N_1} \overline{A}_i \exp(-p_i t)\right) \\ &+ \left(\sum_{j=1}^{2N_2-1} \overline{B}_j \exp(-pp_j t)\right) \end{aligned} \tag{35}$$

For e(t) = u(t) the unit step E(s) = 1/s, (33) will be:

$$X(s) = \left[\left(\sum_{i=0}^{N_1} \frac{\overline{A}_i}{(s+p_i)}\right) + \left(\sum_{j=1}^{2N_2-1} \frac{\overline{B}_j}{(s+pp_j)}\right)\right] \left(\frac{1}{s}\right) \tag{36}$$

$$X(s) = \left(\sum_{i=0}^{N_1} \frac{\overline{A}_i}{(s+p_i)} \left(\frac{1}{s}\right)\right) + \left(\sum_{j=1}^{2N_2-1} \frac{\overline{B}_j}{(s+pp_j)} \left(\frac{1}{s}\right)\right) \tag{37}$$

$$X(s) = \left(\sum_{i=0}^{N_1}\left(\frac{\overline{A}_i}{p_i}\right)\left(\frac{1}{s} - \frac{1}{(s+p_i)}\right)\right) + \left(\sum_{j=1}^{2N_2-1}\left(\frac{\overline{B}_i}{pp_j}\right)\left(\frac{1}{s} - \frac{1}{(s+pp_j)}\right)\right) \tag{38}$$

Hence, the step response of (10) is:

$$x(t) = L^{-1}\{X(s)\} = \left(\sum_{i=0}^{N_1}\left(\frac{\overline{A}_i}{p_i}\right)[1 - \exp(-p_i t)]\right) + \left(\sum_{j=1}^{2N_2-1}\left(\frac{\overline{B}_j}{pp_j}\right)[1 - \exp(-pp_j t)]\right) \tag{39}$$

3.2 Case 2: α = 0.5

From Eq. (31), we have that:

$$H(s) = \frac{X(s)}{E(s)} = \left(\sum_{i=0}^{N_1}\frac{\overline{C}_i}{(s+p_i)}\right) + \left(\frac{\overline{D}}{(s+1/\tau_0)}\right) \tag{40}$$

then,

$$X(s) = \left[\left(\sum_{i=0}^{N_1}\frac{\overline{C}_i}{(s+p_i)}\right) + \left(\frac{\overline{D}}{(s+1/\tau_0)}\right)\right]E(s) \tag{41}$$

For e(t) = δ(t) the unit impulse E(s) = 1, we will have:

$$X(s) = \left[\left(\sum_{i=0}^{N_1}\frac{\overline{C}_i}{(s+p_i)}\right) + \left(\frac{\overline{D}}{(s+1/\tau_0)}\right)\right] \tag{42}$$

Hence, the impulse response of (10), for α = 0.5, is:

$$x(t) = L^{-1}\{X(s)\} = \left(\sum_{i=0}^{N_1}\overline{C}_i \exp(-p_i t)\right) + \left(\overline{D}\exp(-t/\tau_0)\right) \tag{43}$$

For e(t) = u(t) the unit step E(s) = 1/s, (41) will be:

$$X(s) = \left[\left(\sum_{i=0}^{N_1} \frac{\overline{C}_i}{(s+p_i)}\right) + \left(\frac{\overline{D}}{(s+1/\tau_0)}\right)\right]\left(\frac{1}{s}\right) \tag{44}$$

$$X(s) = \left(\sum_{i=0}^{N_1} \frac{\overline{C}_i}{(s+p_i)}\left(\frac{1}{s}\right)\right) + \left(\left(\frac{\overline{D}}{(s+1/\tau_0)}\right)\left(\frac{1}{s}\right)\right) \tag{45}$$

$$\begin{aligned} X(s) = & \left(\sum_{i=0}^{N_1} \left(\frac{\overline{C}_i}{p_i}\right)\left(\frac{1}{s} - \frac{1}{(s+p_i)}\right)\right) \\ & + \left(\overline{D}\tau_0\left(\frac{1}{s} - \frac{1}{(s+1/\tau_0)}\right)\right) \end{aligned} \tag{46}$$

Hence, the step response of f (10), for $\alpha = 0.5$, is:

$$\begin{aligned} x(t) = L^{-1}\{X(s)\} = & \left(\sum_{i=0}^{N_1} \left(\frac{\overline{C}_i}{p_i}\right)[1 - \exp(-p_i t)]\right) \\ & + \left(\overline{D}\,\tau_0[1 - \exp(-t/\tau_0)]\right) \end{aligned} \tag{47}$$

4 Illustrative Example

Let us first consider the fractional system represented by the following fundamental linear fractional order differential equation with $\alpha = 0.35$ and $\tau_0 = 2$ as:

$$(2)^{0.7}\frac{d^{0.7}x(t)}{dt^{0.7}} + x(t) = (2)^{0.35}\frac{d^{0.35}e(t)}{dt^{0.35}} \tag{48}$$

its transfer function is given by:

$$H(s) = \frac{(2s)^{0.35}}{1 + (2s)^{0.7}} \tag{49}$$

Its rational function approximation, in a given frequency band, is given as:

$$H(s) = \frac{(2s)^{0.35}}{1 + (2s)^{0.7}} = \left(\sum_{i=0}^{N_1} \frac{\overline{A}_i}{(s+p_i)}\right) + \left(\sum_{j=1}^{2N_2-1} \frac{\overline{B}_j}{(s+pp_j)}\right) \tag{50}$$

For the fractional order differentiator $(2s)^{0.35}$, the frequency band of approximation is $[\omega_L,\ \omega_H] = [10^{-4}$ rad/s, 10^4 rad/s], around $\omega_0 = (1/\tau_0) = 0.5$ rad/s, $y = 1$ dB, $\delta = 0.1$, and $\beta = 100$. For the fractional system $\frac{1}{1+(2s)^{0.7}}$, the frequency band of

approximation [0, ω_H] = [0, 10^4 rad/s], $\lambda = 4$ and $\beta = 100$. Then, the approximation parameters of H(s) are:

$$a = 1.4251,\ b = 1.9307,\ \omega_c = 10^{-5},\ \omega_{max} = 10^6,$$
$$p_0 = 1.9802{*}10^{-5},\ K_D = 0.0178,\ N_1 = 25,\ and\ N_2 = 11$$

Hence, poles p_i, the residues $\overline{A}_i$ ($0 \le i \le 25$), the poles pp_j and the residues $\overline{B}_j$ ($1 \le j \le 20$), are given by:

$$p_i = \left(1.9802 * 10^{-5}\right)(2.7514)^i$$
$$\overline{A}_i = \sum_{j=1}^{21} \frac{\left[\begin{array}{l}\left(1.1230 * 10^{-7}\right)\left((2.7514)^i(4)^{(j-11)}\right) \\ * \dfrac{\prod_{j=0}^{25}\left[1 - \left((1.4251)(2.7514)^{(i-j)}\right)\right]}{\prod_{j=0, i\neq j}^{25}\left(1 - (2.7514)^{(i-j)}\right)}\end{array}\right]}{\left[\pi\left[(0.5)(4)^{(j-11)} - (1.9802 * 10^{-5})(2.7514)^i\right]\right]} * \left[\frac{\sin[(0.3)\pi]}{\cosh[(0.35)\log((4)^{(11-j)})] - \cos[(0.3)\pi]}\right] \tag{51}$$

$$pp_j = (0.5)(4)^{(j-11)}$$
$$\overline{B}_j = \frac{(0.0057)}{\pi}(4)^{(j-11)}\left[\frac{\sin[(0.3)\pi]}{\cosh[(0.35)\log((4)^{(11-j)})] - \cos[(0.3)\pi]}\right] + \sum_{i=0}^{25}\left\{\begin{array}{l}\dfrac{-(0.0029)(4)^{2(j-11)}\dfrac{\prod_{j=0}^{25}\left[1-(1.4251)(2.7514)^{(i-j)}\right]}{\prod_{j=0, i\neq j}^{25}\left(1-(2.7514)^{(i-j)}\right)}}{\pi\left[(0.5)(4)^{(j-11)} - (1.9802 * 10^{-5})(2.7514)^i\right]} \\ \times\left[\dfrac{\sin[(0.3)\pi]}{\cosh[(0.35)\log((4)^{(11-j)})] - \cos[(0.3)\pi]}\right]\end{array}\right\} \tag{52}$$

Figures 1 and 2 show the bode plots of the fundamental linear fractional order system transfer function of (49) and of its proposed rational function approximation of (50). We can easily see that they are all quite overlapping in the frequency band of interest.

Figures 3 and 4 show, respectively, the impulse and the step responses of the fractional order system of (48).

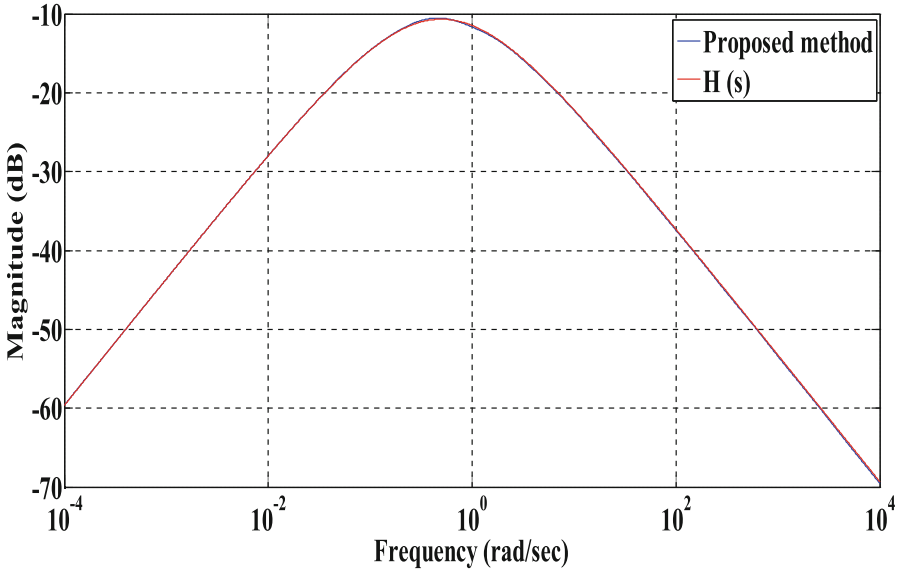

Fig. 1. Magnitude bode plots of (49) and of its proposed approximation.

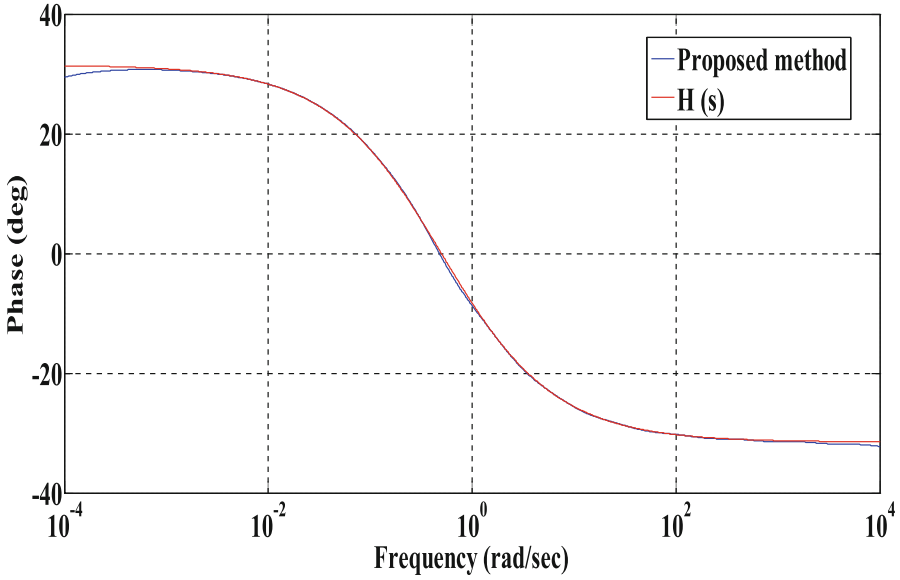

Fig. 2. Phase bode plots of (49) and of its proposed approximation

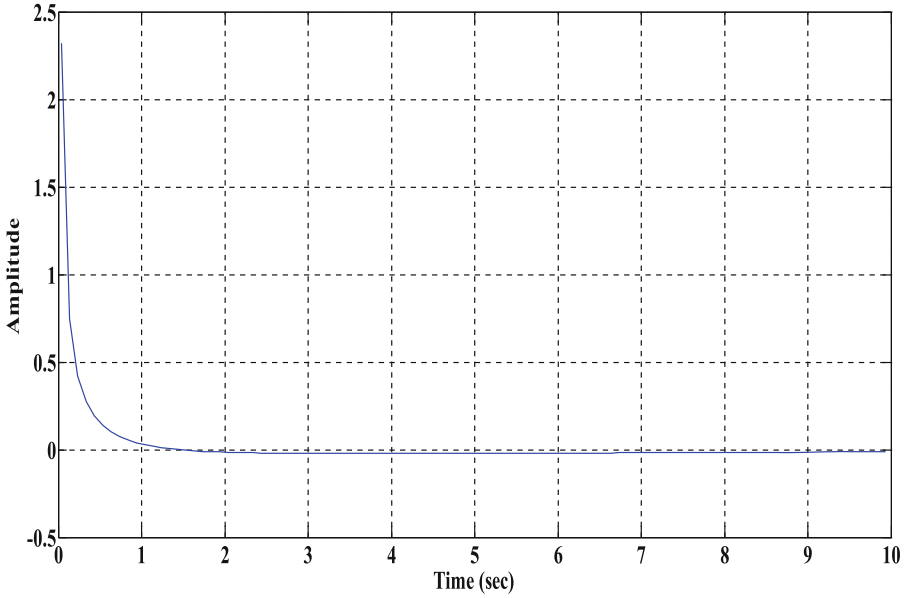

Fig. 3. Impulse response of (48) from its proposed approximation.

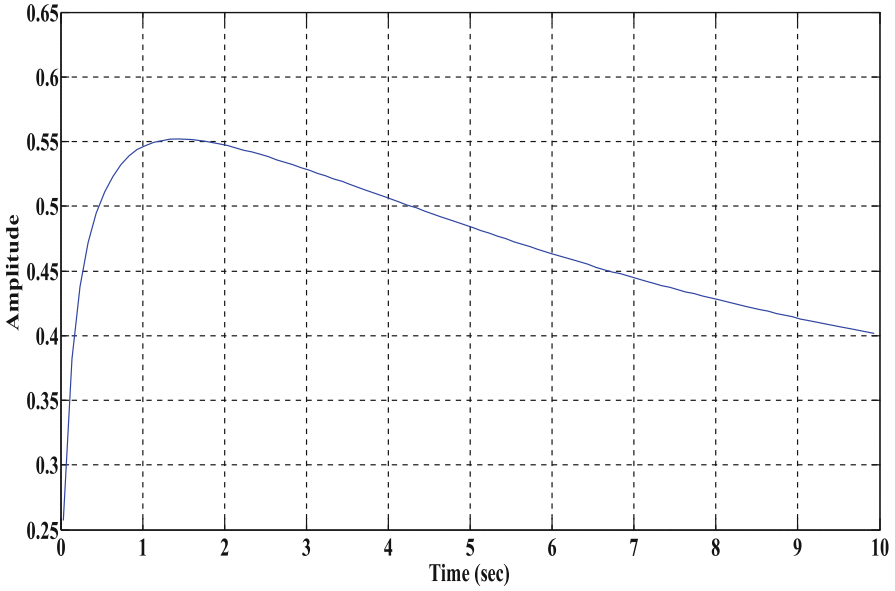

Fig. 4. Step response of (48) from its proposed approximation.

As a second example, we will consider the fractional order system represented by the following fundamental linear fractional order differential equation with $\alpha = 0.5$ and $\tau_0 = 0.16$ as:

$$(0.16)\frac{d\,x(t)}{dt} + x(t) = (0.16)^{0.5}\frac{d^{0.5}e(t)}{dt^{0.5}} \tag{53}$$

its transfer function is given by:

$$H(s) = \frac{(0.16\,s)^{0.5}}{1 + (0.16\,s)} \tag{54}$$

Its rational function approximation, in a given frequency band, is given as:

$$H(s) = \frac{(0.16\,s)^{0.5}}{1 + (0.16\,s)} = \left(\sum_{i=0}^{N_1}\frac{\overline{C}_i}{(s+p_i)}\right) + \left(\frac{\overline{D}}{(s+1/\tau_0)}\right) \tag{55}$$

For the fractional differentiator $(0.16\ s)^{0.5}$, the frequency band of approximation is $[\omega_L,\ \ \omega_H] = [10^{-4}$ rad/s, $\ 10^4$ rad/s], around $\omega_0 = (1/\tau_0) = 6.25$ rad/s, $y = 1$ dB, $\delta = 0.1$, and $\beta = 100$. Then, the approximation parameters of H(s) are:

$$\begin{aligned} &a = 1.5849,\ b = 1.5849,\ \omega_c = 10^{-5},\ \omega_{max} = 10^6,\\ &p_0 = 1.9953 * 10^{-5},\ K_D = 0.0032\ and\ N_1 = 28 \end{aligned}$$

Hence, poles p_i, the residues $\overline{C}_i$ $(0 \le i \le 25)$, and the residue $\overline{D}$, are given by:

$$\begin{aligned} p_i &= \left(1.9953 * 10^{-5}\right)(2.5119)^i\\ \overline{C}_i &= \left(\frac{-(1.5963 * 10^{-7})(2.5119)^i}{\left[(1.9953 * 10^{-5})(2.5119)^i - 6.25\right]}\right)\\ &\quad * \left(\frac{\prod_{j=0}^{28}\left(1 - (1.5849)(2.5119)^{(i-j)}\right)}{\prod_{j=0,\,i\neq j}^{28}\left(1 - (2.5119)^{(i-j)}\right)}\right) \end{aligned} \tag{56}$$

$$\begin{aligned} \overline{D} &= (0.008)\\ &\quad + \sum_{i=0}^{28}\left[\left(\frac{-(0.05)}{\left[6.25 - (1.9953 * 10^{-5})(2.5119)^i\right]}\right)\right.\\ &\quad \left. * \left(\frac{\prod_{j=0}^{28}\left(1 - (1.5849)(2.5119)^{(i-j)}\right)}{\prod_{j=0,\,i\neq j}^{28}\left(1 - (2.5119)^{(i-j)}\right)}\right)\right] \end{aligned} \tag{57}$$

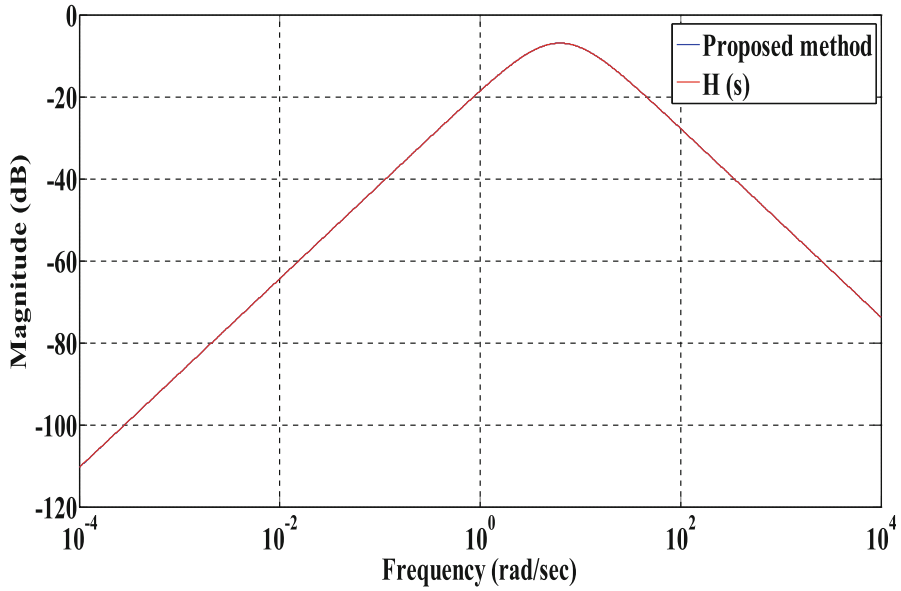

Fig. 5. Magnitude bode plot of (54) and of its proposed approximation.

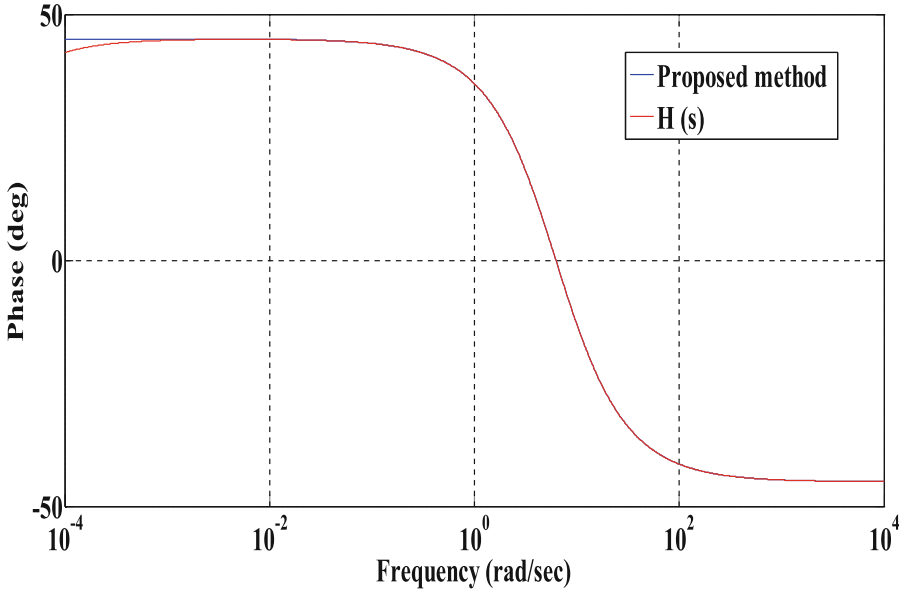

Fig. 6. Phase bode plot of (54) and of its proposed approximation.

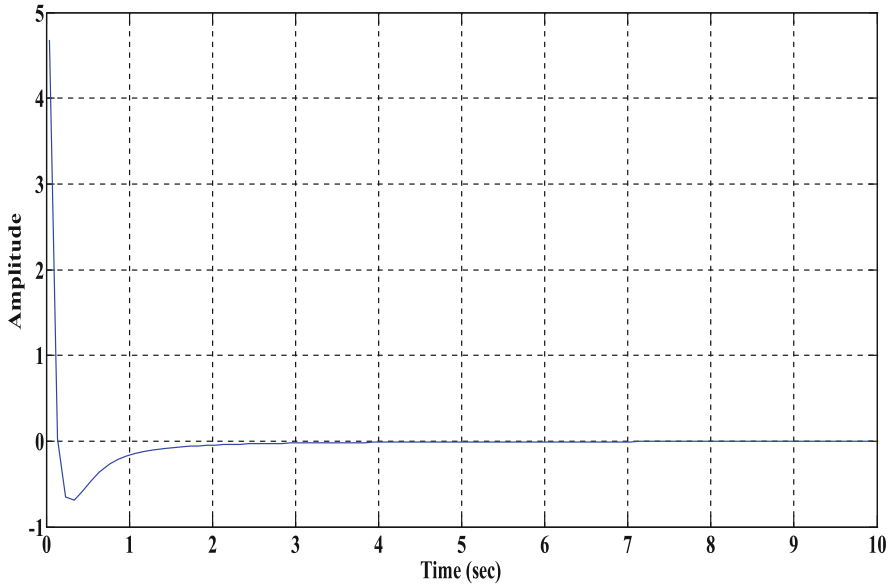

Fig. 7. Impulse response of (53) from its proposed approximation.

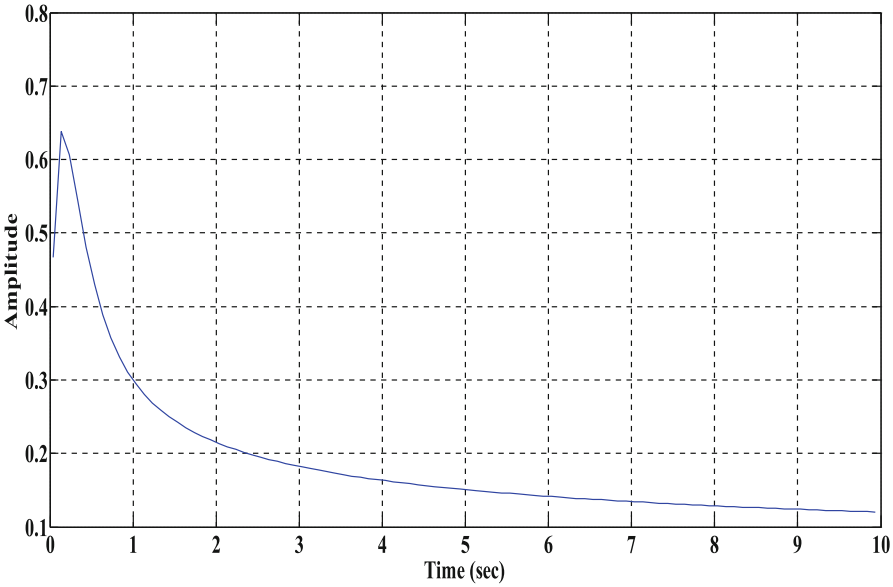

Fig. 8. Step response of (53) from its proposed approximation.

Figures 5 and 6 show the bode plots of the fundamental linear fractional system transfer function of (54) and of its proposed rational function approximation of (55). We note that they are overlapping in the frequency band of interest.

Figures 7 and 8 show, respectively, the impulse and the step responses of the fractional order system of (53).

5 Conclusion

In this paper, we have presented a rational function approximation of the fractional order transfer function $H(s) = \frac{(\tau_0 s)^{\alpha}}{[1+(\tau_0 s)^{2\alpha}]}$, $for\ 0 < \alpha \leq 0.5$. This fractional order transfer function is one of the fundamental functions of the linear fractional system of commensurate order, represented by the linear fractional state-space $D^{\alpha}x(t) = A\,x(t)$. H(s) corresponds to pure complex conjugate eigenvalues of the A matrix. First, closed form of the approximation technique has been derived. Then, the impulse and step responses of this type of fractional system have been obtained. Finally, illustrative examples are presented to show the exactitude and the usefulness of the approximation method.

References

Arikoglu, A., Ozkol, I.: Solution of fractional differential equations by using differential transform method. Chaos Soliton Frac. **40**(2), 521–529 (2009)

Bonilla, B., Rivero, M., Trujillo, J.J.: On systems of linear fractional differential equations with constant coefficients. Appl. Math. Comput. **187**, 68–78 (2007)

Boucherma, D., Charef, A.: Approximation d'une fonction fondamentale d'ordre fractionnaire. In: Proceedings de la seconde conférence sur les systèmes d'ordre fractionnaire et leur applications, SOFA 2011, Tizi-ouzou, Algeria, 24–26 October 2011

Caponetto, R., Dongola, G., Fortuna, L., Petráš, I.: Fractional Order Systems: Modeling and Control Applications. World Scientific Publishing Co. Pte. Ltd, Singapore (2010)

Charef, A.: Modeling and analog realization of the fundamental linear fractional order differential equation. Nonlinear Dyn. **46**, 195–210 (2006a)

Charef, A.: Analogue realisation of fractional order integrator, differentiator and fractional $PI^{\lambda}D^{\mu}$ controllers. IEE Proc. Control Theory Appl. **153**(6), 714–720 (2006b)

Charef, A., Nezzari, H.: On the fundamental linear fractional order differential equation. Nonlinear Dyn. **65**(3), 335–348 (2011)

Hu, Y., Luo, Y., Lu, Z.: Analytical solution of the linear fractional differential equation by Adomian decomposition method. J. Comput. Appl. Math. **215**(1), 220–229 (2008)

Kilbas, A.A., Srivastava, H.M., Trujillo, J.J.: Theory and Applications of Fractional Differential Equations. Elsevier, Amsterdam (2006)

Miller, K.S., Ross, B.: An Introduction to the Fractional Calculus and Fractional Differential Equations. Wiley Inc., New York (1993)

Monje, C.A., Chen, Y.Q., Vinagre, B.M., Xue, D., Feliu, V.: Fractional-Order Systems and Controls Fundamentals and Applications. Springer, England (2010)

Nezzari, H., Charef, A.: Analog realization of generalized fractional order damped sine and cosine functions. In: Proceedings of the Symposium on Fractional Signals and Systems, FSS 2011, Coimbra, Portugal, 4–5 November 2011

Odibat, Z.M.: Analytic study on linear systems of fractional differential equations. Comput. Math Appl. **59**, 1171–1183 (2010)

Oturanç, G., Kurnaz, A., Keskin, Y.: A new analytical approximate method for the solution of fractional differential equations. Int. J. Comput. Math. **85**(1), 131–142 (2008)

Podlubny, I.: Fractional Differential Equations. Academic Press, San Diego (1999)

Robust Adaptive Fuzzy Control for a Class of Uncertain Nonlinear Fractional Systems

Khatir Khettab[1(✉)], Yassine Bensafia[2], and Samir Ladaci[3,4]

[1] Department of Electrical Engineering,
Mohamed Boudiaf University of M'sila, 28000 M'sila, Algeria
zoubirhh@yahoo.fr
[2] Department of Electrical Engineering,
Bouira University, 10000 Bouira, Algeria
bensafiay@yahoo.fr
[3] E.E.A. Department, National Polytechnic School of Constantine,
O. 447, 25000 Constantine, Algeria
samir_ladaci@yahoo.fr
[4] SP-Lab Laboratory, University Mentouri Constantine, Route de Ain El-Bey,
25000 Constantine, Algeria

Abstract. This paper presents a novel fuzzy logic controller (FLC) equipped with an adaptive algorithm to achieve synchronization performance for tow fractional chaotic systems. By introducing the fuzzy control design and robustness tracking approach, a desired synchronization error can be attenuated to a prescribed level, even in the presence of the high level of uncertainties and noisy training data.

Based on recent works of Lin et al. about synchronization of uncertain fractional order chaotic systems, the main contribution of this work is to enhance the control system behavior using the numerical approximation method of Grünwald–Letnikov. Simulation results clearly showed the efficiency of the proposed control scheme.

Keywords: Fractional adaptive fuzzy control · Fractional systems · Robustness · Numerical approximation · Synchronization · Lyapunov stability

1 Introduction

In recent years, fractional calculus deals with derivatives and integrations of arbitrary order [1–3] and has found many applications in many fields of physics, applied mathematics and engineering. Moreover, many real-world physical systems are well characterized by fractional order differential equations, i.e., equations involving both integer and non-integer order derivatives. It is observed that the description of some systems is more accurate when the fractional derivative is used. For instance, electrochemical processes and flexible structures are modeled by fractional order models [1, 4, 5]. Now days, many fractional order differential systems behave chaotically, such as the fractional order *Chua* system [6, 7], the fractional-order *Duffing* system [25, 26], the fractional order *Lü* system, the fractional order *Chen* system [8].

M. Chadli et al. (eds.), *Recent Advances in Electrical Engineering and Control Applications*,
Lecture Notes in Electrical Engineering 411, DOI 10.1007/978-3-319-48929-2_21

Recently, due to its potential applications in secure communication and control processing, the study of chaos synchronization in fractional order dynamical systems and related phenomena is receiving growing attention.

The synchronization problem of fractional order chaotic systems was first investigated by *Deng* and *Li* [9] who carried out synchronization in the case of the fractional *Lü* system. Afterwards, they studied chaos synchronization of the *Chen* system with a fractional order in a different manner [22–24]. Fuzzy logic controllers are generally considered applicable to plants that are mathematically poorly understood and where experienced human operators are available for providing a qualitative "rule of thumb" [10, 11].

Based on the universal approximation theorem [12, 14, 15], (fuzzy logic controllers are general enough to perform any nonlinear control actions) there is rapidly growing interest in systematic design methodologies for a class of nonlinear systems using fuzzy adaptive control schemes. An adaptive fuzzy system is a fuzzy logic system equipped with a training algorithm in which an adaptive controller is synthesized from a collection of fuzzy IF-THEN rules and the parameters of the membership functions characterizing the linguistic terms in the IF-THEN rules change according to some adaptive law for the purpose of controlling a plant to track a reference trajectory.

In this paper, by incorporating the H^{∞} tracking design technique [16] and Lyapunov stability criterion [32], a new adaptive fuzzy control algorithm is proposed so that not only the stability of the adaptive fuzzy control system is guaranteed but also the influence of the approximation error and external disturbance on the tracking error can be attenuated to an arbitrarily prescribed level via the H^{∞} tracking design technique. The proposed design method attempts to combine the attenuation technique, fuzzy logic approximation method, and adaptive control algorithm for the robust tracking control design of the nonlinear fractional order systems with a large uncertainty or unknown variation in plant parameters and structures [32–34].

This paper is organized as follows: in Sect. 1, an introduction to fractional derivatives and its relation to the approximation solution will be addressed and the basic definition and preliminaries for fractional order systems. A description of the TakagiSugeno (T–S) is presented in Sect. 2. Section 3 generally proposes adaptive robust (H^{∞}) control of uncertain fractional order systems in the presence of uncertainty and its stability analysis. In Sect. 4, application of the proposed method on fractional order expression chaotic systems (Duffing system) is investigated. Finally, the simulation results and conclusion will be presented.

2 Basic Definitions and Preliminaries for Fractional Order Systems

Fractional calculus is a mathematical topic more than 300 years bold. It is a generalization of integration and differentiation to non-integer order fundamental operators, denoted by ${}_aD_t^{\gamma}$, where a and t are the limits of the operator.

This operator is a notation for taking both the fractional integral and functional derivative in a single expression defined [13] as:

$$ {}_aD_t^q = \begin{cases} \frac{d^q}{dt^q} & q > 0 \\ 1 & q = 0 \\ \int_a^t (d\tau)^{-q} & q < 0 \end{cases} \tag{1} $$

There are some basic definitions of the general fractional integration and differentiation. The commonly used definitions are *Riemann–Liouville*, *Adams–Bashforth–Moulton* algorithm and the method of *Grünwald-Letnikov*: "Numerical evaluation of the fractional derivative of some usual functions".

The simplest and easiest definition is the *Riemann–Liouville* definition given as:

$$ {}_{t_0}^{RL}D_t^q f(t) = \frac{1}{\Gamma(n-q)} \frac{d^n}{dt^n} \int_{t_0}^{t} (t-\tau)^{n-q-1} f(\tau) d\tau \tag{2} $$

where n is the first integer which is not less than q, i.e., $(n-q) < q < n$, and Γ is the Gamma function.

The numerical simulation of a fractional differential equation is not as simple as that of an ordinary differential equation.

The algorithm which is an improved version of the *Adams–Bashforth–Moulton* [29–31] to find an approximation for fractional order systems based on predictor–correctors is given [30]. Consider the following differential equation

$$ {}_a^{GL}D_t^q y(t) = f(y(t), t) \tag{3} $$

where $0 \le t \le T$ and $y^{(k)}(0) = y_0^{(k)}$ and $k = 0, 1, 2, \ldots, m-1$

Can be expressed as follows

$$ y(t_k) = f(y(t_k), t_k) h^q - \sum_{j=v}^{k} c_j^{(q)} y(t_{k-j}) \tag{4} $$

where ${}_0D_t^q y(t)$ is the Caputo fractional derivative of order q > 0 is defined as:

$$ {}_0D_t^q y(t) = \begin{cases} \frac{1}{\Gamma(m-q)} \int_0^t (t-\tau)^{m-q-1} f^{(m)}(\tau) d\tau, m-1 < q < m \\ \frac{d^m}{dt^m} y(t) q = m \end{cases} \tag{5} $$

and m is the first integer larger than q.

The solution of (4) is equivalent to the Volterra integral equation described as [29–31]:

$$ y(t) = \sum_{k=0}^{[q]-1} y_0^{(k)} \frac{t^k}{k!} + \frac{1}{\Gamma(q)} \int_0^t (t-\tau)^{q-1} f(\tau, y(\tau)) d\tau \tag{6} $$

Let $h = T/N$, $t_n = nh$, $n = 0, 1, 2, \ldots, N$. Then (6) can be described as follows:

$$y_h(t_{n+1}) = \sum_{k=0}^{[q]-1} y_0^{(k)} \frac{t_{n+1}^k}{k!} + \frac{h^q}{\Gamma(q+2)} f\left(y_n^p(t_{n+1}), t_{n+1}\right) + \frac{h^q}{\Gamma(q+2)} \sum_{j=0}^{n} a_{j,n+1} f\left(y_h(t_j), t_j\right) \tag{7}$$

where the predicted value $y_h^p(t_{n+1})$ is determined by the fractional Adams–Bashforth method:

$$y_h^p(t_{n+1}) = \sum_{k=0}^{[q]-1} y_0^{(k)} \frac{t_{n+1}^k}{k!} + \frac{1}{\Gamma(q)} \sum_{j=0}^{n} b_{j,n+1} f\left(y_h(t_j), t_j\right) \tag{8}$$

and

$$a_{j,n+1} = \begin{cases} n^{q+1} - (n-\mathrm{q})(n+1)^q, & \text{if } j = 0 \\ (n-j+2)^{q+1} + (n-j)^{q+1} - 2(n-j+1)^{q+1}, & \text{if } 1 \le \mathrm{j} \le n \\ 1, & \text{if } j = n+1 \end{cases} \tag{9}$$

$$b_{j,n+1} = \frac{h^q}{q}\left((n-j+1)^q - (n-j)^q\right) \tag{10}$$

The approximation error is given as

$$max_{j=0,1,2,\ldots,N} = \left|y(t_j) - y_h(t_j)\right| = O(h^p) \tag{11}$$

$$p = min(2, 1+q).$$

Therefore, the numerical solution of a fractional order system can be obtained by applying the abovementioned algorithm.

In this work, the method of numerical evaluation of the fractional derivative of some usual functions *(Grünwald-Letnikov method)* is given [32], the definition is expressed as:

$${}_{t_0}^{GL}D_t^q f(t) = \lim_{n\to 0} \frac{1}{h^n} \sum_{j=0}^{\left[\frac{t-q}{h}\right]} (-1)^j \binom{q}{j} f(t - jh) \tag{12}$$

where $\left[\frac{t-q}{h}\right]$ indicates the integer part and $(-1)^j \binom{q}{j}$ are binomial coefficients $c_j^{(q)} (j = 0, 1, \ldots)$.

The calculation of these coefficients is done by formula of following recurrence:

$$c_0^{(q)} = 1, \quad c_j^q = \left(1 - \frac{1+q}{j}\right) c_{j-1}^q$$

The general numerical solution of the fractional differential equation

$$ {}_{a}^{GL}D_{t}^{q}y(t) = f(y(t), t), $$

Can be expressed as follows:

$$ y(t_k) = f(y(t_k), t_k)h^q - \sum_{j=v}^{k} c_j^{(q)} y\left(t_{k-j}\right) \tag{13} $$

This approximation of the fractional derivative within the meaning of *Grünwald-Letnikov* is on the one hand equivalent to the definition of *Riemman-Liouville* for a broad class of functions [17], on the other hand, it is well adapted to the definition of *Caputo* (Adams method) because it requires only the initial conditions and has a physical direction clearly.

Remark. As noted in [6, 8], both numerical methods in the time domain mentioned (*Grünwald-Letnikov* and Adams-Bashforth-Moulton) have approximately the same order of accuracy and good digital solutions.

3 Description of the T–S Fuzzy Systems

Fuzzy logic systems address the imprecision of the input and output variables directly by defining them with fuzzy numbers (and fuzzy sets) that can be expressed in linguistic terms (e.g., small, medium and large) [4, 10, 11]. The basic configuration of the T–S system includes a fuzzy rule base, which consists of a collection of fuzzy IF–THEN rules in the following form:

$$ R^{(l)}: IF\ x_1\ is\ F_1^l,\ and \ldots,\ and\ x_n\ is\ F_n^l\ THEN\ y_l = f_i(x) $$
$$ y_l = q_0^l + q_1^l x_1 + \ldots + q_n^l x_n = \underline{\theta}_l^T \left[1\ x^T\right] $$

where $(F_1^l, \ldots, F_i^l, \ldots, F_n^l)$ are input fuzzy sets and $\underline{\theta}_l^T = \left[q_0^l, q_1^l + \ldots + q_n^l\right]$ is a vector of the adjustable factors of the consequence part of the fuzzy rule. Also y_l is a crisp value, and a fuzzy inference engine to combine the fuzzy IF–THEN rules in the fuzzy rule base into a mapping from an input linguistic vector $\underline{x}^T = [x_1 + x_2 \ldots + x_n] \in \Re^n$ to an output variable $y \in R$. Let M be the number of fuzzy IF–THEN rules. The output of the fuzzy logic systems with central average defuzzifier, product inference and singleton fuzzifier can be expressed as

$$ y(\underline{x}) = \frac{\sum_{l=1}^{M} v^l \cdot y_l}{\sum_{l=1}^{M} v^l} = \frac{\sum_{l=1}^{M} v^l \cdot \underline{\theta}_l^T [1x^T]^T}{\sum_{l=1}^{M} v^l} \tag{14} $$

Where $v^l = \prod_{i=1}^{n} \mu_{F_i^l(x_i)}$ is the true value of the lth implication and $\mu_{F_i^l(x_i)}$ is the membership function value of the fuzzy variable x_i [18–20].

Equation (14) can be rewritten as:

$$y(\underline{x}) = \underline{\theta}_l^T \xi(\underline{x}) \tag{15}$$

where $\underline{\theta}_l^T = \left[\underline{\theta}_l^T \underline{\theta}_2^T \ldots \underline{\theta}_M^T\right]$ is an adjustable parameter vector and
$\xi^T(\underline{x}) = \left[\xi^1(\underline{x}), \xi^2(\underline{x}), \ldots, \xi^M(\underline{x})\right]$ is a fuzzy basis function vector defined as

$$\xi^l(\underline{x}) = \frac{v^l[1\underline{x}^T]}{\sum_{l=1}^{M} v^l}$$

When the inputs are fed into the T–S, the true value v^l of the lth implication is computed. Applying the common defuzzification strategy, the output expressed as (14) is pumped out.

Based on the universal approximation theorem [10, 14, 21], the above fuzzy logic system is capable of uniformly approximating any well-defined nonlinear function over a compact set Uc to any degree of accuracy. Also it is straightforward to show that a multi-output system can always be approximated by a group of single-output approximation systems.

4 Adaptive H^∞ Control of Uncertain Fractional Order Systems

Consider an incommensurate fractional order SISO nonlinear dynamic system of the form [4, 15, 32]:

$$\begin{cases} x_1^{(q_1)} = x_2 \\ \vdots \\ x_{n-1}^{(q_{n-1})} = x_n \\ x_n^{(q_n)} = f(\underline{x}, t) + g(\underline{x}, t)u + d(t) \\ y = x_1 \end{cases}$$

If $q_1 = q_2 = \cdots = q_n = q$ the above system is called a commensurate order system, then equivalent form of the above system is described as

$$x^{(nq)} = f(\underline{x}, t) + g(\underline{x}, t)u + d(t) \tag{16}$$

$$y = x_1$$

where $\underline{x} = [x_1, x_2, \ldots, x_n]^T = \left[x, x^{(q)}, x^{(2q)}, \ldots, x^{((n-1)q)}\right]^T \in R^n$ is the state vector, $f(\underline{x}, t)$ and $g(\underline{x}, t)$ are unknown but bounded nonlinear functions which express system dynamics, $d(t)$ is the external bounded disturbance and $u(t) \in R$ is the control input. The control objective is to force the system output $y \in R$ to follow a given bounded reference signal y_d, under the constraint that all signals involved must be bounded.

For simplicity, in this paper adaptive FLC for a commensurate order system is proposed only, since the stability condition for the incommensurate order system can be converted to that for the commensurate order system [15, 18].

To begin with, the reference signal vector y_d and the tracking error vector e will be defined as

$$\underline{y}_d = \left[y_d, y_d^{(q)}, \ldots, y_d^{((n-1)q)}\right]^T \in R^n$$

$$\underline{e} = \underline{y}_d - \underline{y} = \left[e, e^{(q)}, \ldots, e^{((n-1)q)}\right]^T \in R^n,\ e^{(iq)} = y_d^{(iq)} - y^{(iq)}.$$

Let $\underline{k} = [k_1, k_2, \ldots, k_n]^T \in R^n$ to be chosen such that the stability condition $g(eig(A))| > q\pi/2$ is met, where $0 < q < 1$ and $eig(A)$ represents the eigenvalues of the system state matrix.

If the functions $f(\underline{x}, t)$ *and* $g(\underline{x}, t)$ are known and the system is free of external disturbance d, then the control law of the certainty equivalent controller is obtained as [4, 23, 24].

$$u_{eq} = \frac{1}{g(\underline{x}, t)}\left[-f(\underline{x}, t) + y_d^{(nq)} + \underline{k}^T \underline{e}\right] \tag{17}$$

Substituting (17) into (16), we have:

$$e^{(nq)} + k_n e^{(n-1)q} + \cdots + k_1 e = 0$$

Which is the main objective of control, $\lim_{t\to\infty} e(t) = 0$.

However, $f(\underline{x}, t)$ *and* $g(\underline{x}, t)$ are unknown and external disturbance $d(t) \neq 0$, the ideal control effort (17) cannot implemented. We replace $f(\underline{x}, t)$ and $g(\underline{x}, t)$ by the fuzzy logic system $f(\underline{x}|\underline{\theta}_f)$ and $g(\underline{x}|\underline{\theta}_g)$ in a specified form as (14) or (15), i.e.,

$$f(\underline{x}|\underline{\theta}_f) = \xi^T(\underline{x})\underline{\theta}_f \text{ and } g(\underline{x}|\underline{\theta}_g) = \xi^T(\underline{x})\underline{\theta}_g \tag{18}$$

Here the fuzzy basis function $\xi(x)$ depends on the fuzzy membership functions and is supposed to be fixed, while $\underline{\theta}_f$ and $\underline{\theta}_g$ are adjusted by adaptive laws based on a Lyapunov stability criterion.

Therefore, the resulting control effort can be obtained as,

$$u = \frac{1}{g(\underline{x}|\underline{\theta}_g)}\left[-f(\underline{x}|\underline{\theta}_f) + y_d^{(nq)} + \underline{k}^T \underline{e} - u_a\right] \tag{19}$$

where the robust compensator u_a is employed to attenuate the external disturbance and the fuzzy approximation errors. By substituting (19) into (16), we have:

$$\begin{aligned} x^{(nq)} &= f(\underline{x},t) + g(\underline{x},t)u + d(t) + g(\underline{x}|\underline{\theta}_g)u - g(\underline{x}|\underline{\theta}_g)u \\ &= \left[f(\underline{x},t) - f(\underline{x}|\underline{\theta}_f)\right] + y_d^{(nq)} + \underline{k}^T\underline{e} - u_a \\ &\quad + \left[g(\underline{x},t) - g(\underline{x}|\underline{\theta}_g)\right]u + d(t) \end{aligned} \tag{20}$$

then

$$\begin{aligned} e^{(nq)} &= \left[f(\underline{x},t) - f(\underline{x}|\underline{\theta}_f)\right] + \underline{k}^T\underline{e} - u_a + d(t) \\ &\quad + \left[g(\underline{x},t) - g(\underline{x}|\underline{\theta}_g)\right]u = 0 \end{aligned} \tag{21}$$

Equation (21) can be rewritten in state space representation as

$$\underline{e}^{(q)} = A\underline{e} + B\left[f(\underline{x}|\underline{\theta}_f) - f(\underline{x},t) + u_a + \left(g(\underline{x}|\underline{\theta}_g) - g(\underline{x},t)\right)u - d(t)\right] \tag{22}$$

where

$$A = \begin{bmatrix} 0 & 1 & 0 & 0 & \cdots & 0 & 0 \\ 0 & 0 & 1 & 0 & \cdots & 0 & 0 \\ \vdots & \vdots & \vdots & \vdots & \ddots & \vdots & \vdots \\ 0 & 0 & 0 & 0 & \cdots & \vdots & 1 \\ -k_1 & -k_2 & -k_3 & -k_4 & \cdots & -k_{(n-1)} & -k_n \end{bmatrix} \text{ and } B = \begin{bmatrix} 0 \\ 0 \\ \vdots \\ 0 \\ 1 \end{bmatrix}$$

The optimal parameter estimations $\underline{\theta}_f^*$ and $\underline{\theta}_g^*$ are defined as:

$$\underline{\theta}_f^* = arg\ min_{\underline{\theta}_f \epsilon \Omega_f}\left[sup_{x\epsilon\Omega_x}|f(\underline{x}|\underline{\theta}_f) - f(\underline{x},t)|\right] \tag{23}$$

$$\underline{\theta}_g^* = \arg\min_{\underline{\theta}_g \epsilon \Omega_g}\left[\sup_{x\epsilon\Omega_x}|g(\underline{x}|\underline{\theta}_g) - g(\underline{x},t)|\right] \tag{24}$$

where Ω_f, Ω_g and $\Omega_{\underline{x}}$ are constraint sets of suitable bounds on $\underline{\theta}_f$, $\underline{\theta}_g$ *and* x respectively and they are defined as $\Omega_f = \left\{\underline{\theta}_f | |\underline{\theta}_f| \le M_f\right\}$, $\Omega_g = \left\{\underline{\theta}_g | |\underline{\theta}_g| \le M_g\right\}$ et $\Omega_x = \{x||x| \le M_x\}$ where M_f, M_g et M_x are positive constants.

By using (23)–(24), an error dynamic Eq. (22) can be expressed as:

$$\begin{aligned} \underline{e}^{(q)} &= A\underline{e} + B\Big[f(\underline{x}|\underline{\theta}_f) - f(\underline{x}|\underline{\theta}_f^*) + u_a \\ &\quad + \Big(g(\underline{x}|\underline{\theta}_g) - g(\underline{x}|\underline{\theta}_g^*)\Big)u - d(t) + w_1\Big] \end{aligned} \tag{25}$$

where the minimum approximation errors is defined as:

$$w_1 = g(\underline{x}|\underline{\theta}_g^*) - g(\underline{x},t) + f(\underline{x}|\underline{\theta}_f^*) - f(\underline{x},t) - d(t) \tag{26}$$

If $\tilde{\underline{\theta}}_f = \underline{\theta}_f - \underline{\theta}_f^*$ and $\tilde{\underline{\theta}}_g = \underline{\theta}_g - \underline{\theta}_g^*$ can be rewritten as

$$\underline{e}^{(q)} = A\underline{e} + B\left[\xi(\underline{x})^T\tilde{\underline{\theta}}_f + \xi(\underline{x})^T\tilde{\underline{\theta}}_g u + u_a + w_1\right] \tag{27}$$

The following theorem is proposed to show the control performance of the closed loop system [4, 16].

Theorem 1. Consider the commensurate fractional order SISO nonlinear dynamic system (16) with control input (19), if the robust compensator u_a and the fuzzy-based adaptive laws are chosen as:

$$u_a = -\frac{1}{r}B^T P\underline{e} \tag{28}$$

$$\underline{\theta}_f^{(q)} = -r_1\xi(\underline{x})B^T P\underline{e} \tag{29}$$

$$\underline{\theta}_g^{(q)} = -r_2\xi(\underline{x})B^T P\underline{e}u \tag{30}$$

where $r > 0$, $r_i > 0$, $i = 1 \sim 2$, et $P = P^T > 0$ is the solution of the following Riccati-like equation.

$$PA + A^T P + Q - PB\left(\frac{2}{r} - \frac{1}{\rho^2}\right)B^T P = 0 \tag{31}$$

where $Q = Q^T > 0$ is a prescribed weighting matrix. Therefore, the H^∞ tracking performance can be achieved for a prescribed attenuation level ρ which satisfies $2\rho^2 \geq r$ and all the variables of the closed-loop system are bounded [15].

Proof. In order to analyze the closed-loop stability, the Lyapunov function candidate is chosen as

$$V = \frac{1}{2}\underline{e}^T(t)P\underline{e}(t) + \frac{1}{2r_1}\left(\tilde{\underline{\theta}}_f^T\right)\left(\tilde{\underline{\theta}}_f\right) + \frac{1}{2r_2}\left(\tilde{\underline{\theta}}_g^T\right)\left(\tilde{\underline{\theta}}_g\right) \tag{32}$$

Taking the derivative of (32) with respect to time, we get

$$\begin{aligned} V^{(q)}(t) = {} & \frac{1}{2}\left(\underline{e}^{(q)}(t)\right)^T(t) + \frac{1}{2}\underline{e}^T(t)P\underline{e}(t) \\ & + \frac{1}{r_1}\left(\tilde{\underline{\theta}}_f^T\right)\left(\tilde{\underline{\theta}}_f^{(q)}\right) + \frac{1}{r_2}\left(\tilde{\underline{\theta}}_g^T\right)\left(\tilde{\underline{\theta}}_g^{(q)}\right) \end{aligned} \tag{33}$$

$$
\begin{aligned}
&= \frac{1}{2}\left\{A\underline{e} + B\left[\xi(\underline{x})^T\tilde{\underline{\theta}}_f + \xi(\underline{x})^T\tilde{\underline{\theta}}_g u + u_a + w_1\right]\right\}^T P\underline{e} \\
&\quad + \frac{1}{2}\underline{e}^T(e)P\left\{A\underline{e} + B\left[\begin{array}{c}\xi(\underline{x})^T\tilde{\underline{\theta}}_f + \xi(\underline{x})^T\tilde{\underline{\theta}}_g u + u_a \\ + w_1\end{array}\right]\right\} \\
&\quad + \frac{1}{r_1}(\tilde{\underline{\theta}}_f^T)(\tilde{\underline{\theta}}_f^{(q)}) + \frac{1}{r_2}(\tilde{\underline{\theta}}_g^T)(\tilde{\underline{\theta}}_g^{(q)}) \\
&= \frac{1}{2}\underline{e}^T\left(A^TP + PA\right)\underline{e} + \underline{e}^TPBu_a + \underline{e}^TPBw_1 \\
&\quad + \left\{\tilde{\underline{\theta}}_f^T\left[\xi(\underline{x})B^TP\underline{e} + \frac{1}{r_1}(\tilde{\underline{\theta}}_f^{(q)})\right]\right\} \\
&\quad + \left\{\tilde{\underline{\theta}}_g^T\left[\xi(\underline{x})B^TP\underline{e}u + \frac{1}{r_2}(\tilde{\underline{\theta}}_g^{(q)})\right]\right\}
\end{aligned}
\tag{34}
$$

From the robust compensator u_a and the fuzzy-based adaptive laws are given (28)–(30), $V^{(q)}(t)$ in (34) can be rewritten as

$$
\begin{aligned}
V^{(q)}(t) &= -\frac{1}{2}\underline{e}^TQ\underline{e} - \frac{1}{2\rho^2}\underline{e}^TPBB^T\underline{e} + \underline{e}^TPBw_1 \\
&= -\frac{1}{2}\underline{e}^TQ\underline{e} - \frac{1}{2}\left(\frac{1}{\rho}B^TP\underline{e} - \rho w_1\right)^T\left(\frac{1}{\rho}B^TP\underline{e} - \rho w_1\right) + \frac{1}{2}\rho^2w_1^Tw_1 \\
&\le -\frac{1}{2}\underline{e}^TQ\underline{e} + \frac{1}{2}\rho^2w_1^Tw_1.
\end{aligned}
$$

Integrating (34) from $t = 0$ to $t = T$, we have

$$
V(T) - V(0) \le -\frac{1}{2}\int_0^T\left(\underline{e}^TQ\underline{e}dt + \frac{1}{2}\rho^2w_1^Tw_1\right)dt \tag{35}
$$

Since $V(T) \ge 0$, (35) can be rewritten as follows:

$$
\int_0^T \underline{e}^TQ\underline{e}dt \le e^T(0)Pe(0) + \theta^T(0)\theta(0) + \rho^2\int_0^T w_1^Tw_1dt \tag{36}
$$

Therefore, the H^∞ tracking performance can be achieved. The proof is completed.

It is clear that the laws of adaptation (29) and (30) cannot guarantee that $\underline{\theta}_f \in \Omega_f$ and $\underline{\theta}_g \in \Omega_g$, to solve this problem, the algorithm of projection of the parameters is used.

The modified adaptation laws are given as follows:

To adjust the parameters vector $\underline{\theta}_f$ and $\underline{\theta}_g$ [16]:

$$\underline{\theta}_f^{(q)} = \begin{cases} -r_1\xi(\underline{x})B^T P\underline{e}, if \left|\underline{\theta}_f\right| < M_f \\ where\left(\left|\underline{\theta}_f\right| = M_f \, and \, \underline{e}^T PB\xi^T(\underline{x})\underline{\theta}_f \geq 0\right) \\ P_f[-r_1\xi(\underline{x})B^T P\underline{e}], if \left|\underline{\theta}_f\right| = M_f \, and \, \underline{e}^T PB\xi^T(\underline{x})\underline{\theta}_f < 0 \end{cases} \tag{37}$$

$$\underline{\theta}_f^{(q)} = \begin{cases} -r_2\xi(\underline{x})B^T P\underline{e}u, if \left|\underline{\theta}_g\right| < M_g \\ where\left(\left|\underline{\theta}_g\right| = M_g \, and \, \underline{e}^T PB\xi^T(\underline{x})\underline{\theta}_g u \geq 0\right) \\ P_g[-r_2\xi(\underline{x})B^T P\underline{e}u], if \left|\underline{\theta}_g\right| = M_g \, and \, \underline{e}^T PB\xi^T(\underline{x})\underline{\theta}_g u < 0 \end{cases} \tag{38}$$

where the projection operator P [.] is defined as follows:

$$P_f\left[-r_1\xi(\underline{x})B^T P\underline{e}\right] = -r_1\xi(\underline{x})B^T P\underline{e} + r_1 \frac{\underline{e}^T PB\xi^T(\underline{x})\underline{\theta}_f}{\left|\underline{\theta}_f\right|^2}\underline{\theta}_f \tag{39}$$

$$P_g\left[-r_2\xi(\underline{x})B^T P\underline{e}u\right] = -r_2\xi(\underline{x})B^T P\underline{e}u + r_2 \frac{\underline{e}^T PB\xi^T(\underline{x})\underline{\theta}_g u}{\left|\underline{\theta}_g\right|^2}\underline{\theta}_g \tag{40}$$

Proposed algorithm [16]:

1. to define the m_i of set-fuzzy F_i^l whose memberships functions are $\mu_{F_i^l(x_i)}$, where $i = 1,2,...,n$.

   Specifically the basic fuzzy rules of $f\left(\underline{x}|\underline{\theta}_f\right)$ and $g\left(\underline{x}|\underline{\theta}_g\right)$ consist of form rules as:

   $$R_f^{(l)}: IF \, x_1 \, is \, F_1^l, \, and \ldots, \, and \, x_n \, is \, F_n^l \, THEN \, f\left(\underline{x}|\underline{\theta}_f\right) \, is \, G^l$$

   $$R_g^{(l)}: IF \, x_1 \, is \, F_1^l, \, and \ldots, \, and \, x_n \, is \, F_n^l \, THEN \, g\left(\underline{x}|\underline{\theta}_g\right) \, is \, H^l$$

   $l = 1, 2, \ldots, m_i$, G^l and H^l are sets fuzzy in R^l.
   Construction of the fuzzy functions basic as in $\xi^l(\underline{x})$.
2. to specify a symmetrical matrix q definite positive, and to solve the equation of Lyapunov, to obtain the symmetrical matrix $p > 0$.
3. to specify K_i, such as the roots of the $s^{(n)} + k_1 s^{(n-1)} + \cdots + k_n = 0$ are in the left half-plane.
4. to solve the equation of *Riccati* as follows:

$$PA + A^T P + Q - PB\left(\frac{2}{r} - \frac{1}{\rho^2}\right)B^T P = 0$$

5. lastly, the control global law obtains as follows:

$$u = \frac{1}{\xi^T(\underline{x})\underline{\theta}_f}\left[-\xi^T(\underline{x})\underline{\theta}_g + y_d^{(nq)} + \underline{k}^T\underline{e} - u_a\right]$$

where $u_a = -\frac{1}{r}B^T P\underline{e}$, $\underline{\theta}_f^{(q)} = -r_1\xi(\underline{x})B^T P\underline{e}$, and $\underline{\theta}_g^{(q)} = -r_2\xi(\underline{x})B^T P\underline{e}u$.

5 Simulation Results

The chaotic behaviors in a fractional order modified Duffing system studied numerically by phase portraits are given by [27, 28]. In this section, we will apply our adaptive fuzzy H^∞ controller to synchronize two different fractional order chaotic Duffing systems.

Consider the following two fractional order chaotic Duffing systems [27]:

– Drive system:

$$\begin{cases} D^q y_1 = y_2 \\ D^q y_2 = y_1 - 0.25y_2 - y_1^3 + 0.3\cos(t) \end{cases}$$

– Response system:

$$\begin{cases} D^q x_1 = x_2 \\ D^q x_2 = x_1 - 0.3x_2 - x_1^3 + 0.35\cos(t) + u(t) + d(t) \end{cases}$$

where the external disturbance is $d(t) = 0.1sin(t)$.

The main objective is to control the trajectories of the response system to track the reference trajectories obtained from the drive system. The initial conditions of the drive and response systems are chosen as:

$$\begin{bmatrix} x_1(0) \\ x_2(0) \end{bmatrix} = \begin{bmatrix} 0 \\ 0 \end{bmatrix} \text{ and } \begin{bmatrix} y_1(0) \\ y_2(0) \end{bmatrix} = \begin{bmatrix} 0.2 \\ -0.2 \end{bmatrix} \text{ respectively.}$$

The simulations results for deferent values of q (fractional order) are illustrated as follows:

Figure 1 represents the 3D phase portrait of the drive and response systems without control input. It is obvious that the synchronization performance is bad without a control effort supplied to the response system.

The different values of $0 < q < 1$ are considered in order to show the robustness of the proposed adaptive fuzzy H^∞ control with our law.

According to the two state output ranges, the membership functions of x_i, for $f(\underline{x}|\underline{\theta}_f)$ and $g(\underline{x}|\underline{\theta}_g)$ are selected as follows:

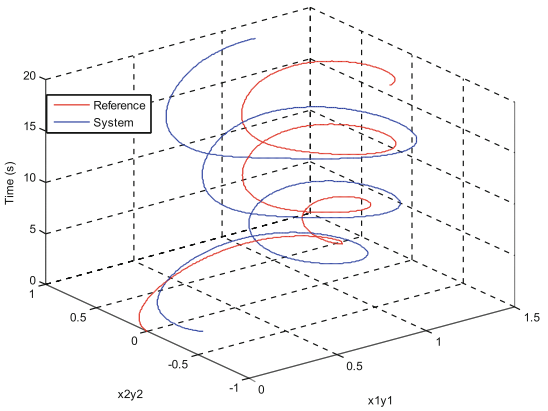

Fig. 1. 3D phase portrait of the drive and response systems without control input (*before* the control input)

$\mu_{F_i^l}(x_i) = \exp\left[-0.5\left(\frac{x_i - \bar{x}}{0.8}\right)^2\right] i = 1, 2$ and $l = 1, \ldots, 7$ where $\bar{x}$ is selected from the interval $[-1, 2]$.

From the adaptive laws (29)–(30) and the robust compensator (28), the control law of the response system can be obtained as:

$$u = \frac{1}{\xi^T(\underline{x})\underline{\theta}_f}\left[-\xi^T(\underline{x})\underline{\theta}_g + y_d^{(nq)} + \underline{k}^T\underline{e} - u_a\right] \tag{41}$$

The figures represent the different simulation results of the drive and response systems with control input (41). It is obvious that the synchronization performance is bad without a control effort supplied the response system.

For the fractional order $q = 0.85$:

For the fractional order $q = 0.98$:

Results and discussion.

- Figures 2 and 7 show a good and fast achievement of the reference and response systems synchronization.
- According to the Figs. 4, 3, 8 and 9, the trajectories of the responses converge accurately to the reference trajectories, even in the presence of external disturbances.
- The control effort for different values of q is illustrated in Figs. 5 and 10.
- It is clearly apparent that a fast synchronization of the reference and response systems is obtained.
- When the fractional order q is reduced we remark that chaos behavior is reduced, and the synchronization error is reduced accordingly.
- Figures 6 and 11 show that the error signals are bounded and converge asymptotically to zero.

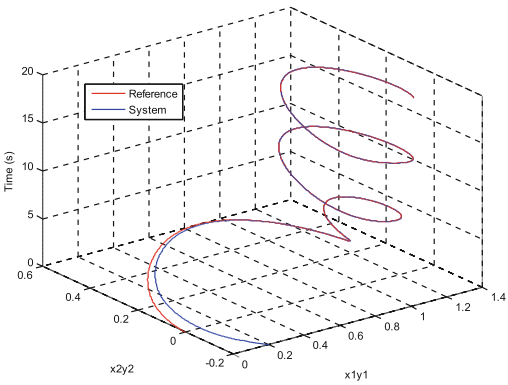

Fig. 2. The 3D phase portrait, synchronization performance, of the drive and response systems.

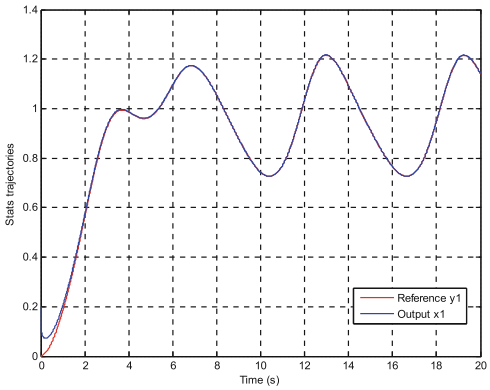

Fig. 3. Trajectories of the state x_1 and y_1.

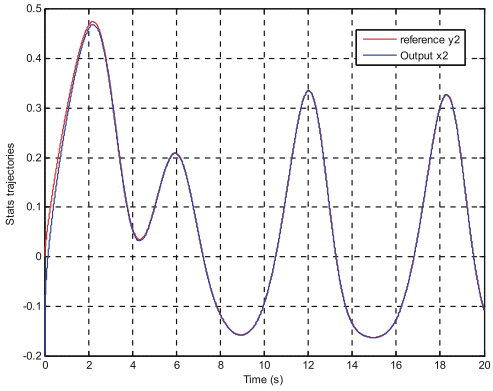

Fig. 4. Trajectories of the state x_2 and y_2.

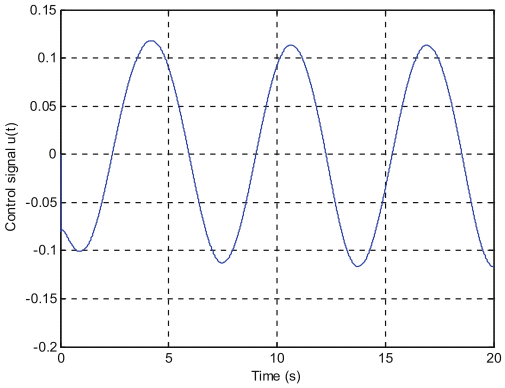

Fig. 5. Trajectory of the control effort.

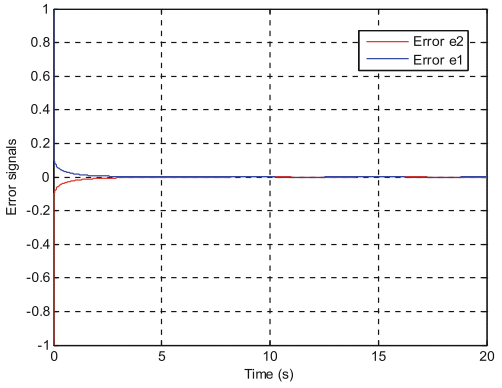

Fig. 6. Trajectory of the errors signals e_1 and e_2.

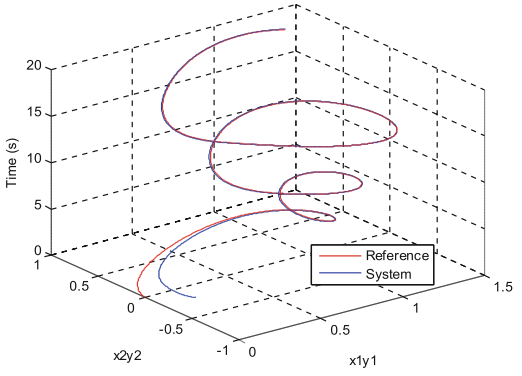

Fig. 7. The 3D phase portrait, synchronization performance of the drive and response systems.

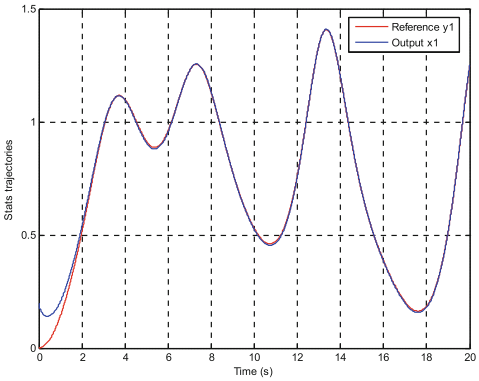

Fig. 8. The trajectories of the states x_1 and y_1.

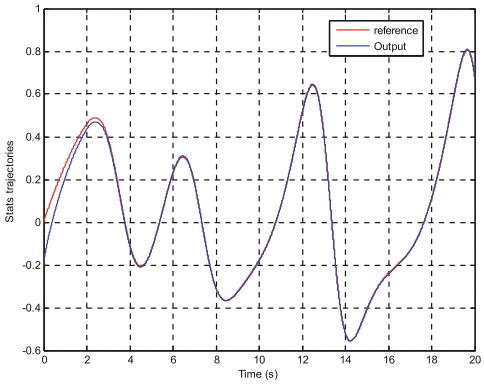

Fig. 9. The trajectories of the states x_2 and y_2.

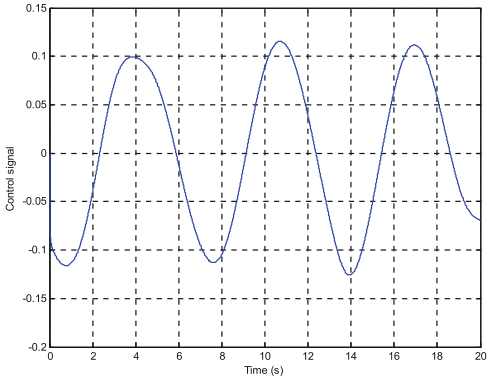

Fig. 10. Trajectory of the control effort.

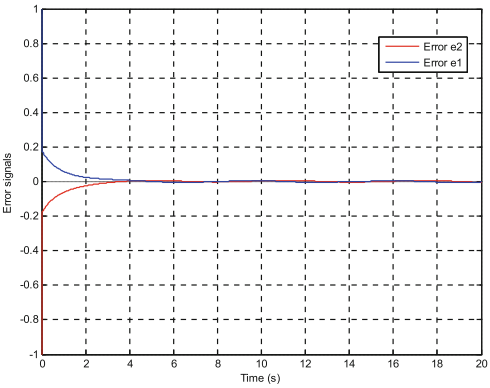

Fig. 11. Trajectory of the errors signals e_1 and e_2.

6 Conclusion

In this paper a novel adaptive fuzzy H^{∞} control is proposed to deal with chaos synchronization between two different uncertain fractional order chaotic systems. Based on the Lyapunov synthesis approach, free parameters of the adaptive fuzzy controller can be tuned on line by the output feedback control law and adaptive laws. However, the determination of the parameter's region is not an easy task in practice, so we introduced a projection algorithm in our control scheme that forces the estimated parameters to stay within a predefined region.

The simulation example, chaos synchronization of two fractional order Duffing systems, is given to demonstrate the effectiveness of the proposed methodology. The significance of the proposed control scheme in the simulation for different values of the fractional order q is manifest. Simulation results show that a fast synchronization of drive and response can be achieved and as q is reduced the chaos is clearly reduced, i.e., the synchronization error is reduced accordingly.

Further researches will be carried out to improve this controller performance using Type-2 Fuzzy sets.

References

1. Lin, T.-C., Lee, T.-Y., Balas, V.E.: Adaptive fuzzy sliding mode control for synchronization of uncertain fractional order chaotic systems. Chaos, Solitons Fractals **44**, 791–801 (2011)
2. Podlubny, I.: Fractional Differential Equations. Academic Press, San Diego (1999)
3. Samko, S.G., Kilbas, A.A., Marichev, O.I.: Fractional Integrals and Derivatives: Theory and Applications. Gordon and Breach, Yverdon (1993)
4. Lin, T.-C., Kuo, C.-H.: H^{∞} synchronization of uncertain fractional order chaotic systems: adaptivefuzzy approach. ISA Trans. **50**, 548–556 (2011)
5. Kilbas, A.A., Srivastava, H.M., Trujillo, J.J.: Theory and Applications of Fractional Differential Equations. Elsevier, Amsterdam (2006)

6. Petráš, I.: A note on the fractional-order Chua's system. Chaos, Solitons Fractals **38**(1), 140–147 (2008)
7. Vinagre, B.M., Feliu, V.: Modeling and control of dynamic systems using fractional calculus: application to electrochemical processes and flexible structures. In: Proceedings of 41st IEEE Conference on Decision and Control (2002)
8. Petráš, I.: A note on the fractional-order cellular neural networks. In: International Proceedings of the IEEE World Congress on Computational Intelligence, International Joint Conference on Neural Networks, pp. 16–21 (2006)
9. Deng, W.H., Li, C.P.: Chaos synchronization of the fractional Lü system. Phys. A **353**, 61–72 (2005)
10. Wang, L.X., Mendel, J.M.: Fuzzy basis function, universal approximation, and orthogonal least square learning. IEEE Trans. Neural Netw. **3**(5), 807–814 (1992)
11. Wang, L.X.: Stable adaptive fuzzy control of nonlinear systems. IEEE Trans. Fuzzy Syst. **1**, 146–155 (1993)
12. Wang, L.X.: Fuzzy systems are universal approximators. In: IEEE International Conference on Fuzzy Systems, San Diego, pp. 1163–1170 (1992)
13. Ross, B. (ed.): Fractional Calculus and Its Applications. LNM, vol. 457. Springer, Heidelberg (1975). doi:10.1007/BFb0067095
14. Wang, L.X.: Adaptive Fuzzy Systems and Control: Design and Stability Analysis. Prentice-Hall, Englewood Cliffs (1994)
15. Lin, T.-C., Kuo, C.-H., Lee, T.-Y., Balas, V.E.: Adaptive fuzzy H^{∞} tracking design of SISO uncertain nonlinear fractional order time-delay systems. Nonlinear Dyn. **69**, 1639–1650 (2012)
16. Chen, B.-S. Lee, C.-H., Chang, Y.-C.: H∞ tracking design of uncertain nonlinear SISO systems: adaptive fuzzy approach. IEEE Trans. Fuzzy Syst. **4**(1), 32–43 (1996)
17. N'Doye, I.: Généralisation du lemme de Grünwall-Bellman pour la stabilisation des systèmes fractionnaires, Ph.D. thesis, Ecole doctorale IAEM Lorraine, Maroc (2011)
18. Lin, T.-C., Wang, C.-H., Liu, H.-L.: Observer-based indirect adaptive fuzzy-neural tracking control for nonlinear SISO systems using VSS and H^{∞} approaches. Fuzzy Sets Syst. **143**, 211–232 (2004)
19. Hilfer, R.: Applications of Fractional Calculus in Physics. World Scientific, New Jersey (2001)
20. Hartley, T.T., Lorenzo, C.F., Qammer, H.K.: Chaos on a fractional Chua's system. IEEE Trans. Circ. Syst. Theor. Appl. **42**(8), 485–490 (1995)
21. Castro, J.L.: Fuzzy logical controllers are universal approximators. IEEE Trans. Syst. Man Cybern. **25**, 629–635 (1995)
22. Lu, J.G., Chen, G.: A note on the fractional-order Chen system. Chaos, Solitons Fractals **27** (3), 685–688 (2006)
23. Wang, C.-H., Liu, H.-L., Lin, T.-C.: Direct adaptive fuzzy-neural control with state observer and supervisory controller for unknown nonlinear dynamical systems. IEEE Trans. Fuzzy Syst. **10**(1), 39–49 (2002)
24. Wang, C.-H., Lin, T.-C., Lee, T.-T., Liu, H.-L.: Adaptive hybrid intelligent control for uncertain nonlinear dynamical systems. IEEE Trans. Syst. **32**(5), 583–597 (2002)
25. Arena, P., Caponetto, R., Fortuna, L., Porto, D.: Chaos in a fractional order Duffing system. In: Proceedings ECCTD, pp. 1259–1262 (1997)
26. Gao, X., Yu, J.: Chaos in the fractional order periodically forced complex Duffing's oscillators. Chaos, Solitons Fractals **26**, 1125–1133 (2005)
27. Ge, Z.-M., Ou, C.-Y.: Chaos in a fractional order modified Duffing system. Chaos, Solitons Fractals **34**(2), 262–291 (2007)

28. Ge, Z.-M., Ou, C.-Y.: Chaos synchronization of fractional order modified Duffing systems with parameters excited by a chaotic signal. Chaos, Solitons Fractals **35**(4), 705–717 (2008)
29. Diethelm, K., Ford, N.J.: Analysis of fractional differential equations. J. Math. Anal. Appl. **265**, 229–248 (2002)
30. Diethelm, K., Ford, N.J., Freed, A.D.: A predictor–corrector approach for the numerical solution of fractional differential equations. Nonlinear Dyn. **29**, 3–22 (2002)
31. Diethelm, K., Ford, N.J., Freed, A.D.: Detailed error analysis for a fractional Adams method. Numer. Algorithms **36**, 31–52 (2004)
32. Khettab, K., Ladaci, S., Bensafia, Y.: Fuzzy adaptive control of fractional order chaotic systems with unknown control gain sign using a fractional order Nussbaum gain. IEEE/CAA J. Automatica Sinica **4**(1), 1–8 (2017)
33. Bensafia, Y., Ladaci, S., Khettab, K.: Using a fractionalized integrator for control performance enhancement. Int. J. Innovative Comput. Inf. Control **11**(6), 2013–2028 (2015)
34. Ladaci, S., Khettab, K.: Fractional order multiple model adaptive control. Int. J. Autom. Syst. Eng. **6**(2), 110–122 (2012)

Signal and Communications (SC)

A Leaky Wave Antenna Based on SIW Technology for Ka Band Applications

Souad Doucha(✉) and Mehadji Abri

Laboratoire de Télécommunications, Faculté de Technologie,
Département de Génie Electrique, Université Abou-Bekr Belkaïd – Tlemcen,
BP 230 Pôle Chetouane, 13000 Tlemcen, Algérie
souadtelecom@gmail.com, abrim2002@yahoo.fr

Abstract. The design of an antenna based on Substrate Integrated Waveguide (SIW) has been realized in this paper. The structure consists of an array of slot antenna designed to operate in Ka 17,3 à 21.2 GHz band applications. The structure of SIW is composed of two rows of cylinders between metal plates; it can be easily produced by the standard method PCB "circuit" or LTCC method. The direction of the main lobe of the antenna radiation pattern can be steered by changing the frequency in the band from backward direction to forward direction.

1 Introduction

The next generation communication networks require ultra-wide bandwidth for which transmission antennas are required to operate in the Ka-band in particular for satellite and mobile communication. Array antennas have several applications in communications systems. They are usually developed using microstrip or waveguide technologies. However, with the development of a novel technology called substrate integrated waveguide (SIW), Substrate integrated waveguide (SIW) technology has been studied very extensively in recent years and has by now become a widely applied technique in planar microwave circuit design [1–3]. These waveguide-like structures are fabricated in planar form and are built up by periodically arranged metallic via-holes or via-slots as shown in Fig. 1 advantage of the well-known characteristics of conventional rectangular waveguides, namely, its high Q-factor and high power capacity, as, well as its low losses. Though they have been studied for the use in antenna applications [4, 5].

A leaky-wave antenna has been widely used in aerospace applications for many years. The main advantage of these antennas is that they save space and can be located on the external surface of various bodies. They are low cost, can be easily fabricated and are therefore suitable for mass production Substrate integrated waveguide (SIW) structures.

An SIW LWA concept was proposed in [8]. This antenna radiates energy through the SIW side wall with sparsely located shortening vias. Inherent limitations of this structure were exposed. The SIW was used as an LWA able to steer the radiation pattern main beam by changing frequency from nearly backward direction to forward direction [9, 10].

M. Chadli et al. (eds.), *Recent Advances in Electrical Engineering and Control Applications*,
Lecture Notes in Electrical Engineering 411, DOI 10.1007/978-3-319-48929-2_22

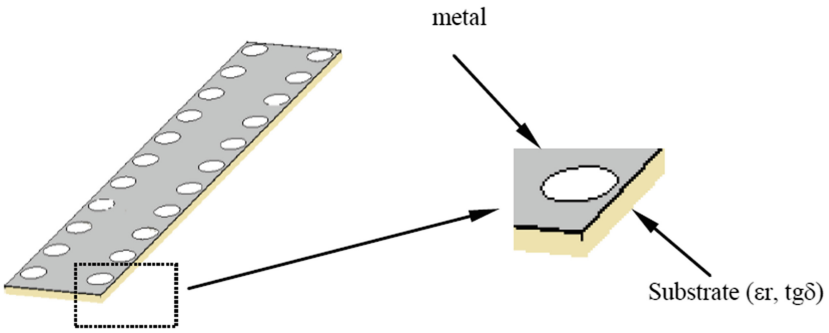

Fig. 1. SIW structure

In this paper, we design a SIW component operating in ka-band for TE10 mode with CST Microwave Studio® commercial software's. To validate the obtained results, a comparison will be made using the moment method of Momentum Software. The design procedures begins by extracting the equivalent width guide and then calculate the width of SIW, by the following formulas design after adapt other parameters such as diameter and the distance between the vias, and for transit SIW to microstrip we use the equations of impedance adaptation. And finely, we designed a leaky-wave antenna based on substrate integrated waveguide (SIW) with transverse slots; the antenna radiates one main beam that can be steered from the backward to the forward direction by changing frequency.

2 Parameters of Substrate Integrated Waveguide

Since SIW design generally works in TE1, 0 mode, so here m = 1, n = 0. Therefore the equation for cutoff frequency reduces to:

$$f_c = \frac{c}{2a} \tag{1}$$

For DFW with same cut off frequency, dimension "ad" is found by:

$$a_d = \frac{a}{\sqrt{\varepsilon_r}} \tag{2}$$

Having determined the dimension ad for the DFW, we can now pass to the design equations for SIW [11].

$$a_s = a / \sqrt{\xi_r} + \left(\frac{d^2}{0.95s} \right) \tag{3}$$

where, a is the total broad side dimension of the rectangular waveguide, as is the separation between via rows (centre to centre), a is the width of DFW, d is the diameter (as shown in Fig. 2) and c is the velocity of light in free space.

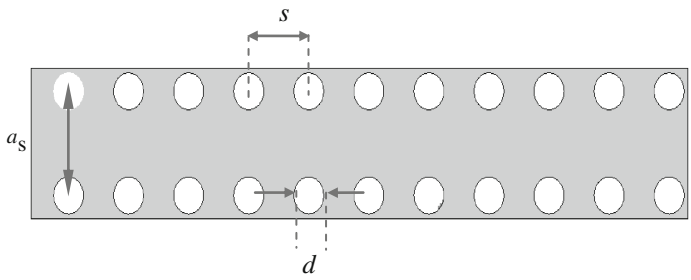

Fig. 2. SIW guide parameters

For SIW design, the following two conditions are required [6]:

$$d \leq \frac{\lambda_g}{5} \tag{4}$$

$$s \leq 2d \tag{5}$$

Where λg (guided wavelength) is [7]

$$\lambda_g = \frac{2\pi}{\sqrt{\frac{(2\pi f)^2 \varepsilon_r}{c^2} - \left(\frac{\pi}{a}\right)^2}} \tag{6}$$

2.1 Feed Design

In order to make an SIW working for ka-band applications we investigated these equations the cutoff frequency of TE10 mode in SIW is selected about 17.3 GHz with the following parameters on Arlon Cu 233lx (lossy), with dielectric constant of εr = 2.33 and tang δ = 0.0013. These parameters are used to construct SIW by using CST Microwave Studio software.

The result of the simulation for the cutoff frequency 17.3 GHz is given by the Fig. 3, it is clear that the transmission between [0–17.3 GHz] is impossible before the cutoff frequency which is 17.3 GHz as theoretically calculated. In this case, the transmission between [17.3–21.2 GHz] is low and this is due to the poor adaptation of the guide.

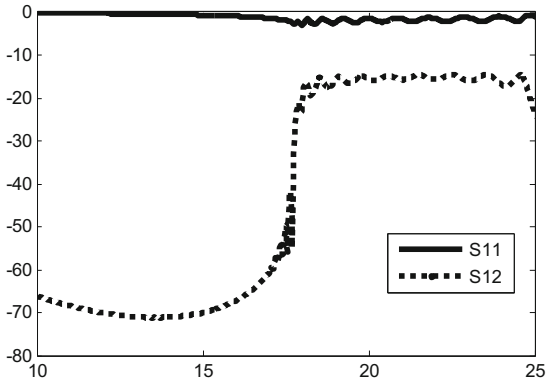

Fig. 3. The reflected power and the transmission coefficient of the SIW waveguide. The SIW waveguide parameters are set to: as = 7.1 mm, d = 1.25 mm, s = 4.9 mm, b = 0.508 mm

2.2 Microstrip Transition Lines in Substrate Integrated Waveguide

Once the SIW is designed, it is necessary to have a transition to a transmission line to ensure a perfect adaptation.

This transition contains two main parameters, the original width W0, the final width W of the profile line. The initial width of the microstrip line W0 must be calculated to obtain the desired characteristic impedance. This width is generally selected for a characteristic impedance of 50 O. For calculating the width W, it is necessary to calculate the impedance of SIW guide, which is given by the following formula. [12]

$$Z_{pi} = Z_{TE} \frac{b\pi^2}{8a_s} \tag{8}$$

For the calculation of the guide impedance, it is also necessary to calculate the wave impedance of TE mode, which is given by [12]

$$Z_{TE} = \sqrt{\frac{\mu}{\xi}} \times \frac{\lambda_g}{\lambda} \tag{9}$$

The calculated parameters are used to construct a taper by using ADS (advanced design system) software. The simulation result of taper and the structure after optimization is shown in Fig. 4. The calculated parameters are used to construct a taper by using ADS (advanced design system) software. The simulation result of taper and the structure after optimization is shown in Fig. 4.

According to the Fig. 4, we see an excellent adaptation between 17-22 GHz. This is necessary to avoid a drop in dB when inserting transition guide with SIW. The physical transition structure of microstrip line with the guide SIW is shown in Fig. 5.

Reflected power and the transmission coefficient of the transition topology with SIW guide is obtained by simulation using CST and Momentum software's, are shown respectively in the Figs. 6 and 7.

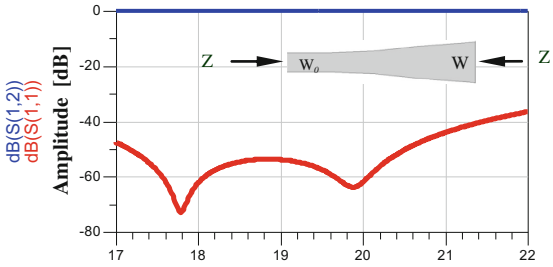

Fig. 4. The return loss and the transmission coefficient of the transition and the geometrical layout of optimized taper. The parameters are set to: Z0 = 50 O, Z = 29.29 O, w0 = 1.52 mm, w = 3.25 mm

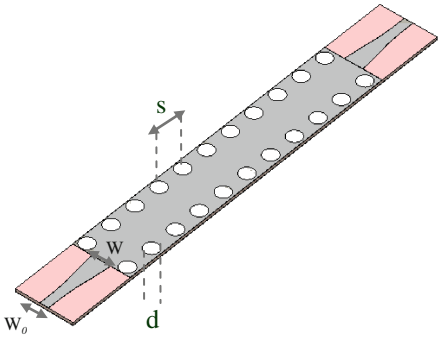

Fig. 5. Topology of transition with SIW guide

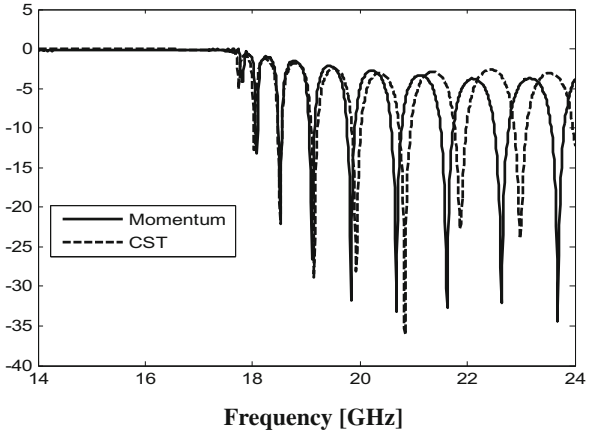

Fig. 6. Return loss of the SIW guide presented in Fig. 4 simulated with CST and Momentum software's

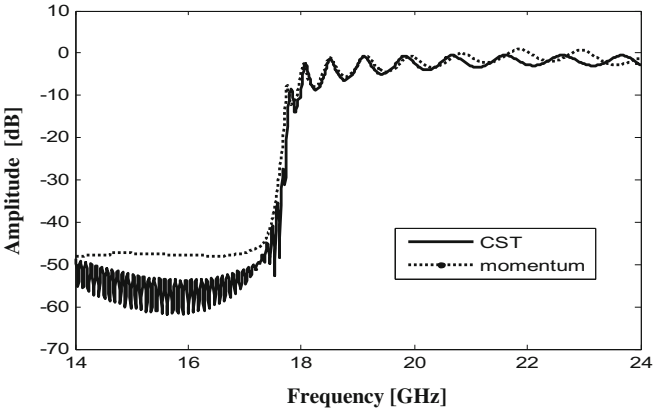

Fig. 7. Transmission coefficient S12 of the waveguide

3 SIW Leaky-Wave Antenna Design

The antenna under consideration is basically a wave guiding structure that possesses a mechanism that permits it to leak power all along its length. In this paconstruct a LWA based on SIW as shown in Fig. 8.

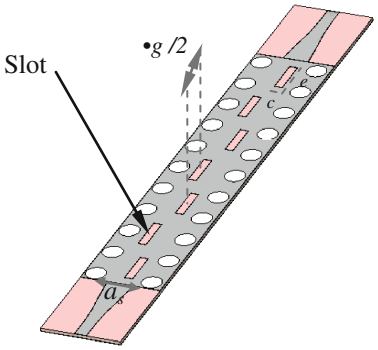

Fig. 8. Top view of the proposed leaky-wave antenna based on Substrate integrated waveguide with d = 1.25 mm, s = 4.9 mm, as = 7.1 mm, w = 3.25 mm, w0 = 1.52 mm, e = 4.3 mm, c = 1 mm and λg = 14.8 mm

The S-parameter of the LWA with 7 uniform slots based in SIW is shown in Fig. 9.

The radiation patterns in 3D representation and in polar coordinates of only one port LWA are depicted respectively in Figs. 10 and 11. From Figs. 9 and 10 the beam directions are 27°, 16°, 8° and 1° calculated respectively the frequencies 19.11 GHz, 19.83 GHz, 20.68 GHz and 21.6 GHz. The scanning is assured using this technique around the broadside direction (θ = 0°). This phenomenon is well shown in polar plot.

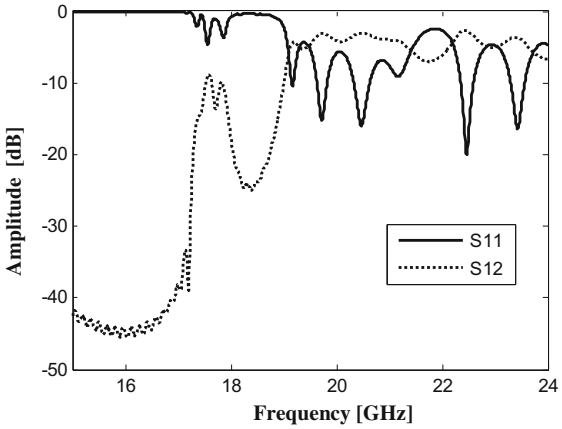

Fig. 9. S-parameter of the LWA based in SIW in band [17.3–21.2 GHz]

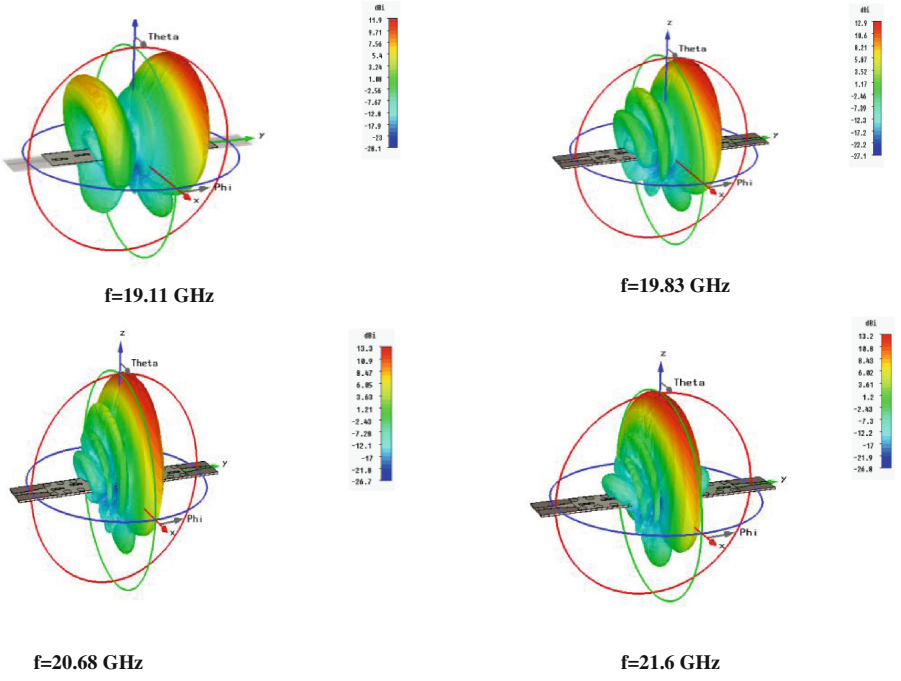

Fig. 10. 3D radiation patterns obtained of LWA with changing frequency. f = 19.11 GHz with Main Lobe Direction MLD = −27°, f = 19.83 GHz with MLD = −16°, f = 20.68 GHz with MLD = 8° and f = 21.6 GHz with MLD = 1°

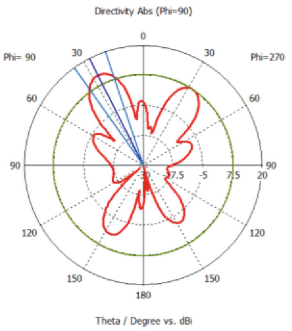

f=19.11 GHz

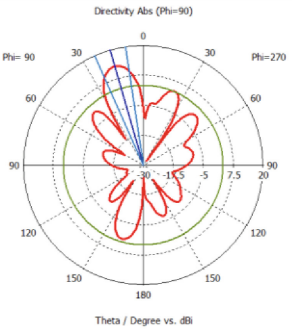

f=19.83 GHz

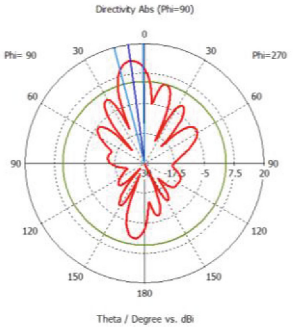

f=20.68 GHz

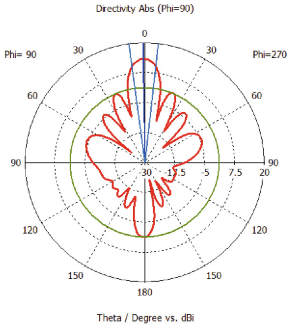

f=21.6 GHz

Fig. 11. Radiation patterns in polar coordinates obtained of LWA with changing frequency

4 Conclusion

In this paper a novel type of substrate integrated waveguide leaky wave antenna has been presented, the structure can find wide application in Ka [17.3–21.2 GHz] band radar and remote sensing mechanism. The design is first passed by calculating the cutoff frequency of the guide. Then we calculated the input impedance of the guide and optimize the taper to make the transition between supply and input guide to ensure a perfect adaptation. After we design a leaky wave antenna based on a substrate integrated waveguide (SIW), the antenna radiates in ka-band and shows the beam scanning possibility from forward direction to backward direction of the radiation.

References

1. Shen, W., Yin, W.Y., Sun, X.W.: Miniaturized dual-band substrate integrated waveguide filter with controllable bandwidths. IEEE Microw. Wirel. Compon. Lett. **21**(8), 418–420 (2011)
2. W. W. Hansen, Radiating Electromagnetic Waveguide. U.S. Patent 2,402,622 (1940)
3. Xu, F., Jiang, X., Wu, K.: Efficient and accurate design of substrate integrated waveguide circuits synthesized with metallic via-slot arrays. IET Microw. Antennas Propag. **2**(2), 188–193 (2008)
4. Kim, D.Y., Chung, W., Park, C., Lee, S., Nam, S.: Design of a 45° Inclined SIW resonant series slot array antenna for Ka-Band. IEEE Antennas Wirel. Propag. Lett. **10**, 318–321 (2011)
5. Lu, H.C., Chu, T.-H.: Equivalent circuit of radiating longitudinal slots in substrate integrated waveguide. In: IEEE AP-S International Symposium on Digest, pp. 2341–2344 (2004)
6. Cassivi, Y., Perregrini, L., Arcioni, P., Bressan, M., Wu, K., Conciauro, G.: Dispersion characteristics of substrate integrated rectangular waveguide. IEEE Microw. Wirel. Compon. Lett. **12**, 333–335 (2002)
7. Rayas-Sanchez, J.E., Gutierrez-Ayala, V.: A general EM-based design procedure for single-layer substrate integrated waveguide interconnects with microstrip transitions. In: IEEE MTT-S International Microwave Symposium on Digest, Atlanta, GA, pp. 983–986, June 2008
8. Yu, I., Chen, X., Wang, C.J., Jou, C.F.: Substrate integrated waveguide leaky-wave antenna: concept and design considerations. In: Asia Pacific Microwave Conference, pp. 4–7, December 2005
9. Tang, X.J., Xiao, S.Q., Wang, B.Z., Wang, J.: A 60-GHz wideband slot antenna based on substrate integrated waveguide cavity. Int. J. Infrared Milli. Waves **28**, 275–281 (2007)
10. Dong, Y., Itoh, T.: Composite right left-handed substrate integrated waveguide leaky-wave antennas. In: 39th European Microwave Conference, October 2009
11. Chen, X., Hong, W., Cui, T., Chen, J., Wu, K.: Substrate integrated waveguide (SIW) linear phase filter. IEEE Microw. Wirel. Compon. Lett. **15**(11), 787–789 (2005)
12. Ban, Y.J.: Tunable ferrite phase shifters using substrate integrated waveguide technique, theses, December 2010

Selective Filters Design Based Two-Dimensional Photonic Crystals: Modeling Using the 2D-FDTD Method

Hadjira Abri Badaoui[1(✉)] and Mehadji Abri[2]

[1] STIC Laboratory, Faculty of Technology, Telecommunication Department, University of Tlemcen, Tlemcen, Algeria
elnbh@yahoo.fr
[2] Telecommunication Laboratory, Faculty of Technology, Telecommunication Department, University of Tlemcen, Tlemcen, Algeria
abrim2002@yahoo.fr

Abstract. The photonic crystals are structures whose dielectric index varies in one or more spatial direction. In these latter appear energy band gap for the electromagnetic field, prohibiting propagation of light in certain directions and in certain energies. These characteristics give the photonic crystals having attractive properties for many applications in integrated optic. Precisely, this work is a contribution to the two-dimensional planar photonic crystals in the field of integrated optics. In this paper, we propose novel selective filter topologies by the use of cascaded wave guides. The performance of such structures in terms of transmission and reflection will be performed and analyzed using 2D-FDTD method.

1 Introduction

The market for data transmission application rates in recent years such as optical transmission has become the major route. The development of optical fibers was the first essential link in the development of this technology routing information. The information is now transmitted on multiple frequencies and is essential components of the optical fiber output to manage such operations multiplexing/demultiplexing. These optical circuits exist but are of the order of one centimeter: therefore they are bulky and therefore not conducive to mass production. Alongside this issue related to the development of the Internet, the electrical interconnections between chips begin to be so close to each other that their performance could be limited. Make optical interconnects can be a solution, provided that the sizes of these components are the same as those of current microelectronic components [1]. Microelectronics has invaded our lives every day and most of the devices around us contain at least one chip. Optical functions have also been developed with semiconductor materials, such as emission and detection of light, paving the way for optoelectronics. Emitting diodes, laser diodes and CCD (Charge Coupled Device) sensors can be cited here.

The light turns out to be a very good vehicle because of its insensitivity to electromagnetic interference and its high frequency, allowing considering high

M. Chadli et al. (eds.), *Recent Advances in Electrical Engineering and Control Applications*, Lecture Notes in Electrical Engineering 411, DOI 10.1007/978-3-319-48929-2_23

transmission rates in the field of optical telecommunications. Among the solutions proposed today would be an interesting way to fabricate photonic devices (waveguide selective filter, multiplexer…) silicon as they are fully compatible with microelectronics industries. This solution would, eventually, a significant advance in microelectronics, but it is very basic and requires a prospective study of optical mechanisms involved in these micro- or nanostructures.

Photons are therefore emerging as efficient information delivery. It is in this context that Eli Yablonovitch suggested, in a seminal paper dated 1987, to extend the concepts of structure and band-gap [2, 3] band. By artificially structural material, it is possible to control the light. Yablonovitch initially wanted to apply this idea to the problem of controlling the spontaneous emission, but soon the more general character of this concept emerged: the photonic crystals (PCs) were born.

The term "photonic crystal" has been proposed for the first time in 1987. The first photonic crystal was conducted in 1991. Photonic crystals are structures with the refractive index varied periodically in one, two or three dimensions. This produces a periodic medium of light propagating in the photonic crystal is similar to that of the periodic potential of the electrons in a crystal effect. Just as there are for electrons allowed energy bands and bandgaps, there are photonic band of allowed states and photonic bandgap. A photonic band (PBG) corresponds to an energy where the propagation of light is prohibited in certain directions in the crystal interval. Photonic crystals have the potential to control the spread of the light, and thus, on the dimensions of the order of magnitude of the wavelength in the material. It is especially this property which makes them attractive for many applications. The adaptation of photonic crystals in optoelectronics allows considering new perspectives such as the realization of integrated optical components with reduced dimensions and the integration of multiple functions on a single substrate. Potential applications of photonic band gap materials BIP- 2D are many and varied: production of resonant cavities of very small size, waveguides, turns, splitters, selective filters, multiplexers-demultiplexers and optical fibers [4–20]. These materials will give rise to new much more efficient and compact than conventional we are currently experiencing optoelectronic components. Achievements selective filters, including point defects and a line in a two-dimensional photonic crystal can be validated. This work will support the design of devices for guiding and selective from 2D - CPs at the wavelength 1.55 μm, which widely used in the fiber-optic telecommunications length filtering.

2 Filtering in Two-Dimensional Photonic Crystals

Most applications of the photonic crystals based on their band gap. To provide a frequency allowed in this inner band gap, it is necessary to introduce defects in the periodic structure. These defects are made locally modifying the geometry of the crystal. A filter is an element or a function whose purpose is to select one or more among the frequency bands of the electromagnetic spectrum and to eliminate others. In this case, we are interested only in selective filters is to say that select a single frequency. They allow you to select the desired signal while rejecting those unwanted.

In this article, we aim to develop selective filters in photonic crystals using the two-dimensional FDTD-2D method. This is a new type of selective filter which is achieved by the combination of two or three W1KA guides having different radii standardized. Filter performance studied in terms of transmission will be discussed and the representation of the magnetic field will be made for different iterations.

3 Two Dimensional FDTD 2D

FDTD aims to numerical solution of Maxwell's equations using finite differences in spatial and temporal domains. The finite difference equations have been applied to both polarizations TE and TM modes [21, 22]:

– TE Mode

$$\begin{cases} H_z|_{i,j}^{n+1/2} = H_z|_{i,j}^{n\,1/2} + \frac{\Delta t}{\mu}\left(\dfrac{\dfrac{E_x|_{i,j+1/2}^{n}\,E_x|_{i,j\,1/2}^{n}}{\Delta y}}{\dfrac{E_y|_{i+1/2,j}^{n}\,E_y|_{i\,1/2,j}^{n}}{\Delta x}}\right) \\ E_x|_{i,j}^{n+1} = E_x|_{i,j}^{n} + \frac{\Delta t}{\varepsilon_{i,j}}\left(\frac{H_z|_{i,j+1/2}^{n+1/2}\,H_z|_{i,j\,1/2}^{n+1/2}}{\Delta y}\right) \\ E_y|_{i,j}^{n+1} = E_y|_{i,j}^{n} + \frac{\Delta t}{\varepsilon_{i,j}}\left(\frac{H_z|_{i+1/2,j}^{n+1/2}\,H_z|_{i\,1/2,j}^{n+1/2}}{\Delta x}\right) \end{cases} \tag{1}$$

– TM Mode

$$\begin{cases} H_x|_{i,j}^{n+1/2} = H_x|_{i,j}^{n\,1/2}\,\frac{\Delta t}{\mu}\left(\frac{E_z|_{i,j+1/2}^{n}\,E_z|_{i,j\,1/2}^{n}}{\Delta y}\right) \\ H_y|_{i,j}^{n+1/2} = H_y|_{i,j}^{n\,1/2} + \frac{\Delta t}{\mu}\left(\frac{E_z|_{i+1/2,j}^{n}\,E_z|_{i\,1/2,j}^{n}}{\Delta x}\right) \\ E_z|_{i,j}^{n+1} = E_z|_{i,j}^{n} + \frac{\Delta t}{\varepsilon_{i,j}}\left(\dfrac{\dfrac{H_y|_{i+1/2,j}^{n+1/2}\,H_y|_{i\,1/2,j}^{n+1/2}}{\Delta x}}{\dfrac{H_x|_{i,j+1/2}^{n+1/2}\,H_x|_{i,j\,1/2}^{n+1/2}}{\Delta y}}\right) \end{cases} \tag{2}$$

The numerical algorithm defined by the Eqs. (1) and (2) imposes an upper bound on the temporal discretization step defined by:

$$\Delta t \;\leq\; \frac{1}{c\sqrt{\left(\frac{1}{\Delta x}\right)^2 + \left(\frac{1}{\Delta y}\right)^2}} \tag{3}$$

And with a spatial resolution $\Delta x = \Delta y \leq \frac{\lambda}{10.\sqrt{\varepsilon_r}}$

The algorithm FDTD-2D, presented in the form shown in Fig. 1, allows a temporal evolution of electric and magnetic fields. The field of solving Maxwell's equations in a bounded domain restreind to limit the amount of memory used and therefore the computation time. This is a mesh structure, knowing that the spatial discretization step depends mainly on the accuracy required and the wavelength used. Furthermore, to ensure numerical stability, the temporal discretization step depends on spatial step.

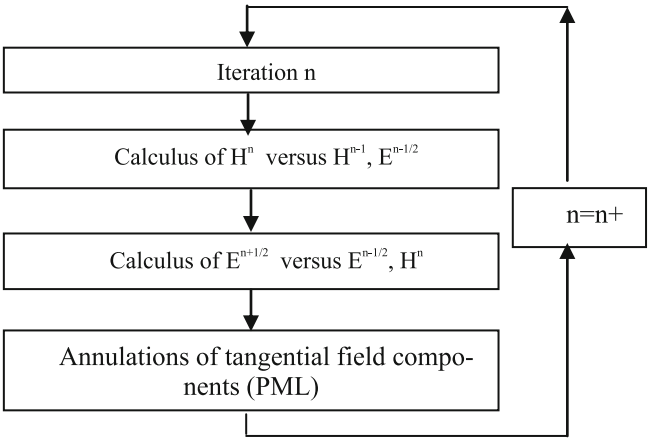

Fig. 1. FDTD flowchart algorithm field.

We used in this work a two-dimensional FDTD code that captures the simulation parameters (spatial discretization step, simulation mode (TE/TM), number of iterations), the boundary conditions. This paper presents only the conditions of absorption of wall type that simulates an infinite domain containing the whole structure study seeking the lowest numerical reflection at interfaces.

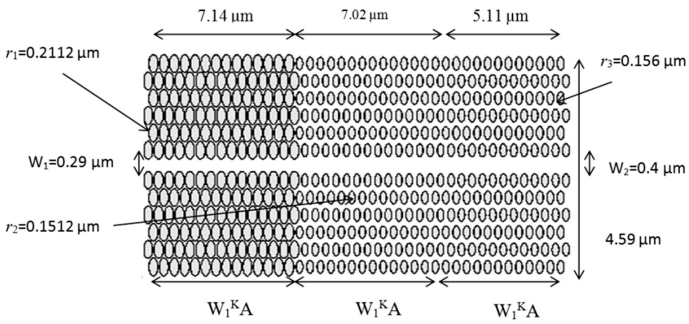

Fig. 2. Selective filter structure composed of a three triangular $W_1{}^K A$ guides.

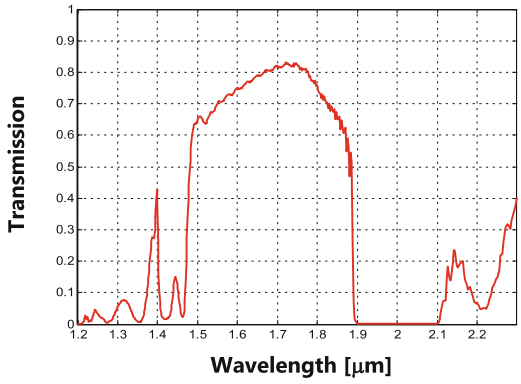

(a)

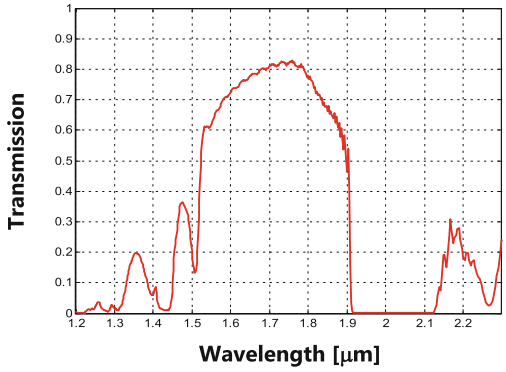

(b)

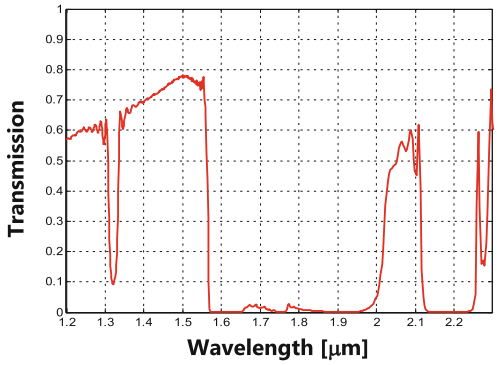

(c)

Fig. 3. Normalized transmission spectra obtained by: (a) triangular guide $W_1{}^KA$ with triangular normalized radius $r_1 = 0.2112$ μm, (b) guide $W_1{}^KA$ with triangular normalized radius $r_2 = 0.1512$ μm, (c) guide $W_1{}^KA$ with triangular normalized radius $r_3 = 0.156$ μm.

The principal visible at the end of the simulation results are maps fields of the various components and the calculation of the coefficients of reflection and transmission.

4 Selective Filter Design

In this part of work, we present the different topologies that we have designed to improve the performance of different selective filters made by coupling two or three guides W1KA in square and triangular structures.

4.1 First Filter Topology Based on Three Cascaded Waveguide in Triangular Lattices

In what follows, we will study the frequency selectivity of three guides W1KA in triangular lattices in cascade based the 2D - CPs with different radii. The parameters of this filter are shown in Fig. 2. Simulation results of each guide W1KA depicted in Fig. 2 are presented in Fig. 3.

The filter transmission performance obtained by the 2D-FDTD method is shown in Fig. 4. From Fig. 4, a low transmission which does not exceed 20% of the range of wavelengths [1.2–1.41] μm and almost zero over the range of wavelengths [1.58–2] μm is observed. The amount of stored transmission at the wavelength 1.55 μm is of the order of 95%. This demonstrates the performance of the studied structure. Note that the high level of transmission is due to the change of the channel width of the various guides constituting the filter, usually called a taper. Studies have shown the effectiveness of the tapers for improving transmission through the structure.

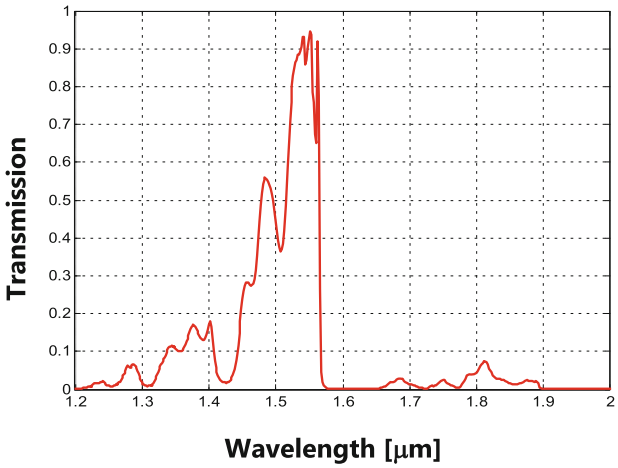

Fig. 4. Filter spectral transmission response.

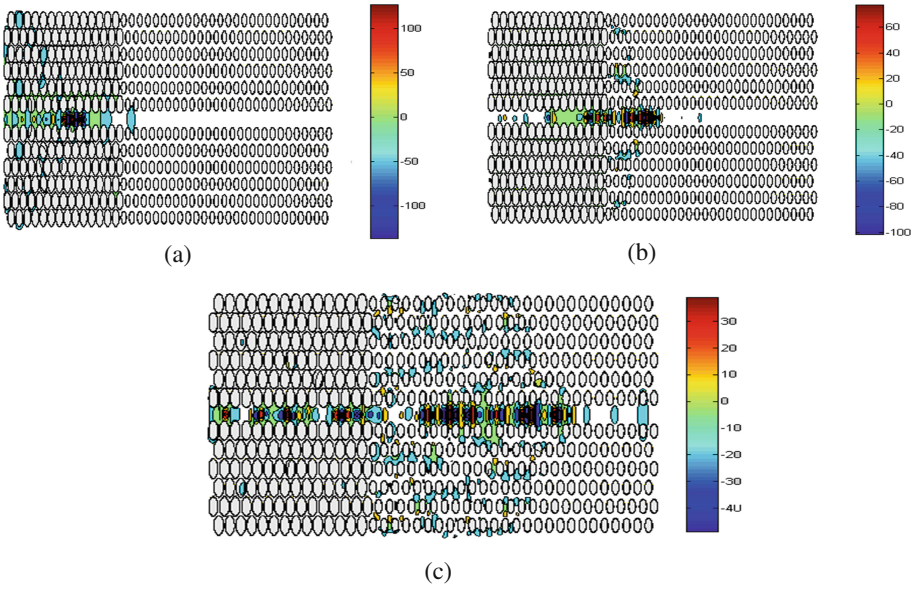

Fig. 5. Distribution of the magnetic field Hz excited in TE mode filter. (a) 2000 iterations, (c) 3500 iterations, (d) 5000 iterations.

The distribution of the magnetic field Hz iterations, 2000, 3500 and 5000 is shown in Fig. 5.

4.2 Second Filter Topology Based on Three Cascaded Wave Guides in Square and Triangular Lattices

To improve the filtering and propose new structures, we made a new type of selective filter obtained by the combination of three $W_1{}^KA$ guides in triangular structure with standardized different radii. The input parameters of the topology are shown in Fig. 6 which illustrates the structure to be simulated. In this topology, the filter is formed by combining two triangular waveguides $W_1{}^KA$ with different radii, respectively $r_1 = r_3 = 0.1416$ µm and 0.2121 µm, and this by means of a third guide $W_1{}^KA$ with normalized radius $r_2 = 0.1968$ µm in square lattice. The structure to be simulated is shown in Fig. 6. Simulation results of each guide $W_1{}^KA$ are shown in Fig. 7.

In Fig. 8 we see a clear selectivity of the filter wave length 1.55 µm, with a maximum transmission which is of about 52% and almost zero in the range [1.25 to 1.53] µm, [1.57–2] µm. This filter provides a good rejection of not more than 10%.

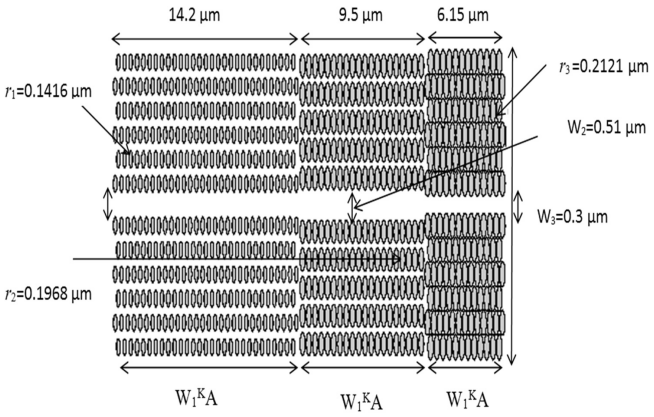

Fig. 6. Structure of a filter consisting of two waveguides $W_1{}^KA$ in triangular a square lattices.

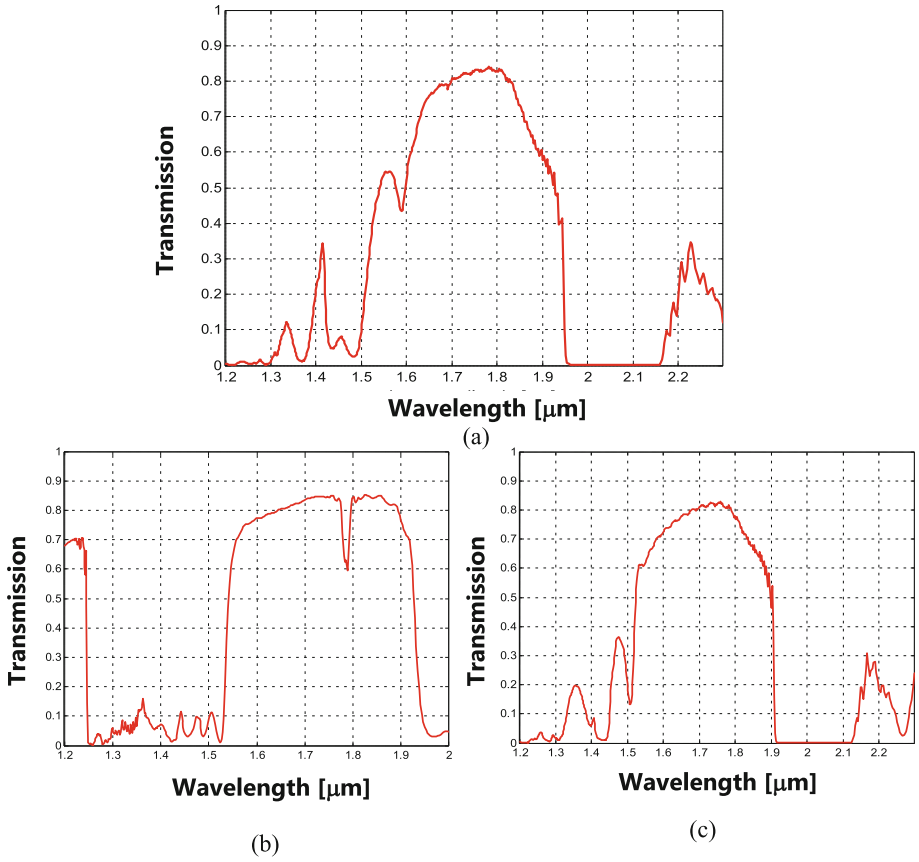

Fig. 7. Standardized transmission spectra obtained from: (a) guide $W_1{}^KA$ in triangular lattice with radius $r_1 = 0.1416$ µm, (b) guide $W_1{}^KA$ in square lattice with radius $r_2 = 0.1968$ µm, (c) guide $W_1{}^KA$ in triangular lattice with radius $r_3 = 0.2121$ µm.

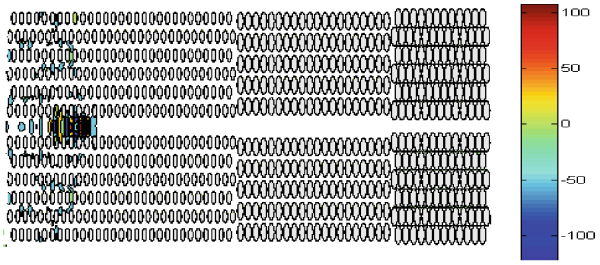

(a)

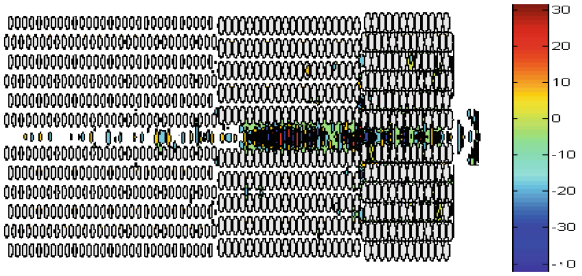

(b)

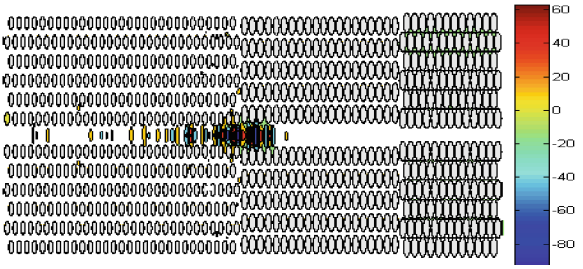

(c)

Fig. 9. Distribution of the magnetic field Hz filter excited with TE mode. (a) 2000 iterations, (b) 5000 iterations (c) 10000 iterations.

Figure 9 represents the distribution of magnetic field in Hz folder for different iterations.

From Fig. 9, a part of the magnetic field reach the filter output, and another portion will be reflected.

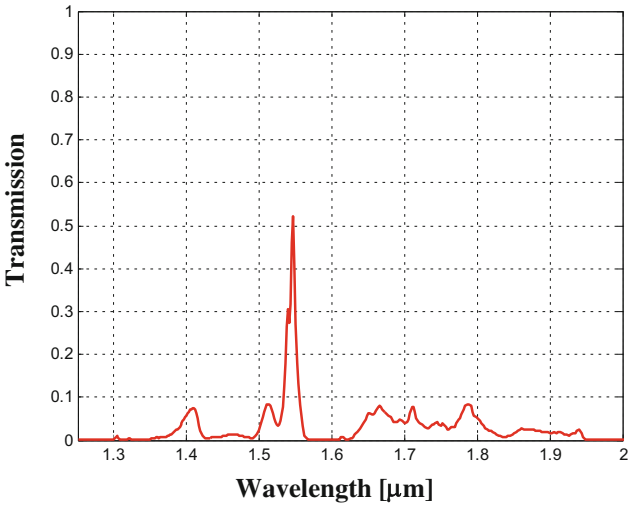

Fig. 8. Spectral transmission response of selective filter studied.

5 Conclusions

The main objective of this paper was to explore a new type of selective filter based on the coupling between waveguides $W_1{}^K A$ CP-2D. The properties of these filters have been investigated by simulations using the two-dimensional finite difference time domain method.

We proposed two selective filter configurations, the first based on the coupling between three $W_1{}^K A$ guides having different radii in triangular lattice and the second one use the same principle with respect to the first but with the use of a guide in square lattices. The numerical results show the existence of a narrow band around the transmitted wavelength 1.55 μm and good selectivity.

References

1. Abri Badaoui, H.: Étude Et Conception Des Microcomposant A Base Des Cristaux Photonique Bidimensionnelles. Thèse de doctorat en télécommunications, Université Tlemcen (2012)
2. Yablonovitch, E.: Inhibited spontaneous emission in solid-state physics and electronics. Phys. Rev. Lett. **58**(20), 2059–2062 (1987)
3. John, S.: Strong localization of photons in certain disordered dielectric superlattices. Phys. Rev. Lett. **58**(23), 2486–2489 (1987)
4. Badaoui, H., Feham, M., Abri, M.: Double bends and y-shaped splitter design for integrated optics. Prog. Electromagn. Res. Lett. **28**, 129–138 (2012)
5. Badaoui, H., Feham, M., Abri, M.: Optimized 1×4 Y shaped splitter for integrated optics. Aust. J. Basic Appl. Sci. **5**(10), 482–488 (2011)

6. Rumpf, R.C., Mehta, A., Srinivasan, P., Johnson, E.G.: Design and optimization of space-variant photonic crystal filters. Appl. Opt. **46**(23), 5755–5761 (2007)
7. Shambat, G., Mirotznik, M.S., Euliss, G., Smolski, V.O., Johnson, E.G., Athal, R.A.: Photonic crystal filters for multi-band optical filtering on a monolithic substrate. J. Nanophotonics **3**, 031506 (2009)
8. Strasser, P., Stark, G., Robin, F., Erni, D., Rauscher, K., Wüest, R., Jäckel, H.: Optimization of a 60° waveguide bend in InP-based 2D planar photonic crystals. J. Opt. Soc. Am. B **25**, 67–73 (2008)
9. Russell, P.S.J., Atkin, D.M., Birks, T.A., Roberts, P.J.: Bound modes of two-dimensional photonic crystal waveguides. In: Rarity, J.G, Weisbuch, C. (eds.) Microcavities and Photonic Bandgaps: Physics and Applications, pp. 203–218. Kluwer Academic, Dordrecht (1996)
10. Atkin, D.M., Russell, P.S.J., Birks, T.A., Roberts, P.J.: Photonic band structure of guided Bloch modes in high index films fully etched through with periodic microstructure. J. Mod. Opt. **43**, 1035–1053 (1996)
11. Kanskar, M., Paddon, P., Pacradoui, V., Morin, R., Busch, A., Young, J.F., Johnson, S.R., Mackenzie, J., Tiedje, T.: Observation of leaky slab modes in an air-bridged semiconductor waveguide with two-dimensional photonic lattice. Appl. Phys. Lett. **70**, 1438–1440 (1997)
12. Johnson, S.G., Fan, S., Villeneuve, P.R., Joannopoulos, J.D., Kolodziejaki, L.A.: Guided modes in photonic crystal slabs. Phys. Rev. B **60**, 5751–5758 (1999)
13. Jiang, B., Zhou, W., Chen, W., Liu, A., Zheng, W.: Design of surface mode photonic crystal T-junction waveguide using coupled-mode theory. J. Opt. Soc. Am. B **28**(8), 2038–2041 (2011)
14. Wright, R.G., Zgol, M., Adebimpe, D., Keenan, E., Mulligan, R., Kirkland, L.V.: Multiresolution nanoscale sensor-based circuit board testing. In: IEEE Autotestcon, 2005, pp. 766–772. IEEE (2005)
15. Chan, W.L., Moravec, M.L., Baraniuk, R.G., Mittleman, D.M.: Terahertz imaging with compressed sensing and phase retrieval. Opt. Lett. **33**, 974–976 (2008)
16. Kawase, K., Ogawa, Y., Watanabe, Y.: Non-destructive terahertz imaging of illicit drugs using spectral finger prints. Opt. Express **11**, 2549–2554 (2003)
17. Zhang, C.H., Wang, Y.Y., Chen, J., Kang, L., Xu, W.W., Wu, P.H.: Continuous-wave terahertz imaging system based on far-infrared laser source. In: Joint 31st International Conference on Infrared Millimeter Waves and 14th International Conference on Teraherz Electronics, 2006. IRMMW-THz 2006, p. 426. IEEE (2006)
18. Ibraheem, A., Krumbholz, N., Mittleman, D., Koch, M.: Low-dispersive dielectric mirrors for future wireless terahertz communication systems. IEEE Microw. Wirel. Compon. Lett. **18**, 67–69 (2008)
19. Abri Badaoui, H., Abri, M.: New design of integrated 2D photonic crystal narrow band filters using the FDTD-2D method. Frequenz **68**(11–12), 511–518 (2014)
20. Abri Badaoui, H., Abri, M.: Optimized 1×8 compact splitter based on photonic crystal using the two-dimensional finite-difference time-domain technique. Opt. Eng. **54**(6), 067104 (2015)
21. Taflove, A.: Computational Electromagnetics: The Finite Difference Time Domain Method. Artech House, Boston (1995)
22. Koshiba, M., Tsuji, Y., Sasaki, S.: High-performance absorbing boundary conditions for photonic crystal waveguide simulations. IEEE Microwave Wirel. Compon. Lett. **11**, 152–154 (2001)

Writer's Gender Classification Using HOG and LBP Features

Nesrine Bouadjenek(✉), Hassiba Nemmour, and Youcef Chibani

LISIC. Lab, Faculty of Electronics and Computer Sciences,
University of Sciences and Technology Houari Boumediene (USTHB),
Algiers, Algeria
{nbouadjenek, hnemmour, ychibani}@usthb.dz

Abstract. The gender identification in handwritten documents becomes to gain importance for various writer authentication purposes. It provides information for anonymous documents for which we need to know if they were written by a Man or a Woman. In this work, we propose a system for writer's gender classification that is based on local textural and gradient features. Especially our proposed features are Histogram of Oriented Gradients (HOG) and Local Binary Patterns (LBP), which are successful in various pattern recognition applications. The classification step is achieved by SVM classifier. The results obtained on samples extracted from IAM dataset showed that the proposed features provide quite promising results.

Keywords: Gender classification · HOG · LBP · SVM

1 Introduction

The writer's gender identification becomes to be employed in various forensic and authentication areas. It is helpful in investigations on anonymous handwritten documents, for which, we want to predict some information such as the handedness, the nationality, the age or the gender of writers. In the last years, the gender information has attracted researchers in several domains. Specifically, the gender influence was investigated on Parkinson disease [1], motor learning [2], dichotic listening [3] as well as on the differences in crimes and violence [4]. Besides, the gender classification (Male or Female) constituted a subject in some pattern recognition applications. For instance, in [5] the gender classification is based on face image processing. Furthermore, since the handwriting is used to identify writers, a straightforward question is that: can the handwriting be used to predict some information about people such as the gender, the handedness or even the age? In [6], authors investigated the relationship between sex hormones and the handwriting style. The findings showed that prenatal sex hormones can affect women handwriting performance. Note that over the past years no great attentions were paid to this subject but requirements in various legal identification tasks imply the prediction of some specific information about the writer. An early work on handwriting-based gender classification was introduced by Cha and Srihari [7]. The aim was to classify US population into various sub-categories such as "white/male/ age group 15–24" and "white/female/ age group 45–64, etc.". Then after,

M. Chadli et al. (eds.), *Recent Advances in Electrical Engineering and Control Applications*,
Lecture Notes in Electrical Engineering 411, DOI 10.1007/978-3-319-48929-2_24

the same research team proposed the use of boosting method for gender detection [8]. In both works, a private dataset of uppercase letters was used. In fact, it seems that the principle reason for which, there are no many research works gender classification is the unavailability of public datasets. Recently, a research group on computer vision and artificial intelligence at Bern University developed the IAM handwriting dataset, which is devoted to writer identification as well as gender and handedness prediction [9]. Using this dataset, Liwicki et al., [10], addressed the gender and handedness prediction using on-line and off-line features. Specifically, SVM and GMM classifiers were used to achieve the classification task. For the off-line characterization, a sliding window was applied in the writing direction to calculate features such as the mean gray value, the center of gravity and the number of black- white transitions. Nevertheless, since more robust features are offered by the pattern recognition theory; in this work, we propose the use of locally computed textural and gradient features. Textural features are based on Local Binary Patterns (LBP), which are used to characterize variations of gray level values of a pixel with respect to its neighborhood. In addition to the classical LBP descriptor, we use the rotation invariant LBP that allows rotation invariance and size reduction. Furthermore, gradient features are based on Histogram of Oriented Gradients (HOG), which are successful for human detection and face recognition applications. Note that these features were already used through classifier combination to solve handwritten signature verification [11]. Motivated by their satisfactory performance, we investigate their applicability for writer's gender classification that is a more complicated task. The rest of this paper is arranged as follows: In Sect. 2, the gender classification system is described. Experimental results are reported in Sect. 3. Section 4 gives the conclusions of this work.

2 Gender Classification System

The proposed gender classification system is designed to automatically classify writers into two classes that are "man" or "woman". As shown in Fig. 1, off-line images of the handwritten text are used to compute local features. The SVM classifier receives data features and decides whether the handwritten text has been written by a man or a woman. Recall that, in [10] the gender classification was based on some conventional offline features. Since no exhaustive investigations were carried out to describe off-line data for gender classification, the main contribution of this work consists of employing more powerful off-line features. Specifically, our attention is focused on local features, which are commonly more suitable for handwriting characterization. These features are presented in what follows.

2.1 Local Binary Patterns

Local Binary Patterns (LBP) are used to perform statistical and structural analysis of textural patterns [12]. They describe the gray level distribution in the neighborhood of each pixel. Specifically, the LBP code is obtained by comparing the gray level value of the central pixel with neighboring gray levels. The LBP takes 1 if the central pixel has a

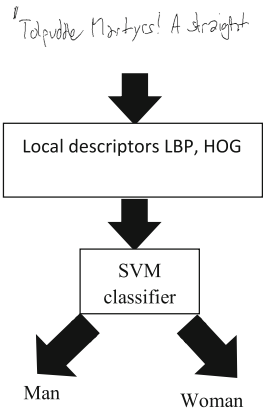

Fig. 1. Proposed gender classification system

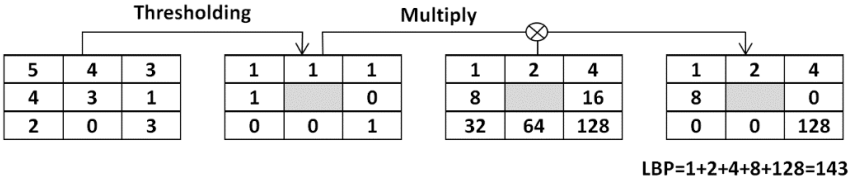

Fig. 2. Working out the LBP code of pixel (x, y). In this case $I(x, y) = 3$, and its LBP code is $\text{LBP}(x, y) = 143$.

lower gray level than the neighboring pixel. Otherwise it takes 0. Figure 2 shows an example of a LBP operator. The LBP code for P neighbors situated on a circle of radius R is computed as follows:

$$LBP_{P,R}(x, y) = \sum_{p=0}^{p} S(g_p - g_c)2^p \tag{1}$$

With

$$S(l) = \begin{cases} 1 & l \geq 0 \\ 0 & l < 0 \end{cases}$$

g_c: gray value of the central pixel.
g_p: gray value of the p^{th} pixel.

Commonly, the neighbors are taken by considering circular neighborhood, consequently, the p^{th} neighbor does not belong into a pixel. Therefore, the adequate gray level value is computed as [13]:

$$g_p = I\left(x + Rsin\frac{2\pi p}{P}, y - Rcos\frac{2\pi p}{P}\right) \tag{2}$$

Then, image features are obtained by considering the LBP histogram.

Furthermore, as reported in [12], to allow invariance with respect to rotation, the LBP^{riu} is used. This operator is defined as follows:

$$LBP^{\text{riu2}}_{P,R}(x,y) = \begin{cases} \sum_{p=0}^{p-1} S(g_p - g_c) & U(x,y) \leq 2 \\ P+1 & otherwise \end{cases} \tag{3}$$

With: $U(x,y) = \sum_{p=1}^{p} \left| s(g_p - g_c) - s(g_{p-1} - g_c) \right|$, and $g_p = g_0$. Moreover the $LBP^{\text{riu2}}_{P,R}$ reduces the size of the LBP histogram to $(P+2)$ [12].

Afterwards, the image is divided into regions where local LBP histograms are concatenated to form an enhanced feature vector as shown in Fig. 3.

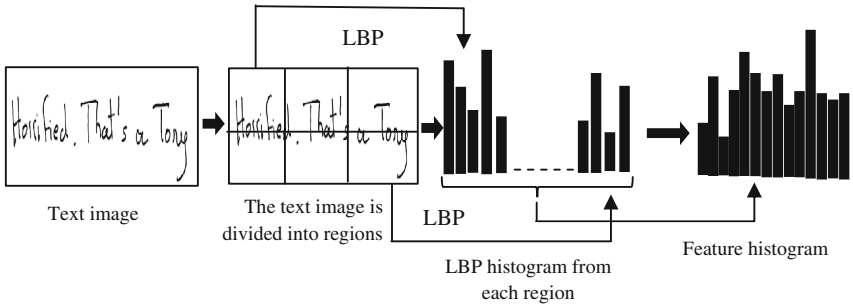

Fig. 3. Computation of LBP histograms over image regions

2.2 Histogram of Oriented Gradients

The Histogram of Oriented Gradients (HOG) features were introduced by Dalal and Triggs for human detection [14]. They are calculated according to the following steps:

- For each pixel $I(x,y)$, the horizontal and vertical gradient information are computed by:

$$\begin{aligned} g_x(x,y) &= I(x+1,y) - I(x-1,y) \\ g_y(x,y) &= I(x,y+1) - I(x,y-1) \end{aligned} \tag{4}$$

- Then, the gradient magnitude and phase are obtained as follows:

$$\begin{aligned} M(x,y) &= \sqrt{g_x(x,y)^2 + g_y(x,y)^2} \\ \varphi(x,y) &= \arctan\left(\frac{g_x(x,y)}{g_y(x,y)}\right) \end{aligned} \tag{5}$$

- Finally, the histogram of gradient orientations is assessed to obtain the HOG features.

Presently, handwritten text images are divided into several regions for each of which, a local histogram of the gradient orientations is calculated. The image HOG descriptor is obtained by concatenating all local histograms [14]. Figure 4 describes the HOG calculation.

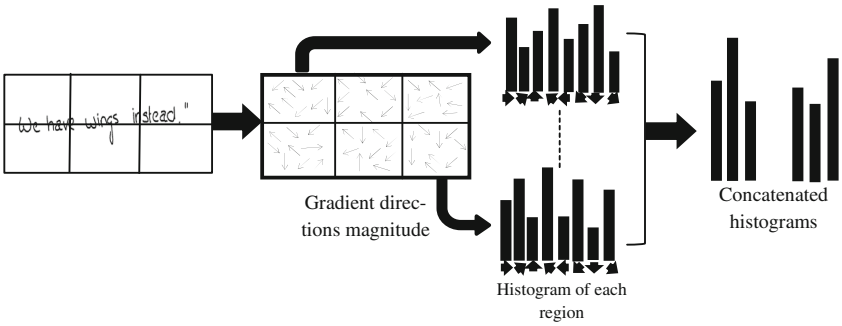

Fig. 4. HOG computation flowchart.

2.3 Support Vector Machines

SVMs construct binary classifiers from a set of training examples such that: $(z_j, y_i) \in RN \times \{\pm 1\}$, $j = 1, \ldots, n$, [15]. The data are mapped into a dot product space via a kernel function such that: $K(z, z_j) = <\phi(z), \phi(z_j)>$. Then, the solution is expressed in terms of kernel expansion as:

$$f(z) = sign\left(\sum\nolimits_{j=1}^{S_v} \alpha_j K(z, z_j) + b\right) \tag{6}$$

S_v is the number of support vectors which are training data for which $0 \leq \alpha_j \leq C$, while the bias b is a scalar. Note that C is the cost parameter. Furthermore, a large number of mathematical functions are eligible to be a SVM-kernel. Here, we use the Radial Basis Function kernel given in Eq. 7 (σ and C are user-defined parameters).

$$K(z, z_j) = \exp\left(-\frac{1}{2\sigma^2}||z - z_j||^2\right) \tag{7}$$

3 Experimental Results

Experiments are performed using samples extracted from the IAM-OnDB dataset. Samples are obtained from more than 200 writers that contribute each, with eight texts which, are averagely composed of seven lines. The classification task aims to identify the writer gender (male or female) for each handwritten text. Thereby, two training sets were selected to perform the experiments. To evaluate our results comparatively with

those obtained in [10], the first training set is composed of 75 samples for men and 75 samples for women. These samples are then divided into three subsets that contain 40 training samples, 10 validation samples and 25 test samples. Furthermore, the second training set contains 175 samples for each class.

3.1 Results Obtained for the First Training Set

In a first test, the results obtained using several LBP and LBP^{riu} configurations are given in Table 1.

Table 1. Classification accuracy using Local Binary Patterns.

P × R	Classification accuracy (%)	
	LBP	LBP^{riu}
4 × 1	56.00	62.00
8 × 1	66.00	64.00
16 × 2	70.00	60.00

The best result was obtained using the classical LBP (P = 16, R = 2) where the classification accuracy is about 70%. Unfortunately, the LBP^{riu} that reduces the histogram size does not bring the same performance.

In a second step, LBP features were computed on image regions. Specifically, LBP (8 × 1) and LBP^{riu}(8 × 1) were evaluated over several image partitions. The results in terms of classification accuracy showed that only the LBP^{riu} provided an accuracy improvement. This outcome is related to the size of LBP(8 × 1), which grows significantly according to the number of regions. In fact, for each region, the LBP(8 × 1) histogram contains 256 components. Thereby, the classification accuracy of the region-based LBP^{riu}(8 × 1) is illustrated in Fig. 5. As can be seen, the highest recognition accuracy which is 68% is obtained when dividing images into 3 × 1 regions. Comparatively to the LBP(16 × 2) for which, the histogram size is about 65536, the region-based LBP^{riu}(8 × 1), allows the best tradeoff between accuracy and size reduction.

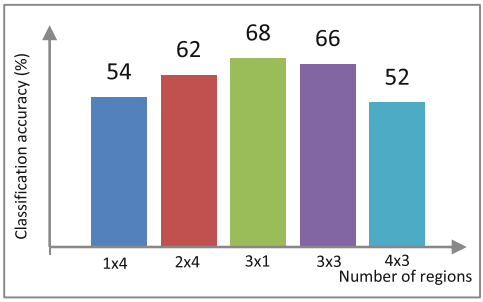

Fig. 5. Precision rates with different partitions of LBP^{riu}(8 × 1)

Furthermore, HOG features were performed by varying the number of regions. In addition, the histogram of oriented gradients was evaluated by considering 4, 8 and 9 directions. As reported in Fig. 6, the best performance is obtained when partitioning images into 3 × 3 regions. Also, we note that histograms based on 9 directions give the best accuracy that reaches 74%.

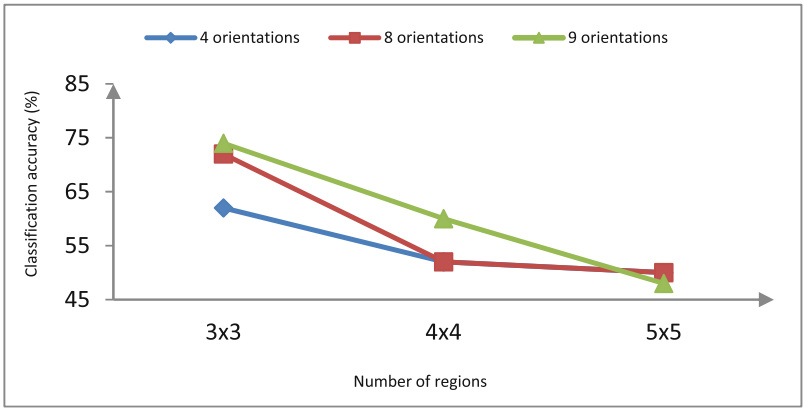

Fig. 6. Gender classification using Histogram of Oriented Gradients.

Finally, Table 2 summarizes the best accuracy rates that are obtained by the proposed features. Also, it gives the best classification rate that was obtained in [10]. It is easy to see that the proposed features provide a gain that reaches 7% using HOG features, over the state of the art accuracy that is about 67.57%. This, latter is achieved by using classifier combination with both on-line and off-line structural features.

Table 2. Gender classification rates fort the first training set

Features	Classification accuracy (%)
LBP(16 × 2)	70.00
$LBP^{riu}(8 \times 1)$	68.00
HOG	74.00
Off-line + On-line + classifier combination [10]	67.57

3.2 Results Obtained for the Second Training Set

In order to confirm again the usefulness of our proposed features, a second set of experiments was performed by considering a larger dataset. Specifically, for each class we use 100 training samples, 25 validation samples and 50 test samples. The best results are reported in Table 3. Roughly speaking, compared to the first dataset the classification accuracy is decreased. Nevertheless, it varies between 59% and 70%, which confirm the robustness of the proposed system. Besides, we note that HOG features allow the best performance that is about 70%.

Table 3. Gender classification rates for the second training set

Features	Classification accuracy (%)
LBP(16 × 2)	63.00
LBP^{riu}(8 × 1)	62.00
HOG	70.00

4 Conclusion and Future Work

In this paper, we proposed a system for gender classification based on off-line handwritten text. Two local descriptors that are, LBP and HOG features were used to improve the gender classification. Experiments were conducted on samples extracted from the IAM database. Two training sets that contain 75 and 175 samples per class were selected. The comparison with the results obtained using the same experimental protocol, indicate that our features provide a significant improvement that reaches 7%. Moreover, HOG features outperform all the others with a classification rate that is about 74% and 70% for the two training sets, respectively. Finally, we infer that local data features constitute a promising approach to solve the gender classification task.

References

1. Shulman, L.M.: Gender differences in Parkinson's disease. Gend. Med. **4**(1), 8–18 (2007)
2. Dorfberger, S., Adi-Japha, E., Karni, A.: Sex differences in motor performance and motor learning in children and adolescents: an increasing male advantage in motor learning and consolidation phase gains. Behav. Brain Res. **198**(1), 165–171 (2009)
3. Voyer, D.: Sex differences in dichotic listening. Brain Cogn. J. **76**, 245–255 (2011)
4. Bennett, S., Farrington, D.P., Huesmann, L.R.: Explaining gender differences in crime and violence: the importance of social cognitive skills. Aggression Violent Behav. **10**(3), 263–288 (2005)
5. Lee, J.D., Lin, C.Y., Huang, C.H.: Novel features selection for gender classification. In: 2013 IEEE International Conference on Mechatronics and Automation (ICMA), pp. 785–790, August 2013
6. Beech, I.C., Mackintosh, J.R.: Do differences in sex hormones affect handwriting style? evidence from digit ratio and sex role identity as determinants of the sex of handwriting? Pers. Individ. Differ. **39**, 459–468 (2005)
7. Cha, S.H., Srihari, S.N.: A priori algorithm for sub-category classification analysis of handwriting. In: Document Analysis and Recognition (IEEE, ed.), pp. 1022–1025, September 2001
8. Bandi, K.R., Srihari, S.N.: Writer demographic classification using bagging and boosting. In: Proceedings of International Graphonomics Society Conference, pp. 133–137 (2005)
9. Liwicki, M., Schlapbach, A., Bunke, H.: Automatic detection of gender and handedness from on-line handwriting. In: Conference of the International Graphonomics Society, pp. 179–183 (2007)
10. Liwicki, M., Schlapbach, A.: Automatic gender detection using on-line and off-line information. Pattern Anal. Appl. **14**, 87–92 (2011)

11. Yilmaz, M., Yanikoglu, B., Tirkaz, C., Kholmatov, A.: Offline signature verification using classifier combination of hog and lbp features. In: 2011 International Joint Conference on Biometrics (IJCB), pp. 1–7, October 2011
12. Vargas, J., Ferrer, M., Travieso, C., Alonso, J.: Off-line signature verification based on grey level information using texture features. Pattern Recogn. **44**(2), 375–385 (2011)
13. Ojala, T., Pietikäinen, M., Harwood, D.: A comparative study of texture measures with classification based on featured distributions. Pattern Recogn. **29**(1), 51–59 (1996)
14. Dalal, N., Triggs, B.: Histograms of oriented gradients for human detection. In: IEEE Computer Society Conference on Computer Vision and Pattern Recognition, CVPR 2005, vol. 1, pp. 886–893, June 2005
15. Burges, C.: A tutorial on support vector machines for pattern recognition. Data Min. Knowl. Disc. **2**(2), 121–167 (1998)

Speech Recognition System Based on OLLO French Corpus by Using MFCCs

Braham Chaouche Youcef[1(✉)], Yessaad Mohamed Elemine[1], Benmaiza Islam[2], and Bouttout Farid[3]

[1] LMSE Laboratory, Department of Electronics, University of Mohamed El Bachir El Ibrahimi, 34265 Bordj Bou Arréridj, Algeria
bcyoucef@gmail.com, yessaad.amine@gmail.com
[2] Laboratory of Spoken Communication and Signal Processing, Faculty of Electronics and Computer Sciences, USTHB, 16000 Algiers, Algeria
islam.bm34@gmail.com
[3] Laboratory of Signal Processing, Department of Electronics, University of Constantine, 25000 Constantine, Algeria
f.bouttout@gmail.com

Abstract. The automatic speech recognition is an area of active study since the early 1950s, and the latest technologies in the field of stochastic processes and the discovery of Hidden Markov Models have given a new direction for this area.

This paper describes an approach of speech recognition by using the Mel-Scale Frequency Cepstral Coefficients (MFCC) from speech recognition experiments done on OLLO French corpus by different features. Our work consists in finding the most appropriate choice for this task using the Mel-Scale Frequency Cepstral Coefficients (MFCC) extracted from speech signal.

To evaluate this analysis, we built an ASR reference system based on the modeling of phonemes by the HMM (Hidden Markov Models) associated with the GMM models (Gaussian Mixture Model) using the HTK tool. The implementation of this system was made using several experiments in order to choose the best parameters used in two main steps to build an ASR system, acoustic analysis and decoding. The experiments show that the choice of 25 Gaussian components provides a good compromise between recognition accuracy and computation time, and we found also that the best parameters leading to good recognition accuracy are MFCC_E_D_A coefficients with 92.5%.

In this paper the quality and testing of speaker recognition and gender recognition system is completed and analysed.

Keywords: ASR system · HMM · MFCC · GMM · OLLO · HTK

1 Introduction

Speech is the most natural means of communication between humans. With the development of information technology and the massive use of computer. Man-Machine Dialogue (MMD) using the word as a means of communication has been an increased interest from both the scientific and the industrial community. Automatic speech recognition (ASR), the main component of the MMD system, is a central topic

M. Chadli et al. (eds.), *Recent Advances in Electrical Engineering and Control Applications*, Lecture Notes in Electrical Engineering 411, DOI 10.1007/978-3-319-48929-2_25

in the broader one of Natural Language Processing (NLP) domain. The general structure of HMM-based speech recognition system [1] consists of two phases: a learning phase whose goal is the construction of acoustic models (HMM models) and recognition phases which the most likely word being imposed. Generally, ASR systems use cepstral parameters called standard parameters as acoustic representation of the speech signal. Cepstral parameters currently the most successful are the MFCCs coefficients (Mel Frequency Cepstral Coefficients). The procedure of calculation of the coefficients is performed on several stages.

The rest of this paper is organized as follows. Section 2 gives a description of Mel-Frequency Cepestral Coefficients (MFCCs). Section 3 introduces a description about OLLO French corpus. The experiments and the results obtained are given in Sect. 4. Concluding remarks are given in Sect. 5.

2 The Mel-Frequency Cepstrum Coefficient (MFCC)

The Mel-frequency Cepstrum Coefficient (MFCC) technique is often used to create the fingerprint of the sound files. The MFCC are based on the known variation of the human ear's critical bandwidth frequencies with filters spaced linearly at low frequencies and logarithmically at high frequencies used to capture the important characteristics of speech. Studies have shown that human perception of the frequency contents of sounds for speech signals does not follow a linear scale [2]. Thus for each tone with an actual frequency, f, measured in Hz, a subjective pitch is measured on a scale called the Mel scale. The following formula is used to compute the Mels for a particular frequency:

$$mel(f) = 2595 \times \log_{10}(1 + \frac{f}{700}) \tag{1}$$

A block diagram of the MFCC processes is shown in Fig. 1. The windowing block minimizes the discontinuities of the signal by narrowing the beginning and end of each frame to zero. The following step consists of applying DFT in order to convert each frame from the time domain to the frequency domain. Then, the signal is passed through the Mel filter bank spectrum to mimic human hearing. In the final step, the Cepstrum, the Mel-spectrum scale is converted back to standard frequency scale. This spectrum provides a good representation of the spectral properties of the signal which is key for representing and recognizing characteristics of the speaker.

3 Coprus

The OLLO French part of the database is a corpus spoken by 10 native French individuals who lived in Belgium. There are six men and four women in different ages [3]. Each person speaks 150 utterances, every utterance is spoken in 6 different style. Each utterance is spoken three times per person.

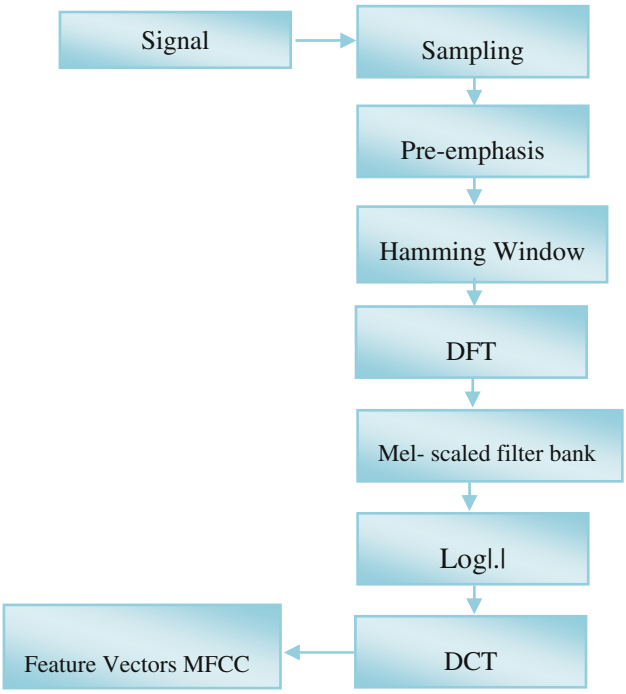

Fig. 1. Block diagram of MFCC

So each person contains 2700 (150*6*3) files. As we are performing dependant speaker recognition tasks, the set of the learning (L1) contains the first of three each logatome's repetitions in the corpus. The remaining two repetitions are contained within the set of test (L2).

The allocation of the corpus is used to build our ASR system. In our experiments, the sampling rate is down to 8 kHz.

To validate our reference system for the phonetic transcription of the speech signal, we took the ACC recognition accuracy as an evaluation criterion, calculated by the formula:

$$Acc = \left(\frac{N - D - S - I}{N}\right) \times 100\% \tag{2}$$

Where:

H: Number of recognized words;
D: Number of deleted words;
S: Number of substituted words;
I: Number of inserted words;
N: Total number of words.

4 Experimental Results and Analyse

Experiments included comparative evaluations of the recognition results using the mel–cepstral using OLLO databases (Fig. 2).

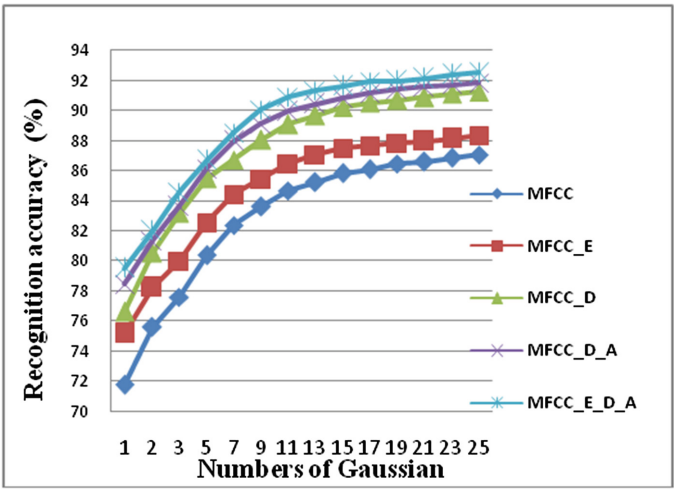

Fig. 2. Comparative accuracy of recognition between static/dynamic coefficients depending on the number of Gaussians.

We used 25 ms speech window with mel–cepstral features [4], due to specific decomposition structure. We also used the same overlapping rate of speech window with the value of 10 ms. Speech feature vector computation included calculation of log energies in the mel–scaled filterbanks [5].

In order to have an effective system of reference, we conducted an experiment to determine the best number of Gaussian mixture components per state and the best type of acoustic parameters MFCC. In this experiment, we set the number of states to three active states [6], then we took the following types of acoustic parameters: MFCC, MFCC_E, MFCC_D, MFCC_D_A and MFCC_E_D_A. In each type of parameters, we varied the number of Gaussian 1 to 25 to determine the best number of Gaussians to have the best accuracy. The basic system uses MFCC coefficients and energy, and the differential coefficients of the parameters.

The logarithm of the energy of the frame is added to the 12 cepstral coefficients to form a vector of 13 coefficients. Differential coefficients of the first and second order, calculated automatically by the tools of HTK [7], are optionally used with the static coefficients.

We tested the contribution of differential coefficients of the first and second order with 13 initial coefficients, working with vectors of dimensions d = 13 (12 MFCC; E), d = 26 (12 MFCC; E; 12 ΔMFCC; ΔE) and d = 39 (12 MFCC; E; 12 ΔMFCC; ΔE; 12 ΔΔMFCC; ΔΔE). The emission probability of each state of the HMM is represented by

a linear combination of Gaussian G with diagonal covariance matrix. All other experimental conditions are those of the already described basic system.

Table 1 shows the accuracy for the five sets of experiments and the number of Gaussian probability density.

Table 1. Comparative accuracy of recognition between static/dynamic coefficients depending on the number of Gaussians.

Numbers of Gaussian	Recognition accuracy (%)				
	MFCC(12)	MFCC(13)	MFCC(24)	MFCC(26)	MFCC(39)
1	71.78	75.17	76.64	78.44	79.50
2	75.59	78.23	80.55	81.36	82.00
3	77.62	79.98	83.18	83.63	84.59
5	80.39	82.55	85.48	86.11	86.68
7	82.38	84.41	86.73	87.97	88.52
9	83.61	85.43	88.06	89.10	90.06
11	84.69	86.47	89.09	89.94	90.89
13	85.22	87.06	89.67	90.44	91.31
15	85.82	87.48	90.23	90.83	91.63
17	86.09	87.66	90.52	91.15	91.92
19	86.46	87.84	90.69	91.41	91.96
21	86.58	87.97	90.88	91.58	92.15
23	86.85	88.12	91.11	91.72	92.40
25	87.05	88.34	91.25	91.85	**92.50**

From Table 1, based on the parameterization MFCC_E_D_A typical system gives very good results. The good performance of the system based on MFCC parameters are due to the nature of their products based on human perception models. The results also show that increasing the number of Gaussian enables better modeling of the acoustic space. In the case of a word recognition system, we achieved the best number of Gaussians that allows stability accuracies of recognition (number of Gaussian equal to 25). It is therefore necessary to find a compromise between the recognition accuracy and the number of parameters. We note that beyond the 13th Gaussian, the system performance is not significantly improved (91.31 to 92.50).

Based on these results, we note the following points:

- The combination of MFCC_E_D_A type gives the best recognition accuracy with 92.50 %. However, this combination of 39 parameters requires more resources and computing time. By combining WCC_D_A against type 21 parameters (or 18 parameters in the case of level 5) provides a more compact representation relative to that MFCC_E_D_A or MFCC_D_A (36 parameters), requiring less time and computing resources. Thus, the combination WCC_D_A provides a good compromise in terms of accuracy and computational resources.

5 Conclusion

Our study is to apply the Mel-Scale Frequency Cepstral Coefficients (MFCC) in the acoustic analysis of speech signal to an ASR task.

To accomplish this task and to evaluate the acoustic analysis, we built a reference ASR system based on HMM models. Acoustic analysis of this reference system is based on the extraction of MFCC parameters. This system is built under the platform HTK and evaluated on the basis of OLLO database.

The construction of the reference system calls for the type of acoustic parameters and the number of Gaussian components for each active state HMM. To this end, we conducted various experiments to determine these two parameters. The results showed us that the most relevant acoustic parameters are MFCC_E_D_A coefficients.

The results also showed that the choice of 25 Gaussian components provides a good compromise between recognition accuracy and computation time. In the present work, After a comparative study between the acoustic analysis based on the MFCC parameters, we found that the best parameters leading to good recognition accuracy are MFCC_E_D_A coefficients. However, the representation of the latter requires a dimension (39 parameters) larger than that based on the parameters.

References

1. Haton, J.-P.: Reconnaissance Automatique de la Parole. Paris (2006)
2. Patel, K., Prasad, R.K.: Speech recognition and verification using MFCC & VQ. Int. J. Emerg. Sci. Eng. (IJESE) **1**(7) (2013). ISSN: 2319–6378
3. Huang, L., Zhang, X.: Speaker independent recognition on OLLO French corpus by using different features. In: 2010 First International Conference on Pervasive Computing, Signal Processing and Applications
4. Modic, R.: Comparative wavelet and MFCC speech recognition experiments on the Slovenian and English SpeechDat2
5. Nguyen, Q.C.: Reconnaissance de la Parole en Langue Vietnamienne. thèse de doctorat, Institut national polytechnique de Grenoble, Juin 2002
6. Bakis, R.: Continuous speech recognition via centisecond acoustic states, 91th. Meeting of the Acoust.Soc, avril 1976
7. Young, S., et al.: The HTK Book (for HTK Version 3.4), p. 198 (2006)

Wavelets Based Image De-Noising: Application to EFTEM Imaging

Sid Ahemd Soumia[1(✉)], Zoubeida Messali[2], Abdeldjalil Ouahabi[3], and Sergio Marco[4]

[1] Faculty of Science and Technology,
Bordj Bou Arreridj University, BBA, El Anasser, Algeria
samasoumia@hotmail.fr
[2] Electrical Engineering Laboratory LGE,
M'sila University, BBA, M'sila, Algeria
messalizoubeida@yahoo.fr
[3] Energy and Electronics Department, Polytechnic School,
University of Tours, (EPU - Polytech Tours), Tours, France
abdeldjalil.ouahabi@univ-tours.fr
[4] Curie Institute, INSERM U759,
University Campus Orsay, 91405 Orsay Cedex, France
sergio.marco@curie.fr

Abstract. Image de-noising is a very important step in Electron Microscopy (EM) image processing, before the three-dimensional reconstruction (tomography reconstruction) of the EM images. They normally have a problem of high noise level, which causes a loss in the contained information. This paper brings out the efficiency of the wavelet transform in the aim of improving the quality of real datasets. These real datasets are an EM images took at different time exposure, meaning reducing the noise level, where it seems better to answer the tradeoff between the use of Low electron doses to reduce the radiation damage, and feasibility to improve SNR after acquisition. In this matter, we have considered both hard and soft thresholding. To assess our results, we have chosen the signal-to-noise-ratio SNR criterion beside the visual quality of the obtained images. As expected, the wavelet was the right choice to perform well in Electron Microscopy and to be efficient in terms of SNR improvement.

Keywords: Electron microscopy · Wavelet · Tomography reconstruction

1 Introduction

The goal of image de-noising methods is to recover the original image from a noisy data. Several methods have been proposed to solve the image de-noising problem [1–3]. Even though, they should remove the additive noise while retaining as much as possible the important signal features.

A wide class of these methods was based on wavelet transform [2, 4–6] due to its effectiveness and simplicity. In brief, the main steps of these algorithms are: first compute the wavelet transform of the noisy image, then apply an estimation process to the wavelet coefficients, and finally take the inverse wavelet transform to recover the

M. Chadli et al. (eds.), *Recent Advances in Electrical Engineering and Control Applications*,
Lecture Notes in Electrical Engineering 411, DOI 10.1007/978-3-319-48929-2_26

de-noised image. Most popular wavelet de-noising algorithms are based on thresholding [7, 8]. The basic idea consists in selecting each wavelet coefficient by applying a thresholding rule that will tend to remove more noise (mostly represented by low wavelet coefficients) than important image edge information (mostly represented by high value coefficients).

Since the work of Donoho & Johnstone [7, 8], there has been abundant interest in improving wavelet de-noising algorithms [9, 10], however few works are specifically designed for medical and electron microscopy (EM) images.

Therefore, in this paper, we explore the use of wavelet transform for de-noising EM images.

We tested the wavelet de-noising algorithms based on thresholding on a set of experimental EM test images. Four datasets of EM images taken with different exposure time are considered (1 s 1×1 s, 2×0.5 s, 5×0.2 s, 10×0.1 s). The final goal of this kind of studies is to enhance the quality of the electron tomography and to generalize and adapt these algorithms to address a wide range of EM images. Note that Electron Tomography or tomographic reconstruction technique allows the computation of three-dimensional reconstructions of objects from a series of projections recorded at various tilt angles.

Due to the sensitivity of biological sample to the radiation damage, the low electron doses conditions used for electron microscopy result in extremely noisy images, so extremely low signal-to-noise ratio, especially in energy filtering transmission electron microscopy (EFTEM) mode [11, 12], as we will show in experimental results.

A de-noising algorithm that is suitable for these applications should be able to preserve as much as possible of the signal while reducing the noise to a sufficiently low level. In fact, wavelet de-noising techniques can be applied in two stages in EM: (a) before reconstructing the three-dimensional structure of the subcellular components to enhance the quality of reconstruction as it will be considered in this paper, (b) at the intermediate processes like bidimensional alignments, to facilitate the process.

We demonstrate the applicability of wavelet thresholding algorithm in improving the signal-to-noise-ratio SNR and the visual quality of EFTEM images, before any tomographic reconstruction. To evaluate the de-noised results Signal-to-Noise-Ratio (SNR) criterion is calculated in addition to the visual quality of the resulting images.

This paper is organized as follows: Sect. 2, briefly overviews the theoretical fundamentals of Electron Microscopy, Transmission Electron Tomography (TET) and Energy Filtering Transmission Electron microscopy (EFTEM). Section 3, includes the basic principles of wavelet de-noising algorithms with a special focus on wavelet thresholding techniques. In Sect. 4, we apply the wavelet thresholding techniques to a set of 2D EFTEM test images. The main goal of this study is to improve the SNR and enhance the visual quality of EFTEM images. Finally, we conclude the paper in Sect. 5.

2 Noise in EM Images

One of the biggest advantages of electron microscopy is the ability to study structural molecular biology thanks to the electron microscope. The electron microscope is a type of microscope that uses a beam of electrons to create an image of the specimen. It is

capable of much higher magnifications and has a greater resolving power than a light microscope, allowing it to see much smaller objects in finer detail. In good approximation, the obtained images are 2D projections of densities from the imaged volume.

In the other hand, Transmission Electron Tomography (TET) is becoming an emerging powerful tool for studying the three dimensional structure of subcellular in their native environment in the cell. This method allows computing the true three-dimensional (3D) information (e.g. electron tomography [11, 13]) from 2D projections of a single object recorded at different tilt angles in the electron microscope. Although electron microscopes are able to image biological objects with a resolution down to 0.3 nm, the structural information is considered to be of poor quality, poor contrast and noisy due to the use of low electron doses. Thus, noise reduction is essential to increase the SNR and to facilitate visual inspection. For the sake of clarity, here we give a definition of electron dose. The level of exposure an EM image receives is called its electron dose, or simply dose, and is measured in electrons per square Angstrom. Low electron doses are used to reduce the radiation damage, which makes the reconstructed volumes exhibit low signal-to-noise ratios (SNR). Several efforts have recently been made to solve this limitation [14, 15].

Energy-filtering transmission electron microscopy (EFTEM) is nowadays well established method in many areas of the biological sciences. Recently, tomographic reconstruction techniques have been combined with energy filtering transmission electron microscopy (EFTEM) for a new structural approach allowing analysis of the 3D distribution of individual chemical elements [16]. Using this approach, relevant information has been obtained in the analysis of iron distribution in magneto tactic bacteria by acquiring tomographic seri. Generally, the EFTEM images are very noisy due to the low SNR. So it is an important job to de-noise and improve the signal to noise ratio (SNR) of EFTEM image before any combination.

In our study, we propose to de-noise the 2D EFTEM test images before the tomographic reconstruction, using wavelet transform. For our purposes, we assume that the EFTEM images are affected by an additive white Gaussian noise.

3 Concrete Steps of Wavelets De-Noising Algorithm in EM

3.1 Basic Assumption

Wavelet de-noising algorithms have become an essential tool for many applications [6]. The simpler way to remove noise from a contaminated 1D or 2D data using these algorithms is to eliminate the small coefficient associated to the noise. The wavelet thresholding methods are usually more suitable. The thresholding can be applied by implementing either hard or soft thresholding method, as it will be considered in this paper. In the hard thresholding (keep or kill), the wavelet coefficient smaller than a given threshold are setting to zero, while in soft thresholding which also called as shrinkage (shrink or kill), the wavelet coefficients are modified (shrinked) by a quantity to the threshold. Note that the hard thresholding is mainly used in medical image processing.

$$y = x + \varepsilon \tag{1}$$

Where x is the desired image, ε is random independent noise and y is the measured image. We assume that the noise is white and normally distrusted with zero mean and constant standard deviation. We denote "D" the wavelet transform operator. Applying wavelet transform to the observed data, we have.

$$\mathrm{D(y)} = \mathrm{D(x)} + \mathrm{e} \tag{2}$$

D(y), D(x) and e represent the noisy observation, clean image and noise in the wavelet domain, respectively. According to the character of wavelet transform, the wavelet transform of Gaussian noise still is Gaussian distribution.

One important point in thresholding methods is to set an appropriate choice of the following parameters: the kind of the wavelet, the threshold type, the decomposition level and the rule for calculating the threshold value which is critical as the estimator leading to destruction, reduction, or increase in the value of a wavelet coefficient.

In our study, we have computed, a global threshold and the noise power, is common to all the scales since the noise is assumed to be white. We decide for the modification of the coefficients to utilize both the hard and the soft thresholding type, following to Eqs. 3 and 4 respectively:

$$\hat{D}_{\mathrm{j}}(y) = \begin{cases} \mathrm{D_j}(y) & \left|\mathrm{D_j}(y)\right| \geq \mathrm{T} \\ 0 & \text{otherwise} \end{cases} \tag{3}$$

$$\hat{D}_{\mathrm{j}}(y) = \begin{cases} \mathrm{sign}(\mathrm{D_j}(y)) \cdot \left(\left|\mathrm{D_j}(y)\right| - \mathrm{T}\right) & \left|\mathrm{D_j}(y)\right| \geq \mathrm{T} \\ 0 & \text{otherwise} \end{cases} \tag{4}$$

Where $\hat{D}_{\mathrm{j}}(y)$ is the de-noised wavelet coefficient at level j, $\mathrm{D_j}(y)$ the noisy wavelet coefficient, and T is the threshold value. We choose the decomposition level, j as five (j = 5), the wavelet "*symlet8*" and the universal rule to calculate the threshold value, given by:

$$\mathrm{T} = \sigma\sqrt{2\log(n)} \tag{5}$$

n is the length of the analyzed image. The standard deviation σ of the data values may be used as an estimator. This parameter is estimated using a robust median estimator for the finest scale of noisy wavelet coefficients [7, 8]

$$\sigma = \frac{\mathrm{median(D}(y))}{0.6745} \tag{6}$$

Where D(y) is the detail subband HH in first scale. This median selection made on the detail coefficient of the analyzed signal.

The threshold estimator in Eq. (5) ensures that every sample in the wavelet transform in which the underlying function is exactly zero will be estimated as zero. Also, the motivation of choosing the "*symlet8*" wavelet is that the mother wavelets

having high oscillation number gives better SNR results. The "*symlet8* wavelet has eight oscillations" in its mother wavelet; it produces better SNR level than the lower ones.

3.2 Concrete Steps of De-noising EM Images

First, we prepare the test EM images for acquisition by the microscope JEOL.

We apply wavelet transform to the noisy data, EM test images with various SNR. Second, we extract important wavelet coefficients with the threshold method (hard/soft). Finally, we reconstruct image by inverse wavelet transform using wavelet coefficients processed by the threshold method.

(1) Get the noisy EM images from the electron microscope. Experiments are conducted on several EM images with different time exposure, so different noise level.
(2) Wavelets transform (image decomposition): we select the whole number (J) of wavelet transform (J = 5), and the "*symlet8*" wavelet, due its proprieties as discussed above.
(3) Thresholding process: we select the hard and soft thresholding for the sake of comparison. We choose the universal rule (Eq. (5)) to calculate the threshold value.
(4) Image reconstruction: reconstructed image is calculated by the inverse wavelet transform of the de-noised wavelet coefficients.
(5) Performance evaluation: SNR is calculated at hard and soft thresholding, to appreciate the robustness of the algorithm in addition to the visual quality of the de-noised EM images.

4 Results

4.1 Experimental Test Data

In this paper, experiments are conducted on four series of acquisition which were performed each with a total exposure time of 1 s (1 × 1 s, 2 × 0.5 s, 5 × 0.2 s, 10 × 0.1 s), corresponding to various SNR (SNR (dB) = 22.59, 18.59, 11.32 and 3.13) respectively. The EM images are of size 440 × 440 each one and were taken using a JEOL 2200FS transmission electron microscope operating at 40000X. The specimen was a lacey formvar film which structure was enforced by a coating of carbon with holes that vary in size from less than a quarter micron to more than 10 microns. The original and de-noised images map at Figs. 1, 2, 3, 4 and 5 respectively.

4.2 Performance Evaluation

SNR values are calculated on each test image at hard and soft thresholding by applying "*symlet8*". Comparison is made from the Table 1 showing SNR at each test image of each dataset.

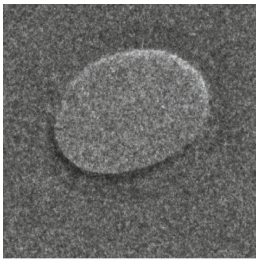

(a)

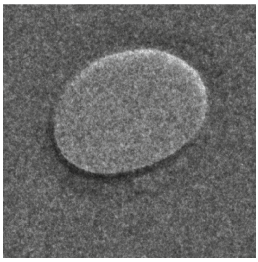

(b)

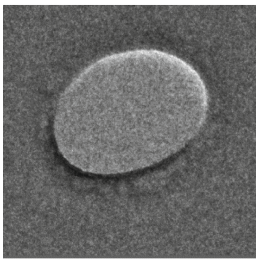

(c)

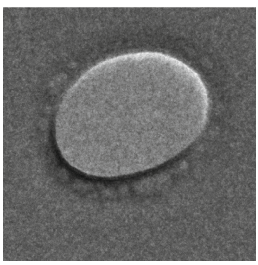

(d)

Fig. 1. Original EM test images at different time exposure: (a) 0.1 s, (b) 0.2 s, (c) 0.5 s and (d) 1 s

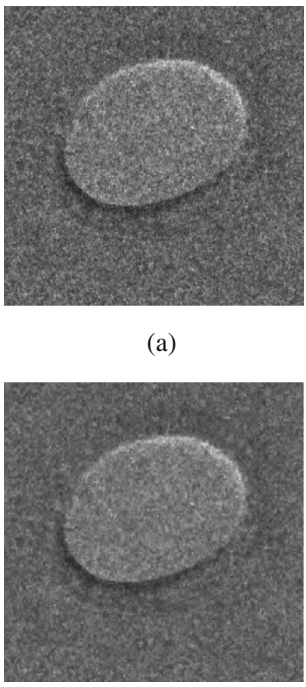

(a)

(b)

Fig. 2. De-noised test image of time exposure 0.1 s: (a) Hard thresholding, (b) Soft thresholding

Unlike to simulate noisy data which are generated by adding white Gaussian noise, and the SNR values are calculated by comparing two images: the original image and the distorted image, with real data, we haven't the original image; we can't use this definition to evaluate the SNR of our test EM images, therefore in our experiments where our data are EM images we calculated the SNR by using the following formula:

$$\mathrm{SNR} = 10\log\left(\left|\frac{\bar{S}-\bar{N}}{\sigma}\right|^2\right) \tag{5}$$

Where $\bar{S}$ and $\bar{\mathrm{N}}$ represent the mean values of the useful signal and the additive noise respectively. σ is the standard deviation of the additive noise.

In order to assess the results, we calculated two SNR on each test image. First, $\mathrm{SNR}_{\mathrm{in}}$ as the difference between the useful signal (the area around the hole, which is the object) and the additive noise (the hole: absence of the object) in the test image, second $\mathrm{SNR}_{\mathrm{out}}$ the difference between the useful signal and the additive noise after the de-noising process for hard and soft thresholding, respectively by applying "*symlet8*". Table 1 shows the SNR values for the ten images with 0.1 s as exposure time, five with 0.2 s, two with 0.5 s and finally 1 with 1 s.

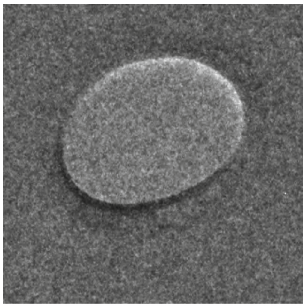

(a)

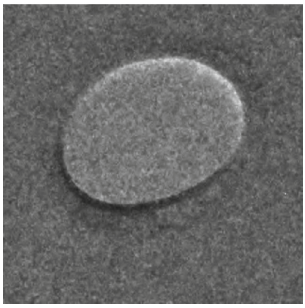

(b)

Fig. 3. De-noised test image of time exposure 0.2 s: (a) Hard thresholding, (b) Soft thresholding

4.3 Results of the De-Noising Algorithm

Table 1 illustrates SNR's of all EM test images employing hard and soft thresholding. As mentioned in the introduction the SNR_{in} is extremely low (Table 1), then witnesses a steady rise until it reaches a peak at exposure time equal to 1 s. The observed increase in the calculated value of SNR is attributed to the exposure time where during the acquisition of the EFTEM test images, they subject to electron beam which causes a shaking of the specimen. Therefore as can be seen in Table 1, the lower exposures time the smaller value of SNR_{in}. Corresponding to the degraded visual quality of the test images from 1 s to 0.1 s (Fig. 1). Low time exposure (low electron dose) is suitable to reduce the radiation damage. So, we should balance the trade-off between low electron dose and the feasibility to improve SNR after acquisition.

We can easily see, from Table 1, that the SNR_{out} values are remarkably improved both in hard and soft thresholding, but, SNR_{out} of soft thresholding method, is bigger than that in hard thresholding for all the datasets. The SNR values in the same dataset are slightly varying because of the non-homogeneity of the EM images.

To highlight the advantages of the used algorithm, Fig. 2 till Fig. 5 show some of our EM tested images after applying hard and soft thresholding. We chose to show one de-noised image from each dataset (0.1 s, 0.5 s, 0.2 s and 1 s). From these figures, we can see that noise is massively reduced in both soft and hard thresholding.The enhancement

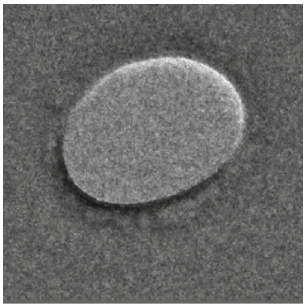

(a)

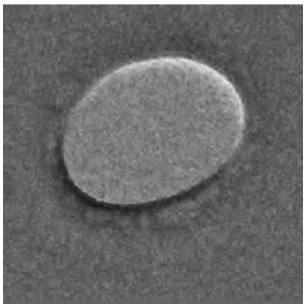

(b)

Fig. 4. De-noised test image of time exposure 0.5 s: (a) Hard thresholding, (b) Soft thresholding

of the visual quality of the de-noised EM images is clearly observed on the noisiest datasets which correspond to 0.1 s and 0.2 s (Figs. 2 and 3 respectively). The visual quality of the de-noised images which obtained by soft thresholding are better than that obtained by hard thresholding for all the datasets.

5 Concluding Remarques

In this paper, de-noising of real Electron microscopy (EM) test images is performed using wavelets at both hard and soft threshold levels. Different real datasets with different time exposure are used. An appropriate choice of mother wavelet, the whole number of decomposition and the thresholding rule, are set to achieve better visual quality and improved SNR values of the processed images. The application of wavelet de-noising procedure to electron microscopy may facilitate the three dimensional reconstruction by improving the image quality as was shown in our experiments. Thus, we demonstrate the applicability of the wavelet representation for de-noising EM data. The need to use low electron doses in microscopy imaging system, make the application of image pre-processing steps like the one described here very important in order to improve SNR values.

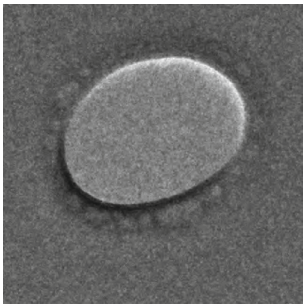

(a)

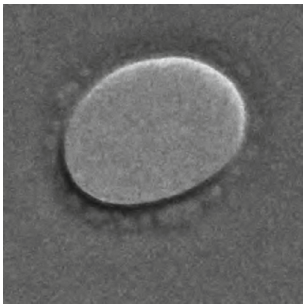

(b)

Fig. 5. De-noised test image of time exposure 1 s: (a) Hard thresholding, (b) Soft thresholding

Table 1. SNR_{in} and SNR_{out} of all test images applying soft and hard thresholding

Different time exposure of dataset of EM images	SNR_{in} (dB)	SNR_{out} (dB)	
		Hard	Soft
0.1 s_0	2.8822	6.7821	12.1781
0.1s_1	2.8495	8.6866	12.4866
0.1s_2	2.9539	7.7134	13.0061
0.1s_3	3.2676	7.5365	12.6419
0.1s_4	4.5934	5.7116	11.7905
0.1s_5	3.4948	7.1098	12.3269
0.1s_6	5.8239	9.7918	14.0187
0.1s_7	2.0041	7.9693	14.2338
0.1s_8	3.1318	9.0966	13.2074
0.1s_9	4.5217	6.3026	12.2574
0.2s_1	11.3218	13.1354	17.3772
0.2s_2	7.5025	11.1387	16.4682
0.2s_3	11.2858	12.9944	17.4572
0.2s_4	9.5248	14.5085	18.1439
0.2s_5	11.0171	14.8471	19.0419
0.5s_1	18.5929	19.4764	22.6002
0.5s_2	15.6158	17.2110	26.6293
1s	22.5953	27.4807	34.0854

In any case, we should balance the contradiction between the use of low electron dose to reduce radiation damage, and the feasibility to improve SNR after acquisition.

Also, we recommend that the integration of wavelet de-noising technique in the pre-processing applied under the software designed for this aim, TomoJ, developed by Messaoudi *et al.* [17, 18], will be given a greater role in enhancing the quality of reconstructed 3D volume.

References

1. Moulin, P., Liu, J.: Analysis of multiresolution image denoising schemes using generalized gaussian and complexity priors. IEEE Inf. Theory **45**(3), 909–919 (1999)
2. Strela, V., Portilla, J., Wainwright, M., Simoncelli, E.P.: Image denoising using gaussian scale mixtures in the wavelet domain. In: Proceedings of SPIE 45th Annual Meeting, San Diego, CA, August 2000
3. Buades, A., Coll, B., Morel, J.M.: A review of image denoising algorithms, with a new one. Simulation **4** (2005)
4. Chang, S.G., Yu, B., Vetterli, M.: Spatially adaptive wavelet thresholding with context modeling for image denoising. IEEE Trans. Image Process. **9**, 1522–1531 (2000)
5. Guo, H., Odegard, J.E., Lang, M., Gopinath, R.A., Selesnick, I.W., Burrus, C.S.: Wavelet based speckle reduction with application to SAR based ATD/R. In: First International Conference on Image Processing, vol. 1, pp. 75–79, November 1994
6. Wufan, C.: Wavelet Analysis and Its Application on Image Processing. Publishing House of Science, Beijing (2011)
7. Donoho, D.L., Johnstone, I.M.: Ideal spatial adaptation by wavelet shrinkage. Biometrika **81** (3), 425–455 (1994)
8. Donoho, D.L.: De-noising by soft-thresholding. IEEE Trans. Inf. Theory **41**(3), 613–627 (1995)
9. Jansen, M., Bulthel, A.: Empirical bayes approach to improve wavelet thresholding for image noise reduction. J. Am. Stat. Assoc. **96**(454), 629–639 (2001)
10. Boudjlel, A., Messali, Z., Boubchir, L., Chetih, N.: Non parametric bayesian estimation structure in the wavelet domain of multiple noisy image copies. In: 6th International Conference: Sciences of Electronic, Technologies of Information and Telecommunications SITIS, 21–24 March, Sousse, Tunisia (2012)
11. Sousa, A.A., Kruhlak, M.J.: Nanoimaging: Methods and Protocols. Springer Protocols. Humana Press, New York (2013)
12. Hayat, M.A.: Principles and Techniques of Electron Microscopy: Biological Application. Cambridge University Press, Cambridge (2000)
13. Frank, J.: Electron Tomography. Three-Dimensional Imaging with the Transmission Electron Microscope. Plenum Press, New York (1992)
14. Marco, S., Boudier, T., Messaoudi, C., Rigaud, J.L.: Electron tomography of biological samples. Biochemistry (Mosc) **69**(11), 1219–1225 (2004)
15. Messaoudi, C., Garreau de Loubresse, N., Boudier, T., Dupuis-Williams, P., Marco, S.: Multiple-axis tomography: applications to basal bodies from Paramecium tetraurelia. Biol. Cell **98**, 415–425 (2006)

16. Boudier, T., Lechaire, J.P., Frebourg, G., Messaoudi, C., Mory, C., Colliex, C., Gaill, F., Marco, S.: A public software for energy filtering transmission electron tomography (EFTET-J): application to the study of granular inclusions in bacteria from Riftia pachyptila. J. Struct. Biol. **151**(2), 151–159 (2005)
17. Messaoudi, C., Boudier, T., Sorzano, C., Marco, S.: TomoJ: tomography software for three-dimensional reconstruction electron microscopy. BMC Bioinform. **6**(8), 288 (2007)
18. http://u759.curie.fr/fr/download/softwares/TomoJ

New Front End Based on Multitaper and Gammatone Filters for Robust Speaker Verification

Fedila Meriem[1,2(✉)], Harizi Farid[1], Bengherabi Messaoud[1(✉)], and Amrouche Abderrahmene[2]

[1] Centre de Développement des Technologies Avancées, Algiers, Algeria
{mfedila, fharizi, mbengherabi}@cdta.dz
[2] University of Sciences and Technology Houari Boumedienne, Algiers, Algeria

Abstract. In this paper we present a novel feature extraction algorithm based on multitaper and Gammatone filters for robust speaker verification systems in mismatched noisy conditions encountered in realistic conditions. The idea is to couple the advantage of the low variance multitaper short term spectral estimators with the noise robustness of the auditory Gammatone filterbanks. Experimental results on the TIMIT corpus, with mismatched environment and low signal to noise ratios (SNR) levels, show that the proposed Multitaper Gammatone Cepstral Coefficient (MGCC) features outperform largely the conventional Mel Frequency Cepstral Coefficients (MFCC). Furthermore, and interestingly the MGCC features outperforms at almost all the operating signal to noise ratios the recently proposed Gammatone Frequency Cepstral Coefficient (GFCC) under white, babble and factory noises. This gain in performance is obtained with both the GMM-UBM baseline and the state-of -the art I-vector speaker verification systems.

Keywords: MFCC · Multitapers · Gammatone filter · Speaker verification · GFCC · Noisex

1 Introduction

The Mel Frequency Cepstral Coefficients (MFCC) short term spectral features which are the standard features in speech and speaker recognition offer better performance than other features in clean environment. However, the performance MFCC's-based recognition systems degrades drastically in certain operational conditions, e.g. noise, room reverberation, or channel variations. This fact has fueled the research community to focus on novel robust features in last years. Recently, multitapering or multiple windows nonparametric spectral estimators proposed in [1] were applied for speaker recognition using the standard Gaussian Mixture Model–Universal Background Model (GMM–UBM) resulting in better robustness to noise [2]. Following this success, the authors in [3, 4] integrate the multitaper features in the state of the art I-vector paradigm using the Probabilistic Linear Discriminant analysis (PLDA) for channel compensation with promising results.

M. Chadli et al. (eds.), *Recent Advances in Electrical Engineering and Control Applications*, Lecture Notes in Electrical Engineering 411, DOI 10.1007/978-3-319-48929-2_27

Other researchers; inspired from the human hearing system-robustness to noise and high capacity of acoustic source separation; have directed their work to the design of new filters which better imitate the human auditory system. The Gammatone filter bank proposed in [5] to model human cochlear filtering attracted many researchers working on speech and speaker recognition.

Recently, a new feature for speaker recognition based on Gammatone filtering namely GFCC (Gammatone Frequency Cepstral Coefficients) demonstrates high robustness in noisy conditions and performs substantially better than the conventional Mel-frequency cepstral coefficients [6, 7]. Furthermore, this feature coupled with Computational Auditory Scene Analysis (CASA) yields to a highly noise-robust speaker identification system [8].

Starting from our belief that there exist a room for further improvement of speaker verification robustness by combining the recently proposed techniques at different system levels, we propose in this work the Multitaper method for Gammatone Cepstral Coefficients MGCC, a new front-end based on combining multitaper windows and Gammatone filterbanks. The contribution of this paper is twofold: first, proposing a novel feature based on the combination of multiple windows and Gammatone filterbanks. Second and differing from previous works using Gammatone filters, the focus is on the robustness of speaker verification systems not speech recognition or speaker identification tasks outlined in previous works [6–8].

The organization of the paper is as follows. In Sect. 2, we introduce the proposed Multitaper Gammatone Cepstral Coefficients (MGCC). In Sect. 3, we give a brief review of Gammatone filterbank. Multitaper Spectrum Estimation is depicted in Sect. 4. In Sect. 5, we describe the experimental setup and analyze the results of the preliminary experiments reported on the TIMIT corpora using the GMM-UBM system [9]. Finally, the conclusion is drawn in Sect. 6.

2 The Proposed Multitaper Gammatone Cepstral Coefficient MGCC

Figure 1 shows the diagram for the extraction of the proposed feature. First, the input speech is divided into frames with a temporal length satisfying wide sense stationarity, e.g. 30 ms, and are shifted a certain temporal length, e.g.10 ms.

Next, each frame is multiplied by a window function to minimize the signal discontinuity at the beginning and end of each frame. The power spectrum of the speech signal is estimated using multitaper spectral estimator, the classical Hamming-windowed spectrum estimates can be obtained as a special case of the multi-taper spectrum estimation method. The spectrum of the speech signal is then filtered by a bank of Gammatone filters. This filterbank was originally designed to model human cochlear; it is derived from psychophysical and physiological observations of the auditory periphery. After that, Equal-loudness is applied to each of the filter outputs, according to the center frequency of the corresponding filter. Additionally, the DCT is applied on the log Gammatone filter bank accumulated energies for de-correlation and dimensionality reduction. Only the lower orders are used for speaker verification.

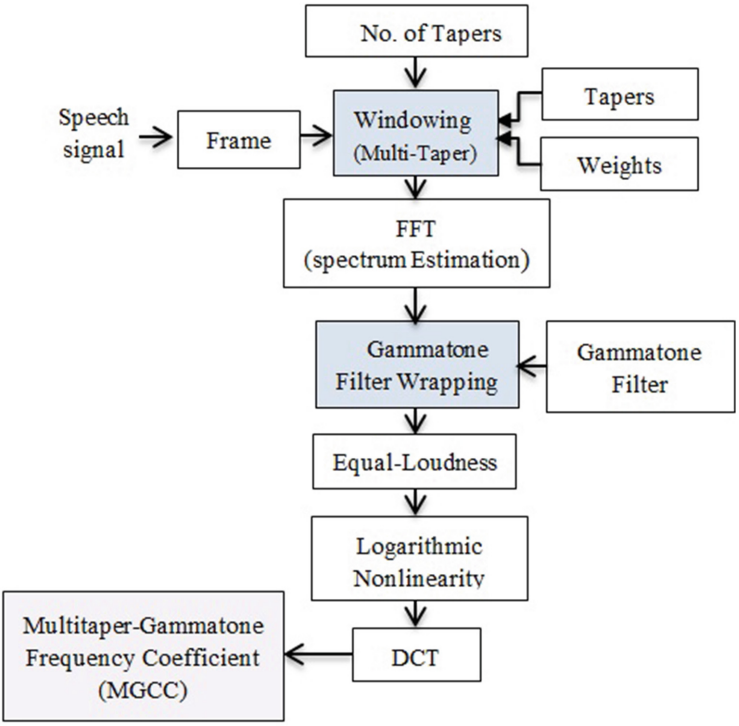

Fig. 1. Block diagram of MGCC feature extraction.

3 Gammatone Filter

The Gammatone filter is described by an impulse response that is the product of a gamma distribution and sinusoidal tone [6]:

$$g(t) = at^{n-1} \exp(-2\pi b\, ERB(f_c)t) \cos(2\pi f_c t + \varphi) \tag{1}$$

The parameter n is the order of the filter; which is generally taken to be 4; f_c is the center frequency of the filter, a and b are constants, φ is the starting phase, and $ERB(f_c)$ is the equivalent rectangular bandwidth of an auditory filter. In [10], human data on the ERB of the auditory filter has been summarized and can be approximated as:

$$ERB(f_c) = 24.7 + 0.108 f_c \tag{2}$$

The Gammatone filter is very similar to the rounded exponential function used in representing the magnitude response of the human auditory filters [5].

Compared to the Mel filterbank, the Gammatone filter has a more smooth form as shown in Fig. 2. The amount of overlap of the Mel filterbank is fixed, so if the number of filters increases, the bandwidth of each triangular filter will decrease. For the Gammatone filter, the bandwidth is determined by its center frequency, so if the

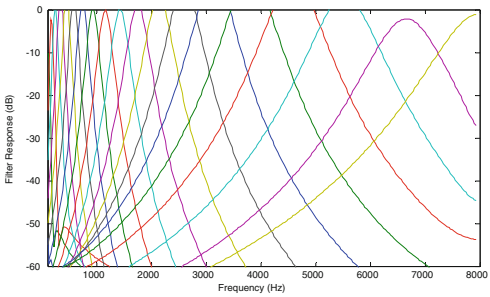

Fig. 2. The frequency characteristics of 20-channel Gammatone filter banks.

number of filters increases, the overlap also increases. The structure of the Gammatone filterbank is more subtle and similar to the human auditory model.

4 Multitaper Spectrum Estimation

In speech processing applications, windowed periodogram is the most popular used power spectrum estimation method. Although windowing reduces the bias (the difference between the estimated spectrum and the actual spectrum), it does not reduce the variance of the spectral estimate [11], and therefore, the variance of MFCC features computed from this estimated spectrum is also large. A multitaper spectrum, as a replacement of the windowed periodogram estimate, can be used to reduce the variance of the MFCC features [2, 3, 12]. The multitaper spectrum estimator, which uses M orthogonal window function rather than a single window, can be expressed as [3]:

$$\hat{S}_{MT}(m,k) = \frac{1}{M}\sum_{p=0}^{M-1} \lambda(p)\left|\sum_{j=0}^{N-1} w_p(j)s(m,j)e^{\frac{-2\pi jk}{N}}\right|^2 \tag{3}$$

Where $s(m, j)$ is the time domain speech signal, N is the frame length, w_p is the pth data taper used for the spectral estimate $\hat{S}_{MT}(\cdot)$, which is also called the pth eigenspectrum, M denotes the number of tapers, and $\lambda(p)$ the weight corresponding to the pth taper. The tapers w_p are chosen to be orthonormal, i.e.,

$$\sum_j w_p(j)w_q(j) = \delta_{pq} = \begin{cases} 1 & p = q \\ 0 & otherwise \end{cases} \tag{4}$$

The windowed periodogram (called also single taper) can be obtained as a special case of Eq. (3), when $p = M = 1$ and $\lambda(p) = 1$:

$$\hat{S}_d(m,k) = \left|\sum_{j=0}^{N-1} w(j)s(m,j)e^{\frac{-j2\pi jk}{N}}\right|^2 \tag{5}$$

In a multitaper spectrum estimation method, the speech signal is, first, multiplied by not only one window but a family of tapers which are resistant to spectral leakage such as Thomson, Multipeak and Sine Weighted Cepstrum Estimator (SWCE) [2].

This yields several tapered speech signals from one record. Taking the discrete Fourier transforms (DFTs) of each of these tapered signal, several eigen-spectra are produced which are combined (using a weighted averaging technique) to form the final multi-taper spectral estimate.

5 Experiment

In this section, we evaluate the noise robustness of the proposed MGCC features for Speaker verification task. We compare the performance of our system using MGCC features with the baseline system using the conventional MFCC features. In addition, we compare it with the recently proposed Gammatone Frequency Cepstral Coefficients (GFCC) [6].

5.1 Experimental Setup

We use the TIMIT corpus [13] for our experiments. It contains a total of 630 (192 female and 438 male) Speakers, from which 530 speakers have been selected for background model training and the remaining 100 (30 female and 70 male) speakers are used for tests. There are 10 short sentences per speaker in TIMIT. For background model training all sentences from all 530 speakers (i.e., 5300 speech recordings in total) are used. For speaker-specific model training 9 out of 10 sentences per speaker are selected and the remaining 1 sentence is kept for tests. Verification trials consist of all possible model-test combinations, resulting in a total of 10,000 trials (100 targets versus 9900 impostor trials).

We utilize a standard Gaussian Mixture Model with Universal Background Model (GMM-UBM) as our baseline. We have utilized the same hyper parameters as in [14], with 256-component Gaussian mixture models. In comparison of the different estimation methods, Results are expressed in terms of Equal Error Rate, Minimum Detection Cost Function as proposed by NIST for 2008 SRE (DCF_{08}) and as proposed for 2010 SRE (DCF_{10}) [15].

EER is the error rate for which the miss rate (Pmiss) and the false alarm rate (Pfa) are equal. DCF_{08} and DCF_{10} correspond to the evaluation metric for the NIST SRE in 2008 and 2010, respectively. In addition, we plot detection error tradeoff (DET) curves which show the full tradeoff curve between false alarms and misses in a normal deviate scale.

For systematic study of the robustness of the feature sets, we consider their performance under additive Babble, factory (drawn from the NOISEX-92 corpus) and White *noises* degradation. The UBM and target model training data are kept untouched, but the noises are added to the test files with a given average segmental signal-to-noise ratio (SNR). We consider six SNR levels: 20, 15, 10, 5, 0 and −5 dB. This scenario simulates real applications where the training is done in controlled environment and the test is uncontrolled.

For comparison we have also implemented two baseline systems, the first is based on MFCC where the features are computed via the standard pipeline: Hamming windowing, DFT magnitude spectrum, 29 mel-frequency spaced filters, logarithm and discrete cosine transform. We keep the lowest 13 MFCCs, excluding c_0. Additionally, for the system based on GFCC we have used the following steps outlined in [6]:

- Pass input signal through a 64-channel Gammatone filterbank.
- At each channel, fully rectify the filter response (i.e. take absolute value) and decimate it to 100 Hz as a way of time windowing. Then take absolute value afterwards.
- Take cubic root on the T-F representation.
- Apply DCT to derive cepstral features.

The toolkit provided by Prof. Wang is used to generate the frequency-domain GFCC[1]. The feature extraction process of MGCC is presented through the block diagram in Fig. 1. MGCC are derived using a frame length of 30 ms with a frame shift of 10 ms. As in [6], Furthermore the spectrum of the speech signal is then filtered by a bank of Gammatone filters (using 64-channel). Finally, we applied DCT and kept only the 30 lower coefficients (excluding c0). Based on studies of T. Kinnunen et al. [2], we fixed the number of tapers as k = 8 for all tapers namely Thomson, SWCE and Multipeak.

5.2 Experimental Results Using GMM-UBM

From Fig. 3, showing the DET curves of different features under clean testing conditions, we can notice the superiority of the MFCC at the EER operating point. Meanwhile the proposed MGCC outperforms MFCC at low false alarm region using both the Thomson and the SWCE tapers (MinDCF). Moreover, both MFCC and MGCC outperform the GFCC. Figures 4 present the experimental results in terms of

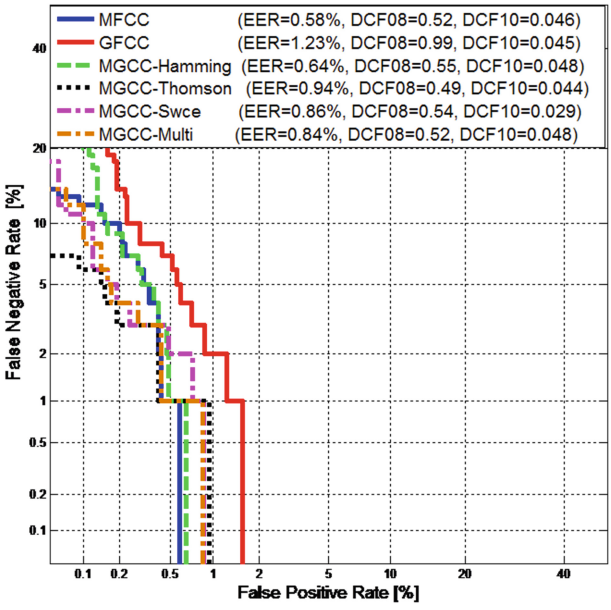

Fig. 3. Performance of MGCC, MFCC and GFCC in clean conditions.

[1] http://www.cse.ohio-state.edu/pnl/shareware/gfcc/ .

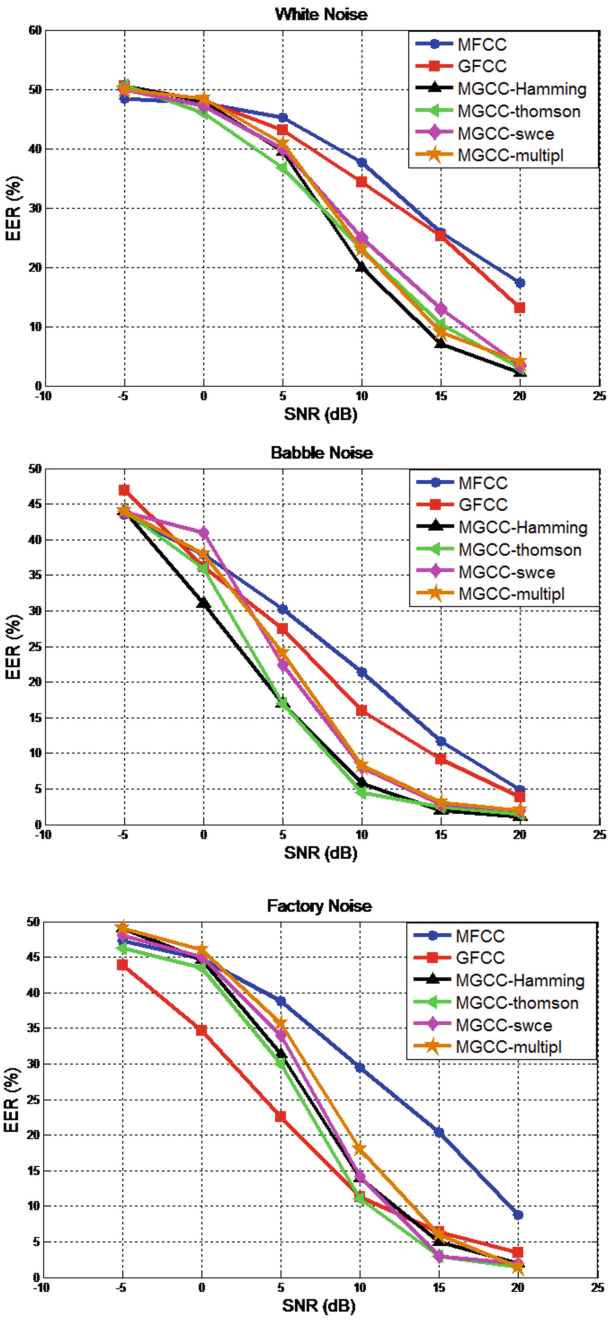

Fig. 4. Evaluation of various features in term of Equal Error Rates under white, babble and factory noises on the Noise Speech test set for SNR values of {−5, 0,5,10,15 and 20 dB}.

EER under White, Babble and Factory noises respectively. Clearly, it is seen a relative permanent improvements (especially when using Thomson tapers) obtained by the use of MGCC features compared to the MFCC and GFCC especially in white and bubble noises and even under the factory noise the performance is better than GFCC at SNR's between 10 and 20 dB generally encountered in forensic speaker recognition.

It is worthy to mention that using hamming window with the Gammatone filterbank results in very interesting results, reinforcing the previous works highlighting the superiority of the Gammatone filterbank over the conventional Mel filterbank [16–18].

Tables 1 and 2 summarize the performance of different Features under white and babble noises respectively at 10 dB. It is apparent from this table the superiority of the proposed features.

Table 1. The performance of various features in term of EER, DCF08 and DCF10 under white noise at SNR = 10 dB.

	MFCC	GFCC	MGCC-Thomson	MGCC-SWCE	MGCC-Multip
EER	37.00	34.00	33.31	32.00	**30.96**
DCF08	9.90	9.55	9.45	9.58	**9.42**
DCF10	0.099	0.099	0.099	0.099	0.099

Table 2. The performance of various features in term of EER, DCF08 and DCF10 under Babble noise at SNR = 10 dB.

	MFCC	GFCC	MGCC-Thomson	MGCC-SWCE	MGCC-Multip
EER	22.00	15.59	9.00	8.80	**7.90**
DCF08	5.70	4.98	5.06	**4.41**	4.55
DCF10	0.090	0.098	0.090	**0.089**	0.089

A second set of experiments are done for a fair comparison with the MFCC by reducing the number of Gammatone filterbank channels to 20 and taking only 13 MGCC coefficients (Set 1).

The performance results depicted in Table 3 demonstrate clearly that the proposed feature still outperforms significantly the MFCC feature despite the decrease in its performance compared to the system using 64 channels and 13 MGCC (Set 2). Interestingly, apart from factory noise, the MGCC outperforms clearly the GFCC for both white and babble noise.

Table 3. EER performance of MGCC features under white, babble and factory noises at SNR = 10 dB.

	White		Babble		Factory	
	Set 1	Set 2	Set 1	Set 2	Set 1	Set 2
MGCC-Thomson	33.3	23.0	9.0	4.4	11.0	6.0
MGCC-Swce	32.0	25.0	8.8	8.0	14.2	6.0
MGCC-Multipl	30.9	23.0	7.9	8.2	18.0	6.7

5.3 Experimental Results Using I-Vector

For the sake of investigating the robustness of the proposed features on the state of the art speaker verification based on total variability paradigm known as I-vector [19]. An i-vector extractor of dimension 400 is trained on a larger set (5300 speech of TIMIT database).

The dimensionality of i-vectors is further reduced to 200 by Linear Discriminant Analysis LDA, followed by Gaussian Probabilistic Linear Discriminant Analysis GLDA [20]. From Tables 4, 5 and 6 we can deduce that, despite the general tendency of I-vector-based speaker verification systems to yield less performance compared to the GMM-UBM systems in this testing conditions characterized by very short testing utterances; which are one of the challenges in the speaker recognition research community [21, 22]; The performance of the proposed features outperform largely the performance of the systems based on the traditional MFCC.

Table 4. EER performance of baseline system compared to i-vector using various features under white noise.

Feature	Classifier	5 dB	10 dB	15 dB	20 dB
MFCC	GMM-UBM	45.00 %	37.00 %	26.00 %	16.93 %
MFCC	I-vector	42.38 %	38.00 %	32.00 %	27.00
MGCC_Hamming	I-vector	**32.00 %**	**21.77 %**	15.45 %	10.00 %
MGCC_Thomson	I-vector	34.00 %	25.00 %	**15.43 %**	9.00 %
MGCC_SWCE	I-vector	34.97 %	26.23 %	15.51 %	**8.00 %**

Table 5. EER performance of baseline system compared to i-vector using various features under babble noise.

Feature	Classifier	5 dB	10 dB	15 dB	20 dB
MFCC	GMM-UBM	32.28 %	22.00 %	12.86 %	4.53 %
MFCC	I-vector	35.81 %	30.62 %	27.66 %	20.00 %
MGCC_Hamming	I-vector	38.00 %	27.10 %	21.00 %	12.71 %
MGCC_Thomson	I-vector	**27.19 %**	**16.44 %**	**10.24 %**	**6.79 %**
MGCC_SWCE	I-vector	35.00 %	25.00 %	13.38 %	9.96 %

Table 6. EER performance of baseline system compared to i-vector using various features under factory noise.

Feature	Classifier	5 dB	10 dB	15 dB	20 dB
MFCC	GMM-UBM	38.00 %	29.00 %	19.00 %	8.00 %
MFCC	I-vector	38.00 %	34.00 %	26.00 %	17.00 %
MGCC_Hamming	I-vector	35.00 %	27.00 %	18.34 %	12.29 %
MGCC_Thomson	I-vector	**33.12 %**	**22.00 %**	**10.57 %**	**6.00 %**
MGCC_SWCE	I-vector	36.40 %	28.00 %	15.59 %	9.35 %

6 Conclusion

In this paper, we have proposed a new feature for speaker verification based on coupling the advantage of the low-variance multi-taper short term spectral estimators and the noise robustness of Gammatone filterbanks.

Experimental speaker verification results on the TIMIT corpus depict that an improvement be obtained by using MGCC, as a front-end. These preliminary results obtained in speaker verification under noisy conditions are very encouraging and shows clearly that Gammatone filters can be a better alternative to the triangular Mel filterbanks and also the possibility to improve more the speaker verification systems via Multitapering.

References

1. Thomson, J.: Spectrum estimation and harmonic analysis. Proc. IEEE **70**(9), 1055–1096 (1982)
2. Kinnunen, T., Saeidi, R., Sandberg, J., Hansson-Sandston, M.: What else is new than the hamming window? robust MFCCs for speaker recognition via multitapering. In: International Speech Communication Association, INTERSPEECH, pp. 2734–2737 (2010)
3. Alam, M.J., Tomi, K., Kenny, P., Ouellettand, P., O'Shaughnessy, D.: Multitaper MFCC and PLP features for speaker verification using I-vectors. Speech Commun. **55**(2), 237–251 (2013)
4. Alam, M.J., Tomi, K., Kenny, P., Ouellettand, P., O'Shaughnessy, D.: Multi-taper MFCC features for speaker verification using I-vectors. In: ASRU, pp. 547–52 (2011)
5. Patterson, R.D., Nimmo-Smith, I., Holdsworth, J., Rice, P.: An efficient auditory filterbank based on the gammatone function. Applied Psychology Unit, Cambridge, UK, APU Rep. 2341 (1988)
6. Zhao, X., Wang, D.L.: Analyzing noise robustness of MFCC and GFCC features in speaker identification. In: International Conference on Acoustics, Speech, and Signal Processing, ICASSP 2013, pp. 7204–7208 (2013)
7. Shaoand, Y., Wang, D.L.: Robust speaker identification using auditory features and computational auditory scene analysis. In: Proceedings of the IEEEICASSP, pp. 1589–1592 (2008)
8. Zhao, X., Shao, Y., Wang, D.L.: CASA-based robust speaker identification. IEEE Trans. Audio Speech Lang. Process. **20**, 1608–1616 (2012)
9. Reynolds, D.A., Quatieri, T.F., Dunn, R.B.: Speaker verification using adapted Gaussian mixture models. Digit. Sig. Process. **10**, 19–41 (2000)
10. Glasbergand, B.R., Moore, B.C.J.: Derivation of auditory filter shapes from notched-noise data. Hear. Res. **47**, 103–108 (1990)
11. Kay, S.M.: Modern Spectral Estimation. Prentice-Hall, Englewood Cliffs (1988)
12. Riedeland, K.S., Sidorenko, A.: Minimum bias multiple taper spectral estimation. IEEE Trans. Signal Process. **43**(1), 188–195 (1995)
13. The DARPA TIMIT Acoustic-Phonetic Continuous Speech Corpus (TIMIT) Training and Test Data, NIST Speech Disc CD1-1.1
14. Sadjadi, S.O., Slaney, M., Heck, L.: MSR Identity Toolbox: A MATLAB Toolbox for Speaker Recognition Research Version 1.0, Microsoft Research, Conversational Systems Research Center (CSRC), October 2013

15. NIST, The NIST year 2008 and 2010 Speaker Recognition Evaluation plans. http://www.itl.nist.gov/iad/mig/tests/sre
16. Dehak, N., Kenny, P., Dehak, R., Dumouchel, P., Ouellet, P.: Frontend factor analysis for speaker verification. IEEE Trans. ASLP **19**, 788–798 (2010)
17. Kenny, P.: Bayesian speaker verification with heavy tailed priors. In: Proceedings of the Odyssey Speaker and Language Recognition Workshop, Brno, Czech Republic (2010)
18. Valero, X., Alias, F.: Gammatone cepstral coefficients: biologically inspired features for non-speech audio classification. IEEE Trans. Multimedia **14**(6), 1684–1689 (2012). doi:10.1109/TMM.2012.2199972. Cited by: Papers (4)
19. Abdulla, W.H.: Auditory based feature vectors for speech recognition. In: Advances in Communications and Software Technologies, pp. 231–236 (2002)
20. Abdulla, W.H., Zhang, Y.: Voice biometric feature using gammatone filterbank and ICA. Int. J. Biometrics **2**(4), 330–349 (2010)
21. Kanagasundaram, A., Vogt, R., Dean, D., Sridharan, S., Mason, M.: I-vector based speaker recognition on short utterances. In: Proceedings of INTERSPEECH, International Speech Communication Association (ISCA), pp. 2341–2344 (2011)
22. Kanagasundaram, A., Dean, D., Sridharan, S., Gonzalez-Dominguez, J., Gonzalez-Rodriguez, J., Ramos, D.: Improving short utterance I-vector speaker recognition using utterance variance modelling and compensation techniques. Speech Commun. **59**, 69–82 (2014)

Comparative Study of Time Frequency Analysis Application on Abnormal EEG Signals

Abdelhakim Ridouh[1(✉)], Daoud Boutana[1], and Messaoud Benidir[2]

[1] Department of Automatic, University of Jijel, Jijel, Algeria
ridouhhakim@yahoo.fr, daoud.boutana@mail.com
[2] Laboratory of Signals and Systems Supelec,
South-Paris University, Paris, France
benidir@Lss.supelec.fr

Abstract. This paper presents a time-frequency analysis for some pathological Electroencephalogram (EEG) signals. The proposed method is to characterize some pathological EEG signals using some time-frequency distributions (TFD). TFDs are useful tools for analyzing the non-stationary signals such as EEG signals. We have used spectrogram (SP), Choi-Williams Distribution (CWD) and Smoothed Pseudo Wigner Ville Distribution (SPWVD) in conjunction with Rényi entropy (RE) to calculate the best value of their parameters. The study is conducted on some case of epileptic seizure of EEG signals collected on a known database. The best values of the analysis parameters are extracted by the evaluation of the minimization of the RE values. The results have permit to visualize in time domain some pathological EEG signals. Also, the Rényi marginal entropy (RME) has been used in order to identify the peak seizure. The characterization is achieved by evaluating the frequency bands using the marginal frequency (MF).

Keywords: EEG · Time-frequency analysis · Rényi entropy

1 Introduction

The brain is considered as the controlling center for all organs of human body including heart and respiration, and it's also the primary center for other functions like: transmitting information to the muscles and body organs, regulation and control of body activities and receiving and interpreting sensory impulses [1].

The Electroencephalogram (EEG) signal is the registration of time-varying potential differences produced by electrical activity which is born from action of brain and produced by the firing of a vast number of neurons recorded from the scalp with electrodes placed on the head [2, 3]. The internationally standardized 10–20 system is the most often system used for these records [4, 5]. The EEG within the brain is a complex random signal, so it is a non-stationary signal [6–8].

The EEG signal analysis is very important [9] for studying and recognizing several neurological disorders. It allows the extraction of information about the brain, with which we can know the current state of the brain and it's used as a diagnostic tool [10].

M. Chadli et al. (eds.), *Recent Advances in Electrical Engineering and Control Applications*, Lecture Notes in Electrical Engineering 411, DOI 10.1007/978-3-319-48929-2_28

A signal taken from a patient suffering from epilepsy, which is the neurological disorder of the brain, contains many typical signal patterns and rhythms. But visually, it's difficult to diagnose neurological disorders using EEG signals [11]. Two useful aspects such as spectral and temporal analysis have been used during the interpretation of an EEG signal. The importance of these two analyses to characterize EEG signal comes from that:

The spectral analysis of an EEG signal determines its wavebands. These wavebands are the rhythms characterizing EEG signal from their frequency: Delta (0–4 Hz), Theta (4–8 Hz), Alpha (8–13 Hz), and Beta (13–45 Hz) [12, 13]. However, the temporal analysis provides information such as: when the rhythms (Delta, Theta, Alpha and Beta) appear and disappear they maintain in the signal a form of normal and abnormal wave. A neurologist can make a diagnosis of the patient by analyzing these different wave forms [14, 15].

There are many mathematical tools to extract information from EEG observations. Time-frequency distributions (TFD) [16, 17] characterize non-stationary signals over time-frequency plane. They may also serve as a basis for signal synthesis, coding, and processing [18]. While EEG signals have non-stationary properties [19, 20], the time-frequency analysis is a powerful tool for EEG signals.

In our work we apply some TFDs to some pathological EEG signals using our own method to study EEG signals. We use our method to detect the abnormality in a specific signal using the Rényi entropy (RE).

The paper is organized as follows. In Sect. 2, we give an overview of all used methods. In Sect. 3, we present the material and data used. In Sect. 4, we present the experimental results. Section 5 we concludes the paper.

2 Methods

2.1 Time-Frequency Analysis

The TFDs constitutes a powerful tool in the analysis of non-stationary signals, i.e. signals whose frequency content varies with time. Two different kinds of TFD are used in our study: the linear class based on the use of SP and the quadratic class included CWD and SPWVD. The quadratic class can be expressed as [21]:

$$C_x(t,f) = \iiint e^{j2\pi(vt-vu-f\tau)} g_x(v,\tau) x\left(u+\frac{\tau}{2}\right) x^*\left(u-\frac{\tau}{2}\right) du\, d\tau\, dv \qquad (1)$$

Where t is the time, f is the frequency, τ is the time-Lag, v is the Doppler frequency and $g_x(v,\tau)$ is the Doppler-Lag kernel of the distribution, x(t) is the analytical form of the signal under consideration, x*(t) its complex conjugate.

A choice of a particular kernel function yields a particular quadratic TFD with its own specificities. To extract information about frequency band, we used the Marginal Frequency (MF) of the distribution given by [21]:

$$m_t(f) = \int_{-\infty}^{+\infty} C_x(t,f)dt \tag{2}$$

Spectrogram. The SP is defined as the squared magnitude of the Short Time Fourier Transform (STFT) which is a windowed Fourier transform [21]:

$$|S(t,f)|^2 = \left| \int_{-\infty}^{+\infty} x(\tau)h(\tau - t)e^{-j2\pi f\tau}d\tau \right|^2 \tag{3}$$

Where x is the signal under consideration, h is the analysis window function and τ represents the parameter of window localization.

Smoothed Pseudo Wigner-Ville Distribution. This distribution is derived from the Wigner-Ville distribution (WVD). It has opened the way for optimizing resolution with cross-terms reduction in the time-frequency plan. The SPWVD is defined as [22]:

$$SPWVD_x(t,f) = \iint h_x(v)g_x(\tau)x\left(t + \frac{\tau}{2}\right)x^*\left(t - \frac{\tau}{2}\right)e^{-j2\pi f\tau}d\tau dv \tag{4}$$

Where $h_x(v)$ and $g_x(\tau)$ are window functions centered at time τ and frequency v respectively, they control the resolution in joint time-frequency plane.

Choi-Williams Distribution. The CWD was a significant step in the field of time-frequency analysis where it opened the way for optimizing resolution with cross-terms reduction. The kernel of the Choi–Williams distribution (CWD) in the Doppler-lag domain is [22]:

$$g_x(v,\tau) = e^{-(\pi v\tau)^2/2\sigma^2} \tag{5}$$

Where σ is a real parameter that can control the resolution and the cross-terms reduction. This two-dimensional exponential kernel has shown excellent performance in reducing cross terms while keeping high resolution, with a compromise between these two requirements decided by the parameter σ.

2.2 Rényi Entropy

The RE is considered as a measure of time-frequency signal concentration. It is used in order to find the best values of analysis parameters such length of the window analysis and giving good concentration everywhere in time-frequency plane and provides high concentration of different components at different locations. The RE of order α is defined as [23, 24]:

$$R_\alpha = \frac{1}{1-\alpha} log_2 \iint C_x^\alpha(t,f)dtdf \tag{6}$$

Where α is the rank of the Rényi measure with $\alpha \geq 2$.

This measure has been used to evaluate the complexity of a signal in the time-frequency plane in Ref. [25]. However the authors in Ref. [26] demonstrate that the minimization of the RE for a given TFD provides the maximizing of its concentration and resolution. So, the best length of analysis window is obtained corresponding to the minimal value of the RE. Moreover the discrete-time formulation of the third RE for TFD with normalization volume is given by [27]:

$$\mathrm{RV}_3 = -\frac{1}{2}\log_2 \sum_{k=-K}^{K} \sum_{n=-N}^{N} \left[\frac{C_x(n,k)}{\sum_{m=-K}^{K} \sum_{l=-N}^{N} |C_x(m,l)|} \right]^3 \tag{7}$$

Where n and k are variables for discrete-time and discrete frequency respectively, (2N+1) and (2K+1) are number of samples in time and frequency respectively.

The RE is integrated with respect to frequency, in order to marginalize the signal's energy distribution over time. In our study, we have used the normalized Rényi marginal entropy (RME) of third order defined as:

$$\mathrm{R}_3(n) = -\frac{1}{2}\log_2 \sum_{k=-K}^{K} \left[\frac{C_x(n,k)}{\sum_{m=-K}^{K} \sum_{l=-N}^{N} |C_x(m,l)|} \right]^3 \tag{8}$$

This criterion has been used successfully [28] on identification and segmentation for pathological phonocardiogram signals.

3 Materials and EEG Data

The EEG data used in our study have been analyzed in Refs. [29–31]. The data comprises five sets: A, B, C, D and E [32], each set contains 100 single registrations of EEG segments. Each segment contains 4096 samples with duration equal to 23.6 s. Sets A and B are extra-cranially recorded for healthy persons, respectively with eyes open and closed. Sets C and D are intra-cranially recorded; C from non-epileptogenic of the opposite hemisphere of the brain and D from within the epileptogenic zone of an epileptic patient during seizure free intervals. Set E was intra-cranially recorded from the epileptic zone during seizure. The data acquisition to a computer system is done with sampling rate of 173.61 Hz [30]. In our studies we use set A and set E in purpose to compare normal and epileptic signals. We have chosen the set E as abnormal signals, and selected visually the signal number sixty five (Fig. 1(a)), and then divided the obtained signal into some segments. Among the 4 obtained fractions, we have chosen one portion noted frame 1 (Fig. 1(b)) on which there is a peak of epilepsy clearly

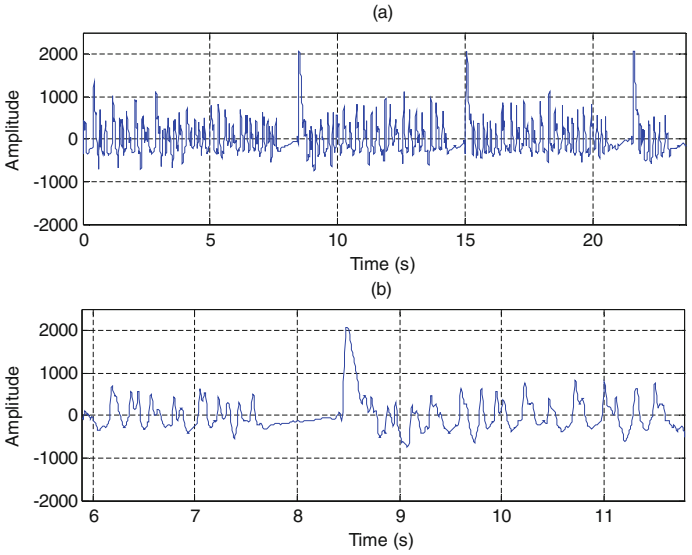

Fig. 1. Time representation of (a) a complete EEG signal and (b) the chosen part signal.

visualized. Each one of these parts comprises 1024 samples corresponding to 5.9 s of recording. The pathological signal is located from 5.9 to 11.8 s such as represented in Fig. 1.

4 Experimental Results

We calculated the RE on EEG signal frame 1 using the discussed methods: SP and SPWVD for various lengths of window and CWD for various values of σ in order to obtain the best parameters giving a better time-frequency resolution. It gives which frequencies having the most frequency resolution and characterizing the abnormal information on EEG signal.

4.1 Time-Frequency Analysis Using Rényi Entropy

The Spectrogram Analysis. The SP analysis using different lengths of window is achieved. The best parameters of the SP are obtained using the RE. Table 1(a) shows the RE values obtained for various lengths of a Hamming window *wl*. The best results are obtained with $wl = 93$ corresponding to the minimum value of the RE = 2.8568 and summarized in Fig. 2(a). Figure 3(a) displays the SP of the EEG signal using this best obtained value where the horizontal axis corresponds to time and the vertical axis to frequency. It can be seen that the analysis permits the visualization of an interesting event in time-frequency domain at 2.6151 s (8.5133 s in the original signal) with a frequency located around 1.5 Hz. A detailed study illustrated by Fig. 4(a) taking a

Table 1. Results of various values of RE using (a) SP, (b) SPWVD and (c) CWD.

SP		SPWVD		CWD	
wl	RE	*wlg*	RE	σ	RE
11	4.3672	11	3.0283	2	2.9365
17	3.8683	17	2.9004	4	2.8830
27	3.4117	27	2.7883	6	2.8618
41	3.0942	41	2.7339	8	2.8529
49	2.9960	**49**	**2.7296**	**10**	**2.8499**
93	**2.8568**	93	2.9060	12	2.8501
151	2.9239	151	2.9060	26	2.8787
205	3.0364	205	3.6117	36	2.9023
255	3.1393	255	3.8331	56	2.9420

profile at frequency f = 1.35 Hz and the MF allows us to observe that the dominant peak is located between frequency 1 Hz and 2 Hz. This frequency band characterizes the epileptic seizure of the signal in consideration.

The SPWVD Analysis. The SPWVD results illustrated in Table 1(b) represents the RE values obtained for various time analyzed window lengths (*wlg*) and the frequency analyzed window fixed with *wlh* = 93. Figure 2(b) illustrates the plot of these results where the best time window length is *wlh* = 49 corresponding to the minimum value of RE equal to 2.7296. The results in Fig. 3(b) show that the most important event is located at 2.6218 s (at 8.5191 s on the original signal). The progressive detailed study in Fig. 4(b) illustrate the profile at frequency f = 2.03 Hz and the MF of SPWVD respectively. This study shows that the dominant event present a peak with frequency between 1 Hz and 4 Hz characterizing the epileptic peak.

The CWD Analysis. The third approach using the CWD gives the results of the RE shown in Table 1(c). It allows us to find the best value obtained for various values of parameter with *wlh* = 93 and *wlg* = 49. Figure 2(c) illustrates the plot of these results given σ = 10 and the minimum value RE = 2.8499 as the best values. These results are illustrated in Fig. 3(c) showing that the most important event is located at 2.5978 s (8.4961 s in the original signal). The continuous study of the time frequency evolution permits to characterize the important events. Figure 4(c) show a profile at frequency f = 2.03 Hz and the MF of the CWD. This observation allows us to specify that an important event is located at 8.49 s with a frequency around 2.03 Hz.

The comparison of the results obtained by the approaches allows us to show that the SPWVD provides the best results in terms of the spectral resolution. So, the peak seizure of the abnormal EEG signal seems to have a frequency band from 2 to 4 Hz.

4.2 Peak Seizure Characterisation

In order to complete the validation of the method, the original signal is divided into consecutive segments or frames with length N = 1024. Figure 5(a, b and c) shows the

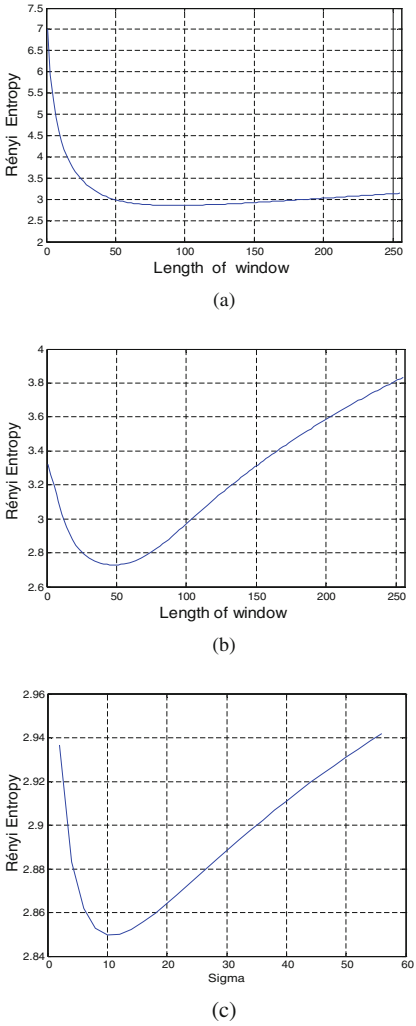

Fig. 2. Variation of RE using (a) SP, (b) SPWVD and (c) CWD.

temporal representation of the used frames noted frame 1, frame 2 and frame 3. In frame 1, the peak is located around second 8 and 9, the seizure continues in frame 2 and may be seen in the time located at 15 s and finally another peak can be seen in frame 3 from 21 s and 22 s.

Temporal Identification Using the Rényi Marginal. Our proposed method for EEG analysis used the RME estimated from the results of SPWVD for identifying the peak seizure in time domain. This approach has been applied in Ref. [33] for best speech segmentation. In this work, we propose the mean value of the RME and investigate its use as a suitable threshold to determine the localization of the peaks seizure of an EEG signal in consideration. The application of these approaches on studied frames using

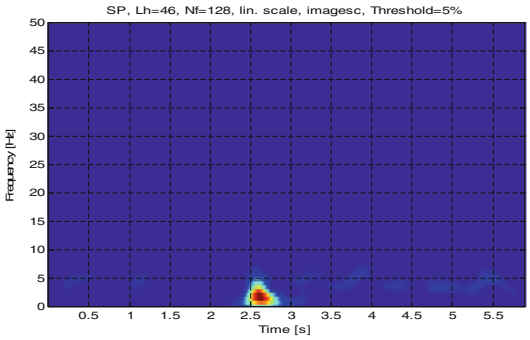

(a)

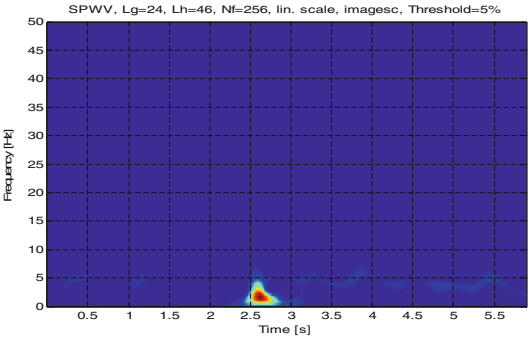

(b)

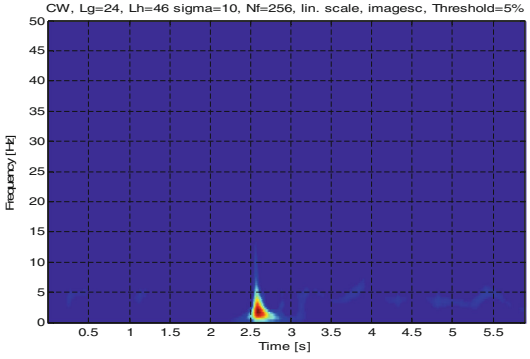

(c)

Fig. 3. Time-frequency representations of EEG signal using (a) SP, (b) SPWVD and (c) CWD.

the SPWVD gives the results illustrated in Fig. 6(A, B and C). These Figures represent a good qualitative identification of the peaks seizure present in the signal where part (a) shows the original signal of frame, part (b) the RME values with the blue plot line

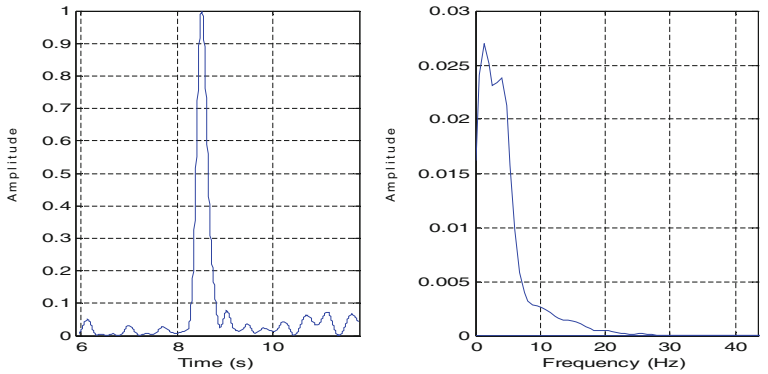

(a)

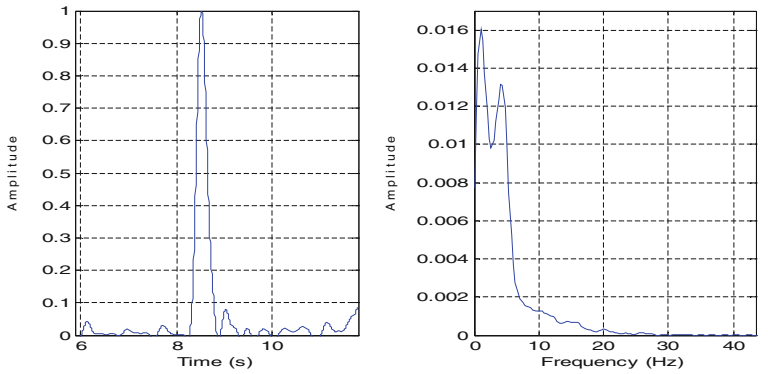

(b)

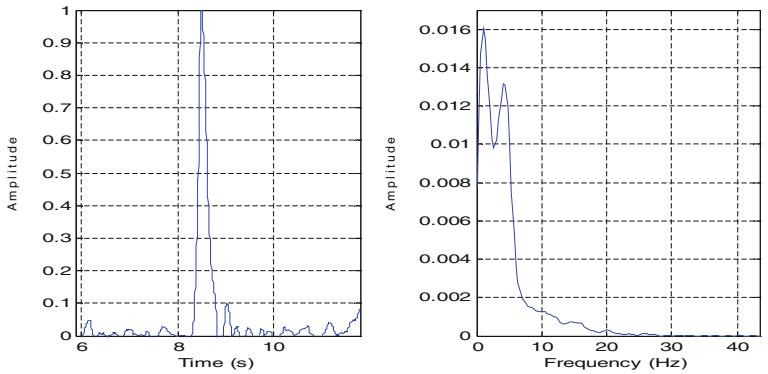

(c)

Fig. 4. Profiles and MF of EEG signal using (a) SP, (b) SPWVD and (c) CWD.

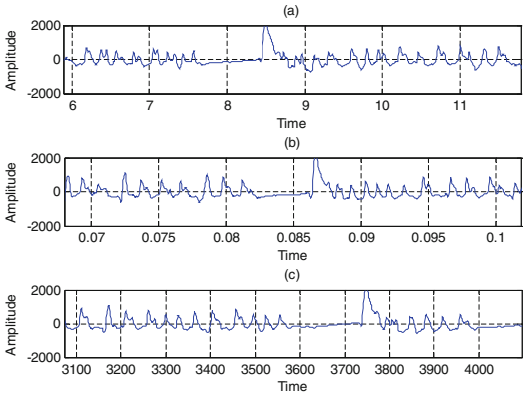

Fig. 5. Different frames of signal; (a) frame 1, (b) frame 2 and (c) frame 3.

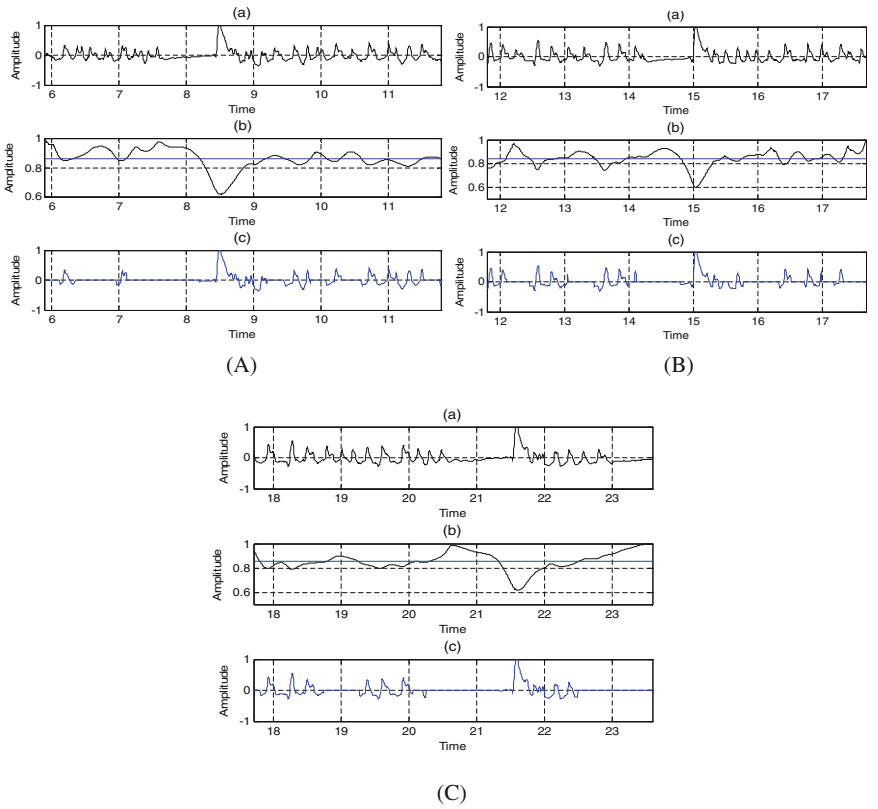

Fig. 6. RME results using SPWVD on (A) frame 1, (B) frame 2 and (C) frame 3: (a) EEG signal frame, (b) RME values and (c) peaks seizure identification.

Table 2. Minimal value of RE.

	Frame 1	Frame 2	Frame 3
SP	2.8568	3.3299	2.8870
CWD	2.8499	3.2090	2.9421
SPWV	2.7296	3.1534	2.8303

Table 3. Frequency bands.

	Frame 1	Frame 2	Frame 3
SP	0–2	0–3	0–2
CWD	0–4	0–4	0–4
SPWV	0–4	0–4	0–4

representing its mean value and in part (c) the peak seizure identification. The observation of all these figures allows identifying an important event located at 8.51 s in frame 1, at 15.04 s in frame 2 and at 21.61 s in frame 3.

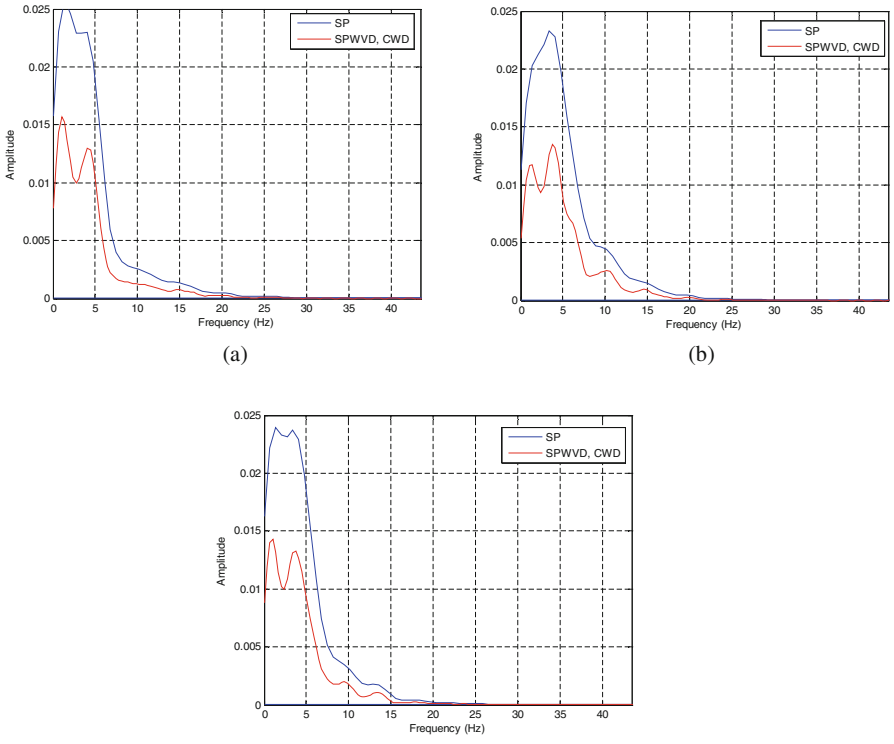

(a) (b)

(c)

Fig. 7. MF of EEG signal (a) frame 1, (b) frame 2 and (c) frame 3 using SP, CWD and SPWVD.

Frequency Band of the Peak Seizure. The time-frequency results obtained by all the used methods to characterize the epileptic seizure are given in Tables 2 and 3. For each method, we have used the optimal parameters obtained by the RE considered as a measure for best time-frequency resolution. The results summarized in Table 2 show the minimal values of the RE. After this step, we continue the evaluation with different MF to obtain the frequency bands for all studied frames shown in Table 3. The MF of the three frames of EEG signal using SP, CWD and SPWVD are represented in Fig. 7 (a, b and c).

5 Conclusion

The contribution deals with the characterization in time-frequency domain of some pathological Electroencephalogram (EEG) signals. The paper presents a comparative study methodology to characterize some real life EEG signals using spectrogram (SP), smoothed pseudo Wigner Ville distribution (SPWVD) and Choi-Williams distribution (CWD) such as time-frequency tools. The best energy concentration of these distributions is obtained using the Rényi entropy (RE) as criterion in order to find the best parameters analysis. Also, the comparative study shows that the SPWVD is very useful for studying in time-frequency plane some pathological EEG signals. Indeed, the Rényi marginal entropy (RME) has permit to identify successfully the localization of the peak of seizure in time. The frequency bands as features characterizing the EEG for epileptic patients have also been found. Work is underway to identify and classify several pathological signals as diagnosis tool.

References

1. Kumari, R., Jose, J.: Seizure detection in EEG using biorthogonal wavelet and fuzzy KNN classifier. Elixir Hum. Physiol. **41**, 5766–5770 (2011)
2. Berger, H.: On the EEG in humans. Arch. Psychiatr. Nervenkr. **87**, 527–570 (1929)
3. Mihandoust, S., Amirani, M.: Epileptic seizure detection using GARCH model on EEG signals. In: 1st International Conference on Computer and Knowledge Engineering, Mashhad, pp. 100–104. IEEE Press (2011)
4. Jasper, H.: The ten-twenty electrode system of the international federation. Electroenceph. Clin. Neuroph. **10**, 371–375 (1958)
5. Shin, Y., Lee, S., Ahn, M., Choa, H., Juna, S., Lee, H.: Simple adaptive sparse representation based classification schemes for eeg based brain-computer interface applications. Comput. Biol. Med. **66**, 29–38 (2015)
6. Sugimoto, H., Ishi, N., Iwata, A., Suzumura, N.: Stationarity and normality test for biomedical data. Comput. Prog. Biomed. **7**, 293–304 (1977)
7. Sugimoto, H., Ishii, N., Iwata, A., Suzumura, N., Tomita, T.: On the stationarity and normality of the electroencephalographic data during sleep stages. Comput. Prog. Biomed. **8**, 224–234 (1978)
8. Alonso, L., Corralejo, R., Pilar, J., Alvarez, D., Hornero, R.: Adaptive semi-supervised classification to reduce intersession non-stationarity in multiclass motor imagery-based brain-computer interfaces. Neurocomputing **159**, 186–196 (2015)

9. Ubeyli, E.: Statistics over features: EEG signals analysis. Comput. Biol. Med. **39**, 733–741 (2009)
10. Mihandoost, S., Amirani, M., Mazlaghani, M., Mihandoost, A.: Automatic feature extraction using generalised autoregressive conditional heteroscedasticity model: an application to electroencephalogram classification. IET Sig. Proc. **6**, 829–838 (2012)
11. Islam, M., Ahmed, T., Yusuf, M., Ahmad, M.: Cognitive state estimation by effective feature extraction and proper channel selection of EEG signal. J. Circ. Syst. Comput. **24**, 1540005 (1)–1540005(24) (2015)
12. Zietsch, B., Hansen, J., Hansell, N., Geffend, G., Martin, N., Wright, M.: Common and specific genetic influences on EEG power bands delta, theta, alpha, and beta. Biol. Psyc. **75**, 154–164 (2007)
13. Ahmad, M., Majeed, W., Khan, N.: An alive electroencephalogram analysis system to assist the diagnosis of epilepsy. In: 22nd European Conference Signal Processing (EUSIPCO), Lisbon, pp. 2340–2344. IEEE Press (2014)
14. Wallace, B., Collutura, T.: Imaging ability and visual processing of EEG waveforms. Bull. Psyc. Soc. **31**, 4–6 (1993)
15. Singh, M., Kau, S.: Feature selection for epilepsy detection using EEG. Int. J. Inf. Technol. Knowl. Manage. **6**, 7–9 (2012)
16. Boashash, B., Azemib, G., Khana, N.: Principles of time-frequency feature extraction for change detection in non-stationary signals: applications to newborn EEG abnormality detection. Patt. Recog. **48**, 616–627 (2015)
17. Flandrin, P.: Time-frequency representations of non stationary signals. Sig. Proc. **6**, 89–101 (1989)
18. Hlawatsch, F., Boudreaux-Bartels, F.: Linear and quadratic time-frequency signal representations. IEEE Sig. Proc. Mag. **9**, 21–67 (1992)
19. Tzallas, A., Tsipouras, M., Fotiadis, D.: Automatic seizure detection based on time-frequency analysis and artificial neural networks. Comput. Intell. Neuros. **2007**, 1–13 (2007)
20. Ansari, K., Bellanger, J., Bartolomei, F., Wendling, F., Senhadji, L.: Time-frequency characterization of interdependencies in nonstationary signals: application to epileptic EEG. IEEE Trans. Biomed. Eng. **52**, 1218–1226 (2005)
21. Tzallas, A., Tsipouras, M., Fotiadis, D.: Epileptic seizure detection in EEGs using time-frequency analysis. IEEE Trans. Inf. Tech. Biomed. **13**, 703–710 (2009)
22. Boubal, O., Oksman, J.: Application of the reallocated smoothed pseudo Wigner-Ville distribution to knock detection. Sig. Proc. **15**, 337–347 (1998)
23. Renyi, A.: On measures of entropy and information. In: 4th Berkeley Symposium on Mathematical Statistics and Probability. Contributions to the Theory of Statistics, California, vol. 1, pp. 547–561 (1961)
24. Sucica, V., Sauliga, N., Boashash, B.: Analysis of local time-frequency entropy features for nonstationary signal components time supports detection. Dig. Sig. Proc. **34**, 56–66 (2014)
25. Williams, W., Hsie, T.: Adaptive RID kernels which minimize time frequency uncertainty. In: IEEE-SP International Symposium on Time-Frequency and Time-Scale Analysis, Philadelphia, pp. 96–99. IEEE Press (1994)
26. Hsie, T., Williams, W.: Rényi information and signal dependent optimal kernel design. In: International Conference on Acoustics, Speech, and Signal Processing (ICASSP), Detroit, pp. 997–1000. IEEE Press (1995)
27. Aviyente, S., Williams, W.: Minimum entropy time-frequency distributions. IEEE Sig. proc. Lett. **12**, 37–40 (2005)
28. Boutana, D., Benidir, M., Barkat, B.: Segmentation and identification of some pathological phonocardiogram signals using time-frequency analysis. IET Sig. Proc. **5**, 527–537 (2011)

29. Drzejak, R., Lehnertz, K., Mormann, F., Rieke, C., David, P., Christian, E.: Indications of nonlinear deterministic and finite dimensional structures in time series of brain electrical activity: dependence on recording region and brain state. Phys. Rev. **64**, 061907(1)–061907 (8) (2001)
30. Gautama, T., Mandic, D., Hulle, M.: Indications of nonlinear structures in brain electrical activity. Phys. Rev. **67**, 046204(1)–046204(5) (2003)
31. Harikrishnan, K., Misra, R., Ambika, G., Kembhavi, A.: A non-subjective approach to the GP algorithm for analysing noisy time series. Phys. D Nonl. Phen. **215**, 137–145 (2006)
32. Bonn Epileptology database online. http://epileptologie-bonn.de/cms/front_content.php?idcat=193&lang=3
33. Boutana, D., Benidir, M.: Benefits of prior speech segmentation for best time-frequency visualisation using Renyi's entropy. In: 13th IEEE International Conference on Electronics, Circuits and Systems, Nice, pp. 688–691. IEEE Press (2006)

Performance Evaluation of Segmentation Algorithms Based on Level Set Method: Application to Medical Images

Messaouda Larbi[1(✉)] and Zoubeida Messali[2,3]

[1] Science and Technology Department, University of Batna, Batna, Algeria
larbi_messaouda@yahoo.fr
[2] Science and Technology Department, University of Bordj Bou Arreridj, El Anasser, Bordj Bou Arreridj, Algeria
zoubeidamessali@yahoo.fr
[3] Laboratoire de Génie Electrique LGE, M'sila, Algeria

Abstract. Currently, the phase of segmentation is an important step in the treatment and the interpretation of the medical images; it represents one of the most difficult step for the extraction of the relevant parameters of the image and fact part of a very active field and rich of research. In this paper, we present an overview about segmentation methods based on level set technique, namely *Caselle method, Chan Vese method*, *Chumming Li method*, *Lankton method*, *Bernard method and Shi method*. The performance of each method can be evaluated either visually, or from similarity measurements between a reference and the results of the segmentation. We have applied each method for different medical images. We present a comparative evaluation of the considered segmentation methods, with respect to four criteria, given specific medical datasets. Through simulated results, we have demonstrated that the best results are achieved by Shi method and Chan & Vese method.

Keywords: Image segmentation · Level set · Active contours · Medical images

1 Introduction

Image segmentation is a technique of partitioning a digital image into multiple segments. It has been used in the fields including computer vision, medical images, image analyze and so on. The main aim of segmentation is to simplify and/or change the representation of an image into something that is more meaningful and easier to analyze [1, 2]. Image segmentation is typically used to locate objects and boundaries (lines, curves, etc.) in images. Numerous segmentation methods have been developed in the past two decades for extraction of organ contours on medical images.

In recent years, level set model has also become an important method for medical image segmentation task. The level set method is a robust method for image segmentation, was initially proposed to track moving interfaces by Osher and Sethian in 1987 and has spread across various imaging domains in the late nineties. It can be used to efficiently address the problem of curve/surface etc. In this paper, we present an

M. Chadli et al. (eds.), *Recent Advances in Electrical Engineering and Control Applications*, Lecture Notes in Electrical Engineering 411, DOI 10.1007/978-3-319-48929-2_29

overview of various segmentation methods based on level set technique with respect to four performance metrics.

2 Level Set Method in Image Segmentation

The level set method is a numerical technique for capturing moving fronts, and was introduced by Osher and Sethian [3] in 1987. The formulation of moving fronts (contours C) in level set method, the fronts are represented by the zero level set:

$$C = \{(x, y) : \phi(x, y) = 0\}, \forall (x, y) \in \Omega \tag{1}$$

Where:

$\phi(x, y) : \Omega \rightarrow IR$ level set function **LSF**.

Ω: plan of the image.

The level set evolution equation can be written in the following general form (partial differential equation PDE):

$$\frac{\partial \phi}{dt} = F|\nabla \phi| \tag{2}$$

F: Speed function (depend on the LSF and image data).

∇: is the gradient operator.

The advantage of the level set method is that numerical computations involving curves and surfaces on a fixed Cartesian grid without having to parameterize the points on a contour as in parametric active contour models. Another advantage of level set methods is that they can represent contours of complex topology and are able to handle topological changes, such as splitting and merging, in a natural and efficient way, which is not allowed in parametric active contour models [4–6] unless extra indirect procedures are introduced in the implementations [7].

2.1 Level Sets

Caselles Method. This geodesic approach for object segmentation allows to connect classical "snakes" based on energy minimization and geometric active contours based on the theory of curve evolution [8] so it is a contour-based method. The gradient of the image is used to compute the force function. The curve will thus be driven to regions with high gradient. This method does not require any regularization term, as it is intrinsic to the method. The Caselles evolution equation is given by:

$$\frac{\partial \phi}{dt}(x) = g(I(x))\|\nabla \phi(x)\|(c + k) + \nabla g(I(x))\nabla \phi(x) \tag{3}$$

where:

$k = div\left(\frac{\nabla\phi(x)}{\|\nabla\phi(x)\|}\right)$: curvature of the evolving contour.

c: constant that acts as a balloon force.

Energy criterion of this method is:

$$E(\Gamma) = \int_0^1 g(I(\Gamma(q)))\left\|\Gamma'(q)\right\|dq \tag{4}$$

where:

$$g(I) = \frac{1}{1 + \|\nabla(G * I)\|^2} \tag{5}$$

$I(.)$: corresponds to the image intensity.
Γ: corresponds to the parametric curve.
G: corresponds to Gaussian filter variance which is equal to 1.

Chan and Vese Method. It is a new model for image segmentation based on Mumford-Shah functional and level sets, and is widely used in medical imaging field [9]. This model does not depend on the gradient of the image as stopping term. Therefore, it can be used in images with ambiguous boundaries. It should be noted that this algorithm is a region-based method. It tends to separate the image into two homogeneous region. The LSF $\phi(x, y)$ is implemented as a signed distance function and is reinitialized at each iteration.

The evolution equation is as follows:

$$\frac{\partial\phi}{dt}(x) = \delta(\phi(x))((I(x) - v)^2 - (I(x) - u)^2) + \lambda\delta(\phi(x))k \tag{6}$$

The Energy criterion:

$$E(\phi) = \int_\Omega F(I(x), \phi(x))dx + \lambda \int_\Omega \delta(\phi(x))\|\nabla\phi(x)\|dx \tag{7}$$

$$F(I(x), \phi(x)) = H(\phi(x))(I(x) - v)^2 + (1 - H(\phi(x)))(I(x) - u)^2 \tag{8}$$

where:

δ: the dirac function.
H: the Heaviside function.

$$u = \frac{\int_{\Omega} (1 - H(\phi(x))).I(x)dx}{\int_{\Omega} 1 - H(\phi(x))dx} \tag{9}$$

$$v = \frac{\int_{\Omega} H(\phi(x)).I(x)dx}{\int_{\Omega} H(\phi(x))dx} \tag{10}$$

u and v are two parameters updated at each iteration.

Chumming Li Method. In this method, the evolution equation is as follows:

$$\begin{aligned}\frac{\partial \phi}{dt}(x) = \delta(\phi(x))(\lambda_1 \int_{\Omega} K_\sigma(x-y)|I(y) - f_1(x)|^2 dy \\ + \lambda_2 \int_{\Omega} K_\sigma(x-y)|I(y) - f_2(x)|^2 dy) + v\delta(\phi(x))k + \mu(\nabla^2\phi(x) - k)\end{aligned} \tag{11}$$

The Energy criterion is:

$$\begin{aligned}E(\phi) = \lambda_1 \int_{\Omega}\int_{\Omega} K_\sigma(x-y)|I(y) - f_1(x)|^2 H(\phi(x))dxdy \\ + \lambda_2 \int_{\Omega}\int_{\Omega} K_\sigma(x-y)|I(y) - f_2(x)|^2 (1 - H(\phi(x)))dxdy) \\ + v\int_{\Omega} \delta(\phi(x))\|\nabla\phi(x)\|dx + \mu\int_{\Omega} \frac{1}{2}(\|\nabla\phi(x)\| - 1)^2 dx\end{aligned} \tag{12}$$

Where:

$I(x)$: the image intensity at pixel x.
H: the Heaviside function.
$K_{\sigma:}$ is a Gaussian kernel defined as:

$$K_\sigma(u) = \frac{1}{(2\pi)^{n/2}\sigma^n} e^{-\|u\|^2/2\sigma^2} \tag{13}$$

with a scale parameter $\sigma \succ 0.\ 1$, and f_1 ,f_2 are two functions centered at pixel x and computed at each iteration by:

$$f_1(x) = \frac{K_\sigma * (H(\phi(x))I(x)}{K_\sigma * (H(\phi(x))} \tag{14}$$

$$f_2(x) = \frac{K_\sigma * (1 - H(\phi(x))I(x)}{K_\sigma * (1 - H(\phi(x))} \tag{15}$$

The two first integrals of Eq. 12 correspond to data attached term, which are localized around each point x. The third integral corresponds to the usual regularization term that smoothes the curve during its evolution. The last integral is a regularization term that forces the level-set to keep signed distance properties over the evolution process. Note that this method segments the whole image.

Lankton Method. The evolution equation is as follows [11]:

$$\frac{\partial \phi}{dt}(x) = \delta(\phi(x)) \int_\Omega B(x,y) \nabla_\phi F(I(y), \phi(y) dy) + \lambda \delta(\phi(x)) k \tag{16}$$

where:

δ: the dirac function.
B: is a ball of radius r centered at point x and defined as follow:

$$B(x,y) = \begin{cases} 1 & \|x - y\| \leq r \\ 0 & otherwise \end{cases} \tag{17}$$

The Energy criterion is:

$$\begin{aligned} E(\phi) = & \int_\Omega \delta(\phi(x)) \int_\Omega B(x,y) F(I(y), \phi(y)) dy dx) \\ & + \lambda \int_\Omega \delta(\phi(x)) \|\nabla \phi(x)\| dx \end{aligned} \tag{18}$$

$$F(I(y), \phi(y)) = \begin{cases} H(\phi(y))(I(y) - v(x))^2 + (1 - H(\phi(y)))(I(y) - u(x))^2, & Chanvese \\ (v(x) - u(x))^2, & Yezzi \end{cases} \tag{19}$$

$$u = \frac{\int_\Omega B(x,y).(1 - H(\phi(y))).I(y) dy}{\int_\Omega B(x,y).(1 - H(\phi(y))) dy} \tag{20}$$

$$v = \frac{\int_\Omega B(x,y).H(\phi(y)).I(y) dy}{\int_\Omega B(x,y).H(\phi(y)) dy} \tag{21}$$

This algorithm is a region-based method. Its feature term is locally computed. This property allows the algorithm to segment non-homogeneous objects. However, this make the method sensitive to initialization.

Bernard Method. This algorithm computes the level-set evolution overall image. So new contours could emerge far from the initialization. It is a region-based method and tries to separate the image into two homogeneous region [12]. It is formulated as follows:

Let Ω be a bounded open subset of IR^d and let f: $\Omega \rightarrow IR$ be a given d-dimensional image. In the B-spline level-set formalism, the evolving interface $\Gamma \subset\rightarrow IR^d$ is represented as the zero level-set of an implicit function $\phi(.)$ expressed as a linear combination of B-spline basis functions:

$$\phi(x) = \sum_{K \in Z^d} c[K] \beta^n \left(\frac{x}{h} - K\right) \tag{22}$$

β^n: is the uniform symmetric d-dimensional B-spline of degree n. The Energy criterion is defined as:

$$E(\phi) = \int_{\Omega} F(I(x), \phi(x))\, dx \tag{23}$$

$$\begin{aligned} F(I(x), \phi(x)) &= H(\phi(x))(I(x) - v)^2 \\ &\quad + (1 - H(\phi(x)))(I(x) - u)^2 \end{aligned} \tag{24}$$

Shi Method. This method is a fast algorithm based on the approximation of the level-set based curve evolution [13]. The implicit function is approximated by a piece-wise constant function taking only four values (−3, −1, 1, 3) corresponding respectively to the interior points, the interior points adjacent to the evolving curve, the exterior points adjacent to the evolving curve and the exterior points. The two narrow-bands that enclosed the evolving contours are gathered into two lists that are updated at each iteration from simple rules, making the algorithm particularly fast.

The evolution equation used here is given by:

$$\begin{aligned} F(I(x), \phi(x)) &= H(\phi(x))(I(x) - v)^2 \\ &\quad + (1 - H(\phi(x)))(I(x) - u)^2 \end{aligned} \tag{25}$$

H: the Heaviside function.

2.2 Performance Evaluation

To evaluate the performance of the considered segmentation algorithms, we have computed five similarity criteria, in addition to the visual criterion which compares

between the final contours of each selected algorithm and the reference image. The calculated criteria are: Dice criterion, Peak Signal-to-Noise Ratio PSNR, Hausdorff Distance (HD), Mean Sum of Square Distance (MSSD) and the computation running time, the time that each algorithm needed to reach convergence. The considered criteria Dice coefficient, PSNR, HD and MSSD measure the closeness between the reference segmentation and the segmentation provided by each selected algorithm.

Dice Criterion. Dice criterion is defined by:

$$Dice = \frac{2(A \cap B)}{A + B} \tag{26}$$

A and B are the reference mask region and the result mask region of an algorithm.

PSNR.

$$PSNR = 10 \log_{10}\left(\frac{d}{MSE(A,B)}\right) \tag{27}$$

d: the maximum possible value of the image.
$MSE\,(A,B)$: Mean Square Error.

$$MSE(A,B) = \frac{1}{MN}\sum_{m=1}^{M}\sum_{n=1}^{N}\|A(m,n) - B(m,n)\|^2 \tag{28}$$

Hausdorff Distance.

$$Hausdorff = \max(D_1(A,B), D_1(B,A)) \tag{29}$$

where:

- A: the reference contour.
- B: the result contour of an algorithm.
- $D_1(A,B) = \max_{x \in A}(\min_{y \in B}(\|x - y\|))$

Mean Sum of Square Distance (MSSD).

$$MSSD = \frac{1}{N}\sum\nolimits_{n=1}^{N} D_2^2(A, B(x_n)) \tag{30}$$

where:

- A: the reference contour.
- B: the result contour of an algorithm.
- N: is the size of the result contour.
- $D_2(A, B(x_n)) = \min_{y \in A}(\|y - x\|)$.

3 Experimental Results

In this section we discuss the performances of the considered segmentation methods.

Data Sets. We have use three data sets of medical images with different modalities. These images present Brain MRI image obtained from [14], Two Cells Microscopy image obtained from [12], and Vessel CTA image obtained from [10]. Figures 1, 2 and 3 illustrate these test images. The comparison is carried out in term of the running time, Dice coefficient, PSNR, HD and MSSD criteria. We have used, to compute the different criteria, creaseg interface proposed in [15], except the computation of the running time. Note that the discussed algorithms are implemented in Matlab 7.0 on 2.79-GHz Intel Pentium IV PC. For the sake of comparison, we have used the same initialization (a circle) for all algorithms. In Fig. 1, we want to segment the whole Brain image. In Fig. 2, we want to segment the Two Cells Microscopy image. In Fig. 3, we want to segment the whole Vessel_CTA1 image.

Example 1:

Table 1. The coefficients: times, Dice, PSNR, Hausdorff and MSSD of the six methods obtained for the segmentation of Brain MRI image.

Methods	Time (S)	Dice	PSNR	Hausdorff	MSSD
Caselles	3.09	0.71	10.76	20.59	57.58
Chan & Vese	1.42	0.69	8.84	33.11	168.1
Li	11.2	0.49	6.58	14.04	37.77
Lankton	1.99	0.5	9.17	22.47	96.16
Bernard	1.7	0.6	7.17	17.46	61.84
Shi	0.96	0.7	9	20.62	49.83

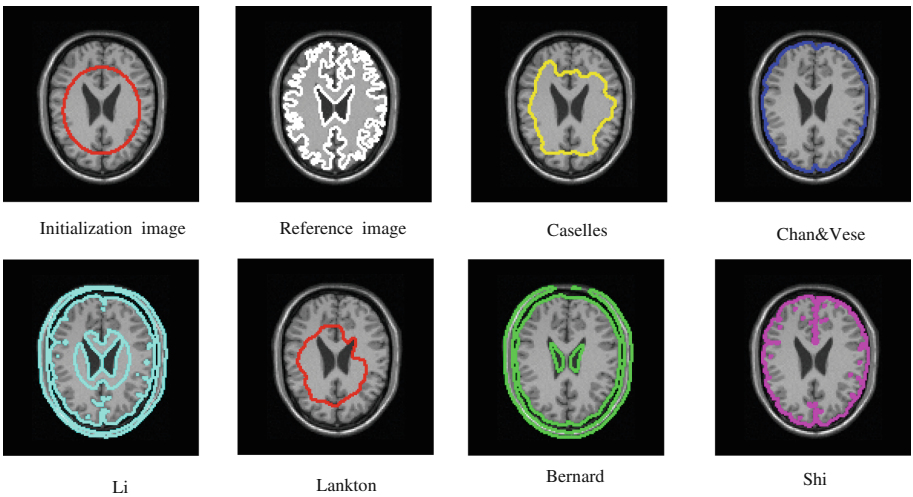

Fig. 1. Segmentation of Brain_MRI image

Example 2:

Table 2. The coefficients: times, Dice, PSNR, Hausdorff and MSSD of the six methods obtained for the segmentation of TwoCells_Microscopy image

Methods	Time (S)	Dice	PSNR	Hausdorff	MSSD
Caselles	2.01	0.31	1.12	40.61	724.39
Chan & Vese	1.31	0.9	14.29	5	4.07
Li	7.1	0.49	9.03	9.9	7.87
Lankton	4.06	0.54	5.24	25.81	135.5
Bernard	1.89	0.7	9.63	19.21	25.05
Shi	1.16	0.85	12.65	12.21	11.15

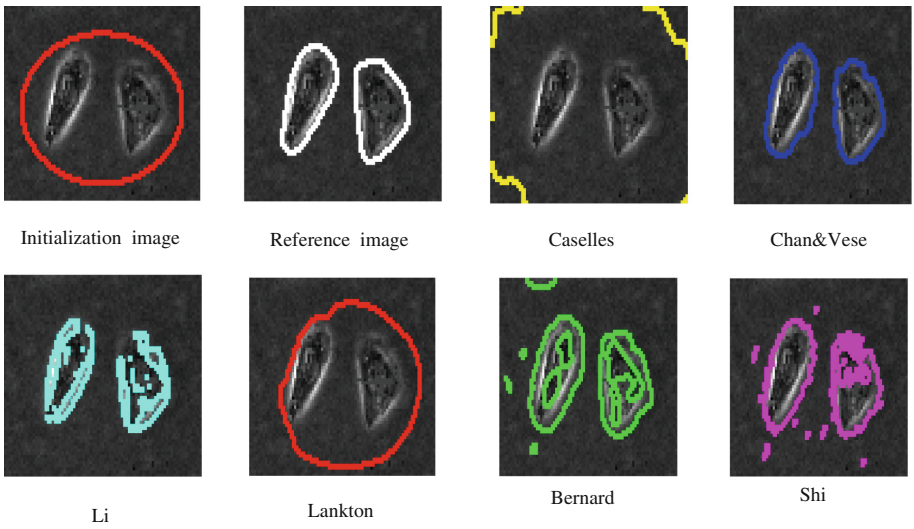

Fig. 2. Segmentation of TwoCells_Microscopy image

Example 3:

Table 3. The coefficients: times, Dice, PSNR, Hausdorff and MSSD of the six methods obtained for the segmentation of Vessel CTA image

Methods	Time (S)	Dice	PSNR	Hausdorff	MSSD
Caselles	2.53	0.22	3.25	41.44	406.17
Chan & Vese	2.16	0.68	9.87	15.62	24.68
Li	10.57	0.32	5.32	27.89	84.19
Lankton	6.34	0.29	5.9	47.43	282.29
Bernard	4.77	0.65	8.66	42.95	187.46
Shi	3.06	0.84	13.68	17.46	18.45

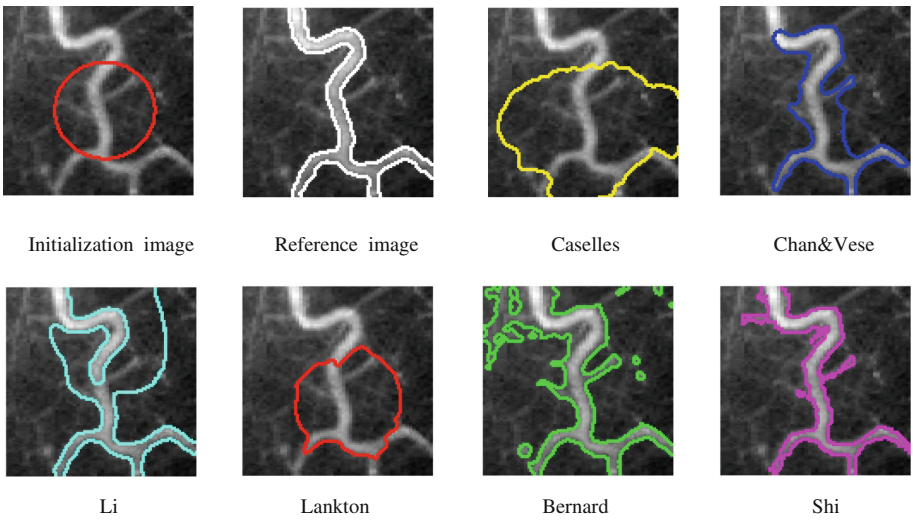

Fig. 3. Segmentation of Vessel_CTA image

There are methods evolve on the whole image (Li and Bernard method: the evolution of these methods is whole band) and others recover only the part of the image (narrow band).

From Tables 1, 2 and 3, it can be see that two methods succeed for segmentation the image Shi and Chan & Vese, in the sense of the computed criteria.

- The Dice coefficient:

  1. For Brain MRI image; this coefficient equal to 0.69 for Chan & Vese and 0.7 for Shi method. The maximum value of this coefficient is obtained for Caselles method and equal to 0.71. However, this approach required the highest computation time to reach convergence (3.09 s).
  2. For Two Cells Microscopy image, the maximum value of this coefficient (0.90) is obtained for Chan & Vese.
  3. For Vessel CTA1 image; Dice coefficient equal to 0.68 for Chan & Vese and 0.84 for Shi method.

- The PSNR coefficient:

  1. For Brain MRI image, the maximum value of PSNR (10.76) is obtained by applying Caselles method. However, this approach required the highest computation time to reach convergence (3.09 s).
  2. For Two Cells Microscopy image, the maximum value of this coefficient (14.29) is obtained from Chan & Vese method.
  3. For Vessel_CTA1 image, the maximum value of PSNR (13.68) is found for Shi method.

- The Hausdorff coefficient (HD):

  1. For Brain MRI image, this coefficient is equal to 33.11 for Chan & Vese, 20.62 for Shi method and 22.47 for Lankton method. But this approach has the Dice coefficient equal to 0.5 (the value minimum).
  2. For Two Cells Microscopy image; this coefficient is equal to 5.00 for Chan & Vese and 12.21 for Shi method.
  3. For Vessel CTA1 image, Hausdorff coefficient is equal to 15.62 for Chan & Vese and 17.46 for Shi method.

- The MSSD coefficient:

  1. For Brain image; this coefficient equal to168.10 for Chan & Vese and 49.83 for Shi method, also we see this coefficient for caselles method equal to 0.71 (the value maximum) but this approach required the highest computation time to reach convergence (3.09 s).
  2. For Two-Cells_Microscopy image; this coefficient equal to 4.07 (the value maximum) for Chan & Vese and 11.15 for Shi method.
  3. For Vessel_CTA1 image; MSSD coefficient equal to 24.68 for Chan & Vese and 18.45 for Shi method.

We easily conclude, from the obtained results that for all coefficients, the best results are achieved by Shi method.

4 Concluding Remarques

In this work, we have established a complete quantitative comparison of segmentation algorithms based on level set method for medical images. We have used three test medical images with three different modalities. The considered level set algorithms are compared in the sense of five metrics. From the experimental results, we easily conclude that Shi method gives the best segmentation results.

References

1. Shapiro, L.G., George, C.S.: Computer Vision. Prentice-Hall, New Jersey (2000). pp. 279–325
2. Barghout, L., Lee, L.W.: Perceptual information processing system. Paravue Inc. U.S. Patent Application 10/618,543. Accessed 11 July 2003
3. Osher, S., Sethian, J.A.: Fronts propagating with curvature-dependant speed: algorithms based on Hamilton-Jacobi formulations. J. Comput. Phys. **79**(1), 12–49 (1988)
4. Kass, M., Witkin, A., Terzopoulos, D.: Snakes: active contour models. Int. J. Comput. Vision **1**(4), 321–331 (1988)

5. Zhu, S.-C., Yuille, A.: Region competition: unifying snakes, region growing, and bayes, MDL for multiband image segmentation. IEEE Trans. Pattern Anal. Mach. Intell. **18**(9), 884–900 (1996)
6. Xu, C., Prince, J.: Snakes, shapes, and gradient vector flow. IEEE Trans. Image Process. **7** (3), 359–369 (1998)
7. Li, C., Chenyang, X., Gui, C., Martin, D.: Distance regularized level set evolution and its application to image segmentation. IEEE Trans. Image Process. **19**(12), 3243–3254 (2010)
8. Caselles, V., Kimmel, R., Sapiro, G.: Geodesic active contours. Int. J. Comput. Vision **22**(1), 61–79 (1997)
9. Chan, T., Vese, L.: Active contours without edges, Technical report 9853, Computational Applied Math Group, UCLA (1998)
10. Li, C., Kao, C.-Y., Gore, J.C., Ding, Z.: Minimization of region-scalable fitting energy for image segmentation. IEEE Trans. Image Process. **17**, 1940–1949 (2008)
11. Lankton, S., Tannenbaum, A.: Localizing region-based active contours. IEEE Trans. Image Process. **17**, 2029–2039 (2008)
12. Bernard, O., Friboulet, D., Thevenaz, P., Unser, M.: Variational B-spline level-set: a linear filtering approach for fast deformable model evolution. IEEE Trans. Image Process. **18**, 1179–1191 (2009)
13. Shi, Y., Karl, W.C.: A real-time algorithm for the approximation of level-set based curve evolution. IEEE Trans. Image Process. **17**, 645–656 (2008)
14. Brain MRI.png: borrowed from http://www.itk.org
15. Dietenbeck, T., Alessandrini, M., Friboulet, D., Bernard, O.: CREASEG: a free software for the evaluation of image segmentation algorithms based on level-set. In: IEEE International Conference on Image Processing, Hong Kong, China (2010)

Design of Antipodal Linearly Tapered Slot Antennas (ALTSA) Arrays in SIW Technology for UWB Imaging

Benzerga Fellah(✉) and Mehadji Abri(✉)

Laboratoire de Télécommunications, Faculté de Technologie,
Université Abou-BekrBelkaïd –Tlemcen,
BP 230 Pôle Chetouane, 13000 Tlemcen, Algeria
fellahttl@yahoo.fr, abrim2002@yahoo.fr

Abstract. The aim of this paper, a new configuration of antipodal linear tapered slot antenna (ALTSA) using micro strip to Substrate Integrated Waveguide (SIW) transition with ultra wideband UWB imaging system performance is proposed and demonstrated. The antenna consists of a SIW and a linear tapered slot structure which is connected to the substrate integrated waveguide. It is designed in the form of a substrate integrated waveguide (SIW) array with respect to side lobe level constraints. The proposed antenna features a small size, low-profile and low cost, and can achieve a 10-dB return loss from frequency range [55–70] GHz, stable radiation patterns and linear phase response, thus capable for applications in UWB radar imaging systems. For side lobe reduction, a simple quasi triangular distribution is proposed and is accomplished uniquely by means of 3 dB power dividers. A 2-way series feed network with T-junction is designed and demonstrate.

1 Introduction

In these days, millimeter wave electronics for commercial applications, such as short range broadband wireless communications, automotive collision avoidance radars and local cellular radio network (LCRN) require low fabrication cost, excellent performance, high level of integration, and small transverse spacing between array elements. Therefore, it has been widely applied in the development of millimeter wave integrated circuits and systems. A novel substrate integrated waveguide (SIW) feeding architecture based on the scheme of antipodal linearly tapered slot antenna (ALTSA) has recently been proposed and experimentally demonstrated with excellent performances [5].

Several low-cost and highly efficient antenna structures based on SIW technology have recently been presented [1–6], which have the advantages of being planar structure, and also they can easily be connected to active components and micro strip line. Nevertheless, most of them exhibit relatively narrow bandwidth, e.g., slot arrays [1, 2] and H plane horn antennas [3, 4]. SIW-fed antipodal linearly tapered slot antenna (ALTSA) [5, 6] and Vivaldi antennas [7] were presented for wideband applications. Using SIW feed can effectively remove the bandwidth limited balun in conventional ALTSA. The antipodal tapered slot antenna (ATSA) has already demonstrated a multi-octave bandwidth, low profile and high gain. This type of antenna is easily fed by

M. Chadli et al. (eds.), *Recent Advances in Electrical Engineering and Control Applications*,
Lecture Notes in Electrical Engineering 411, DOI 10.1007/978-3-319-48929-2_30

SIW lines, which can effectively avoid the use of baluns in the design. The level of cross-polarization is low in this type of antenna, thus making it an excellent candidate to be used in the realization of a dual polarization. In this paper, a compact millimeter wave linearly antenna array with SIW feeding network was presented, which can achieve a UWB performance and offer several advantages over other counterparts such as relatively low insertion loss, good design tolerance and circuit size compactness at the millimeter wave (MMW) range [8]. This antenna configuration can be easily adapted to millimeter wave applications with a conventional low-cost PCB fabrication process [9]. The simulation results indicate that the antenna has good performance in V-band. The work of this article is organized as follows. The Single linearly antenna element in Sect. 2. SIW bends design in Sect. 3. Design of SIW power 2-way divider with ALTSA in Sect. 4. Resultants simulation in Sect. 5. Also in Sect. 6: present electromagnetic fields in SIW bends. Finally a conclusion is drawn.

2 Single Antenna Element

A single-element linearly antenna used in arrays is shown in Fig. 1. The antenna is fed by SIW implemented by via holes of the diameter d and the space between the via holes s. The width of linear antenna W_a is given by spacing of the elements and the width of SIW feed W_{siw} is given by the cutoff frequency f_c of the equivalent waveguide. The optimized variables of the single antenna element were the antenna length L_a and the parameters *dw* of the linear taper profile designed by gradually flaring the metallic covers on opposite sides of the substrate. The output micro-strip has a resistance of 50Ω and a width of W_{50}, w_{taper} and L_{taper} are for the width and length of SIW micro strip taper transition, respectively.

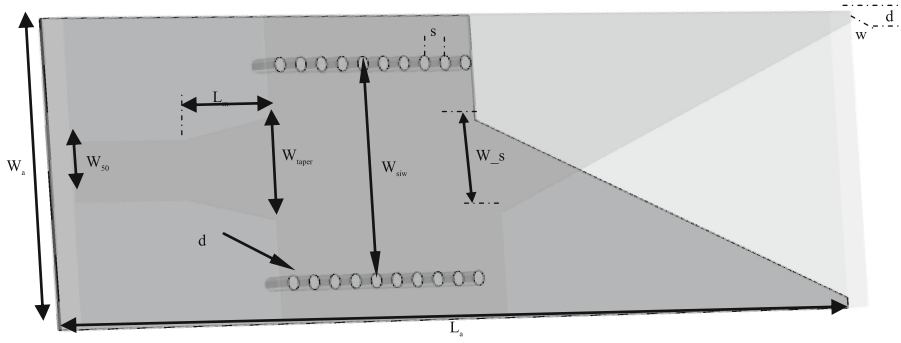

Fig. 1. Millimeter-wave antipodal linearly tapered slot antenna (ALTSA) feed by SIW structure and micro-strip to SIW transition of width $w_{siw} = 5.5$, diameter d = 0.37 and space between vias s = 0.7 and micro-strip to SIW transition of the width $w_{50} = 1.25, w_{taper} = 2.57$ and $L_{taper} = 5$ (all parameters in millimeters).

A single linear-TSA has been designed to cover the band of interest [55–70] GHz for imaging array applications. The SIW line is used to feed the linear-TSA. The antenna has been simulated and optimized with CST MWS to achieve a narrower beam with w_a = 5.5 mm, L_a = 21.93 mm, dw = 0.28 mm and w_s = 2.4 mm. Substrate Arlon Cu 217LX (lossy) with thickness of 0.508 mm and dielectric constant of ε_r = 2.2 is used. The optimized values of geometric parameters are presented in Fig. 1. The simulated results for this antenna are provided in Fig. 2.

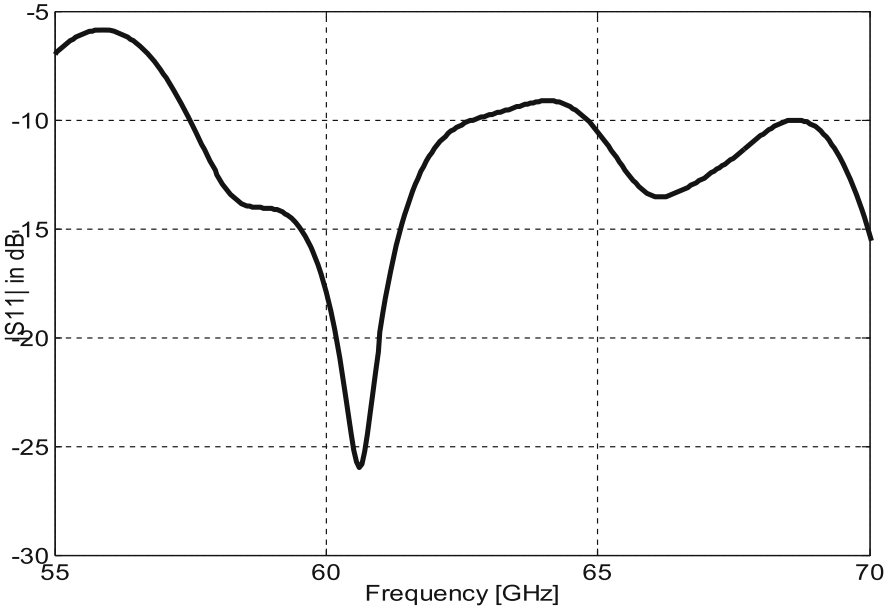

Fig. 2. Return loss of element LTSA millimeter.

The Fig. 2 shows the antenna has a wide operating bandwidth. The lowest operating frequency for this antenna is determined by the cut-off frequency f_c of the SIW which has a high-pass characteristic.

It was stated in Fig. 1, that the designed single-element antenna is aimed to operate at the frequency band of [55–70] GHz. The return loss characteristics previously mentioned proves that the bandwidth aim is met in terms of return loss. Next, the simulation results for the radiation patterns of ALTSA configurations were observed for 55–60–65–70 GHz in order to see the radiation patterns at the frequency band boundaries and the mediums (Fig. 3).

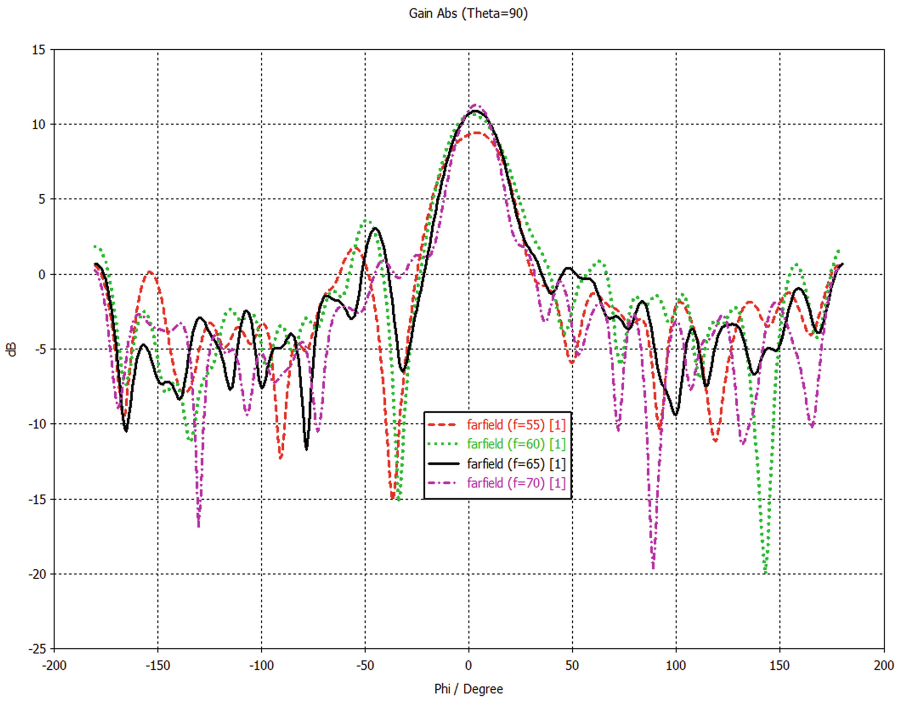

Fig. 3. Simulation patterns radiation in different frequency point of linearly antenna element.

3 SIW Bends Design

The T-junction power divider with its geometric parameters is shown in Fig. 4. The designed T-junction two-way power divider has the same width for both input SIW and output SIWs, which are designed to only support TE_{10} mode in the whole operating frequency range with a width of W_{siw}. The input power is equally divided into the two output SIWs by the metallic-vias in the middle. To reduce its reflection, P_1 and P_2 are placed. By optimizing the positions h, h_p and diameter d_1, of these posts, good performances for the T-junction two-way power divider can be obtained. In Fig. 5 the result of the simulation is plotted, where the simulated S11 is below −10 dB from 57.3 to 65.28 GHz, which corresponds to 53,2%.

4 Design of SIW Power 2-Way Divider with ALTSA

The prototype ALTSA fed by a SIW power 2-way divider is shown in Fig. 4. At the input port, the inductive matching post diameter d_1 and position h and h_p can greatly affect the average and peak frequency of the return loss. The initial goal with this structure was to obtain a lower return loss at f_c = 62 GHz. The optimal post diameter d_1 = 0.2 mm and position h = 1.2 mm, h_p = 2 mm.

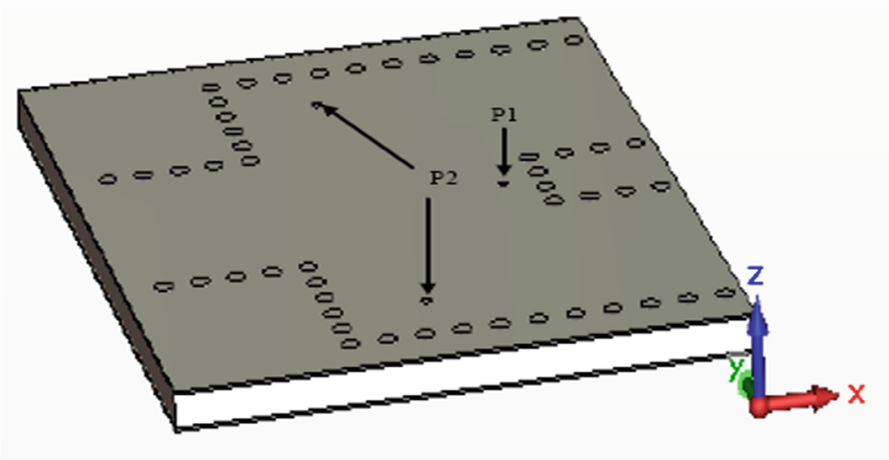

Fig. 4. T-junction SIW power divider.

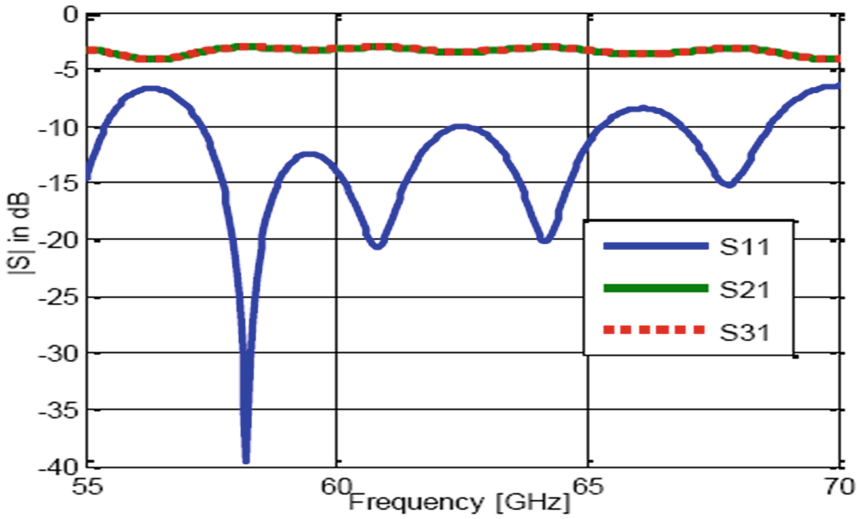

Fig. 5. Insertion loss and return loss of the T-junction SIW power divider.

After simulation and optimization, a linearly antenna was proposed at the frequency V-band constructed by a single ALTSA element, which is fed by a SIW power divider. The whole system was integrated on a Arlon Cu 217LX dielectric substrate having a thickness of 0.508 mm and a relative permittivity of 2.2, respectively. The values of parameters are provided in Fig. 1.

The simulated S-parameter characteristics of the novel three-dimensional structure are shown in Fig. 5. The results return loss is better than 10 dB over 66.67% of the considered bandwidth [55–70 GHz] simulation using CST MicroWave Studio.

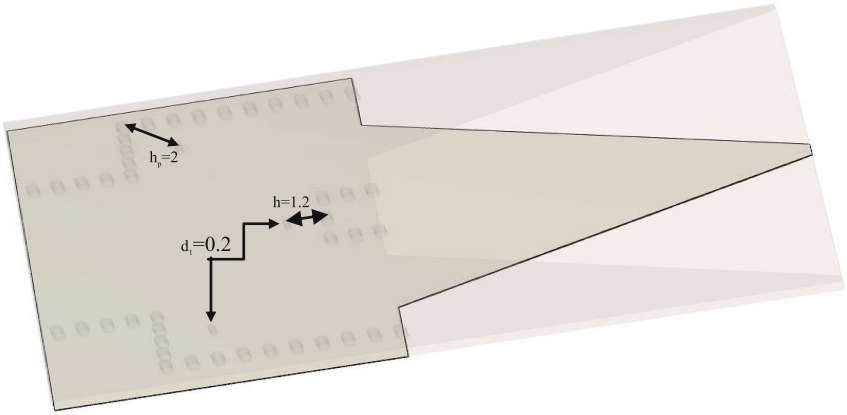

Fig. 6. The LTSA divided into two sub-antennas in consideration Manufactured SIW wide band power divider.

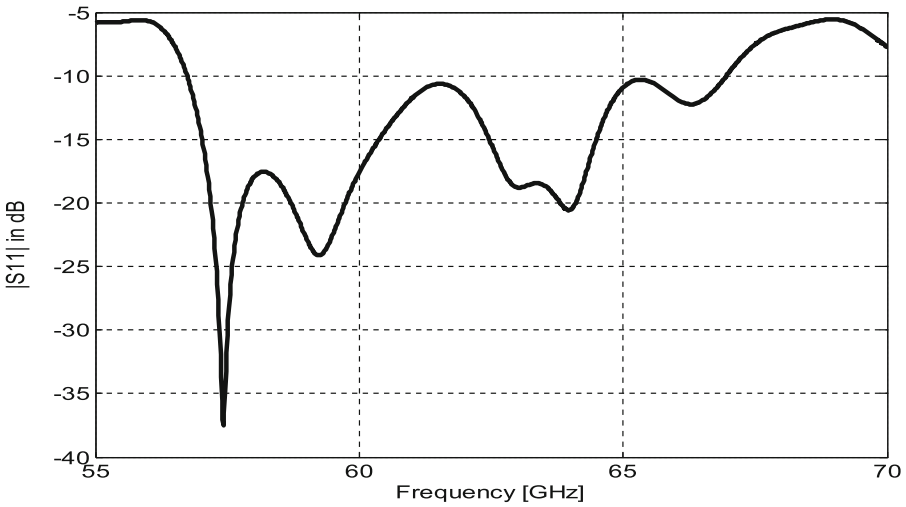

Fig. 7. Return loss of LTSA array.

5 Resultants and Simulation

The simulation input VSWR is shown in Fig. 6. The input VSWR of the array is, for the most part, better than 2 over a 40 GHz bandwidth, which is acceptable. A gain of 10 dB is the lowest over the 40 GHz bandwidth for the two-element array (Figs. 8 and 9).

The array gain radiation patterns simulated at different frequency is given in Fig. 7. It was also tested at 55–60–65–70 GHz, respectively. This type of antipodal antenna has good performances over a broad bandwidth. The whole component was simulated the return loss a shown in Fig. 5.

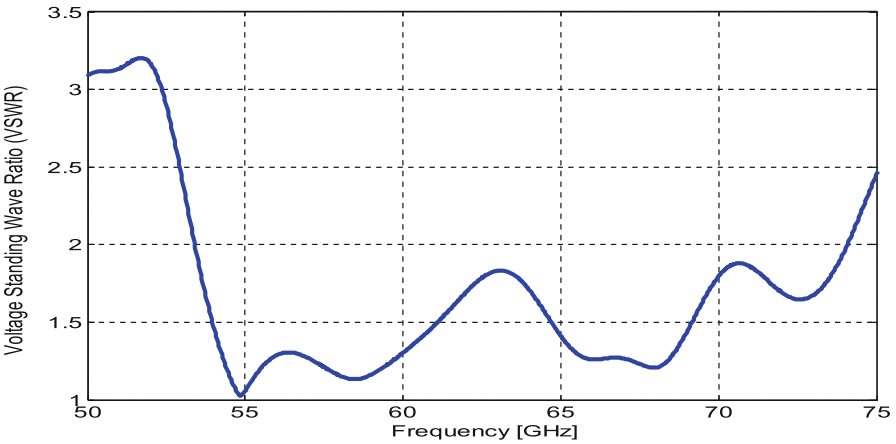

Fig. 8. The corresponding VSWR.

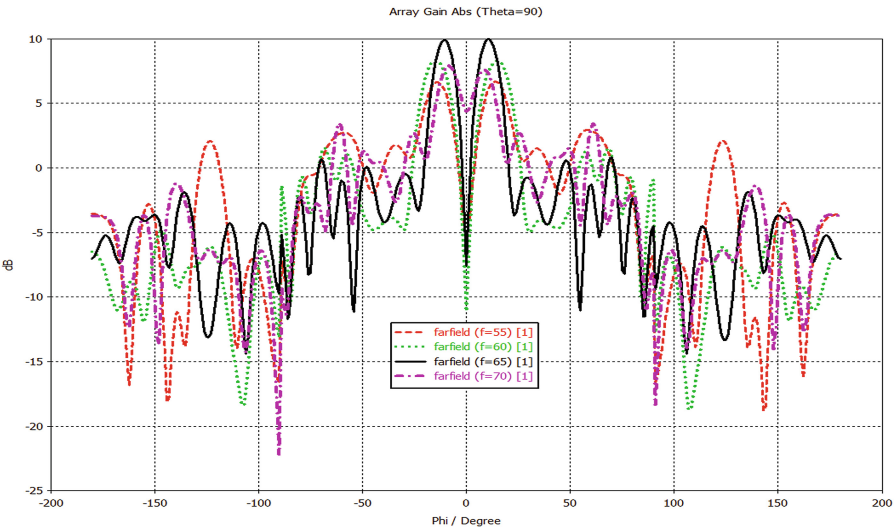

Fig. 9. LTSA Radiation Pattern in the range of 55 to 70 GHz.

6 Present Electromagnetic Fields in SIW Bends

Figure 10 shows the field distribution when power divider working in 65 GHz. From the figure, electromagnetic field enter form SIW port and transmit to SIW feeding port matching part then go to SIW bends.

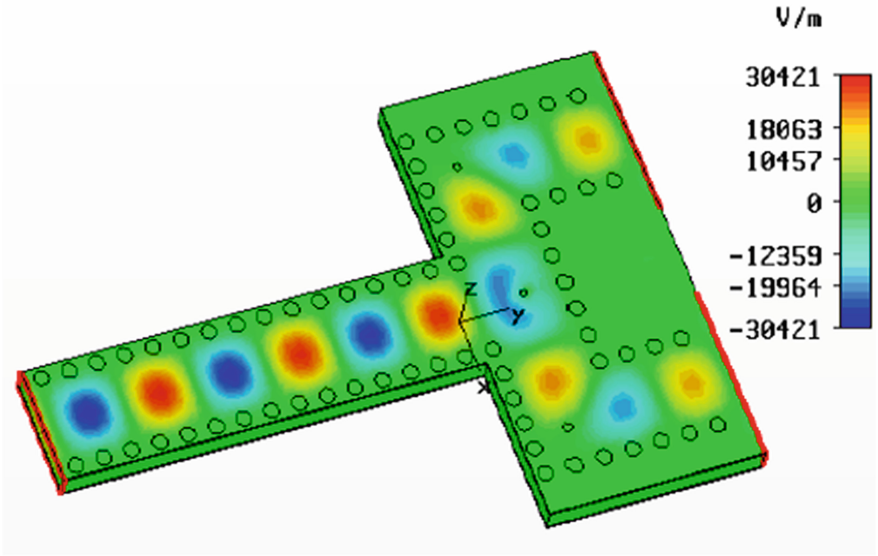

Fig. 10. Electric field distribution in 65 GHz.

7 Conclusion

A novel low-cost, high-gain and highly efficient antenna based on substrate integrated technology (SIW) was presented for UWB imaging. The proposed antenna and the SIW feed are all integrated in a planar single layer substrate, resulting in a low-cost and easy to fabricate using standard PCB process.

The developed linearly antenna array employs compact size two way power divider replacing the conventional binary feeding network and is complemented by a wideband SIW to micro strip transition to minimize the insertion loss.

References

1. Li, Z., Wu, K.: 24-GHz frequency-modulation continuous-wave radar front-end system-on-substrate. IEEE Trans. Microw. Theory Tech. **56**, 278–285 (2008)
2. Kramer, O., Djerafi, T., Wu, K.: Very small footprint 60 GHz stacked Yagi antenna array. IEEE Trans. Antennas Propag. **59**(9), 3204–3210 (2011)
3. Li, Z.L., Wu, K.: A new approach to integrated horn antenna. In: Proceedings International Symposium on Antenna Technology and Applied Electromagnetics, pp. 535–538, July 2004
4. Che, W., Fu, B., Yao, P., Chow, Y.L.: Substrate integrated waveguide horn antenna with dielectric lens. Microw. Optic. Technol. Lett. **49**(1), 168–170 (2007)
5. Hao, Z.C., Hong, W., Chen, J.X., Chen, X.P., Wu, K.: A novel feeding technique for antipodal linearly tapered slot antenna array. In: Proceedings of IEEE IMS, Long Beach, CA, USA, 12–17 June 2005, pp. 1641–1644 (2005)

6. Chen, Y.J., Hong, W., Wu, K.: Design of a monopulse antenna using a dual V-type linearly tapered slot antenna. IEEE Trans. Antennas Propag. **56**(9), 2903–2909 (2008)
7. Kazemi, R., Fathy, E., Sadeghzadeh, R.: Dielectric rod antenna array with substrate integrated waveguide planar feed network for wideband applications. IEEE Trans. Antennas Propag. **60** (3), 1312–1319 (2012)
8. Patrovsky, A., Daigle, M., Wu, K.: Millimeter-wave wideband transition from CPW to substrate integrated waveguide on electrically thick high-permittivity substrates. In: IEEE Microwave Conference, pp. 138–141, October 2007
9. Ghassemi, N., Wu, K.: Planar high-gain dielectric-loaded antipodal linearly tapered slot antenna for E- and H–band gigabyte point-to-point wireless services. IEEE Trans. Antennas Propag. **61**(4), 1748–1755 (2013)

Large Scale Systems (SI03)

Optimized Sliding Mode Control of DC-DC Boost Converter for Photovoltaic System

A. Khoudiri[1,2,3(✉)], K. Guesmi[1,2,3], and D. Mahi[1,2,3]

[1] Djelfa University, Djelfa, Algeria
a.khoudiri@yahoo.fr, kamel.guesmi@univ-reims.fr
[2] CReSTIC, IUT de Troyes, 09 Rue de Quebec, 10026 Troyes, France
[3] LEDMaSD, Laghouat University, Laghouat 03000, Algeria

Abstract. DC–DC converters are an important element in photovoltaic systems to attain desired level of energy and to shape it according to the demand. This paper proposes new optimized sliding mode controller (SMC) with fixed switching frequency for a boost converter to step up a fluctuating solar panel voltage to a higher constant DC voltage. Based on the converter functioning principle, a sliding mode controller (SMC) is proposed. Then, a method for SMC parameters selection using simplex and PSO techniques is given. The simplex method allows obtaining the admissible ranges for SMC parameters while taking into account practical considerations about the converter. Then, theses ranges will be used by the particle swarm optimization technique (PSO) to find optimal values for controller parameters.

Keywords: Photovoltaic · Boost converter · Sliding mode control · Optimization · Simplex · PSO

1 Introduction

Recent environmental issues have increased the demand of PV systems due to the fact that they are pollution free and relatively cheap compared to other renewable energy systems [1, 2]. In many cases high efficiency boost DC-DC converters are required as an interface between low voltage sources (PV panels) and the standalone load or DC-AC inverters in the case of grid-connected applications.

The control of DC-DC converters is a key step to guarantee a fixed output voltage despite of load and input voltage variations. In this context, the SMC presents an adequate choice due to its robustness and efficiency [3]. Indeed, many works focused on obtaining a fixed switching frequency SMC schemes using PWM bloc and considering the SMC equivalent control as a modulated wave in both modes continuous and discontinuous conduction [4–8]. However, the motion toward the sliding surface and remaining on this surface is related to the choice of controller gains. Generally, an admissible range for each gain can be obtained based on the system model linearization around an equilibrium point taking into account some practical limitations to achieve a desired dynamics and local asymptotic stability of the converter [9–11]. Nevertheless, the obtained performances are valid only around the chosen equilibrium point. In addition, the obtained response of the system is depending on the chosen gains values

M. Chadli et al. (eds.), *Recent Advances in Electrical Engineering and Control Applications*, Lecture Notes in Electrical Engineering 411, DOI 10.1007/978-3-319-48929-2_31

in the admissible range. Hence, optimal values of the controller parameters can enhance the system robustness against input voltage variation (PV module voltage fluctuation) or load variation.

In this paper, a sliding mode control for PV system with optimal choice of sliding mode controller gains is proposed. To attain this goal, first, the sliding surface attractiveness is proven taking into account practical considerations. Then, the optimization of the controller is done in two steps. First, the simplex method is used to define the allowable values for SMC gains under some practical constraints. Second, the obtained gains ranges are used as search space by the particle swarm optimization technique (PSO) to select the finest values for controller gains.

2 System Configuration and Sliding Mode Control Strategy

The system configuration is given in Fig. 1. It contains a PV array, DC-DC Boost converter and a sliding mode control mechanism with a resistive load. E and i_L are, respectively, the supply voltage and the inductance current, R and u_0 designate the load and the output voltage respectively. The clock period T is imposed by an external PWM block. According to the control mode, the reference to be attained may be voltage (V_{ref}) or current (i_{ref}).

The circuit objective is to keep the output voltage at a desired value regardless of input voltage and load variations.

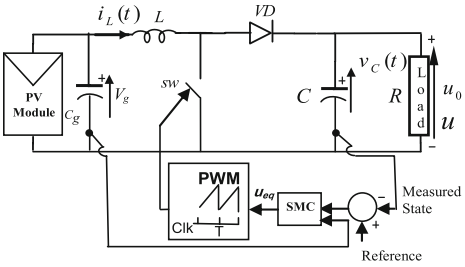

Fig. 1. System configuration.

Considering the ideal case (neglected ESRs), the converter model is given by:

$$\begin{cases} \frac{di_L(t)}{dt} = \frac{V_g}{L} - u\frac{v_C(t)}{L} \\ \frac{dv_C(t)}{dt} = -\frac{v_C(t)}{RC} + u\frac{i_L(t)}{C} \end{cases} \quad (1)$$

If $x(t) = [v_C \;\; i_L]^T$. is the state vector of the system, (1) can be expressed as:

$$\begin{cases} \dot{x}_1(t) = \frac{V_g}{L} - u\frac{x_2(t)}{L} \\ \dot{x}_2(t) = -\frac{x_2(t)}{RC} + u\frac{x_1(t)}{C} \end{cases} \tag{2}$$

with $u \in \{0, \;\; 1\}$ is the position of the switch *sw*.

System (2) has the generalized form:

$$\dot{x}(t) = f(x,t) + g(x,t)\,u \tag{3}$$

and over one clock cycle it becomes:

$$\dot{x}(t) = f(x,t) + g(x,t)u_{eq} \tag{4}$$

where the equivalent control u_{eq} is the average value of u over a cycle.

As a result, u_{eq} can be replaced by the duty cycle d to obtain:

$$\dot{x}(t) = f(x,t) + g(x,t)\,d \tag{5}$$

With

$$d = \frac{Num(x)}{Den(x)} = u_{eq} \tag{6}$$

If $Num(x) = \phi(x)$ and $Den(x) = g_p$ with ϕ a smooth scalar function and $g_p > 0$, then σ can be given as:

$$\sigma = k_a \int_0^t \big(\phi(x(\tau)) - g_p u(\tau)\big)d\tau + k_b \tag{7}$$

k_a and k_b are constants.

This SMC can be easily implemented using a PWM block as described in the following diagram (Fig. 2):

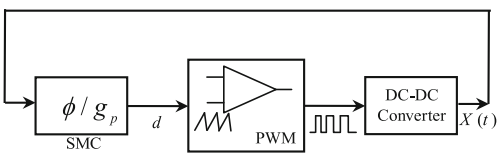

Fig. 2. Fixed switching frequency sliding mode control of DC-DC converter.

If $k_a = 1,\ k_b = 0$, and

$$\phi = G\int_0^{\tau}\left(V_g - u(s)x_2(s)\right)ds + G\,k_p\left(x_2(t) - V_{ref}\right) + G\,k_i\int_0^{\tau}\left(x_2(s) - V_{ref}\right)ds$$

Then, the sliding surface to be optimized is:

$$\sigma = \int_0^{t}\left(G\int_0^{\tau}\left(V_g - u(s)x_2(s)\right)ds + G\,k_p\left(x_2(t) - V_{ref}\right) + G\,k_i\int_0^{\tau}\left(x_2(s) - V_{ref}\right)ds - g_p u(\tau)\right)d\tau \tag{8}$$

With

$$u = \begin{cases} 0 & \text{if } \sigma(x,t) < 0 \\ 1 & \text{if } \sigma(x,t) > 0 \end{cases} \tag{9}$$

The constants $G,\ g_p,\ k_p$ and k_i are the design parameters to be adjusted to ensure the existence of the sliding mode [10].

2.1 Validity of the Control Methodology

Let $V_{ref},\ V_g,\ R,\ C,\ L,\ k_p,\ k_i,\ g_p$ be positive constants and $V_{ref} > V_g$.

Authors in [10] consider the convergence time as:

$$t_{\sigma 1} = \frac{k_p V_{ref}}{V_g - k_i V_{ref}} \tag{10}$$

If $0 < k_i \frac{V_{ref}}{V_g} < 1$, then

$$0 < k_i < 1 - D \tag{11}$$

and any trajectory of the system with control u goes into a sliding motion on the surface $\sigma(x,t) = 0$ with $t > t_{\sigma 1}$.

Proof. The time derivative of σ is:

$$\dot{\sigma}(t) = \phi(x(t),t) - g_p u(t) \tag{12}$$

The surface $\sigma = 0$ is locally attractive, if there is a subset $S_\sigma \subset R^2$ where $\sigma\dot{\sigma} < 0$. In this case, any trajectory will hit the surface $\sigma = 0$ within the set S_σ.

Taking into consideration in [10, 11], two cases can be identified:

1. $\sigma < 0$.

According to the switching policy (9) the switching position $u = 0$, and

$$\begin{aligned}\dot{\sigma}(t) &= \phi(x(t),t)|_{u=0} \\ &= G\int_0^t V_g d\tau + G k_p(x_2(t) - V_{ref}) + G k_i \int_0^t (x_2(\tau) - V_{ref})d\tau\end{aligned}$$

Hence, $\dot{\sigma}|_{u=0} > 0$ in the following set:

$$S_{\sigma 1} = \left\{ x \in R^2, t > 0 \,:\, k_p(x_2(t) - V_{ref}) + k_i \int_0^t (x_2(\tau) - V_{ref})d\tau > -\int_0^t V_g d\tau \right\} \tag{13}$$

2. $\sigma > 0$.

In this case, $u = 1$, and

$$\begin{aligned}\dot{\sigma}(t) &= \phi(x(t),t)|_{u=1} - g_p \\ &= G\int_0^t (V_g - x_2(\tau))d\tau + G k_p(x_2(t) - V_{ref}) + G k_i \int_0^t (x_2(\tau) - V_{ref})d\tau - g_p\end{aligned}$$

Therefore, $\dot{\sigma}|_{u=0} < 0$ in the following set:

$$S_{\sigma 2} = \left\{ x \in R^2, t > 0 \,:\, k_p(x_2(t) - V_{ref}) + k_i \int_0^t (x_2(\tau) - V_{ref})d\tau < (g_p/G) + \int_0^t (x_2(\tau) - V_g)d\tau \right\} \tag{14}$$

Thus, $\sigma\dot{\sigma} < 0$ in the set $S_\sigma = S_{\sigma 1} \cap S_{\sigma 2}$:

$$S_\sigma = \left\{ x \in R^2, t > 0 \,:\, -\int_0^t V_g < k_p(x_2(t) - V_{ref}) + k_i \int_0^t (x_2(\tau) - V_{ref})d\tau < (g_p/G) + \int_0^t (x_2(\tau) - V_g)d\tau \right\} \tag{15}$$

Any trajectory eventually hits the surface $\sigma = 0$ at x within the set S_σ and for $t > t_{\sigma 1}$.

The adequate choice of the two parameters G, g_p and the controller gains k_p end k_i is crucial in the design of the SMC. To simplify the study, authors in [10] take $G = 1$

and the choice of g_p can be made according to the external PWM characteristics. Therefore, the DC-DC boost converter stability can be ensured only by k_p and k_i.

In order to complete the proof, if one considers that the Boost converter elements are well dimensioned, the capacitor voltage mean value $V_{Cmoy(i)}$ at each switching period i is given by:

$$\begin{aligned} V_{Cmoy(i)} = V_{ref} &= \frac{V_{CMax} + V_{C\min}}{2} \\ &= V_{C\min} + \frac{\Delta V_C}{2} = V_{CMax} - \frac{\Delta V_C}{2} \end{aligned} \tag{16}$$

With

$$\begin{cases} V_{CMax(i)} = V_{CMax(i+1)} = V_{CMax} \\ V_{C\min(i)} = V_{C\min(i+1)} = V_{C\min} \\ \Delta V_C = V_{CMax} - V_{C\min} \end{cases} \tag{17}$$

Figure 3 gives the steady state typical response of the system:

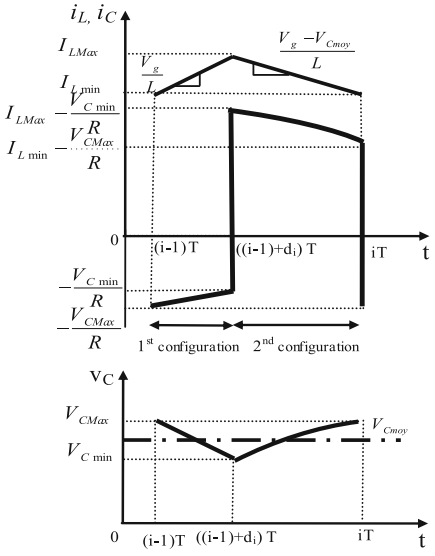

Fig. 3. Typical steady states waveforms.

Based on Fig. 3, the output voltage ripple is:

$$\begin{aligned} \Delta V_C &= -(V_{C\min} - V_{CMax}) \\ &= -\frac{1}{C} \int_{(i-1)T}^{((i-1)+d_i)T} i_C(t)dt \end{aligned} \tag{18}$$

Taking into account that the capacitor current in the 1st configuration is given by: $i_C(t) = -i_R(t)$, So:

$$\begin{aligned}\Delta V_C &= \frac{V_{CMax} + V_{C\min}}{2}\frac{DT}{RC} \\ &= \frac{V_{ref}}{RC}DT\end{aligned} \tag{19}$$

And, the output voltage extremes values will be:

$$\begin{cases} V_{CMax} = V_{ref}\left(1 + \frac{DT}{2RC}\right) \\ V_{C\min} = V_{ref}\left(1 - \frac{DT}{2RC}\right) \end{cases} \tag{20}$$

Using (20) and according to the sign of σ, two cases can be identified:

- 1st case: $\sigma < 0$, $u = 0$

$$\begin{aligned}\dot{\sigma}(t) &= \phi(x(t), t)|_{u=0} \\ &= G\int_0^t V_g d\tau + G\,k_p(x_2(t) - V_{ref}) + G\,k_i\int_0^t (x_2(\tau) - V_{ref})d\tau\end{aligned}$$

According to [9]: $x_2 \rightarrow V_{C\min}$ in this case, and

$$\dot{\sigma} \rightarrow G\left(tV_{in} + (k_p + tk_i)(V_{C\min} - V_{ref})\right)$$

$t \rightarrow DT$ and $V_g = V_{ref}(1 - D)$,
Therefore,

$$\dot{\sigma} \rightarrow GV_{ref}\left(\frac{DT}{2RC}\right)\left(2RC(1 - D) - (k_p + DTk_i)\right) \tag{21}$$

and σ increases until becomes zero, then hitting the surface $\sigma = 0$.
Stability of the system conducts to $\dot{\sigma} > 0$ in the following set:

$$S_{K1} = \left\{\exists(k_p, k_i) \in \mathbb{R}^2 : k_p + DTk_i < 2RC(1 - D)\right\} \tag{22}$$

- 2nd case: $\sigma > 0$, $u = 1$

$$\begin{aligned}\dot{\sigma}(t) &= \phi(x(t), t)|_{u=1} - g_p \\ &= G\int_0^t (V_g - x_2(\tau))d\tau + G\,k_p(x_2(t) - V_{ref}) + G\,k_i\int_0^t (x_2(\tau) - V_{ref})d\tau - g_p\end{aligned}$$

Based on comments in [9]: $x_2 \rightarrow V_{CMax}$.

$$\dot{\sigma} \rightarrow G\big(t(V_g - V_{CMax}) + (k_p + tk_i)(V_{CMax} - V_{ref})\big) - g_p$$

$t \rightarrow (1-D)T$ and $V_g = V_{ref}(1-D)$.
Hence,

$$\dot{\sigma} \rightarrow GV_{ref}\left(\frac{DT}{2RC}\right)\big((k_p + (1-D)Tk_i) - ((1-D)(2RC+T)) + \big) - g_p \qquad (23)$$

σ decreases until attaining zero, and hitting the surface $\sigma = 0$.
And the system stability leads to $\dot{\sigma} < 0$ in the following set:

$$S_{K2} = \left\{\exists(k_p, k_i) \in \mathbb{R}^2 : k_p + (1-D)Tk_i < (1-D)(2RC+T) + \frac{2RC\ g_p}{G\,DT\,V_{ref}}\right\} \qquad (24)$$

Finally, the controller gains k_p end k_i that satisfy $\sigma\dot{\sigma} < 0$ are in the set $S_K = S_{K1} \cap S_{K2}$:

$$S_K = \left\{\begin{array}{c}\exists(k_p, k_i) \in \mathbb{R}^2 : (k_p + (1-D)Tk_i < (1-D)(2RC+T) + \frac{2RC\ g_p}{G\,DT\,V_{ref}}) \\ \& \ (\ k_p + DTk_i < 2RC(1-D))\end{array}\right\} \qquad (25)$$

To obtain optimal values for gains (k_p, k_i), the simplex method is used in what fellow to define allowable intervals for gains and particle swarm optimization technique to obtain optimal values for controller parameters in the obtained allowable intervals.

3 Optimization of the Sliding Mode Control Strategy

3.1 Simplex Method to Delimitate Sliding Mode Controller Gains

Let's consider the vectors $\mathrm{C} = [c_1, \ldots, c_n]^T$, $\mathrm{B} = [b_1, \ldots, b_m]^T$ and

$$A = \begin{bmatrix} a_{11} & a_{12} & \ldots & a_{1n} \\ a_{21} & a_{22} & \ldots & a_{2n} \\ . & . & . & . \\ a_{m1} & a_{m2} & \ldots & a_{mn} \end{bmatrix}$$

In Simplex method, the standard maximum problem is formulated as follows [12, 13]:

- Maximize the objective function: $C^T Y$
- Subject to constraint: $AY < B$, with $Y = [y_1, \ldots, y_n]^T \geq 0$

where m is the number of constraints and n the number of decision variables.

In this case, the set S_K with the condition of the convergence time (10) can be combined and reformulated as follows:

- Objective function to be maximized is:$Z(Y) = y_1$, $k_p = y_1$ and $k_i = y_2$, with $y_{2\,Max} = (1 - D)$ known from (10).
- Constraints: $AY < B$, with:

$$\begin{bmatrix} 1 & DT \\ 1 & (1-D)T \\ 0 & 1 \end{bmatrix}, \quad B = \begin{bmatrix} 2RC(1-D) \\ (2RC+T)(1-D) + \frac{2RC\, g_p}{GDT\, V_{ref}} \\ 1-D \end{bmatrix}, \quad Y = [y_1 \quad y_2]^T \tag{26}$$

One start by adding the so-called s*lack variables (*temporary variables)s_i, the problem becomes: $Z(Y) = y_1 + \sum_{i=1}^{2} s_i$, then,

$$\begin{cases} y_1 + DTy_2 + s_1 = 2RC(1-D) \\ y_1 + (1-D)Ty_2 + s_2 = (1-D)(2RC+T) + \frac{2RC\, g_p}{GDT\, V_{ref}} \\ y_1 > 0 \ , \ y_2 > 0 \end{cases} \tag{27}$$

The initial simplex table is:

C_i		1	0	0	0	b_i
Coeff.	**Variable**	y_1	y_2	S_1	S_2	
0	S_1	1	DT	1	0	$2RC(1-D)$
0	S_2	1	$(1-D)T$	0	1	$(1-D)(2RC+T) + \frac{2RC\, g_p}{GDT\, V_{ref}}$
Z		0	0	0	0	0
Ci-Z		1	0	0	0	

the next step,

C_i		1	0	0	0	b_i
Coeff.	**Variable**	y_1	y_2	S_1	S_2	
1	y_1	1	DT	1	0	$2RC(1-D)$
0	S_2	1	$(1-2D)T$	−1	1	$(1-D)(2RC+T) + \frac{2RC\, g_p}{GDT\, V_{ref}}$
Z		1	DT	1	0	$2RC(1-D)$
Ci-Z		0	$-DT$	−1	0	

Finally:

$$Z_{\max}(y) = 2RC(1-D) \tag{28}$$

and the controller gains can be defined as follows:

$$\begin{cases} 0 < k_p < 2RC(1-D) \\ 0 < k_i < 1-D \end{cases} \tag{29}$$

These inequalities define the possible values for SMC gains and will be used as a search space for the PSO algorithm.

3.2 PSO-Based Optimization of Sliding Mode Controller Gains

The Particle Swarm Optimization (PSO) [14], is a population-based algorithm that mimics swarm behavior in birds flocking. The population is called the swarm and its individuals are called the particles. To give a brief presentation of this technique, let $\Phi \subset R^n$ be the search space and $f: \Phi \rightarrow \Gamma \subseteq R$ be the objective function.

The swarm is defined as a set:

$$S = \{\chi_1, \chi_2, \ldots, \chi_N\} \tag{30}$$

of N particles, defined as:

$$x_i = (\chi_{i1}, \chi_{i2}, \ldots, \chi_{in})^T \in \Phi, \quad i = 1, 2, \ldots, N \tag{31}$$

Each particle has to move within the search space Φ and can reach any region in Φ. This can be done using a proper shifting (*velocity* v_i) of its position:

$$v_i = (v_{i1}, v_{i2}, \ldots, v_{in})^T, \quad i = 1, 2, \ldots, N \tag{32}$$

Hence, at each iteration t_e, each particle (i) is defined by the couple $(\chi_i(t_e),\ v_i(t_e))$; its current position and velocity respectively. It can change its velocity by using the information on the previous positions and it can store the best position p_i it has ever visited during its search. This position is defined as:

$$p_i(t) = \arg\min f_i(t_e) \tag{33}$$

Then, the best positions of swarm are set in memory as:

$$P = \{p_1, p_2, \ldots p_N\} \tag{34}$$

In order to simulate the collective behavior of the particle, PSO estimated the general best position ever visited by all particles.

$$p_\beta(t_e) = \arg\min f_i(p_i(t_e)) \tag{35}$$

with β the index of the best position with the lowest function value in P at a given iteration t_e.

The PSO dynamics is defined by the following Eq. (15):

$$\begin{cases} v_{ij}(t_e+1) = \omega\, v_{ij}(t_e) + R_p\psi_p(p_{ij}(t_e) - \chi_{ij}(t_e)) + R_\beta\psi_\beta(p_{\beta j}(t_e) - \chi_{ij}(t_e)) \\ \chi_{ij}(t_e+1) = \chi_{ij}(t_e) + v_{ij}(t_e+1) \\ i = 1, 2, \ldots, N, \quad j = 1, 2, \ldots, n \end{cases} \tag{36}$$

where R_p and R_β are random variables uniformly distributed within the interval [0, 1]. ω, ψ_p, ψ_β are weighting factors called *inertia*, *cognitive* and *social* respectively. After an iteration (t_e+1), the update and the evaluation of particles, the best positions are also updated and the PSO gives a new index β for the updated best positions. Therefore, the new best position of χ_i at iteration (t_e+1) is defined as follows [12]:

$$p_i(t_e+1) = \begin{cases} \chi_i(t_e+1) & \text{if } f(\chi_i(t_e+1)) \leq p_i(t_e) \\ p_i(t_e) & \text{otherwise} \end{cases} \tag{37}$$

In this case and in order to calculate the optimal values for $k_p$and k_i controller parameters given in (8) and (9), the PSO is used *off-line* to minimize the error between the reference voltage V_{ref} and the output voltage $v_C(t)$. The PSO algorithm compare the chosen reference voltage V_{ref} with the obtained voltage with different values of k_p and k_i, then it chose the values that can give the minimum error.

The *quadratic errors* e_{RQ} are defined as:

$$\begin{cases} e_{RQ}(t_i) = (V_{ref} - v_C(t_i))^2 \\ e_{RQ}(t_{i+1}) = (V_{ref} - v_C(t_{i+1}))^2 = (V_{ref} - v_C(t_i+T))^2 \end{cases} \tag{38}$$

The objective function f to be minimized is chosen as the norm of the quadratic error:

$$f = norm(E_{RQ}) \tag{39}$$

with E_{RQ} the vector that contains all errors $e_{RQ}(t_i)$.

The PSO algorithm test the search space Φ given in (29) using N particles according to (36) and (37). Each particle (i) moves in Φ and stores its best position p_i (k_p and k_i), then, it compares all positions to finally take out the chosen $k_{p-optimum}$ and $k_{i-optimum}$ that give the minimum value of the objective function f.

4 Simulation Results

To validate the proposed optimized controller a voltage controlled Boost converter with the following parameters is considered:

$V_g = 10\ V,\ L = 2\ mH, C = 47\ \mu F,\ R = 25\,\Omega$ with switching period $T = 0.1\ ms$. The chosen reference voltage is $V_{ref} = 20\,V$.

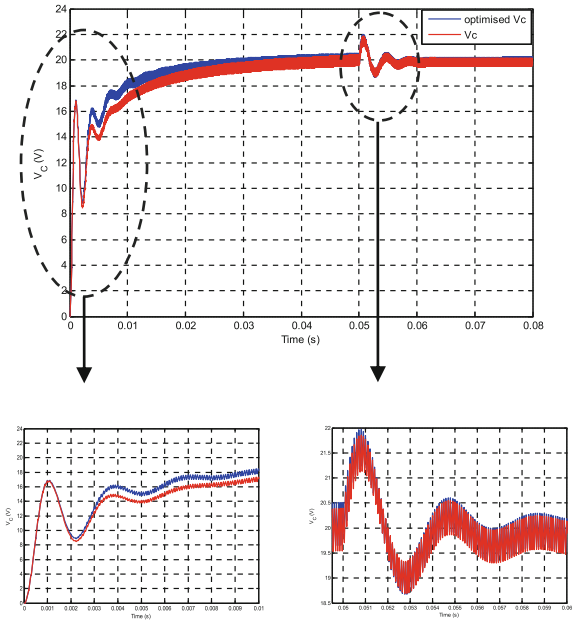

(a)

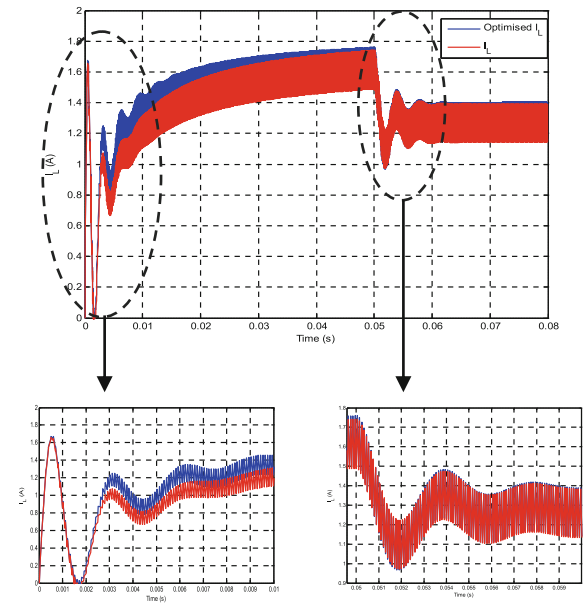

(b)

Fig. 4. Boost converter response (with zoom). (a) Capacitor voltage, (b) inductor current.

In this case, the simplex algorithm gives:

$$\begin{cases} 0 < k_p < 8.25 \cdot 10^{-4} \\ 0 < k_i < 0.5 \end{cases} \tag{40}$$

For PWM gains choice, one take $G = 1$ and $g_p = 0.05$ as given in [10].

for the PSO algorithm, the following standard parameters are considered:$N = 20,\ \omega = 0.5,\ \psi_p = \psi_\beta = 2$, to obtain The following optimized values:

$$\begin{cases} k_{p-optimum} = 7.8385 \cdot 10^{-4} \\ k_{i-optimum} = 0.1156 \end{cases} \tag{41}$$

With these parameters, the system response simulation results are given by Fig. 4. In this last, the system response is obtained using the optimized controller gains and compared to a non-optimized response of the same system when the controller gains are taken arbitrarily in the middle of the ranges obtained by the simplex approach given by (40): $k_p = 4.125 \cdot 10^{-4}$, $k_i = 0.25$.

In addition, In order to validate the system robustness, a load variation from $R = 25\,\Omega$ to $R = 32\,\Omega$ is also considered for $t > 0.05\,s$. Result is given in the same figure.

From the simulation results, it can be seen that the DC-DC power converter present a fast response with practically zero steady state error while keeping the switching frequency fixed. The proposed optimized controller allows the system to move in the sliding surface with faster dynamics and reduced convergence time compared to the non-optimized case. Also, a difference can be noticed between the two responses, and the enhancement introduced by the proposed approach in the transient and steady states. The load variation test confirm that the inductor current $i_L(t)$ changes with load changing which have a small effect on output voltage (less than 10 % variation) with fast establishment time (about *1 ms*) which prove the robustness of the optimized control technique.

5 Conclusion

An optimized PWM-based sliding mode controller of DC-DC converters for photovoltaic systems has been proposed. First, the converter control law is proved taking into account practical limitations, then, an optimization process is proposed. The simplex algorithm is used to obtain the search space for SMC gains and PSO technique is used to select the optimal values for controller gains. The simulation results validated the proposed approach and showed its efficiency and robustness.

References

1. Baggini, A.: Handbook on Power Quality. Wiley, Hoboken (2008)
2. Christoph, K., Thomas, S., Jessica, T., Sebastian, N., Johannes, M.: Levelized Cost of Electricity Renewable Energies, Edition: May 30, Fraunhofer Institute for Solar Energy Systems ISE Germany (2012)
3. Utkin, V., Guldner, J., Shi, J.X.: Sliding Mode Control in Electromechanical Systems. Taylor & Francis, London (1999)
4. Erickson, R.W., Maksi-movic, D.: Fundamentals of Power Electronics. Kluwer Academic Publishers, London (1999)
5. De Battista, H., Mantz, R.J.: Variable structure control of a photovoltaic energy converter. IEE Proce-Control Theory Appl. **149**(4), 303–310 (2002)
6. Adragna, C., Simone, S.D., Gattavari, G.: New Fixed Off-Time PWM Modulator Provides Constant Frequency Operation in Boost PFC Pre-regulators. SPEEDAM (2008)
7. Xiaoru, X., Xiaobo, W., Xiaolang, Y.: A Quasi Fixed Frequency Constant On Time Controlled Boost Converter. IEEE (2008)
8. Tan, S.C., Lai, Y.M., Tse, C.K.: A Fast-Response Sliding-Mode Controller for Boost-Type Converters with a Wide Range of Operating Conditions. IEEE. Trans. End. Elec. (2007)
9. Tan, S.C., Lai, Y.M., Tse, C.K.: Implementation of pulse-width-modulation based sliding mode controller for boost converters. IEEE Power Electr. Lett. **3**(4), 130–135 (2006)
10. Navarro-Lopez, E.M., Cortes, D., Castro, C.: Design of particle sliding-mode controllers with constant switching frequency for power converters. Electr. Power Syst. Res. **79**, 796–802 (2009)
11. Guesmi, K.: Comments on: Design of particle sliding-mode controllers with constant switching frequency for power converters. Electr. Power Syst. Res. **79**, 796–802 (2009)
12. Singiresu, S.R.: Engineering Optimization: Theory and Practice. Wiley, Hoboken (2009)
13. Yang, X.-S.: Engineering Optimization. Wiley, Hoboken (2009)
14. Eberhart, R.C., Shi, Y.: Particle Swarm Optimization and Intelligence: Developments, Applications and Resources. IEEE (2001)

Modeling of MOSFET Transistor by MLP Neural Networks

K. Lamamra[1,3(✉)] and S. Berrah[2,3]

[1] Department of Electrical Engineering, University of Oum El Bouaghi, Oum El Bouaghi, Algeria
l_kheir@yahoo.fr
[2] Department of Electrical Engineering, University of Bejaia, Bejaia, Algeria
sm_berrah@yahoo.fr
[3] Laboratory of Mastering of Renewable Energies, University of Bejaia, Bejaia, Algeria

Abstract. In this paper neural networks are used to model a MOSFET transistor, the structure of the neural model and its training are performed by the genetic algorithm which evolves to minimize the difference between the desired values resulting from practical measurements and the neural model values. The neuronal model consists of three layers, an input layer with two neurons, one for the drain voltage and the other to the error that we want to minimize; an output layer for the drain current of the neural model and a hidden layer with varying number of neurons. After applying this approach, several models are found and that offer a very low modeling error, and the obtained results are very satisfactory.

Keywords: MOSFET · Neural network · Genetics algorithm · Modeling

1 Introduction

The appearance of the transistor has shaken the technological evolution with a big step forward. Current needs of science (technical, computing, medicine and others) fact that the miniaturization of components has become essential for better adaptation [1, 2]. However, at the microscopic level, several phenomena are related to the physical dimensions of the component and their negligible influence on the macroscopic scale participate largely to the formation of microscopic characteristics of the component. This consideration leads us to consider the design or development of new models to describe and predict perfectly the functioning of the microscopic component [3, 4].

In this work we propose the development of a model based on artificial neural networks to predict the static characteristic of the drain-source current of Metal Oxide Semiconductor Field Effect Transistor (MOSFET) based on experimental measurements, and without having a knowledge about the fact of physical phenomena that lead to these results. The neural model of the transistor is based on a neural network type Multi-Layer Perceptron (MLP) in which the structure is optimized by genetic algorithms. Thus, the main role of genetic algorithms is to find the best structure of a neural network which provides the best model of the transistor, for this the fitness function to

M. Chadli et al. (eds.), *Recent Advances in Electrical Engineering and Control Applications*, Lecture Notes in Electrical Engineering 411, DOI 10.1007/978-3-319-48929-2_32

be optimized by genetic algorithms is the error that is the difference between the real drain current (of experimental measurements) and the drain current of the neural model.

This paper is organized as follows: in the Sect. 2 we present briefly the MOS transistor, its structure and types, in the Sect. 3 we present the basic principles of neural networks, in the Sect. 4 we present the genetic algorithms, its operating principle and its application in our method, and in the Sect. 5 the learning of MLP neural networks by genetic algorithms is presented, and finally we present the simulation results of the developed method in the Sect. 6.

2 The Metal Oxide Semiconductor (MOS) Transistor

The MOS transistor comprises a semiconductor substrate on which is deposited a thin layer of insulating oxide (SiO_2) with thickness t_{ox}. A conducting layer (metal or highly doped poly-silicon), called gate electrode that is also deposited on the oxide. Finally, two heavily doped regions of depth X_j, called source and drain, are disposed in the substrate on both sides of the gate.

The region between the junctions of the source and drain is referred to as the channel region and it's defined by a length L and width W. Figure 1, illustrates the basic structure of a MOS transistor [5, 6].

There are two types of MOS transistors, depletion MOSFET (D-MOSFET) and enhancement mode MOSFET (MOSFET-E), in the first type, transistor is conductive even in the absence of polarization (the channel already exists). The drain-source current may be reduced by acting on the gate-substrate voltage (Vgb). In the second type transistor is blocked in the absence of polarization (no channel), so that the drain-source current exists, it is necessary that the gate-substrate voltage is higher than the threshold voltage of the MOS capacitance of the transistor ($Vgs > V_T$). In each of these two basic types there are two other categories, the n-channel MOSFET (nMOS), when the substrate is doped with acceptor atoms type and the minority carriers are electrons. The source region and drain region are heavily doped with donor atoms type. On the p-channel MOSFETs, the transistor has a doped with donor atoms type substrate and the minority carriers are holes. The source regions and drain regions are heavily doped with acceptor atoms category [7–9].

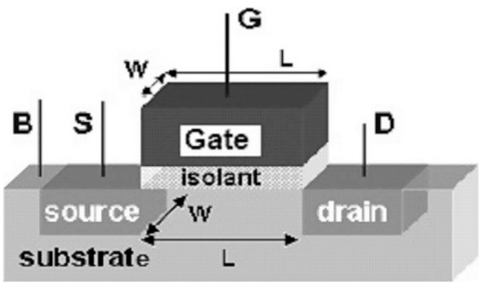

Fig. 1. Basic structure of a MOS transistor

In this work we model the MOSFET transistor with neural networks optimized by genetic algorithms. The model is generally a theoretical representation of reality. Its usefulness to describe, interpret and predict events in the context of this reality. A mathematical model is a translation of reality to be able to apply the tools, techniques and mathematical theories, and generally in the opposite direction, the translation of mathematical results in predictions or transactions in reality. Usually there is no single model since it is always linked to what is intended. As well, a model is never perfect and totally representative of reality, and we orient parameters to study some characteristics and results in particular.

3 Artificial Neuron Networks ANN

Artificial neural networks, is a branch of artificial intelligence research that aims to simulate intelligent behavior by mimicking the way that biological neural networks work. Most of artificial intelligence methods seek to reproduce human intelligence by imitating "what we do", artificial neural networks seek to reproduce it by imitating "the way that we do it".

An artificial neural network is generally composed of a succession of layers, each of which takes its inputs from outputs of the previous one. Each layer is composed of neurons, and the neurons of each layer are connected together by synaptic weights. A neural network has the ability to adapt to the conditions imposed by any environment, and easy change when there are changes of the parameters of this environment, which allows it to solve problems previously qualified as difficult [10–12].

Generally, artificial neural networks are classified into two categories: Multi-Layer Perceptron (MLP) and Radial basis function (RBF), in this work we used the MLP ANN type.

3.1 Structure of ANN

ANN are sets of formal neurons interconnected by very specific connections. Like their biological counterparts, ANN can perform parallel processing of information through the simultaneous operation of neurons and are able to adapt to new data. The links connect neurons together, and they are associated (for a connection between two neurons) to a weight that reflects the influence of one neuron to another.

The neural network have independent neurons layers; each layer has its own organization. There are three kinds of layers: input layer, hidden layers and output layer, each layer is composed of a number of neuron unit. According to the neurons connection there are two types of networks: static networks (or non-recurring) and dynamic networks (or recurrent) [11, 13, 14]. In the static neural network, at each layer, each neuron receives signals from neurons of the previous layer and it sends the result of its treatment to the neurons of the next layer, so there is no communication between neurons of the same layer, the information flows in one direction. In the dynamics neural network each neuron can be connected with himself as it can send its treatment to neurons of layers that precede it and those who follow, the information flows in both directions [11, 13, 14].

In Fig. 2, is shown an example of MLP neural network with two neurons at the input layer (x_1, x_2), four neurons at the hidden layer, and one neuron at the output layer (y). w and z are respectively the weights connecting the input layer to the hidden layer and this last at the output layer.

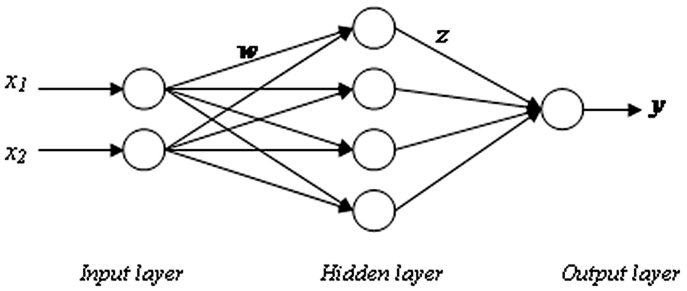

Fig. 2. Example of a MLP neural network structure

3.2 Training of an ANN

Learning consists to determine the weights value in order that the output of the neural network will be as near as possible to the desired target.

The major problem to build a neural network is how to determine the number of units (neurons) in the hidden layer required to achieve a good approximation because a wrong choice can lead to mediocre network performance [15]. The first attempts to resolve the problem of determining the structure have been to test several networks with different architectures until it achieve the desired performance [16].

Many studies have been devoted to developing methods to optimize the architecture of neural network. The main proposed algorithms can be classified into three families: Pruning algorithms: detect and remove the weights or units that contribute little to the network performance [17]. Constructive algorithms or ascending: start from an approximate solution to the problem with a simple network, and then add if necessary units or hidden layers to improve performance of network [18]. Direct algorithms: define a suitable architecture after performing learning, or achieve both operations simultaneously, such as genetic algorithms [12, 19].

In this work, the training of neural networks (neural model of the MOSFET transistor) is made by genetic algorithms.

4 Genetic Algorithms GA

Genetic algorithms are optimization techniques based on the Darwinian principle of natural evolution of species in genetics [20]. They act on a population of individuals that evolve over a series of iterations called generations until a stopping criterion which ensure in advance that the quality of solutions obtained is verified. Only individuals well adapted to their environment can survive and reproduce. The individual is

composed of one or more chromosomes, which are constituted of genes that contain the hereditary characteristics of the individual [21].

The purpose of GA is to determine the extremes of a function f: $E \rightarrow R$, where E is a set called search space and f is called fitness function or evaluation function or adaptation function. For GA the fitness function acts as a black box. Therefore, very complex problems can be approached by genetic programming without special understanding of the problem. For a given optimization problem, an individual represents a point in the state space. The value of the criterion to be optimized is associated with this individual. Then, the algorithm generates iteratively populations of individuals on which is applied some operators [22, 23]. In our work, the GA should minimize the error function, which is the difference between a desired value and the real value of a neural model of the MOSFET transistor.

The genetic operators are applied to an initial population so as to produce, over time, successive populations of high quality. The basic genetic operators are: reproduction, selection, crossover and mutation.

Reproduction is the process by which individuals of population are selected according to the value of their objective function f (function to be optimized). In maximization problem, more the value of the objective function of an individual is the higher this individual is likely to be selected for reproduction. If an individual does not have a high value of objective function, it has little chance of being selected for reproduction. Thus, it will disappear because their genes will not be found in the next generations, and inversely for the minimization problem.

The crossover operator aims to enrich the diversity of the population by handling the components of chromosomes. Typically, crossovers are planned with two parents and generate two children. From two parent individuals, we obtain two new individuals (children) that inherit the characteristics of their parents. The crossover selects genes from both parents and from these genes are generated children. The probability of crossover represents the frequency at which the hybridization is applied [20, 21, 24].

The mutation operator brings to GA the necessary gene value for efficient exploration of space to create a new individual that did not exist before. This operator ensures that the GA will be able to reaching all parts of the state space, without browse through in the resolution process. The purpose is to avoid the GA to converge to local extreme of the function and allow the creation of original elements. If it generates a weaker individual it will be eliminated. The probability of mutation represents the frequency of changing at which a gene on chromosome is mutated. The final selection will identify the best individuals among individuals of the two populations (parents and children) and eliminate the bad individuals [20, 21, 24].

5 Applying of Genetic Algorithms for Neural Network Training

The GA is used herein for optimizing the parameters of the neural model of the MOSFET transistor while ensuring its training [12, 25]. For this, the GA tends to provide the best connection weights of the three layers of the MLP neural network. The input layer is composed of two input neurons, the first is the drain voltage (V_d) of the

transistor, and the second is the instantaneous error (e_i) which is the difference between the desired output I_{dr} (the real drain current of practical measurements) and the output of the neural model of the transistor I_{dm} (Eq. (1)).

The output layer is composed of a single neuron corresponding to the output of the neural model that is the drain current of model (I_{dm}).

$$e_i = I_{dr} - I_{dm} \tag{1}$$

Regarding the hidden layer, it is composed of a variable number of neurons, thus in each test, we chose a model structure (i.e. a number of neuron for each structure with its weights) and after execution, the best obtained individual, who present the minimal error is registered and in the end we take only the model which objective function is minimal for all structures and all generations.

The objective function optimized by GA is the cumulative squared error (e_c) which is the quadratic some of all instantaneous errors during the training phase (Eq. (2)).

$$e_c(w) = \sum_{k=1}^{m} e_i(k)^2 \tag{2}$$

Where:

e_i: is the instantaneous error
w: is the matrix of the weights
m: is the number of training data

The chromosome of an individual is composed of the connection weights of the different layers of the neural model. Because of the number of neurons in the hidden layer is variable, the length of the chromosome is variable according to the network structure. Thus, the chromosome length (L_c) is given by the formula (3):

$$L_c = 3N_n \tag{3}$$

Where: N_n is the number of neurons of the hidden layer.

For example; if the number of neurons of the hidden layer equal to 3, the length of the chromosome is equal to 9, which corresponds to six weights between the input layer and the hidden layer (three weights for the first input (the drain voltage V_d), and three for the second input (the instantaneous error e_i)), and three weights between the hidden layer and the output layer (drain current model).

6 Simulation Results

The physical characteristics of the used MOSFET transistor are:

- Length of channel region L = 0.23 µm
- Width of channel region W = 0.30 µm

– The gate-source voltage V_{gs} is fixed to a given value, the results below correspond to V_{gs} = 12 v.
– The drain voltage (V_d) varying step is equal to 0.01 v

As it is mentioned previously, the number of neurons in the hidden layer is not fixed, it is variable and each time we try a number and at the end we have chosen one where the neural model structure is composed of five neurons in layer hidden because it gave the best result with a cumulative error equal to: $er_{qc} = 8.6031e^{-9}$ for a single feature.

The Fig. 3, shows the drain current of the neural model (I_{dm}) and the real drain current of the practical measurements that is the desired output (I_{dr}).

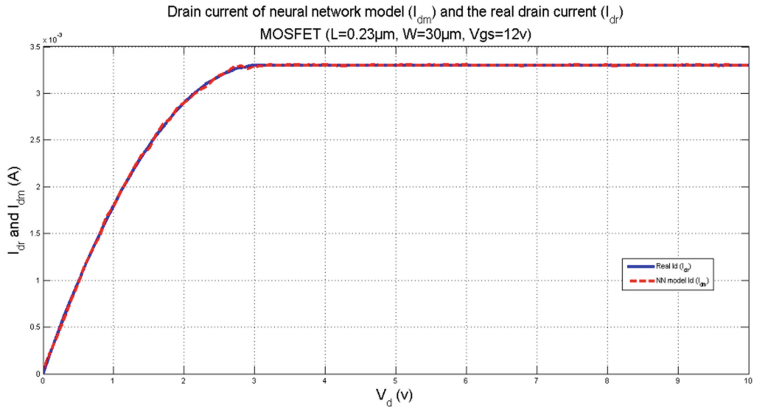

Fig. 3. Drain current of the neural model and the real drain current of practical measurements

Figure 4, represents the instantaneous error, which is the difference between the desired output (I_{dr}) and the output of the neural model of the transistor (I_{dm}).

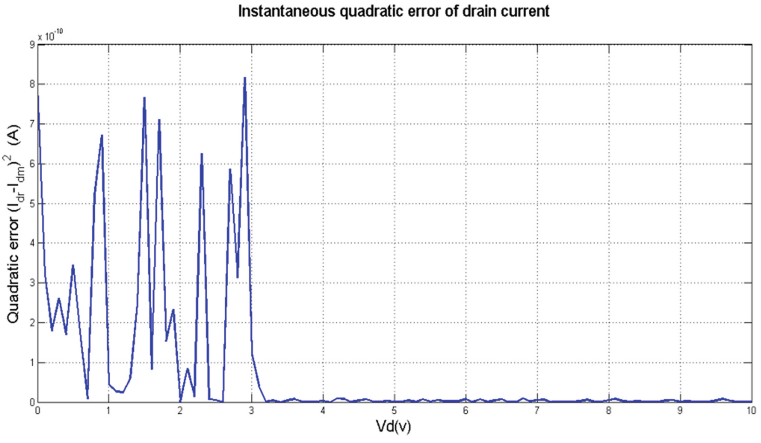

Fig. 4. Instantaneous error

Analyzing these figures, we can observe that the output of MLP neural network model has perfectly followed the desired output, so we can notice that the genetic algorithm has found a good neural network model to the MOSFET chosen for our case, and genetic algorithms provides a good tool for building neural network particularly in the field of modeling.

7 Conclusion

In this work we designed a MOSFET transistor by MLP neural network; which must be well structured and well trained. To ensure this, we have used genetic algorithms that have the task of finding the best structure of the neural model and ensure its training by minimizing the error between the desired values and the output of the neural model of the transistor. The model structure has two neurons in the input layer, one neuron in the output layer, but the hidden layer neurons number is not fixed, each time we change the number and at the end we chose the one which gives good results. After applying this approach, we have found that the results are very satisfactory.

In future work we suggest the use of multi-objective genetic algorithms to make the number of neurons in the hidden layer also a parameter to be optimized, thus and testing several values of neurons number in the hidden layer will not be of temptation.

References

1. Abraham, A., Thakur, P.K., Mahapatra, S.: Bipolar poisson solution for independent double-gate MOSFET. IEEE Trans. Electron Devices **60**, 498–501 (2013)
2. Sun, K., Wu, H., Lu, J., Xing, Y., Huang, L.: Improved modeling of medium voltage SiC MOSFET within wide temperature range. IEEE Trans. Power Electron. **29**, 2229–2237 (2014)
3. Yang, T.P., Ma, Q.S.: MOSFET modeling based on electromagnetic interference (EMI). Appl. Mech. Mater. **268**, 1299–1303 (2013)
4. Aoki, H., Kobayashi, H.: Typical n-MOSFET modeling using a skewing method - an n-MOSFET modeling method for RF analog circuit design centering (2013)
5. Galup-Montoro, C., Schneider, M.C.: MOSFET Modeling for Circuit Analysis and Design. World Scientific, River Edge (2007)
6. Saha, D.: Verilog-a modeling of FD-SOI/SON MOSFET and performance study of high speed ultra low power SRAM (2013)
7. Cheng, Y., Hu, C.: MOSFET Modeling & BSIM3 User's Guide. Springer, New York (1999)
8. Banqueri, J., Carvajal, M.A., Palma, A.J.: Modeling of radiation effects in MOSFETs. In: 2013 Spanish Conference on Electron Devices (CDE), pp. 33–36. IEEE (2013)
9. Yuksel, H., Yang, D., Molnar, A.C.: A circuit-level model for accurately modeling 3rd order nonlinearity in CMOS passive mixers. In: Radio Frequency Integrated Circuits Symposium, 2014 IEEE, pp. 127–130. IEEE (2014)
10. Binder, M.D., Hirokawa, N., Windhorst, U.: Artificial neural networks. In: Encyclopedia of Neuroscience, pp. 185–185. Springer, Heidelberg (2009)
11. Mallot, H.A.: Artificial neural networks. In: Mallot, H.A. (ed.) Computational Neuroscience, pp. 83–112. Springer International Publishing, Cham (2013)

12. Lamamra, K., Belarbi, K., Bosche, J., Hajjaji, A.E.L.: A neural network controller optimized with multi objective genetic algorithms for a laboratory anti-lock braking system. Sci. Technol. J. Constantine 1 Univ. (2012)
13. Levine, D.S., Aparicio IV, M.: Neural Networks for Knowledge Representation and Inference. Psychology Press, Routledge (2013)
14. Villa, A.E.P., Duch, W., Érdi, P., Masulli, F., Palm, G.: Artificial Neural Networks and Machine Learning – ICANN 2012: 22nd International Conference on Artificial Neural Networks, Lausanne, Switzerland, September 11-14, 2012, Proceedings, Part I. Springer, Heidelberg (2012). Springer e-books: Imprint: Springer: Springer e-books, Berlin, Heidelberg, Germany
15. Ripley, B.D.: Statistical ideas for selecting network architectures. In: Kappen, B., Gielen, S. (eds.) Neural Networks: Artificial Intelligence and Industrial Applications, pp. 183–190. Springer, London (1995)
16. Knerr, S., Personnaz, L., Dreyfus, G.: Single-layer learning revisited: a stepwise procedure for building and training a neural network. In: Fogelman Soulié, F., Hérault, J. (eds.) Neurocomputing, pp. 41–50. Springer, Heidelberg (1990)
17. Morse, J.N.: Reducing the size of the non-dominated set: pruning by clustering. Comput. Oper. Res. **7**, 55–66 (1980)
18. Giles, D.C.: Constructive learning of recurrent neural networks: limitations of recurrent cascade correlation and a simple solution. IEEE Trans. Neural Netw. **6**, 829–836 (1995)
19. Angeline, P.J., Saunders, G.M., Pollack, J.B.: An evolutionary algorithm that constructs recurrent neural networks. Trans. Neural Netw. **5**, 54–65 (1994)
20. Goldberg, D.E.: Genetic Algorithms. Pearson Education India, New Delhi (2006)
21. Grefenstette, J.J.: Genetic Algorithms and Their Applications: Proceedings of the Second International Conference on Genetic Algorithms. Psychology Press, Hillsdale (2013)
22. Horn, J., Goldberg, D.E.: Genetic algorithm difficulty and the modality of fitness landscapes. In: Foundations of Genetic Algorithms 3. Citeseer (1994)
23. Goldberg, D.E., Richardson, J.: Genetic algorithms with sharing for multimodal function optimization. In: Genetic Algorithms and Their Applications: Proceedings of the Second International Conference on Genetic Algorithms, pp. 41–49. Lawrence Erlbaum, Hillsdale (1987)
24. Harik, G.R., Lobo, F.G., Goldberg, D.E.: The compact genetic algorithm. IEEE Trans. Evol. Comput. **3**, 287–297 (1999)
25. Lamamra, K., Belarbi, K.: Comparison of neural networks and fuzzy logic control designed by multi-objective genetic algorithm. Int. J. Adv. Comput. Technol. **3**, 137–143 (2011)

Author Index

M. Chadli et al. (eds.), *Recent Advances in Electrical Engineering and Control Applications*, Lecture Notes in Electrical Engineering 411, DOI 10.1007/978-3-319-48929-2